Green Energy and Technology

Dawei Liang · Joana Almeida · Cláudia Vistas · Bruno Tibúrcio · Dário Garcia

Solar-Pumped Lasers

With Examples of Numerical Analysis of Solid-State Lasers

Springer

Green Energy and Technology

Climate change, environmental impact and the limited natural resources urge scientific research and novel technical solutions. The monograph series Green Energy and Technology serves as a publishing platform for scientific and technological approaches to "green"—i.e. environmentally friendly and sustainable—technologies. While a focus lies on energy and power supply, it also covers "green" solutions in industrial engineering and engineering design. Green Energy and Technology addresses researchers, advanced students, technical consultants as well as decision makers in industries and politics. Hence, the level of presentation spans from instructional to highly technical.

Indexed in Scopus.

Indexed in Ei Compendex.

Dawei Liang · Joana Almeida · Cláudia Vistas ·
Bruno Tibúrcio · Dário Garcia

Solar-Pumped Lasers

With Examples of Numerical Analysis of Solid-State Lasers

Springer

Dawei Liang
Physics Department
Universidade Nova de Lisboa
Lisbon, Portugal

Joana Almeida
Physics Department
Universidade Nova de Lisboa
Lisbon, Portugal

Cláudia Vistas
Physics Department
Universidade Nova de Lisboa
Lisbon, Portugal

Bruno Tibúrcio
Physics Department
Universidade Nova de Lisboa
Lisbon, Portugal

Dário Garcia
Physics Department
Universidade Nova de Lisboa
Lisbon, Portugal

ISSN 1865-3529 ISSN 1865-3537 (electronic)
Green Energy and Technology
ISBN 978-3-031-24784-2 ISBN 978-3-031-24785-9 (eBook)
https://doi.org/10.1007/978-3-031-24785-9

© The Editor(s) (if applicable) and The Author(s), under exclusive license to Springer Nature Switzerland AG 2023
This work is subject to copyright. All rights are solely and exclusively licensed by the Publisher, whether the whole or part of the material is concerned, specifically the rights of translation, reprinting, reuse of illustrations, recitation, broadcasting, reproduction on microfilms or in any other physical way, and transmission or information storage and retrieval, electronic adaptation, computer software, or by similar or dissimilar methodology now known or hereafter developed.
The use of general descriptive names, registered names, trademarks, service marks, etc. in this publication does not imply, even in the absence of a specific statement, that such names are exempt from the relevant protective laws and regulations and therefore free for general use.
The publisher, the authors, and the editors are safe to assume that the advice and information in this book are believed to be true and accurate at the date of publication. Neither the publisher nor the authors or the editors give a warranty, expressed or implied, with respect to the material contained herein or for any errors or omissions that may have been made. The publisher remains neutral with regard to jurisdictional claims in published maps and institutional affiliations.

This Springer imprint is published by the registered company Springer Nature Switzerland AG
The registered company address is: Gewerbestrasse 11, 6330 Cham, Switzerland

Contents

1 Brief History of Solar-Pumped Lasers 1
Joana Almeida
1.1 Solar-Pumped Solid-State Lasers 1
1.1.1 Progress in Multimode Solar-Pumped Lasers 2
1.1.2 Progress in TEM_{00}-mode, Doughnut-Shaped Mode, and Low-Order Mode Solar-Pumped Lasers 5
1.1.3 Progress in Solar-Pumped Laser Beam Stability 10
1.2 Solar-Pumped Gas Lasers 13
1.2.1 Blackbody Pumped CO_2 Solar Lasers 14
1.2.2 Iodine Solar-Pumped Lasers 15
1.3 Potential Applications 16
1.3.1 Space-Based Solar-Pumped Laser Applications 16
1.3.2 Earth-Based Solar-Pumped Laser Applications 17
References 18

2 Numerical Tools for Solid-State Laser Design 25
Dário Garcia and Dawei Liang
2.1 Design of Solid-State Lasers by Zemax® Software 25
2.1.1 Main Window 25
2.1.2 Pumping Sources for Solar Pumped Lasers 38
2.1.3 Objects for Solar-Pumped Laser 41
2.1.4 Detectors for Ray-Tracing Analysis 45
2.1.5 Raytracing 46
2.2 Evaluation of Solid-State Laser Output Performance by LASCAD™ Software 49
2.2.1 Starting the Program 50
2.2.2 LASCAD™ Windows 50
2.2.3 Crystal, Pump Beam, and Material Parameter Window 51
2.2.4 Analysis of Thermal Lensing Effects by FEA 52

2.2.5 Laser Beam Analysis by Beam Propagation Method (BPM) 54
2.2.6 Computation of Laser Output Power and Beam Quality 57
2.3 Examples of Numerical Solar Pumped Lasers Design: Side-Pumped Solar Laser 59
2.3.1 Zemax® 60
2.3.2 LASCAD™ 64
References 72

3 Solar-Pumped Solid-State Laser Theory 75
Dawei Liang
3.1 Brief Introduction 75
3.2 Properties of Laser Radiation 76
3.2.1 Directionality 76
3.2.2 Monochromaticity 77
3.2.3 Coherence 77
3.2.4 High Brightness 79
3.3 Photons 80
3.3.1 Concept and Properties of Photon 80
3.3.2 Photon Energy 81
3.3.3 Photon Momentum 81
3.4 Blackbody Radiation—Planck' Law 82
3.5 Solar Spectral Irradiance from Planck's Formula 83
3.6 Stefan-Boltzmann's Law 84
3.7 Wien's Displacement Law 85
3.8 Spontaneous Emission, Stimulated Absorption and Simulated Emission Probabilities 85
3.8.1 Spontaneous Emission Probability 86
3.8.2 Stimulated Absorption Probability 87
3.8.3 Stimulated Emission Probability 88
3.9 Einstein's Relations 89
3.10 Photon Degeneracy in Light from Laser 90
3.11 Laser Gain and Stimulated Emssion Cross Section 91
3.12 Upper Level Laser Rate Equation 94
3.13 Light Intensity Increment Along Active Medium 95
3.14 Laser Oscillation Threshold Condition 98
3.15 Laser Rate Equation Involving Resonant Cavity 100
3.16 Calculation of Photon Density Within a Laser Resonant Cavity 101
3.17 Solar Concentration Ratio 102
3.18 Transfer Efficiency 102
3.19 Absorption Efficiency 103
3.20 Deviation Angle and Effective Absorption Length 104
3.21 Upper State Efficiency 106

3.22 Beam Overlap Efficiency 107
3.23 Atom Number Density and Solar Pump Rate Calculations 109
3.24 Solar Laser Output Power Calculation 110
3.25 Solar Spectral Irradiance and Simplified Model for Nd:YAG Absorption Spectrum 112
3.26 Absorbed Solar Power Density and Absorbed Pump Photon Number Density Calculations 113
3.27 Output Power Analysis of a Side-Pumped Nd:YAG Solar Laser 114
3.27.1 Modified Analytical Method for the Side-Pumped Nd:YAG Solar Laser 114
3.27.2 Classical Analytical Method of Side-Pumped Solar Laser 123
3.27.3 LASCAD™ Analysis of the Side-Pumped Solar Laser 124
3.27.4 Comparison of Different Analysis Methods of the Side-Pumped Solar Laser 126
3.28 Output Power Analysis of an End-Side-Pumped Nd:YAG Solar Laser 127
3.28.1 Modified Analytical Method for the End-Side-Pumped Nd:YAG Solar Laser 127
3.28.2 Classical Analytical Method of the End-Side-Pumped Laser 134
3.28.3 LASCAD™ Numerical Analysis of the End-Side-Pumped Solar Laser 136
3.28.4 Comparison of Different Analyses for the End-Side-Pumped Solar Laser 137
Homework with Solution 1 138
Calculation of Resonant Modes Numbers within a Cavity 138
Homework with Solution 2 140
Deriving Solar Spectral Irradiance from Planck's Law 140
Homework with Solution 3 142
Deriving Stefan-Boltzmann's Law from Planck's Law 142
Homework with Solution 4 143
Deriving Wien's Displacement Law from Planck's Law 143
References 144

4 Laser Materials for Solar-Pumped Lasers 147
Cláudia R. Vistas
4.1 Host Materials 147
4.2 Active Ions 149
4.3 Nd:YAG 151
4.3.1 Physical and Laser Properties of Nd:YAG 151
4.3.2 Spectral Overlap Between Nd:YAG Absorption and Solar Emission Spectra 155

4.4 Cr:Nd:YAG 155
4.4.1 Physical and Laser Properties of Cr:Nd:YAG 155
4.4.2 Spectral Overlap Between Cr:Nd:YAG Absorption and Solar Emission Spectra 159
4.5 Ce:Nd:YAG 159
4.5.1 Physical and Laser Properties of Ce:Nd:YAG 160
4.5.2 Spectral Overlap Between Ce:Nd:YAG Absorption and Solar Emission Spectra 166
4.6 Other Materials 166
References 167

5 Primary Solar Concentrators 173
Dário Garcia
5.1 Parabolic Concentrator 178
5.1.1 Solar Concentration Principles 178
5.1.2 Example of Numerical Analysis with Zemax® 179
5.2 Fresnel Lenses 182
5.2.1 Solar Concentration Principles 182
5.2.2 Example Numerical Analysis with Zemax® 184
5.3 Elliptical-Shaped Fresnel Lens (ESFL) 187
5.3.1 Solar Concentration Principles 187
5.3.2 Example Numerical Analysis with Zemax® 192
5.4 Single-Ring Array Concentrator 193
5.4.1 Solar Concentration Principles 193
5.4.2 Example Numerical Analysis with Zemax® 196
5.5 3D Ring Array Concentrator 198
5.5.1 Solar Concentrator Principle 198
5.5.2 Example Numerical Analysis with Zemax® 199
5.6 Focal Spot Analysis of Primary Solar Concentrators with ANSYS™ Software 202
References 204

6 Multimode Solar-Pumped Lasers 207
Joana Almeida and Dawei Liang
6.1 Solar-Pumped Lasers with Imaging and Nonimaging Primary, Secondary and Tertiary Concentrators 207
6.1.1 Configurations for Solar Energy Collection and Concentration 207
6.1.2 Parabolic Mirrors and Fresnel Lens as Primary Imaging Concentrators 210
6.1.3 Secondary Imaging Concentrators 215
6.1.4 Secondary Nonimaging Concentrators 221
6.1.5 Tertiary Imaging and Nonimaging Concentrators 227
6.2 Examples of Numerical Analysis of Milestone Solar-Pumped Lasers 232

6.2.1 Zemax® and LASCAD™ Numerical Analysis of 12.3 W Solar Laser with DTIRC Secondary and Conical Tertiary Concentrators 232
6.2.2 Zemax® and LASCAD™ Numerical Analysis of 28 W Solar Laser with a Fused Silica Light Guide Homogenizer and a 2D-CPC Pump Cavity 238
6.2.3 Zemax® and LASCAD™ Numerical Analysis of Simultaneous Solar Laser Emissions from Three Ce:Nd:YAG Laser Rods Within a Single Pump Cavity 242
References 247

7 High Brightness Solar-Pumped Lasers 251
Cláudia R. Vistas
7.1 Solar Laser Pumping Configurations for TEM_{00}-mode 251
7.1.1 Side-Pumping Configuration 252
7.1.2 End-Side-Pumping Configuration 260
7.2 Solar Laser Pumping Configurations for Doughnut-Shaped and Low-Order Modes Emissions 262
7.2.1 Side-Pumping Configuration 264
7.2.2 End-Side-Pumping Configuration 265
7.3 Techniques of TEM_{00}-Mode Solar Laser Power Extraction 267
7.3.1 Thermal Lensing Effect and Thermal Focal Length 267
7.3.2 Influence of Laser Resonant Cavity Parameters 269
7.3.3 Influence of Solar Pumping Conditions 271
7.3.4 Influence of Laser Rod Dimensions 275
References 276

8 Solar Tracking Error in Solar-Pumped Lasers 279
Bruno D. Tibúrcio
8.1 Brief Introduction 279
8.2 Sun Trajectory and Error Formation in Solar Energy Collection and Concentration Systems 279
8.2.1 Sun Trajectory in the Sky During the Day 279
8.2.2 Error Formation in Solar Energy Collection and Concentration Systems 280
8.3 Solar Tracking Systems 284
8.3.1 Direct Solar Tracking Mode 284
8.3.2 Indirect Solar Tracking Mode by Heliostats 285
8.4 Tracking Error in Different Primary Solar Concentrators 288
8.4.1 Solar Tracking Error in Parabolic Mirrors 288
8.4.2 Solar Tracking Error in Fresnel Lenses 290
8.4.3 Solar Tracking Error in Ring-Array Concentrators 290
8.5 Tracking Error Compensation Techniques 292
8.5.1 Monolithic Fused Silica Twisted Light Guide 292
8.5.2 Multi-Rod Pumping Approach 294

8.6 Example of Numerical Modeling of Solar-Pumped Lasers with Tracking Error Compensation Capacity 304
8.6.1 Zemax® and LASCAD™ Analysis of the Tracking Error Compensation Capacity Using Multi-Rod Configurations 304
References 308

Chapter 1
Brief History of Solar-Pumped Lasers

Joana Almeida

In this chapter, a short overview of the main achievements of solar-pumped lasers is provided. The main progresses in solar-pumped lasers to date are based on solid-state active medium. Advances in multimode, TEM_{00}-mode, doughnut-shaped mode and low-order mode solar-pumped solid-state lasers, as well as solar laser beam stability, are described. Previous efforts on solar-pumped gas lasers are also mentioned in this chapter. Potential applications of solar-pumped lasers in space and on Earth are finally discussed.

1.1 Solar-Pumped Solid-State Lasers

Solar-pumped laser (or sun-pumped laser) uses solar energy for pumping an active medium, directly converting incoherent solar radiation into coherent laser radiation. This idea is nearly as old as the laser itself [1]. The first solar-pumped laser was reported by Kiss et al. in [2], based on a calcium fluoride crystal doped with divalent dysprosium (Dy^{2+}:CaF_2) system, achieving laser action at 2.36 μm. Between the mid-1960s and 2000s, solid [3–9], liquid [10, 11] and especially gas [12–30] active media have all been evaluated as candidates for solar-pumped lasers. However, this research has converged in systems with bulk solid-state optical gain media, namely the yttrium aluminum garnet ($Y_3Al_5O_{12}$) doped with the rare earth ion neodymium (Nd^{3+}) [31–64], emitting at 1064 nm. The favorable combination of the spectroscopic properties of the Nd^{3+} active ion with the mechanical and optical properties of the YAG host material [65], in conjunction with the advances in the optical pumping designs, have contributed to the progress of solar-pumped lasers performance.

Efficiency is generally regarded of primary importance to evaluate the laser performance. For solar-pumped lasers, the evaluation of their efficiency has been essentially done through three figures of merit:

- **Collection efficiency**, defined as the laser output power per each square meter of solar collector area. Since the early 2000s, achieving high collection efficiency

© The Author(s), under exclusive license to Springer Nature Switzerland AG 2023

D. Liang et al., *Solar-Pumped Lasers*, Green Energy and Technology,
https://doi.org/10.1007/978-3-031-24785-9_1

has become a desirable goal for solar laser researchers to get more laser power as well as to save primary mirror area.

- **Slope efficiency**, defined as the slope of the curve obtained by plotting the laser output power versus the pump power of a laser system. A clear advantage of the slope efficiency, in relation to collection efficiency, lies in its independency on solar irradiance at each location. The evaluation of the slope efficiency at the focus of the primary concentrator has been adopted by several researchers. Nevertheless, it ignores the influence of the solar power losses associated with the primary solar collectors. For a fair evaluation of the entire solar laser system slope efficiency, the incoming solar power must be accounted for.
- **Solar-to-laser conversion efficiency**, defined as the ratio between solar laser output power and the corresponding input solar power. It is a valuable parameter for the assessment of solar laser, being also independent of the solar irradiance. Analogously to the slope efficiency, the solar-to-laser conversion efficiency should account for all losses in the laser system for a fairer assessment of its efficiency.

1.1.1 Progress in Multimode Solar-Pumped Lasers

The first attempt at solar-pumping a Nd:YAG laser medium was reported by Young in 1966 [4], who obtained continuous wave (cw) laser output power of 1 W by using a 61 cm diameter paraboloidal primary concentrator. Between the mid-1980s and mid-1990s, there was a tendency to increase the laser output power in multimode regime [5, 6, 8]. In 1984, Arashi et al. achieved 18 W cw solar laser power by side-pumping a 4 mm diameter, 75 mm length Nd:YAG rod within a water-cooled flow tube at the focus of a large parabolic mirror [5]. The solar laser output power was later improved to more than 60 W cw by Weksler and Schwartz, who, in 1988, side-pumped a Nd:YAG laser rod through a secondary two-dimensional (2D) compound parabolic concentrator (CPC), which was designed to increase the coupling of the solar radiation from the primary mirror into the laser rod [6]. In 1993, Krupkin et al. reported the highest cw solar laser output power of 500 W, obtained from an array of laser rods pumped by a 660 m^2 primary collector [8]. Nevertheless, the solar laser collection efficiency was only 0.76 W/m^2 [9].

It was around the mid-1990s and early 2000s that the maximization of the solar laser efficiency, namely collection efficiency, became one of the main goals in solar laser research [9]. With a 6.75 m^2 astigmatic corrected target-aligned (ACTA) solar collector and CPC secondary and tertiary concentrators, solar laser collection efficiency was boosted to 6.7 W/m^2 in 2003 by Lando et al. [9]. Significant progresses were later achieved with the adoption of Fresnel lens as primary concentrator [31–36]. The interest in enhancing the solar laser performance by co-doping the Nd:YAG with chromium (Cr) ions has also been pointed out since then [31, 33]. 18.7 W/m^2 solar laser collection efficiency was reported in 2007 by Yabe et al. who pumped a 3–9 mm diameter, 100 mm length Cr:Nd:YAG ceramic laser rod with a 1.3 m^2 area Fresnel lens [31]. A total solar-to-laser conversion efficiency of 1.93% was

found in this case. In 2011, Liang et al. achieved a solar laser collection efficiency of 19.3 W/m^2 by exciting a 4 mm diameter, 25 mm length Nd:YAG single-crystal rod through a 0.64 m^2 area Fresnel lens [32], leading to total slope and conversion efficiencies of 2.75% and 2.17%, respectively. These results triggered the discussions about which medium, Cr:Nd:YAG ceramics or Nd:YAG single-crystal, would be more suitable for solar lasers. In 2012, a substantial improvement in solar laser collection efficiency was reported by Dinh et al. [33]. They added a liquid light-guide lens into a conical cavity to increase the intensity of the pump light into a 6 mm diameter, 100 mm length Nd:YAG single-crystal rod. 120 W cw laser output power was attained, leading to high collection efficiency of 30 W/m^2. Total slope and conversion efficiencies of 4.3% and 3.26% were also obtained. The authors also compared the solar laser performance of Nd:YAG single crystal rod with that of Cr:Nd:YAG ceramic rod, where the former was unexpectedly better [33]. Since then, most efforts to improve the solar laser efficiency have been made using Nd:YAG as active medium [34–40]. In 2014, Xu et al. employed a Nd:YAG rod with grooved sidewall in an end-side-pumping solar laser scheme with a 1.03 m^2 Fresnel lens primary concentrator [34]. The grooved surface offers a larger interface with cooling liquid, compare to common rods, and hence better heat dissipation, reducing the thermal lensing effect, which in turn may improve the solar laser efficiency and beam quality. The maximum output power of 27 W from the grooved rod was 1.54 times higher than that from the unpolished rod, leading to total slope and conversion efficiencies of 4.09% and 2.91%, respectively [34]. In 2018, Guan et al. reported a record Nd:YAG solar laser collection efficiency of 32.1 W/m^2, by pumping a 6 mm diameter, 95 mm length diffusion-bonded Nd:YAG/YAG rod through a Fresnel lens with 1.03 m^2 collection area [36]. Total slope efficiency of 5.4% and solar-to-laser conversion efficiency of 3.3% were also reached.

The use of Fresnel lenses in solar-pumped laser systems have become popular because of their low weight and cost, availability in large size and adequacy for mass production. However, they have the disadvantage of spreading the solar radiation spectrum along its focal zone, hindering the coupling of light in the laser medium. For this reason, large laser rods, with diameters ranging from 6 to 9 mm, were generally utilized in the abovementioned solar laser systems [31, 33, 34, 36], resulting in poor laser beam quality. Parabolic mirrors, instead, collect all pumping wavelengths to a small focal spot without dispersion, thus allowing for a more efficient pumping of a small diameter laser rod. Since the laser rod acts as an aperture, high-order resonator modes can be suppressed by pumping laser rods of small diameter and the laser beam quality improves. Also, the smaller the rod diameter is, the greater its thermal resistance is.

For these reasons, since 2012 the solar laser research team from FCT NOVA has insisted on improving the solar laser efficiency using parabolic mirrors as primary concentrators [37–47]. In 2017, Liang et al. registered the highest solar laser collection and total slope efficiencies of 31.5 W/m^2 and 5.25%, respectively, with Nd:YAG laser medium, which was end-side-pumped at the focus of a 1.18 m^2 parabolic mirror concentrator [38]. In 2018, records in collection, slope and solar-to-laser conversion

efficiencies of 32.5 W/m^2, 6.7% and 3.74%, respectively, were attained by end-side-pumping a Cr:Nd:YAG single-laser rod with 4.5 mm diameter and 35 mm length through a heliostat–parabolic mirror system with 1.0 m^2 collection area [42]. Later in 2022, Garcia et al. reported the most efficient single-rod solar laser with 38.22 W/m^2 collection efficiency, 6.8% total slope efficiency and 4.5% solar-to-laser conversion efficiency [46], using Nd:YAG co-doped with cerium (Ce) as an ative medium, which provides a broader absorption band to overlap with the solar emission spectrum, when compared to Nd:YAG [66, 67]. The Ce:Nd:YAG rod with 2.5 mm diameter and 25 mm length was end-side-pumped by the same heliostat-parabolic mirror system with an effective collection area of only 0.293 m^2. The lowest threshold solar power for bulk solid-state solar laser of only 88 W was also reported [46].

Although the most efficient multimode solar laser systems had end-side-pumping configurations [31–38, 42], side-pumping is suitable for laser power scaling as it allows a more uniform pump light distribution along the laser rod axis, minimizing the thermal loading problems. Therefore, efforts were also made to improve the solar laser efficiency with side-pumping configurations [39, 44]. In 2019, 15.3 W cw solar laser power was measured from a 3.0 mm diameter, 30 mm length Nd:YAG single-crystal laser rod side-pumped by a heliostat-parabolic mirror system with 0.9 m^2 collection area [39]. This corresponded to 17.0 W/m^2 collection efficiency, 5.4% total slope efficiency and 2.43% total solar-to-laser conversion efficency. In 2021, the side-pumping of a Ce:Nd:YAG laser rod at the same solar facility provided an increase in laser power of more than 1.5 times compared to that of the Nd:YAG laser rod under the same solar pumping conditions [44], resulting in record collection and solar-to-laser conversion efficiencies of 23.6 W/m^2 and 2.8% with side-pumping configuration. Nonetheless, side-pumping is not an ideal configuration for maximum pumping efficiency. In this type of pumping, the pump light is injected into the laser medium transversely to its optical axis. This means that the optical path within the laser rod is much less than that in an end-side-pumping configuration, where most of the pump light is directly focused onto the end face of the laser rod.

To overcome these drawbacks, the potential of end-side-pumping several laser media simultaneously has been investigated [40, 47, 48]. In these systems, the highly concentrated solar radiation could be evenly shared by several laser rods, ensuring a substantial alleviation of the thermal lensing effects. In 2020, the first simultaneous emission of three 1064 nm cw solar laser beams was reported by end-side-pumping three 3 mm diameter, 25 mm length Nd:YAG rods within a single conical pump cavity at the focus of a heliostat-parabolic system [40]. 18.3 W multimode solar laser power was measured at an effective collection area of 1.0 m^2, resulting in 18.3 W/m^2 laser collection efficiency, 5.1% total slope efficiency and 2.2% solar-to-laser conversion efficiency. Substantial improvement in the laser rods thermal performance was confirmed, when compared to that of a single rod with similar volume under the same pumping conditions [40]. The concept of pumping several laser rods within a single pump cavity is of great importance since it allows the sharing of pump energy between the lasers rods, which may lead to a significant rise in solar laser conversion efficiency, while reducing the system complexity. The records in collection, slope, and solar-to-laser conversion efficiencies sits at 41.3 W/m^2, 7.64%,

and 4.64%, respectively, attained in 2022 through the simultaneous pumping of three 2.5 mm diameter, 25 mm length Ce:Nd:YAG laser rods within a single conical pump cavity [47, 48].

Table 1.1 summarizes the main advances in multimode solar laser efficiency.

1.1.2 Progress in TEM_{00}-mode, Doughnut-Shaped Mode, and Low-Order Mode Solar-Pumped Lasers

For solar-pumped laser to be an alternative renewable energy system in many scientific and industrial applications, the pursuit of highly efficient solar lasers with high beam quality is essential. However, despite the significant efforts to achieve high efficiency multimode solar lasers, the relatively poor laser beam quality remains a bottleneck issue. One of the main limitations in scaling the solid-state lasers power without losing its beam quality is the heat accumulated in the active medium, which is heavily dependent on the pump power and laser rod diameter [68, 69]. Substantial improvement in solar laser beam quality had only been possible by pumping small diameter laser rods within a large-mode volume resonator configuration, enabling efficient extraction of fundamental TEM_{00}-mode solar laser [38, 50–55]. Since the laser rod acts as an aperture, high-order resonator modes can be suppressed by pumping laser rods of small diameter. Consequently, beam quality improves, but with the loss of efficiency as a counterpart. Also, the smaller the rod diameter is, the greater its thermal resistance is.

Fundamental TEM_{00}-mode laser emission is of utmost importance in laser-based material processing [70], becoming of vital importance in solar-pumped lasers. Gaussian TEM_{00}-mode laser beam produces the smallest beam divergence, the highest power density and the ability to be focused to a diffraction-limited spot [68]. Nevertheless, the importance of this laser beam profile in solar laser research had been overshadowed by the search for an increase in laser power [5, 6, 8] and efficiency [31–33] until 2013, with the report of a solar-pumped TEM_{00}-mode laser by side-pumping a 3.0-mm diameter Nd:YAG rod with a Fresnel lens installed on a solar tracker [50]. The choice of a large-mode volume resonator configuration was essential for the maximum extraction of 2.3 W cw TEM_{00}-mode power, leading to 2.93 W/m^2 and 0.329% collection and conversion efficiencies, respectively. This experiment resulted in a brightness figure of merit of 1.9 W, which was 6.6 times more than the highest solar laser beam brightness at that time in multimode regime [49]. The brightness figure of merit is one of the most important parameters of a laser beam, being defined as the ratio between laser output power and the product of M_x^2 and M_y^2 factors [9], which quantify the laser beam quality. Since then, Liang's research group had insisted on improving the TEM_{00}-mode solar laser efficiency and laser beam brightness [38, 51–55]. For this purpose, parabolic mirrors have been used as primary concentrators since they can focus the sunlight into a small spot with no chromatic aberration, thus pumping more efficiently a small diameter laser rod.

Table 1.1 Summary of the progress of solid-state solar-pumped laser efficiency in multimode regime

Year Authors References	Primary concentrator (Effective collection area)	Pumping type Active medium (dimensions)	Laser output power (cw)	Laser collection efficiency	Slope efficiency (total/at the focus)	Solar-to-laser conversion efficiency (total/at the focus)
1963 Kiss et al. [2]	Spherical mirror (0.099 m^2)	– Dy:CaF_2 (6.35 mm × 3.16 mm × 25.4 mm)	–	–	– /–	– /–
1966 Young [4]	Parabolic mirror (0.29 m^2)*	Side-pumping Single Nd:YAG rod (∅3 mm × 30 mm)	1.0 W	–	– /–	– /–
1984 Arashi et al. [5]	Segmented parabolic mirror (13.1 m^2)	Side-pumping Single Nd:YAG rod (∅4 mm × 75 mm)	18.0 W	~1.4 W/m^{2*}	– /–	– /~1.6%
1988 Weksler and Schwartz [6]	Segmented mirror concentrator (~12.8 m^2)	Side-pumping Single Nd:YAG rod (∅6.35 mm × 76.2 mm)	~66 W	~5.2 W/m^{2*}	– /2.1%	– /~1.5%*
1993 Krupkin et al. [8]	Heliostats/Paraboloidal mirrors (660 m^2)	Side-pumping Array of Nd:YAG rods (–)	500 W	0.76 W/m^2	– /–	– /–
2003 Lando et al. [9]	ACTA solar concentrator (6.75 m^2)	Side-pumping Single Nd:YAG rod (∅6 mm × 72 mm)	45.0 W	6.7 W/m^2	– /–	– /–
2007 Yabe et al. [31]	Fresnel lens (1.3 m^2)	End-side-pumping Single Cr:Nd:YAG rod (∅3-9 mm × 100 mm)	24.4 W	18.7 W/m^2	~8.3%*†/12.5 ± 1.5%†	~1.93%*/2.9%

(continued)

Table 1.1 (continued)

Year Authors References	Primary concentrator (Effective collection area)	Pumping type Active medium (dimensions)	Laser output power (cw)	Laser collection efficiency	Slope efficiency (total/at the focus)	Solar-to-laser conversion efficiency (total/at the focus)
2011 Liang and Almeida [32]	Fresnel lens (0.636 m^2)	End-side-pumping Single Nd:YAG rod (∅4 mm × 25 mm)	12.3 W	19.3 W/m^2	2.75%*/3.5%	2.17%*/2.76%*
2012 Dinh et al. [33]	Fresnel lens (4.0 m^2)	End-side-pumping Single Nd:YAG rod (∅6 mm × 100 mm)	120 W	30 W/m^2	4.3%/8.6%	3.26%*/6.52%*
2014 Xu et al. [34]	Fresnel lens (1.03 m^2)	End-side-pumping Single Nd:YAG grooved rod (∅6 mm × 100 mm)	27 W	26.2 W/m^2	4.09%*/9.04%	2.91%*/6.44%
2017 Liang et al. [38]	Parabolic mirror (1.18 m^2)	End-side-pumping Single Nd:YAG rod (∅4 mm × 35 mm)	37.2 W	31.5 W/m^2	5.25%*/8.9%	3.14%*/5.31%*
2018 Guan et al. [36]	Fresnel lens (1.03 m^2)	End-side-pumping Single Nd:YAG/YAG rod (∅6 mm × 95 mm)	33.1 W	32.1 W/m^2	5.4%/–	3.3%/–
2018 Liang et al. [42]	Parabolic mirror (1.0 m^2)	End-side-pumping Single Nd:YAG rod (∅4.5 mm × 35 mm)	32.5 W	32.5 W/m^2	6.7%/8.96%*	3.74%*/5.0%*
2019 Liang et al. [39]	Parabolic mirror (0.9 m^2)	Side-pumping Single Nd:YAG rod (∅3 mm × 30 mm)	15.3 W	17.0 W/m^2	5.4%/7.22%*	2.43%*/3.25%*
2020 Liang et al. [40]	Parabolic mirror (1.0 m^2)	End-side-pumping Three Nd:YAG rods (∅3 mm × 25 mm)	18.3 W (6.1 W each)	18.3 W/m^2	5.1%/6.82%*	2.2%*/2.95%*

(continued)

Table 1.1 (continued)

Year Authors References	Primary concentrator (Effective collection area)	Pumping type Active medium (dimensions)	Laser output power (cw)	Laser collection efficiency	Slope efficiency (total/at the focus)	Solar-to-laser conversion efficiency (total/at the focus)
2021 Vistas et al. [44]	Parabolic mirror (0.7 m^2)	Side-pumping Ce:Nd:YAG rod (∅4 mm × 35 mm)	16.5 W	23.6 W/m^2	4.4%/5.88%*	2.8%/3.74%*
2022 Garcia et al. [46]	Parabolic mirror (0.293 m^2)	End-side-pumping Single Ce:Nd:YAG rod (∅2.5 mm × 25 mm)	11.2 W	38.2 W/m^2	6.8%/9.09%*	4.5%/6.02%*
2022 Liang et al. [47]	Parabolic mirror (0.4 m^2)	End-side-pumping Three Ce:Nd:YAG rods (∅2.5 mm × 25 mm)	16.5 W (5.5 W each)	*41.3* W/m^2	*7.64%*/10.2%*	*4.64%*/6.20%*

* The value is not indicated in the publication, but it can be calculated based on the reported parameters.
† The value was overestimated, considering only a few laser output data points at high solar input power to calculate the slope efficiency

Fused silica light-guides were proposed and tested to pump uniformly either a 3.0 mm or a 4.0 mm diameter, 30 mm length Nd:YAG rod, resulting in 4.0 W laser beam brightness [51] and 5.5 W cw TEM_{00}-mode power [52]. The collection and solar-to-laser efficiencies were lower than that of the first TEM_{00}-mode solar laser [50], due in part to the low light coupling efficiency between the output end of the light guide and the laser rod. Therefore, alternative side-pumping configurations were subsequently tested, where the concentrated solar radiation at the focus of the parabolic mirror was more efficiently coupled to the laser rod through either a cylindrical lens [54] or an ellipsoidal-shaped lens [55], attaining collection and conversion efficiencies of 4.0 W/m^2 and 0.442%, respectively [55]. Most of these solar laser prototypes had side-pumping configuration. However, substantial progress in collection efficiency, solar-to-laser conversion efficiency and beam brightness figure of merit in TEM_{00}-mode regime was registered by end-side-pumping a 4.0 mm diameter, 35 mm length, 1.0 at.% Nd:YAG rod in 2017 [38]. The collection efficiency was almost doubled, reaching 7.9 W/m^2. Solar-to-laser conversion efficiency of 0.788% was also calculated. Moreover, record-high beam brightness of 6.46 W was achieved. These values remain the experimental records in solar laser collection efficiency, solar-to-laser conversion efficiency and brightness figure of merit, respectively, in fundamental mode regime.

Aside from the typical Gaussian intensity profiles, non-conventional laser beam shapes, such as annular beams, open new perspectives in fundamental laser-matter interactions, enabling unique material responses with control down to the nanoscale [70]. An annular beam, also called doughnut-shaped beam (TEM_{01*}-mode), is a beam with an intensity distribution concentrated in a ring with no on-axis intensity. This profile is crucial for applications in which temperature is a key parameter, such as laser heat treatment or laser hardening [70]. Doughnut-shaped laser beams have also attracted significant attention for applications in advanced trapping techniques, acting as optical tweezers for trapping atoms and molecules [71].

In 2018, doughnut-shaped solar laser emission with 3.0 W cw laser power from a side-pumped grooved Nd:YAG rod by a heliostat-parabolic mirror system was reported for the first time [56]. 2.0 W cw Gaussian TEM_{00}-mode solar laser power was also registered. The selective oscillation of these laser modes was possible with the adoption of an asymmetric laser resonator operating close to the border of the resonator stability zone [56]. This allowed the formation of the doughnut-shaped beam without the need of inserting additional spatial light modulators [72, 73], optical phase elements [74], or apertures [75] to the laser cavity, thus reducing laser power losses and laser system complexity. Consequently, the generated doughnut-shaped beam had less diffraction losses than the Gaussian beam, which was achieved by slightly extending the laser resonator [56]. Slight adjustments in the rotation of the optical resonator mirrors influenced significantly the radial intensity distribution of the doughnut-shaped beams [56]. In 2019, significant improvement in doughnut-shaped solar laser beam power from a Nd:YAG rod was reported by using an end-side pumping configuration. 4.5 W cw solar laser power was achieved [57], corresponding to 4.5 W/m^2 collection efficiency, which was 1.65 times higher than that of the previous doughnut-shaped solar laser beam [56]. To produce this kind of laser beam

pattern, a large-mode laser resonator was also adopted. With a slight reduction of the laser resonator length, a four-petal like Gaussian solar laser beam of 5.1 W was also observed [57]. This kind of laser light patterns have also been used in optical tweezing experiments [76] and atom optics applications [77].

Table 1.2 summarizes the main advances in TEM_{00}-mode and other low-order mode solar laser efficiencies.

1.1.3 Progress in Solar-Pumped Laser Beam Stability

The pursuit of stable solar laser emission is an indispensable step for solar-pumped lasers to be an alternative renewable energy system in many scientific and industrial applications. However, there were only a few reports on solar laser beam stability measurements [5, 9, 59, 61, 63, 64], some of them in short periods of time [5, 59, 61]. Three studies were found that reported continuous solar laser oscillation for more than one hour [9, 63, 64].

The first detailed report of solar laser continuous operation for duration exceeding five hours was presented by Lando et al. [9], who took advantage of the variation of solar irradiance throughout the day to study the durability and stability of the Nd:YAG solar laser side-pumped with a 2D-CPC secondary concentrator at the focus of the ACTA solar concentrator [9]. During these measurements, maximum cw laser power of about 11 W was registered, which kept nearly constant during the period around noon.

In most solar laser systems, Fresnel lenses and parabolic mirrors were used to harvest sunlight to pump bulk solid-state laser media. However, the relatively large systems accompanied by a tracker or a heliostat are apt to be mechanically unstable. Moreover, the exposure of a single bulk laser rod to high pumping radiation can cause significant thermal lensing and thermal stress effects, which may compromise the resonator stability of a solar-pumped laser. Therefore, efforts have been made to compact down the solar-pumped laser, by drastically reducing the size of the solar concentrators [63, 64, 78, 79] or even eliminating them using luminescent solar collectors [62, 80, 81], avoiding also the need for a water-forced cooling system. In 2017, continuous solar lasing of one hour was reported by Motohiro et al., who developed a compact solar-pumped laser with no water-cooling system [63]. An off-axis parabolic mirror with an aperture of 76.2 mm diameter and a Cr:Nd:YAG ceramic rod of 1 mm diameter and 10 mm length were employed and mounted on a solar-tracking system for an astrometric telescope. Maximum laser output power of more than 30 mW was registered, decreasing to about 20 mW after one hour. By using a similar compact solar laser in 2019, Suzuki et al. reported continuous oscillation of solar laser exceeding 6.5 h [64], being the longest measurements of solar laser power variation as a function of time. During these experiments, maximum solar laser power of about 12 mW was registered between 12:00 and 13:00 and kept going over 10 mW until 14:30, from which it started to decrease continuously.

Table 1.3 summarizes the abovementioned solar laser beam stability experiments.

Table 1.2 Summary of the progress of solid-state solar-pumped laser in TEM_{00}-mode, doughnut-shaped and other low-order modes regime

Year Authors Reference	Primary concentrator (Effective collection area)	Pumping type Active medium (dimensions)	Laser beam profile (M^2) Laser output power	Collection efficiency	Solar-to-laser conversion efficiency (Total)	Brightness figure of merit
2013 Liang et al. [50]	Fresnel lens (0.785 m^2)	Side-pumping Single Nd:YAG rod (∅3 mm × 30 mm)	TEM_{00} ($M^2 \leq 1.1$) 2.3 W	2.93 W/m2	0.329%*	1.9 W
2015 Liang et al. [51]	Parabolic mirror (2.3 m^2)	Side-pumping Single Nd:YAG rod (∅3 mm × 30 mm)	TEM_{00} ($M^2 \leq 1.05$) 4.4 W	1.9 W/m2	0.233%*	4.0 W
2015 Almeida et al. [52]	Parabolic mirror (1.92 m^2)	Side-pumping Single Nd:YAG rod (∅4 mm × 30 mm)	TEM_{00} ($M^2 \leq 1.25$) 5.5 W	2.84 W/m2	0.295%*	3.52 W*
2015 Vistas et al. [53]	Parabolic mirror (1.1 m^2)	Side-pumping Single Nd:YAG grooved rod (∅4 mm × 34 mm)	TEM_{00} ($M^2 \leq 1.15$) 4.0 W	3.6 W/m2	0.410%*	3.0 W
2016 Liang et al. [55]	Parabolic mirror (1.13 m^2)	Side-pumping Single Nd:YAG grooved rod (∅4 mm × 34 mm)	TEM_{00} ($M^2 \leq 1.1$) 4.5 W	4.0 W/m2	0.442%*	3.72 W*
2017 Liang et al. [38]	Parabolic mirror (1.18 m^2)	End-side-pumping Single Nd:YAG rod (∅4.0 mm × 35 mm)	TEM_{00} ($M^2 \leq 1.2$) 9.3 W	7.9 W/m2	*0.788%**	*6.46* W

(continued)

Table 1.2 (continued)

Year Authors Reference	Primary concentrator (Effective collection area)	Pumping type Active medium (dimensions)	Laser beam profile (M^2) Laser output power	Collection efficiency	Solar-to-laser conversion efficiency (Total)	Brightness figure of merit
2018 Almeida et al. [56]	Parabolic mirror (1.1 m^2)	Side-pumping Single Nd:YAG grooved rod (∅4.0 mm, 34 mm)	Doughnut-shaped 3.0 W	2.73 W/m2*	0.307%*	–
2019 Vistas et al. [57]	Parabolic mirror (1.0 m^2)	Side-pumping Single Nd:YAG grooved rod (∅4.0 mm, 34 mm)	Doughnut-shaped 4.5 W	4.5 W/m2	0.529%*	–
			Four-petal like 5.1 W	5.1 W/m2	0.60%*	–

* The value is not indicated in the publication, but it can be calculated based on the reported parameters

Table 1.3 Summary of the progress of solid-state solar-pumped laser beam stability

Year Authors References	Primary concentrator (Collection area)	Laser head configuration Active medium (dimensions)	Maximum laser output power (cw) Regime	Duration (h)
2003 Lando et al. [9]	ACTA solar concentrator (6.75 m^2)	Side-pumping Single Nd:YAG rod (⌀10 mm × 130 mm)	~11 W Multimode	5
2017 Motohiro et al. [63]	Off-axis parabolic mirror (4.56 × 10^{-3} m^2)	End-pumping Single Cr:Nd:YAG rod (⌀1.0 mm × 10 mm)	>30 mW –	1
2019 Suzuki et al. [64]	Off-axis parabolic mirror (4.56 × 10^{-3} m^2)	End-pumping Single Cr:Nd:YAG rod (⌀1.0 mm × 10 mm)	12 mW –	≥6.5

The drawback of the downsized single-rod solar-pumped lasers is the low laser power (in milliwatt level) and poor solar laser efficiency due to the low available collection area for sunlight harvesting [62–64, 78–81]. The development of alternative approaches for simultaneous pumping of more than one laser rod, enabling both enhanced thermal performance and efficiency, can constitute a way to solve the abovementioned issues [40, 47, 60]. In 2022, Tibúrcio et al. reported the first experimental results in solar laser tracking error compensation capacity with a dual-rod solar laser head side-pumped at the focus of a heliostat-parabolic mirror system with effective collection area of 1.05 m^2 [60]. The solar laser beam stability was measured with no Sun tracking for one minute, by stopping the operation of the heliostat during that time. A maximum tracking error width of 1.4° at 10% laser power loss ($TEW_{10\%}$) was registered, representing a substantial increase in solar tracking error tolerance; 23 times over the numerical results with the most efficient end-side-pumped Nd:YAG solar laser with heliostat-parabolic mirror system [38, 60]. Besides, good solar laser collection efficiency of 14.1 W/m^2 for side-pumping configuration was calculated [60]. This study demonstrated the significance of pumping several laser rods simultaneously within a single cavity, providing stable solar laser beam emission with good efficiency and enhanced thermal performance, while helping to reduce the cost of high precision solar trackers.

1.2 Solar-Pumped Gas Lasers

In the late 1970s, interest arose in pumping gas lasers with sunlight [14] thanks to the previous successful reports of solid-state solar laser emission [2–4].

1.2.1 Blackbody Pumped CO_2 Solar Lasers

The direct solar pumping of gas lasers can be very inefficient due to the narrow absorption spectrum in relation to the solar radiation emission spectrum. In addition, many gas lasants have infrared absorption bands which do not lie near the region of the solar spectrum with the highest energy density. This implies an overall low solar laser system efficiency [12].

To overcome the severe limitations of direct solar pumping of gas media, the blackbody-pumped solar laser concept was proposed by Christiansen in 1978 [12]. This concept consisted of using the concentrated solar radiation to heat an intermediate body, a blackbody, which when heated could release infrared thermal radiation to pump the gas laser medium. Any radiation not absorbed by the lasant gas could be re-absorbed by the blackbody cavity walls and then re-emitted. An advantage of the blackbody-pumped solar laser system would be the inherent energy storage capacity of the blackbody cavity, which might enable laser operation even when sunlight was unavailable [17]. Because of the potential of this idea, several non-solar proof-of-concept researches have been carried out since the late 70s to the early 90s, using an electrically heated oven as a solar simulator [13–20]. Carbon dioxide (CO_2), which has an absorption linewidth at 4.25 μm and lases at 10.6 μm, was chosen as the laser medium for demonstrating the feasibility of blackbody pumped gas lasers.

The blackbody-pumped CO_2 laser concept can be divided in two types [19]: the direct blackbody-pumped laser cavity and the blackbody-pumped transfer laser. In the direct blackbody-pumped laser cavity, the laser tube lies within the blackbody, whereby it is directly subjected to the thermal radiation from the solar heated blackbody. Usually, the lasant gas in this cavity laser is a mixture of CO_2, helium (He), and argon (Ar) [13–16]. The limitation of this laser concept lies in the fact that only a very small fraction of the blackbody power is absorbed by the CO_2, further limiting the laser power and efficiency. In the the blackbody-pumped transfer laser, the CO_2 laser cavity is external to the blackbody cavity. Instead, other potential diatomic molecules are vibrationally excited by the heated blackbody cavity. The vibrationally excited high-pressure gas is then transported through a nozzle into the external laser cavity with lower pressure, transferring energy to CO_2 [19].

In 1978 and 1979, Yesil and Christiansen began to explore the feasibility of the direct blackbody-pumped laser cavity concept [13, 14], but it was only in 1984 that continuous lasing was reported with output powers reaching 8–10 mW [15, 16]. Shortly thereafter, in 1985, Sirota and Christiansen investigated the use of nitrous oxide (N_2O) and CO_2 isotopes as laser media for this type of gas laser [18], once their combination allows the broadening of the laser media absorption spectrum [18, 20]. Continuous lasing action with laser output powers of up to 0.16 W were registered with the combination of these isotopes [18]. A blackbody-pumped CO_2–N_2 transfer laser was experimentally demonstrated in 1984 by De Young and Higdon [17]. Continuous lasing of N_2-pumped CO_2 at 10.6 μm approaching 1.4 W was reached, being the highest power reported from a blackbody-pumped CO_2 cw laser [17].

1.2.2 Iodine Solar-Pumped Lasers

The use of a gas lasant could be advantageous for easy removal of waste heat and lasant replenishment. Some of these characteristics are inherent in the alkyl-iodide photodissociation laser [25].

After the successful demonstration of a solar simulator-pumped iodine laser in 1981 [21], this kind of gas laser was studied extensively at NASA Langley Research Center, where the performance of various perfluoroalkyl iodides were tested under solar simulator pumping with concentrated extraterrestrial air-mass zero (AM0) radiation for potential utilization in space applications [21–27]. The effective pump band of the perfluoroalkyl iodides lasants is in the near ultraviolet at 275 nm with a bandwidth of approximately 50 nm. Lasing occurs at 1.315 μm [24]. In the first atomic iodine solar simulator-pumped gas laser, a quartz tube filled with perfluoro-n-propyl iodide (n-C_3F_7I) was pumped by a 4 kW xenon (Xe) arc solar simulator with the help of a conical aluminum secondary concentrator [21]. Similar experimental apparatus was used in 1983, through which continuous lasing for over 10 ms was reached [22]. However, the cw laser power was below 0.5 W [21, 22]. In 1986, by pumping the same gas lasant with an argon-arc lamp, 2 W cw laser power was obtained for over one hour [23]. In 1990, Lee et al. tested the feasibility of the perfluoro-n-hexyl iodide (n-$C_6F_{13}I$) as a lasant in a solar-simulator-pumped cw laser system [26]. The cw laser output from the n-$C_6F_{13}I$ reached 10 W, which was closely comparable to that of n-C_3F_7I under similar pumping conditions. Nevertheless, the n-$C_6F_{13}I$ proved to have nearly unlimited reusability after chemical treatment in contrast with n-C_3F_7I [26]. In 1994, Tabibi et al. decided to investigate the cw iodine laser performance of perfluoro-tert-butyl iodide (t-C_4F_9I) [27]. t-C_4F_9I could increase the solar spectrum utilization due to the red-shifted photodissociation absorption peak and broader half-width in relation to n-C_3F_7I. A four-fold increase in cw laser power compared to that with n-C_3F_7I was reported. A maximum cw output power of 46 W was achieved with the t-C_4F_9I laser system. This was the highest reported cw output laser power from a solar simulator-pumped iodine gas laser [27].

In 1996, Terry et al. design and built the first iodine gas laser pumped by concentrated UV terrestrial solar radiation [28]. The laser system consisted of a parabolic trough reflector, an optical resonator cavity and a lasant gas flow system with t-C_4F_9I as the lasant material. Nevertheless, the solar irradiation measurements at the focus of the parabolic trough showed an average solar concentration of 15–20 suns, below the predicted threshold of 40 suns, making the laser emission impossible [28].

In addition to the study of perfluoroalkyl iodides, the feasibility of other types of iodides have been also investigated as alternative lasant materials for solar-pumped lasers, albeit to a lesser extent. In 1982, the operating characteristics of a flashlamp-pumped iodine monobromide (IBr) laser were investigated to evaluate its suitability for solar-pumped laser applications [82]. The iodine monobromide peak absorption is located at 500 nm, at the peak of the solar energy flux and has a wide absorption bandwidth of approximately 150 nm. Laser action occurs because of emission from Br at a wavelength of 2.7 μm. Another advantage lies in the fact that the I

and Br photodissociation products reconstitute themselves to form IBr again within milliseconds. The experimental results demonstrated a lower threshold and a higher laser output from the IBr compared to that of C_3F_7I [82]. However, the feasibility of this iodine laser material under cw regime was not investigated.

In the early 2000s, the feasibility of a solar-pumped fullerene–oxygen–iodine laser has also been studied [29] once fullerene absorption band covers a significant part of the visible region of the solar spectrum [30]. Lasing experiments in pulsed regime with a fullerene-oxygen-iodine pumped by a solar simulator were realized in 2009, reaching a mean output power of 30 W [30]. Still, there is no reports of the performance of this type of gas laser in cw regime under true solar pumping.

1.3 Potential Applications

Solar-pumped lasers can be considered as one of the most promising technologies in renewable energy and laser technology researches. This type of renewable system is unique since it does not require any artificial pumping source along with its associated electrical power generation equipment, offering the prospects of a drastic reduction in the cost of lasers production and maintenance.

1.3.1 Space-Based Solar-Pumped Laser Applications

Solar-pumped laser systems are especially suited for applications in places where sunlight is plentiful and other forms of energy sources are scarce [48]. Therefore, this renewable technology appears to be the best candidate for space-based applications, such as free space optical communications [84, 85], power transmission [86, 87] and laser propulsion [88]. If scalable to sufficiently high powers, the solar pumped laser could be used for power beaming from a central space station to other space stations [87] equipped with receivers for spacecraft laser-powered propulsion [22, 88], electric power generation [89] and energy storage [22]. The principal advantage of laser power transmission resides in its capacity of tight collimation, thus requiring a relatively small receiving antenna or collector when compared to microwave beaming [22]. Therefore, solar-pumped lasers may be used as a noncontact method to transmit collected solar energy across large distances, either from space to earth or to deep space, which may pave the way for the future development of sustainable industrialization in space [24, 45].

Specific applications of solar-pumped lasers may also include the power transmission for space-based science missions [22] and removal of orbital debris [90, 91]. The feasibility of using a multi-spacecraft system equipped with solar-pumped lasers for asteroid deflection was also a subject of research [92]. The main idea was to have a formation of spacecraft flying in the proximity of the asteroid with all the

spacecraft beaming to the same location to achieve the required thrust to deflect the asteroid [92].

The idea of space-to-Earth power transmission is also a very promising manner for bringing more cleaner energy onto the Earth, which can be used for laser-based materials processing and/or fuel production [22]. The solar laser beam generated in space can be also transmitted to the surface of photovoltaic panels on Earth to generate electricity more efficiently than the direct solar panel plant [93]. Communications, telemetry [93], lidars [94], military air defense [95] and the transmission of power to space-based users [94] are applications that could also benefit from this renewable technology.

1.3.2 Earth-Based Solar-Pumped Laser Applications

Solar-pumped lasers have also attracted attention owing to their potential in terrestrial applications, such as fossil-fuel free energy cycles [96]. Researchers at the Tokyo Institute of Technology in Japan have for some time investigating the idea of using a magnesium combustion engine as a source of green energy [97–100]. Magnesium is a relatively light metal suitable for transportation and has ten times the energy-storage density of hydrogen. It is also the eighth most abundant element on the earth's crust and the second richest metal element in seawater [97]. However, magnesium cannot be found in its elemental form and the magnesium oxide to magnesium transformation requires an extremely high temperature (in excess of 4000 K). Therefore, the renewable deoxidation of the magnesium oxide could only be possibly driven by solar-pumped laser [96]. Ablation of pure magnesium oxide through a home-made continuous-wave Cr:Nd:YAG ceramic solar laser was reported for the first time in 2016 by the researchers of FCT NOVA [101]. The feasibility of a renewable energy cycle for hydrogen production using solar-pumped laser and metal oxide nanoparticles was also studied by Saiki and his co-workers [102, 103]. The reduced metals can be also used in metal-air fuels that extract energy from reactions between hydrogen and metals [103]. The application of solar-pumped lasers in solar-energy conversion methodologies can also involve the illumination of photovoltaic cells for high solar-to-electrical conversion efficiency [104], which can be used to feed electric-drive vehicles [63].

The recent progress in dual-rod [60] and three-rod [40, 47] solar lasers has also aroused interested in the future utilization of multibeam solar-pumped lasers in laser-based materials processing, such as laser microprocessing [105, 106] and surface texturing [107]. Additionally, solar-pumped laser may also constitute a cost-effective alternative, non-competitive technology, for healthcare in many Sun-rich developing countries [108]. In 2019, the first solar laser—tissue interaction was reported, revealing a more effective penetration of 1064 nm solar laser radiation into the biological samples in relation to that with concentrated solar radiation spectrum [109],

References

1. Maiman, T.H.: Stimulated optical radiation in ruby. Nature **187**(4736), 493–494 (1960). https://doi.org/10.1038/187493a0
2. Kiss, Z.J., Lewis, H.R., Duncan, R.C.: Sun pumped continuous optical maser. Appl. Phys. Lett. **2**(5), 93–94 (1963). https://doi.org/10.1063/1.1753794
3. Simpson, G.R.: Continuous sun-pumped room temperature glass laser operation. Appl. Opt. **3**(6), 783–784 (1964). https://doi.org/10.1364/AO.3.000783
4. Young, C.G.: A sun-pumped cw one-watt laser. Appl. Opt. **5**(6), 993–997 (1966). https://doi.org/10.1364/AO.5.000993
5. Arashi, H., Oka, Y., Sasahara, N., Kaimai, A., Ishigame, M.: A solar-pumped cw 18 W Nd:YAG laser. Japan. J. Appl. Phys. **23**(Part 1, No. 8), 1051–1053 (1984). https://doi.org/10.1143/jjap.23.1051
6. Weksler, M., Shwartz, J.: Solar-pumped solid-state lasers. IEEE J. Quantum Electron. **24**(6), 1222–1228 (1988). https://doi.org/10.1109/3.247
7. Benmair, R.M.J., Kagan, J., Kalisky, Y., Noter, Y., Oron, M., Shimony, Y., Yogev, A.: Solar-pumped Er, Tm, Ho:YAG laser. Opt. Lett. **15**(1), 36–38 (1990). https://doi.org/10.1364/OL.15.000036
8. Krupkin, V., Kagan, J., Yogev, A.: Nonimaging optics and solar laser pumping at the Weizmann Institute. In: SPIE's 1993 International Symposium on Optics, Imaging, and Instrumentation, vol. 2016. SPIE (1993)
9. Lando, M., Kagan, J., Linyekin, B., Dobrusin, V.: A solar-pumped Nd:YAG laser in the high collection efficiency regime. Opt. Commun. **222**(1), 371–381 (2003). https://doi.org/10.1016/S0030-4018(03)01601-8
10. Schneider, R.T., Kurzweg, U.H., Cox, J.D., Weinstein, N.H.: Research on solar pumped liquid lasers. In: NASA Report 172121 (1983). https://ntrs.nasa.gov/citations/19830015317
11. Lee, J.H., Kim, K.C., Kim, K.H.: Threshold pump power of a solar-pumped dye laser. Appl. Phys. Lett. **53**(21), 2021–2022 (1988). https://doi.org/10.1063/1.100308
12. Christiansen, W.H.: A new concept for solar pumped lasers. Progress in Astronautics and Aeronautics, January 01, 1978. https://doi.org/10.2514/5.9781600865350.0346.0356
13. Yesil, O., Christiansen, W.H.: Solar pumped continuous wave carbon dioxide laser **61**, 357 (1978). https://doi.org/10.2514/5.9781600865350.0357.0367
14. Yesil, O., Christiansen, W.H.: Optically pumped carbon dioxide laser mixtures (using solar radiation). J. Energy **3**(5), 315–318 (1979). https://doi.org/10.2514/3.48008
15. Insuik, R.J., Christiansen, W.H.: Blackbody-pumped CO_2 laser experiment. AIAA J. **22**(9), 1271–1274 (1984). https://doi.org/10.2514/3.8771
16. Insuik, R., Christiansen, W.: A radiatively pumped CW CO2laser. IEEE J. Quantum Electron. **20**(6), 622–625 (1984). https://doi.org/10.1109/JQE.1984.1072446
17. Deyoung, R.J.: A blackbody-pumped N2–CO2 transfer laser. 17th Fluid Dynamics, Plasma Dynamics, and Lasers Conference (1984). https://doi.org/10.2514/6.1984-1653
18. Sirota, J., Christiansen, W.: Lasing in N_2O and CO_2 isotope mixtures pumped by blackbody radiation. IEEE J. Quantum Electron. **21**(11), 1777–1781 (1985). https://doi.org/10.1109/JQE.1985.1072593
19. Deyoung, R.J.: Scaling blackbody laser to high powers. (1985). https://ntrs.nasa.gov/citations/19850015981
20. Chang, J.J., Christiansen, W.H.: Waveguide CO/sub 2/lasers pumped by broad-band radiation. IEEE J. Quantum Electron. **29**(5), 1412–1422 (1993). https://doi.org/10.1109/3.236156
21. Lee, J.H., Weaver, W.R.: A solar simulator-pumped atomic iodine laser. Appl. Phys. Lett. **39**(2), 137–139 (1981). https://doi.org/10.1063/1.92659
22. Weaver, W.R., Lee, J.H.: A solar pumped gas laser for the direct conversion of solar energy. J. Energy **7**(6), 498–501 (1983). https://doi.org/10.2514/3.62689
23. Lee, J.H., Weaver, W.R., Humes, D.H., Williams, M.D., Lee, M.H.: Solar-pumped photodissociation iodine laser*. **146**(1), 179–180 (1986). https://doi.org/10.1063/1.35844

24. Young, R.D.: Low threshold solar-pumped iodine laser. IEEE J. Quantum Electron. **22**(7), 1019–1023 (1986). https://doi.org/10.1109/JQE.1986.1073096
25. De Young, R.J., Weaver, W.R.: Low-threshold solar-pumped laser using C2F5I **49**(7), 369–370 (1986). https://doi.org/10.1063/1.97589
26. Lee, J.H., Tabibi, B.M., Humes, D.H., Weaver, W.R.: Perfluoro-n-hexyl iodide as gain media for high power, continuous solar-pumped lasers. Opt. Commun. **74**(6), 380–385 (1990). https://doi.org/10.1016/0030-4018(90)90222-F
27. Tabibi, B.M., Terrell, C.A., Lee, J.H., Miner, G.: CW iodine laser performance of t-C4F9I under closely-simulated air-mass-zero solar pumping. Opt. Commun. **109**(1), 86–92 (1994). https://doi.org/10.1016/0030-4018(94)90743-9
28. Terry, C.K., Peterson, J.E., Goswami, D.Y.: Terrestrial solar-pumped iodine gas laser with minimum threshold concentration requirements. J. Thermophys. Heat Transfer **10**(1), 54–59 (1996). https://doi.org/10.2514/3.752
29. Belousova, I.M., Danilov, O.B., Mak, A.A., Belousov, V.P., Zalesskii, V.Y., Grigor'ev, V.A., Kris'ko, A.V., Sosnov, E.N.: Feasibility of the solar-pumped fullerene-oxygen-iodine laser (Sun-light FOIL). Opt. Spectros. **90**(5), 773–777 (2001). https://doi.org/10.1134/1.1374668
30. Mak, A.A., Belousova, I.M., Kiselev, V.M., Grenishin, A.S., Danilov, O.B., Sosnov, E.N.: Converting solar energy into laser radiation using a fullerene-oxygen-iodine laser with solar pumping. J. Opt. Technol. **76**(4), 172–186 (2009). https://doi.org/10.1364/JOT.76.000172
31. Yabe, T., Ohkubo, T., Uchida, S., Yoshida, K., Nakatsuka, M., Funatsu, T., Mabuti, A., Oyama, A., Nakagawa, K., Oishi, T., Daito, K., Behgol, B., Nakayama, Y., Yoshida, M., Motokoshi, S., Sato, Y., Baasandash, C.: High-efficiency and economical solar-energy-pumped laser with Fresnel lens and chromium codoped laser medium. Appl. Phys. Lett. **90**(26), 261120 (2007). https://doi.org/10.1063/1.2753119
32. Liang, D., Almeida, J.: Highly efficient solar-pumped Nd:YAG laser. Opt. Express **19**(27), 26399–26405 (2011). https://doi.org/10.1364/OE.19.026399
33. Dinh, T.H., Ohkubo, T., Yabe, T., Kuboyama, H.: 120 watt continuous wave solar-pumped laser with a liquid light-guide lens and an Nd:YAG rod. Opt. Lett. **37**(13), 2670–2672 (2012). https://doi.org/10.1364/OL.37.002670
34. Xu, P., Yang, S., Zhao, C., Guan, Z., Wang, H., Zhang, Y., Zhang, H., He, T.: High-efficiency solar-pumped laser with a grooved Nd:YAG rod. Appl. Opt. **53**(18), 3941–3944 (2014). https://doi.org/10.1364/AO.53.003941
35. Smyth, C.J.C., Mirkhanov, S., Quarterman, A.H., Wilcox, K.G.: 27.5 W/m^2 collection efficiency solar laser using a diffuse scattering cooling liquid. Appl. Opt. **57**(15), 4008–4012 (2018). https://doi.org/10.1364/AO.57.004008
36. Guan, Z., Zhao, C., Li, J., He, D., Zhang, H.: 32.1 W/m^2 continuous wave solar-pumped laser with a bonding Nd:YAG/YAG rod and a Fresnel lens. Opt. Laser Technol. **107**, 158–161 (2018). https://doi.org/10.1016/j.optlastec.2018.05.039
37. Almeida, J., Liang, D., Guillot, E., Abdel-Hadi, Y.: A 40 W cw Nd:YAG solar laser pumped through a heliostat: a parabolic mirror system. Laser Phys. **23**(6), 065801 (2013). https://doi.org/10.1088/1054-660x/23/6/065801
38. Liang, D., Almeida, J., Vistas, C.R., Guillot, E.: Solar-pumped Nd:YAG laser with 31.5W/m^2 multimode and 7.9W/m^2 TEM_{00}-mode collection efficiencies. Solar Energy Mater. Solar Cells **159**, 435–439 (2017). https://doi.org/10.1016/j.solmat.2016.09.048
39. Liang, D., Vistas, C.R., Almeida, J., Tiburcio, B.D., Garcia, D.: Side-pumped continuous-wave Nd:YAG solar laser with 5.4% slope efficiency. Solar Energy Mater. Solar Cells **192**, 147–153 (2019). https://doi.org/10.1016/j.solmat.2018.12.029
40. Liang, D., Almeida, J., Garcia, D., Tibúrcio, B.D., Guillot, E., Vistas, C.R.: Simultaneous solar laser emissions from three Nd:YAG rods within a single pump cavity. Sol. Energy **199**, 192–197 (2020). https://doi.org/10.1016/j.solener.2020.02.027
41. Liang, D., Almeida, J., Guillot, E.: Side-pumped continuous-wave Cr:Nd:YAG ceramic solar laser. Appl. Phys. B-Lasers Opt. **111**(2), 305–311 (2013). https://doi.org/10.1007/s00340-013-5334-4

42. Liang, D., Vistas, C.R., Tibúrcio, B.D., Almeida, J.: Solar-pumped Cr:Nd:YAG ceramic laser with 6.7% slope efficiency. Solar Energy Mater. Solar Cells **185**, 75–79 (2018). https://doi.org/10.1016/j.solmat.2018.05.020
43. Vistas, C.R., Liang, D., Garcia, D., Almeida, J., Tibúrcio, B.D., Guillot, E.: Ce:Nd:YAG continuous-wave solar-pumped laser. Optik **207**, 163795 (2020). https://doi.org/10.1016/j.ijleo.2019.163795
44. Vistas, C., Liang, D., Almeida, J., Tibúrcio, B., Garcia, D., Catela, M., Costa, H., Guillot, E.: Ce:Nd:YAG side-pumped solar laser. J. Photon. Energy (1), 018001 (2021). https://doi.org/10.1117/1.JPE.11.018001
45. Almeida, J., Liang, D., Garcia, D., Tibúrcio, B.D., Costa, H., Catela, M., Guillot, E., Vistas, C.R.: 40 W continuous wave Ce:Nd:YAG solar laser through a fused silica light guide. Energies **15**(11), 3998 (2022). https://doi.org/10.3390/en15113998
46. Garcia, D., Liang, D., Vistas, C.R., Costa, H., Catela, M., Tibúrcio, B.D., Almeida, J.: Ce:Nd:YAG solar laser with 4.5% solar-to-laser conversion efficiency **15**(14), 5292 (2022). https://doi.org/10.3390/en15145292
47. Liang, D., Vistas, C.R., Garcia, D., Tibúrcio, B.D., Catela, M., Costa, H., Guillot, E., Almeida, J.: Most efficient simultaneous solar laser emissions from three Ce:Nd:YAG rods within a single pump cavity. Sol. Energy Mater. Sol. Cells **246**, 111921 (2022). https://doi.org/10.1016/j.solmat.2022.111921
48. Johnson, S.C.: Solar pumping converts broadband sunlight into efficient laser light. In: Laser Focus World: Lasers & Sources (2022). https://www.laserfocusworld.com/lasers-sources/article/14283698/solar-pumping-converts-broadband-sunlight-into-efficient-laser-light
49. Almeida, J., Liang, D., Guillot, E.: Improvement in solar-pumped Nd:YAG laser beam brightness. Opt. Laser Technol. **44**(7), 2115–2119 (2012). https://doi.org/10.1016/j.optlastec.2012.03.017
50. Liang, D., Almeida, J.: Solar-pumped TEM00 mode Nd:YAG laser. Opt. Express **21**(21), 25107–25112 (2013). https://doi.org/10.1364/OE.21.025107
51. Liang, D., Almeida, J., Vistas, C.R., Guillot, E.: Solar-pumped TEM00 mode Nd:YAG laser by a heliostat—parabolic mirror system. Sol. Energy Mater. Sol. Cells **134**, 305–308 (2015). https://doi.org/10.1016/j.solmat.2014.12.015
52. Almeida, J., Liang, D., Vistas, C.R., Bouadjemine, R., Guillot, E.: 5.5 W continuous-wave TEM_{00}-mode Nd:YAG solar laser by a light-guide/2V-shaped pump cavity. Appl. Phys. B **121**(4), 473–482 (2015). https://doi.org/10.1007/s00340-015-6257-z
53. Vistas, C.R., Liang, D., Almeida, J.: Solar-pumped TEM00 mode laser simple design with a grooved Nd:YAG rod. Sol. Energy **122**, 1325–1333 (2015). https://doi.org/10.1016/j.solener.2015.10.049
54. Vistas, C.R., Liang, D., Almeida, J., Guillot, E.: TEM00 mode Nd:YAG solar laser by side-pumping a grooved rod. Opt. Commun. **366**, 50–56 (2016). https://doi.org/10.1016/j.optcom.2015.12.038
55. Liang, D., Almeida, J., Vistas, C.R., Oliveira, M., Gonçalves, F., Guillot, E.: High-efficiency solar-pumped TEM00-mode Nd:YAG laser. Sol. Energy Mater. Sol. Cells **145**, 397–402 (2016). https://doi.org/10.1016/j.solmat.2015.11.001
56. Almeida, J., Liang, D., Vistas, C.R.: A doughnut-shaped Nd:YAG solar laser beam. Opt. Laser Technol. **106**, 1–6 (2018). https://doi.org/10.1016/j.optlastec.2018.03.029
57. Vistas, C.R., Liang, D., Almeida, J., Tibúrcio, B.D., Garcia, D.: A doughnut-shaped Nd:YAG solar laser beam with 4.5 W/m^2 collection efficiency. Solar Energy **182**, 42–47 (2019). https://doi.org/10.1016/j.solener.2019.02.030
58. Bouadjemine, R., Liang, D., Almeida, J., Mehellou, S., Vistas, C.R., Kellou, A., Guillot, E.: Stable TEM00-mode Nd:YAG solar laser operation by a twisted fused silica light-guide. Opt. Laser Technol. **97**, 1–11 (2017). https://doi.org/10.1016/j.optlastec.2017.06.003
59. Mehellou, S., Liang, D., Almeida, J., Bouadjemine, R., Vistas, C.R., Guillot, E., Rehouma, F.: Stable solar-pumped TEM_{00}-mode 1064 nm laser emission by a monolithic fused silica twisted light guide. Sol. Energy **155**, 1059–1071 (2017). https://doi.org/10.1016/j.solener.2017.07.048

60. Tibúrcio, B.D., Liang, D., Almeida, J., Garcia, D., Catela, M., Costa, H., Vistas, C.R.: Tracking error compensation capacity measurement of a dual-rod side-pumping solar laser. Renew. Energy **195**, 1253–1261 (2022). https://doi.org/10.1016/j.renene.2022.06.114
61. Dinh, T.H., Ohkubo, T., Yabe, T.: Development of solar concentrators for high-power solar-pumped lasers **53**, 2711 (2014). https://doi.org/10.1364/ao.53.002711
62. Reusswig, P.D., Nechayev, S., Scherer, J.M., Hwang, G.W., Bawendi, M.G., Baldo, M.A., Rotschild, C.: A path to practical solar pumped lasers via radiative energy transfer. Sci. Rep. **5**(1), 14758 (2015). https://doi.org/10.1038/srep14758
63. Motohiro, T., Takeda, Y., Ito, H., Hasegawa, K., Ikesue, A., Ichikawa, T., Higuchi, K., Ichiki, A., Mizuno, S., Ito, T., Yamada, N., Luitel, H.N., Kajino, T., Terazawa, H., Takimoto, S., Watanabe, K.: Concept of the solar-pumped laser-photovoltaics combined system and its application to laser beam power feeding to electric vehicles. Japan. J. Appl. Phys. **56**, 08MA07 (2017). https://doi.org/10.7567/jjap.56.08ma07
64. Suzuki, Y., Ito, H., Kato, T., Phuc, L.T.A., Watanabe, K., Terazawa, H., Hasegawa, K., Ichikawa, T., Mizuno, S., Ichiki, A., Takimoto, S., Ikesue, A., Takeda, Y., Motohiro, T.: Continuous oscillation of a compact solar-pumped Cr, Nd-doped YAG ceramic rod laser for more than 6.5 h tracking the sun. Solar Energy **177**, 440–447 (2019). https://doi.org/10.1016/j.solener.2018.10.071
65. Lupei, V., Lupei, A., Gheorghe, C., Ikesue, A.: Emission sensitization processes involving Nd^{3+} in YAG. J. Lumin. **170**, 594–601 (2016). https://doi.org/10.1016/j.jlumin.2015.04.045
66. Payziyev, S., Makhmudov, K., Abdel-Hadi, Y.A.: Simulation of a new solar Ce:Nd:YAG laser system. Optik **156**, 891–895 (2018). https://doi.org/10.1016/j.ijleo.2017.12.071
67. Payziyev, S., Sherniyozov, A., Bakhramov, S., Zikrillayev, K., Khalikov, G., Makhmudov, K., Ismailov, M., Payziyeva, D.: Luminescence sensitization properties of Ce: Nd: YAG materials for solar pumped lasers. Opt. Commun. **499**, 127283 (2021). https://doi.org/10.1016/j.optcom.2021.127283
68. Koechner, W.: Solid-state laser engineering. Springer (2006). https://doi.org/10.1007/0-387-29338-8
69. Clarkson, W.A.: Thermal effects and their mitigation in end-pumped solid-state lasers. J. Phys. D Appl. Phys. **34**(16), 2381–2395 (2001). https://doi.org/10.1088/0022-3727/34/16/302
70. Duocastella, M., Arnold, C.B.: Bessel and annular beams for materials processing **6**(5), 607–621 (2012). https://doi.org/10.1002/lpor.201100031
71. Chu, S.-C., Ohtomo, T., Otsuka, K.: Generation of doughnutlike vortex beam with tunable orbital angular momentum from lasers with controlled Hermite-Gaussian modes. Appl. Opt. **47**(14), 2583–2591 (2008). https://doi.org/10.1364/AO.47.002583
72. Rioux, M., Tremblay, R., Bélanger, P.A.: Linear, annular, and radial focusing with axicons and applications to laser machining. Appl. Opt. **17**(10), 1532–1536 (1978). https://doi.org/10.1364/AO.17.001532
73. Cherezova, T.Y., Chesnokov, S.S., Kaptsov, L.N., Kudryashov, A.V.: Doughnut-like laser beam output formation by intracavity flexible controlled mirror. Opt. Express **3**(5), 180–189 (1998). https://doi.org/10.1364/OE.3.000180
74. Watanabe, T., Fujii, M., Watanabe, Y., Toyama, N., Iketaki, Y.: Generation of a doughnut-shaped beam using a spiral phase plate **75**(12), 5131–5135 (2004). https://doi.org/10.1063/1.1819555
75. Ganic, D., Gan, X., Gu, M.: Focusing of doughnut laser beams by a high numerical-aperture objective in free space. Opt. Express **11**(21), 2747–2752 (2003). https://doi.org/10.1364/OE.11.002747
76. Yu, J., Zhou, C., Jia, W., Wu, J., Zhu, L., Lu, Y., Xiang, C., Li, S.: Generation of controllable rotating petal-like modes using composited Dammann vortex gratings. Appl. Opt. **54**(7), 1667–1672 (2015). https://doi.org/10.1364/AO.54.001667
77. Franke-Arnold, S., Leach, J., Padgett, M.J., Lembessis, V.E., Ellinas, D., Wright, A.J., Girkin, J.M., Öhberg, P., Arnold, A.S.: Optical ferris wheel for ultracold atoms. Opt. Express **15**(14), 8619–8625 (2007). https://doi.org/10.1364/OE.15.008619

78. Mizuno, S., Ito, H., Hasegawa, K., Suzuki, T., Ohishi, Y.: Laser emission from a solar-pumped fiber. Opt. Express **20**(6), 5891–5895 (2012). https://doi.org/10.1364/OE.20.005891
79. Masuda, T., Iyoda, M., Yasumatsu, Y., Endo, M.: Low-concentrated solar-pumped laser via transverse excitation fiber-laser geometry. Opt. Lett. **42**(17), 3427–3430 (2017). https://doi.org/10.1364/OL.42.003427
80. Masuda, T., Iyoda, M., Yasumatsu, Y., Dottermusch, S., Howard, I.A., Richards, B.S., Bisson, J.-F., Endo, M.: A fully planar solar pumped laser based on a luminescent solar collector. Commun. Phys. **3**(1), 60 (2020). https://doi.org/10.1038/s42005-020-0326-2
81. Masuda, T., Zhang, Y., Ding, C., Liu, F., Sasaki, K., Shen, Q., Endo, M.: All-inorganic cesium lead halide perovskite nanocrystals for solar-pumped laser application **127**(24), 243104 (2020). https://doi.org/10.1063/5.0011945
82. Zapata, L.E., Young, R.J.D.: Flashlamp-pumped iodine monobromide laser characteristics **54**(4), 1686–1692 (1983). https://doi.org/10.1063/1.332827
83. Giuliano, C.R., Hess, L.D.: Reversible photodissociative laser. System **40**(6), 2428–2430 (1969). https://doi.org/10.1063/1.1658010
84. Hemmati, H., Biswas, A., Djordjevic, I.B.: Deep-space optical communications: future perspectives and applications. Proc. IEEE **99**(11), 2020–2039 (2011). https://doi.org/10.1109/JPROC.2011.2160609
85. Zhao, C., Zhang, H., Guan, Z., Cai, Z., He, D., Wang, Y.: Solar pumped lasers for free space laser communication. In: PHOTOPTICS (2019). https://doi.org/10.5220/0007569702680275
86. Brauch, U., Opower, H., Wittwer, W., Muckenschnabel, J.: Solar-pumped solid state lasers for space—space power transmission. In: SPS 91—Power from Space, January 01, 1991, pp. 320–326
87. Deyoung, R.J., Walker, G.H., Williams, M.D., Schuster, G.L., Conway, E.J.: Preliminary design and cost of a 1-megawatt solar-pumped iodide laser space-to-space transmission station. (1987). https://ntrs.nasa.gov/citations/19870017752
88. Deyoung, R.J., Walberg, G.D., Conway, E.J., Jones, L.W.: A NASA high-power space-based laser research and applications program. (1983). https://ntrs.nasa.gov/citations/19830018929
89. Mori, M., Nagayama, H., Saito, Y., Matsumoto, H.: Summary of studies on space solar power systems of the national space development agency of Japan. Acta Astronaut. **54**(5), 337–345 (2004). https://doi.org/10.1016/S0094-5765(03)00033-X
90. David, L.: Space junk removal is not going smoothly. In: Scientific American (2021). https://www.scientificamerican.com/article/space-junk-removal-is-not-going-smoothly/
91. Liang, D.: Advances in high-efficiency TEM00-mode solar-pumped laser. In: 1st Workshop Laser Solutions for Orbital Space Debris, Paris (2015). https://gargantua.polytechnique.fr/siatel-web/app/linkto/mICYYYUA65Z
92. Vasile, M., Maddock, C.A.: Design of a formation of solar pumped lasers for asteroid deflection. Adv. Space Res. **50**(7), 891–905 (2012). https://doi.org/10.1016/j.asr.2012.06.001
93. Abdel-Hadi, Y.A.: Space-based solar laser system simulation to transfer power onto the earth. NRIAG J. Astron. Geophys. **9**(1), 558–562 (2020). https://doi.org/10.1080/20909977.2020.1815497
94. Zapata, L.E., Williams, M.D.: Analysis of Nd3+:glass, solar-pumped, high-power laser systems, vol. 89, p. 17855 (1989). https://ntrs.nasa.gov/citations/19890008484
95. Crouse, M.: High-energy laser weapons move quickly from prototype to deployment. In: Military+Aerospace Electronics (2021). https://www.militaryaerospace.com/power/article/14207816/highenergy-laser-weapons-move-quickly-from-prototype-to-deployment
96. Graydon, O.: A sunny solution. Nat. Photon. **1**(9), 495–496 (2007). https://doi.org/10.1038/nphoton.2007.155
97. Yabe, T., Uchida, S., Ikuta, K., Yoshida, K., Baasandash, C., Mohamed, M.S., Sakurai, Y., Ogata, Y., Tuji, M., Mori, Y., Satoh, Y., Ohkubo, T., Murahara, M., Ikesue, A., Nakatsuka, M., Saiki, T., Motokoshi, S., Yamanaka, C.: Demonstrated fossil-fuel-free energy cycle using magnesium and laser. Appl. Phys. Lett. **89**(26), 261107 (2006). https://doi.org/10.1063/1.2423320

98. Yabe, T., Bagheri, B., Ohkubo, T., Uchida, S., Yoshida, K., Funatsu, T., Oishi, T., Daito, K., Ishioka, M., Yasunaga, N., Sato, Y., Baasandash, C., Okamoto, Y., Yanagitani, K.: 100 W-class solar pumped laser for sustainable magnesium-hydrogen energy cycle. J. Appl. Phys. **104**(8), 083104 (2008). https://doi.org/10.1063/1.2998981
99. Sato, Y., Yabe, T., Sakurai, Y., Mohamed, M.S., Uchida, S., Baasandash, C., Ohkubo, T., Mori, Y., Sato, H.: Experimental study of magnesium production with laser for clean energy cycle, **997**(1), 546–552 (2008). https://doi.org/10.1063/1.2931925
100. Takashi, Y., Tomomasa, O., Hung, D.T., Hiroki, K., Junichi, N., Kouta, O.: Demonstration of solar-pumped laser-induced magnesium production form magnesium oxide. In: Mathaudhu, S.N., Sillekens, W.H., Neelameggham, N.R., Hort, N. (eds.) Magnesium technology 2012, pp. 55–58. Springer International Publishing, Cham (2012). https://doi.org/10.1007/978-3-319-48203-3_10
101. Oliveira, M., Liang, D., Almeida, J., Vistas, C.R., Goncalves, F., Martins, R.: A path to renewable Mg reduction from MgO by a continuous-wave Cr:Nd:YAG ceramic solar laser. Sol. Energy Mater. Sol. Cells **155**, 430–435 (2016). https://doi.org/10.1016/j.solmat.2016.06.046
102. Okada, T., Saiki, T., Taniguchi, S., Ueda, T., Nakamura, K., Nishikawa, Y., Iida, Y.: Hydrogen production using reduced-iron nanoparticles by laser ablation in liquids. ISRN Renew. Energy **2013**, 827681 (2013). https://doi.org/10.1155/2013/827681
103. Saiki, T., Taniguchi, S., Nakamura, K., Iida, Y.: Development of solar-pumped lasers and its application, **199**(2), 3–9 (2017). https://doi.org/10.1002/eej.22961
104. Takeda, Y., Iizuka, H., Mizuno, S., Hasegawa, K., Ichikawa, T., Ito, H., Kajino, T., Ichiki, A., Motohiro, T.: Silicon photovoltaic cells coupled with solar-pumped fiber lasers emitting at 1064 nm, **116**(1), 014501 (2014). https://doi.org/10.1063/1.4885758
105. Bruening, S., Du, K., Jarczynski, M., Jenke, G., Gillner, A.: Ultra-fast laser micro processing by multiple laser spots. Procedia CIRP **74**, 573–580 (2018). https://doi.org/10.1016/j.procir.2018.08.084
106. Oliveira, J.P., Panton, B., Zeng, Z., Andrei, C.M., Zhou, Y., Miranda, R.M., Fernandes, F.M.B.: Laser joining of NiTi to Ti6Al4V using a niobium interlayer. Acta Mater. **105**, 9–15 (2016). https://doi.org/10.1016/j.actamat.2015.12.021
107. Strite, T., Gusenko, A., Grupp, M., Hoult, T.: Fiber Lasers: multiple laser beam materials processing. In: Laser Focus World: Lasers & Sources (2016). https://www.laserfocusworld.com/lasers-sources/article/16547084/fiber-lasers-multiple-laser-beam-materials-processing
108. Pearson, H.: Solar surgery hots up. Nature (2002). https://doi.org/10.1038/news020812-12
109. Catela, M., Liang, D., Almeida, J., Vistas, C.R.: Homogenization and penetration effects of 1064 nm Nd:YAG solar laser and concentrated solar radiations on ex vivo chicken breast samples, **31**(2), 022010 (2019). https://doi.org/10.2351/1.5088051

Chapter 2
Numerical Tools for Solid-State Laser Design

Dário Garcia and Dawei Liang

2.1 Design of Solid-State Lasers by Zemax® Software

This chapter introduces the basic knowledge necessary for solar laser modeling with the ray tracing software: Zemax®. This commercially available program is an extensive and powerful optical tool that allows any user to model, analyze, assist, and optimize an envisioned optical system. This software offers two modes of operation: Sequential mode and Non-sequential mode. The reader will familiarize the Zemax® user interface (UI) for Non-Sequential mode, learn to add and edit optical objects; modify a virtual source to emit a complete solar spectrum; add a new type of active medium, such as Nd:YAG or editing materials in the glass catalog; extraction of relevant information's of a detector and analyzing its content.

The most common UIs used in Zemax® Non-sequential ray tracing modeling:

- Main window: The software's working space. It is a window with a large grey background, a title bar, a menu bar, and a toolbar at the top, as shown in Fig. 2.1.
- Editor Windows: The Non-Sequential Component Editor (NSC Editor), as shown in Fig. 2.2.
- Dialog boxes: pop-up windows that cannot be resized. These windows are for changing options and settings of a particular item, such as graphics, text, and number of rays on a layout plot, and changing the data of the system, such as field angles, wavelengths, apertures, surface types, etc.
- Windows: Displays the data in graphic form
- Text windows: Displays the data in text form.

2.1.1 Main Window

The main window consists of a title bar, a menu bar, a toolbar, and a large empty grey background for the workplace, as shown in Fig. 2.1. The title bar shows the current file location, as well as the name of the file. The menu bar has several dropdown

© The Author(s), under exclusive license to Springer Nature Switzerland AG 2023

D. Liang et al., *Solar-Pumped Lasers*, Green Energy and Technology,
https://doi.org/10.1007/978-3-031-24785-9_2

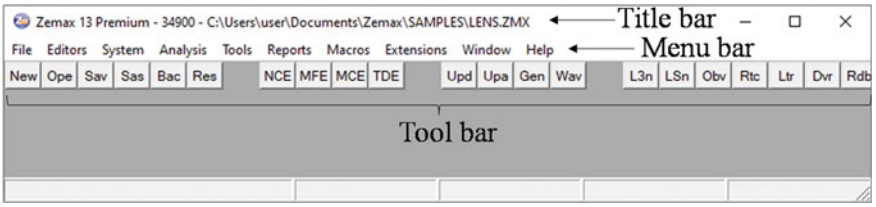
Zemax 13 Premium - 34900 - C:\Users\user\Documents\Zemax\SAMPLES\LENS.ZMX
Title bar
File Editors System Analysis Tools Reports Macros Extensions Window Help
Menu bar
New Ope Sav Sas Bac Res NCE MFE MCE TDE Upd Upa Gen Wav L3n LSn Obv Rtc Ltr Dvr Rdb
Tool bar

Fig. 2.1 Zemax® *Main* window

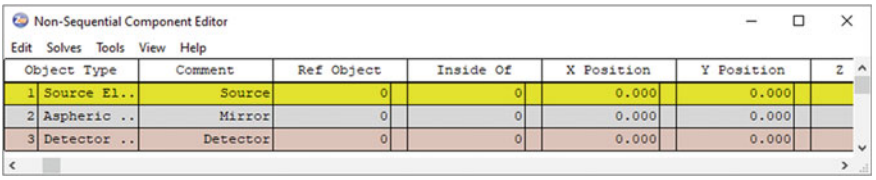
Non-Sequential Component Editor
Edit Solves Tools View Help
Object Type Comment Ref Object Inside Of X Position Y Position Z
1 Source El.. Source 0 0 0.000 0.000
2 Aspheric .. Mirror 0 0 0.000 0.000
3 Detector .. Detector 0 0 0.000 0.000

Fig. 2.2 *Non-sequential component editor* window, listing three objects. The first object is *source eclipse* (Yellow), the second object is *aspheric surface* (Grey), and the third object is *detector rectangle* (Purple)

menu headings which are used to access its features. The toolbar is an access button that quickly accesses the features in the menu bars.

Some options in the dropdown menu are identical to Windows operating system and many of these options are self-explanatory. In this section, only the relevant options listed are relevant to solar-pumped laser modeling.

Fi*le menu*	
Sequential or mixed sequential/non-sequential mode	The dropdown option starts as checked by default
Non-sequential mode	If checked, the current Zemax® workplace turns into a non-sequential mode. This mode must be enabled for solar-pumped laser modeling
Preferences	Opens an options window to change the preferences of the file directory, color representations, numerical representation limits, font sizes, language, and the encoding type of the output text files
E*ditor menu*	Invokes any editor windows
Non-sequential components	Open the editor window and see Sect. 2.1.1.1 non-sequential component (NSC) editor
S*ystem menu*	Invokes any editor windows
Wavelengths	Defines the system's wavelengths in the current project. It accepts up to 24 sets of wavelength data. See Sect. 2.1.2 Pumping sources for solar pumped lasers

(continued)

(continued)

A*nalysis menu*	Menu for optical model analysis
Layout	Opens four options for layout viewers
• NSC 3D layout	Opens a 3D layout plot window in line with the wire representation of the components in the NSC editor. See Sect. 2.1.1.5 layouts
• NSC shaded model	Opens a 3D shaded solid model window representation of the components in the NSC editor. See Sect. 2.1.1.5 layouts
Ray tracing	Opens the options related to ray tracing
• Ray trace …	Opens a ray trace control dialog box. It is used to set up the ray tracing conditions and start the ray tracing process. See Sect.2.1.5.1 ray trace control
• Detector viewer	Opens a window that allows one to view the results of the chosen detector after the ray tracing. See Sect.2.1.5.2 Post-ray tracing: detector viewer
T*ools menu*	Provides incorporated tools that improve or aid the analytical process. Some tools such as optimization, tolerancing, test plate fitting, and others are not covered in this book
Catalogs	
• Glass catalogs …	It opens a window for editing or adding new optical material into Zemax®. See Sect. 2.1.1.4 Glass catalog dialog box
• Editing coating file	Edits the existing coating file in Zemax®
• Reload coating file	Reload the newly edited coating file
W*indow menu*	Select from the list of already open windows which window to move to the front of the display

2.1.1.1 Non-sequential Component (NSC) Editor

The *Non-Sequential Component Editor* window or *NSC editor* window serves as a central workbench for modeling an optical system. This window works similarly to a Microsoft Excel spreadsheet, as shown in Fig. 2.2. Each **row** is equivalent to an **object** and each **column** within a row represents a specific **parameter** of that object. An intersection of a row and a column forms a cell. A single cell (asides from the first and second column) is subdivided into two rectangles, the larger input rectangle is reserved for data input and the smaller one is for the cell-solving condition. The highlighted cell has a black background. The arrow key from the keyboard or left-clicking the mouse serves as a navigation tool to select the intended cell. All column's

widths are modified by hovering on the dividing line between two columns at the top row (white row).

The most used options in the Edit Menu in the *NSC Editor* window:

- "Object Properties…"—Opens the *Object Properties* dialog box or right-click on the object type to open this window.
- "Reload Object"—Reloads and recreates the selected object defined by an external data file.
- "Reload All Objects"—Reloads all objects in the *NSC Editor* window.
- "Insert Object"—This inserts a new empty object into the spreadsheet ***before*** the selected row.
- "Insert After"—This inserts a new empty object into the spreadsheet ***after*** the selected row.
- "Set Row Colors"—Selects either default or none for the color for each row in the spreadsheet. Individual row colors may be set using the row color setting on the object properties dialog box (Right-clicking on the object).

Objects Properties

An object property is edited in the *Properties* dialog box, as shown in Fig. 2.3. This dialog box accessed from "Object Properties…" at the Edit menu bar in the *NSC Editor* window, or by right-clicking on the first column of the object.

The *Type* and *Draw* tabs are the most utilized configurations in the object property for solar-pumped laser modeling.

- *Type* tab (Fig. 2.3a)
  - Type—Accesses all the object types, such as surfaces, volumes, sources, detectors, and imported objects.

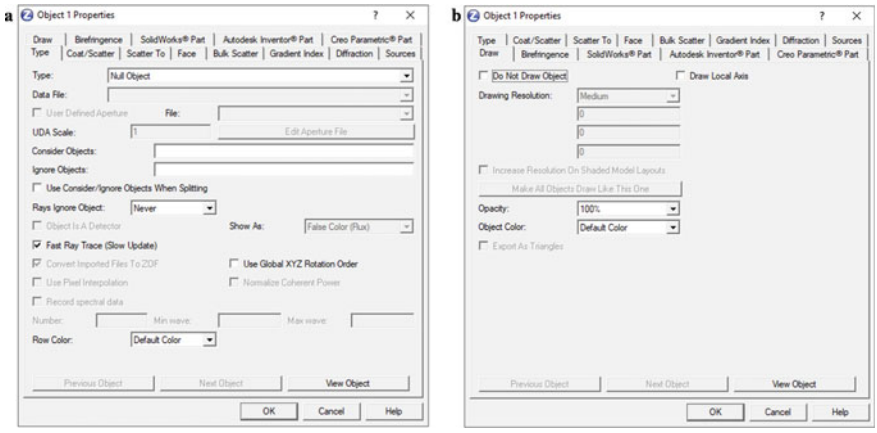

Fig. 2.3 Object properties of object 1 in the *NSC Editor*. **a** *Type* tab and **b** *Draw* tab

– Rays Ignored Objects—Dropdown box menu for selecting the state of the object.

  Never—Rays never ignore the interaction with the object (Default).
  Always—Rays ignore the object as if there is no glass or medium in the path. However, the object's appearance will still be present in the layout window if the draw options are enabled.

> **Note**: The "Ray Ignored Objects" is useful for quickly testing optical models by switching different objects by either enabling or disabling them.

– Row Color—Changes the row color of that object in the NSC editor window.

- *Draw* tab (Fig. 2.3b)
  – Do Not Draw Object—By default, the tick box is disabled. If enabled, the object is hidden in both the *NSC layout* window and the *NSC shaded model* window.

> **Warning**: Even if the object has the "Do Not Draw Object" enabled, the condition of "Rays Ignored Object" marked as disabled. Then the object will not show in the layout, however, the system's ray would still be interacting with the invisible object. This can be an issue and it can tamper with any results.

  – Opacity—Dropdown box menu for numerical percentage. It edits the transparency of the object in the *NSC Shaded Model* window.
  – Object Color—Changes the color of the object in the *NSC Shaded Model* window.

Common Parameters Cells

All the objects within the *NSC editor* share the same type of cell composition in the first eleven columns.

- Column 1—Object Type: It indicates the type of object selected for that row. Right-clicking on this cell opens the *Object row <number> Properties* dialog box.
- Column 2—Comment: It uses for comments, it can accept no more than 225 characters.

- Column 3—Ref Object: It copies the position and orientation of the target object row number. The referenced number must be lower than the current object number.
- Column 4—Inside of: Puts the current object inside of the target object row number. The referenced number must be lower than the current object number.
- Column 5—X Position: X coordinate position of the object in millimeters.
- Column 6—Y Position: Y coordinate position of the object in millimeters.
- Column 7—Z Position: Z coordinate position of the object in millimeters.
- Column 8—Tilt about X: X rotation at the X plane at a degree angle.
- Column 9—Tilt about Y: Y rotation at the Y plane at a degree angle.
- Column 10—Tilt about Z: Z rotation at the Z plane at a degree angle.
- Column 11—Material: Defines the material of the current object if applicable. The material written by the use must be a valid named material found in the "Glass catalog" list (Sect. 2.1.1.4 Glass catalog dialog box and Glass table).

NSC Editor: Cell

Each cell apart from the first two columns ("Object type" and "Comments") subdivides into a larger rectangular cell (left) and a smaller rectangular cell (right).

- Large rectangular cell—Input text box which accepts integer numbers, decimal numbers, or a string of words depending on the cell's specification.

  A numerical cell can do basic arithmetic functions of plus (+), minus (-), multiplication (*), and division (/). For example, adding "+5.5" onto an existing "20" within the cell will result in a "25.5" when pressing the Enter key or by moving to another cell.

Note: To subtract a number, the sequence starts with a plus before a minus. For example "+−10".

- Small rectangular cell—Shows the solve condition of the parameter. Zemax® offers four solve types, as shown in Fig. 2.4:

  – Empty: The parameter is a fixed solve type.

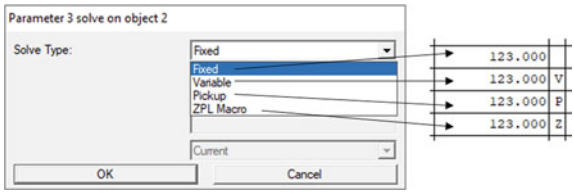

Fig. 2.4 Solve type dialog box of parameter 3 on object 2

– V: The parameter is a variable solve type.
– P: The parameter is a pickup solve type.
– Z: The parameter run by a ZPL macro.

Object Nesting Volumes and Surfaces

The order in which the objects placed in the *NSC Editor* window has a significant role in the ray-objects interaction. The number of nesting objects by default in Zemax® is five and the minimum is four, special models may need a higher nesting number to function properly. The nesting object limit is changeable in the *Main menu* → *System* → *General…* → *Non-sequential* tab.

Nesting volumes

Volumetric objects are often refractors. Zemax® keeps tracking the index of refraction through which the ray is propagating from one object to another.

The general rules are:

> If a ray strikes more than one object at the exact point in space; the ***last*** object listed in the *NSC Editor* determines the properties of the surface or volume at that point.

Considered a silica sphere with a cylindrical hole in the middle, and continuously pumped by a collimated light source in the air, as shown in Fig. 2.5. In the *NSC editor* window, the order of source object placed before the other two objects. According to the nesting rule, the cylinder volume (#2) of vacuum material must placed **after** the sphere object (#1) of silica material in the *NSC editor* window, as shown in Fig. 2.5a.

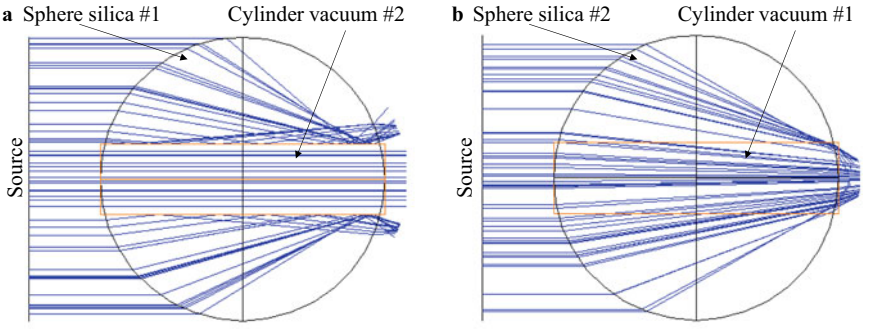

Fig. 2.5 Nesting order of a Sphere in silica with a cylinder volume in a vacuum. **a** The correct object nesting order, **b** the wrong nesting order

The difference between Fig. 2.5a, b is evident. In Fig. 2.5a, the light passes normally through the cylindrical hole, while the rays inside of the silica sphere reflects due to the difference in the refraction index of both silica and air. Figure 2.5b shows the incorrect nesting procedure since the passing ray continues as if no hole is present.

Nesting surfaces

The nesting surface rules are the same as the nesting volumes.

> If a ray strikes more than one object at the same point in space; the ***last*** object listed in the *NSC Editor* determines the properties of the surface at that point.

For nesting surfaces, additional rules should consider when there is more than one surface existing at the ray intercepting point:

1. The last surface listed will determine the properties of the surface.
2. If the last surface listed is a mirror, then the ray will reflect.
3. If the last surface listed is an absorber, then the ray will absorb.
4. If the last surface listed is neither a mirror nor an absorber, the ray will ignore the surface.
5. Surface objects may not share boundaries with volume objects unless the surface object is reflective or absorbing, or unless the volume object listed after the surface object; in which case the volume defines the properties of the common boundary.

2.1.1.2 Wavelength Data Window

The system's wavelength is configurable in *Wavelength Data* dialog box, shown in Fig. 2.6, access from *Main menu* → *System* → *Wavelengths*. A total of 24 wavelength entries can be accepted at a time. Each wavelength has its respective unitless weight. Each tick box activates and deactivate the selected wavelengths or to sort, save and load the wavelength data. A minimum and maximum computational wavelength can be set for the system. The list of wavelengths saved and loaded from a *.WAV file. This file is editable by any text editor software, such as Notepad.

The wavelength measured in micrometers and referenced to the system's air temperature and pressure. The default system temperature is set at 20 °C, and the default air pressure is at 1.0 atmospheres. If a new system with modified temperature and pressure, then a new set of wavelengths must be manually adjusted.

Fig. 2.6 *Wavelength data* dialog box. 22 solar wavelengths with their respective weights selected from the solar spectrum overlapped with the absorption bands of Nd:YAG

Spectrum File

The *Wavelength Data* dialog box is the most direct and common way to introduce wavelengths into the ray tracing system, however, it can only accept up to a maximum of 24 wavelengths. Spectrum file is an alternative method to increase the number of system wavelengths, up to 200 and no less than 3 sets. Notepad with *.SPCD extension used for Spectrum files, and by default placed in the Object *Sources**Spectrum Files* folder. The Spectrum file consists of two sets of columns, a column of wavelength in micrometers and other columns as a dimensionless relative weight value, shown in the following format:

```
# comment <optional>
wavelength1 weight1
wavelength2 weight2
etc…
```

Any blank line or a line starting with the "#" or "!" symbol assumed to be a comment and ignored.

The spectrum file can only be accessed from the object's property under the *Sources* tab and by selecting the dropdown box of "Source color". The "System Wavelengths" is the default option and the "Spectrum file" option selected from that dropdown box, which enables a new dropdown list menu of spectrum files with *.SPCD extension. Any spectrum file selected will supersede the default system wavelength data. Figure 2.7a, shows the resulting 200 wavelengths and weight distribution of a direct AM 1.5 solar spectrum.

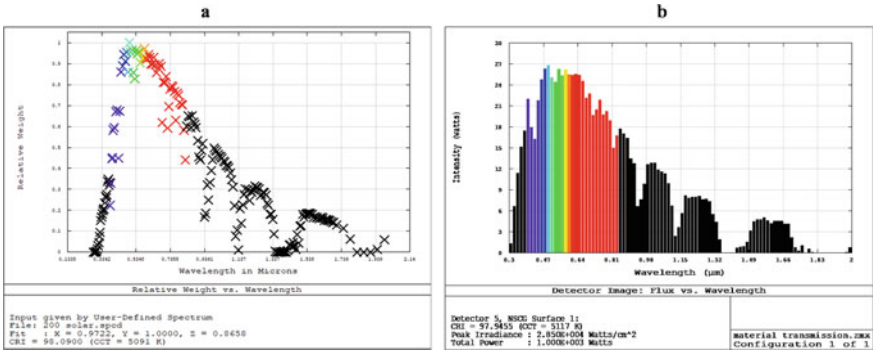
a
b
Relative Weight
Wavelength in Microns
Relative Weight vs. Wavelength
Input given by User-Defined Spectrum
File: 200 solar.spcd
Fit : X = 0.9722, Y = 1.0000, Z = 0.8658
CRI = 98.0900 (CCT = 5091 K)
Intensity (Watts)
Wavelength (µm)
Detector Image: Flux vs. Wavelength
Detector 5, NSCG Surface 1:
CRI = 97.5455 (CCT = 5117 K)
Peak Irradiance : 2.850E+004 Watts/cm^2
Total Power : 1.000E+003 Watts
material transmission.zmx
Configuration 1 of 1

Fig. 2.7 **a** Spectrum file with 200 spectral lines from the direct AM 1.5 solar spectrum. **b** Solar spectrum distribution measured from a source of 1000 W with loaded spectrum file of Fig. 2.7a

Rays Selection from a Spectrum

Once a spectrum defined either from *wavelength data* or from a *spectrum file*, the ray tracing process randomly chooses wavelengths from the spectrum based on their relative weight. A wavelength with twice the relative weight as another wavelength will traced twice more often, and therefore twice of that wavelength will be traced. If a wavelength has a low relative weight, fewer rays traced. If the source units are in Watts or Joules, every ray would have the same amount of power (or energy). Figure 2.7b shows the resulting power distribution influenced by the weight at each wavelength from a 1000 W source with the solar Spectrum file of Fig. 2.7a. Wavelengths with higher weights have a higher power distribution due to the higher number of wavelengths hitting on the detector and vice-versa for wavelengths with a lower weight. The combined final total power (on the detector) of all the wavelengths is equal to the initial power attributed from the source (1000 W).

2.1.1.3 Objects Material

The NSC objects in the *NSC Editor* window can be set as any type of optical material of the user's choosing, by typing the name of the material into the "Material" column. The object can have all its facets set to be reflective with *MIRROR*; or by *ABSORB* as a black body material; leave it blank to be as transparent as the system "air"; or name an existing material name found in the Glass table or Glass catalog.

No material defined (blank cell)

Nameless material treated as a unity index of air.

MIRROR

MIRROR as a material can reflect all incident rays from all or selected facets of the object. The efficiency of the reflection edited by changing the coating.

– Coating mirror editing accessed from the object property under the Coat/Scatter tab. The coating intensity manually added into the text file at *Main menu* → *Tools* → *Catalogs* → *Edit Coating File*. Adding a separate line within the "COAT I.XX" lines with the "XX" values as the desired transmission ratio:

```
! Samples of defining simple ideal coatings using I. format; defines transmitted intensity; rest is assumed to be reflected
! Format: I.transmission
COAT I.01
COAT I.02
COAT I.05
COAT I.06
…
```

Any blank line or a line starting with the "!" symbol assumed to be a comment and ignored.

ABSORB

A material set as *ABSORB* will extinguish any ray that touches this object. This material used in detectors.

Glass name or Glass table:

Naming a material found in the glass catalog or glass table will set the object into that material, which the object will benefit all the optical aspects of that material. Materials such as WATER, PMMA, and SILICA used in solar-pumped laser modeling. Unique materials such as Nd:YAG introduces into the glass catalog.

2.1.1.4 Glass Catalog Dialog Box And Glass Table

Every physical and optical aspect of the material found in Zemax® can be consulted and edited. An optical material is called "glass". Zemax® provides pre-existing standard catalogs from various prominent optical companies. New glasses and catalogs are created, added, and shared. Any objects with volume may attribute a glass material by writing the glass name into the "Material" column, for example, WATER, which Zemax® will look for the matching name in the glass catalog or the glass table.

Glass catalog

The *Glass Catalog* dialog box, as shown in Fig. 2.8, accessed from the *Main menu* → *Tools* → *Catalogs* → *Glass Catalogs*…. Distinct groups of glass lists can be accessed at different catalog lists. Each glass may have a separate set of parameters

that tie to its dispersion formulas; refraction index; operating temperature; maximum and minimum wavelength; etc.… Each parameter within this dialog box is editable and saved into a separate glass catalog.

The transmission at a different wavelength within the material consulted and edited in the *Transmission Data* dialog box, through the *Transmission* button, as shown in Fig. 2.9.

The first column is the wavelength, the second column is the transmission weight calculated through Beer's law Eq. (2.1) at a known thickness (τ) in mm. The absorption coefficient (α) is a measured identity tied to a respective wavelength.

$$t(\lambda) = e^{-\alpha(\lambda)\tau} \tag{2.1}$$

Material: Nd:YAG

The material of "NdYAG" does not exist in the Zemax® catalog. The material of S-LAM60M in the *ARCHER* catalog has an identical refraction index of a Nd:YAG crystal. The user should copy and rename it into "NdYAG", then replace the transmission data for the Nd^{3+} ion at the correct concentration through Beer's law described in Eq. (2.1). Table 2.1 shows the transmission data of an Nd(1%):YAG at $\tau = 10$ mm. The transmission weight is converted through Eq. (2.1) from a known absorption coefficient distribution [1].

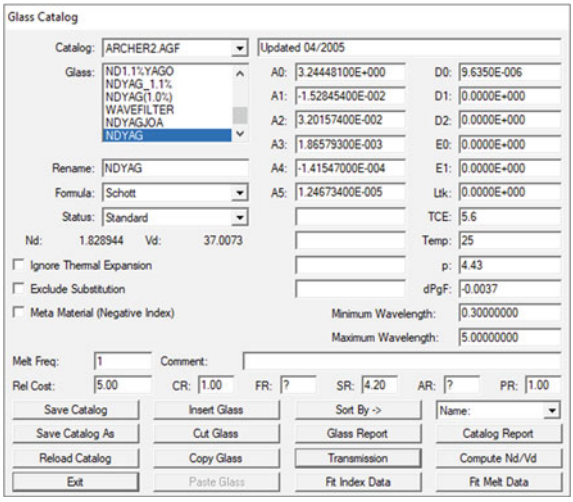

Fig. 2.8 *Glass catalog* dialog box. "NdYAG" as the selected material

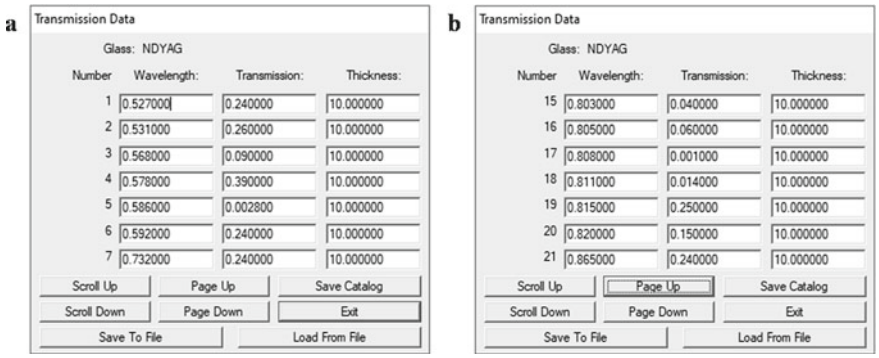

Fig. 2.9 *Transmission data* dialog box of Nd:YAG. **a** Is the transmission of wavelengths at 10 mm thickness for the initial batch of seven wavelengths starting from 0.2 μm to **b** as the 15–21 bulk of wavelength data

Table 2.1 Nd(1%):YAG absorption band [1] and the related transmission weight at 10 mm material length

Wavelength (nm)	Transmission weight
527	0.24
531	0.26
568	0.09
578	0.39
586	0.0028
592	0.24
732	0.24
736	0.09
743	0.16
746	0.002
753	0.024
758	0.039
790	0.35
793	0.056
803	0.04
805	0.06
808	0.001
810	0.014
815	0.25
820	0.15
865	0.24
880	0.40

2.1.1.5 Layouts

This chapter provides a detailed description of the layouts analysis features in Zemax® that widely used for solar-pumped laser modeling. These windows accessed from *Main Menu* → *Analysis* → *Layout*.

NSC 3D Layout window

This window draws all the objects from the *NSC Editor* window in wireframes, as shown in Fig. 2.10a sphere object is drawn with simple lines. Any selected object in the *NSC Editor* window will turn red in the *NSC 3D layout* window, otherwise, the object's colors will be black.

NSC Shaded Model window

This layout draws the objects into a shaded solid model, as shown in Fig. 2.10b. Its functions are the same as the *NSC 3D Layout* windows.

2.1.2 Pumping Sources for Solar Pumped Lasers

A pumping source or simply source is a ray-emitting object in Zemax® that spreads rays at a predefined intensity, angle, and wavelength. A Zemax® model without a source object cannot do any ray tracing.

In solar-pumped laser modeling, only the surface-type sources used:

- Source Ellipse—An elliptical surface that emits light from a virtual source point.
- Source Rectangle—A rectangular surface that emits light from a virtual source point.

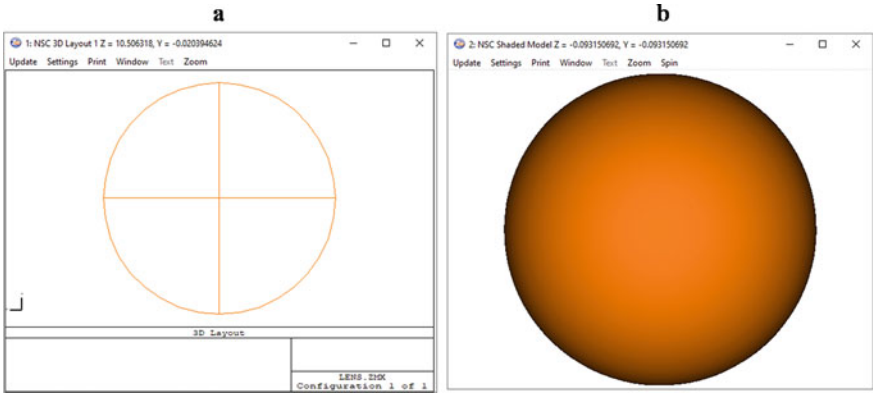

Fig. 2.10 A 10 mm radius sphere with its center at the origin point. **a** Is the *NSC 3D Layout* window and **b** is the *NSC Shaded Model* window

Common parameters used in all source objects

All source objects have the same parameters 1 through 5:

- Parameter 1—# Layout Rays: Defines the number of random rays launched from the source in the layout plots.
- Parameter 2—# Analysis Rays: Defines the number of random rays launched when performing ray tracing.
- Parameter 3—Power: The total power provided to the optical system. The source unit used is in the *General* dialog box under the *Units* tab. In solar-pumped laser, the source units are in Watts. The amount of power (W) calculated according to the size of the source, the solar irradiance, and the overlapped absorbed material with the solar spectrum, see Sect. 2.1.2.1 Source power.
- Parameter 4—Wavenumber: If the value is zero or empty, then the system randomly chooses a wavelength based on the weighting probability in the *Wavelength Data* dialog box. The source becomes monochromatic if any number is larger than 0, the number sets the wavelength emitted found in the *Wavelength Data* dialog box.
- Parameter 5—Color #: Changes the color of the drawing ray. If zero, then uses the system default color.

Source Ellipse

The *Source Ellipse* is a flat elliptical (and optionally annular) surface. The rays launched lie on the surface of the ellipse with a uniform distribution. The distribution of the ray direction follows a Gaussian distribution from the following Eq. (2.2):

$$I(l, m) \approx I_0 e^{-(G_x l^2 + G_y m^2)} \tag{2.2}$$

where l and m are the direction cosine of the rays in the X and Y axis direction and G_x and G_y are constants. This form defines a far-field pattern that is different in the X or Y directions. The larger G_x and G_y are, the narrower the distribution. If both G_x and G_y are zero, then all rays will emit from a virtual point source as collimated light.

The values of G_x and G_y are in parameters 10 and 11 of the *Source Ellipse* object.

Source Rectangle

The *Source Rectangle* is a flat rectangular surface. The parameter of this object is identical to the *Source Ellipse.*

2.1.2.1 Source Power Calculation

Source power calculation for general use

The value of the source power (parameter 3) is dependent on the solar irradiance (I_s) and the effective collection area (A_{ef}). Equation (2.3) is the generic solar source power for the full solar broadband wavelength. For example, considering an elliptical source with an effective area of 1 m^2, irradiated by 1000 W/m^2 solar irradiance, then the power of the source is 1000 W.

$$Power = A_{ef} I_S \tag{2.3}$$

The calculated solar power for the source through Eq. (2.3) used solely for ray tracing if the whole solar spectrum used by the system, either through *Wavelength data* or *Spectrum file.*

Source power calculation for solar-pumped laser

For solar-pumped lasers, only a portion of the solar wavelength useful for the laser medium. A 22 set of wavelengths on the source configured to pump the absorption wavelength of Nd^{3+} from the Nd:YAG crystal, as shown in see Fig. 2.6. The source power of each laser material is recalculated through the amount of overlapping absorbing bands with the whole solar spectrum and the solar power provided from the effective source size at a constant solar irradiance.

Nd:YAG

In the case of Nd:YAG crystal, the amount of available energy is the overlapped solar energy with the absorption bands of Nd^{3+} ion ($\eta_{overlap,Nd^{3+}}$), which is roughly about 16% of the total solar power [2–4]. The associated energy transfer of Nd:YAG and the overlapped solar energy with Nd^{3+} ion described in Sect. 2.4.

$$P_{Nd:YAG} = A_{ef} I_S \eta_{overlap,Nd^{3+}} \tag{2.4}$$

Ce:Nd:YAG

The Ce:Nd:YAG crystal has both Nd^{3+} and Ce^{3+} ions that contribute directly and indirectly to the output of the 1064 nm laser, see Sect. 2.4. The Ce:Nd:YAG is remarkably similar to the Nd:YAG in many aspects, therefore the Nd:YAG crystal can be used as a preliminary substitute for Ce:Nd:YAG, changing only the amount of energy available for absorption at the source. In Zemax® ray tracing, two separate sources considered to pump the crystal.

The first source emits all the relevant overlapped wavelengths of the solar spectrum with the Nd^{3+} ion absorption spectrum, as well as the wavelength data that includes the Ce^{3+} quantum cutting down conversion of non-radiative transfer to Nd^{3+}. The simulated power of source 1 ($P_{source1}$) follows Eq. (2.5) [4].

$$P_{\text{source 1},Ce:Nd:YAG} = A_{ef} I_S \left(\eta_{overlap,Nd^{3+}} + \eta_{overlap,Ce^{3+}} \times \eta_{NR:Ce^{3+}\rightarrow Nd^{3+}}\right) \quad (2.5)$$

The $\eta_{overlap,Nd^{3+}}$ is the overlapped solar energy with the Nd^{3+} ion (~16%), $\eta_{overlap,Ce^{3+}}$ is the overlapped solar energy with the Ce^{3+} ion (~15.7%) and $\eta_{NR:Ce^{3+}\rightarrow Nd^{3+}}$ is the Ce^{3+} quantum cutting down conversion of non-radiative transfer to Nd^{3+} (~70%) [3–5].

The second source accounts for 30% of the absorbed energy by Ce^{3+} that was transferred radiatively to Nd^{3+} ($\eta_{R:Ce^{3+}\rightarrow Nd^{3+}}$), as shown in Eq. (2.6) [3–5].

$$P_{\text{source 2},Ce:Nd:YAG} = A_{ef} I_S \left(\eta_{overlap,Ce^{3+}} \times \eta_{R:Ce^{3+}\rightarrow Nd^{3+}}\right) \quad (2.6)$$

2.1.3 Objects for Solar-Pumped Laser

The solar-pumped laser modeling in Zemax® consists of various well-placed and optimized optical objects. The most used objects briefly described in Sect. 2.1.3.1 Zemax® objects. Imported custom-made CAD objects described in Sect. 2.1.3.2 Imported CAD objects. Section 2.1.1.3 Objects material defines the method of establishing the material for the object. Section 'Object Nesting Volumes and Surfaces' Object nesting refers to object nesting, the order of priority of objects within the NSC ray tracing.

2.1.3.1 Zemax® objects

Primary Concentrator

Large optical devices concentrate vast amounts of solar radiation onto a tight focal spot, see Chap. 3 (Fig. 2.11).

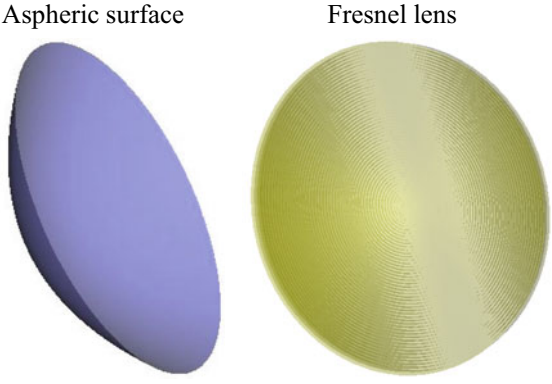

Fig. 2.11 Commonly used primary concentrator objects: *Aspheric surface* and *Fresnel lens*

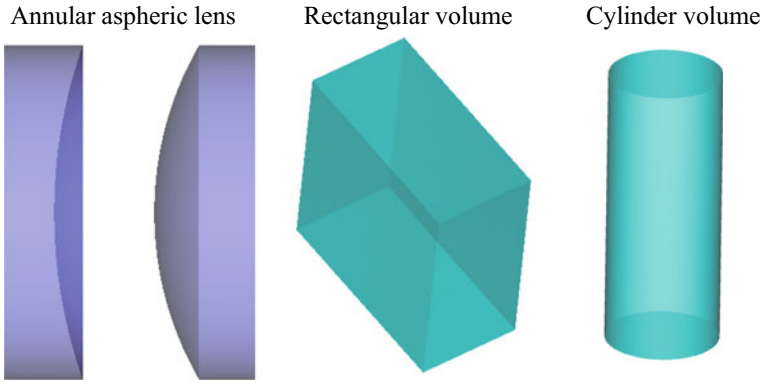

Fig. 2.12 Commonly used secondary concentrator objects: *annular aspheric* lens, *rectangular volume*, and *cylinder volume*

Aspheric Surface—This object commonly used as a parabolic mirror. See Sect. 5.1 Parabolic mirror.

Fresnel lens—A general radial symmetric or cylindrical solid Fresnel lens constructed by modeling the detailed faces of the Fresnel surface, see Sect. 5.2 Fresnel lens.

Secondary Concentrator

Optical devices that further concentrate or distribute the solar radiation of the primary concentrator to the active medium crystal. These optical objects made of fused silica (Fig. 2.12).

Annular Aspheric Lens—The *Annular aspheric lens* is an annular solid with a conic asphere with even aspheric polynomial terms. It further increases the concentration and reduce the size of the focusing solar radiation from the primary concentrator.

Rectangular volume—It used as an optical light guide to homogeneously distribute the focusing radiation onto the crystal. This object used as a body of water for cooling the active medium.

Cylinder volume—Used as a rod when both the front-end and back-end have the same radial size. The cylinder used as a light guide or an active medium. In form of solid cone used to designed as focusing light guide when the front-end radius is different from the back-end radius.

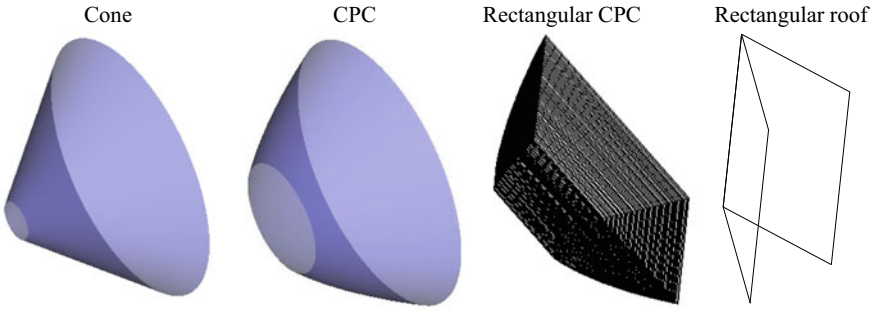

Fig. 2.13 Commonly used pumping cavity objects: *cone*, *CPC*, *rectangular CPC*, and *rectangular roof*

Pumping Cavity

Optical devices redirect the concentrated solar radiation into the crystal, achieving multiple reabsorptions of the energy into the crystal. These surface-type objects are mostly mirrors (Fig. 2.13).

Cone—A hollow conic and reflective cavity used as end-side-pumping, an active medium.

CPC and Rectangular CPC—Compound parabolic concentrators used to concentrate light entering one end to another end. This type of CPC is the same as the "Basic CPC" described in [6].

Rectangular roof—A reflective folding surface with controllable folding angles. Used as a side-pumping cavity to achieve reabsorption by reflecting any light into the active medium rod.

Others

Annulus—An elliptical surface used as a reflective ring (Fig. 2.14).

Rectangle and Ellipse—Used as folding mirrors or parts of an optical or mechanical apparatus.

Sphere—Used anywhere.

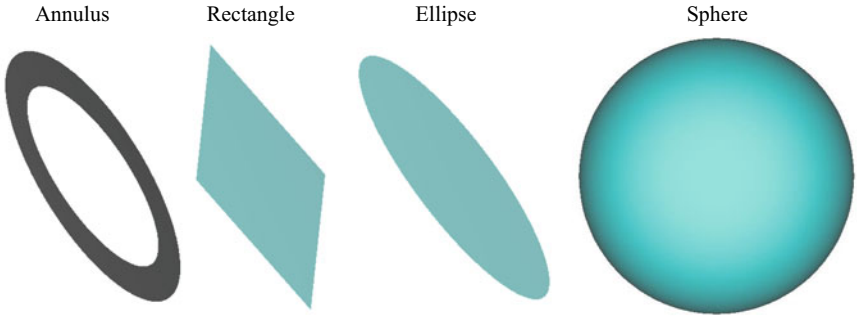

Fig. 2.14 Other useful objects: *annulus*, *rectangle*, *ellipse*, and *sphere*

2.1.3.2 Imported CAD Objects

Objects shapes not found in Zemax® objects database imported from other Computer Aid Designs (CAD) programs, such as Standard Triangle Language (STL), Initial Graphics Exchange Specification (IGES), Standard for the Exchange of Product Data (STEP) and Standard ACIS Text (SAT). Zemax® also accepts dynamically linked objects such as Autodesk Inventor™, Creo Parametric™, and SolidWorks®.

There are no limits on the shape, complexity, or number of objects imported and interacted with. Multiple objects imported in a single file. The imported object has a disadvantage in reducing ray tracing speed and it may lower ray tracing accuracy results.

The ray tracing accuracy of an imported CAD object depends on the complexity of its shape and the number of facets. For instance, an imported cylinder, if done correctly, would have the same optical accuracy as a native Zemax® cylinder object in ray tracing. Moreover, most CAD approximations are mostly suitable for mechanical designs, and not optimized for optical precision in ray tracing, where surfaces must be well known into tiny fractions due to the sensibility of ray wavelength into surface interaction.

Tip: To increase the accuracy of the ray tracing with an imported Autocad® object, it is advisable to export with the largest number of facets possible. This can be achieved by modifying the object polygon count to the maximum with the *Facetress* command.

Some CAD objects may automatically convert an imported object into a Zemax® Object Format (ZOF), a native file format easily recognizable by Zemax® and improves the simulation time. This newly converted object will have an extra extension of *.ZOF at the end of the original file name. For example, if the original file name is Object.IGES then becomes an Object.IGES.ZOF. An imported CAD object in Zemax® used as any other object type.

- CAD Part: STEP/IGES/SAT—Uses imported CAD objects in IGES, STEP, and SAT format. The imported file will automatically convert into a ZOF (Zemax®'s native format).
- CAD Part: STL—The STL object is an open-ended user-defined object. It defines an open polygon surface or a closed polygon volume such as a prism or other solid. The STL Object format is based on a collection of 3D triangles. This format supported by mechanical CAD programs. There are no fixed limits to the total number of vertices or polygons imported.

2.1.4 Detectors for Ray-Tracing Analysis

The detector object stores data. The qualitative data stored in the detector depends on the number of rays that touches its surface. The detector can be reflective, transparent, or absorbing, as in *MIRROR*, blank, or *ABSORB*, respectively. Each detector types offers unique analysis and functions. In this book, there are only two types of detectors used in solar-pumped lasers:

2.1.4.1 2D Detectors

Detector Rectangle

The detector rectangle object stores energy data from rays that strike or pass through it. The resulting data distributions viewed for incoherent light in spatial or angular domains, spatially coherent irradiance or phase, or coherent irradiance as a point spread function.

2.1.4.2 3D Detectors

Detector Volume

The amount of energy stored in each voxel depends on the material absorbance (Transmission data, Sect. 1.1.4 Glass catalog dialog box and Glass table). The resulting data distributions viewed as incident flux, absorbed flux, or absorbed flux per unit volume. Detector volumes may be transparent or be any valid glass material. Detector volumes may also be nested within or straddled with other objects. The *Detector Volume* object shaped like a box, with its origin point at its center.

Note: In solar-pumped laser modeling, the laser crystal rod nested ***inside*** of a water *Detector Volume*.

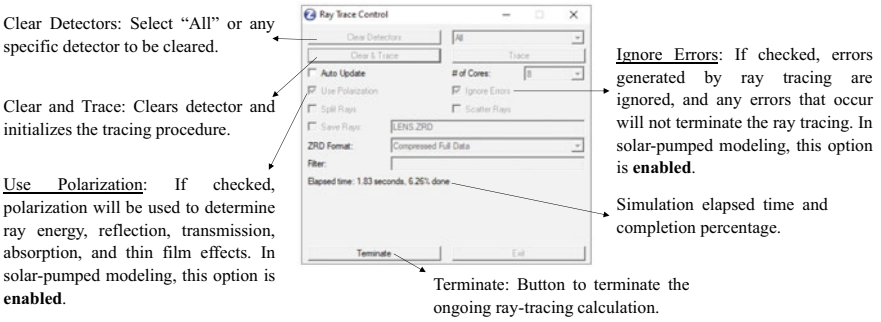
Clear Detectors: Select "All" or any specific detector to be cleared.
Clear and Trace: Clears detector and initializes the tracing procedure.
Use Polarization: If checked, polarization will be used to determine ray energy, reflection, transmission, absorption, and thin film effects. In solar-pumped modeling, this option is enabled.
Ray Trace Control
Clear Detectors
All
Clear & Trace
Trace
Auto Update
# of Cores:
Use Polarization
Ignore Errors
Split Rays
Scatter Rays
Save Rays:
LENS.ZRD
ZRD Format:
Compressed Full Data
Filter:
Elapsed time: 1.83 seconds. 6.26% done
Terminate
Exit
Ignore Errors: If checked, errors generated by ray tracing are ignored, and any errors that occur will not terminate the ray tracing. In solar-pumped modeling, this option is enabled.
Simulation elapsed time and completion percentage.
Terminate: Button to terminate the ongoing ray-tracing calculation.

Fig. 2.15 *Ray trace control* dialog box

2.1.4.3 Objects as Detectors

Some objects have the options to become a detector. Flat-surfaced objects such as polygons, imported objects, and rectangular volume objects used as detectors. Curved surfaced or "round" solids that use rendering as resolution settings, such as the aspheric surface, toroidal lens, biconic lens, and other complex shapes, also serve as a detector. Enabling "Object is a detector" in the object properties turns the object into a detector. The ray tracing results extracted and viewed only in text form. See Sect. 2.1.5.2 Post-ray tracing: Detector Viewer.

2.1.5 Raytracing

2.1.5.1 Ray Trace Control

The *Ray Trace Control* dialog box used to initialize ray tracing analysis. The controls within this dialog box are shown in Fig. 2.15.

Note: The ray tracing session should start with all the detectors cleared.
If the ray tracing calculation terminated during tracing, then a new ray tracing must start with all detectors cleared.

2.1.5.2 Post-ray Tracing: Detector Viewer

The *Detector Viewer* is a window that displays data of a detector in either a graphic or text format. This window accessed at the *Main Menu* → *Analysis* → *Ray Tracing* → *Detector Viewer*. Figure 2.16 shows the *Detector Viewer* window in Incoherent Irradiance after raytracing. Each pixel in the graph corresponds to an intensity color value. The bottom part of the detector viewer shows the information and summary of the detector, such as the detector object number (in this case, the 20th object), the size of the detector, the number of pixels per axis, the total number of rays hit, the peak irradiance and the accumulative total power.

Detector Viewer controls

Right-clicking on the *Detector viewer* window, or clicking on "Settings", a *Detector Viewer* dialog box will appear.

- Show As: Set the display method in the Detector Viewer. Choose a greyscale or false color display, or cross-section plot of rows or columns.
- Z-Plane: Applicable only for detector volume. The Z-Plane selects which cross-section of a volume detector to display. The number of Z-Planes in a detector volume is set by the number of voxels in the Z direction. Pressing the left and right arrow keys while viewing detector volume data will cycle through all the Z-Planes.
- Show Data: determines type of displayed data.
  For 2D detectors:
  - Incoherent irradiance: Incoherent power per area as a function of spatial position on the detector.
  - Coherent Irradiance: Coherent power per area as a function of spatial position on the detector.

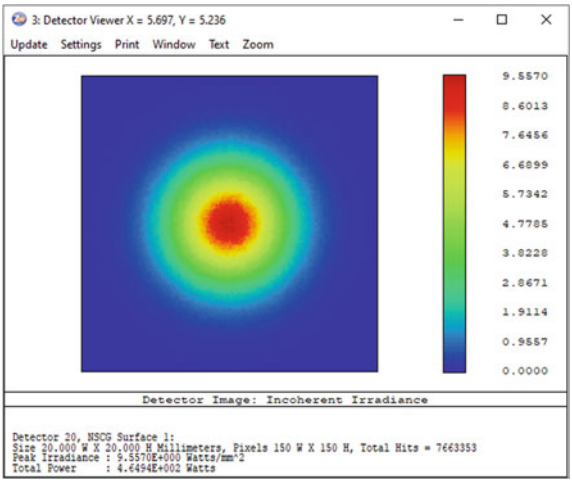

Fig. 2.16 *Detector viewer* window

– Coherent Phase: The phase angle of the complex amplitude sum used in Coherent Irradiance.
– Radiant Intensity: The power per solid angle in steradians as a function of incident angle upon the detector.
– Radiance (Position Space): The power per area per solid angle in steradians as a function of spatial position on the detector.
– Flux vs. Wavelength: For detector color objects, the spectral distribution of the flux incident on the detector. The plot will be shown as a bar chart or point-crosses if the bar char is not enabled, as shown in Fig. 2.7b.

For 3D detectors:

– Incident Flux: The incident flux is the flux entering each voxel, measured in source units (watts, lumens, or joules).
– Absorbed Flux: The absorbed flux is the flux absorbed within each voxel, measured in source units (watts, lumens, or joules).
– Absorbed Flux/Volume: The absorbed flux/volume is the flux absorbed within each voxel, measured in source units (watts, lumens, or joules) per unit volume measured in cubic lens units.
– Minimum and maximum Plot Scale: Define the absolute minimum and maximum of the shown data. If these values are both zero, it applies the default scaling.

Detector Viewer Text window

Clicking the "Text" button on the menu in the *Detector Viewer* window in Fig. 2.16 will opens a new text-based window shown in Fig. 2.17a. The text *Detector Viewer* shows all the relevant information related to the detector, such as the size, the position, and the type of power on each pixel or voxel, depending on the option chosen in "Show Data".

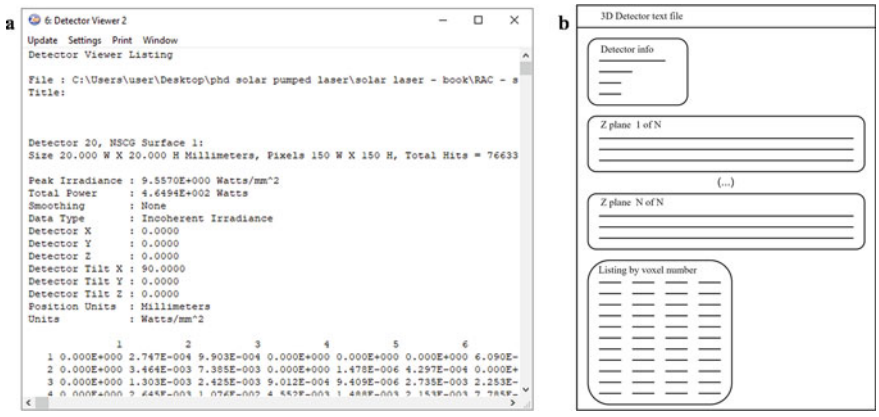
a
6: Detector Viewer 2
Update Settings Print Window
Detector Viewer Listing
File : C:\Users\user\Desktop\phd solar pumped laser\solar laser - book\RAC - s
Title:
Detector 20, NSCG Surface 1:
Size 20.000 W X 20.000 H Millimeters, Pixels 150 W X 150 H, Total Hits = 76633
Peak Irradiance : 9.5570E+000 Watts/mm^2
Total Power : 4.6494E+002 Watts
Smoothing : None
Data Type : Incoherent Irradiance
Detector X : 0.0000
Detector Y : 0.0000
Detector Z : 0.0000
Detector Tilt X : 90.0000
Detector Tilt Y : 0.0000
Detector Tilt Z : 0.0000
Position Units : Millimeters
Units : Watts/mm^2
1 2 3 4 5 6
1 0.000E+000 2.747E-004 9.903E-004 0.000E+000 0.000E+000 0.000E+000 6.090E-
2 0.000E+000 3.464E-003 7.385E-003 0.000E+000 1.478E-006 4.297E-004 0.000E+
3 0.000E+000 1.303E-003 2.425E-003 9.012E-004 9.409E-006 2.735E-003 2.253E-
b
3D Detector text file
Detector info
Z plane 1 of N
(...)
Z plane N of N
Listing by voxel number

Fig. 2.17 **a** Is the text-based *detector viewer*. **b** Is the 3D detector text file structure

The data shown in text mode depends on the type of detector used:

- Two-dimension detector: Pixel data listed into a two-dimensional x–y matrix.
- The three-dimension detector: Voxel data listing is like a two-dimension detector, with a two-dimension x–y matrix listed in each z layer, and a list of voxels sorted by coordinates, as shown in Fig. 2.17b.
- Imported object as a detector: The pixelation data have the same order of sequence as the drawing coordinate sequence of the imported object.

Any text-based *Detector Viewer* saved into a text file from *Window* → *Save Text*. The detector text file used as an intermediate file for importing into other software. A three-dimensional detector text file required to load into LASCAD™ as a thermally loaded crystal and then used for calculating the laser power.

Important Note: Some software may only accept some type of text encoding architecture. LASCAD™ only accepts ANSI file encoding architecture, while ANSYS™ and other more advanced software can accept both ANSI and Unicode encoding architecture. In the Zemax® *Main Menu* → *File* → *Preference…* → *Miscellaneous (tab)* has the option to change the encoding architecture.

2.2 Evaluation of Solid-State Laser Output Performance by LASCAD™ Software

This chapter introduces the necessary knowledge to calculate the laser power and the conditions to attain multi-mode and single-mode (TEM_{00}) laser through LASCAD™, a laser cavity modeling software. The reader will be familiarized with the LASCAD™ UI and learn its basic operations.

LASCAD™ software allows the combination of simulation algorithms to optimize the laser resonator design: thermal and structural Finite Element Analysis (FEA); the ABCD Gaussian Beam Propagation Code; and the propagation algorithm of non-Gaussian beams—the Beam Propagation Method (BPM). It models resonant cavities through the analysis of the thermal lensing effects; multimode and TEM_{00} mode output power and laser efficiency; laser beam quality and its respective profile, as well as laser beam propagation outside the laser cavity, by considering laser parameters, such as reflectivity, the radius of curvature and distance between cavity components, diffraction losses, gain saturation, etc.

2.2.1 Starting the Program

Starting LASCAD™ prompts a directory dialog box to select the working directory. Then a *New Project* dialog box will show options for the Standing Wave Resonator, Ring Resonator, and External Beam options for this type of simulation. In solar-pumped laser research, only uses the option of **Standing Wave Resonator**, then selects the number of face elements either **3** (for end-pump) or **4** (for side-pump).

Three new windows will then appear. The *Main menu* window with the project name appears at the top of the screen, a *Standing Wave Resonator* window in the middle of the screen, then lastly the *Parameter Field* window occupies the bottom of the screen.

Any existing saved LASCAD™ project file *.LCD loaded and started directly by double-clicking on it.

2.2.2 LASCAD™ Windows

2.2.2.1 Standing Wave Resonator Window

The *Standing Wave Resonator* window represents the laser cavity, as shown in Fig. 2.18a. This shows a single window with a black background with green horizontal lines (mode plot). If astigmatism configured in the *Miscellaneous* tab in the *Parameter Field* window, then the *Standing Wave Resonator* window would present two mode plots, with the upper box in the x–z-plane, and the lower one in the y–z-plane, respectively.

The optical elements represented in vertical white lines with the center-numbered box as the number of that element. The y-axis value shows the maximum calculated spot size within the cavity. The x-axis value shows the distance between each optical element within the resonant cavity. The distance edited at the "distance (mm)" row at the *Parameter Field* window (Fig. 2.18).

The optical elements represented by vertical lines within the mode plot represented by three types of elements, identified by triangular symbols.

- Mirrors: Filled rectangular triangles.
- Dielectric interfaces: Open rectangular triangles.
- Lenses: Filled isosceles triangles.

2.2.2.2 Parameter Field Window

The *Parameter Field* window controls the aspects of the laser cavity, as shown in Fig. 2.8. It controls the RoC (radius of curvature) of each element in both *x-Plane Param.* and *y-Plane Param.* tabs; define the size of the element in the *Apertures* tab;

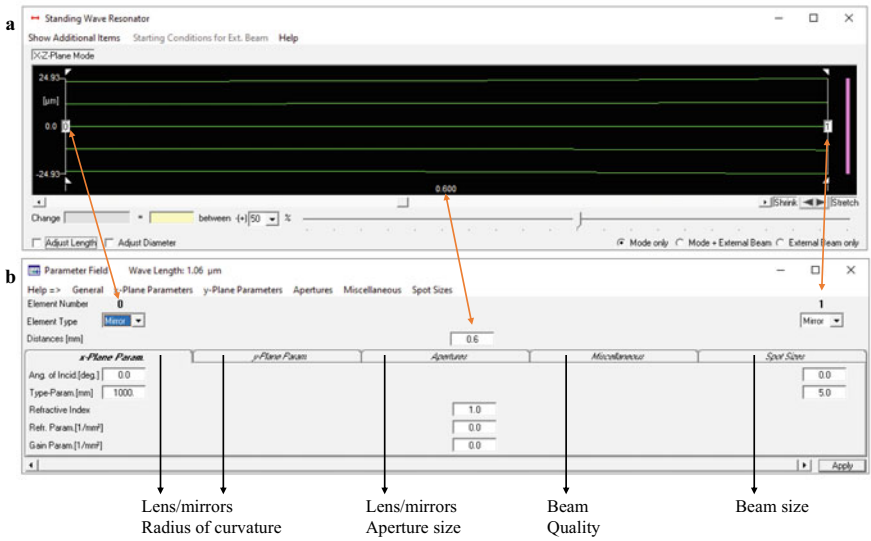

Fig. 2.18 **a** Is the *standing wave resonator* window and **b** is the *parameter field* window

define/consult the output beam quality for both the x and y axis in the *Miscellaneous* tab; consult the beam size of any element in the *Spot Sizes* tab.

2.2.3 Crystal, Pump Beam, and Material Parameter Window

LASCAD™ uses Finite Element Analysis (FEA) to compute the temperature distribution, deformation, and stress of a thermally loaded crystal. The dimension of the crystal defined by the imported thermally loaded crystal data from Zemax® in form of a text file as mentioned in Sect. 2.1.5 Raytracing. A 3D visualization of the thermally loaded crystal later shown in Sect. 2.2.5.2 3D Visualizer.

The *Crystal, Pump Beam, and Material Parameters* window or FEA window accessed through the *Main menu* → *FEA* → *FEA/Parameter Input & Start of FEA Code*, as shown in Fig. 2.19.

This dialog box consists of six accessible tabs *Models*, *Pump Light*, *Boundaries*, and *Mat. Param*, *Doping and Mats,* and *FEA Options*.

Each tab serves as input conditions for FEA calculation for a single thermally loaded crystal and filled according to the physical conditions of the laser system to get an accurate numerical calculation.

"Apply and Run FEA" Button

Clicking on the "Apply and Run FEA" button for the first time, without defining the FEA output directory, will prompt a window to save the FEA calculation directory. It

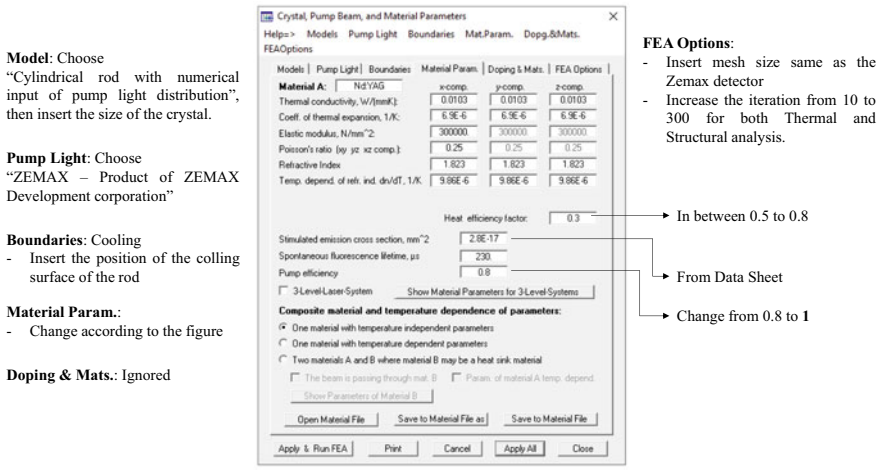
Model: Choose "Cylindrical rod with numerical input of pump light distribution", then insert the size of the crystal.
Pump Light: Choose "ZEMAX – Product of ZEMAX Development corporation"
Boundaries: Cooling
- Insert the position of the colling surface of the rod
Material Param.:
- Change according to the figure
Doping & Mats.: Ignored
Crystal, Pump Beam, and Material Parameters
Help=> Models Pump Light Boundaries Mat.Param. Dopg.&Mats. FEAOptions
Models | Pump Light | Boundaries | Material Param. | Doping & Mats. | FEA Options
Material A: Nd:YAG
x-comp. y-comp. z-comp.
Thermal conductivity, W/(mK):
Coeff. of thermal expansion, 1/K:
Elastic modulus, N/mm^2:
Poisson's ratio (xy yz xz comp.):
Refractive Index
Temp. depend. of refr. ind. dn/dT, 1/K
Heat efficiency factor:
Stimulated emission cross section, mm^2:
Spontaneous fluorescence lifetime, µs:
Pump efficiency:
3-Level-Laser-System
Show Material Parameters for 3-Level-Systems
Composite material and temperature dependence of parameters:
One material with temperature independent parameters
One material with temperature dependent parameters
Two materials A and B where material B may be a heat sink material
The beam is passing through mat. B
Param. of material A temp. depend.
Show Parameters of Material B
Open Material File
Save to Material File as
Save to Material File
Apply & Run FEA
Print
Cancel
Apply All
Close
FEA Options:
- Insert mesh size same as the Zemax detector
- Increase the iteration from 10 to 300 for both Thermal and Structural analysis.
In between 0.5 to 0.8
From Data Sheet
Change from 0.8 to **1**

Fig. 2.19 *Crystal, pump beam, and material parameters* window

is advisable to save within the same directory as the working LASCAD™ file. FEA output files written in text file format.

After clicking on "Apply and Run FEA", it prompts a directory window to select the Zemax®'s detector data file. When the FEA calculation starts, a loading *Finite Element Analysis* dialog box will then pop up showing computational progress. During FEA calculation, it shows the iteration number, the maximum thermal analysis value, or the value of the maximum nodal displacement for the structural analysis. The "Skip" button stops the iteration process and finishes the numerical computation of thermal or structural analysis. A "FEA finished successfully!" message appears when the last iteration computation of structural analysis is complete.

2.2.4 Analysis of Thermal Lensing Effects by FEA

2.2.4.1 2D Data Profiles and Parabolic Fit

This window accessed from the *Main menu → FEA → 2D data profiles & parabolic fit*. A directory window will then ask to load a "*FEA_x_y.out*" file, i.e., the FEA output files from the previous subsection.

The window *2D data profiles & parabolic fit* shown in Fig. 2.20. Each 2D profile has a single curved blue line, which represents the loaded FEA data. The x-axis is the same size as the crystal rod diameter and the y-axis changes depending on the selection of the Show Profile.

After clicking on the "Refresh and Fit" button, a small yellow instruction dialog box will then prompt to remind the user to insert the calculated thermally loaded

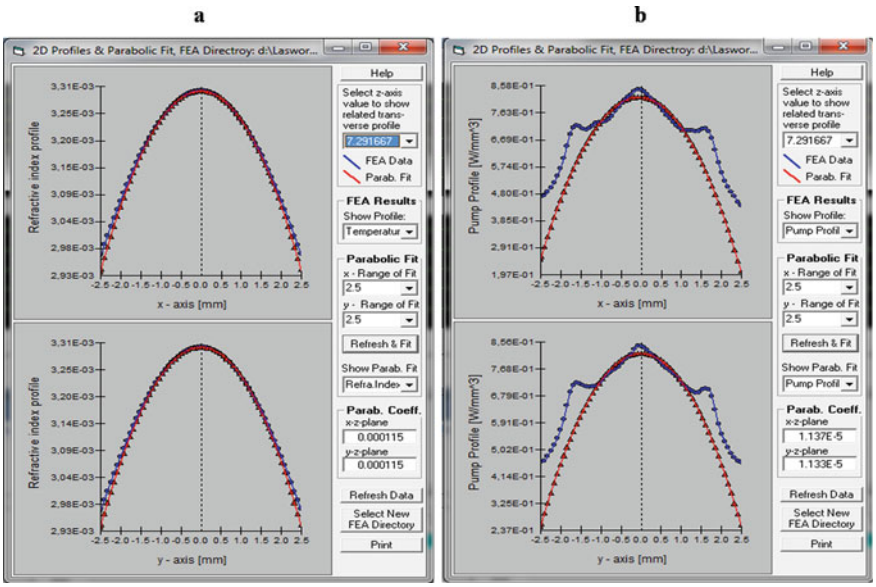

Fig. 2.20 *2D profiles and parabolic fit* windows. **a** Temperature fitting. **b** Pump profile fitting

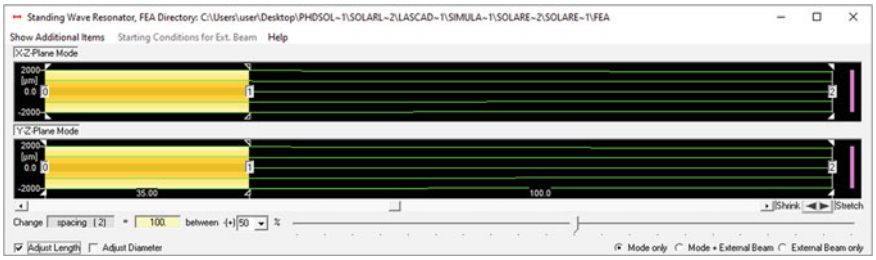

Fig. 2.21 *Standing wave resonator* windows after inserting the thermally loaded crystal (orange) between elements 0 and 1. The end-pump resonant cavity is defined by three elements: coated mirror (element 0), a dielectric interface (element 1), and an output mirror (element 2)

crystal in the *Standing Wave Resonator* window in between two elements by pressing both the ALT key and left-clicking with the mouse. A yellow-colored thermal lens (thermally loaded crystal) will add to the plot, as shown in Fig. 2.21. The inserted crystal automatically changes the diameter for both elements and sets its distance based on its length in the *Parameter Field* window.

Note: The old thermal lens in the *Standing Wave Resonator* window must be cleared beforehand, by pressing the CTRL key and clicking with the left mouse button on the thermally loaded crystal.

2.2.4.2 3D Visualizer

The LASCAD™ *3D Visualizer* window, as shown in Fig. 2.22, accessed after the FEA simulation at any time by selecting the *View* option in the LASCAD™ *Main menu* window. Various physical representations of thermally loaded crystal in terms of heat load, temperature, stress intensity, structural deformation, and absorption is changeable in the *View* menu.

2.2.5 *Laser Beam Analysis by Beam Propagation Method (BPM)*

The beam propagation method (BPM) is an alternative approximation that takes full advantage of the 3D distribution of the refractive index and the structural deformation obtained from the FEA by considering the physical optics code, based on FFT (Fast Fourier Transform). Unlike ABCD-based optical coding, the BPM does not consider

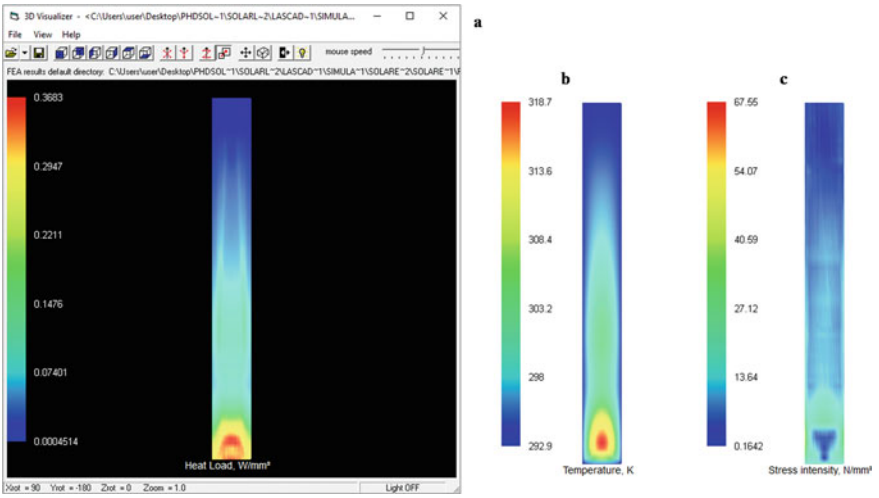

Fig. 2.22 **a** Heat load of the thermally loaded crystal in *3D visualizer* window. **b** Is the temperature and **c** is the stress intensity of the thermally loaded crystal

parabolic approximation. This method takes wavefront propagation through each FEA crystal layer. The cavity configuration shaped by the Gaussian algorithm (at the *Parameter Field* window), and it used as an input for BPM. The beam profile is computed using an iterative computation of the Fox and Li round-trip procedure that involves a more complex computation method [7]. The iterative process shows the convergence of the theoretical approximated spot size generated in the cavity. Simultaneously, a 3D graphical representation of the intensity distribution windows in the output-coupling mirror after each round-trip. At the end of a single iteration process, it displays the phase profile.

2.2.5.1 BPM Computation Parameters

The Beam Propagation Method dialog box (Fig. 2.23) accessed from the *Main menu* → *BPM* → *Run BPM*.

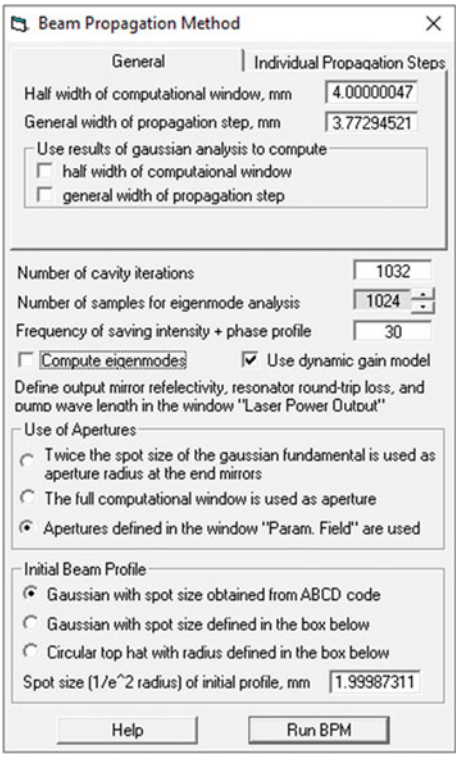
Beam Propagation Method
General
Individual Propagation Steps
Half width of computational window, mm
4.00000047
General width of propagation step, mm
3.77294521
Use results of gaussian analysis to compute
half width of computaional window
general width of propagation step
Number of cavity iterations
1032
Number of samples for eigenmode analysis
1024
Frequency of saving intensity + phase profile
30
Compute eigenmodes
Use dynamic gain model
Define output mirror refelectivity, resonator round-trip loss, and pump wave length in the window "Laser Power Output"
Use of Apertures
Twice the spot size of the gaussian fundamental is used as aperture radius at the end mirrors
The full computational window is used as aperture
Apertures defined in the window "Param. Field" are used
Initial Beam Profile
Gaussian with spot size obtained from ABCD code
Gaussian with spot size defined in the box below
Circular top hat with radius defined in the box below
Spot size (1/e^2 radius) of initial profile, mm
1.99987311
Help
Run BPM

Fig. 2.23 *Beam propagation method* window

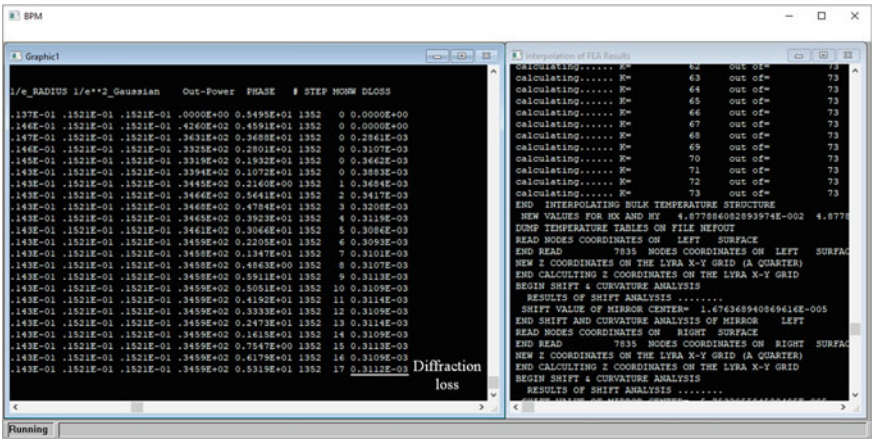

Fig. 2.24 *BPM* window with child window of *graphic1* and *interpolation of FEA Results*. The most recent diffraction loss value is needed for the round-trip loss calculation in Eq. (2.7)

"Run BPM" Button

A large BPM window housing two child command prompt windows should appear, as shown in Fig. 2.24. One of the child windows is *Graphic1* (BPM Output), which shows and records the progress of the Fox and Li type iteration. The other child window for *Interpolation of FEA Results* records the progress of interpolation.

After the first Fox and Li iteration is completed, two additional graphical windows will then appear, showing the convergence of laser beam radius with cavity iteration (Sect. 2.2.5.2 Convergence of laser beam radius with cavity iteration), and the beam profile at the right mirror (Sect. 2.2.5.3 Laser beam profile on the right end mirror).

2.2.5.2 Convergence of Laser Beam Radius with Cavity Iteration Window

The *convergence of laser beam radius at the cavity iteration* window appears after a single Fox and Li iteration, as shown in Fig. 2.25, with the x-axis as the cavity iteration and the y-axis as the spot size of in micrometer. The y-axis information can be switched from radius at $1/e^2$ or 1/e with the option control below the graph. The input text box can change the accuracy of the graph at box axes, respectively.

2.2.5.3 Laser Beam Profile on the Right End Mirror

The *Intensity Profile on the Transversal Plane—Compaq Array Viewer* window shows the laser beam intensity profile at the right end mirror (Fig. 2.26). The plot

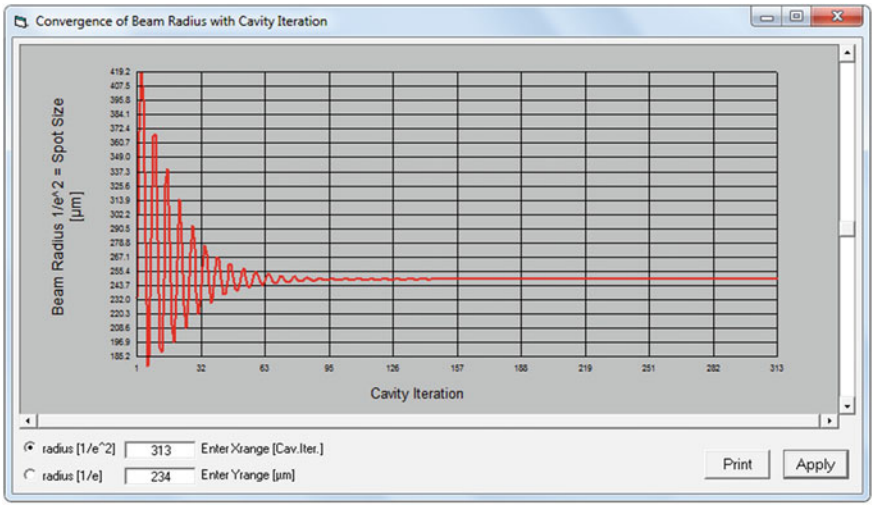

Fig. 2.25 *Convergence of beam radius with cavity iteration* windows of 250 µm spot size at 313th cavity iteration

refreshes each cavity iteration. The BPM menu item "View/Intensity along beam path" shows the intensity distribution along the resonator axis and x-axis.

2.2.6 Computation of Laser Output Power and Beam Quality

The *Laser Power Output* window (Fig. 2.27) accessed from the LASCAD™ *Main* window.

The top side of the window defines the lasing parameter of the cavity, such as the reflectivity of the output mirror, the percentage of a complete resonator round-trip loss, the pumping wavelength, and the absorbed pump power.

The complete resonator round-trip loss follows Eq. (2.7), see Sect. 2.3

$$\text{Round trip loss } (\%) = 2\alpha L + \gamma + D_{loss} \tag{2.7}$$

where the α is the absorption and scattering coefficient, L is rod length. γ is the miscellaneous losses accounting the imperfect optical 1064 nm coating losses of both laser rod end-faces and HR mirrors and D_{loss} is the diffraction loss found in the BPM computational calculation at the right-most column, as shown in Fig. 2.24. For Nd:YAG crystal, the α_s is typically 0.002 cm^{-1} (or 0.2%) and I_{mp} is about 0.004 (or 0.4%).

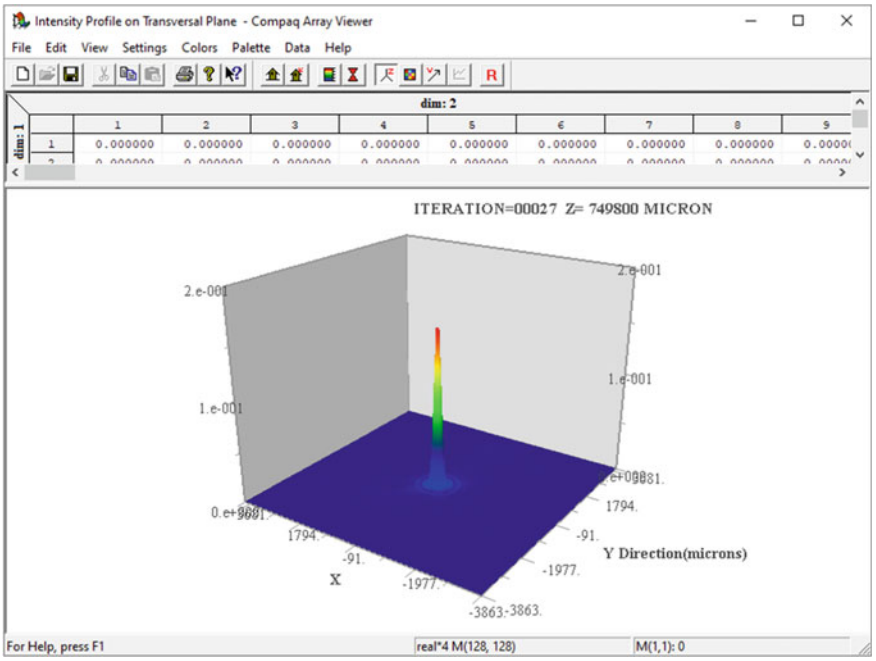

Fig. 2.26 *Intensity profiled on transversal plane—compaq array viewer* window at 27th iteration

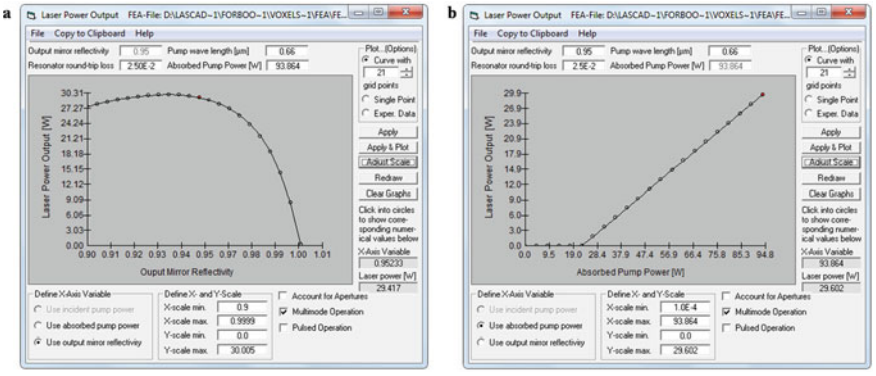

Fig. 2.27 *Laser power output* window. **a** Laser output power in function of output mirror reflectivity, and **b** laser output power in function of absorbed pump power

2.3 Examples of Numerical Solar Pumped Lasers Design: Side-Pumped Solar Laser

This section will use the "Side-pumped continuous-wave Nd:YAG solar laser with 5.4% slope efficiency" by Liang et al. [8] as an example of how to calculate the multimode laser output power.

Section 2.3.1 Zemax® will establish the necessary NSC objects to model the solar concentrating system and the associated laser head based on the publication, as shown in Fig. 2.28. Then in Sect. 2.3.2 LASCAD shows the step-by-step procedure to calculate the laser output.

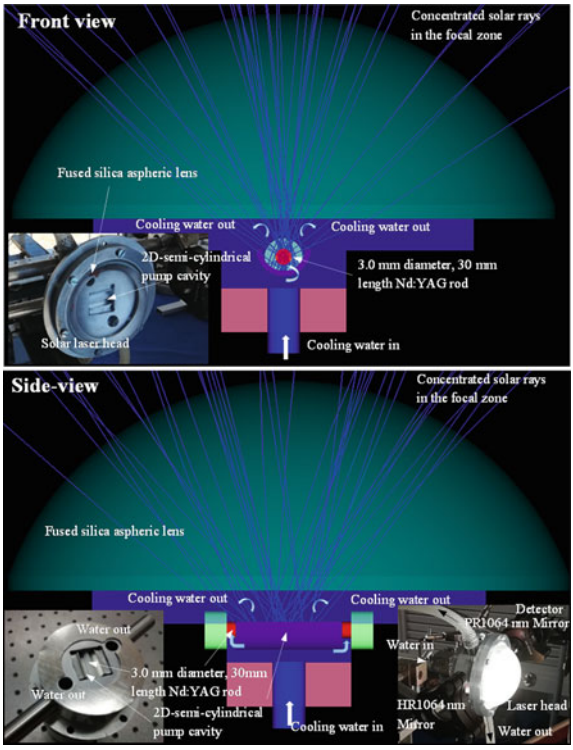

Fig. 2.28 Front and side views of the solar laser head, showing the water-cooling scheme for the laser rod through the space between the fused silica aspheric lens and the two-dimensional semi-cylindrical pump cavity. Inset photos on the left show the mechanical design details of the solar laser head. The inset photo on the right shows the external resonant laser cavity and solar laser head being pumped at the focus of the parabolic mirror [8]

2.3.1 *Zemax*®

According to the published article, the concentrating system pumped by the NOVA stationary heliostat-parabolic mirror with a 1.16 m diameter parabolic mirror and only 0.9 m^2 effective solar collection area accounted for pumping the laser head (discounted 0.15 m^2 of the shadow area caused laser head and its supporting structure). The combined reflectivity of both the parabolic mirror and the heliostat mirror was about 74.8%. The measured local solar irradiance at that time was around 700 W/m^2.

The laser head has consisted of a secondary concentrator of 40 mm diameter fused silica with 44 mm radius of curvature, −0.002 of the first order of even aspheric coefficient, and 32 mm of thickness; running cooling water separates the fused silica lens with the crystal rod with 6 mm in depth was needed for water circulation; the Nd:YAG crystal rod of 3 mm diameter and 30 mm length was fixed at both ends by two mechanical fixture, seizing 3 mm of the rod at both ends; an optimized sized and high reflective sized toroidal mirror of 4.5 mm diameter was positioned 3 mm below the crystal rod, enabling reabsorption of the transmitted rays and reflect any missed solar rays into the crystal.

Zemax®: Non-sequential Component Editor

A Fig. 2.29a shows the necessary objects to model this solar-pumped laser system, as well as the correct object's nesting order. Figure 2.29b shows the resulting layout.

A Fig. 2.30 shows the position of each object in the NSC editor. The x, y, and z-axis positions of each object offset to have its center at the origin. The bulk of objects 4–11 is referenced in object 3, using the object's 3 coordinates and rotation as reference. Object's 3 "Y Position" is set as a variable (V), this markup serves as an indicator for optimizing the laser output in the function of the laser head position on the Y-axis. **Note**: The center of the crystal/detector is at the origin point Fig. 2.30.

Information: Solve type variable (V). The value of a solve type variable parameter changes dynamically with the Zemax® optimization function (not covered

a

	Object Type	Comment	Ref Object		Material
1	Source Ellipse	Nd absorption spectrum	0		-
2	Aspheric Surface	Primary concentrator	0		MIRROR
3	Null Object	Move laser head reference	0		-
4	Annular Aspheric Lens	Fused silica aspheric lens	3		SILICA
5	Rectangular Volume	Cooling water lens surf	3		WATER
6	Rectangular Volume	Cooling water cavity	3		WATER
7	Cylinder Volume	Fixture	3		MIRROR
8	Cylinder Volume	Fixture	3		MIRROR
9	Rect. Torus Volume	Torus mirror	3		MIRROR
10	Detector Volume	Detector	3		WATER
11	Cylinder Volume	NdYAG rod	3		NDYAG

b

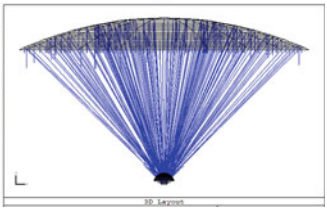

Fig. 2.29 **a** List of objects in the *NSC editor* window for modeling the side-pumped solar laser and **b** the resulting layout

	Object Type	Ref Object	Inside Of	X Position	Y Position	Z Position	Tilt About X	Tilt About Y	Tilt About Z
1	Source Ellipse	0	0	0.000	520.000	0.000	-90.000	0.000	0.000
2	Aspheric Surface	0	0	0.000	660.000	0.000	90.000	0.000	0.000
3	Null Object	0	0	0.000	0.000 V	0.000	0.000	0.000	0.000
4	Annular Aspheric Lens	3	0	0.000	7.500	0.000	-90.000	0.000	0.000
5	Rectangular Volume	3	0	0.000	7.500	0.000	90.000	0.000	0.000
6	Rectangular Volume	3	0	0.000	1.500	0.000	90.000	0.000	0.000
7	Cylinder Volume	3	0	0.000	0.000	12.000	0.000	0.000	0.000
8	Cylinder Volume	3	0	0.000	0.000	-15.000	0.000	0.000	0.000
9	Rect. Torus Volume	3	0	0.000	1.500	0.000	-90.000	0.000	0.000
10	Detector Volume	3	0	0.000	0.000	0.000	0.000	0.000	0.000
11	Cylinder Volume	3	0	0.000	0.000	-15.000	0.000	0.000	0.000

Fig. 2.30 Positions of objects in the NSC editor

in this book). A common practice to use the "V" to mark the parameter most likely to be changed.

Figure 2.31a shows the rest of the parameters used for all objects in the *NSC editor* window and Fig. 2.31b shows the resulting layout of the laser head.

Information: Solve type variable (P) for pick up. The parameter marked with a (P) outputs a modified (or copied) numerical value of a target numerical value of a cell.

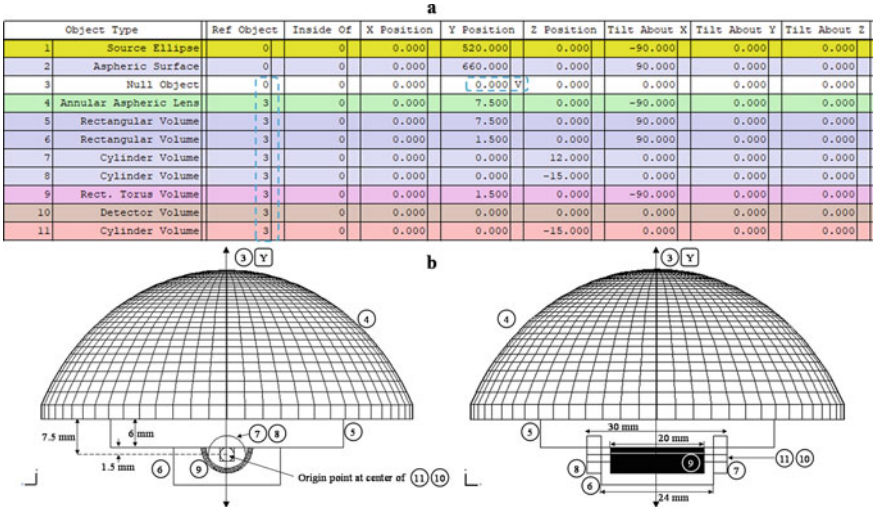

Fig. 2.31 **a** Objects parameters in NSC editor. **b** Laser head layout

The numerical value with the pickup condition changes according to Eq. (2.8).

$$\text{Output parameter value} = \text{Target parameter value} \times \text{scale factor} + \text{offset} \tag{2.8}$$

Object description:

Object 1: solar source (Nd^{3+} absorption spectrum)			
Object type	Power (W)	X/Y half width (mm)	Gauss G_x/G_y
Source ellipse	100.8[a]	580/580	32,000/32,000

[a] The power is calculated from Eq. (2.4) in Sect. 2.1.2.1 Source power. ($P = 0.9 \times 700 \times 0.16 = 100.8$ W). *Note* According to the journal article, the effective area is 0.9 m^2

Object 2: parabolic concentrator				
Object type	Material	Radius of curvature (mm)	Conic	Max/min aper (mm)
Aspheric surface	Mirror (I.25)[a]	1320[b]	−1	580/0

[a] Combined reflectivity of the parabolic mirror and the heliostat of 74.8%
[b] The focal length (Y Position) is exactly half the value of the Radius of curvature

Object 4: aspheric lens					
Object type	Material	Maximum front/back aperture (mm)	Rear radius of curvature (mm)	Thickness (mm)	Rear r^2
Annular aspheric lens	Silica	40/40	−44	32	−0.002

Objects 5 and 6: cooling water				
Object type	Material	X1/Y1 half width (mm)	Z length (mm)	X2/Y2 half width (mm)
Rectangular volume	Water	25/25	6[a]	25/25
Rectangular volume	Water	12/12	8	12/12

[a] The water depth: distance between silica and crystal rod

Objects 7 and 8: fixture-crystal holder				
Object type	Material	Front R (mm)	Z length (mm)	Back R (mm)
Cylinder volume	Mirror (I.06)[a]	4	3[b]	4

[a] High reflective silver-coated aluminum foil sheet
[b] The crystal rod held tightly at each side by 3 mm. *Note* 6 mm out of 30 mm length rod is not pumped

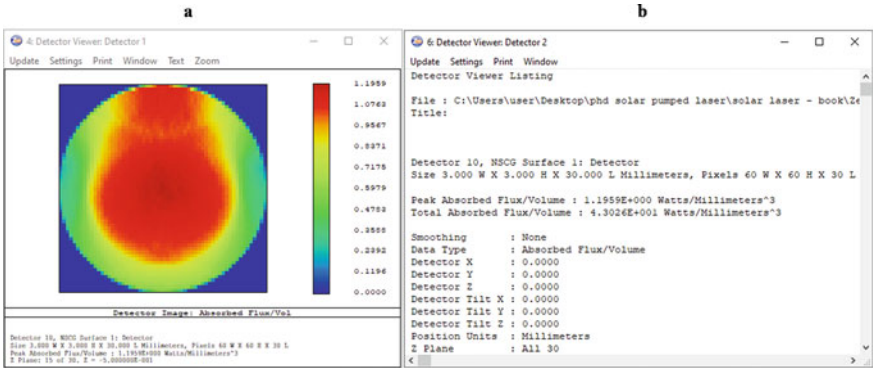

Fig. 2.32 **a** *Detector viewer* of the central layer of the crystal. **b** The same *detector viewer* in text form

Object 9: reflecting cavity				
Object type	Material	Outer R/Inner R (mm)	Starting/Stop angle (°)	Thickness (mm)
Rectangular torus volume	Mirror (I.06)[a]	5.5/4.5	90/270	20[b]

[a] High reflective silver-coated aluminum foil sheet
[b] This is the length of the object. The subtraction of the 30 mm length rod with the 6 mm held part of the rod and 4 mm gap for the inflow of cooling water

Object 10: detector				
Object type	Material	X/Y half width (mm)	Z half length (mm)	X/Y/Z pixels
Detector volume	Water	1.5/1.5	15	60/60/30

Object 10: detector				
Object type	Material	Front R (mm)	Z length (mm)	R (mm)
Cylinder volume	Nd:YAG[a]	1.5	30	1.5

[a] The Transmission data of Nd:YAG used is in Sect. 2.1.1.4 Glass catalog dialog box and Glass table

Ray Tracing

Figure 2.32a shows the ray-tracing results of the energy distribution in the center layer of the crystal in the *Detector viewer* windows. Figure 2.32b shows the numerical data file generated from the detector after clicking on the Text button on the menu bar in Fig. 2.32a.

Note: The total absorbed power value may vary when the number of rays is insufficient, it is advisable to export a detector file for laser calculation in LASCAD™ with at least ten million rays traced.

2.3.2 LASCAD™

2.3.2.1 Multimode Laser Power

The procedure for calculating the multimode laser power in LASCAD™:

1. Choose **Standing Wave Resonator** to initialize the LASCAD™ program for solar-pumped lasers (see Sect. 2.2.1 Starting the program).
   1.1 Change from 2 to **4** elements. One element for the HR mirror, two elements for the crystal rod, and one last element for the PR mirror.
2. Open the *Crystal, Pump Beam, and Material Parameters* window *Main Menu → FEA → FEA/Parameter Input & Start of FEA Code.* (See Sect. 2.2.4 Crystal, Pump Beam, and Material Parameter window).
   2.1 *Model* tab: select "Cylindrical rod with numerical input of pump light distribution". Then insert the length of the rod as ***30*** mm and the diameter of the rod as ***3*** mm.
   2.2 *Pump Light* tab: select "Zemax—Product of ZEMAX Development Corporation".
   2.3 *Boundaries* tab: Select "Barrel surface" and set the value of "Surface extends from z = " to ***0*** mm, and "to z = " as ***30*** mm. Enable the "Fluid Cooling" checkbox. Change both "Temperature, K" and "Reference temperature, K" to 300 K.
   2.4 *Material Parameters* tab: Change the "Heat efficiency factor:" from 0.5 to ***0.65***, "Pump efficiency" from 0.8 to ***1***, and "emission cross-section" to ***2.8 × 10⁻¹⁹*** cm^2.

   Note: The emission cross-section comes from the datasheet of the laser crystal.

   2.5 *Doping and Mats* tab: Change the values inside of the text boxes of "from x = " and "from y = " to $-$***1.5*** mm. The values from "to x=", and "to y = " to ***1.5*** mm. "to z=" to ***30*** mm.

2.6 *FEA options* tab: The value of "Mesh size in x- and y-direction [mm]" is the division of the rod diameter with the pixel number (defined in Zemax®), in this case, is 3/60 = ***0.05***. The "Mesh size in z-direction [mm]" is 30/30 = ***1***. Click on the "Estimated number of elements" and the calculated number of elements superseded the previous value. Set the convergence limits as 1.E−7 or increase it if needed. Increase the "Maximum number of iterations" for both "Thermal analysis" and "Structural analysis" to ***300***.

2.7 Click on the "Apply and Run FEA" button. Import the detector file from Zemax®. Wait until the FEA simulation ends.

3. Open the *2D Profiles & Parabolic Fit* window from the main menu under the FEA option.

3.1 Select the "Open fit window" option.

3.2 Click on the "Refresh and fit" button. If successful, it will prompt an instructing dialog box to add the fitted thermally loaded crystals into the *Standing Wave Resonator* window by pressing both the Alt key and the mouse's left-click button in between the two elements.

3.3 Add the thermally loaded crystal between the two elements in the *Standing Wave Resonator* window, and an orange rectangle will then appear between the two elements, as shown in Fig. 2.33a.

4. In the *Parameter Field* window: after inserting the thermally loaded crystal, the distance between elements 1 and 2 will automatically set the length of the crystal.

4.1 In *x-Plane Param.* tab set "Type-Param. [mm]" to ***1000*** mm for both elements 0 (HR) and 3 (PR). This ensures both mirrors will have a radius of curvature of −1 m.

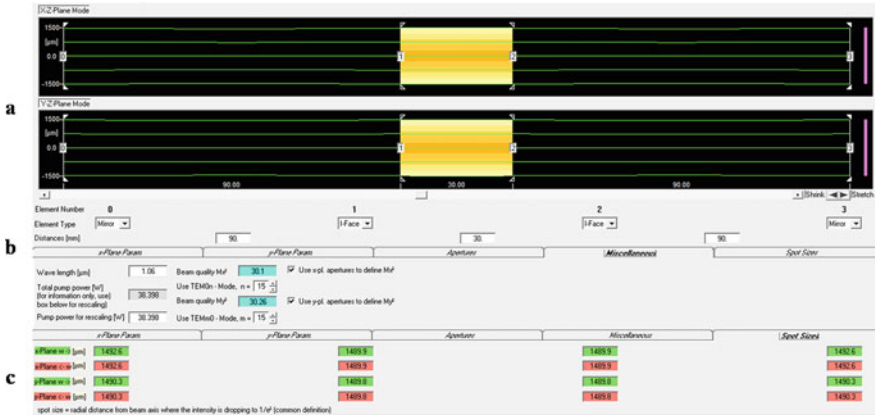

Fig. 2.33 **a** *Standing wave resonator* window: HR mirror (element 0) positioned 90 mm at the left side of the thermally loaded crystal (between elements 1 and 2) and an output PR mirror (element 0) at 90 mm at the other end. **b** *Parameter field* window: maximum output beam quality computed by enabling both checkboxes in the *Miscellaneous* tab. **c** *Spot sizes* for each element

4.2 Define the aperture of the HR, and PR mirrors as ***12,500*** μm (the size of commercially available mirrors) and ***1500*** μm for the crystal (radius of the crystal).

Note: In LASCAD™, the ***positive*** radius of curvature has the curved part of the lens facing toward the laser rod. These lenses have a ***negative*** radius of curvature for commercially available mirror couplers.

5. Set the distance of both the HR mirror (element between 0 and 1) and the PR mirror (element between 2 and 3) to ***90*** mm, as shown in Fig. 2.33. (90 mm is the distance between HR and PR mentioned in the publication.)
6. Use maximum beam quality at that position by ***enabling*** the checkbox of both "Use x-pl, aperture to define M_x^2" and the "Use y-pl, aperture to define M_y^2" in the *Miscellaneous* tab in the *Parameter Field* window, as shown in Fig. 2.33b.
7. Run the BPM from the BPM dialog box with all the checkboxes disabled (as in Fig. 2.23).
8. Determine the most probable beam size:
   - 8.1. Observe the 3D Beam Profile in *Intensity Profiled on Transversal Plane—Compaq Array Viewer* window with each consecutive BPM computational iteration. **Note**: look for the most recurring pattern.
   - 8.2. Add grid lines to the 3D beam profile and rotate the 3D beam profile into Top View. The Grid option can be enabled from the *Height plot settings* dialog box, accessed from the *Main menu* → *Setting* → *Graph* of the *Intensity Profiled on Transversal Plane—Compaq Array Viewer*.
   - 8.3. Take a ***Print Screen***.
   - 8.4. Count the number of segments at the X, and Y axis and the total of segments on one of the axes, as shown in Fig. 2.34.
   - 8.5. Calculate the beam size for both axes following Eq. (2.9):

$$\text{Beam size (radius)} = \frac{1}{2} \times \frac{\text{Diameter segments}}{\text{Total segments}} \times \text{Total grid size} \tag{2.9}$$

     The calculated Beam size at each axis has about ***±1428.55*** μm (0.5 × 20/42 × 6000 μm).
   - 8.6. The last D_{loss} registered was ***0.4E−4*** from BPM's ***Graphic1*** window.
9. Stop BPM.
10. Uncheck all "Use x-pl, aperture to define M_x^2" and the "Use y-pl, aperture to define M_y^2" in the *Miscellaneous* tab in the *Parameter Field* window, as shown in Fig. 2.35a.

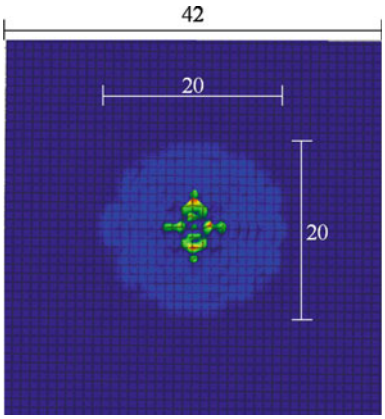

Fig. 2.34 Top view of the multimode laser from the *3D beam profile in the Intensity profile on transversal plane—compaq array viewer* window grid enabled

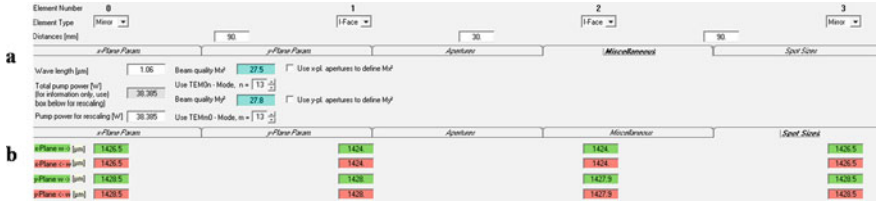

Fig. 2.35 Setting correct (most likely) beam quality to be the same spot size at the output mirror in the *parameter field* window. **a** *Miscellaneous* tab by unchecking "use x-pl, aperture to define $M_x{}^2$" and the "use y-pl, aperture to define $M_y{}^2$" and change the "beam quality $M_x{}^2$" and "beam quality $M_y{}^2$" value until, **b** green boxes at the right to be the same as the beam size from 8.5 in the *spot sizes* tab

11 Change both the numerical box of "Beam quality $M_x{}^2$" and "Beam quality $M_y{}^2$" in the *Miscellaneous* tab, until both output beam size values (green boxes) of the last element in the *Spot size* tab are the same as the calculated beam size of $\pm$***1428.55*** μm in step 8.4, as shown in Fig. 2.35.

12 Calculate laser power in the *Laser Power Output* window.

- 12.1 Select "Use absorbed pump power" in the "Define X-axis variable".
- 12.2 Calculate then insert the round-trip loss from Eq. (2.7) including the D_{loss} value acquired from step 8.6 into the "Resonator round-trip loss" input box.
- 12.3 Check the "Account multimode operation".
- 12.4 Use ***94%*** reflectivity in "Output Mirror Reflectivity".
- 12.5 Increase the number of grid points to ***16***.
- 12.6 Click on "Apply and Plot". The laser power results shown in Fig. 2.36.

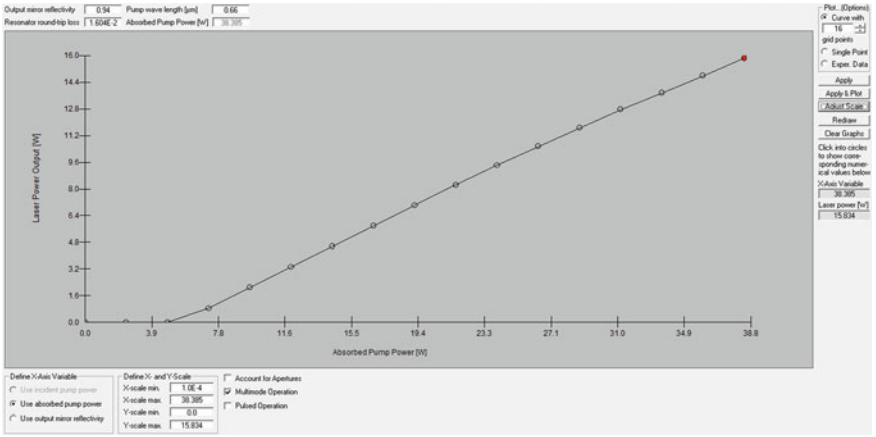

Fig. 2.36 Multimode-mode laser output power with 0.94% output mirror reflectivity

The calculated multimode laser power of 15.834 W was close to the measured laser power of 15.3 W [8].

2.3.2.2 Single-Mode Laser Power

According to the publication [8], the solar irradiance shifted between 770 and 830 W/m^2. Furthermore, the position of the HR mirror positioned 400 mm away from the crystal rod. In Zemax® simulation it has opted for an average irradiance of 770 W/m^2 and a Gaussian distribution of 32,000 at the source.

1. Choose ***Standing Wave Resonator*** to initialize the LASCAD™ program for solar-pumped lasers (see Sect. 2.2.1 Starting the program).

   1.1 Change 2 elements to ***4*** elements. One element for HR, two elements for crystal rod, and one last element for PR.

2. Open the *Crystal, Pump Beam, and Material Parameters* window from the "Parameter Input and Start" of FEA Code at the FEA option in the main menu.

   2.1 *Model* tab: select "Cylindrical rod with numerical input of pump light distribution". Then insert the length of the rod as ***30*** mm and the diameter of the rod as ***3*** mm.

   2.2 *Pump Light* tab: select "Zemax—Product of ZEMAX Development Corporation".

   2.3 *Boundaries* tab: Select "Barrel surface" and set the value of "Surface extends from z = " to ***0*** mm, and "to z = " as ***30*** mm. Enable the "Fluid Cooling" checkbox. Change both "Temperature, K" and "Reference temperature, K" to 300 K.

2.4 *Material Parameters* tab: Change the "Heat efficiency factor:" to ***0.65***, "Pump efficiency" to ***1***, and "emission cross-section" to $\boldsymbol{2.8 \times 10^{-19}}$ mm^2.

> **Note**: The emission cross-section comes from the datasheet of the laser crystal.

2.5 *Doping and Mats* tab: Change the values inside of the text boxes of "from x = " and "from y=" to $-$***1.5*** mm. The values from "to x=", and "to y=" to ***1.5*** mm. "to z=" to ***30*** mm.

2.6 *FEA options* tab: The value of "Mesh size in x- and y-direction [mm]" is the division of the rod diameter with the pixel number (defined in Zemax®), in this case, is 3/60 = ***0.05***. The "Mesh size in z-direction [mm]" is 30/30 = ***1***. Click on the "Estimated number of elements" and the calculated number of elements superseded the previous value. Leave the convergence limits as 1.E−7 or increase it if needed. Increase the "Maximum number of iterations" for both "Thermal analysis" and "Structural analysis" to ***300***.

> **Note**: It is advisable to define a coarser mesh in the z-direction in favor of reducing computational efforts. According to the LASCAD™ manual, the change of physical quantities is much slower in the longitudinal (Z-axis) than in the transverse direction (XY-Axis) [7].

2.7 Click on the "Apply and Run FEA" button. Import the detector file from Zemax®. Wait until the iterative simulation ends.

3. Open the *2D Profiles & Parabolic Fit* window from the *Main menu* window under the FEA option.

3.1 Select the "Open fit window" option.

3.2 Click on the "Refresh and fit" button. If successful, it will prompt an instructing dialog box to add the fitted thermally loaded crystals into the *Standing Wave Resonator* window by pressing both the Alt key and the mouse's left-click button in between the two elements.

3.3 Add the thermally loaded crystal between elements 1 and 2, in the *Standing Wave Resonator* window, and an orange rectangle will then appear between these two elements, as shown in Fig. 2.37a.

4. In the *Parameter Field* window: the distance between elements 1 and 2 will automatically set the size of the crystal.

4.1 In the *x-Plane Param.* tab set the lens radius of curvature of "Type-Param. [mm]" to ***1000*** mm for both elements 0 (HR) and 3 (PR).

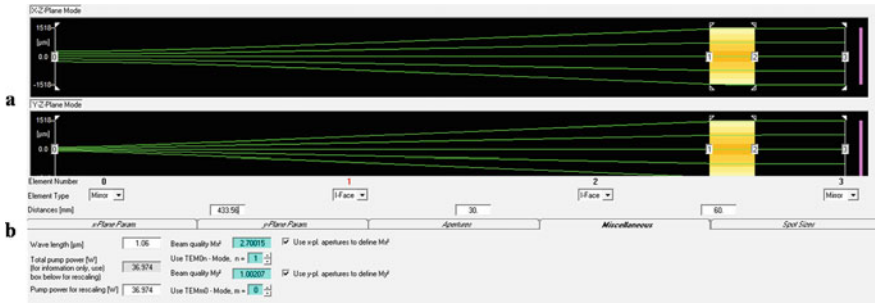

Fig. 2.37 **a** Is the *standing wave resonator* window: HR mirror (element 0) positioned 433.56 mm (step 6) at the left side of the thermally loaded crystal (between elements 1 and 2) and an output PR mirror (element 0) at 60 mm at the other end. **b** Is the miscellaneous tab in the *parameter field* window with beam quality close to 1.00 (steps 5 and 6)

> **Note**: In LASCAD™, the ***positive*** radius of curvature has the curved part of the lens facing toward the laser rod. These lenses have a ***negative*** radius of curvature for commercially available mirror couplers.

4.2 Define the aperture of HR, and PR mirrors as ***12,500*** µm (the size of commercially available mirrors) and ***1500*** µm for the crystal (radius of the crystal).

4.3 Set the distance of the HR mirror (element between 0 and 1) to ***400*** mm and the PR mirror (element between 2 and 3) to ***30*** mm.

5. Enable both the checkboxes of "Use x-pl, aperture to define M_x^2" and "Use y-pl, aperture to define M_y^2" in the *Miscellaneous* tab in the *Parameter Field* window, as shown in Fig. 2.37b.
6. In this case, only the HR mirror was needed to move into a distance (L) of **433.56** mm to find the thermal focal spot by $M_x^2 = 2.70015$ and $M_y^2 = 1.00207$. See Fig. 2.37.
7. Run BPM. Note: BPM can be paused at any time.

7.1 Wait until the beam radius [$1/e^2$] converges onto a single value in the *Convergence of Beam Radius with Cavity Iteration* window, then register this value. See Fig. 2.38a.

7.2 Register the newest D_{loss} value (***0.0207E−2***) from BPM's *Graphic1* window. See Fig. 2.38c.

8. Change the distance of the HR mirror (between elements 0 and 1) until either the beam size of the X or Y axis (green box of element 4) is the same beam waist value of ***813.2 µm*** found in step 7.1.

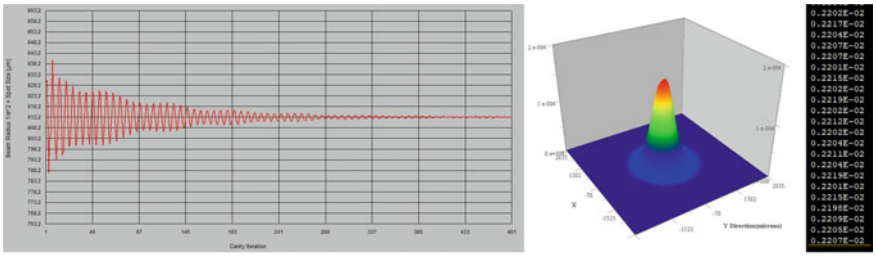

Fig. 2.38 BPM calculation. **a** Stabilized beam radius of 813.2 μm after 481 iterations. **b** Is the laser beam Gaussian distribution in 481 iterations. **c** Diffraction loss (D_{loss}) in 481 iterations

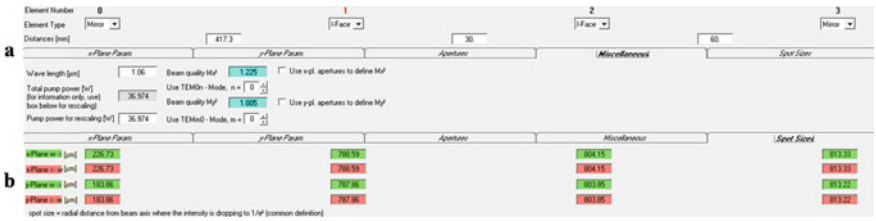

Fig. 2.39 Beam size correction. **a** Is the *miscellaneous* tab and **b** is the *spot size* tab from the *parameter field* window

In this case, reducing the distance from 433.56 mm to ***417.3*** mm was enough for the beam size at the Y axis to become 813.2 μm, shown in Fig. 2.39.

9. Uncheck both "Use x-pl, aperture to define M_x^2" and "Use y-pl, aperture to define M_y^2" in the *Miscellaneous* tab in the *Parameter Field* window.
10. Change the M_x^2 value, until the value of spot size is close to 813.2 μm, as shown in Fig. 2.39.
11. Calculate laser power in the *Laser Power Output* window.

    11.1 Select "Use absorbed pump power" in the "Define X-axis variable".
    11.2 Insert a round-trip loss value of ***1.82E−2***, calculated from Eq. (2.9) by including the D_{loss} value acquired from step 7.2 into the "Resonator round-trip loss" input box.
    11.3 Check the "***Account multimode operation***".
    11.4 Use ***98%*** reflectivity in "Output Mirror Reflectivity".
    11.5 Increase the number of grid points to ***20***.
    11.6 Click on "Apply and Plot". The laser power results shown in Fig. 2.40.

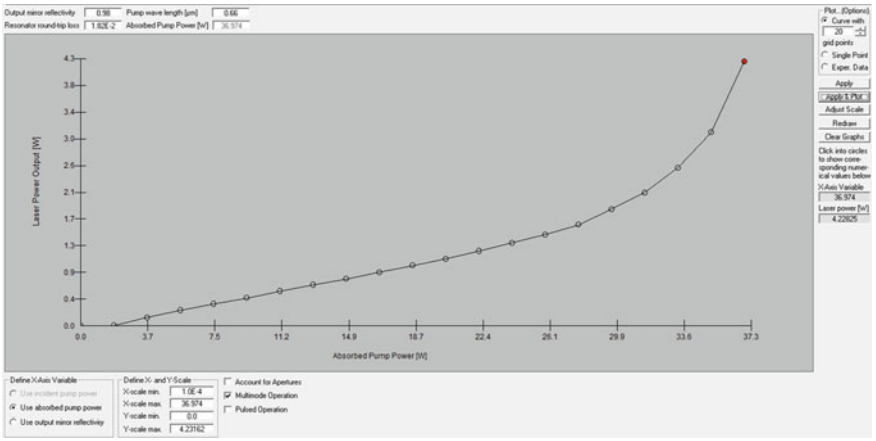

Fig. 2.40 TEM_{00}-mode laser output power with 98% output mirror reflectivity

The calculated TEM_{00}-mode laser power was about 4.23 W, which is higher than the practical results of 2.8 W measured [8], and both results were in the same range. The measured results were inevitably always lower than the ideal setup found in the simulation. Small mechanical errors and the erratic oscillation of solar irradiance may contribute to this difference. Moreover, a steeper slope gain of laser power per input power could be found at the maximum solar irradiation, as shown in Fig. 2.40, hence, a small variance may lead to lower laser power.

References

1. Powell, R.C.: Physics of Solid-State Laser Materials. Springer, New York (1998)
2. Zhao, B., Changming, Z., He, J., Yang, S.: Study of active medium for solar-pumped solid-state lasers. Guangxue Xuebao/Acta Optica Sinica **27**, 1797–1801 (2007)
3. Liang, D., Vistas, C.R., Garcia, D., Tibúrcio, B.D., Catela, M., Costa, H., Guillot, E., Almeida, J.: Most efficient simultaneous solar laser emissions from three Ce:Nd:YAG rods within a single pump cavity. Sol. Energy Mater. Sol. Cells **246**, 111921 (2022). https://doi.org/10.1016/j.solmat.2022.111921
4. Garcia, D., Liang, D., Vistas, C.R., Costa, H., Catela, M., Tibúrcio, B.D., Almeida, J.: Ce:Nd:YAG solar laser with 4.5% solar-to-laser conversion efficiency. Energies **15**(14), 5292 (2022)
5. Tai, Y., Zheng, G., Wang, H., Bai, J.: Near-infrared quantum cutting of Ce3+–Nd3+ co-doped Y3Al5O12 crystal for crystalline silicon solar cells. J. Photochem. Photobiol. A **303–304**, 80–85 (2015). https://doi.org/10.1016/j.jphotochem.2015.02.009

6. Welford, W.T., Winston, R.: CHAPTER 4—nonimaging concentrators: the compound parabolic concentrator. In: Welford, W.T., Winston, R. (eds.), High Collection Nonimaging Optics, pp. 53–76. Academic Press (1989)
7. LASCAD 3.3.5 Manual. LAS-CAD GmbH (2007)
8. Liang, D., Vistas, C.R., Almeida, J., Tibúrcio, B.D., Garcia, D.: Side-pumped continuous-wave Nd:YAG solar laser with 5.4% slope efficiency. Solar Energy Materials and Solar Cells **192**, 147–153 (2019). https://doi.org/10.1016/j.solmat.2018.12.029

Chapter 3
Solar-Pumped Solid-State Laser Theory

Dawei Liang

3.1 Brief Introduction

Properties of laser radiation and photons are firstly introduced. To comprehend solar irradiance and solar-pumped solid-state laser theory, Planck's law, Stefan-Boltzmann's law and Wien's law are presented and reinforced by several homework with solutions. The concept of spontaneous emission, stimulated absorption, stimulated emission, Einstein coefficients and thermodynamic treatment are then explained, leading to the definition of important parameters such as photon degeneracy, laser gain and stimulated emission cross section. Upper level laser rate equation, light increment along an active medium and laser oscillation threshold condition are consequently defined. More importantly, laser rate equation involving a laser resonant cavity is presented, permitting laser photon density calculation within the resonant cavity. To calculate solar laser output power, important definitions like solar concentration ratio, transfer efficiency, absorption efficiency, upper state efficiency, beam overlap efficiency and output coupling efficiency are explained. With the help of Zemax® software, the deviation angles and the effective absorption length of a solar pump ray within a laser rod are determined. A simplified Nd:YAG absorption spectrum is also provided, facilitating considerably the calculation of absorbed solar power density and absorbed pump photon number density within five simplified absorption bands of the Nd:YAG medium. Consequently, a modified analytical method for solar laser power calculation is put forward. Solar laser power from both a side-pumped laser and an end-side-pumped laser are finally calculated by the modified, classical, Zemax® and LASCAD™ analysis methods. In this chapter, we shall outline the basic theory underlying the operation of solar-pumped solid-state lasers. In-depth treatments of laser physics can be found in a number of excellent textbooks [1–6].

© The Author(s), under exclusive license to Springer Nature Switzerland AG 2023

D. Liang et al., *Solar-Pumped Lasers*, Green Energy and Technology,
https://doi.org/10.1007/978-3-031-24785-9_3

3.2 Properties of Laser Radiation

Laser radiation is characterized by an extremely high degree of directionality, monochromaticity, coherence, and brightness.

3.2.1 Directionality

Laser emits a well-defined beam in a specific direction, which implies laser light is of very small divergence. This is a direct consequence of the fact that a laser beam comes from a resonant cavity, and only waves propagating along the optical axis can be sustained in the cavity. The direction of the beam is governed by the orientation of the mirrors in the cavity. The directionality is described by the light beam divergence angle. For perfect spatial coherent light, a beam of aperture diameter D will have unavoidable divergence because of diffraction. From diffraction theory, the divergence angle θ_d is given by

$$\theta_d = \frac{\beta\lambda}{D} \tag{3.1}$$

where λ and D are the wavelength and the diameter of the beam respectively. β is a coefficient whose value is around unity and depends on the type of light amplitude distribution and the definition of beam diameter. θ_d is defined as diffraction limited divergence.

For a Nd:YAG laser beam with: $\lambda = 1.06\ \mu\text{m}$, $D = 3$ mm, $\beta = 1.1$, $\theta_d = \frac{\beta\lambda}{D} = 0.02227^{\circ}$.

Therefore, a laser beam provides a **Very Low Beam Divergence**.

Consequently, a laser beam ensures **a Very High Focusability**.

A fundamental mode laser beam can be focused to a diffraction-limited spot size [7] (Fig. 3.1).

$$w_f = \frac{\lambda f}{\pi w_0} = \frac{630\ \text{nm} \times 10\ \text{mm}}{3.14 \times 1\ \text{mm}} = 2\,\mu\text{m} \tag{3.2}$$

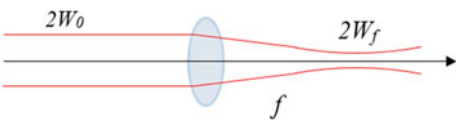

Fig. 3.1 A collimated 630 nm laser beam with $2w_0 = 2$ mm beam waist can be focused into a light spot with only $2w_f = 4\ \mu$m beam waist

According to (3.2), for a collimated beam, the diffraction-limited focal spot size $2w_f$ of a laser beam depends on its wavelength λ, the size of the parallel beam $2w_0$ at the focusing lens and the focal length f of that lens.

3.2.2 Monochromaticity

Monochromaticity refers to a pure spectral color of a single wavelength. A laser cavity forms a resonant system. The photons are emitted by the stimulated emission where all the photons are in the same phase and in the same state of polarization. Oscillations can sustain only at the resonance frequency of the cavity. This leads to the narrowing of the laser line width. So, the laser light is usually very pure in wavelength, and the laser is therefore said to have the property of monochromaticity. In situations where only a single resonator mode has sufficient laser gain to oscillate, a single longitudinal mode can be selected, obtaining single-frequency operation. For a laser beam with $\upsilon_0 = 5 \times 10^{14}$ Hz (yellow color), typical value of $\Delta\upsilon =$ 1 kHz − 1 MHz can be achieved by a gas laser. Using additional techniques for stabilizing the frequency, the linewidth can be further reduced by a massive extent. Some laser systems serve as optical frequency standards with a linewidth below 1 Hz [8], attaining an elevated spectral purity of 10^{-15}.

$$\frac{\Delta v}{v} = 10^{-15} \tag{3.3}$$

Quality factor of monochromaticity is defined as:

$$Q_{Monocromaticity} = \frac{\upsilon}{\Delta\upsilon} \tag{3.4}$$

3.2.3 Coherence

A very important characteristic of laser light is coherence. Coherence means that light waves are in phase. Lasers have a high degree of both spatial and temporal coherence.

Spatial coherence—for light impinging on a surface, the light is coherent if the waves (or photons) at any two points selected at random on the plane maintain a constant phase difference over time.

Temporal coherence characterizes how well a wave can interfere with itself at two different times and increases as a source becomes more monochromatic (Fig. 3.2).

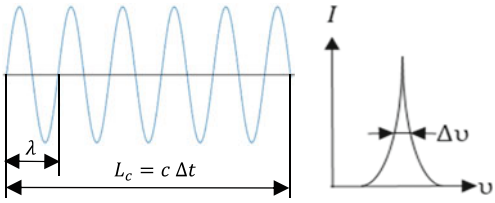

Fig. 3.2 Lightwave train of wavelength λ and temporal coherence Δt from a single atom and its frequency spectrum υ with Δυ linewidth

Definition of coherence length

Coherence length is defined as

$$L_c = c\Delta t \tag{3.5}$$

The coherence length L_c is the coherence time Δt times the vacuum velocity of light c, and thus also characterizes the temporal coherence via the propagation length over which coherence is lost.

Since $\Delta\upsilon \simeq 1/\Delta t$, coherence length can also be presented as

$$L_c = \frac{C}{\Delta\upsilon} \tag{3.6}$$

Relations between Δt and $\Delta\upsilon$

The temporal coherence Δt comes from the monochromaticity of a laser beam. The narrower the line width Δυ of the light source, the better is its temporal coherence Δt.

$$\Delta t \simeq \frac{1}{\Delta\upsilon} \tag{3.7}$$

Relation between $\Delta\lambda$ and $\Delta\upsilon$

Since $\lambda = \frac{c}{\upsilon}$,

$$d\lambda = -\frac{c}{\upsilon^2}d\upsilon = -\frac{\lambda^2}{c}d\upsilon, \quad \text{then } \frac{d\lambda}{\lambda} = -\frac{d\upsilon}{\upsilon} \tag{3.8}$$

We obtain the relationship between Δλ and Δυ

$$\frac{\Delta\lambda}{\lambda} = -\frac{\Delta\upsilon}{\upsilon}, \quad \left|\frac{\Delta\lambda}{\lambda}\right| = \left|-\frac{\Delta\upsilon}{\upsilon}\right| = \left|\frac{\Delta\upsilon}{\upsilon}\right| \tag{3.9}$$

Based on (3.9), the quality factor of coherence and monocromaticity is defined

$$Q_{coherence} = \frac{\lambda}{\Delta\lambda} \tag{3.10}$$

Finally, we can deduce the relations between coherence length L_c and central wavelength λ with linewidth $\Delta\lambda$.

$$L_c = c\Delta t = \frac{C}{\Delta\upsilon} = \frac{\lambda C}{\Delta\lambda\nu} = \frac{\lambda^2}{\Delta\lambda} \tag{3.11}$$

Example 1 (Homework) For a He–Ne gas laser with $\lambda = 630$ nm central wavelength and $\Delta\lambda = 0.002$ nm linewidth.

$$L_{c\ 630\ \text{nm}} = \frac{\lambda^2}{\Delta\lambda} = \frac{630^2\ \text{nm}}{0.002\ \text{nm}} = 198.45\ \text{m},$$
$$Q_{630\ \text{nm}} = \frac{\lambda}{\Delta\lambda} = \frac{630\ \text{nm}}{0.002\ \text{nm}} = 315000$$

For a Nd:YAG solid-state laser with $\lambda = 1064$ nm central wavelength and $\Delta\lambda = 5$ nm linewidth.

$$L_{c\ 1064\ \text{nm}} = \frac{\lambda^2}{\Delta\lambda} = \frac{1064^2\ \text{nm}}{5\ \text{nm}} = 0.226\ \text{mm},$$
$$Q_{1064\ \text{nm}} = \frac{\lambda}{\Delta\lambda} = \frac{1064\ \text{nm}}{5\ \text{nm}} = 212.8$$

Consequently, the coherence length and coherence quality factor of a He–Ne gas laser with $\lambda = 630$ nm central wavelength and $\Delta\lambda = 0.002$ nm linewidth are about 880, 1480 times higher than that of a Nd:YAG solid-sate laser with $\lambda = 1064$ nm central wavelength and $\Delta\lambda = 5.0$ nm linewidth, respectively.

3.2.4 High Brightness

While summing up the above descriptions of directionality (low divergence angle $\Delta\Omega$) and consequently focusability (small focal spot area Δs), as well as monochromaticity (narrow line width $\Delta\nu$) of a laser beam, its brightness cannot be missed out, which is defined as the power emitted per unit surface area per unit frequency and per solid angle, as indicated by (3.12). The units are watts per square meter per unit frequency and per Steradian.

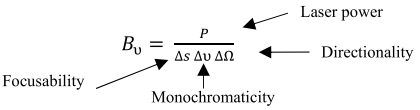

(3.12)

where:

B_υ is defined as laser beam brightness.
P is the laser beam power contained within Δs, $\Delta\upsilon$ and $\Delta\Omega$.
Δs is source area, which is related to laser beam focusability.
$\Delta\nu$ is frequency band width, which is related to laser beam monochromaticity.
$\Delta\Omega$ is solid angle, which is related to laser beam directionality.

Since a laser beam is featured by an excellent focusablity, monochromaticity and directionality, Δs, $\Delta\nu$, $\Delta\Omega$ are substantially smaller than that of classical light source such as lamps, offering therefore unprecedented laser beam brightness.

TEM_{00}-mode laser beam brightness can also be easily defined

$$B_\upsilon = \frac{P}{A\Delta\upsilon_0\left(\pi\,\theta_0^2\right)} \tag{3.13}$$

where

B_υ represents TEM_{00}-mode laser beam brightness.
P denotes laser power.
A is beam cross-section area.
$\Delta\upsilon_0$ is laser linewidth.
θ_0 is beam divergence angle in the far field.

3.3 Photons

3.3.1 Concept and Properties of Photon

Photons are fundamental subatomic particles that carry the electromagnetic force. As quanta of light, photons are the smallest possible packets of electromagnetic energy. Photons are integer spin-1 ($\pm\hbar$) particles (making them bosons) and does not obey the Pauli Exclusion Principle like other half-integer spin-1/2 ($\pm\hbar/2$) fermions (electrons, protons and neutrons), but obeys the Bose–Einstein statistics.

Photons have no electric charge or rest mass. Thereore, photons are electrically neutral and are not deflected by electric and magnetic fields. Photon travels at the speed of light in empty space ($c = 2.998 \times 10^8$ m/s). However, in the presence of matter, a photon can be slowed or even absorbed, transferring energy momentum proportional to its frequency. Like all quanta, the photon has both wave and particle properties; it exhibits wave—particle duality. Today, the role of the photon as a carrier of energy is perhaps its most important attribute. The light coming from the Sun has

different wavelengths or energy and on the basis of it, we have different regions like visible, infrared, ultraviolet and many more. But one thing is common in all these regions is photon, but of different frequency and so different energy.

Photons are emitted in many natural processes, e.g., when a charge is accelerated, when an atom or a nucleus jumps from a higher to lower energy level, or when a particle and its antiparticle are annihilated (for example, electron–positron annihilation). Photons are absorbed in the time-reversed processes which correspond to those mentioned above. Photons can have particle-like interactions (i.e. collisions) with electrons and other particles, such as in the Compton Effect in which particles of light collide with atoms, causing the release of electrons.

3.3.2 Photon Energy

Each photon has a definite energy depending upon the frequency υ of the incident radiation and not on its intensity. If the intensity of light of a given wavelength is increased, there is an increase in the number of photons emitted by the incident radiations on a given area in a given time. But the energy of each photon remains unchanged.

$$E = h\upsilon = \frac{hc}{\lambda} \tag{3.14}$$

where $h = 6.626 \times 10^{-34}$ J s is Planck's constant, $c = 2.998 \times 10^{8}$ m/s is the speed of light and λ is the wavelength of light. All photons travel at the speed of light. The energy of a photon depends on radiation frequency; there are photons of all energies from high-energy gamma and X-rays, through visible light, to low-energy infrared and radio waves. The photon energy is inversely proportional to the wavelength of the electromagnetic wave. The shorter the wavelength, the more energetic is the photon. The longer the wavelength, the less energetic is the photon.

3.3.3 Photon Momentum

There is a relationship between photon energy E and photon momentum p and that is consistent with the relation for the relativistic total energy of a particle

$$E^2 = (pc)^2 + (mc)^2 \tag{3.15}$$

We know m is zero for a photon, but p is not, so that (3.15) becomes

$$E = p\,c \tag{3.16}$$

The momentum of a photon is related to its wavelength λ and can be calculated using the following formula

$$p = \frac{E}{c} = \frac{h\upsilon}{c} = \frac{h}{\lambda} \tag{3.17}$$

Photons carry linear momentum and spin angular momentum when circularly or elliptically polarized. During light—matter interaction, transfer of linear momentum leads to optical forces, whereas transfer of angular momentum induces optical torque. Optical forces including radiation pressure and gradient forces have long been used in optical tweezers and laser cooling. Space sails have been proposed that use the momentum of sunlight reflecting from gigantic low-mass sails to propel spacecraft in the solar system.

3.4 Blackbody Radiation—Planck' Law

The term blackbody comes from a theoretical model of an object absorbing all incident radiation, as shown in Fig. 3.3a that is used to develop the quantum mechanics equations. The radiated energy can be considered to be produced by standing wave or resonant modes of the cavity which is radiating. It turns out that all objects behaves like blackbodies, regardless if they are actually black or not, as shown in Fig. 3.3b.

To explain the spectral-energy distribution of radiation emitted by a blackbody, Max Planck put forward the concept of quantification of radiation energy. Energy emitted by a resonator of frequency could only take on discrete values or quanta. Planck contributed to the advancement of physics by his discovery of "Quanta".

According to Plank, for each frequency υ (each mode) $\rightarrow$ it has the energy U

$$U = \frac{h\upsilon}{e^{\frac{h\upsilon}{kT}} - 1} \tag{3.18}$$

For frequency interval, $\upsilon \leftrightarrow \upsilon + d\upsilon$.

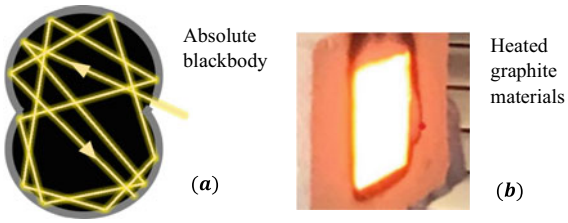

Fig. 3.3 **a** Absolute blackbody schematics. **b** Blackbody radiation from a heated graphite material

The number of radiation modes within a blackbody cavity can be calculated (See homework with solution 1)

$$n_\upsilon = \frac{8\pi\upsilon^2}{c^3} \tag{3.19}$$

Consequently, the energy density $\rho(\nu)$ in frequency interval $\upsilon \leftrightarrow \upsilon + \mathrm{d}\upsilon$ can be calculated

$$\rho(\nu) = \frac{8\pi\upsilon^2}{c^3} U \tag{3.20}$$

When electromagnetic radiation in a cavity is in thermal equilibrium at the absolute temperature T, Planck hence formulated the theory of spectral distribution of thermal radiation

$$\rho(\upsilon) = \frac{8\pi\upsilon^2}{c^3} \frac{h\upsilon}{e^{\frac{h\upsilon}{kT}} - 1} \tag{3.21}$$

Planck's law for the energy radiated $\rho(\upsilon)$ per unit volume by a cavity of a blackbody in the frequency interval ν to $\nu + \Delta\nu$ ($\Delta\nu$ denotes an increment of frequency) can be written in terms of Planck's constant ($h = 6.626 \times 10^{-34}$ J s), the speed of light $\left(C = 2.998 \times 10^8 \text{ m s}^{-1}\right)$, the Boltzmann constant $\left(\kappa = 1.3806 \times 10^{-23} \text{ J k}^{-1}\right)$, and the absolute temperature (T).

3.5 Solar Spectral Irradiance from Planck's Formula

In experimental work, blackbody radiation distribution according to wavelength is much more preferred.

We can deduce the spectral density $\rho(\lambda)$ in (3.22) from $\rho(\upsilon)$ in (3.21). (See homework with solution 2).

$$\rho(\lambda) = \frac{2hc}{\lambda^5} \frac{1}{e^{\frac{hc}{\lambda kT}} - 1} \tag{3.22}$$

Solar spectral irradiance $I(\lambda)$ in $\text{W m}^{-2}\text{nm}^{-1}$ can be obtained by multiplying spectral energy density $\rho(\lambda)$ by light velocity c.

$$I(\lambda) = \rho(\lambda)\, c \tag{3.23}$$

$$I(\lambda) = \frac{2hc^2}{\lambda^5} \frac{1}{e^{\frac{hc}{\lambda kT}} - 1} \tag{3.24}$$

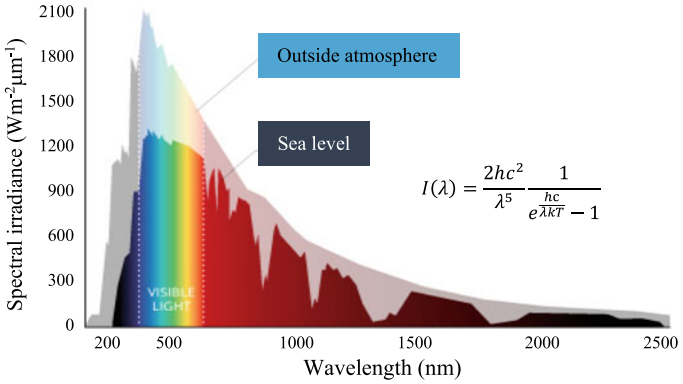

Fig. 3.4 Solar spectral irradiance at sea level and in outside atmospheric for wavelengths ranging from 240 nm to 2.5 μm. $I(\lambda) = \frac{2hc^2}{\lambda^5}\frac{1}{e^{\frac{hc}{\lambda kT}} - 1}$ can be used to approximate the solar spectral radiance curve

Equation (3.24) denotes the power emitted at a given wavelength per unit solid angle (one Steradian), per unit area (Fig. 3.4).

3.6 Stefan-Boltzmann's Law

The total radiant flux I, in unit [$\mathrm{W\,m^{-2}} = \mathrm{J\,m^{-2}s^{-1}}$], emitted from the surface of a black body at temperature T is expressed by the Stefan-Boltzmann law:

$$I = \frac{P}{A} = \varepsilon\,\sigma\,T^4 \tag{3.25}$$

where σ denotes a fundamental physical constant called the Stefan-Boltzmann constant, σ equals to 5.67×10^{-8} $\mathrm{w/m^2K^4}$. ε is the emissivity of the blackbody ($\varepsilon \leq 1$).

Total radiation energy density can be obtained by integrating the energy density $\rho(\nu, T)$ over all wavelengths λ. (See homework with solution 3).

Stefan-Boltzmann's law gives the radiant intensity of a single object. By Stefan-Boltzmann's law, we can also determine the radiation heat transfer between two objects. Two bodies that radiate toward each other have a net radiant power between them, as given by (3.26).

$$P_{1-2} = \varepsilon\,\sigma\,A_{1-2}\left(T_1^4 - T_2^4\right) \tag{3.26}$$

The area factor $A_{1\text{-}2}$ is the area viewed by body 2 of body 1. In many cases, body 1 can be surrounded by body 2, as shown by Fig. 3.5.

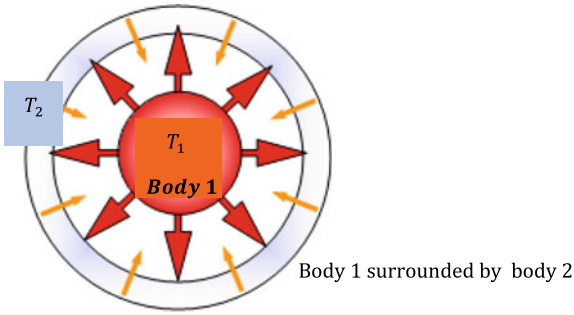

Fig. 3.5 Thermal energy transfer from body 1 to body 2, which surrounds body 1

3.7 Wien's Displacement Law

Wien's displacement law is a law of physics that states that there is an inverse relationship between the wavelength of the peak of the emission of a black body and its temperature. The spectral radiance of black body radiation per unit wavelength $\rho(\lambda, T)$ peaks at the wavelength λ_{max}, as given by (3.27)

$$\lambda_{max} = \frac{b}{T} = \frac{2.898 \times 10^{-3}\ \text{m K}}{T} \tag{3.27}$$

where T is the absolute temperature in Kelvins, b is a constant of proportionality, known as Wien's displacement constant, which equals to 2.898×10^{-3} m K.

By taking derivative of Eq. (3.24) versus wavelength λ, the peak $\rho(\lambda)$ of blackbody distribution curve can be found at λ_{max} (See homework with solution 4).

Example 2 (Homework)

Calculation of different peak wavelengths for different blackbody temperatures by (3.27).

Human body: $T = 310$ K $\rightarrow$ Answer ($\boldsymbol{\lambda_{max}} = 9.35$ μm).

Molten iron: $T = 1810$ K $\rightarrow$ Answer ($\boldsymbol{\lambda_{max}} = 1.60$ μm).

The Sun: $T = 5800$ K $\rightarrow$ Answer ($\boldsymbol{\lambda_{max}} = 500$ nm).

3.8 Spontaneous Emission, Stimulated Absorption and Simulated Emission Probabilities

In the early twentieth century, Max Planck formulated the theory of spectral distribution of thermal radiation. Albert Einstein, by combining Planck's theory and the Boltzmann statistics gave a theory of stimulated emission which is the governing principle of lasers. Let us assume that the material is placed in a blackbody cavity

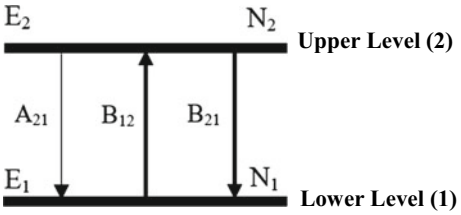

Fig. 3.6 Simplified 2-energy level diagram

whose walls are kept at a constant temperature T. Once thermodynamic equilibrium is reached, energy density with a spectral distribution $\rho(\upsilon)$ will be established and the material will be immersed in this radiation. In this material, both stimulated-emission and absorption processes will occur, in addition to the spontaneous-emission process. There are three ways in which an incident radiation can interact with the energy levels of atoms.

To describe the phenomenon of spontaneous emission, stimulated absorption and radiations, let us consider two energy levels, lower level 1 and upper level 2, of some atom or molecule of a given material, their energies being E_1 and E_2 ($E_1 < E_2$) (Fig. 3.6). It is important to note that the two levels could be any two out of the infinite set of levels possessed by the atom.

3.8.1 Spontaneous Emission Probability

Atoms which are in excited states are not in thermal equilibrium with their surroundings. Such atoms will eventually return to their ground state by emission of a photon. The population of the upper level will decrease due to spontaneous transition to the lower level with emission of radiation. The rate of emission will depend on the population of the upper level. Spontaneous emission is a statistical function of space and time. With a large number of spontaneously emitting atoms, there is no phase relationship between the individual emission processes; the quanta emitted are incoherent. Spontaneous emission probability A_{21} is only related to the properties of the atom itself and does not depend on with the radiation field $\rho(\upsilon)$ (Fig. 3.7).

Definition of spontaneous emission probability A_{21}

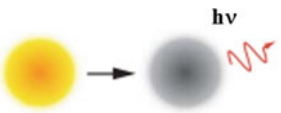

Fig. 3.7 Spontaneous emission: an excited atom from level (2) (lighter) transits to level (1) (darker) by releasing a photon (wiggly line)

$$A_{21} = \left(\frac{dn_{21}}{dt}\right)_{sp} \frac{1}{n_2} \tag{3.28}$$

Equation (3.28) has a solution:

$$n_2(t) = n_{20} e^{-A_{21}t} = n_{20} e^{-\frac{t}{\tau_s}} \tag{3.29}$$

where τ_s is the lifetime for spontaneous radiation of level 2. This radiation lifetime is equal to the reciprocal of the Einstein's coefficient.

$$A_{21} = \frac{1}{\tau_s} \tag{3.30}$$

Unit $A\left[\frac{1}{\text{s}}\right] = \frac{1}{230\ \mu\text{s}}$ for Nd:YAG medium.

3.8.2 *Stimulated Absorption Probability*

In the presence of an electromagnetic field, an atom in a lower level can undergo transitions to the upper level provided that the frequency of the radiation field $\rho(\upsilon)$ satisfies (3.31), (Fig. 3.8).

$$E_2 - E_1 = h\nu \tag{3.31}$$

However, this process is not a spontaneous one, because the atom is "stimulated to absorb" by the incident light field $\rho(\upsilon)$, W_{12} is the stimulated absorption probability of radiation, as defined below

$$W_{12} = \left(\frac{dn_{12}}{dt}\right)_{st} \frac{1}{n_1} \tag{3.32}$$

Unit $W_{12}\left[\frac{1}{\text{s}}\right]$.

$$W_{12} = B_{12}\rho(\upsilon) \tag{3.33}$$

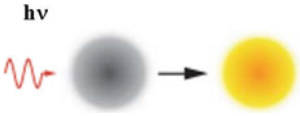

Fig. 3.8 Stimulated absorption: by absorption of a photon (wiggly line), the atom in the lower energy level (1) (darker) is excited to the upper level (2) (lighter)

Dimensional analysis $W_{12}\left[\frac{1}{s}\right] = B_{12}\rho(\upsilon)\left[\frac{m^3}{J\cdot s^2}\right]\left[\frac{J\cdot s}{m^3}\right]$.

Absorption pump probability W_{12} is related not only to Einstein absorption constant B_{12} but energy density of radiation $\rho(\upsilon)$ as well.

3.8.3 Stimulated Emission Probability

In 1917, Einstein showed that under certain conditions, emission of light may be stimulated by radiation incident on an excited atom. This happens when an electron is in an excited state and a photon whose energy is equal to the difference between and the energy of upper and lower energy levels. The incident photon induces the electron in the excited state to make a transition to the lower level by emission of a photon. The emitted photon travels in the same direction as the incident photon. Significantly, the new photon has the same energy as that of the incident photon and is perfectly in phase with it. When a sizable population of electrons resides in upper levels, this condition is called a "population inversion", and it sets the stage for stimulated emission of multiple photons. This is the precondition for the light amplification which occurs in a laser, and since the emitted photons have a definite time and phase relation to each other, the light has a high degree of coherence (Fig. 3.9).

W_{21} is the stimulated emission probability, as defined below:

$$W_{21} = \left(\frac{dn_{21}}{dt}\right)_{st}\frac{1}{n_2} \tag{3.34}$$

Unit $W_{21}\left[\frac{1}{s}\right]$.

$$W_{21} = B_{21}\rho(\upsilon) \tag{3.35}$$

Dimensional analysis $W_{21}\left[\frac{1}{s}\right] = B_{21}\rho(\upsilon)\left[\frac{m^3}{J\cdot s^2}\right]\left[\frac{J\cdot s}{m^3}\right]$.

Stimulated emission probability W_{12} is related not only to Einstein emission constant B_{21} but energy density of radiation $\rho(\upsilon)$ as well.

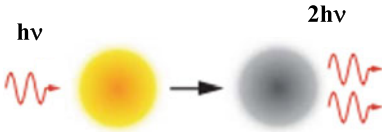

Fig. 3.9 Stimulated emission: an incident photon stimulates the excited atom to transit to lower level (1) by emitting a second photon which has the same frequency, polarization, and direction as the incident one

3.9 Einstein's Relations

Although Einstein coefficients A_{21}, B_{12}, and B_{21} are associated to different transition processes, they are all directly related to each other. If we know one of them, we can work out the rest.

Laser rate equation of upper level

$$\frac{dN_2}{dt} = \rho(\upsilon)B_{12}N_1 - \rho(\upsilon)B_{21}N_2 - A_{21}N_2 \tag{3.36}$$

Under steady state of transition

$$\frac{dN_2}{dt} = 0,\ \rho(\upsilon)B_{12}N_1 - \rho(\upsilon)B_{21}N_2 = A_{21}N_2 \tag{3.37}$$

Therefore

$$\rho(\upsilon) = \frac{A_{21}N_2}{B_{12}N_1 - B_{21}N_2} = \frac{\frac{A_{21}}{B_{21}}}{\frac{N_1}{N_2}\frac{B_{12}}{B_{21}} - 1} \tag{3.38}$$

From Boltzmann equation

$$\frac{N_1}{N_2} = e^{-\left(\frac{E_1-E_2}{kT}\right)} = e^{\left(\frac{E_2-E_1}{kT}\right)} = e^{\frac{h\upsilon}{kT}} \tag{3.39}$$

By inserting (3.39) into (3.38)

$$\rho(\upsilon) = \frac{\frac{A_{21}}{B_{21}}}{\frac{B_{12}}{B_{21}}e^{\frac{h\upsilon}{kT}} - 1} \tag{3.40}$$

By comparing (3.40) with Planck's formula (3.21),

$$\rho(\upsilon) = \frac{8\pi h\upsilon^3}{c^3}\frac{1}{e^{\frac{h\upsilon}{kT}} - 1} \tag{3.21}$$

We can finally find the relations of Einstein coefficients A_{21}, B_{12}, and B_{21}.

$$\frac{B_{12}}{B_{21}} = 1 \tag{3.41}$$

$$\frac{A_{21}}{B_{21}} = \frac{8\pi h\upsilon^3}{c^3} = \frac{8\pi h}{\lambda^3} \tag{3.42}$$

3.10 Photon Degeneracy in Light from Laser

From Planck's blackbody formula

$$\rho(\upsilon) = \frac{8\pi h\upsilon^3}{c^3}\frac{1}{e^{\frac{h\upsilon}{kT}} - 1} \tag{3.21}$$

We obtain

$$\frac{\rho(\upsilon)}{\frac{8\pi h\upsilon^3}{c^3}} = \frac{1}{e^{\frac{h\upsilon}{kT}} - 1} \tag{3.43}$$

From Einstein relation

$$\frac{A_{21}}{B_{21}} = \frac{8\pi h\upsilon^3}{c^3} \tag{3.42}$$

We obtain

$$\frac{\rho(\upsilon)}{\frac{8\pi h\upsilon^3}{c^3}} = \frac{\rho(\upsilon)}{\frac{A_{21}}{B_{21}}} = \frac{B_{21}\rho(\upsilon)}{A_{21}} = \frac{W_{21}}{A_{21}} = \frac{1}{e^{\frac{h\upsilon}{kT}} - 1} \tag{3.44}$$

Photon degeneracy $\overline{n}$ is finally deduced [9]

$$\overline{n} = \frac{W_{21}}{A_{21}} = \frac{1}{e^{\frac{h\upsilon}{kT}} - 1} \tag{3.45}$$

where

$W_{21} = \frac{\left(\frac{dn_{21}}{dt}\right)_{st}}{n_2} = B_{21}\rho(\upsilon)$ denotes stimulated emission probability (3.34).

$A_{21} = \frac{\left(\frac{dn_{21}}{dt}\right)_{st}}{n_2}$ denotes spontaneous emission probability (3.28).

To attain laser radiation, stimulated emisssion probability should be higher than spontaneous emission probability $W_{21} > A_{21}$, or photon degeneracy should be more than unity, $\overline{n} \geq 1$.

Example 3 (Homework)

Calculation of photon degeneracy for $\lambda = 0.6$ μm visible lightwave at different temperatures by

$$\overline{n} = \frac{W_{21}}{A_{21}} = \frac{1}{e^{\frac{h\upsilon}{kT}} - 1} \tag{3.45}$$

1. $T = 300$ K, $\lambda = 0.6$ μm
   (Answer $\overline{n} = 10^{-35}$), not possible for laser emission.

2. $T = 5000\ K, \lambda = 0.6\ \mu m$
   (Answer $\overline{n} = 0.08$), not possible for laser emission.
3. $T = 50000\ K, \lambda = 0.6\ \mu m$
   (Answer $\overline{n} = 1.54$), possible for laser emission.

Example 4 (Homework)

Calculation of photon degeneracy for $\lambda = 30$ cm microwave radiation at $T = 300\ K$.
Answer:

$$\upsilon = \frac{c}{\lambda} = \frac{30 \times 10^9 \frac{\text{cm}}{\text{s}}}{30\ \text{cm}} = 1\ \text{GHz},$$

$$\overline{n} = \frac{1}{e^{\frac{h\upsilon}{kT}} - 1} = \frac{1}{e^{\frac{6.63\times10^{-34}\ \text{J}\cdot\text{s}\times10^9\ \text{s}^{-1}}{1.38\times10^{-23}\frac{\text{J}}{\text{K}}\times300\ \text{K}}} - 1} = \frac{1}{e^{0.00016} - 1} = 6250 \gg 1$$

Conclusion

As shown by example 3, stimulated emission process may be significant for optical frequencies, but this requires extremely high temperature ($T = 50000$ K) to attain the minimum laser emission condition.

$W_{21} > A_{21}$, or photon degeneracy should be more than one, $\overline{n} \geq 1$.

For microwave frequencies, however, the stimulated emission processes can be significant even at room temperature ($T = 300$ K), as calculated by example 4. This explains why Microwave Amplification by Stimulated Emission of Radiation "MASER" was more early and easily attained than Light Amplification by Stimulated Emission of Radiation "LASER".

3.11 Laser Gain and Stimulated Emssion Cross Section

Laser rate equation for the upper level N_2 can be presented

$$\frac{dN_2}{dt} = \rho(\upsilon)B_{12}N_1 - \rho(\upsilon)B_{21}N_2 - A_{21}N_2 \tag{3.46}$$

Atomic energy levels are not infinitely sharp, but have some width associated with them. As a result, the spectrum of transition is not shap lines but have some distribution. By considering laser line shape function $g(\upsilon)$ [1–6], change in population density by stimulated emission N_{21} and change in population density by stimulated absorption N_{12} are defined:

$$N_{21} = B_{21}\,\rho(\upsilon)\,N_2\,g(\upsilon) \tag{3.47}$$

$$N_{12} = B_{12}\rho\,(\upsilon)\,N_1\,g(\upsilon) \tag{3.48}$$

$N_{21} - N_{12}$ denotes net change in population density: N_{21}^{net}.

$$N_{21}^{net} = N_{21} - N_{12} = (N_2 - N_1)\, B_{21} g(\upsilon)\, \rho(\upsilon) \tag{3.49}$$

where

$$B_{21} = B_{12}$$

Since light energy intensity $I(\upsilon)$ with unit $\left[\frac{\mathrm{J}}{\mathrm{m}^2}\right]$ equals to the product of photon energy density $\rho(\upsilon)$with unit $\left[\frac{\mathrm{J}}{\mathrm{m}^3 \mathrm{H_z}}\right] = \left[\frac{\mathrm{J \cdot s}}{\mathrm{m}^3}\right]$ and light velocity within the laser medium $\frac{c}{n}$ with unit $\left[\frac{\mathrm{m}}{\mathrm{s}}\right]$.

$$I(\upsilon) = \rho(\upsilon)\, \frac{c}{n}, \tag{3.50}$$

$$\rho(\upsilon) = I(\upsilon) \frac{n}{c} \tag{3.51}$$

Dimensional analysis of (3.50)

$$I(\upsilon)\left[\frac{\mathrm{J}}{\mathrm{m}^2}\right] = \rho(\upsilon) \frac{c}{n} \quad \left[\frac{\mathrm{J \cdot s}}{\mathrm{m}^3}\right]\left[\frac{\mathrm{m}}{\mathrm{s}}\right]$$

Photon energy density $\rho(\upsilon)$ in (3.49) can hence be replaced by $I(\upsilon)\frac{n}{c}$.
Relation between N_{21}^{net} and $I(\upsilon)$ is found

$$N_{21}^{net} = (N_2 - N_1)\, B_{21}\, g(\upsilon) \frac{n}{c} I(\upsilon) \tag{3.52}$$

By adding photon energy to the active volume in Fig. 3.10.

$$N_{21}^{net}\, h\upsilon\, A\, dx \tag{3.53}$$

Light intensity increament inside the volume can be calculated:

$$dI = N_{21}^{net} h\upsilon\, dx = (N_2 - N_1)\, B_{21}\, g(\upsilon)\, \frac{n}{c} I\,(\upsilon)\, h\upsilon dx \tag{3.54}$$

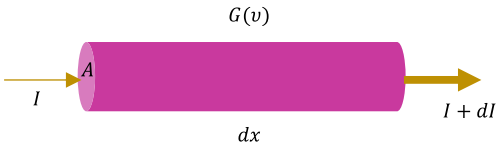

Fig. 3.10 Light intensity I increment along an active medium with A cross-section and dx length

By considering laser gain definition

$$G(\upsilon) = \frac{\frac{dI(\upsilon)}{dx}}{I(\upsilon)} \tag{3.55}$$

$$dI = G(\upsilon)I(\upsilon)dx \tag{3.56}$$

By comparing (3.54) and (3.56), we obtain

$$G(\upsilon) = (N_2 - N_1)B_{21}g(\upsilon)\frac{n}{c}h\upsilon \tag{3.57}$$

From Einstein relation in active medium with refractive index n.

$$B_{21} = \frac{c^3}{8\pi n^3 h\upsilon^3}A_{21} \tag{3.42}$$

We finally obtain the analytical presentation of laser gain $G(\upsilon)$

$$G(\upsilon) = (N_2 - N_1)\frac{c^3 A_{21}}{8\pi n^3 h\upsilon^3}g(\upsilon)\frac{n}{c}h\upsilon = (N_2 - N_1)\frac{\lambda^2 A_{21}}{8\pi n^2}g(\upsilon) \tag{3.58}$$

A more simplified presentation of $G(\upsilon)$ is reached by using

$$A_{21} = \frac{1}{\tau_{21}} \tag{3.30}$$

$$G(\upsilon) = (N_2 - N_1)\frac{\lambda^2}{8\pi n^2 \tau_{21}}g(\upsilon) \tag{3.59}$$

One of the most important parameter of laser physics: **Stimulated Emission Cross Section** $\sigma(\upsilon)$ is finally defined as

$$\sigma(\upsilon) = \frac{\lambda^2}{8\pi n^2 \tau_{21}}g(\upsilon) \tag{3.60}$$

Sitmulated emission cross-section is purely related to the property of laser active medium, depending only on upper level lifetime τ_{21}, refractive index n, laser wavelength λ and line shape function $g(\upsilon)$ of the laser medium. Consequently, laser gain can be more simply defined as the product of the stimulated emission cross section $\sigma(\upsilon)$ and the population inversion $N_2 - N_1$.

$$G(\upsilon) = \sigma(\upsilon)(N_2 - N_1) \tag{3.61}$$

3.12 Upper Level Laser Rate Equation

In a four-level laser, a pump excites atoms, molecules, or other atomic systems from the ground state level to an excited state (pump level). A sustained laser emission can be achieved by using atoms that have two relatively stable levels between their ground level and pump level. The atoms first drop to a long-lived metastable state (Upper level N_2) where they can be stimulated to emit excess energy. However, instead of dropping to the ground level, they stop at lower level N_1 above the ground level from which they can more easily be excited back up to the higher metastable state, thereby maintaining the population inversion needed for continuous laser operation. By taking into account the contribution of pumping W_p and laser lineshape function $g(\upsilon)$, the upper level laser rate equation can be presented: (Details on how to calculate solar pump rate W_p will be explained in Sect. 3.23), (Fig. 3.11).

$$\frac{dN_2}{dt} = W_p + \rho(\upsilon)B_{12}N_1 g(\upsilon) - \rho(\upsilon)B_{21}N_2 g(\upsilon) - A_{21}N_2 \tag{3.62}$$

From Einstein relation

$$B_{21} = B_{12} \tag{3.41}$$

$$\frac{dN_2}{dt} = W_p - \rho(\upsilon)B_{21}g(\upsilon)(N_2 - N_1) + A_{21}N_2 \tag{3.63}$$

Since

$$\rho(\upsilon) = I(\upsilon)\frac{n}{c} \tag{3.51}$$

$$B_{21} = A_{21}\frac{c^3}{8\pi n^3 h\upsilon^3} \tag{3.42}$$

$$\rho(\upsilon)B_{21}g(\upsilon) = I(\upsilon)\frac{n}{c}A_{21}\frac{c^3}{8\pi n^3 h\upsilon^3}g(\upsilon) = \frac{A_{21}\lambda_0^2}{8\pi n^2}g(\upsilon)\frac{I(\upsilon)}{h\upsilon} = \sigma(\upsilon)\frac{I(\upsilon)}{h\upsilon} \tag{3.64}$$

where $\sigma(\upsilon) = \frac{A_{21}\lambda_0^2}{8\pi n^2}g(\upsilon)$.

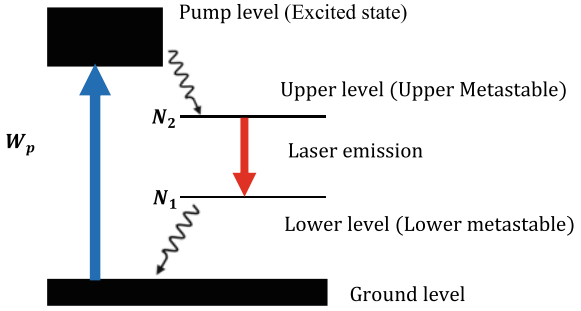

Fig. 3.11 Schematics of a four-level laser system. Wiggle lines indicate fast non-radiative transitions. Blue solid line for pump transition and red solid line for slow laser transition

We can finally replace $\rho(\upsilon)B_{21}g(\upsilon)$ by $\sigma(\upsilon)\frac{I(\upsilon)}{h\upsilon}$ in (3.63).

Finally, we obtain an important laser rate equation involving pump rate W_p, stimulated emission cross section $\sigma(\upsilon)$, number of photons per unit area per unit time $\frac{I(\upsilon)}{h\upsilon}$, upper level pupulation N_2, lower level population N_1 and spontaneous emission constant A_{21}.

$$\frac{dN_2}{dt} = W_p - \sigma(\upsilon)\frac{I(\upsilon)}{h\upsilon}(N_2 - N_1) + A_{21}N_2 \tag{3.65}$$

Pump rate | Stimulated emission cross-section | Number of photons per unit area per unit time | Stimulated emission | Absorption | Spontaneous emission

3.13 Light Intensity Increment Along Active Medium

At steady state oscillation, the populations is independent of time

$$\frac{dN_2}{dt} = 0 \tag{3.66}$$

Due to the rapid transition from lower level to ground level, zero population $N_1 = 0$ for the lower level is assumed.

Consequently

$$\frac{dN_2}{dt} = W_p - \sigma\frac{I}{h\upsilon}(N_2 - 0) + A_{21}N_2 = 0 \tag{3.67}$$

Since

$$A_{21} = \frac{1}{\tau} \tag{3.30}$$

$$\frac{dN_2}{dt} = W_p - \frac{\sigma I}{h\upsilon}N_2 - \frac{N_2}{\tau} = 0 \tag{3.68}$$

Then

$$N_2 = \frac{W_p\tau}{1 + \frac{\sigma\tau}{h\upsilon}I} = \frac{W_p\tau}{1 + \frac{I}{\frac{h\upsilon}{\sigma\tau}}} = \frac{W_p\tau}{1 + \frac{I}{I_S}} \tag{3.69}$$

where W_p is the pump rate in unit $\left[\frac{1}{\mathrm{s}}\right]$.

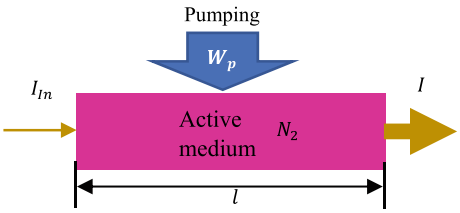

Fig. 3.12 Laser light intensity increament along an active medium

Saturation intensity I_S is hence defined

$$I_S = \frac{h\upsilon}{\sigma\tau} \tag{3.70}$$

$$I_S = \frac{h\upsilon}{\sigma\tau} = 2.9\frac{\text{kW}}{\text{cm}^2} \text{ for Nd:YAG medium}$$

When $I = 0$, population inversion N_2 reaches its maximum value

$$N_2(0) = W_p\tau \tag{3.71}$$

Therefore, the relation between population inversion in upper level N_2 and laser light intensity I is found (Fig. 3.12).

$$N_2 = \frac{N_2(0)}{1 + \frac{I}{I_{Sat}}} \tag{3.72}$$

By laser gain definition

$$G(\upsilon) = \frac{\frac{dI(\upsilon)}{dx}}{I(\upsilon)} \tag{3.55}$$

$$dI = G(\upsilon)I(\upsilon)dx = \sigma(\upsilon)(N_2 - N_1)I(\upsilon)dx \tag{3.73}$$

By assuming zero lower level pupulation $N_1 = 0$ for (3.73) and using (3.72)

$$\frac{dI}{dx} = \sigma I(N_2 - N_1) \approx \sigma I N_2 = \sigma I \frac{N_2(0)}{1 + \frac{I}{I_{Sat}}} \tag{3.74}$$

Therefore

$$\int_{I_{in}}^{I} \frac{dI}{I} + \int_{I_{in}}^{I} \frac{dI}{I_{Sat}} = \int_0^l \sigma N_2(0)dx \tag{3.75}$$

$$ln\frac{I}{I_{in}} + \frac{I - I_{in}}{I_{Sat}} = \int_0^l \sigma N_2(0)dx \tag{3.76}$$

Equation (3.76) can be solved numerically.
Simplified solution for (3.76) can be found in two following cases

1. $I \ll I_{Sat}$ (Weak pumping), $\frac{I}{I_{Sat}}$ is negligible in (3.74)

   Therefore (Fig. 3.13)

$$\frac{dI}{I} = \sigma N_2(0) dx \tag{3.77}$$

$$I(z) = e^{\sigma N_2(0) x} \tag{3.78}$$

2. $I \gg I_{Sat}$ (Very strong pumping), ln $\frac{I}{I_{In}}$ is negligible in (3.76)

   Equation (3.76) can then be simplified to (Fig. 3.14)

$$\frac{I - I_{in}}{I_{Sat}} = \int_0^l \sigma N_2(0)\, dx \tag{3.79}$$

$$I = I_{in} + I_{Sat} \int_0^l \sigma N_2(0) dx \tag{3.80}$$

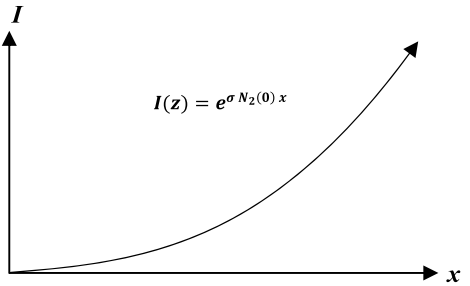

Fig. 3.13 Light intensity inceases exponentially with x

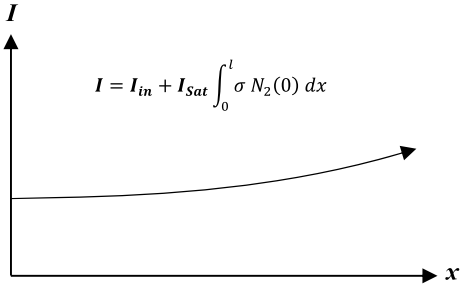

Fig. 3.14 Light intensity increases much more slowly, as compared to that of Fig. 3.13

3.14 Laser Oscillation Threshold Condition

Laser intensity enhencement I' after one round-trip, starting from I at point A and ending at the same point (Fig. 3.15).

$$I' = I\,R_1R_2(1-L_i)^2e^{2\sigma[N_2-N_1]l} \tag{3.81}$$

For a laser resonator composed of a HR end mirror with laser wavelength reflectance of R_1 (approaching 100%), a PR output mirror with laser wavelength reflectance of R_2 (may vary between 40 and 99% for example), an active medium with rod length l and loss L_i, laser oscillation threshold condition can be determined by assuming $I' = I$, leading to the following equation

$$R_1R_2(1-L_i)^2e^{2\sigma\,[N_2-N_1]l} = 1 \tag{3.82}$$

$$e^{2\sigma[N_2-N_1]l} = \frac{1}{R_1R_2(1-L_i)^2} \tag{3.83}$$

Therefore

$$2\sigma[N_2-N_1]l = -[\ln(R_1R_2) + 2\ln(1-L_i)] \tag{3.84}$$

Threshold population inversion density can be calculated

$$N_2 - N_1 = -\frac{1}{2\sigma l}[\ln(R_1R_2) + 2\ln(1-L_i)] \tag{3.85}$$

It is convenient to introduce some new quantities γ, which can be described as the logarithmic loss per pass, namely.

$$\gamma_1 = -\ln \mathrm{R}_1 = -\ln(1-\mathrm{T}_1) \tag{3.86}$$

$$\gamma_2 = -\ln \mathrm{R}_2 = -\ln(1-\mathrm{T}_2) \tag{3.87}$$

$$\gamma_\mathrm{i} = -\ln(1-\mathrm{L}_\mathrm{i}) \tag{3.88}$$

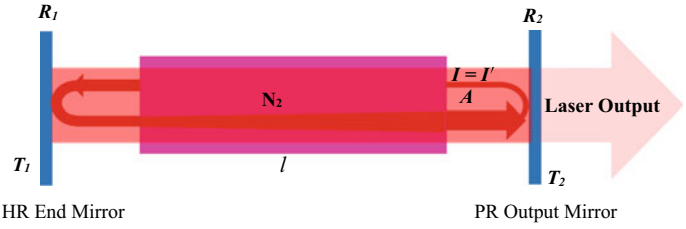

Fig. 3.15 Schematics of laser intensity variation in round-trip within a laser resoant cavity

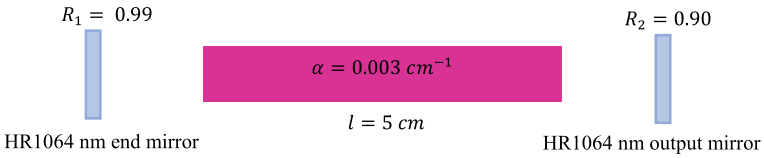

Fig. 3.16 Laser resoant cavity composed of a Nd:YAG rod, a HR1064 nm end mirror and a PR1064 nm output mirror

γ_1 and γ_2 are the logarithmic losses per pass due to the mirror transmission and γ_i is the logarithmic internal loss per pass. T_1 and T_2 are laser wavelength reflectivities of the HR end mirror and the PR output mirror, respectively. The logarithmic loss notation proves to be the most convenient way of representing laser losses, given the exponential character of the laser gain. Threshold population inversion density $N_2 - N_1$ can hence be presented.

$$N_2 - N_1 = \frac{1}{2\sigma l}\left[\gamma_1 + \gamma_2 + 2\gamma_i\right] = \frac{1}{\sigma l}\left[\gamma_i + \frac{1}{2}(\gamma_1 + \gamma_2)\right] = \frac{\gamma}{\sigma l} \tag{3.89}$$

Example 5 Calulation of threshold population inversion density $N_2 - N_1$ for a laser resonator with a $l = 5$ cm length Nd:YAG rod with $\sigma = 3 \times 10^{-19}$ cm^2 stimulated emission cross section and $\alpha = 0.003$ cm^{-1} absorption and scattering loss coefficient.

By using laser resoant cavity parameters indicated in Fig. 3.16

$$\gamma_1 = -\ln R_1 = -\ln 0.99 = 0.01, \qquad \gamma_2 = -\ln R_2 = -\ln 0.90 = 0.105$$
$$L_i = 2\alpha l = 2 \times 0.003\ \text{cm}^{-1} \times 5\ \text{cm} = 0.03 \qquad \gamma_i == -\ln(1 - L_i) = \ln(1 - 0.03) = 0.03$$

Threshold population inversion density $N_2 - N_1$ for the Nd:YAG medium can be calculated by (3.89)

$$\begin{aligned} N_2 - N_1 &= \frac{1}{2\sigma l}\left[\gamma_1 + \gamma_2 + 2\gamma_i\right] \\ &= \frac{1}{2 \times 3 \times 10^{-19}\ \text{cm}^2 \times 5\ \text{cm}}(0.01 + 0.105 + 0.06) \\ &= 5.83 \times 10^{16}\ \text{cm}^{-3} \end{aligned}$$

3.15 Laser Rate Equation Involving Resonant Cavity

As shown in Fig. 3.17, by photon absorption, atoms are excited to upper laser level at a pump rate W_p per second per unit volume, the rate equations for a four-level material can be used [10]

$$\frac{dN}{dt} = W_p(N_t - N) - \rho\sigma cN - \frac{N}{\tau_e} \tag{3.90}$$

$$\frac{d\rho}{dt} = \frac{c}{L'}(\sigma lN - \gamma)\rho \tag{3.91}$$

where W_p is the pump rate, N is the population inversion density, N_t is the total number density of the active atoms in the laser rod (for 1.0 at.% $Nd^{3+}YAG$ medium, $N_t = 1.38 \times 10^{20}$ cm^{-3}), c is the velocity of light in vacuum, σ is the stimulated emission cross section, τ_e is the effective lifetime of the upper laser level, and ρ is the photon density in the laser cavity. L' is the effective cavity length and is given as

$$L' = L_C + (n-1)l \tag{3.92}$$

where L_C is the length between the two cavity mirrors, n is the refractive index of the laser host material, and $\boldsymbol{l}$ is the length of the laser material.

For a laser resonator with an active medium, γ represents the logarithmic loss by the scattering and absorption of the laser light in the laser material and by the transmission of the two laser cavity mirrors, γ is thus given as

$$\gamma = \alpha l + \frac{1}{2}\left[\ln\left(\frac{1}{R_1}\right) + \ln\left(\frac{1}{R_2}\right)\right] \tag{3.93}$$

where α is the scattering and absorption losses per unit length, R_1 is the reflectance of the full mirror, and R_2 is the reflectance of the output coupler mirror.

The first term on the right-hand side of (3.91) represents the rate of photon density increase in the laser cavity by stimulated emission and the second term represents the

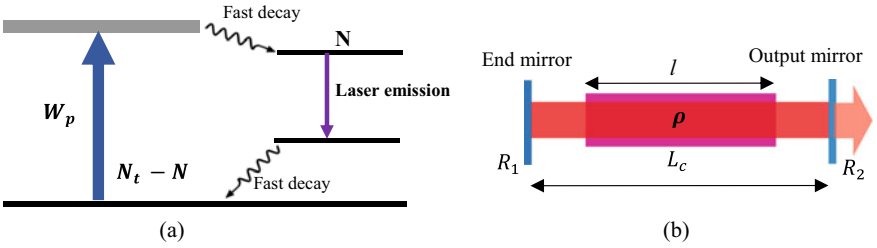

Fig. 3.17 **a** Simplified energy-level diagram of a four-level laser, **b** Schematics of a laser resonant cavity

photon loss rate due to the scattering and to the transmittance of the cavity mirrors. The photon loss rate coefficient can hence be written as

$$\frac{\gamma c}{L'} = \frac{\alpha c l}{L'} + \frac{c}{2L'}\left[\ln\left(\frac{1}{R_1}\right)\right] + \frac{c}{2L'}\left[\ln\left(\frac{1}{R_2}\right)\right] \tag{3.94}$$

3.16 Calculation of Photon Density Within a Laser Resonant Cavity

The population inversion in the laser cavity while the laser is in CW oscillation can be calculated from the photon rate Eq. (3.90) by applying the time invariant condition of the population density: $\frac{dN}{dt} = 0$

$$W_p N_t = \left(W_p + \rho\sigma c + \frac{l}{\tau_e}\right)N \tag{3.95}$$

Also, by applying the time invariant condition of the photon density $\frac{d\rho}{dt} = 0$ to (3.91) at the threshold

$$\sigma l N_c - \gamma = 0 \tag{3.96}$$

$$N_c = \frac{\gamma}{\sigma l} \tag{3.97}$$

where threshold inversion population N_c is proportional to the single-trip cavity loss γ and inversely proportional to the product of the stimulated emission cross-section σ and the rod length l.

Since the population inversion density N is clamped at the threshold inversion density N_c [1]

$$N = N_c = \frac{\gamma}{\sigma l} \tag{3.98}$$

By applying (3.98) to (3.95)

$$W_p N_t = \left(W_p + \rho\sigma c + \frac{l}{\tau_e}\right)\frac{\gamma}{\sigma l} \tag{3.99}$$

The photon density ρ within the laser cavity is finally obtained.

$$\rho = \frac{1}{\sigma c}\left[\left(\frac{N_t \sigma l}{\gamma} - 1\right)W_p - \frac{1}{\tau_e}\right] \tag{3.100}$$

3.17 Solar Concentration Ratio

The ratio between the concentrated flux on the receiver and the ambient flux from the sun is called the optical concentration ratio. Geometric concentration ratio C is defined as the area of solar collector S_a divided by the surface area of the receiver S_r. The laser rod surface can be considered as a receiver.

$$C = \frac{S_a}{S_r} = \frac{S_a}{\pi Dl} \tag{3.101}$$

where S_a is primary solar collector area, πDl is the laser rod side surface area exposed to concentrated solar pump rays.

3.18 Transfer Efficiency

Transfer Efficiency η_T can be defined as the ratio between the solar power incident on laser active medium and the incoming solar power reaching the primary solar collector [11].

$$\eta_T = \frac{\int_{\lambda_1}^{\lambda_2} \eta_{tg}\, \eta_{tl}(\lambda) \boldsymbol{I}(\boldsymbol{\lambda}) d\boldsymbol{\lambda}}{\int_{\lambda_1}^{\lambda_2} \boldsymbol{I}(\boldsymbol{\lambda}) d\boldsymbol{\lambda}} \tag{3.102}$$

where

η_{tg} is a geometrical transfer factor from the solar collector to the surface of the laser medium and is usually independent of wavelength.

$\eta_{tl}(\lambda)$ takes into account the reflection and transmission losses of primary, secondary solar concentrators and laser pump cavity.

The absorption by cooling liquid, the reflection and scattering losses at the laser medium and flow tube should be considered.

The integral in (3.102) is taken over the wavelength range between λ_1 and λ_2, which are useful for pumping the upper laser level. As an example, solar spectral irradiance $I(\lambda)$ and complex absorption spectra $\alpha(\lambda)$ of 1.0 at. % Nd:YAG medium are presented by orange and blue lines, respectively in Fig. 3.18. The integral in (3.102) is taken over the wavelength range from $\lambda_1 = 530$ nm to $\lambda_2 = 880$ nm for pumping the upper laser level.

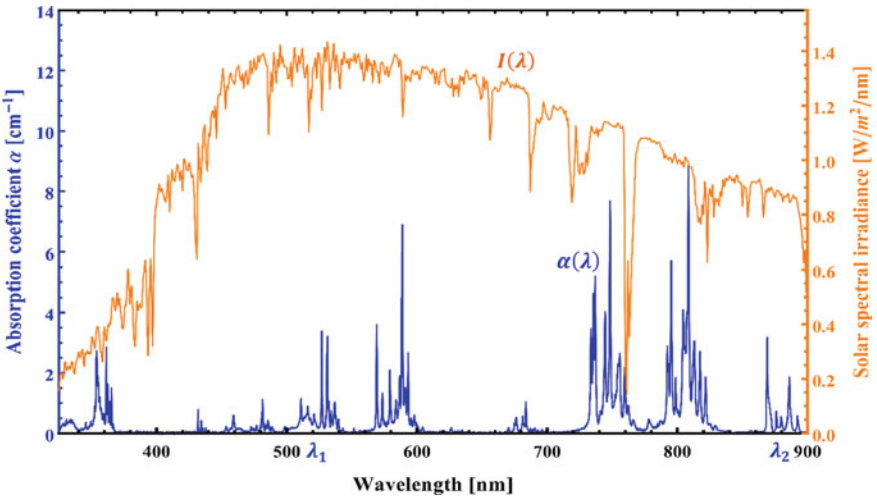

Fig. 3.18 Standard solar emission spectrum $I(\lambda)$ (orange line), Nd:YAG absorption spectrum $\alpha(\lambda)$ (blue line)

3.19 Absorption Efficiency

Absorption Efficiency η_A describes conversion of incident solar power incident on the surface of the active medium to the total absorbed pump power by the same medium.

Absorption efficiency η_A can be defined as [11]

$$\eta_A = \frac{P_a}{\int_{\lambda_1}^{\lambda_2} P_{e\lambda} d\lambda} \tag{3.103}$$

where:

P_a is the total absorbed solar power by the active medium.
$P_{e\lambda}$ is the power per unit wavelength incident on the medium.

For solar-pumped solid-state lasers, absorption efficiency calculations require the absorption spectra of the laser material and the solar emission spectra, as shown in Fig. 3.18, where pump source is characterized by solar spectral distribution $I(\lambda)$, and the laser material is characterized by absorption coefficients $\alpha(\lambda)$.

In addition, the angular distribution of the concentrated solar light on the laser material, as well as the geometry of the laser material and its refractive index also need to be known.

For solid-state lasers, the pump source is characterized by a relative spectral distribution $I(\lambda)$, and the laser material is characterized by an absorption coefficient $\alpha(\lambda)$, as shown in Fig. 3.18.

The pump photons have a distribution of incident angles $F(\theta, \varphi)$, and travel a path length $L(\theta, \varphi)$ in the laser material which depends on the incident angles θ and φ.

Given this, the absorption efficiency can be found [12]

$$\eta_A = \frac{\int_{\lambda_1}^{\lambda_2} \int_0^{\frac{\pi}{2}} \int_0^{\frac{\pi}{2}} \frac{\lambda}{\lambda_L} I(\lambda) F(\theta, \phi)\{1 - exp[-\alpha(\lambda)L]\} sin\theta d\theta d\phi d\lambda}{\int_{\lambda_1}^{\lambda_2} \int_0^{\frac{\pi}{2}} \int_0^{\frac{\pi}{2}} I(\lambda) F(\theta, \phi) d\theta d\phi d\lambda} \tag{3.104}$$

where

Integration is over all incident angles allowed by the angular distribution $F(\theta, \phi)$.

Integration over wavelength is all wavelengths emitted by the pump source.

L is defined as the effective absorption length of pump light within the laser rod.

$\alpha(\lambda)$ is the absorption coefficient of the laser medium.

λ_L is the laser wavelength.

I/λ_L is used to normalize so the efficiency is dimensionless.

Integration may vary between $\lambda_1 = 0.3$ μm to $\lambda_2 = 2.4$ μm for solar-pumped lasers.

However, when an active medium has a limited absorption bandwidth, integration over wavelength may vary only from $\lambda_1 = 0.5$ μm to $\lambda_2 = 0.88$ μm, as for the case of solar pumping of Nd:YAG material, as indicated in Fig. 3.18.

3.20 Deviation Angle and Effective Absorption Length

Numerically, the non-sequential method of Zemax® program can be used for calculating the above mentioned transfer efficiency η_T by (3.102) and absorption efficiency η_a by (3.103).

As shown in Fig. 3.19, a detector rectangle can be placed beneath the laser rod surface in Zemax® program. The deviation angles of α and β in transversal and longitudinal directions, respectively, can be detected by using the irradiance (angle space) function of the detector rectangle in Zemax® program [13].

Once α and β are found, the most important parameter in Fig. 3.19, defined as the deviation angle of the solar pump ray within the laser rod, β' can be calculated

$$\tan \beta' = \cos \alpha \tan \beta \tag{3.105}$$

Effective absorption length L of the solar pump ray can be finally calculated

$$L = \frac{D}{\cos \alpha \cos \beta'} \tag{3.106}$$

As compared to the complicated analytical modeling by (3.102) and (3.104), transfer efficiency η_T and absorption efficiency η_a can be more accurately and easily calculated by Zemax® software.

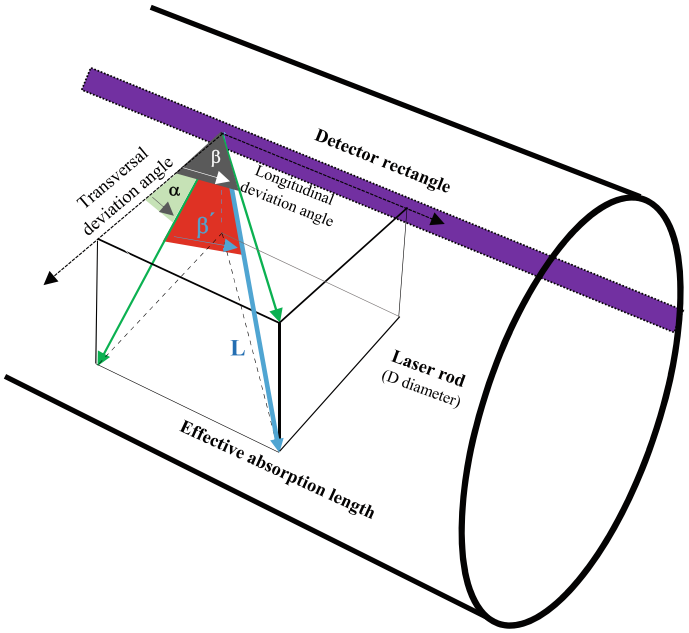

Fig. 3.19 Sun ray propagation geometry within a laser rod with D diameter. In Zemax® analysis, a rectangular detector can be positioned beneath the rod surface to detect the transversal deviation angle α and longitudinal deviation angle β of a solar pump ray within the laser rod, so as to calculate the deviation angle of solar pump ray β'. Effective absorption length L can be consequently determined

By assuming an infinite absorption coefficient $\alpha(\lambda) = \infty$ for a laser medium, all the incident rays are considered absorbed by the laser rod surface.

A rectangular volume detector can be used to calculate the total solar pump power incident on the surface of the laser rod, as shown in Fig. 3.20. Consequently, transfer efficiency can hence be calculated by (3.107).

$$\eta_T = \frac{P_{Rod\ surface}}{P_{Primar\ collector}} \tag{3.107}$$

where

$P_{Rod\ surface}$ denotes the solar pump power incident on the surface of the laser rod, as indicated by Fig. 3.20.

$P_{Primar\ collector}$ denotes the total incoming solar power reaching the primary solar collector.

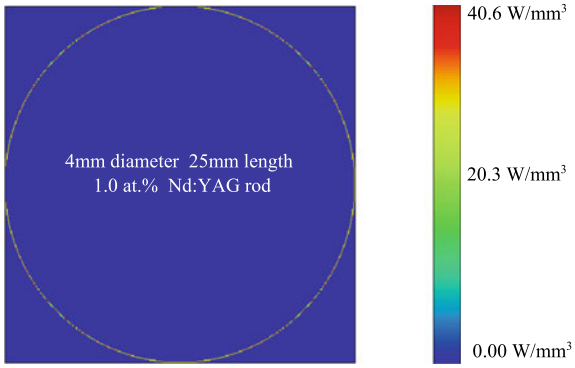

Fig. 3.20 Zemax® rectangular volume detector for the simulation of solar power reaching the surface of a Nd:YAG laser rod. Red color means near maximum solar energy absorption, whereas blue means little or no absorption. Numerical simulation data was obtained by analyzing the absorbed flux/volume profile of a 4 mm diameter, 25 mm length 1.0 at.% Nd:YAG pumped by a 0.636 m^2 Fresnel lens [14]

3.21 Upper State Efficiency

Upper State Efficiency $\eta_U(\lambda)$ is defined as the product of two contributing factors

1. Quantum efficiency $\eta_Q(\lambda)$.
2. Quantum defect efficiency $\eta_s(\lambda)$, also referred as Stokes factor.

$$\eta_U(\lambda) = \frac{P_U}{P_A} = \eta_Q(\lambda)\,\eta_S(\lambda) \tag{3.108}$$

Quantum Efficiency $\eta_Q(\lambda)$ can be defined as the ratio of the number of atoms raised to the upper laser level to the number of absorbed pump photons [11]. It relates the probability of an absorbed photon producing an atom in the upper laser level. We can thus write:

$$\eta_Q(\lambda) = \frac{h\nu \int \frac{dN_2}{dt} dV}{P_a} = \frac{\frac{hc}{\lambda} \int \frac{dN_2}{dt} dV}{P_a} \tag{3.109}$$

where N_2 denotes upper level population, P_a denotes the absorbed solar pump power.

Photons absorbed in a pump manifold may bypass the upper laser manifold by radiative decay to a manifold that is lower. In all probability, the decay from the pump to the upper laser manifold occurs by non-radiative transitions. If the upper laser manifold is directly below the pump manifold, the quantum efficiency is approximately [12].

$$\eta_Q = \frac{\frac{1}{\tau_{NR}}}{\left[\frac{1}{\tau_{NR}} + \frac{1}{\tau_{RAD}}\right]} \tag{3.110}$$

where τ_{NR} and τ_{RAD} are the pump manifold non-radiative and radiative lifetimes, respectively.

Quantum Defect Efficiency $\eta_S(\lambda)$, also called Stokes factor, is the ratio of the photon energy emitted at the laser transition, to the energy of a pump photon [11].

$$\eta_s = \frac{h\nu_L}{h\nu_p} = \frac{\lambda_p}{\lambda_L} \tag{3.111}$$

where: λ_p and λ_L are the pump transition and laser wavelengths, respectively.

In solar-pumped solid-sate lasers, the pump wavelength is defined as the mean absorbed and intensity-weighted solar radiation wavelength [15]

$$\lambda_p = \frac{\int_{\lambda_1}^{\lambda_2} I(\lambda)\lambda \, d\lambda}{\int_{\lambda_1}^{\lambda_2} I(\lambda) d\lambda} \tag{3.112}$$

where the integration is performed over the laser absorption bands between λ_1 and λ_2 and $I(\lambda)$ is the standard solar spectral irradiance, as shown in Fig. 3.18.

Since the laser wavelength of Nd:YAG laser material is $\lambda_L = 1064$ nm for solar-pumped Nd:YAG laser, $\lambda_P = 660$ nm was calculated by (3.112), $\eta_S = 0.62$ quantum defect efficiency is calculated for the Nd:YAG emission wavelength of $\lambda_L = 1064$ nm by (3.111).

Typically, upper state efficiencies of a Nd:YAG medium show a variation of $\eta_U(\lambda)$ from 0.58 to 0.60 [11], revealing its slight dependence on laser rod diameter. Consequently, upper state efficiency of $\boldsymbol{\eta_U(\lambda) = 0.59}$ is adopted in the following sections.

3.22 Beam Overlap Efficiency

Beam Overlap Efficiency η_B expresses the spatial overlap between the laser resonator modes and the pumped region of the laser medium, which can be given by an overlap integral [11].

$$\eta_B = \frac{\left(\iiint \varepsilon(x,y,z)\omega(x,y,z)dV\right)^2}{\iiint \varepsilon(x,y,z)^2\omega(x,y,z)dV} \tag{3.113}$$

where

$$\varepsilon(x,y.z) = \frac{\rho(x,y,z)}{\rho_0} \tag{3.114}$$

$\rho(x,y,z)$ is cavity mode energy density and ρ_0 is the total value of the energy density.

$$\iiint \omega(x, y, z) dV = 1 \tag{3.115}$$

$$\omega(x, y.z) = \frac{W_p(x, y, z)}{W_{p0}} \tag{3.116}$$

$W_p(x, y, z)$ denotes the pump rate per unit volume, W_{p0} is the total number of absorbed photons.

The relation between pump rate and absorbed power is given by

$$\iiint W_p(x, y, z) dV = \frac{P_a}{h\nu_p} \tag{3.117}$$

Choice of laser geometry can have a profound effect on overlap efficiency and average power capability. Historically, laser geometries were often in the form of cylinders. They can also be useful for end pumping of laser materials with low absorption coefficients. Laser rods pose a hard aperture making extraction of the population inversion near the periphery of the laser rod more difficult. If laser operation is restricted to TEM_{00} modes, the beam radius is often set at about 0.6 of the laser rod radius. This restricts the overlap efficiency to roughly 0.36 [12].

In addition, cooling was usually achieved by flowing coolant over the lateral surface of the laser rod. This leads to radial thermal gradients and thermal lensing that degrades beam quality and limits average power.

Consequently, analytical calculation of the beam overlap efficiency of a solid-state laser by (3.113) is rather complex, since it is strongly dependent on the resonator parameters such as radius of curvature of cavity mirrors, cavity length, rod diameter and, more importantly, also on solar pumping conditions such as tracking errors of either a heliostat or a solar tracker in the case of solar-pumped lasers.

Therefore, it is very important to note that laser output power from a resonant cavity with a certain length L presents usually a considerably reduced laser output power level due to the influence of the beam overlap efficiency of less than unity ($\eta_B < 1$), as compared to that of a closely coupled laser resonant cavity with $\eta_B = 1$. Zemax® and LASCAD™ analyses of laser output power from a laser cavity with a certain length L was presented in Sect. 2.3 of Chap. 2. Detailed examples will also be provided in Sect. 6.2 of Chap. 6.

Finally, it is important to note that in the pump rate and the solar laser output power analysis in the following sections, $\eta_B = 1$ is usually assumed, corresponding to a laser cavity with HR and PR mirrors closely positioned near the laser rod, allowing the maximum extraction of laser power from that rod.

3.23 Atom Number Density and Solar Pump Rate Calculations

By considering a solar laser collection and concentration system with concentration factor C, the concentrated solar spectral irradiance $I'(\lambda)$ incident on the laser rod surface can be calculated

$$I'(\lambda) = \eta_T(\lambda) I(\lambda) C \tag{3.118}$$

where $I(\lambda)$ is the one-Sun solar spectral irradiance, as indicated by Fig. 3.18. $\eta_T(\lambda)$ is the solar power transfer efficiency from the primary solar collector to the surface of the laser medium.

The absorbed photon number by the laser rod with diameter D and effective absorption length L can hence be calculated

$$N_a = \pi D l \times \int \frac{I'(\lambda)}{h\nu_p(\lambda)} \{1 - exp[-\alpha(\lambda)L]\} d\lambda \tag{3.119}$$

$$= \pi D l \times \int \frac{\eta_T(\lambda) I(\lambda) C}{h\nu_p(\lambda)} \{1 - exp[-\alpha(\lambda)L]\} d\lambda \tag{3.120}$$

Atom number density N_U (unit $\frac{1}{\text{cm}^3}$) in the upper laser level can be calculated by considering upper state efficiency $\eta_U(\lambda)$ and laser rod volume

$$N_U = \frac{1}{\pi \left(\frac{D}{2}\right)^2 l} \times \pi D l \times \int \frac{\eta_T(\lambda) I(\lambda) C}{h\nu_p(\lambda)} \eta_U(\lambda) \{1 - exp[-\alpha(\lambda)L]\} d\lambda \tag{3.121}$$

Since $\eta_T(\lambda)$ varies only slightly with wavelength λ within each simplified absorption band in Fig. 3.21 in Sect. 3.2, atom number density N_U in upper laser level can be finally obtained

$$N_U = \eta_T \times \frac{4C}{D} \times \int \frac{I(\lambda)}{h\nu_p(\lambda)} \eta_U(\lambda) \{1 - exp[-\alpha(\lambda)L]\} d\lambda \tag{3.122}$$

In the calculation of the output power, one of the most important parameters is the pump rate W_p. By dividing the atom number density N_U in the upper level by the total number density of the active ions in the laser rod N_t (for 1.0 at.% $Nd^{3+}YAG$ medium, $N_t = 1.38 \times 10^{20}$ cm^{-3}), the pump rate W_p can then be calculated

$$W_p = \frac{N_U}{N_t} = \eta_T \times \frac{4C}{N_t D} \times \int \frac{I(\lambda)}{h\nu_p(\lambda)} \eta_U(\lambda) \{1 - exp[-\alpha(\lambda)L]\} d\lambda \tag{3.123}$$

3.24 Solar Laser Output Power Calculation

The laser output power P_{out} of a continuous-wave laser is calculated from the following relation

$$P_{out} = \left[photon\ density\right] \times \left[lasing\ volume\ in\ the\ cavity\right] \times \left[photon\ loss\ rate\ through\ output\ mirror\right] \times \left[photon\ energy\right] \quad (3.124)$$

and

$$V = AL' \quad (3.125)$$

where V is defined as lasing volume in the cavity, where A is the laser beam cross section, and L' is the effective cavity length

$$L' = L_C + (n-1)l \quad (3.92)$$

Since photon loss rate through output mirror is presented by the third term on the right-hand side of (3.94)

$$P_{out} = \rho \times AL' \times \frac{c}{2L'} ln \frac{1}{R_2} \times h\nu \quad (3.126)$$

Photon loss rate through output mirror is also defined as laser power extraction efficiency.

Extraction Efficiency η_E

Laser extraction efficiency is determined by (3.127)

$$\eta_E = \frac{c}{2L'} ln \frac{1}{R_2} \quad (3.127)$$

By applying photon density ρ of (3.100)

$$P_{out} = \frac{1}{\sigma c}\left[\left(\frac{N_t \sigma l}{\gamma} - 1\right) W_p - \frac{1}{\tau_e}\right] \times AL' \times \frac{c}{2L'} ln \frac{1}{R_2} \times h\nu \quad (3.128)$$

$$= \frac{Ah\nu}{\sigma}\left(\frac{N_t \sigma l}{\gamma} - 1\right) \frac{1}{2} ln \frac{1}{R_2}\left[W_p - \frac{1}{\tau_e\left(\frac{N_t \sigma l}{\gamma} - 1\right)}\right] \quad (3.129)$$

Since normally, $\frac{N_t \sigma l}{\gamma} \gg 1$, we can reach a simplified equation for P_{out}

$$P_{out} = Ah\nu\left(\frac{N_t l}{\gamma}\right) \frac{1}{2} ln \frac{1}{R_2}\left[W_p - \frac{\gamma}{\sigma \tau_e N_t l}\right] \quad (3.130)$$

We then reach a simplified presentation for laser output power

$$P_{out} = \eta_s'\left(W_p - W_{pth}\right) \tag{3.131}$$

where: η_s' is defined as laser slope efficiency

$$\eta_s' = Ah\nu\left(\frac{N_t l}{\gamma}\right)\frac{1}{2}ln\frac{1}{R_2} \tag{3.132}$$

W_{pth} is defined as threshold pump rate.

$$W_{pth} = \frac{\gamma}{\sigma\tau_e N_t l} \tag{3.133}$$

From (3.133), it is important to note that W_{pth} is directly proportional to resonant cavity loss γ, and inversely proportional to the product of four important laser gain parameters, e.g. stimulated emission cross section σ, upper level lifetime τ_e, active ion number N_t and laser rod length l. Consequently, threshold pump rate can be either reduced by diminishing γ or by increasing σ, τ_e, N_t, l values.

By considering solar concentration ratio definition.

$$C = \frac{S_a}{S_r} = \frac{S_a}{\pi Dl} \tag{3.101}$$

Incoming solar laser can be calculated by (3.134)

$$P_{in} = S_a I_0 = \pi DlCI_0 \tag{3.134}$$

where I_0 is the one-sun solar insolation in unit of power per unit area (Standard one-Sun irradiance value: $I_0 = 1000\frac{\mathrm{W}}{\mathrm{m}^2}$).

Solar power to laser power conversion efficiency can then be calculated

$$\begin{aligned}\eta_c &= \frac{P_{out}}{P_{in}} = \frac{P_{out}}{\pi DlCI_0} = Ah\nu\left(\frac{N_t l}{\gamma}\right)\frac{1}{2}ln\frac{1}{R_2}\left[W_p - \frac{\gamma}{\sigma\tau_e N_t l}\right]\frac{1}{\pi DlI_0 C} \\ &= \eta_s'\left(Wp - W_{pth}\right)\frac{1}{\pi DlI_0 C}\end{aligned} \tag{3.135}$$

Maximum pump power to threshold pump power ratio is defined

$$\frac{P_{in}}{P_{th}} = \frac{W_p}{W_{th}} = x \tag{3.136}$$

Solar laser slope efficiency can also be calculated

$$\eta_{slope} = \frac{P_{out}}{P_{in} - P_{th}} = \frac{P_{out}}{P_{in}}\frac{1}{1 - \frac{P_{th}}{P_{in}}} = \frac{P_{out}}{P_{in}}\frac{1}{1 - \frac{W_{th}}{W_p}} = \eta_c\frac{x}{x-1} \tag{3.137}$$

3.25 Solar Spectral Irradiance and Simplified Model for Nd:YAG Absorption Spectrum

As shown in Fig. 3.21, the absorption spectra of Nd:YAG laser materials are rather complex. The absorption curve is composed of a couple of bands. Moreover, each band has a complex structure. Consequently, the analytical estimation of the pump rate by unit solar constant is rather difficult.

We therefore modeled the adsorption curves of the Nd:YAG laser material for the convenience of calculation. Five simplified absorption bands centered at 530 nm, 580 nm, 750 nm, 810 nm and 860 nm along with their respective absorption bandwidths of 28 nm, 28 nm, 31 nm, 33 nm, and 22 nm respectively (green color numbers in Fig. 3.21) are considered.

A simplified absorption coefficient value $\sigma_a\left(\frac{\lambda_a+\lambda_b}{2}\right)$ for each band is assumed, corresponding to 40% of the peak absorption coefficient of that band, so that the area under the modelled absorption curve (black color) could be equal to that under the real absorption curve (blue color) in each band, as shown in Fig. 3.22.

Consequently, simplified absorption coefficients 1.39 cm^{-1}, 2.87 cm^{-1}, 3.11 cm^{-1}, 3.64 cm^{-1} and 1.23 cm^{-1} are determined for 530 nm, 580 nm, 750 nm, 810 nm and 860 nm bands, respectively, as indicated by Fig. 3.21. Correspondingly, 1.35 W/m^2/nm, 1.31 W/m^2/nm, 1.12 W/m^2/nm, 1.00 W/m^2/nm, 0.87 W/m^2/nm solar

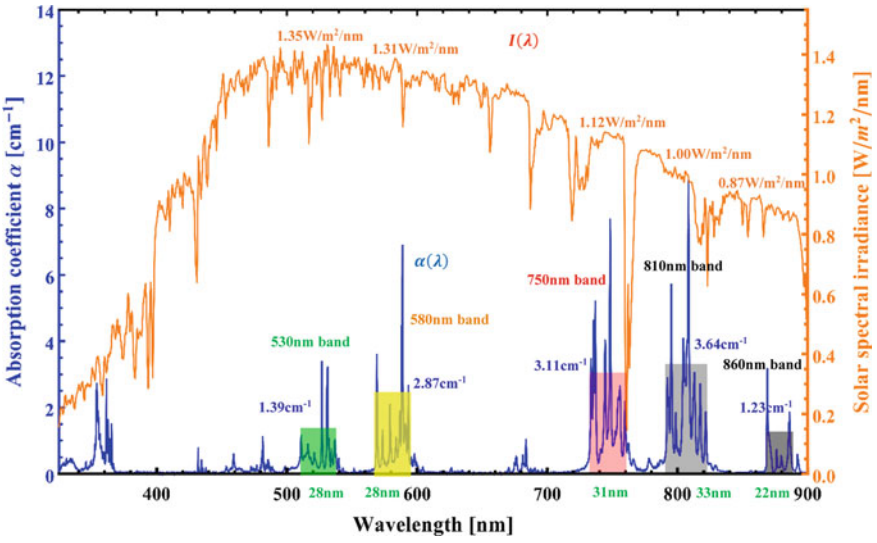

Fig. 3.21 Solar spectral irradiance and complex absorption spectra of 1.0 at.% Nd:YAG medium are presented by orange and blue lines, respectively. Five simplified absorption bands (530 nm, 580 nm, 750 nm, 810 nm and 860 nm) and their respective bandwidth (28 nm, 28 nm, 31 nm, 33 nm, and 22 nm) are indicated

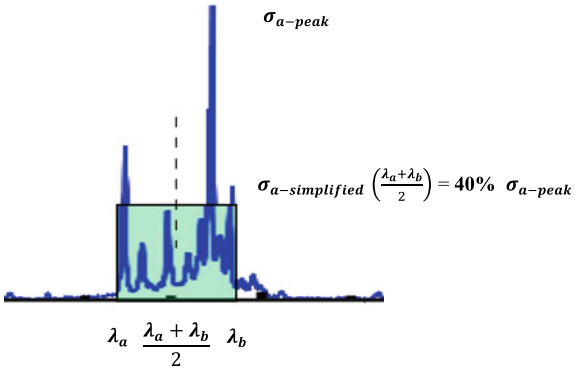

Fig. 3.22 Simplified rectangular absorption band (light green color) centered at $\frac{\lambda_a+\lambda_b}{2}$. The simplified band is limited by the minimum wavelength λ_a and the maximum wavelength λ_b. Simplified absorption coefficient corresponds to 40% of the peak absorption coefficient value of that band $\sigma_a\left(\frac{\lambda_a+\lambda_b}{2}\right) = 40\%\ \sigma_{a-peak}$

irradiance values are found to match the five simplified absorption bands centered at 530 nm, 580 nm, 750 nm, 810 nm and 860 nm, respectively.

Other absorption band of the Nd:YAG medium at UV wavelength in Fig. 3.21 is not considered since it does not contribute to 1064 nm laser emission process.

3.26 Absorbed Solar Power Density and Absorbed Pump Photon Number Density Calculations

To calculate absorbed solar power density and photon number density in each of the five simplified absorption band, as shown in Fig. 3.21, the following parameters are assumed constant within each of the simplified absorption band.

$$I(\lambda) = I\left(\frac{\lambda_a+\lambda_b}{2}\right)\ \textit{Constant solar spectral irradiance for each band} \quad (3.138)$$

$$\eta_U(\lambda) = \eta_U\left(\frac{\lambda_a+\lambda_b}{2}\right)\ \textit{Constant upper state efficiency for each band} \quad (3.139)$$

$$\sigma_a(\lambda) = \sigma_a\left(\frac{\lambda_a+\lambda_b}{2}\right) = 40\,\%\,\sigma_{a-peak}\ \textit{Constant absorption coefficient for each band} \quad (3.140)$$

Consequently, the absorption integral $\int I(\lambda)\eta_U(\lambda)\{1-exp[-\sigma_a(\lambda)L]\}d\lambda$ for each of the five absorption band can be simplified as

$$= I\left(\frac{\lambda_a+\lambda_b}{2}\right)\eta_U\left(\frac{\lambda_a+\lambda_b}{2}\right)\left\{1-exp\left[-\sigma_a\left(\frac{\lambda_a+\lambda_b}{2}\right)L\right]\right\}\int_{\lambda_a}^{\lambda_b} d\lambda \quad (3.141)$$

$$= I\left(\frac{\lambda_a+\lambda_b}{2}\right)\eta_U\left(\frac{\lambda_a+\lambda_b}{2}\right)\left\{1-exp\left[-\sigma_a\left(\frac{\lambda_a+\lambda_b}{2}\right)L\right]\right\}(\lambda_b-\lambda_a) \quad (3.142)$$

We then reach a simplified equation for calculating the absorbed solar power density within each band with $\Delta\lambda = \lambda_b - \lambda_a$ bandwidth.

Absorbed solar power density in each band

$$= I\left(\frac{\lambda_a+\lambda_b}{2}\right)\eta_U\left(\frac{\lambda_a+\lambda_b}{2}\right)\left\{1-exp\left[-\sigma_a\left(\frac{\lambda_a+\lambda_b}{2}\right)L\right]\right\}\Delta\lambda \quad (3.143)$$

Absorbed photon number density in each band may also be simplified according the constant parameter conditions of (3.138), (3.139) and (3.140).

Simplification of integral $\int \frac{I(\lambda)}{h\nu_p(\lambda)}\eta_U(\lambda)\{1-exp[-\alpha(\lambda)L]\}d\lambda$ for each band

$$\begin{aligned}
&= \frac{1}{h}I\left(\frac{\lambda_a+\lambda_b}{2}\right)\eta_U\left(\frac{\lambda_a+\lambda_b}{2}\right)\left\{1-exp\left[-\sigma_a\left(\frac{\lambda_a+\lambda_b}{2}\right)L\right]\right\}\int_{\lambda_a}^{\lambda_b}\frac{1}{\nu_p(\lambda)}d\lambda \\
&= \frac{1}{h}I\left(\frac{\lambda_a+\lambda_b}{2}\right)\eta_U\left(\frac{\lambda_a+\lambda_b}{2}\right)\left\{1-exp\left[-\sigma_a\left(\frac{\lambda_a+\lambda_b}{2}\right)L\right]\right\}\int_{\lambda_a}^{\lambda_b}\frac{\lambda_p}{c}d\lambda \\
&= \frac{1}{hc}I\left(\frac{\lambda_a+\lambda_b}{2}\right)\eta_U\left(\frac{\lambda_a+\lambda_b}{2}\right)\left\{1-exp\left[-\sigma_a\left(\frac{\lambda_a+\lambda_b}{2}\right)L\right]\right\}\frac{\left(\lambda_b^2-\lambda_a^2\right)}{2} \\
&= \frac{1}{h\frac{c}{\frac{\lambda_a+\lambda_b}{2}}}I\left(\frac{\lambda_a+\lambda_b}{2}\right)\eta_U\left(\frac{\lambda_a+\lambda_b}{2}\right)\left\{1-exp\left[-\sigma_a\left(\frac{\lambda_a+\lambda_b}{2}\right)L\right]\right\}\Delta\lambda \quad (3.144)
\end{aligned}$$

Absorbed photon number density in each absorption band is finally calculated

$$= \frac{1}{h\upsilon\left(\frac{\lambda_a+\lambda_b}{2}\right)}I\left(\frac{\lambda_a+\lambda_b}{2}\right)\eta_U\left(\frac{\lambda_a+\lambda_b}{2}\right)\left\{1-exp\left[-\sigma_a\left(\frac{\lambda_a+\lambda_b}{2}\right)L\right]\right\}\Delta\lambda \quad (3.145)$$

3.27 Output Power Analysis of a Side-Pumped Nd:YAG Solar Laser

3.27.1 Modified Analytical Method for the Side-Pumped Nd:YAG Solar Laser

An astigmatic corrected target aligned (ACTA) primary parabolic mirror with $S_a = 6.85\ m^2$ collection area was used to both collect and concentrate incoming solar power to a single-stage 2-dimensional compound parabolic concentrator (2D-CPC)

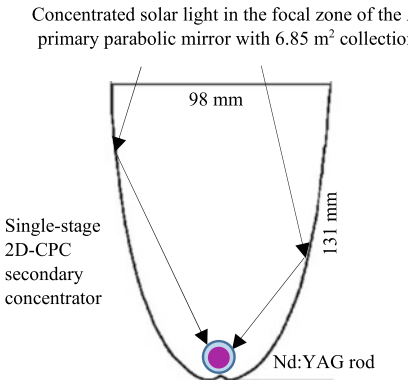

Fig. 3.23 The cross-sectional profile of the single-stage two-dimensional compound parabolic concentrator (2D-CPC). Concentrated solar lights in the focal zone were reflected to the Nd:YAG rod within the flow tube via the 2D-CPC secondary concentrator. Definite laser resonant cavity length $L = 430$ mm was adopted [16]

with 8.9 cm × 9.8 cm rectangular input face. A $D = 10$ mm diameter and $l = 130$ mm length 1.1% Nd:YAG laser rod was mounted inside a quartz flow tube, which was located along the 2D-CPC axis, as depicted in Fig. 3.23 [16].

Solar concentration ratio *C*

Absorbed pump power distribution of the Nd:YAG laser rod is presented by Fig. 3.24.

Since only 10 cm length of the laser rod is exposed to concentrated solar radiation within the 2D CPC pump cavity, the surface area of this exposed section of the rod is considered as a receiver, consequently.

$$S_r = \pi D L_e = 3.14 \times 1.0 \times 10 = 31.4 \left(\text{cm}^2\right)$$

By considering $S_a = 6.75$ m^2 ACTA primary solar collector area, the solar concentration ratio can be calculated

$$C = \frac{S_a}{S_r} = \frac{6.75 \times 10^4 \text{ cm}^2}{31.4 \text{ cm}^2} = 2150 \tag{3.146}$$

Effective absorption length *L*

To calculate the absorption path length L of solar pump light within the 10 mm diameter, 130 mm length Nd:YAG rod in Figs. 3.23 and 3.24, eight rectangular detectors are equally spaced around the internal surface of the rod, as indicated by Fig. 3.25. As shown in Fig. 3.19, the deviation angles of α and β of the solar ray in each detector position can be detected, so that deviation angle β' and, consequently, effective pump absorption path L at each of the eight detector positions can be calculated by (3.105), (3.106), respectively.

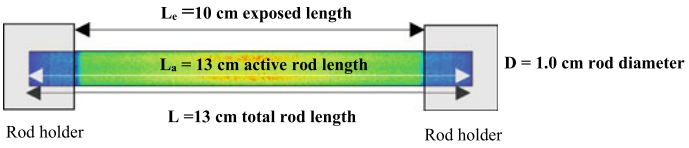

Fig. 3.24 Absorbed pump power distribution along the 10 mm diameter, 130 mm length Nd:YAG rod

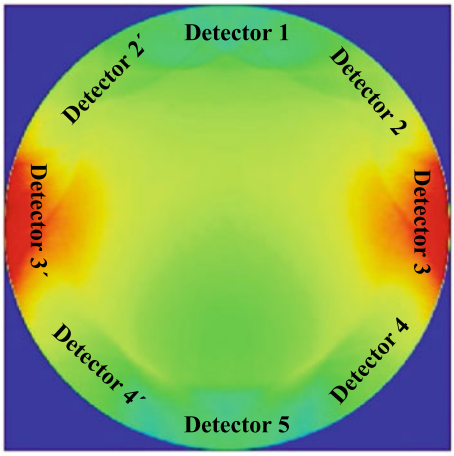

Fig. 3.25 Detection of deviation angles α and β by Zemax® angle-space method. Eight detectors are positioned in equal space beneath the rod surface. Solar pump power and incident pump ray angles at each detector position can be detected simultaneously

Figures 3.26, 3.27, 3.28, 3.29 and 3.30 below show the Zemax® non-sequential ray tracing results of angle space distribution obtained from each detector rectangle. Deviation angles α and β are determined by cross section row FWHM X-coordinate value and cross section column FWHM Y-coordinate value of detectors 1–5, respectively.

Since the 2D-CPC secondary concentrator ensures a symmetric pump profile for the rod, Detector 2′, Detector 3′ and Detector 4′ in Fig. 3.25 present the same amount of detected power, the same deviation angles of α and β, and consequently, the same absorption lengths as that of Detector 2, Detector 3 and Detector 4, respectively.

Table 3.1 summarize the detected pump power for each detector. Relative weight for each detector can also be calculated. Effective absorption length in different detector positions, ranging from L_1 to L_5, are finally listed.

Finally, weighted effective absorption length L can be finally calculated

$$L = 6.47\%L_1 + 22.66\%L_2 + 41.73\%L_3 + 20.35\%L_4 + 8.79\%L_5 = 1.27(\text{cm}) \tag{3.147}$$

Calculation of absorbed solar power and absorbed photon number density in the five bands

Once the weighted effective absorption length is calculated ($L = 1.27$ cm), the amounts of absorbed pump power density and absorbed photon density within each

ZEMAX® angle-space distribution

Detector 1

Detected power 16.72W

Deviation angles

$\alpha = 7^{\circ}$, $\beta = 6^{\circ}$

$Tan\,\beta' = Cos\,\alpha\ Tan\,\beta = 0.104$

$\beta' = 5.96^{\circ}$

Optical absorption path length

$L_1 = \frac{D}{Cos\,\alpha\,Cos\,\beta'} = 1.01\ (cm)$

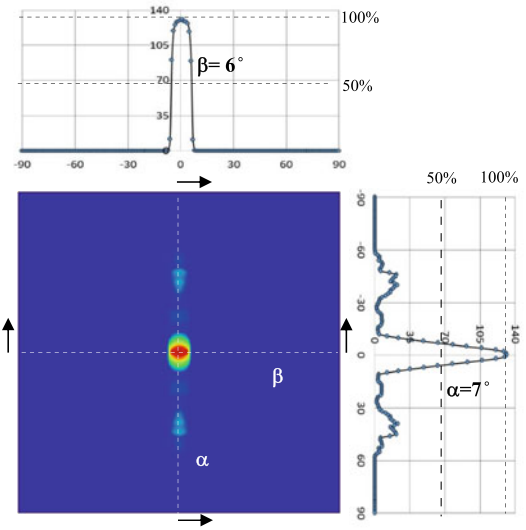

Fig. 3.26 Zemax® angle-space distribution of detector 1

ZEMAX® angle-space distribution

Detector 2

Detected power 29.26W

Deviation angles

$\alpha = 33^{\circ}$, $\beta = 3^{\circ}$

$Tan\,\beta' = Cos\,\alpha\ Tan\,\beta = 0.044$

$\beta' = 2.52^{\circ}$

Optical absorption path

$L_2 = \frac{D}{Cos\,\alpha\,Cos\,\beta'} = 1.19\ (cm)$

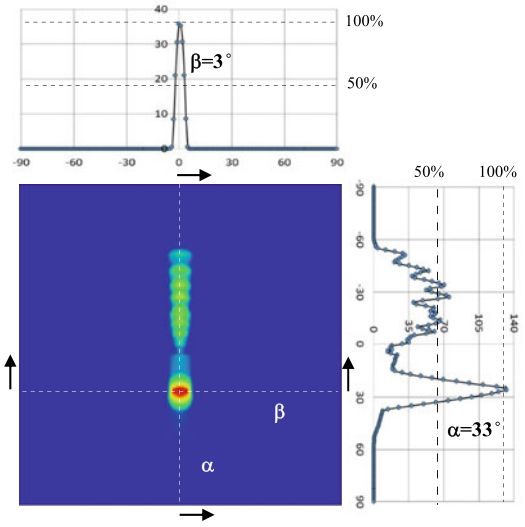

Fig. 3.27 Zemax® angle-space distribution of detector 2

of the five simplified absorption band in Fig. 3.21 can be finally calculated by using (3.143) and (3.145).

It is also important to note that simplified absorption coefficient of each band corresponds to 40% of the peak absorption coefficient value of that band $\sigma_a\left(\frac{\lambda_a+\lambda_b}{2}\right) = 40\%\ \sigma_{a-peak}$, as indicated in Fig. 3.21 by blue color text.

ZEMAX® angle-space distribution

Detector 3

Detected power 53.89W

Deviation angles

α= 39°, β = 6°

$Tan\,\beta' = Cos\,\alpha\ Tan\,\beta = 0.082$

β′ = 2.72°

Optical absorption path

$L_3 = \frac{D}{Cos\,\alpha\,Cos\,\beta'} = 1.29\ (cm)$

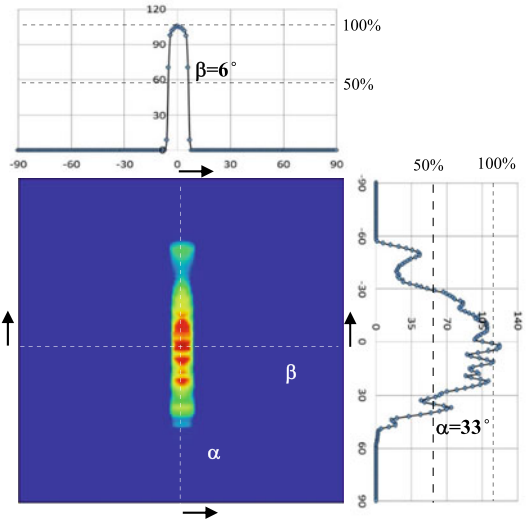

Fig. 3.28 Zemax® angle-space distribution of detector 3

ZEMAX® angle-space distribution

Detector 4

Detected power 26.28W

Deviation angles

α= 41°, β = 3°

$Tan\,\beta' = Cos\,\alpha\ Tan\,\beta = 0.040$

β′ = 2.27°

Optical absorption path

$L_4 = \frac{D}{Cos\,\alpha\,Cos\,\beta'} = 1.33(cm)$

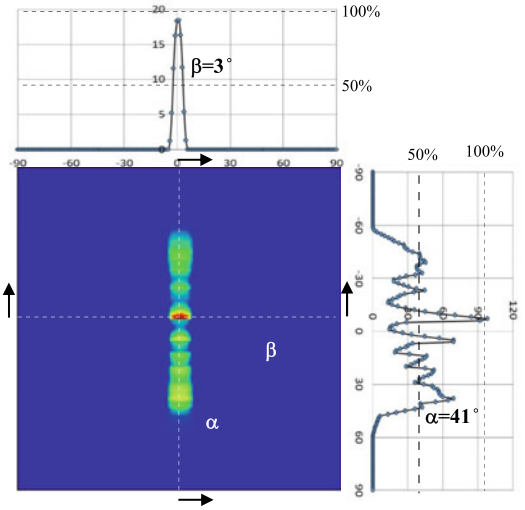

Fig. 3.29 Zemax® angle-space distribution of detector 4

By adopting Eq. (3.143):

$$I\left(\frac{\lambda_a+\lambda_b}{2}\right)\left\{1-exp\left[-\sigma_a\left(\frac{\lambda_a+\lambda_b}{2}\right)L\right]\right\}\Delta\lambda$$

ZEMAX® angle-space distribution

Detector 5

Detected power 22.72W

Deviation angles

$\alpha = 44^{\circ}, \beta = 6^{\circ}$

$Tan\,\beta' = Cos\,\alpha\ Tan\,\beta = 0.076$

$\beta' = 4.32^{\circ}$

Optical absorption path

$L_5 = \frac{D}{Cos\,\alpha\,Cos\,\beta'} = 1.39\ (cm)$

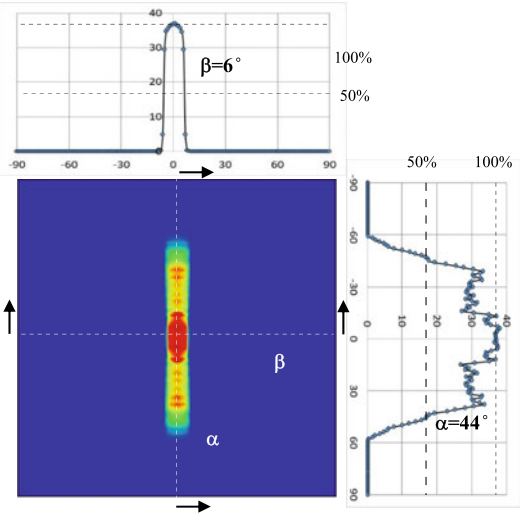

Fig. 3.30 Zemax® angle-space distribution of detector 5

Table 3.1 Effective absorption lengths determined by the deviation angles of 8 detectors. Since each detector detect different amount of solar pump power, different weight are calculated accordingly, indicating non-homogeneous solar pumping around the laser rod, as indicated by Fig. 3.25

	Detected solar pump power (W)	Weight (%)	Effective absorption length (cm)
Detector 1	16.72	6.47	$L_1 = 1.01$
Detectors $2 + 2'$	$2 \times 29.26 = 58.52$	22.66	$L_2 = 1.19$
Detectors $3 + 3'$	$2 \times 53.89 = 107.78$	41.73	$L_3 = 1.29$
Detectors $4 + 4'$	$2 \times 26.28 = 52.56$	20.35	$L_4 = 1.33$
Detector 5	22.72	8.79	$L_5 = 1.39$
	Total detected power 258.30 W	100.00	Weighted absorption length L = 1.27 cm

Absorbed solar pump power density in 530 nm band can be calculated

$$
\begin{aligned}
&= I(530\ \text{nm})\{1 - \exp[-\alpha_a(530\ \text{nm})L]\}28\ \text{nm} \\
&= 1.35\frac{\text{W}}{\text{m}^2\text{nm}}\left\{1 - \exp\left[-1.53\ \text{cm}^{-1} \times 1.27\ \text{cm}\right]\right\}28\ \text{nm} \\
&= 32.40\ \frac{\text{W}}{\text{m}^2}
\end{aligned}
$$

By adopting Eq. (3.145):

$$\frac{1}{h\upsilon\left(\frac{\lambda_a+\lambda_b}{2}\right)} I\left(\frac{\lambda_a+\lambda_b}{2}\right)\left\{1 - \exp\left[-\sigma_a\left(\frac{\lambda_a+\lambda_b}{2}\right)L\right]\right\}\Delta\lambda$$

Absorbed solar photon number density in 530 nm band can also be calculated

$$= \frac{32.40 \frac{\mathrm{W}}{\mathrm{m}^2}}{h\upsilon(530\ \mathrm{nm})} = \frac{32.40 \frac{\mathrm{W}}{\mathrm{m}^2}}{3.75 \times 10^{-19}\ \mathrm{J}} = 0.864 \times 10^{20} \frac{1}{\mathrm{m}^2\mathrm{s}}$$

In the same way, absorbed solar pump power density in 580 nm band

$$\begin{aligned} &= I(580\ \mathrm{nm})\{1 - \exp[-\alpha_a(580\ \mathrm{nm})L]\}28\ \mathrm{nm} \\ &= 1.31 \frac{\mathrm{W}}{\mathrm{m}^2\mathrm{nm}} \left\{1 - \exp\left[-3.16\ \mathrm{cm}^{-1} \times 1.27\ \mathrm{cm}\right]\right\} 28\ \mathrm{nm} \\ &= 36.02 \frac{\mathrm{W}}{\mathrm{m}^2} \end{aligned}$$

Absorbed solar photon number density in 580 nm band

$$= \frac{36.02 \frac{\mathrm{W}}{\mathrm{m}^2}}{h\upsilon(580\ \mathrm{nm})} = \frac{36.02 \frac{\mathrm{W}}{\mathrm{m}^2}}{3.43 \times 10^{-19}\ \mathrm{J}} = 1.050 \times 10^{20} \frac{1}{\mathrm{m}^2\mathrm{s}}$$

Absorbed solar pump power density in 750 nm band

$$\begin{aligned} &= I(750\ \mathrm{nm})\{1 - \exp[-\alpha_a(750\ \mathrm{nm})L]\}31\ \mathrm{nm} \\ &= 1.12 \frac{\mathrm{W}}{\mathrm{m}^2\mathrm{nm}} \left\{1 - \exp\left[-3.42\ \mathrm{cm}^{-1} \times 1.27\ \mathrm{cm}\right]\right\} 31\ \mathrm{nm} \\ &= 34.27 \frac{\mathrm{W}}{\mathrm{m}^2} \end{aligned}$$

Absorbed solar photon number density in 750 nm band

$$= \frac{34.27 \frac{\mathrm{W}}{\mathrm{m}^2}}{h\upsilon(750\ \mathrm{nm})} = \frac{34.27 \frac{\mathrm{W}}{\mathrm{m}^2}}{2.65 \times 10^{-19}\ \mathrm{J}} = 1.293 \times 10^{20} \frac{1}{\mathrm{m}^2\mathrm{s}}$$

Absorbed solar pump power density in 810 nm band

$$\begin{aligned} &= I(810\ \mathrm{nm})\{1 - \exp[-\alpha_a(810\ \mathrm{nm})L]\}33\ \mathrm{nm} \\ &= 1.00 \frac{\mathrm{W}}{\mathrm{m}^2\mathrm{nm}} \left\{1 - \exp\left[-4.00\ \mathrm{cm}^{-1} \times 1.27\ \mathrm{cm}\right]\right\} 33\ \mathrm{nm} \\ &= 32.80 \frac{\mathrm{W}}{\mathrm{m}^2} \end{aligned}$$

Absorbed solar photon number density in 810 nm band

$$= \frac{32.80 \frac{\mathrm{W}}{\mathrm{m}^2}}{h\upsilon(810\ \mathrm{nm})} = \frac{32.80 \frac{\mathrm{W}}{\mathrm{m}^2}}{2.45 \times 10^{-19}\ \mathrm{J}} = 1.339 \times 10^{20} \frac{1}{\mathrm{m}^2\mathrm{s}}$$

Absorbed solar pump power density in 860 nm band

$$\begin{aligned}
&= I(860\text{ nm})\{1-\exp[-\alpha_a(860\text{ nm})L]\}22\text{ nm}\\
&= 0.87\frac{\text{W}}{\text{m}^2\text{nm}}\left\{1-\exp\left[-1.35\text{ cm}^{-1}\times 1.27\text{ cm}\right]\right\}22\text{ nm}\\
&= 15.71\frac{\text{W}}{\text{m}^2}
\end{aligned}$$

Absorbed solar photon number density in 860 nm band

$$= \frac{15.71\frac{\text{W}}{\text{m}^2}}{h\upsilon(860\text{ nm})} = \frac{15.71\frac{\text{W}}{\text{m}^2}}{2.31\times 10^{-19}\text{ J}} = 0.680\times 10^{20}\frac{1}{\text{m}^2\text{s}}$$

Finally, we obtain the total absorbed solar power density of the five absorption bands

$$\begin{aligned}
\sum\nolimits_1^5 P_i &= 32.40\frac{\text{W}}{\text{m}^2}+36.02\frac{\text{W}}{\text{m}^2}+34.27\frac{\text{W}}{\text{m}^2}+32.80\frac{\text{W}}{\text{m}^2}+15.71\frac{\text{W}}{\text{m}^2}\\
&= 151.20\frac{\text{W}}{\text{m}^2}
\end{aligned}\tag{3.148}$$

And the total absorbed photon number density from the five bands:

$$\begin{aligned}
\sum\nolimits_1^5 F_i &= 0.864\times 10^{20}\frac{1}{\text{m}^2\text{s}}+1.050\times 10^{20}\frac{1}{\text{m}^2\text{s}}\\
&\quad +1.293\times 10^{20}\frac{1}{\text{m}^2\text{s}}+1.339\times 10^{20}\frac{1}{\text{m}^2\text{s}}+0.680\times 10^{20}\frac{1}{\text{m}^2\text{s}}\\
&= 5.226\times 10^{20}\frac{1}{\text{m}^2\text{s}} = 5.226\times 10^{16}\frac{1}{\text{cm}^2\text{s}}
\end{aligned}\tag{3.149}$$

Calculation of one sun pump rate W_p'

The astigmatic corrected target aligned (ACTA) parabolic mirror with 6.75 m^2 collection area was used to both collect and concentrate incoming solar power. For $950\frac{\text{W}}{\text{m}^2}$ solar irradiance, 6412.5 W incoming solar power was calculated. By assuming infinite absorption coefficient $\alpha_a(\lambda)=\infty$, 4225.8 W absorbed power at rod surface was detected by Zemax® software.

Consequently, $\boldsymbol{\eta_T} = \frac{4225.8\boldsymbol{W}}{6412.5\boldsymbol{W}} = 0.659$ transfer efficiency was calculated.

As discussed in Sect. 3.20, $\boldsymbol{\eta_U(\lambda)} = 0.59$ upper state efficiency was assumed in our analysis [11].

Since both which $\eta_T(\lambda)$ and $\eta_U(\lambda)$ remain nearly constant within each of the five absorption bands, we then reach simplified equation for one sun pump rate

$$W_p' = \eta_T \eta_U \frac{4}{N_t D} \int \frac{I(\lambda)}{h\upsilon(\lambda)} \{1 - \exp[-\alpha(\lambda)L]\} d\lambda = \eta_T \eta_U \frac{4}{N_t D} \sum_1^5 F_i$$
$$= 0.493 \times 0.59 \times \frac{4}{1.518 \times 10^{20}\ \text{cm}^{-3} \times 1.0\ \text{cm}} \times 5.226 \times 10^{16} \frac{1}{\text{cm}^2\text{s}}$$
$$= 0.40 \times 10^{-3} \frac{1}{\text{s}} \tag{3.150}$$

Calculation of threshold pump rate W_{pth}

For 1.1 at.% Nd:YAG rod, $\sigma = 6.5 \times 10^{-19}$ cm^2, $l = 13$ cm, $D = 1$ cm, $A = 0.785$ cm^2 $R_1 = 0.998$, $R_2 = 0.95$, $N_t = 1.518 \times 10^{20}$ cm^{-3}.

The single-trip loss of the laser resonant cavity is firstly calculated

$$\gamma = \alpha l + \frac{1}{2}\left[\ln\left(\frac{1}{R_1}\right) + \ln\left(\frac{1}{R_2}\right)\right]$$
$$= 0.003\ \text{cm}^{-1} \times 13\ \text{cm} + \frac{1}{2}\left[\ln\left(\frac{1}{0.998}\right) + \ln\left(\frac{1}{0.95}\right)\right] = 6.57\% \tag{3.151}$$

Then we can calculate the threshold solar pump rate

$$W_{pth} = \frac{\gamma}{\sigma \tau_e N_t l} = \frac{0.0657}{6.5 \times 10^{19}\ \text{cm}^2 \times 230 \times 10^{-6}\ \text{s} \times 1.518 \times 10^{20}\ \text{cm}^{-3} \times 13\ \text{cm}}$$
$$= 0.223\ \text{s}^{-1} \tag{3.152}$$

Calculation of solar laser output power

$$P_{out} = Ah\nu \left(\frac{N_t l}{\gamma}\right) \frac{1}{2} ln \frac{1}{R_2} \left[C W_p' - \frac{\gamma}{\sigma \tau_e N_t l}\right]$$
$$= 0.785\ \text{cm}^2 \times 6.63 \times 10^{-34}\ \text{J S} \times 2.82 \times 10^{14}\ \text{S}^{-1}$$
$$\times \left(\frac{1.518 \times 10^{20}\ \text{cm}^{-3} \times 13\ \text{cm}}{0.0657}\right) \frac{1}{2} ln$$
$$\times \frac{1}{0.95}\left(2150 \times 0.40 \times 10^{-3} \frac{1}{\text{s}} - 0.223 \frac{1}{\text{s}}\right) = \eta_s' \left(C W_p' - W_{pth}\right)$$
$$= 113.1\text{J}\left(0.860\ \text{S}^{-1} - 0.223\ \text{S}^{-1}\right) = 72.0\ \text{W} \tag{3.153}$$

Calculation of $\frac{P_{in}}{P_{pth}}$ ratio

$$x = \frac{P_{in}}{P_{pth}} = \frac{W_p}{W_{pth}} = \frac{C W_p'}{W_{pth}} = \frac{0.860\ \text{S}^{-1}}{0.223\ \text{S}^{-1}} = 3.86 \tag{3.154}$$

Calculation of threshold pump power P_{pth}

$$P_{\text{pth}} = \frac{P_{\text{in}}}{x} = \frac{6412.5\,\text{W}}{3.86} = 1661.3\,\text{W} \tag{3.155}$$

Calculation of solar to laser power conversion efficiency η

With 6.75 m^2 collection area, at 950 W/m^2 solar irradiance, 6412.5 W incoming solar power is calculated.

$$\eta = \frac{P_{out}}{P_{in}} = \frac{72.0\ \text{W}}{6412.5\ \text{W}} = 1.12\% \tag{3.156}$$

Calculation of solar laser slope efficiency η_{slope}

$$\begin{aligned} \eta_{slope} &= \frac{P_{out}}{(P_{in} - P_{th})} = \frac{P_{out}}{P_{in}\left(1 - \frac{P_{th}}{P_{in}}\right)} = \eta \frac{1}{\left(1 - \frac{1}{x}\right)} \\ &= \eta \frac{x}{x-1} = 1.12\% \frac{3.86}{3.86 - 1} = 1.51\% \end{aligned} \tag{3.157}$$

3.27.2 *Classical Analytical Method of Side-Pumped Solar Laser*

The following equations are commonly used classical analytical method for calculating laser output power P_{out}, slope efficiency η_{s} and threshold pump power P_{th} of solid-state lasers [2].

$$P_{out} = \frac{1-R}{1+R}\left(\frac{2\eta_{OVP}\eta_T\eta_A\eta_U\eta_B}{\delta - lnR}P_{in} - AI_{\text{s}}\right) \tag{3.158}$$

$$\eta_{\text{s}} = \frac{1-R}{1+R}\left(\frac{2\eta_{OVP}\eta_T\eta_A\eta_U\eta_B}{\delta - lnR}\right) \tag{3.159}$$

$$P_{th} = \frac{\delta - lnR}{2\eta_{OVP}\eta_T\eta_A\eta_U\eta_B}AI_{\text{s}} \tag{3.160}$$

where:

$$I_s = \frac{h\upsilon}{\tau\sigma} = \frac{6.63 \times 10^{-34}\ \text{JS} \times 2.82 \times 10^{14}\ \text{s}^{-1}}{230 \times 10^{-6}\ \text{S} \times 6.5 \times 10^{-19}\ \text{cm}^2} = 1.2506\ \text{kW/cm}^2$$

For the side-pumped solar laser in Fig. 3.23, all other important parameters and laser output power are calculated by (3.158), (3.159) and (3.160) and listed by Table 3.2.

Table 3.2 Design parameters and output power of the side-pumped solar laser

Parameters	
Irradiance (W/m^2)	950
Collection area (m^2)	6.75
P_{IN} (W)	6412.5
Rod diameter (cm)	1
Length l (cm)	13
A (cm^2)	0.785
I_S (kW/cm^2)	1.2506
$A\ I_S$ (W)	981.7
α (cm^{-1})	0.003
$2\alpha l$	0.078
δ_M	0.004
δ_D	0.000
$\delta = 2\alpha l + \delta_M + \delta_D$	0.082
R	0.95
(1-R)/(1 + R)	0.02564
$\delta - \ln R$	0.1333
η_{ovp}	0.16
P_{SOURCE} (Zemax) (W)	1026
$P_{TRANSFER}$ (Zemax) (W)	505.93
η_T	0.493
$P_{ABSORBED}$ (Zemax) (W)	423.58
η_A	0.837
η_U	0.59
$\eta = \eta_{OVP}\eta_T\eta_A\eta_U\eta_B$	0.03895
Analytical calculation	
P_{OUT} (W)	70.9
Total η_{SLOPE} (%)	1.50
P_{TH} (W)	1679.4
Solar-to-laser conversion efficiency (%)	0.94

3.27.3 LASCAD™ Analysis of the Side-Pumped Solar Laser

Similar to the Zemax® and LASCAD™ solar laser analysis examples in Chap. 2, the absorbed pump flux data from the Zemax® analysis of the side-pumped solar laser in Figs. 3.23 and 3.24 can be processed by LASCAD™ software to evaluate laser output performances.

The stimulated emission cross-section of 6.5×10^{-19} cm^2, the fluorescence life time of 230 μs and an absorption and scattering loss of 0.003 cm^{-1} for the 1.1

at.% Nd:YAG medium were adopted in LASCAD™ analysis. The mean absorbed and intensity-weighted solar pump wavelength of 660 nm [14] was also used in the analysis. For the 10.0 mm diameter, 1.1 at.% Nd:YAG rod with length $L_R = 130$ mm, the amount of absorption and scattering losses was $2\,\alpha\,L_R = 5.2\%$. Assuming 0.4% of imperfect HR and AR coating losses, the round-trip loss was increased to 5.6%. The diffraction losses depend heavily on rod diameter, resonator length and RoC of the resonator mirrors. LASCAD™ beam propagation method (BPM) resulted in a negligible diffraction loss when HR1064 nm end mirror and PR1064 nm output mirror, all with RoC $= \infty$, were placed very close to the laser rod. Final round-trip loss of 5.6% was calculated. Consequently, 72.5 W multimode solar laser power was numerically calculated.

By considering the incoming solar power of 6412.5 W and for the maximum solar laser output power of 72.5 W, solar-to-laser conversion efficiency of 1.13% is calculated. Effective threshold solar pump power and maximum effective solar power of 104.4 W, 417.0 W was indicated in Fig. 3.31, respectively, corresponding to 1587.3 W threshold solar power and the maximum incoming solar power of 6412.5 W, respectively. Solar laser slope efficiency of 1.5% was hence be calculated. Maximum pump power/threshold pump power ratio of 4.04 was calculated. All the above mentioned parameters are indicated in Table 3.3.

Under the same pumping conditions for the laser resonator with L = 430 mm length, 45.9 W laser output power, 1687.5 W threshold pump power, 0.716% solar-to-laser conversion efficiency, 0.97% laser slope efficiency and 3.8 maximum pump power/threshold pump power ratio were calculated by LASCAD™ software, as shown in Fig. 3.32.

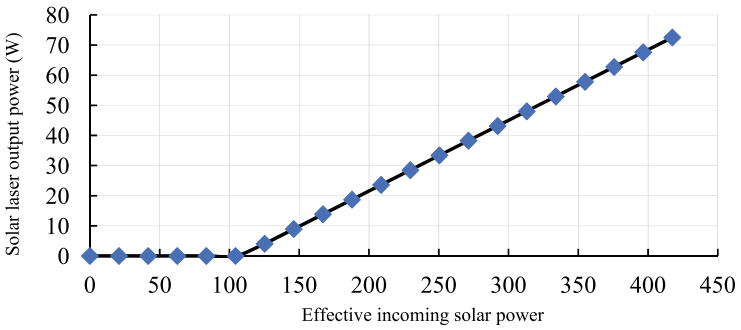

Effective solar pump power	104.4W	417.0W
Incoming solar power	1587.3W	6412.5W

Fig. 3.31 Numerically calculated solar laser output power versus effective incoming solar power by assuming a closely coupled resonant cavity

Table 3.3 Side-pumped solar laser output performance by different analysis methods

	Laser output power (W)	Threshold pump power (W)	Solar-to-laser conversion efficiency (%)	Laser slope efficiency (%)	Maximum pump power/threshold pump power ratio
Modified analysis	72.0	1661.3	1.120	1.51	3.86
Classical analysis	70.9	1680.2	1.106	1.50	3.82
$\text{LASCAD}_{\text{Max}}$	72.5	1587.3	1.130	1.50	4.04
$\text{LASCAD}_{\text{L430mm}}$	45.9	1687.5	0.716	0.97	3.80
Experimental	46.0	2596.2	0.717	1.20	2.47

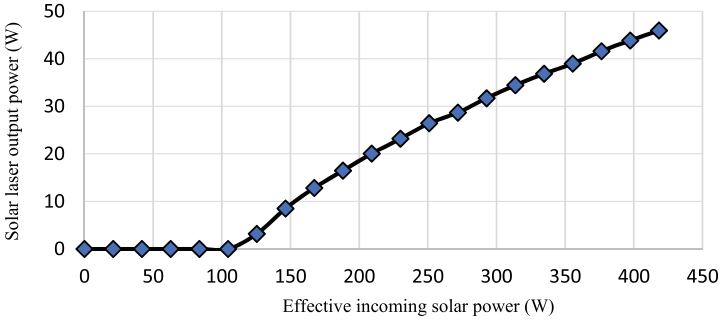

Fig. 3.32 Numerically calculated solar laser output power versus effective incoming solar power for the laser resonant cavity with $L = 46$ cm length

3.27.4 Comparison of Different Analysis Methods of the Side-Pumped Solar Laser

Discussions

As shown by Table 3.3, both the modified and the LASCAD™ analyses predicted nearly the same maximum extractable multimode laser power and solar-to-laser conversion efficiency when the HR1064 nm end mirror and PR1064 nm output mirrors were closely placed near the Nd:YAG laser rod. This happened when unity overlap efficiency ($\eta_B = 1$) was assumed in the modified method. Classical analytical method offered a considerably reduced prediction accuracy for laser power and efficiency, as indicated by Table 3.3.

However, it is important to note that both the modified and the classical analyses were not effective in predicting the output power from a laser resonant cavity with a certain cavity length L ($\eta_B < 1$), since it was very difficult to calculate analytically the beam overlap efficiency of solar-pumped lasers, as mentioned in Sect. 3.22.

Zemax® and LASCAD™ analyses were effective in the laser output power prediction of a solar laser with certain cavity length, as explained in Sect. 2.26 of Chap. 2. Detailed analysis method will be provided in Sect. 6.2.1 of Chap. 6.

When the HR1064 nm end mirror and the PR1064 nm output mirror were positioned 430 mm away from each other, there was a noticeable reduction in beam overlap efficiency ($\eta_B < 1$), consequently, 45.9 W solar laser output power was calculated by Zemax® and $\text{LASCAD}_{\text{L430mm}}$ analyses, as shown by Fig. 3.32 and confirmed by experimental result [16].

As for the prediction of threshold solar pump power, all the analyses including LASCAD™ failed to a considerable extent, leading normally to a much smaller threshold power prediction accuracy, as compared to the experimental result in Table 3.3.

3.28 Output Power Analysis of an End-Side-Pumped Nd:YAG Solar Laser

3.28.1 Modified Analytical Method for the End-Side-Pumped Nd:YAG Solar Laser

Solar concentration factor *C*

The Fresnel lens collector has the collection area of $S_A = \pi R^2 = 6358.5\ \text{cm}^2$ (Fig. 3.33).

The $D = 0.4$ cm, $l = 2.1$ cm rod has an exposed surface area of $S_R = \frac{\pi D^2}{4} + \pi D l = 2.763\,\text{cm}^2$.

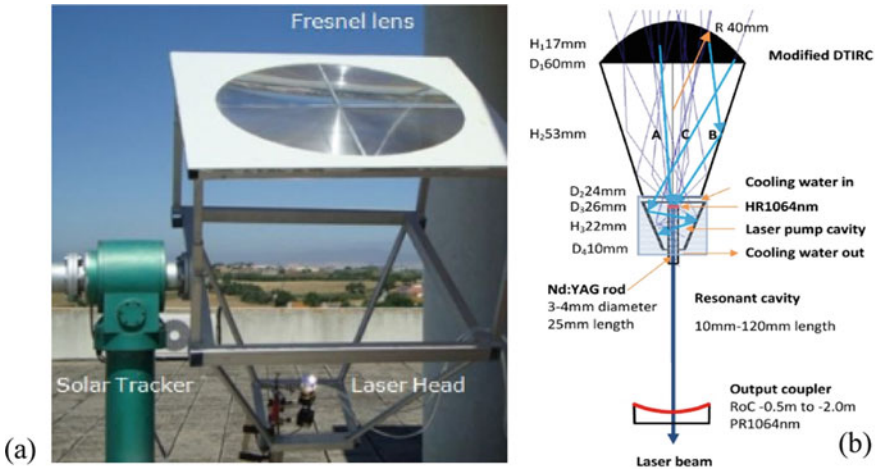

Fig. 3.33 **a** The Nd:YAG solar-pumped laser system with a 0.9 m diameter Fresnel lens and **b** a laser head positioned in the focal zone of the Fresnel lens [14]

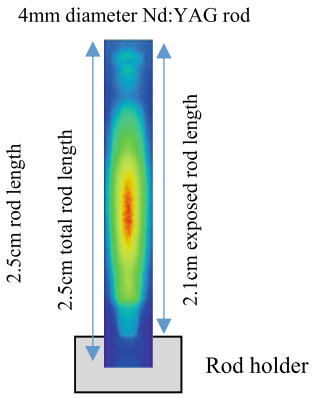

Fig. 3.34 Absorbed pump power distribution along a 4 mm diameter, 25 mm length Nd:YAG rod

The solar concentration ratio C is hence calculated:

$$\boldsymbol{C} = \frac{\boldsymbol{S_A}}{\boldsymbol{S_R}} = 2301.3 \tag{3.161}$$

Effective absorption length L

By Zemax® analysis, 24.8% of all the solar pump ray were found to enter the $D = 4$ mm diameter and $l = 25$ mm length Nd:YAG rod through its HR1064 nm end face, ensuring the most efficient pump light absorption through end-pumping configuration. Similar to the divergence angle analysis of the solar pump rays within a laser rod in in Sect. 3.27, a square detector (Detector 1) was placed beneath the HR1064 nm end face of the D = 4 mm diameter and l = 25 mm length Nd:YAG rod, as indicated by Figs. 3.34 and 3.35. $\gamma_x = \gamma_y = 20^\circ$ divergence angles were detected. Effective absorption length $L_{\text{End-pumping}} = 2.81$ cm was consequently calculated.

By Zemax® analysis, 69.6% of all the solar pump ray were found to enter the D = 4 mm diameter and l = 25 mm length Nd:YAG rod through its side barrel face, ensuring also an efficient pump light absorption through three-pass side-pumping configuration, a detector rectangle (Detector 2) was placed beneath the side face of the D = 4 mm = 0.4 cm diameter and l = 25 mm length Nd:YAG rod, as indicated by Fig. 3.36. α=32°, β=21° divergence angles were detected. Effective absorption length $L_{\text{Three-pass}}$=1.39 cm was calculated. End-pumping solar pump rays in Fig. 3.35 were also detected by Detector 2.

By Zemax® analysis, only 5.6% of all the solar pump ray were found to enter the D = 4 mm diameter and l = 25 mm length rod through its side face in one-pass pumping approach, leading to an inefficient pump light absorption. A short detector rectangle (Detector 3) was placed beneath the side face of the Nd:YAG rod, as indicated by Fig. 3.37. α = 25°, β = 28° divergence angles were detected. Effective absorption length $L_{\text{One-pass}} = 0.49$ cm was calculated. To detect the one-pass rays

ZEMAX® angle-space distribution

Detector 1

End-pumping

Deviation angles:

$\gamma_x = 20^\circ,\ \gamma_y = 20^\circ$

$Tan\,\beta' = Cos\,\gamma_x\ Tan\,\gamma_y = 0.342$

$\gamma' = 18.9^\circ$

Effective absorption length:

$$L_{End-pumping} = \frac{2.5}{Cos\ \gamma_x Cos\,\gamma'} = 2.81(cm)$$

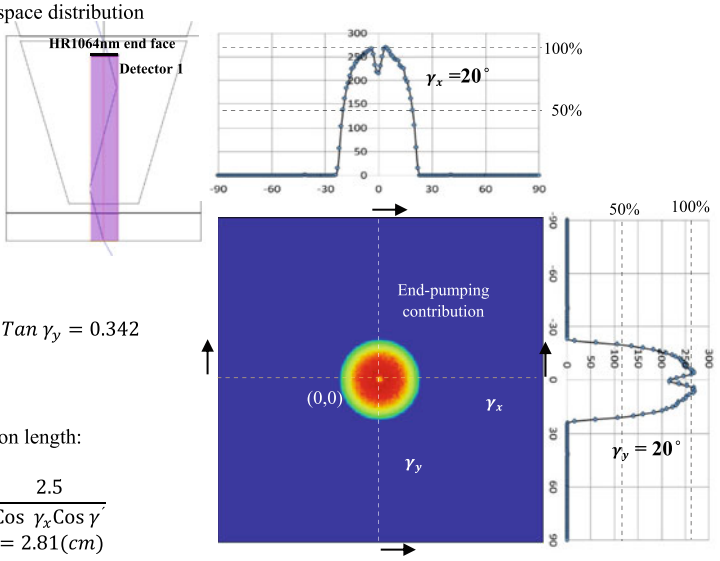

Fig. 3.35 Zemax® angle-space distribution of detector 1 for end-pumping

ZEMAX® angle-space distribution

Detector 2

Side-pumping

Deviation angles

α= 32°, β = 21°

$Tan\,\beta' = Cos\,\alpha\ Tan\,\beta = 0.326$

$\beta' = 18.0^\circ$

Effective absorption length

$$L_{Three-pass} = 2 \times \frac{D}{Cos\,\alpha\ Cos\,\beta'} + 4 = 1.39(cm)$$

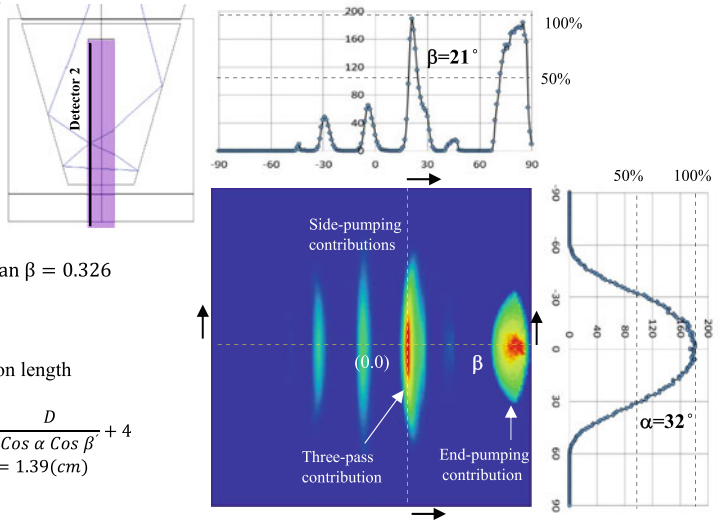

Fig. 3.36 Zemax® angle-space distribution of detector 2 for three-pass side-pumping

more effectively, Detector 3 was positioned near the output end of the rod. Besides, since Detector 3 also had a much shorter length than that of Detector 2, contribution of the solar rays through the HR 1064 nm end face was much less pronounced in Fig. 3.37, as compared to that in Fig. 3.36.

Zemax® analysis of different effective absorption lengths and their relative weights for different passes (Table 3.4)

$$\begin{aligned} \mathrm{L} &= 24.8\% \times L_{\text{End-pumping}} + 69.6\% \times L_{\text{Three-pass}} + 5.6\% \times L_{\text{One-pass}} \\ &= 24.8\% \times 2.81 + 69.6\% \times 1.39 + 5.6\% \times 0.49 = 1.69\,(\text{cm}) \end{aligned} \tag{3.162}$$

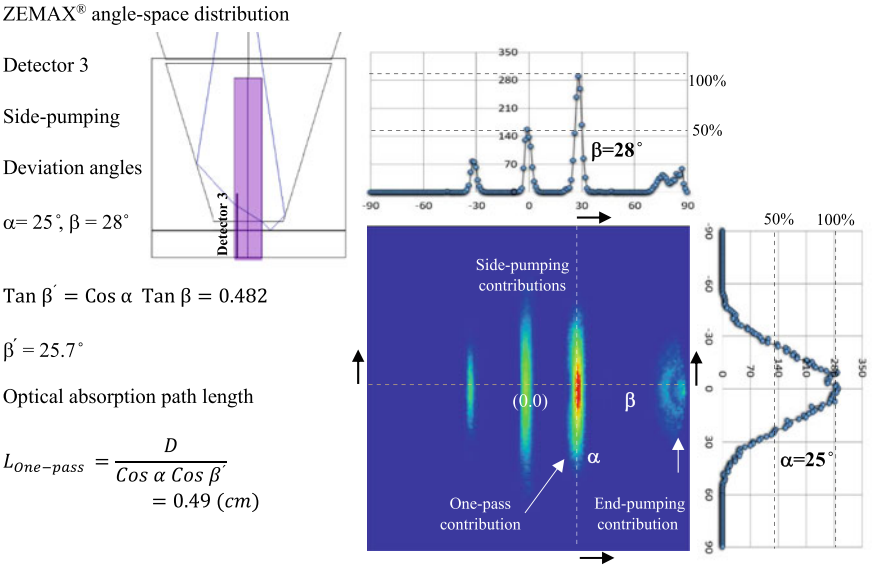

Fig. 3.37 Zemax® angle-space distribution of detector 3 for one-pass side-pumping

Table 3.4 Effective absorption length for end-side-pumping approach

	End-pumping	Three-pass side pumping	One-pass side pumping
Weight	24.8%	69.6%	5.6%
Type	$L_{\text{End-pumping}}$	$L_{\text{Three-pass}}$	$L_{\text{One-pass}}$
Effective absorption length	2.81 cm	1.39 cm	0.49 cm

Calculation of absorbed solar power and absorbed photon number density in the five bands

Once the weighted effective absorption length ($L = 1.69$ cm) is found, the amounts of absorbed pump power density and absorbed photon density within each of the five simplified absorption band in Fig. 3.21 can be finally calculated by using (3.143) and (3.145).

By adopting Eq. (3.143): $I\left(\frac{\lambda_a+\lambda_b}{2}\right)\left\{1-\exp\left[-\sigma_a\left(\frac{\lambda_a+\lambda_b}{2}\right)L\right]\right\}\Delta\lambda$.

Absorbed solar pump power density in 530 nm band

$$\begin{aligned}&= I(530\text{ nm})\{1-\exp[-\alpha_a(530\text{ nm})L]\}28\text{ nm}\\&= 1.35\frac{\text{W}}{\text{m}^2\text{nm}}\left\{1-\exp\left[-1.39\text{ cm}^{-1}1.69\text{ cm}\right]\right\}28\text{ nm}\\&= 34.19\frac{\text{W}}{\text{m}^2}\end{aligned}$$

By adopting Eq. (3.145): $\frac{1}{h\upsilon\left(\frac{\lambda_a+\lambda_b}{2}\right)}I\left(\frac{\lambda_a+\lambda_b}{2}\right)\left\{1-\exp\left[-\sigma_a\left(\frac{\lambda_a+\lambda_b}{2}\right)L\right]\right\}\Delta\lambda$

Absorbed solar photon density in 530 nm band

$$= \frac{34.19\frac{\text{W}}{\text{m}^2}}{h\upsilon(530\text{ nm})} = \frac{34.19\frac{\text{W}}{\text{m}^2}}{3.75\times10^{-19}\text{ J}} = 0.912\times10^{20}\frac{1}{\text{m}^2\text{s}}$$

Similarly, absorbed solar pump power density in 580 nm band

$$\begin{aligned}&I(580\text{ nm})\{1-\exp[-\alpha_a(580\text{ nm})L]\}\ 28\text{ nm}\\&= 1.31\frac{\text{W}}{\text{m}^2\text{nm}}\left\{1-\exp\left[-2.87\text{ cm}^{-1}1.69\text{ cm}\right]\right\}\ 28\text{ nm}\\&= 36.39\frac{\text{W}}{\text{m}^2}\end{aligned}$$

Absorbed solar photon number density in 580 nm band

$$= \frac{36.39\frac{\text{W}}{\text{m}^2}}{h\upsilon(580\text{ nm})} = \frac{36.39\frac{\text{W}}{\text{m}^2}}{3.43\times10^{-19}\text{ J}} = 1.061\times10^{20}\frac{1}{\text{m}^2\text{s}}$$

Absorbed solar pump power density in 750 nm band

$$\begin{aligned}&I(750\text{ nm})\{1-\exp[-\alpha_a(750\text{ nm})L]\}\ 31\text{ nm}\\&= 1.12\frac{\text{W}}{\text{m}^2\text{nm}}\left\{1-\exp\left[-3.11\text{ cm}^{-1}1.69\text{ cm}\right]\right\}\ 31\text{ nm}\\&= 34.54\frac{\text{W}}{\text{m}^2}\end{aligned}$$

Absorbed solar photon number density in 750 nm band

$$= \frac{34.54\frac{\text{W}}{\text{m}^2}}{h\upsilon(750\text{ nm})} = \frac{34.54\frac{\text{W}}{\text{m}^2}}{2.65\times10^{-19}\text{ J}} = 1.303\times10^{20}\frac{1}{\text{m}^2\text{s}}$$

Absorbed solar pump power density in 810 nm band

$$\begin{aligned} & I(810\text{ nm})\{1-\exp[-\alpha_a(810\text{ nm})L]\}\ 33\text{ nm} \\ &= 1.00\frac{\text{W}}{\text{m}^2\text{nm}}\left\{1-\exp\left[-3.64\text{ cm}^{-1}1.69\text{ cm}\right]\right\}\ 33\text{ nm} \\ &= 32.93\ \frac{\text{W}}{\text{m}^2} \end{aligned}$$

Absorbed solar photon number density in 810 nm band

$$= \frac{32.93\frac{\text{W}}{\text{m}^2}}{h\upsilon(810\text{ nm})} = \frac{32.93\frac{\text{W}}{\text{m}^2}}{2.45\times10^{-19}\text{ J}} = 1.344\times10^{20}\frac{1}{\text{m}^2\text{s}}$$

Absorbed solar pump power density in 860 nm band

$$\begin{aligned} & I(860\text{ nm})\{1-\exp[-\alpha_a(860\text{ nm})L]\}\ 22\text{ nm} \\ &= 0.87\frac{\text{W}}{\text{m}^2\text{nm}}\left\{1-\exp\left[-1.23\text{ cm}^{-1}1.69\text{ cm}\right]\right\}\ 22\text{ nm} \\ &= 16.75\ \frac{\text{W}}{\text{m}^2} \end{aligned}$$

Absorbed solar photon number density in 860 nm band

$$= \frac{16.75\frac{\text{W}}{\text{m}^2}}{h\upsilon(860\text{ nm})} = \frac{16.75\frac{\text{W}}{\text{m}^2}}{2.31\times10^{-19}\text{ J}} = 0.725\times10^{20}\frac{1}{\text{m}^2\text{s}}$$

Finally, total absorbed solar power density from the five bands

$$\begin{aligned} \sum\nolimits_1^5 P_i &= 34.19\frac{\text{W}}{\text{m}^2} + 36.39\frac{\text{W}}{\text{m}^2} + 34.54\frac{\text{W}}{\text{m}^2} + 32.93\frac{\text{W}}{\text{m}^2} + 16.75\frac{\text{W}}{\text{m}^2} \\ &= 154.8\frac{\text{W}}{\text{m}^2} \end{aligned} \tag{3.163}$$

Total absorbed photon number density from the five bands

$$\begin{aligned} \sum_1^5 F_i &= 0.912\times10^{20}\frac{1}{\text{m}^2\text{s}} + 1.061\times10^{20}\frac{1}{\text{m}^2\text{s}} + 1.303\times10^{20}\frac{1}{\text{m}^2\text{s}} \\ &\quad + 1.344\times10^{20}\frac{1}{\text{m}^2\text{s}} + 0.725\times10^{20}\frac{1}{\text{m}^2\text{s}} = 5.345\times10^{20}\frac{1}{\text{m}^2\text{s}} \\ &= 5.345\times10^{16}\frac{1}{\text{cm}^2\text{s}} \end{aligned} \tag{3.164}$$

Calculation of one Sun pump rate W_p'

For the Fresnel lens with 0.63585 m^2 collection area and $890\frac{\text{W}}{\text{m}^2}$ solar irradiance, 565.9 W incoming solar power was calculated. By assuming infinite absorption

coefficient $\boldsymbol{\alpha_a(\lambda) = \infty}$, 372.9 W absorbed solar power at rod surface was detected by Zemax® software.

Consequently, $\boldsymbol{\eta_T = \frac{372.9W}{565.9W} = 0.659}$ transfer efficiency was calculated.

As mentioned in Sect. 3.20, $\boldsymbol{\eta_U(\lambda) = 0.59}$ upper state efficiency was also assumed [11].

Since both which $\eta_T(\lambda)$ and $\eta_U(\lambda)$ remain nearly constant within each of the five absorption bands, we then reach simplified equation for one Sun pump rate.

$$W_p' = \eta_T \eta_U \frac{4}{N_t D} \int \frac{I(\lambda)}{h\upsilon(\lambda)} \{1 - exp[-\alpha(\lambda)L]\} d\lambda$$
$$= \eta_T \eta_U \frac{4}{N_t D} \sum_1^5 F_i \tag{3.146}$$

$$= 0.659 \times 0.59 \times \frac{4}{1.38 \times 10^{20}\ \mathrm{cm}^{-3} \times 0.4} \times 5.345 \times 10^{16} \frac{1}{\mathrm{cm}^2 \mathrm{s}}$$
$$= 1.506 \times 10^{-3}\ \frac{1}{\mathrm{s}} \tag{3.165}$$

Calculation of threshold pump rate W_{pth}

For the 2.5 cm length Nd:YAG laser rod

$$\sigma = 2.8 \times 10^{-19}\ \mathrm{cm}^2, N_t = 1.38 \times 10^{20}\ \mathrm{cm}^{-3} \quad R_1 = 0.998 \quad R_2 = 0.98$$

$$\gamma = \alpha + \frac{1}{2}\left[\ln\left(\frac{1}{R_1}\right) + \ln\left(\frac{1}{R_2}\right)\right]$$
$$= 0.002\,\mathrm{cm}^{-1} \times 2.5\,\mathrm{cm} + \frac{1}{2}(0.002 + 0.0202) = 1.61\% \tag{3.166}$$

$$W_{pth} = \frac{\gamma}{\sigma \tau_e N_t l} = \frac{0.0161}{2.8 \times 10^{19}\ \mathrm{cm}^2 \times 230 \times 10^{-6}\ \mathrm{s} \times 1.38 \times 10^{20}\ \mathrm{cm}^{-3} \times 2.5\ \mathrm{cm}}$$
$$= 0.725\,\mathrm{s}^{-1} \tag{3.167}$$

Calculation of solar laser output power

$$P_{out} = Ah\nu\left(\frac{N_t l}{\gamma}\right)\frac{1}{2} ln \frac{1}{R_2}\left[CW_p' - \frac{\gamma}{\sigma \tau_e N_t l}\right] = \eta_s'\left(CW_p' - W_{pth}\right)$$
$$= 0.1256\ \mathrm{cm}^2 \times 6.63 \times 10^{-34}\ \mathrm{J\,S} \times 2.82 \times 10^{14}\ \mathrm{S}^{-1}$$
$$\times \left(\frac{1.38 \times 10^{20}\ \mathrm{cm}^{-3} \times 2.5\ \mathrm{cm}}{0.0161}\right)\frac{1}{2} ln \frac{1}{0.98}$$
$$\times \left(2301.3 \times 1.506 \times 10^{-3}\frac{1}{\mathrm{s}} - 0.725\frac{1}{\mathrm{s}}\right)$$
$$= 5.085\,\mathrm{J}\left(3.468\frac{1}{\mathrm{s}} - 0.725\frac{1}{\mathrm{s}}\right) = 13.94\ \mathrm{W} \tag{3.168}$$

Calculation of $\frac{P_{in}}{P_{pth}}$ ratio

$$x = \frac{P_{in}}{P_{pth}} = \frac{W_p}{W_{pth}} = \frac{\boldsymbol{CW_p'}}{W_{pth}} = \frac{3.468\frac{1}{s}}{0.725\frac{1}{s}} = 4.784$$

Calculation of threshold pump power P_{pth}

$$P_{pth} = \frac{P_{\text{in}}}{x} = \frac{565.9\ W}{4.784} = 118.3\ W$$

Calculation of solar to laser power conversion efficiency η

With 0.636 m^2 collection area, at 890 W/m^2 solar irradiance, 565.9 W incoming solar power was calculated.

$$\eta = \frac{P_{out}}{P_{in}} = \frac{13.94\ \text{W}}{565.9\ \text{W}} = 2.46\%$$

Calculation of solar laser slope efficiency η_{slope}

$$\eta_{slope} = \frac{P_{out}}{(P_{in} - P_{th})} = \frac{P_{out}}{P_{in}\left(1 - \frac{P_{th}}{P_{in}}\right)} = \eta\frac{1}{\left(1 - \frac{1}{x}\right)}$$
$$= \eta\frac{x}{x-1} = 2.46\%\frac{4.784}{4.784 - 1} = 3.11\%$$

3.28.2 Classical Analytical Method of the End-Side-Pumped Laser

The following equations are commonly used classical analytical method for calculating laser output power P_{out}, slope efficiency η_s and threshold pump power P_{th} of solid-state lasers [2].

$$P_{out} = \frac{1-R}{1+R}\left(\frac{2\eta_{OVP}\eta_T\eta_A\eta_U\eta_B}{\delta - lnR}P_{in} - AI_s\right) \tag{3.158}$$

$$\eta_s = \frac{1-R}{1+R}\left(\frac{2\eta_{OVP}\eta_T\eta_A\eta_U\eta_B}{\delta - lnR}\right) \tag{3.159}$$

$$P_{th} = \frac{\delta - lnR}{2\eta_{OVP}\eta_T\eta_A\eta_U\eta_B}AI_s \tag{3.160}$$

where $I_s = \frac{h\upsilon}{\tau\sigma} = \frac{6.63\times10^{-34}\ \text{JS}\times2.82\times10^{14}\ \text{s}^{-1}}{230\times10^{-6}\ \text{S}\times2.8\times10^{-19}\ \text{cm}^2} = 2.90\ \frac{\text{kW}}{\text{m}^2}$.

For the side-pumped solar laser in Fig. 3.23, all other important parameters and laser output power are calculated by (3.158), (3.159) and (3.160) and listed by Table 3.5.

Table 3.5 Design parameters and output performance of the end-side-pumped solar laser

Parameters	
Irradiance (W/m^2)	890
Collection area (m^2)	0.636
P_{IN} (W)	565.9
Rod diameter (mm)	4
Length l (mm)	25
A (cm^2)	0.1256
I_S (kW/cm^2)	2.90
AI_S (W)	364.2
α (cm^{-1})	0.002
$2\,\alpha\,l$	0.01
δ_M	0.004
δ_D	0.000
$\delta = 2\alpha l + \delta_M + \delta_D$	0.014
R	0.98
(1-R)/(1 + R)	0.0101
δ - lnR	0.0342
η_{OVP}	0.16
P_{SOURCE} (Zemax) (W)	90.545
$P_{TRANSFER}$ (Zemax) (W)	59.65
η_T	0.659
$P_{ABSORBED}$ (Zemax) (W)	49.05
η_A	0.822
η_U	0.59
η_B	1.00
$\eta = \eta_{OVP}\eta_T\eta_A\eta_U\eta_B$	0.0511
Analytical Calculation	
P_{OUT} (W)	13.41
Total η_{SLOPE} (%)	3.02
P_{TH} (W)	121.9
Solar-to-laser conversion efficiency (%)	2.37

3.28.3 *LASCAD™ Numerical Analysis of the End-Side-Pumped Solar Laser*

The absorbed pump flux data from the Zemax® analysis of the end-side-pumped solar laser in Fig. 3.34 was processed by LASCAD™ software to evaluate its solar laser output performances. The stimulated emission cross-section of 2.8×10^{-19} cm^2, the fluorescence life time of 230 μs and an absorption and scattering loss of 0.002 cm^{-1} for the Nd:YAG medium were adopted in LASCAD™ analysis. The mean absorbed and intensity-weighted solar pump wavelength of 660 nm [14] was also used in the analysis. For the 25 mm diameter, 1.0 at.% Nd:YAG rod with length $L_R = 25$ mm, the amount of absorption and scattering losses was $2\,\alpha\, L_R = 1.0\%$. Assuming 0.4% of imperfect HR and AR coating losses, the round-trip loss was increased to 1.4%. The diffraction losses depend heavily on rod diameter, resonator length and RoC of the resonator mirrors. LASCAD™ beam propagation method (BPM) resulted in a negligible diffraction loss when HR1064 nm end mirror and PR1064 nm output mirror, all with RoC = ∞, were placed very close to the laser rod. Final round-trip loss of 1.4% was calculated. Consequently, 13.96 W multimode solar laser power was numerically obtained, as shown by Fig. 3.38.

By considering the incoming solar power of 565.9 W and for the maximum solar laser output power of 13.96 W, solar-to-laser conversion efficiency of 2.47% was calculated for the closely coupled resonant cavity. Effective threshold solar pump power of 9.7 W and maximum effective solar power of 48.3 W was calculated, corresponding to 113.7 W threshold solar power and 565.9 W maximum incoming solar power, respectively. Solar laser slope efficiency of 3.09% was hence calculated. Maximum pump power/ threshold pump power ratio of 4.98 was calculated. All the above mentioned parameters are indicated in Table 3.6.

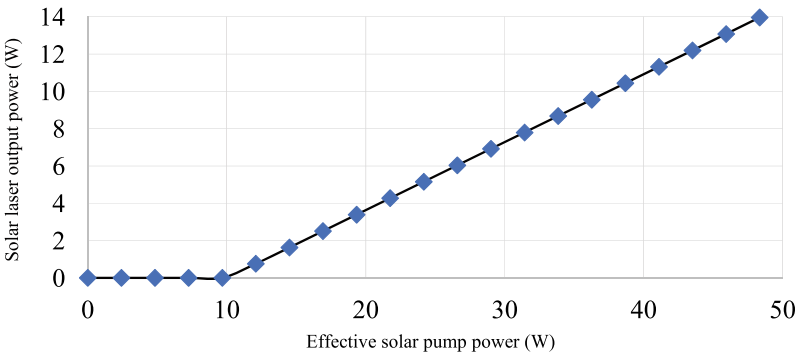

Fig. 3.38 Numerically calculated solar laser output power versus effective incoming solar power (Detector pixies 40 × 40 × 25) for 1 mm laser cavity length

Table 3.6 Solar laser output performance by different analysis methods

	Laser output power (W)	Threshold pump power (W)	Solar-to-laser conversion efficiency (%)	Laser slope efficiency (%)	Maximum pump power/threshold pump power ratio
Modified analysis	13.94	118.4	2.46	3.11	4.78
Classical analysis	13.41	121.9	2.37	3.02	4.64
$LASCAD_{Max}$	13.96	113.7	2.47	3.09	4.98
$LASCAD_{120\ mm}$	12.26	106.8	2.17	2.67	5.30
Experimental	12.30	125.8	2.17	2.79	4.50

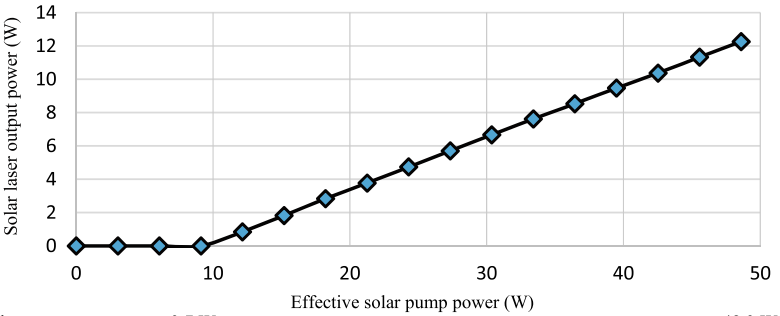

Fig. 3.39 Numerically calculated solar laser output power versus effective incoming solar power (Detector pixies 40 × 40 × 25) for 120 mm cavity length

Similarly, for the laser resonator with $L = 120$ mm length, as shown in Fig. 3.39 and under the same pumping condition, 12.26 W laser output power, 106.8 W threshold pump power, 2.17% solar-to-laser conversion efficiency, 2.67% laser slope efficiency and 5.30 maximum pump power/threshold pump power ratio were calculated by LASCAD© software, as shown in Table 3.6. (See Chaps. 2 and 5 for Zemax® and LASCAD™ laser power calculation methods for the solar laser with definite resonant cavity).

3.28.4 Comparison of Different Analyses for the End-Side-Pumped Solar Laser

Discussions

As shown by Table 3.6, both the modified and the $LASCAD_{Max}$ analyses predicted nearly the same amount of maximum extractable multimode laser power and solar-to-laser conversion efficiency when a PR1064 nm output mirror was closely placed near

the Nd:YAG laser rod. This happened when $\eta_B = 1$ overlap efficiency was assumed in the modified analysis. Classical analysis offered a slightly reduced accuracy in laser output power and efficiency predictions, as shown by Table 3.6.

It is important to point out that both the modified and the classical analyses were not effective in predicting the output power from a laser resonant cavity with a certain cavity length L ($\eta_B < 1$), since it was very difficult to calculate analytically the beam overlap efficiency of solar pumped solid-state lasers, as mentioned in Sect. 3.22.

Zemax® and LASCAD™ analyses, however, were effective in the laser output power prediction of a solar laser with certain cavity length. Detailed analysis method will be provided in Sect. 6.2.1 of Chap. 6.

When the PR1064 nm output mirror was positioned 120 mm away from the rod, there was a noticeable reduction in beam overlap efficiency ($\eta_B < 1$), consequently, 12.26 W solar laser power was numerically calculated by Zemax® and $\text{LASCAD}_{120\,\text{mm}}$ analyses, as shown by Fig. 3.39 and confirmed by experimental result [14]. As for the prediction of threshold solar pump power, all the analyses failed to a considerable extent, leading normally to a much smaller threshold power prediction, as compared to the experimental value in Table 3.6.

Homework with Solution 1

Calculation of Resonant Modes Numbers within a Cavity

Solution

For a single plane wave: $\vec{E}\left(\vec{r}, t\right) = \vec{E}_0 e^{i2\pi\nu t - i\vec{k}\cdot\vec{r}}$.

Where $\vec{E}_0$ is field amplitude, ν is light wave frequency, $\vec{r}$ is space coordinate vector and $\vec{k}$ is light wave vector. In free space, $\vec{k}$ can be any value. However, in hollow cavity, "ν" are with bounding limitations, only discrete values can exist. We consider stationary waves within a cubic hollow cavity (Fig. 3.40).

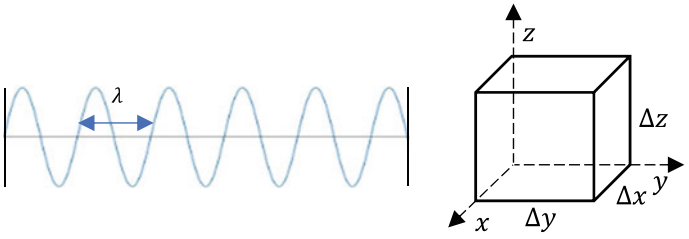

Fig. 3.40 Schematics of a stationary wave and a cubic hollow cavity with Δx, Δy, Δz dimension

We therefore obtain

$$\Delta x = m\frac{\lambda}{2} \quad \Delta y = n\frac{\lambda}{2} \quad \Delta z = q\frac{\lambda}{2} \tag{3.169}$$

where: m, n, q can be any integers

For $k = \frac{2\pi}{\lambda}$ the three components of k should meet the following conditions (Fig. 3.41)

$$k_x = \frac{\pi}{\Delta x}m, \quad k_y = \frac{\pi}{\Delta y}n, \quad k_z = \frac{\pi}{\Delta z}q \tag{3.170}$$

The interval between modes can hence be calculated

$$\Delta k_x = \frac{\pi}{\Delta x}, \quad \Delta k_y = \frac{\pi}{\Delta y}, \quad \Delta k_z = \frac{\pi}{\Delta z} \tag{3.171}$$

Each mode occupies a unit volume element in "k" space (Fig. 3.42)

$$\Delta k_x \Delta k_y \Delta k_z = \frac{\pi^3}{\Delta x \Delta y \Delta z} = \frac{\pi^3}{\mathrm{V}} \tag{3.172}$$

In $\vec{k}$ space, the volume between $\left|\vec{k}\right|$ and $\left|\vec{k}\right| + d\left|\vec{k}\right|$ is:

$$\frac{1}{8}4\pi\left|\vec{k}\right|^2 d\left|\vec{k}\right| \tag{3.173}$$

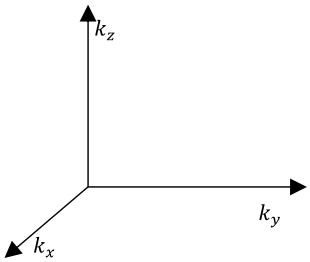

Fig. 3.41 Presentation of k-space in k_x, k_y, k_z components

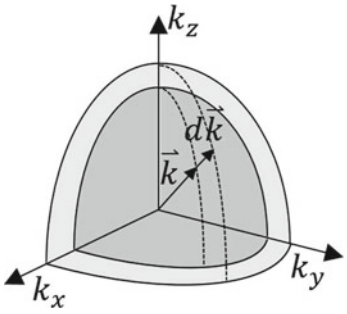

Fig. 3.42 $\vec{k}$ space presentation for calculating the volume between $\vec{k}$ and $\vec{k} + d\left|\vec{k}\right|$

Therefore, the number of modes within $\left|\vec{k}\right|$ and $\left|\vec{k}\right| + d\left|\vec{k}\right|$

$$\frac{\frac{1}{8}4\pi\left|\vec{k}\right|^2 d\left|\vec{k}\right|}{Unit\ volume\ of\ k\ space} = \frac{\frac{1}{8}4\pi\left|\vec{k}\right|^2 d\left|\vec{k}\right|}{\frac{\pi^3}{V}} = \frac{1}{8}4\pi\left|\vec{k}\right|^2 d\left|\vec{k}\right|\frac{V}{\pi^3} \tag{3.174}$$

Since

$$\left|\vec{k}\right| = \frac{2\pi}{\lambda} = \frac{2\pi}{\frac{c}{\upsilon}} = \frac{2\pi\upsilon}{c} \tag{3.175}$$

$$d\left|\vec{k}\right| = \frac{2\pi}{c}d\upsilon \tag{3.176}$$

Also since there are two modes (spin angular momentum of $(\pm\hbar)$) possible for each value of k, the total number of modes within $\upsilon \leftrightarrow \upsilon + d\upsilon$

$$2 \times \frac{1}{8}4\pi\left(\frac{2\pi\upsilon}{c}\right)^2\frac{2\pi}{c}d\upsilon\frac{V}{\pi^3} = \frac{8\pi\upsilon^2}{c^3}Vd\upsilon \tag{3.177}$$

where V is the volume of the cavity. $\rho(\upsilon)$ is defined as the number of modes per unit volume and per unit frequency range, the number of mode per unit volume per unit frequency is therefore calculated.

$$Number\ of\ modes = \frac{8\pi\upsilon^2}{c^3} \tag{3.178}$$

Homework with Solution 2

Deriving Solar Spectral Irradiance from Planck's Law

In experimental work, solar irradiance distribution as a function of wavelength is preferred and the radiation law take the form

$$I(\lambda, T) = \frac{2hc^2}{\lambda^5}\frac{1}{e^{\frac{hc}{\lambda kT}} - 1} \tag{3.22}$$

Please deduce solar spectral irradiance (3.22) from Planck's law (3.21)

$$\rho(\upsilon, T) = \frac{8\pi h\upsilon^3}{c^3}\frac{1}{e^{\frac{h\upsilon}{kT}} - 1} \tag{3.21}$$

Solution

By considering energy inavariance in wavelength and frequency domains

$$\rho(\lambda, T)d\lambda = -\rho(\upsilon, T)d\upsilon \tag{3.179}$$

then

$$\rho(\lambda, T) = -\rho(\upsilon, T)\frac{d\upsilon}{d\lambda} \tag{3.180}$$

Since

$$\upsilon = \frac{c}{\lambda}, \ \frac{d\upsilon}{d\lambda} = -\frac{c}{\lambda^2} \tag{3.181}$$

then

$$\rho(\lambda, T) = \rho(\upsilon, T)\frac{c}{\lambda^2} \tag{3.182}$$

Since full solid angle equals 4π,
Planck's formula per Steradian is therefore obtained by dividing (3.21) by 4π.

$$\rho(\upsilon, T) = \frac{2h\upsilon^3}{c^3}\frac{1}{e^{\frac{h\upsilon}{kT}} - 1} \tag{3.21}$$

Consequently, $\rho(\lambda, T)$ can be deduced from $\rho(\upsilon, T)$

$$\rho(\lambda, T) = \rho(\upsilon, T)\frac{c}{\lambda^2} = \frac{2h\upsilon^3}{c^3}\frac{1}{e^{\frac{h\upsilon}{kT}} - 1}\frac{c}{\lambda^2} = \frac{2hc}{\lambda^5}\frac{1}{e^{\frac{hc}{\lambda kT}} - 1} \tag{3.183}$$

Solar spectral irradiance $I(\lambda)$ can be obtained by multiplying (3.183) by c

$$I(\lambda, T) = \rho(\lambda)c \tag{3.23}$$

Consequently, we obtain solar spectral irradiance as a function of wavelength λ (as well as temperature T)

$$I(\lambda, T) = \frac{2hc^2}{\lambda^5}\frac{1}{e^{\frac{hc}{\lambda kT}} - 1} \tag{3.22}$$

Homework with Solution 3

Deriving Stefan-Boltzmann's Law from Planck's Law

Please deduce Stefan-Boltzmann's law (3.25)

$$I = \frac{P}{A} = \sigma T^4 = \frac{2\pi^5}{15}\frac{k^4}{c^2h^3}T^4 = 5.67 \times 10^{-8} \times T^4\left[\frac{\mathrm{W}}{\mathrm{m}^2}\right] \tag{3.25}$$

from Plank's formula (3.21)

$$\rho(\upsilon) = \frac{8\pi h\upsilon^3}{c^3}\frac{1}{e^{\frac{h\upsilon}{kT}} - 1} \tag{3.21}$$

Solution

Plank's formula in terms of photon irradiance

$$I(\upsilon) = \rho(\upsilon)c = \frac{8\pi h\upsilon^3}{c^2}\frac{1}{e^{\frac{h\upsilon}{kT}} - 1} \tag{3.184}$$

Total photon irradiance I over the whole frequency spectrum

$$I = \frac{P}{A} = \int_0^\infty I(\upsilon)d\upsilon = \int_0^\infty \frac{8\pi h\upsilon^3}{c^2}\frac{1}{e^{\frac{h\upsilon}{kT}} - 1}d\upsilon = \frac{8\pi h}{c^2}\int_0^\infty \frac{\upsilon^3}{e^{\frac{h\upsilon}{kT}} - 1}d\upsilon \tag{3.185}$$

If we assume

$$x = \frac{h\upsilon}{kT} \quad \text{then} \quad \upsilon = \frac{kT}{h}x,\ d\upsilon = \frac{kT}{h}dx \tag{3.186}$$

For 4π solid angle

$$\begin{aligned} I = \frac{P}{A} &= \frac{8\pi h}{c^2}\int_0^\infty \frac{\left(\frac{kT}{h}x\right)^3}{e^x - 1}\frac{kT}{h}dx = \frac{8\pi k^4T^4}{c^2h^3}\int_0^\infty \frac{x^3}{e^x - 1}dx \\ &= \frac{8\pi k^4T^4}{c^2h^3}\frac{\pi^4}{15} = \frac{8\pi^5}{15}\frac{k^4}{c^2h^3}T^4 \\ &= \sigma' T^4 \end{aligned} \tag{3.187}$$

Since

$$h = 6.63 \times 10^{-34}\ \mathrm{J}\cdot\mathrm{s} \quad k = 1.38 \times 10^{-23}\frac{\mathrm{J}}{\mathrm{K}}$$

Radiation constant $\sigma = \frac{1}{4}\sigma'$ of Stefan-Boltzmann's law can be calculated

$$I = \frac{P}{A} = \sigma T^4 = \frac{2\pi^5}{15}\frac{\mathrm{k}^4}{c^2h^3}T^4 = 5.67 \times 10^{-8} \times T^4 \tag{3.25}$$

according to 2019 redifinition of SI base units

$$I = \frac{2\pi^5}{15}\frac{\mathrm{k}^4}{c^2h^3}T^4 \quad \text{Dimensional analysis}: \quad \left[\frac{\mathrm{W}}{\mathrm{m}^2}\right] = \left[\frac{\mathrm{J}}{\mathrm{m}^2 \cdot \mathrm{s}}\right] = \left[\frac{\frac{\mathrm{J}^4}{\mathrm{K}^4} \cdot \mathrm{K}^4}{\frac{\mathrm{m}^2}{\mathrm{s}^2} \cdot \mathrm{J}^3 \cdot \mathrm{s}^3}\right] \tag{3.188}$$

Homework with Solution 4

Deriving Wien's Displacement Law from Planck's Law

Please deduce Wien's displacement law (3.27)

$$\lambda_{\max} T = 2.898\,\mu\mathrm{m} \cdot \mathrm{K} \tag{3.27}$$

from Planck's law (3.22)

$$\rho(\lambda) = \frac{8\pi hc}{\lambda^5}\frac{1}{e^{\frac{hc}{\lambda kT}} - 1} \tag{3.22}$$

Solution

By taking derivative of $\rho(\lambda)$ with respect to λ:

$$\frac{d\rho(\lambda)}{d\lambda} = \frac{d}{d\lambda}\left(\frac{8\pi hc}{\lambda^5}\frac{1}{e^{\frac{hc}{\lambda kT}} - 1}\right) \tag{3.189}$$

$$\begin{aligned}\frac{d\rho(\lambda)}{d\lambda} &= \frac{8\pi hc}{e^{\frac{hc}{\lambda kT}} - 1}\frac{d}{d\lambda}\left(\lambda^{-5}\right) + \frac{8\pi hc}{\lambda^5}\frac{d}{d\lambda}\left(\frac{1}{e^{\frac{hc}{\lambda kT}} - 1}\right) \\ &= \frac{8\pi hc}{e^{\frac{hc}{\lambda kT}} - 1}\frac{-5}{\lambda^6} + \frac{8\pi hc}{\lambda^5}\frac{-1}{\left(e^{\frac{hc}{\lambda kT}} - 1\right)^2}e^{\frac{hc}{\lambda kT}}\frac{d\left(\frac{hc}{\lambda kT}\right)}{d\lambda}\end{aligned} \tag{3.190}$$

Peak $\rho(\lambda)$ can be found by applying

$$\frac{d\rho(\lambda)}{d\lambda} = 0 \tag{3.191}$$

Then

$$\frac{d\rho(\lambda)}{d\lambda} = \frac{-8\pi hc}{e^{\frac{hc}{\lambda kT}} - 1}\frac{5}{\lambda^6} + \frac{-8\pi hc}{\lambda^5}\frac{e^{\frac{hc}{\lambda kT}}}{\left(e^{\frac{hc}{\lambda kT}} - 1\right)^2}\left(-\frac{hc}{kT}\frac{1}{\lambda^2}\right) = 0 \tag{3.192}$$

$$\frac{8\pi hc}{e^{\frac{hc}{\lambda kT}} - 1}\frac{5}{\lambda^6} = \frac{8\pi hc}{\lambda^7 kT}hc\frac{e^{\frac{hc}{\lambda k}}}{\left(e^{\frac{hc}{\lambda kT}} - 1\right)^2} \tag{3.193}$$

Finally

$$5 = \frac{hc}{\lambda kT}\frac{e^{\frac{hc}{\lambda kT}}}{e^{\frac{hc}{\lambda kT}} - 1} \tag{3.194}$$

If we assume

$$\frac{hc}{\lambda kT} = x \tag{3.195}$$

Then:

$$5 = x\frac{e^x}{e^x - 1}, \quad xe^x = 5\left(e^x - 1\right) \tag{3.196}$$

where $x = 4.965$ equalize both side of the above equation.

Consequently

$$\frac{hc}{\lambda kT} = 4.965 \tag{3.197}$$

Which happens when $\lambda = \lambda_{\max}$

$$\lambda_{\max} T = \frac{hc}{4.965\ \mathrm{k}} = \frac{6.63 \times 10^{-34} \times 3 \times 10^8}{4.965 \times 1.38 \times 10^{-23}} \tag{3.198}$$

Wien's displacement law is finally deduced

$$\lambda_{\max} T = 2.898\ \mu\mathrm{m}\ K \tag{3.27}$$

References

1. Svelto, O.: Principles of Lasers, 5th edn. Springer, New York, NY (2016). https://books.google.pt/books/about/Principles_of_Lasers.html?id=ioywRI5W2HEC&redir_esc=y
2. Koechner, W.: Solid-State Laser Engineering, 6th edn. Springer, Berlin Heidelberg (2006). https://link.springer.com/book/10.1007/978-3-662-14219-6

3. Yariv, A., Gordon, J. P.: The Laser*. Proceedings of the IEEE (1963). https://www.mindat.org/reference.php?id=12781943
4. Renk, K. F.: Basics of Laser Physics, 2nd edn. Springer Science & Business Media (2012). https://books.google.pt/books/about/Basics_of_Laser_Physics.html?id=dpVDTLPySTQC&redir_esc=y
5. Haken, H.: Laser Theory. Springer, Berlin Heidelberg (1984). https://books.google.pt/books/about/Laser_Theory.html?id=wzLtCAAAQBAJ&redir_esc=y
6. Siegman, A.E.: Lasers. University Science Books, Mill Valley, CA (1986). https://books.google.pt/books/about/Lasers.html?id=1BZVwUZLTkAC&redir_esc=y
7. Dickson, L.: Characteristics of a propagating gaussian beam. Appl. Opt. **9**, 1854–1861 (1970). https://opg.optica.org/ao/abstract.cfm?uri=ao-9-8-1854
8. Stoehr, H., Mensing, F., Helmcke, J., Sterr, U.: Diode laser with 1 Hz linewidth. Opt. Lett. **31**, 736–738 (2006). https://opg.optica.org/ol/abstract.cfm?uri=ol-31-6-736
9. Mandel, L.: Photon degeneracy in light from optical maser and other sources*. J. Opt. Soc. Am. **51**, 797–798 (1961). https://opg.optica.org/josa/abstract.cfm?uri=josa-51-7-797
10. Hwang, I. H., Lee, J. H.: Efficiency and threshold pump intensity of CW solar-pumped solid-state lasers. IEEE J. Quantum Electron. **27**(9), 2129–2134 (1991). https://ieeexplore.ieee.org/document/135171
11. Laporta, P., Magni, V., Svelto, O.: Comparative study of the optical pumping efficiency in solid-state lasers. IEEE J. Quantum Electron. **21**(8), 1211–1218 (1985). https://ieeexplore.ieee.org/document/1072800
12. Barnes, N. P. Solid state laser from an efficiency perspective. IEEE J. Sel. Top. Quantum Electron. (June 2007). https://ieeexplore.ieee.org/document/4244407
13. Liang, D., Vistas, C. R., Garcia, D., Tibúrcio, B. D., Catela, M., Costa, H., Guillot, E., Almeida, J.: Most efficient simultaneous solar laser emissions from three Ce:Nd:YAG rods within a single pump cavity. Sol. Energy Mater. Sol. Cells. **246**, 111921 (2022). https://www.sciencedirect.com/science/article/abs/pii/S0927024822003403#!
14. Liang, D., Almeida, J.: Highly efficient solar-pumped Nd:YAG laser. Opt. Express **19**, 26399–26405 (2011). https://opg.optica.org/oe/fulltext.cfm?uri=oe-19-27-26399&id=225792
15. Weksler, M., Shwartz, J.: Solar-pumped solid-state lasers. IEEE J. Quantum Electron. **24**(6), 1222–1228 (1988). https://ieeexplore.ieee.org/document/247
16. Lando, M., Kagan, J., Linyekin, B., Dobrusin, V.: A solar-pumped Nd:YAG laser in the high collection efficiency regime. Opt. Commun. **222**, 1 (2003). https://www.sciencedirect.com/science/article/abs/pii/S0030401803016018

Chapter 4
Laser Materials for Solar-Pumped Lasers

Cláudia R. Vistas

Solar laser active media play an essential role in the success of solar laser emission. Physical and laser properties of the commonly used Nd:YAG and Cr:Nd:YAG solar laser media are firstly explained. Ce:Nd:YAG is then introduced as recent solar laser material for enhancement of solar laser efficiencies. Other laser media as Cr:Nd:GSGG and Alexandrite are briefly described.

4.1 Host Materials

The active media of solid-state lasers have their active ions embedded as an impurity into an insulating host material. Active ions are the responsible for the lasing action by its energy levels, while the host material influences the laser efficiency by its physical properties. Several important books discuss in detail laser host materials and active ions [1–6].

The desirable properties for a host material to be useful in solid-state laser applications include:

(1) Optical properties

   a. low refractive index variation to minimize inhomogeneous propagation of light through the material, avoiding thus poor beam quality.
   b. minimum parasitic absorptions and scattering centers.
   c. high transparency for the wavelengths of pump and laser radiation.

(2) Mechanical properties

   a. hardness for easy polishing and growth to fabricate surfaces with high optical quality.
   b. high stress fracture limit.

© The Author(s), under exclusive license to Springer Nature Switzerland AG 2023

D. Liang et al., *Solar-Pumped Lasers*, Green Energy and Technology,
https://doi.org/10.1007/978-3-031-24785-9_4

(3) Thermal properties

   a. high thermal conductivity to rapidly dissipate the heat formed by the excitation energy.
   b. small thermal expansion and thermal-optic coefficients to minimize thermal lensing and thermally induced birefringence effects.

(4) Chemical stability
(5) At microscopic level, the host lattice must accept the active ions, replacing a chemically similar element.
(6) Finally, the active medium must be fabricated on a large scale, maintaining high optical quality and high yield.

No material fulfills all the requirements. The specific application determines the medium to be used. The main groups of materials used as hosts in solid-state lasers are: crystals, glasses and ceramics.

A comparison between crystalline and glass hosts shows that crystals with ordered structures offer advantages such as narrow emission (fluorescence) linewidths, high emission cross-sections and low threshold. Also, crystals have good thermal conductivity (usually by an order of magnitude greater than in glasses), tolerating thus high pump power before thermal lensing impairs the laser, and, in most cases, great hardness and therefore high durability. Contrastingly, glasses benefit from easy and cheap fabrication with great size capability, high doping level and very good optical quality. Candidates for crystalline hosts are oxides and fluorides, and for glasses are silicates and phosphates. Among the group of oxides, garnets are of great relevance for lasers, especially for solar-pumped lasers.

The most useful synthetic garnets as laser hosts are: yttrium aluminum garnet, $Y_3Al_5O_{12}$ (YAG); gadolinium scandium aluminum garnet, $Gd_3Sc_2Al_3O_{12}$ (GSGG); and gadolinium gallium garnet, $Gd_3Ga_5O_{12}$ (GGG). These are known by their stability, hardness, optical isotropy and good thermal conductivities. YAG is the most widely used host in solid-state lasers, particularly in solar-pumped lasers, as a result of its remarkable combination of properties. This crystal has high thermal conductivity, is very hard and fabricated with high optical quality.

The YAG crystal is usually grown by the conventional Czochralski method, which is based on high temperature melting. Although this method produces high optical quality crystals, they are limited in size and doping concentration. Advanced sintering process has allowed the fabrication of polycrystalline ceramic laser materials at a low temperature, below the melting point. This fabrication technology is very simple, inexpensive, and enables the production of polycrystalline oxide ceramics, such as YAG, with high dopant concentration and large size, compared to the Czochralski method. The ceramic is an aggregate of randomly oriented fine crystals, which has the appearance of a single crystal and properties that are similar or even better than those of the corresponding crystals. Some of the advantages of ceramic laser materials over their crystalline and glass counterparts include lower scattering loss, greater

mechanical toughness, less residual stress, and a comparable or better laser damage threshold [7–9].

4.2 Active Ions

Active ions are implanted into a host material by replacing a chemically similar element. In general, some parameters should match between the impurity and the replaced ion, such as ion valency, size. However, the disparate parameters, such as mass, ionic radius, limit the impurity concentration on the host, whose increase can lead to thermal stress.

The two most important groups of active elements are the rare earth (particularly the lanthanide series), such as Nd, Ce, Er and Ho, and the transition metal ions, such as Cr and Ti. The electronic transitions of active ions in the local ligand field environment of the host are responsible by the optical spectral properties of the laser material. Desirable properties include long lifetime of the metastable state, which allows good storage of the pump energy, and favorable absorption bands that match the pump source emission.

Rare earth atoms generally have a ground state electronic configuration consisting of [Xe] $4f^n$ $5d$ $6s^2$ or [Xe] $4f^{n+1}$ $6s^2$, where $0 \leq n \leq 14$ and [Xe] denotes the electronic configuration of xenon:

$$1s^2\ 2s^2\ 2p^6\ 3s^2\ 3p^6\ 3d^{10}\ 4s^2\ 4p^6\ 4d^{10}\ 5s^2\ 5p^6.$$

The filled core is equal to xenon, while the 4f orbit (capable of holding up to 14 electrons) is partially filled by the optically active electrons, which is shielded by the electrons in the outermost 5s through 6s orbits.

As example, the rare earth element cerium has only one electron in the f orbit

$$\text{Ce: [Xe] } 4f\ 5d\ 6s^2,$$

and the most common rare earth neodymium has four electrons in the f orbit

$$\text{Nd: [Xe] } 4f^4\ 6s^2.$$

Rare earth ions normally exhibit +3 oxidation state. In the formation of the trivalent ion, the atom loses its outermost electrons—the two 6s electrons and either the 5d electron or one of the 4f electrons—leaving an electronic configuration of [Xe] $4f^n$. The 4f remains the inner shell, being screened by the outermost $5s^2$ and $5p^6$ shells. As example, the trivalent cerium ion has the configuration

$$Ce^{3+}\text{: [Xe] } 4f,$$

and the trivalent neodymium ion has the configuration

$$Nd^{3+}: [Xe]\ 4f^3.$$

The lost electrons are used for the ionic binding when inserted in a host material. The electronic transitions within the 4f configuration (4f–4f transitions) give rise to the absorption and fluorescence spectra of rare earth ions. The 4f electrons organize themselves in different states of the 4f shell, resulting in a large number of energy levels. The splitting of the degenerate 4f orbital energy level is caused by three types of interaction within the ion. The 4f states are first divided into sublevels by the strongest Coulomb interaction. Each term is then divided into manifolds, with a spectral range ~10^3 cm^{-1}, by the spin–orbit coupling. Further split of each manifold into Stark sublevels with a spectral range ~10^2 cm^{-1} results from the weakest crystal field interaction. Crystal field refers to the electrostatic interaction between electrons of the 4f shell and those of the neighboring host ions. As regards the Nd^{3+} ion, since the unfilled 4f electron shell is screened from the external field of the ligands by the filled 5s and 5p shells, the crystal field is weaker than the spin–orbit coupling. Consequently, the emission lines are relatively narrow, and the energy level structure is almost independent of the host material.

The manifolds are determined according to the Russell–Saunders notation, which have the form of $^{2S+1}L_J$, where S is the total spin angular momentum, L is the total orbital angular momentum (L = 0, 1, 2, 3, 4, …, expressed by the letters S, P, D, F, G, …) and J is the total angular momentum.

Neodymium is by far the most popular active ion in the rare earth group. Several host materials have been exploited to incorporate this ion and thus obtain stimulated emission, being YAG the ideal choice for Nd. The strongest lasing wavelength of Nd-doped materials is just beyond 1 μm. Nd:YAG is one of the best lasing materials, particularly for solar-pumped lasers, and it is described in Sect. 4.3.

Transition metal atoms have a ground state electronic configuration consisting of [Ar] $3d^{n+1}$ $4s^2$ or [Ar] $3d^{n+2}$ 4s, where $0 \leq n \leq 9$ and [Ar] denotes the argon electronic configuration core, $1s^2$ $2s^2$ $2p^6$ $3s^2$ $3p^6$. The optically active electrons are in the partially filled 3d orbitals. As example, the chromium atom has six electrons distributed in the d and s orbitals

$$Cr: [Ar]\ 3d^5\ 4s.$$

In the formation of the trivalent ion, the transition metal atom loses three electrons from the outer shells leaving an electronic configuration of [Ar] $3d^n$. As example, the trivalent chromium ion has the configuration

$$Cr^{3+}: [Ar]\ 3d^3.$$

The remaining 3d electrons determine the optical proprerties of the ion. In contrast to rare earth ions, the 3d shell is not screened by outer shells of electrons, being the outermost one. Since the unshielded 3d electrons easily interact with the surrounding ligands, the crystal field interaction is stronger than that of the 4f electrons in the rare earths (more than an order of magnitude), being stronger than the spin–orbit

coupling. Consequently, the 3d-3d transitions have a vibronic character, leadind to broad absorption and emission bands.

Chromium is the most exploited ion in the transition metal group. Lasing on chromium ions has been produced in a large range of wavelengths for quite different hosts. The broad linewidth feature results in a signicant tunability of the laser output wavelength. Chromium ion is used, for example, in alexandrite (Cr-doped chrysoberyl, $BeAl_2O_4$), ruby (Cr-doped aluminium oxide) and Cr-doped GSGG.

Some rare earth and transition metal ions, such as Ce^{3+} and Cr^{3+}, respectively, can be used as sensitizers of the active ion emission. Sensitization by co-doping these ions in the doped host material is an important way to increase the efficiency of solid-state lasers. The sensitizer ion, which has better absorption properties, absorbs the pump energy and transfers efficiently the excitation energy to the emitting active ion (activator), which has better emission properties. The key condition is the spectral overlap between the sensitizer emission spectrum and the activator absorption spectrum. Co-doped crystals are of particular interest to solar-pumped lasers, such as Cr:Nd:YAG, Ce:Nd:YAG and Cr:Nd:GSGG.

4.3 Nd:YAG

The first demonstration of the Nd:YAG laser operation took place in 1964 by Geusic et al. [10]. Soon after, the first Nd:YAG solar-pumped laser was reported by Young in 1966 [11]. The Nd:YAG laser is the most frequently used solid-state laser in scientific, medical, industrial, and military applications, as a result of its unique combination of optical, thermal and mechanical properties. Nd:YAG lasers are very versatile as they can be operated in a continuous wave or as a pulsed mode, can be pumped by solar energy, flash lamps or laser diodes, and can generate from a few milliwatts up to several kilowatts of output power. Light emission is primarily at a wavelength of 1064 nm, but 532, 355, or 266 nm emission wavelengths can be produced by frequency doubling, tripling and quadrupling, respectively.

4.3.1 Physical and Laser Properties of Nd:YAG

In the Nd:YAG crystal, Nd^{3+} ions replace a few percent of Y^{3+} ions. As the radius of the Nd^{3+} ion is slightly larger than that of the Y^{3+} ion, the crystal lattice is distorted if the doping concentration surpasses the limit of approximately 1.5 at.%, which in turn leads to a decrease in the fluorescence lifetime. The typical concentration of Nd^{3+} ions for Nd:YAG crystals is around 1.0 at.%, corresponding to a density of Nd^{3+} ions of 1.38×10^{20} cm^{-3}. Nd:YAG laser rods can be produced with a maximum diameter of around 15 mm and a length of up to 150 mm.

In Table 4.1 is listed some of the physical, optical and thermal properties of the Nd:YAG. This crystal is characterized by its high damage threshold, great thermal

Table 4.1 Properties of the Nd:YAG laser at room temperature [1]

Property	Value
Nd doping	1.0 at.%
Neodymium atoms concentration	1.38×10^{20} cm^{-3}
Density	4.56 g/cm^3
Tensile strength	200 MPa
Emission wavelength	1064 nm
Fluorescence lifetime	230 μs
Linewidth	120 GHz
Stimulated emission cross-section	2.8×10^{-19} cm^2
Saturation intensity	2.9 kW/cm^2
Saturation fluence	0.67 J/cm^2
Refractive index	1.82
Thermal conductivity	0.14 W cm^{-1} K^{-1}
Specific heat	0.59 W s g^{-1} K^{-1}
Thermal diffusivity	0.046 cm^2 s^{-1}
Thermal expansion	7.5×10^{-6} K^{-1}
$\partial n/\partial T$	7.3×10^{-6} K^{-1}

conductivity, high emission cross-section with long fluorescence lifetime, and narrow fluorescence linewidth that leads to high gain efficiency and low threshold pump power.

The fluorescence lifetime is temperature independent [12, 13]. However, it is Nd concentration dependent, decreasing with increasing doping concentration, an effect usually referred to as concentration quenching [13]. The stimulated emission cross-section of the main laser line is temperature dependent, decreasing with increasing temperature [13–15]. Regarding the Nd concentration dependence, Dong et al. reported that the stimulated emission cross-section is nearly independent of doping concentration [13]. While Sato et al. demonstrated that the emission cross-section depends not only on the doping concentration, but also on the fabrication process [16]. The difference between these two works could rely on the spectral resolution in fluorescence measurements, in which Sato et al. used a fine resolution of 0.05 nm [16], compared to 0.4 nm in Dong et al. [13]. The higher spectral resolution could provide more accurate results in general. The small-signal gain of Nd:YAG crystal has been proved to decrease with increasing temperature [17].

In Fig. 4.1 is shown the energy level diagram of Nd:YAG. As discussed above, the levels are denoted according to the Russell–Saunders coupling scheme, with the manifolds having the form of $^{2S+1}L_J$. For example, the $^4I_{9/2}$ ground level has $S = 3/2$, $L = 6$ and $J = L - S = 9/2$. Each manifold is then divided into $J + 1/2$ Stark sublevels by the crystal field of YAG (Fig. 4.1). Thus, the $^4I_{9/2}$ is split into five sublevels.

The absorption spectrum of Nd:YAG is shown in Fig. 4.2.

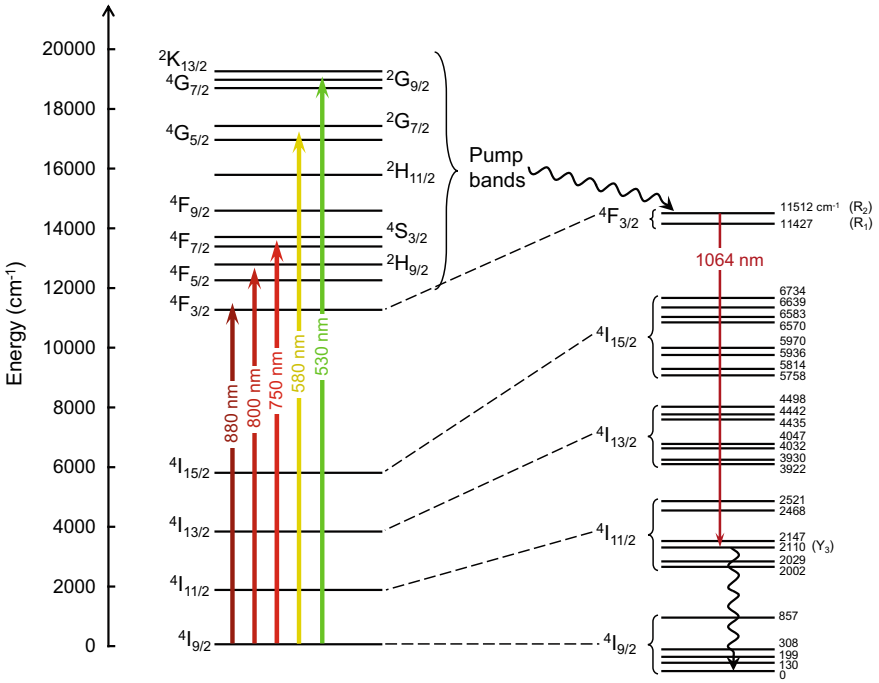

Fig. 4.1 Energy-level diagram of the Nd^{3+} in YAG (adapted from [3]). On the right-hand side is shown the Stark splitting of the manifolds by the crystal field of YAG. The Stark splitting is only shown for the levels that directly participate in lasing. Thick and thin solid arrows represent the main pump and laser transitions, respectively, and wavy arrows indicate non-radiative transitions

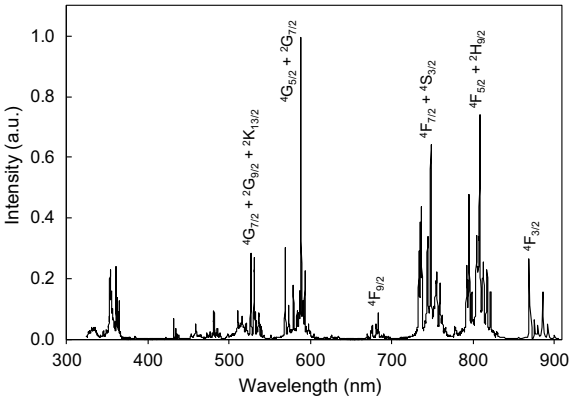

Fig. 4.2 Absorption spectrum of Nd:YAG (adapted from [1, 18])

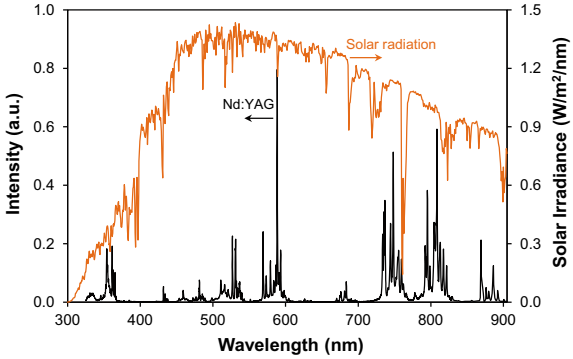

Fig. 4.3 Standard solar emission spectrum (orange line) [21], and Nd:YAG (black line) absorption spectrum (adapted from [1, 18])

The major absorption bands of the Nd:YAG crystal correspond to the transitions from the $^4I_{9/2}$ ground to the following pump levels (Figs. 4.1 and 4.2):

- $\lambda \approx 880$ nm $\rightarrow$ $^4F_{3/2}$
- $\lambda \approx 800$ nm $\rightarrow$ $^4F_{5/2} + {}^2H_{9/2}$
- $\lambda \approx 750$ nm $\rightarrow$ $^4F_{7/2} + {}^4S_{3/2}$
- $\lambda \approx 580$ nm $\rightarrow$ $^4G_{5/2} + {}^2G_{7/2}$
- $\lambda \approx 530$ nm $\rightarrow$ $^4G_{7/2} + {}^2G_{9/2} + {}^2K_{13/2}$.

The remain absorption bands have small cross-sections, contributing less to laser pumping. The pump band around 808 nm is the main one for laser diode pumping. The absorption regions around 810 nm and 750 nm are relevant for arc lamp pumping, while around 530 nm and 580 nm are relevant for flash-lamp pumping. As shown in Fig. 4.3, all absorption pump bands of Nd:YAG in the 300–900 nm range play an important role for solar pumping.

As a result of light pumping absorption, the Nd^{3+} ions excited to these energy bands decay non-radiatively and rapidly to the $^4F_{3/2}$ upper laser level (Fig. 4.1). This level is metastable and has a relatively long lifetime because the nearest lower level is separated from it by a large energy gap, accumulating thus a large fraction of the excitation energy. The $^4F_{3/2}$ level is split into two Stark sublevels R_1 and R_2, with relative population at room temperature of about 60% and 40%, respectively, according to Boltzmann's law. Whenever R_2 sublevel is depleted by stimulation emission, it is replenished by R_1 population by thermal transitions.

From the upper laser level, ions decay mainly by radiative transitions to the ^4I lower levels, with a fluorescence lifetime of 230 μs. The strongest transition occurs from the $^4F_{3/2}$ level (R_2 sublevel) to the $^4I_{11/2}$ level (Y_3 sublevel), emitting light at a wavelength of 1064 nm with the highest effective emission cross-section of 2.8×10^{-19} cm^2. The $^4I_{11/2}$ lower laser level is then rapidly depleted by non-radiative transitions to the $^4I_{9/2}$ ground level (Fig. 4.1). The lower level is practically unpopulated at room temperature because the energy difference between it and the ground level is about an order of magnitude greater than the kT value, according to Boltzmann's law. Therefore, the Nd:YAG laser is a four-level system, exhibiting a relatively low threshold.

Other laser transitions at 1319 nm or 1338 nm ($^4F_{3/2} \rightarrow {}^4I_{13/2}$), as well as at 946 nm ($^4F_{3/2} \rightarrow {}^4I_{9/2}$) are also used. However, they have low gain and thus are difficult to lase, requiring the use of frequency-selective elements.

4.3.2 Spectral Overlap Between Nd:YAG Absorption and Solar Emission Spectra

The absorption spectrum of Nd:YAG spans the ultraviolet to near infrared range, overlapping the solar emission spectrum, as shown in Fig. 4.3. However, the absorption lines are weak and narrow, corresponding to only 14–16% overlap with the solar spectrum [19, 20].

4.4 Cr:Nd:YAG

The Cr:Nd:YAG single crystal was introduced by Kiss and Duncan in 1964 [22], soon after the development of the Nd:YAG crystal. Under solar pumping, the Cr:Nd:YAG crystal was first investigated by Reno in 1966 [23]. The absorption spectrum of Nd^{3+} ions consists of weak and narrow lines in the ultraviolet, visible and near infrared regions that overlap poorly with the solar and lamps emission spectra. The sensitizer Cr^{3+} ion has broader and stronger absorption bands in the visible region than that of the Nd^{3+} ion, absorbing more light from solar and lamps pump radiation. This excitation energy can then be transferred to the Nd^{3+} ion. Therefore, co-doping Nd:YAG crystals with Cr^{3+} ions has been envisaged to improve the laser efficiency under broadband pumping.

4.4.1 Physical and Laser Properties of Cr:Nd:YAG

Despite the endeavor to double the efficiency of Nd:YAG crystal through the incorporation of the Cr^{3+} ion [22], the poor optical quality of Cr:Nd:YAG crystals never allowed to achieve this goal. The production of melt-grown Cr:Nd:YAG single crystals is very challenging because of the large Cr^{3+} ion radius that leads to local distortion, and the partial conversion of Cr^{3+} ions to Cr^{4+} ions, which have an absorption band at 1064 nm, degrading thus the lasing performance.

The implementation of ceramic technology in the fabrication of doped YAG materials has renewed the interest in the Cr:Nd:YAG laser [24–26]. Since the first development of highly transparent Cr:Nd:YAG ceramics [25], their optical quality has continually progressed, and the laser performance under broadband pumping has been improved [26]. This technology allows to increase the concentration and uniformity of doping ions in the host, and to suppress the transformation of Cr^{3+} ions to

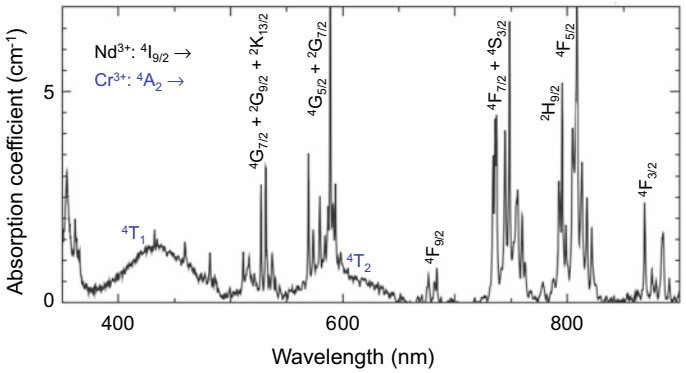

Fig. 4.4 Absorption spectrum of Cr:Nd:YAG (adapted from [30])

Cr^{4+} ions because the sintering process occurs below the melting point of the host material.

The optical and laser properties of the Cr:Nd:YAG ceramics have been explored and they are similar to those for the single crystal counterparts [27–38]. In these media, Cr^{3+} ions substitute a few percent of Al^{3+} ions, without creating significant lattice distortion. As shown in Fig. 4.4, the absorption spectrum of Cr:Nd:YAG consists of two broad absorption bands from about 400 nm to 700 nm caused by Cr^{3+} ions, and several narrow lines contributed by Nd^{3+} ions.

In Fig. 4.5 is shown the energy level diagram of Cr:Nd:YAG. In consequence of pump absorption at around 440 nm and 590 nm, the Cr^{3+} ions are excited from the $^4A_2$ ground state to the broad pump bands $^4T_1$ and $^4T_2$, respectively. As the lifetime at these pump bands is too short, the ions relax non-radiatively to the long-life metastable state ^2E. The energy transfer process between Cr^{3+} and Nd^{3+} ions in the YAG matrix is temperature dependent [27]. At low temperatures ($T < 77$ K), Cr^{3+} luminescence is dominated by the $^2E \rightarrow {}^4A_2$ transition, consisting mainly of the sharp line at 687 nm and the side-bands at 704 nm and 723 nm [26, 27], which overlap with the $^4F_{9/2}$ and very poorly with the $^4F_{7/2}$ and $^4S_{3/2}$ high-energy levels, respectively, of the Nd^{3+} absorption spectrum (Fig. 4.2). This leads to low resonant energy transfer efficiency from Cr^{3+} to Nd^{3+} ions. At higher temperatures like 300 K, a large fraction of the population in the ^2E level is thermally excited to the $^4T_2$ level, which then relaxes to the $^4A_2$ level in the form of a wider luminescence band at longer wavelengths (to the 800 nm range). This results in stronger spectral overlap with the $^4F_{7/2}$, $^4S_{3/2}$ and $^4F_{5/2}$, $^2H_{9/2}$ absorption bands of the Nd^{3+} ion, leading to higher energy transfer efficiency than that at low temperatures [26, 27]. The energy transferred to the excited levels of Nd^{3+} eventually decays non-radiatively into the metastable $^4F_{3/2}$ level and then radiatively to the $^4I_{11/2}$ level, leading to Nd laser emission. All this results in an increase in pump efficiency and a decrease in threshold pump power.

The fluorescence lifetime of Cr:Nd:YAG transparent ceramics is longer than that of 230-μs Nd:YAG. Its value depends on the Cr^{3+} ions concentration, pumping conditions and temperature, as shown in Table 4.2 [29, 32, 39]. As at low temperatures, the $^2E \rightarrow {}^4A_2$ transition dominates, long fluorescence lifetimes are observed. While increasing the temperature, the short-lifetime $^4T_2$ level is thermally populated,

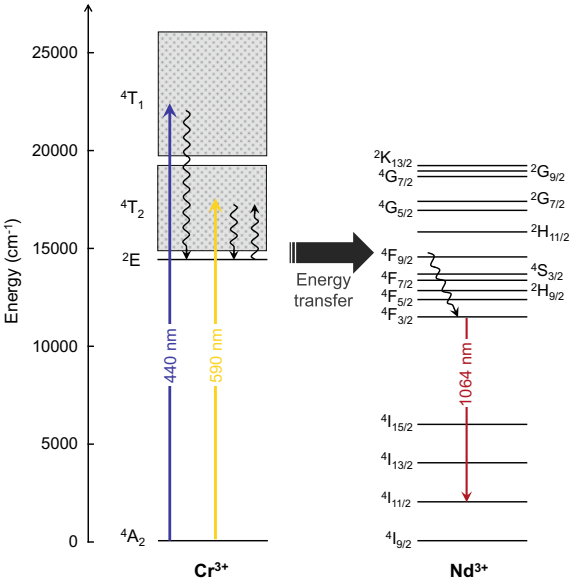

Fig. 4.5 Energy-level diagram of Cr^{3+} (adapted from [35]) and Nd^{3+} (adapted from [3]) ions in YAG, illustrating the energy transfer mechanism between Cr^{3+} and Nd^{3+} ions in the Cr:Nd:YAG active medium. Solid arrows indicate the excitation and emission processes, and wavy arrows represent the non-radiative transitions

contributing to more $^4T_2 \rightarrow {}^4A_2$ transitions, leading to a decrease in fluorescence lifetime [40], as shown in Table 4.2. The effective lifetime is longer when excited with white light from a xenon flash lamp than that when excited with the Cr^{3+} absorption wavelengths, such as 440 nm or 590 nm (Table 4.2), because more pumping power is absorbed by Cr^{3+} ions.

Table 4.2 Effective fluorescence lifetime of Cr:Nd(1.0 at.%):YAG at 1064 nm

Cr^{3+} ions concentration	Excitation	Temperature	Lifetime (μs)	References
0.1 at.%	440 nm	RT	732	[39]
	590 nm	RT	228	[39]
	White light	292 K	1100	[29]
		400 K	570	[29]
0.7 at.%	440 nm	RT	459	[39]
	590 nm	RT	306	[39]
2.0 at.%	610 nm	77 K	890	[32]
		450 K	520	[32]
3.0 at.%	440 nm	RT	389	[39]
	590 nm	RT	365	[39]
	White light	292 K	1000	[29]
		400 K	500	[29]

RT Room temperature

The value of the stimulated emission cross-section of the laser line of Cr:Nd:YAG at room temperature has been reported [28, 38]. Saiki et al. estimated an effective stimulated emission cross-section close to 2.0×10^{-18} cm^2 and 2.3×10^{-18} cm^2 for the Cr:Nd(1.0 at.%):YAG ceramics with Cr^{3+} ions content of 0.1 at.% and 3.0 at.%, respectively, when excited with an arc metal halide lamp [28]. These values are higher than the ~2.0×10^{-19} cm^2 estimated by Honda et al. for the Cr (2.0 at.%):Nd (1.0 at.%):YAG ceramics, which use the 610 nm pump wavelength of Cr^{3+} ions as the excitation source [38]. The effective stimulated emission cross-section is higher when excited with a broadband pump source due to greater power absorption by Cr^{3+} ions. The temperature dependence was also investigated [29, 38]. Honda et al. demonstrated that the stimulated emission cross-section of the Cr:Nd:YAG ceramic excited at 610 nm decreased slightly and linearly over the temperature range of 300–500 K [38]. While Saiki et al. reported that the effective stimulated emission cross-section of the Cr (0.1 at.%):Nd (1.0 at.%):YAG ceramic excited with xenon flash lamp remained intact from 300 K to 500 K [29].

Unlike the Nd:YAG material, which exhibits a substantial gain reduction with increasing temperature [17], the small-signal gain of Cr:Nd:YAG ceramics has been reported to increase with the temperature in the 300–500 K range when excited at 610 nm [38], or to remain constant at temperatures up to 473 K when excited with an arc-metal halide lamp [41]. Overall, Cr:Nd:YAG ceramics are expected to be a good active medium for high-efficiency lasers operating at high temperature.

The Cr:Nd:YAG ceramics have been successfully applied in lamp and solar-pumped laser systems [39, 42–50]. The Cr:Nd:YAG laser efficiency was already found to be more than twice than that of a Nd:YAG laser using a lamp source [39, 42, 43]. However, in solar-pumped lasers, Cr doping has not shown very enlightening results in terms of increasing their efficiency [45–48, 51]. Kato et al. investigated the effect of the Cr content in Cr:Nd (1.0 at.%):YAG ceramics on the performance of a compact solar-pumped laser [50]. They demonstrated that the output laser power was maximum at a Cr content of 0.4 at.%, with 8.5 times more than that of a Nd (1.0 at.%):YAG ceramic. Above the Cr content of 0.4 at.% to 1.0 at.%, the laser power gradually decreased, which may result from increased round-trip loss due to scattering by the Cr dopants [50].

The same authors went even further by studying the effect of the Cr content on the quantum efficiency of the energy transfer from Cr^{3+} to Nd^{3+} ions in a solar-pumped laser [37]. Several studies have been performed to assess the energy transfer efficiency, where pumping conditions, assessment methods and Cr contents in the sample varied between them [30–34, 36, 37]. Nevertheless, Kato et al. were the first to report energy transfer efficiencies for Cr:Nd:YAG lasers pumped by sunlight [37]. They found the maximum transfer efficiency of 0.45 at 0.4 at.% Cr content, which confirms the positive effect of increased absorption of the solar radiation by Cr^{3+} ions [37]. The Cr and Nd content most frequently used in Cr:Nd:YAG ceramics for broadband-pumped lasers is 0.1 at.% and 1.0 at.%, respectively [39, 44–49]. Nevertheless, as some studies have demonstrated, these concentrations may not be the ideal choice [35, 37, 50]. High concentrations of Cr^{3+} ions enhance the absorbed power; however, too high concentrations can be responsible for a large scattering

loss within the medium and an increased heat generation due to the large quantum defect. An optimization of the Cr^{3+} ions concentration is thus essential to attain high efficiency.

4.4.2 *Spectral Overlap Between Cr:Nd:YAG Absorption and Solar Emission Spectra*

The Cr:Nd:YAG ceramics has two broad absorption bands in the visible region provided by Cr^{3+} ions, in addition to narrow Nd lines, which match well with the solar emission spectrum (Fig. 4.6). A typical Cr:Nd:YAG ceramic with 0.1 at.% Cr and 1.0 at.% Nd concentration ensures an overlap of absorption spectrum with the solar radiation of about 23% [34].

4.5 Ce:Nd:YAG

In addition to Cr^{3+} ions, Ce^{3+} ions are also sensitizers of the Nd^{3+} ion emission in the doped YAG host because they have strong and broad absorption bands from visible to ultraviolet at broadband light pumping as well as efficient energy transfer from Ce^{3+} to Nd^{3+} ions. Since the first study on the luminescence properties of Ce:Nd:YAG crystal by Holloway and Kestigian in 1969 [52], several reports on the sensitization mechanism of energy transfer from Ce^{3+} to Nd^{3+} ions have demonstrated the potential of this medium to enhance the pump and laser efficiency of Nd^{3+} emission [53–61]. In 1984, Kvapil et al. demonstrated for the first time the increase in the output laser power of Ce:Nd:YAG laser rod in comparison with Nd:YAG [62].The first laser emissions

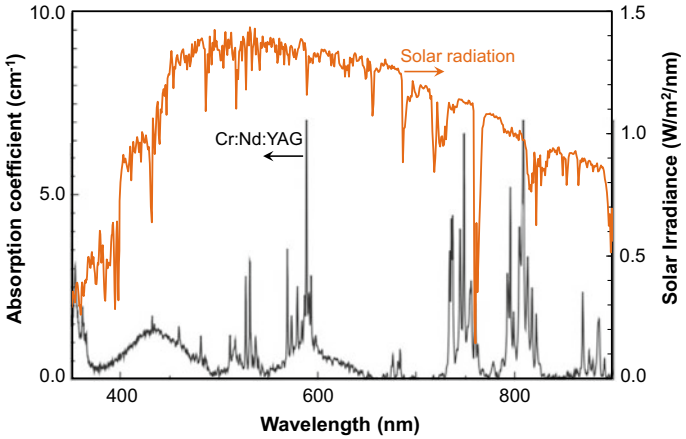

Fig. 4.6 Standard solar emission spectrum (orange line) [21], and Cr:Nd:YAG (black line) absorption spectrum (adapted from [30])

from a Ce:Nd:YAG rod pumped by solar radiation were reported by Vistas et al., in 2020 and 2021, using end-side-pumping [63] and side-pumping [64] configurations, respectively. The later configuration allowed an enhanced laser power of 1.57 times higher than the one obtained with a Nd:YAG solar laser under the same pumping conditions [64], as discussed in the next section.

4.5.1 Physical and Laser Properties of Ce:Nd:YAG

In Ce:Nd:YAG medium, Ce^{3+} ions substitute a few percent of Y^{3+} ions. Since the Ce^{3+} ionic radius is larger than that of the Y^{3+} ion, local distortion or local strains can occur in the lattice [65]. Commercial Ce:Nd:YAG single crystals are formed by the Czochralski method. However, the production of crystals with large dimensions and/or with high concentration of Ce^{3+} ions using this method is not easy because of the mismatch in the ionic radii of dopant and host ions. Therefore, the ceramic technology has also been implemented in the fabrication of Ce co-doped Nd:YAG materials [56–58].

Unlike other rare earth ions, the ground state of Ce^{3+} ion is a 4f shell level while the excitation state is a 5d shell level. Since the d-f transition is a spin and parity allowed transition, the Ce^{3+} ion has more efficient absorption and consequently more efficient fluorescence than the other rare earth ions, which have partially forbidden f-f transition. Its absorption cross section of $1–5 \times 10^{-18}$ cm^2 [66] is more than ten times greater than that of Nd^{3+} ion in YAG, 6.7×10^{-20} cm^2 [2], its fluorescence quantum efficiency is near-unity [66], and its fluorescence lifetime is the shortest among lanthanide ions, with values of 60–70 ns for Ce:YAG [66–68].

In the Ce^{3+} free ion, the 5d excited state is split into $^2D_{3/2}$ and $^2D_{5/2}$ manifolds and the 4f ground state is divided into $^2F_{5/2}$ and $^2F_{7/2}$ manifolds by the spin–orbit coupling (Fig. 4.7). Incorporated in a host, the 4f electrons are weakly affected by the crystal field because they are shielded by the outer 5s and 5p shells, unlike the excited 5d electrons, whose orbital extends well beyond the 5s and 5p. Therefore, the host lattice exerts a strong crystal field on the 5d level, splitting it into two to five sublevels depending on the occupied site symmetry, as shown in Fig. 4.7. In the garnet crystal structure of YAG, the Ce^{3+} ion is accommodated in the dodecahedral site with D_2 point symmetry of the Y^{3+} ion, which has an eightfold oxide cubic coordination with an additional tetragonal distortion [69]. In the cubic symmetry, the 5d state is split into a higher t_{2g} and a lower e_g states, which are further split into five Stark sublevels because of the tetragonal distortion (Fig. 4.7). This results into five absorption bands—two well-known around 460 and 340 nm, corresponding to transitions from $^2F_{5/2}$ to the $5d_1$ and $5d_2$ sublevels, respectively; and three other bands that overlap each other between 205 and 225 nm, corresponding to transitions from $^2F_{5/2}$ to the $5d_3$, $5d_4$ and $5d_5$ sublevels [70, 71]—as shown in Figs. 4.7 and 4.8. The first two bands are the strongest and most important to solar-pumped lasers because they match well with the solar light emission.

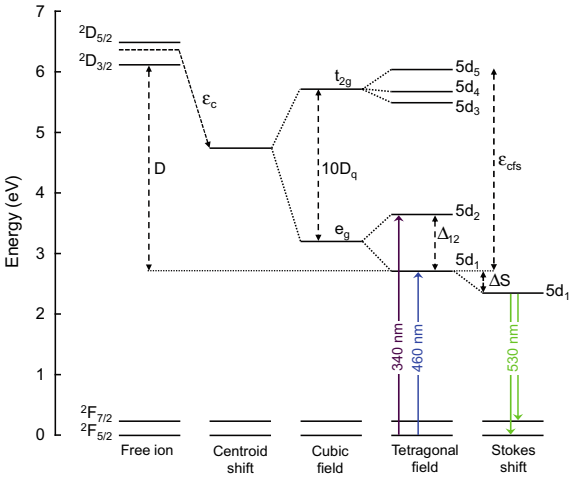

Fig. 4.7 Energy-level diagram of Ce^{3+} ion in the free-ion state and when embedded in YAG, illustrating the centroid shift (ε_c) and crystal-field splitting under cubic and tetragonal symmetries (ε_{cfs}). Both effects lead to a reduction of the $5d_1$ level by an amount denominated as redshift or depression (D). $10D_q$ indicates the crystal splitting energy caused by the cubic crystal field, Δ_{12} indicates the additional crystal splitting energy between $5d_1$ and $5d_2$ caused by the tetragonal crystal field, ΔS represents the Stokes shift responsible for a small additional redshift emission. Adapted from [71, 73]

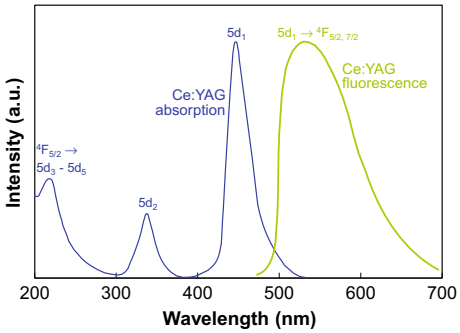

Fig. 4.8 Absorption and fluorescence spectra of Ce:YAG (adapted from [67])

In addition to the crystal field splitting, other effect is determinant to the photoluminescence properties, influencing the energy for the electron in the 5d state—the nephelauxetic effect, which is related to a decrease in the interelectron repulsion [72]. This results in a large centroid shift that refers to a reduction in the average energy of the 5d levels, as shown in Fig. 4.7. Both crystal field splitting and centroid shift effects are responsible for reducing the energy gap between the lowest $5d_1$ level and the 4f ground state, designated as spectral redshift. A small additional redshift of the emission is caused by the Stokes shift (Fig. 4.7). The Ce^{3+} radiative transition occurs from the Stokes shifted $5d_1$ level to the two $^2F_{5/2}$ and $^2F_{7/2}$ levels, emitting

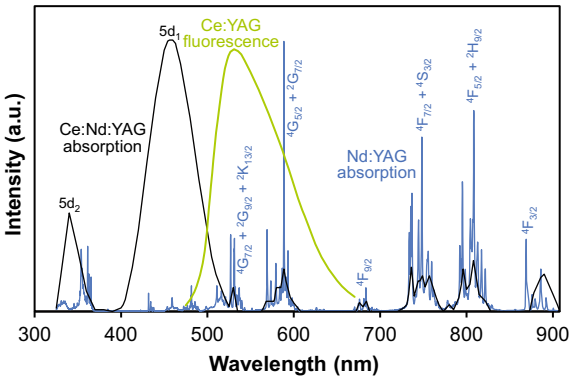

Fig. 4.9 Absorption spectra of Ce:Nd:YAG (adapted from [60]) and Nd:YAG (adapted from [1, 18]), and fluorescence spectrum of Ce:YAG (adapted from [60])

a broad band spectrum of yellow-green light, which loses its doublet character and forms one asymmetric Gaussian curve at room temperature [68].

In Fig. 4.8 is presented the absorption and fluorescence spectra of Ce:YAG, illustrating the broad absorption bands corresponding to the transitions from the $^2F_{5/2}$ ground state to the $5d_1$–$5d_5$ sublevels, and the broad emission band corresponding to the transition from the lowest $5d_1$ sublevel to the $^2F_{5/2}$ and $^2F_{7/2}$ states, respectively.

The optical and laser properties as well as the energy transfer mechanisms have been reported for Ce:Nd:YAG crystals [53, 54, 60, 61], ceramics [56–58] and powders [55, 59]. Co-doping both Ce^{3+} and Nd^{3+} ions in the YAG matrix combines the excellent absorption spectral properties of the Ce^{3+} ion, which has the two broad absorption bands centered around 340 nm and 460 nm, and the absorption bands characteristic of the Nd^{+3} ion between 525 nm and 900 nm, as represented in Fig. 4.9. In the YAG host, the Ce^{3+} ion broad fluorescence band, peaked around 530 nm, overlaps well with the intense absorption lines of the Nd^{3+} ion between 510 nm and 600 nm, as shown in Fig. 4.9.

The energy transfer from Ce^{3+} to Nd^{3+} ions in the Ce:Nd:YAG material has been found to occur via both radiative and non-radiative mechanisms [53–61]. In Fig. 4.10 is shown the energy transfer mechanisms between Ce^{3+} and Nd^{3+} ions depicted in an energy level diagram.

The radiative energy transfer has been confirmed by the superposition of the Ce emission band with the Nd absorption lines [53–58, 60, 61]. When pump photons at wavelengths around 340 nm and 460 nm are absorbed, Ce^{3+} ions are excited from the $^2F_{5/2}$ ground state to the broad pump bands $5d_2$ and $5d_1$, respectively. The electrons in the $5d_2$ could relax non-radiatively to the lower $5d_1$ pump band. Then, the electrons decay radiatively to the $^2F_{5/2}$ and $^2F_{7/2}$ ground states, emitting the broad band in the green and yellow spectral region. This radiative energy is then transferred to the Nd^{3+} ions, exciting them from the $^4I_{9/2}$ ground state to the $^4G_{7/2} + {}^2G_{9/2} + {}^2K_{13/2}$ levels grouped around 530 nm and the $^4G_{5/2} + {}^2G_{7/2}$ levels around 580 nm, because of the good overlap with the Ce fluorescence band (Figs. 4.9 and 4.10). Subsequently, the electrons relax non-radiatively to the $^4F_{3/2}$ level and then transit radiatively to the $^4I_{11/2}$ level, emitting light at 1064 nm (Fig. 4.10, pathway 1).

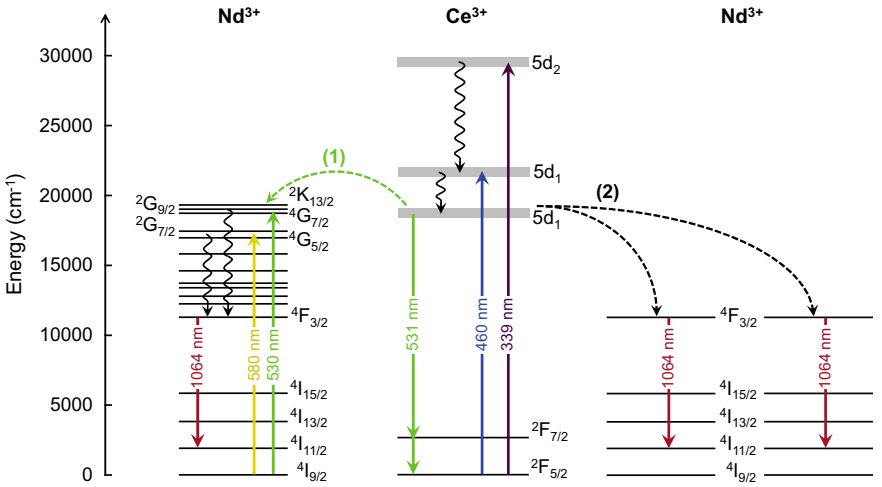

Fig. 4.10 Energy-level diagram of Nd^{3+} (adapted from [3]) and Ce^{3+} (adapted from [60]) ions in YAG, illustrating the energy transfer mechanisms between Ce^{3+} and Nd^{3+} ions in the Ce:Nd:YAG active medium (adapted from [60]). (1) Radiative energy transfer pathway. (2) Quantum cutting down-conversion pathway. Solid arrows indicate the excitation and emission processes, wavy and dashed arrows represent the non-radiative transitions and energy-transfer processes, respectively

The energy of the excited Ce^{3+} ions is also transferred to Nd^{3+} ions non-radiatively. The resonance energy transfer via dipole–dipole coupling has been deemed as a non-radiative mechanism in Ce:Nd:YAG [54, 56, 59]. Nevertheless, Tai et al. explored the quantum cutting process as a route for non-radiative $Ce^{3+} \rightarrow Nd^{3+}$ energy transfer [60]. The near-infrared quantum cutting involves the cooperative down-conversion of an absorbed visible photon to the emission of two near-infrared photons. Since the energy of the transition $5d_1 \rightarrow {}^2F_{5/2}$ of Ce^{3+} ion is approximately twice the energy of the transition ${}^4F_{3/2} \rightarrow {}^4I_{11/2}$ of Nd^{3+} ion, the energy of one excited Ce^{3+} ion can be cooperatively transferred into two nearby Nd^{3+} ions, Ce^{3+}: $5d_1 \rightarrow Nd^{3+}$: ${}^4F_{3/2}$ + Nd^{3+}: ${}^4F_{3/2}$, leading to near-infrared emission [60, 74], as shown in Fig. 4.10, pathway 2.

The energy transfer efficiency from Ce^{3+} to Nd^{3+} ions has been quantitatively determined in several works, with values varying from 50% to 84% [55, 58–60, 75, 76], as shown in Table 4.3. This efficiency discrepancy is mainly due to the difference of Ce^{3+} and Nd^{3+} ions concentration in YAG and the measurement methods. Most studies performed the measurement of the donor Ce lifetime to determine the energy transfer efficiency [55, 59, 60, 75]. However, this technique assesses only the non-radiative part since this causes a decrease in the donor fluorescence lifetime in the presence of the activator (Nd) (the lifetime does not depend on the radiative part). Yamaga et al. examined the transfer efficiency based on the quantum yields of the Ce^{3+} and Nd^{3+} luminescence [58]. They estimated that about 70% amount of Ce^{3+} ions transfers to Nd^{3+} ions, and 30% of Ce^{3+} ions radiatively transfer energy to Nd^{3+} ions [58]. Payziyev et al. relied on the measurement of the luminescence spectra of

Table 4.3 Summary of the energy transfer efficiencies from Ce^{3+} to Nd^{3+} ions in Ce:Nd:YAG

References	Energy transfer efficiency (%)	Active medium	Measurement method
Meng et al. [55]	84.0	Ce(5%):Nd(5%):YAG	Donor lifetime
Yamaga et al. [58]	70.0	Ce(0.05 mol.%): Nd(0.9 mol.%):YAG	Quantum yield
Wang et al. [75]	67.6	$Ce_{0.05}Nd_{0.05}$YAG	Donor lifetime
Wang et al. [59]	50.0	Ce(1%):Nd(2%):YAG	Donor lifetime
Tai et al. [60]	65.4	0.01Ce:0.01Nd:YAG	Donor lifetime
Payziyev et al. [76]	76.0	Ce(0.1 at.%): Nd(1.0 at.%):YAG	Luminescence spectrum

Nd:YAG and Ce:Nd:YAG media to assess the overall efficiency of energy transfer from Ce^{3+} to Nd^{3+} ions, estimating a value of 76% [76].

The fluorescence lifetime for Nd^{3+} emission at 1064 nm in Ce:Nd:YAG has been demonstrated to be slightly shorter than that in the Nd:YAG [56, 61]. Li et al. reported 256 μs for $Ce_{0.009}$:$Nd_{0.03}$:YAG against 269 μs for Nd:YAG [56], while Guo et al. reported 209.57 μs for $Ce_{0.003}$:$Nd_{0.03}$:YAG against 220.17 μs for Nd:YAG [61].

The laser performance of the Ce:Nd:YAG crystal has proved to be better than that of the Nd:YAG, pumped by either flash lamps or solar energy [61, 62, 64, 77]. Zhao et al. also demonstrated that the laser efficiency of the Ce:Nd:YAG was greater at high temperatures from 50 °C to 140 °C than that of the Nd:YAG crystal [77]. Pumping an Ce:Nd:YAG crystal with a xenon flash lamp, Guo et al. reported an output energy, energy efficiency and slope efficiency 1.62, 1.64 and 1.46 times, respectively, higher than those obtained with Nd:YAG [61]. When pumped by solar energy, Vistas et al. reported an output energy, energy efficiency and slope efficiency for an Ce:Nd:YAG crystal 1.57, 1.56 and 1.47 times, respectively, higher than those obtained with Nd:YAG [64]. These values are very similar than the ones observed by Guo et al. [61], and also the threshold pump power for the Ce:Nd:YAG was lower than that for the Nd:YAG crystal in both works [61, 64]. This demonstrates the great efficiency of the Ce:Nd:YAG laser regardless of the pumping source. However, an appropriate pumping configuration is necessary when solar energy is used as pumping source [63, 64, 78, 79].

The Ce:Nd:YAG solar-pumped laser systems design must take into account the pumping distribution due to thermal loading issues. The first solar laser emission from a Ce:Nd:YAG crystal used an end-side-pumping configuration, which was not the most effective for this medium as it led to the rod fracture in its upper-end region [63]. This made the laser unable to reach great power, being lower than that of Nd:YAG [63]. In this type of configuration, the concentrated solar radiation is mainly focused on the upper-end region of the rod, creating hot pump spots that can lead to thermal fracture. In the following year, Vistas et al. used a side-pumping configuration to allow uniform pump light absorption and homogeneous laser rod heating [64]. A significant increase in the Ce:Nd:YAG solar laser efficiency was obtained, corresponding to 1.57

times higher than the one obtained with a Nd:YAG solar laser [64]. In order to scale the laser power, Vistas et al. also studied the influence of the pump light distribution of two side-pumping configurations on the output performance of the Ce:Nd:YAG solar laser [78]. Using a point-focusing fused silica aspherical lens as a secondary concentrator resulted in an uneven light distribution along the laser rod, leading to its fracture when adding more incoming solar power. Contrariwise, using a fused silica rectangular light guide as a secondary concentrator enabled better light spreading on the rod, which led to a more uniform absorbed pump distribution along the rod, reducing thus the accumulated heat within the laser medium [78]. Although the output power was lower using the light guide than that using the aspherical lens, the reduction of the thermal load issues on the rod prevented the Ce:Nd:YAG medium fracture at high input solar power levels [78]. Moreover, Almeida et al. demonstrated the power scalability potential of the side-pumping configuration using the rectangular light guide through the emission of 40 W solar laser from a Ce:Nd:YAG medium [79].

Another way to circumvent thermal loading problems is to pump several small diameter laser rods within a single pump cavity. The exposure of a single laser rod to high pumping solar energy can produce severe thermal induced effects, limiting the laser power scalability. Therefore, the distribution of the concentrated radiation among multiple rods, as well as the use of small diameter rods, leads to an alleviation of thermal loading issues. In this sense, Liang et al. developed a three-rod Ce:Nd:YAG solar laser prototype able to produce 41.25 W/m^2 collection efficiency, 4.64% solar-to-laser conversion efficiency and 7.64% slope efficiency, which are records to date [80].

It is interesting to note that the thermal loading issues in the Ce:Nd:YAG are not manifested in the same fashion as in the Nd:YAG active medium. The Nd:YAG crystal rod also fractured using an end-side-pumped solar laser configuration [81]. However, its incoming solar power was at a very high level of 2585 W [81] compared with the low 964 W incoming power that caused the Ce:Nd:YAG rod fracture in an end-side-pumping configuration [63]. The main reason behind these results may rely on the Stokes shift (η_s), which is the spectral difference between the emission ($\lambda_{Emission}$) and the pump (λ_{Pump}) peak wavelengths. The Nd:YAG pumped by sunlight has a Stokes efficiency of 0.62 ($\eta_s = \lambda_{Pump}/\lambda_{Emission} = 660$ nm/1064 nm $= 0.62$ [19]); thus, 38% of the pump photon energy can be dissipated as heat to the crystal. The Ce:Nd:YAG has a lower Stokes efficiency of about 0.43 ($\eta_s = \lambda_{Pump}/\lambda_{Laser} = 460$ nm/1064 nm $= 0.43$ [82]); thereby, about 57% of the energy of the pump photon ions can be lost in the form of heat. This lower Stokes efficiency results in a higher thermal load in the active medium. Therefore, the thermal effects under solar pumping are more pronounced in the Ce:Nd:YAG, making this crystal more susceptible to thermal fracture [63, 78] than the Nd:YAG crystal [51, 81].

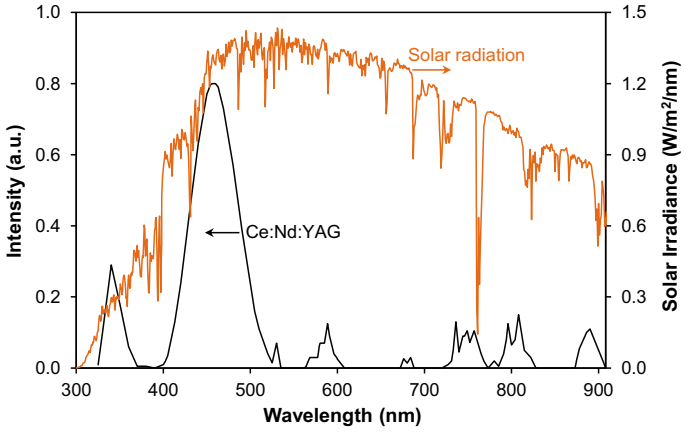

Fig. 4.11 Standard solar emission spectrum (orange line) [21], and Ce:Nd:YAG (black line) absorption spectrum (adapted from [60])

4.5.2 Spectral Overlap Between Ce:Nd:YAG Absorption and Solar Emission Spectra

The Ce:Nd:YAG active medium has two strong and broad absorption bands centered around 340 nm and 460 nm characteristic of the Ce^{3+} ions, and other absorption bands above 525 nm characteristic of the Nd^{3+} ions, which overlap well with the solar spectrum (Fig. 4.11). Liang et al. and Garcia et al. estimated efficiencies of overlap between the emission spectrum of solar radiation and the absorption spectra of Ce^{3+} and Nd^{3+} ions of around 15% and 16%, respectively [80, 83].

4.6 Other Materials

Throughout the history of solar laser, other active media have been explored, as Cr:Nd:GSGG and alexandrite. However, they have not been very successful in solar-pumped lasers.

Aside from the YAG matrix, other crystalline materials have been used as laser hosts, such as the GSGG, which can also be activated by Nd^{3+} ions and sensitized by Cr^{3+} ions. The Cr:Nd:GSGG crystal was introduced in the early 80's [84, 85]. This medium had been considered a good candidate for solar lasers because of the two strong and broad Cr absorption bands peaked at 450 nm and 640 nm and narrow Nd lines, which match the solar spectrum. In addition, the energy difference between the levels $^4T_2$ and ^2E is small due to the low cubic-crystal field strength in GSGG [86, 87] compared to YAG. The reduced energy difference increases the population

of the $^4T_2$ level, and thus the energy transfer from Cr^{3+} to Nd^{3+} ions is higher than that in YAG.

From Cr:Nd:GSGG laser experiments using either flashlamp [85, 88–90] or solar [91, 92] pumping, high efficiency was obtained compared to that of a Nd:YAG laser. However, the laser performance of the Cr:Nd:GSGG crystal at high pump powers is poor due to its low thermal conductivity (0.06 W/cm K) that is almost 2.5 times lower than that of Nd:YAG [87]. Moreover, the widening of the absorption bands causes a large increase of heat deposited in the crystal. All this results in strong thermal effects, such as severe thermal lensing, thermally induced birefringence and thermal fracture [89, 91], making this crystal unattractive to high-power solar-pumped lasers.

Alexandrite, the popular name for chromium-doped chrysoberyl (Cr^{3+}:$BeAl_2O_4$) crystal, was developed in the late 70's [93, 94]. Its excellent optical, thermal and mechanical properties have made it one of the leading materials in solid-state lasers. The alexandrite crystal has a thermal conductivity (0.23 W/cm K) almost twice that of YAG, and a thermal fracture limit 5 times higher than that of YAG [94]. As a chromium-doped material, it has two strong and broad absorption bands in the visible region, centered at 410 nm and 590 nm [94], which match well with lamps and solar emission spectra. The alexandrite laser emission is tunable in the 701–818 nm spectral range, because of the $^4T_2 \rightarrow {}^4A_2$ electronic–vibrational transitions in Cr^{3+} ions [1]. The stimulated emission cross-section at room temperature is low (7×10^{-21} cm^2), requiring high pump fluence for efficient gain extraction, but this is offset by its high optical damage threshold [1].

Despite the potential of this material for solar-pumped lasers due to its suitable properties, only few works were performed [19, 95–97]. Lando et al. was the first and only to experimentally test the alexandrite crystal in a solar-pumped laser [96]. The remained studies were performed through numerical analysis [19, 95, 97]. Lando et al. obtained a laser output power of 12 W; however, the efficiency of the alexandrite solar laser was not reported [96]. Weskler et al. and Payziyev et al. predicted a solar-to-laser conversion efficiency of about 14%, based on numerical analysis [19, 97]. The high threshold pump power to initiate the alexandrite laser is considered as the main limiting factor for visible solar-pumped lasers [19, 95–97]. This is the main reason for not having more studies on alexandrite solar lasers, being a real challenge to have such a great solar intensity with the existing solar concentrating systems.

References

1. Koechner, W.: Solid-State Laser Engineering, 6th edn. Springer, New York (2006)
2. Silfvast, W.T.: Laser Fundamentals, 2nd edn. Cambridge University Press, Cambridge (2004)
3. Powell, R.C.: Physics of Solid-State Laser Materials. Springer-Verlag, New York (1998)
4. Hooker, S., Webb, C.: Laser physics. Oxford University Press, New York, Oxford (2010)
5. Svelto, O.: Principles of Lasers, 5th edn. Springer, US, New York (2010)
6. Kaminskii, A.A.: Laser Crystals: Their Physics and Properties, 2nd edn. Springer-Verlag, Berlin, Heidelberg (1990)
7. Ikesue, A., Aung, Y.L.: Synthesis and performance of advanced ceramic lasers. J. Am. Ceram. Soc. **89**(6), 1936–1944 (2006). https://doi.org/10.1111/j.1551-2916.2006.01043.x

8. Ikesue, A., Aung, Y.L.: Ceramic laser materials. Nat. Photonics **2**(12), 721–727 (2008). https://doi.org/10.1038/nphoton.2008.243
9. Sanghera, J., Kim, W., Villalobos, G., Shaw, B., Baker, C., Frantz, J., Sadowski, B., Aggarwal, I.: Ceramic laser materials. Materials **5**(2) (2012). https://doi.org/10.3390/ma5020258
10. Geusic, J.E., Marcos, H.M., Van Uitert, L.G.: Laser oscillations in Nd-doped yttrium aluminum, yttrium gallium and gadolinium garnets. Appl. Phys. Lett. **4**(10), 182–184 (1964). https://doi.org/10.1063/1.1753928
11. Young, C.G.: A sun-pumped CW one-watt laser. Appl. Opt. **5**(6), 993–997 (1966). https://doi.org/10.1364/AO.5.000993
12. Brauch, U., Muckenschnabel, J.: Temperature dependence of flashlamp-pumped Nd:YAG and Nd:Cr:GSGG lasers. Opt. Commun. **73**(1), 62–66 (1989). https://doi.org/10.1016/0030-4018(89)90241-1
13. Dong, J., Rapaport, A., Bass, M., Szipocs, F., Ueda, K.-I.: Temperature-dependent stimulated emission cross section and concentration quenching in highly doped Nd^{3+}:YAG crystals. physica status solidi (a) **202**(13), 2565–2573 (2005). https://doi.org/10.1002/pssa.200421122
14. Rapaport, A., Zhao, S., Xiao, G., Howard, A., Bass, M.: Temperature dependence of the 1.06-μm stimulated emission cross section of neodymium in YAG and in GSGG. Appl. Opt. **41**(33), 7052–7057 (2002). https://doi.org/10.1364/AO.41.007052
15. Sato, Y., Taira, T.: Temperature dependencies of stimulated emission cross section for Nd-doped solid-state laser materials. Opt. Mater. Express **2**(8), 1076–1087 (2012). https://doi.org/10.1364/OME.2.001076
16. Sato, Y., Taira, T.: Variation of the stimulated emission cross section in Nd:YAG caused by the structural changes of Russell-Saunders manifolds. Opt. Mater. Express **1**(3), 514–522 (2011). https://doi.org/10.1364/OME.1.000514
17. Buchenkov, V.A., Vitrishchak, I.B., Evdokimova, V.G., Soms, L.N., Stepanov, A.I., Stupnikov, V.K.: Temperature dependence of giant pulse amplification in YAG:Nd^{3+}. SvJQE **11**(6), 702–705 (1981). https://doi.org/10.1070/qe1981v011n06abeh007030
18. Prahl, S.: Nd:YAG - Nd:$Y_3Al_5O_{12}$. https://omlc.org/spectra/lasermedia/html/052.html (2017)
19. Weksler, M., Shwartz, J.: Solar-pumped solid-state lasers. IEEE J. Quantum Electron. **24**(6), 1222–1228 (1988). https://doi.org/10.1109/3.247
20. Zhao, B., Zhao, C., He, J., Yang, S.: The study of active medium for solar-pumped solid-state lasers. AcOpS **27**, 1797–1801 (2007)
21. ASTM G173–03, Standard tables for reference solar spectral irradiances: direct normal and hemispherical on 37° tilted surface. ASTM International, West Conshohocken, Pennsylvania (2012)
22. Kiss, Z.J., Duncan, R.C.: Cross-pumped Cr^{3+}−Nd^{3+}:YAG laser system. Appl. Phys. Lett. **5**(10), 200–202 (1964). https://doi.org/10.1063/1.1723587
23. Reno, G.W.: Solar-pumped modulated laser. RCA Rev. **149** (1966)
24. Ikesue, A., Kinoshita, T., Kamata, K., Yoshida, K.: Fabrication and optical properties of high-performance polycrystalline Nd:YAG ceramics for solid-state lasers. J. Am. Ceram. Soc. **78**(4), 1033–1040 (1995). https://doi.org/10.1111/j.1151-2916.1995.tb08433.x
25. Ikesue, A., Kamata, K., Yoshida, K.: Synthesis of Nd3+, Cr3+-codoped YAG ceramics for high-efficiency solid-state lasers. J. Am. Ceram. Soc. **78**(9), 2545–2547 (1995). https://doi.org/10.1111/j.1151-2916.1995.tb08699.x
26. Ikesue, A., Aung, Y.L., Lupei, V.: Ceramic Lasers. Cambridge University Press, Cambridge (2013)
27. Hong, P., Zhang, X.X., Struck, C.W., Di Bartolo, B.: Luminescence of Cr^{3+} and energy transfer between Cr^{3+} and Nd^{3+} ions in yttrium aluminum garnet. J. Appl. Phys. **78**(7), 4659–4667 (1995). https://doi.org/10.1063/1.359813
28. Saiki, T., Motokoshi, S., Imasaki, K., Fujioka, K., Fujita, H., Nakatsuka, M., Izawa, Y., Yamanaka, C.: Effective Fluorescence Lifetime and Stimulated Emission Cross-Section of Nd/Cr:YAG Ceramics under CW Lamplight Pumping. Jpn. J. Appl. Phys. **47**(10), 7896–7902 (2008). https://doi.org/10.1143/jjap.47.7896

29. Saiki, T., Nakatsuka, M., Fujioka, K., Motokoshi, S., Imasaki, K., Iida, Y.: Increase in effective fluorescence lifetime by cross-relaxation effect depending on temperature of Nd/Cr:YAG ceramic using white-light pump source. Opt. Photonics Lett. **6**(1), 1350003 (2013). https://doi.org/10.1142/S1793528813500032
30. Endo, M.: Optical characteristics of Cr^{3+} and Nd^{3+} codoped $Y_3Al_5O_{12}$ ceramics. Opt. Laser Technol. **42**(4), 610–616 (2010). https://doi.org/10.1016/j.optlastec.2009.10.012
31. Yamaga, M., Oda, Y., Uno, H., Hasegawa, K., Ito, H., Mizuno, S.: Formation probability of Cr-Nd pair and energy transfer from Cr to Nd in $Y_3Al_5O_{12}$ ceramics codoped with Nd and Cr. J. Appl. Phys. **112**(6), 063508 (2012). https://doi.org/10.1063/1.4752403
32. Honda, Y., Motokoshi, S., Jitsuno, T., Miyanaga, N., Fujioka, K., Nakatsuka, M., Yoshida, M.: Temperature dependence of optical properties in Nd/Cr:YAG materials. J. Lumin. **148**, 342–346 (2014). https://doi.org/10.1016/j.jlumin.2013.12.044
33. Hasegawa, K., Ichikawa, T., Mizuno, S., Takeda, Y., Ito, H., Ikesue, A., Motohiro, T., Yamaga, M.: Energy transfer efficiency from Cr^{3+} to Nd^{3+} in solar-pumped laser using transparent Nd/Cr:$Y_3Al_5O_{12}$ ceramics. Opt. Express **23**(11), A519–A524 (2015). https://doi.org/10.1364/OE.23.00A519
34. Lupei, V., Lupei, A., Gheorghe, C., Ikesue, A.: Spectroscopic and de-excitation properties of (Cr, Nd):YAG transparent ceramics. Opt. Mater. Express **6**(2), 552–557 (2016). https://doi.org/10.1364/OME.6.000552
35. Lupei, V., Lupei, A., Gheorghe, C., Ikesue, A.: Emission sensitization processes involving Nd^{3+} in YAG. J. Lumin. **170**, 594–601 (2016). https://doi.org/10.1016/j.jlumin.2015.04.045
36. Honda, Y., Motokoshi, S., Jitsuno, T., Fujioka, K., Nakatsuka, M., Yoshida, M., Yamada, T., Kawanaka, J., Miyanaga, N.: Temperature-dependent fluorescence decay and energy transfer in Nd/Cr:YAG ceramics. Opt. Mater. **90**, 215–219 (2019). https://doi.org/10.1016/j.optmat.2019.02.032
37. Kato, T., Ito, H., Hasegawa, K., Ichikawa, T., Ikesue, A., Mizuno, S., Takeda, Y., Ichiki, A., Motohiro, T.: Energy transfer efficiency from Cr^{3+} to Nd^{3+} in Cr, Nd YAG ceramics laser media in a solar-pumped laser in operation outdoors. Opt. Mater. **110**, 110481 (2020). https://doi.org/10.1016/j.optmat.2020.110481
38. Honda, Y., Motokoshi, S., Jitsuno, T., Fujioka, K., Yamada, T., Yoshida, M.: Temperature dependence of the small-signal gain of a Cr^{3+} and Nd^{3+} co-doped $Y_3Al_5O_{12}$ ceramic. Jpn. J. Appl. Phys. **60**(7), 072003 (2021). https://doi.org/10.35848/1347-4065/ac06b3
39. Yagi, H., Yanagitani, T., Yoshida, H., Nakatsuka, M., Ueda, K.: The optical properties and laser characteristics of Cr^{3+} and Nd^{3+} co-doped Y3Al5O12 ceramics. Opt. Laser Technol. **39**(6), 1295–1300 (2007). https://doi.org/10.1016/j.optlastec.2006.06.016
40. Zhang, Z., Grattan, K.T.V., Palmer, A.W.: Temperature dependences of fluorescence lifetimes in Cr^{3+}-doped insulating crystals. PhRvB **48**(11), 7772–7778 (1993). https://doi.org/10.1103/PhysRevB.48.7772
41. Saiki, T., Funahashi, K., Motokoshi, S., Imasaki, K., Fujioka, K., Fujita, H., Nakatsuka, M., Yamanaka, C.: Temperature characteristics of small signal gain for Nd/Cr:YAG ceramic lasers. Opt. Commun. **282**(4), 614–616 (2009). https://doi.org/10.1016/j.optcom.2008.10.032
42. Saiki, T., Imasaki, K., Motokoshi, S., Yamanaka, C., Fujita, H., Nakatsuka, M., Izawa, Y.: Disk-type Nd/Cr:YAG ceramic lasers pumped by arc-metal-halide-lamp. Opt. Commun. **268**(1), 155–159 (2006). https://doi.org/10.1016/j.optcom.2006.07.002
43. Saiki, T., Motokoshi, S., Imasaki, K., Fujita, H., Nakatsuka, M., Yamanaka, C.: Nd/Cr:YAG ceramic rod laser pumped using arc-metal-halide-lamp. Jpn. J. Appl. Phys. **46**(1), 156–160 (2007). https://doi.org/10.1143/jjap.46.156
44. Yabe, T., Ohkubo, T., Uchida, S., Yoshida, K., Nakatsuka, M., Funatsu, T., Mabuti, A., Oyama, A., Nakagawa, K., Oishi, T., Daito, K., Behgol, B., Nakayama, Y., Yoshida, M., Motokoshi, S., Sato, Y., Baasandash, C.: High-efficiency and economical solar-energy-pumped laser with Fresnel lens and chromium codoped laser medium. Appl. Phys. Lett. **90**(26), 261120 (2007). https://doi.org/10.1063/1.2753119
45. Dinh, T.H., Ohkubo, T., Yabe, T., Kuboyama, H.: 120 watt continuous wave solar-pumped laser with a liquid light-guide lens and an Nd:YAG rod. Opt. Lett. **37**(13), 2670–2672 (2012). https://doi.org/10.1364/ol.37.002670

46. Liang, D., Almeida, J., Guillot, E.: Side-pumped continuous-wave Cr:Nd:YAG ceramic solar laser. Appl. Phys. B-Lasers O. **111**(2), 305–311 (2013). https://doi.org/10.1007/s00340-013-5334-4
47. Liang, D., Almeida, J., Garcia, D.: Comparative study of Cr:Nd:YAG and Nd:YAG solar laser performances. In: Proc. SPIE 8785, 8th Iberoamerican Optics Meeting and 11th Latin American Meeting on Optics, Lasers, and Applications, Porto (2013)
48. Liang, D., Vistas, C.R., Tiburcio, B.D., Almeida, J.: Solar-pumped Cr:Nd:YAG ceramic laser with 6.7% slope efficiency. Sol. Energy Mater. Sol. Cells **185**, 75–79 (2018). https://doi.org/10.1016/j.solmat.2018.05.020
49. Suzuki, Y., Ito, H., Kato, T., Phuc, L.T.A., Watanabe, K., Terazawa, H., Hasegawa, K., Ichikawa, T., Mizuno, S., Ichiki, A., Takimoto, S., Ikesue, A., Takeda, Y., Motohiro, T.: Continuous oscillation of a compact solar-pumped Cr, Nd-doped YAG ceramic rod laser for more than 6.5 h tracking the sun. Sol. Energ. **177**, 440–447 (2019). https://doi.org/10.1016/j.solener.2018.10.071
50. Kato, T., Ito, H., Hasegawa, K., Ichikawa, T., Ikesue, A., Mizuno, S., Takeda, Y., Ichiki, A., Motohiro, T.: Effect of Cr content on the output of a solar-pumped laser employing a Cr-doped Nd:YAG ceramic laser medium operating in sunlight. Jpn. J. Appl. Phys. **58**(6), 062007 (2019). https://doi.org/10.7567/1347-4065/ab22de
51. Liang, D., Almeida, J., Vistas, C.R., Guillot, E.: Solar-pumped Nd:YAG laser with 31.5 W/m^2 multimode and 7.9 W/m^2 TEM00-mode collection efficiencies. Sol. Energy Mater. Sol. Cells **159**, 435–439 (2017). https://doi.org/10.1016/j.solmat.2016.09.048
52. Holloway, W.W., Kestigian, M.: Optical properties of cerium-activated garnet crystals. J. Opt. Soc. Am. **59**(1), 60–63 (1969). https://doi.org/10.1364/JOSA.59.000060
53. Mareš, J.: Energy transfer in YAlG: Nd codoped with Ce. CzJPB **35**(8), 883–891 (1985). https://doi.org/10.1007/BF01959456
54. Mareš, J., Jacquier, B., Pédrini, C., Boulon, G.: Energy transfer mechanisms between Ce^{3+} and Nd^{3+} in YAG : Nd, Ce at low temperature. Rev. Phys. Appl. **22**(2), 145–152 (1987)
55. Meng, J.X., Li, J.Q., Shi, Z.P., Cheah, K.W.: Efficient energy transfer for Ce to Nd in Nd/Ce codoped yttrium aluminum garnet. Appl. Phys. Lett. **93**(22), 221908 (2008). https://doi.org/10.1063/1.3035849
56. Li, Y., Zhou, S., Lin, H., Hou, X., Li, W.: Intense 1064nm emission by the efficient energy transfer from Ce^{3+} to Nd^{3+} in Ce/Nd co-doped YAG transparent ceramics. Opt. Mater. **32**(9), 1223–1226 (2010). https://doi.org/10.1016/j.optmat.2010.04.003
57. Samuel, P., Yanagitani, T., Yagi, H., Nakao, H., Ueda, K.I., Babu, S.M.: Efficient energy transfer between Ce^{3+} and Nd^{3+} in cerium codoped Nd: YAG laser quality transparent ceramics. J. Alloys Compd. **507**(2), 475–478 (2010). https://doi.org/10.1016/j.jallcom.2010.07.207
58. Yamaga, M., Oda, Y., Uno, H., Hasegawa, K., Ito, H., Mizuno, S.: Energy transfer from Ce to Nd in $Y_3Al_5O_{12}$ ceramics. Phys. Status Solidi C **9**(12), 2300–2303 (2012). https://doi.org/10.1002/pssc.201200200
59. Wang, Q., Qiu, J.B., Song, Z.G., Yang, Z.W., Yin, Z.Y., Zhou, D.C.: Optical properties of Ce^{3+}–Nd^{3+} co-doped YAG nanoparticles for visual and near-infrared biological imaging. Spectrochim. Acta Part A Mol. Biomol. Spectrosc. **149**, 898–903 (2015). https://doi.org/10.1016/j.saa.2015.04.082
60. Tai, Y., Zheng, G., Wang, H., Bai, J.: Near-infrared quantum cutting of Ce^{3+}–Nd^{3+} co-doped $Y_3Al_5O_{12}$ crystal for crystalline silicon solar cells. J. Photochem. Photobiol. A **303–304**, 80–85 (2015). https://doi.org/10.1016/j.jphotochem.2015.02.009
61. Guo, Y., Huang, J., Ke, G., Ma, Y., Quan, J., Yi, G.: Growth and optical properties of the Nd, Ce:YAG laser crystal. J. Lumin. **236**, 118134 (2021). https://doi.org/10.1016/j.jlumin.2021.118134
62. Kvapil, J., Kvapil, J., Perner, B., Kubelka, J., Mánek, B., Kubeček, V.: Laser properties of YAG: Nd, Cr. Ce. CzJPB **34**(6), 581–588 (1984). https://doi.org/10.1007/BF01595714
63. Vistas, C.R., Liang, D., Garcia, D., Almeida, J., Tibúrcio, B.D., Guillot, E.: Ce:Nd:YAG continuous-wave solar-pumped laser. Optik **207**, 163795 (2020). https://doi.org/10.1016/j.ijleo.2019.163795

64. Vistas, C.R., Dawei, L., Joana, A., Bruno, D.T., Dário, G., Miguel, C., Hugo, C., Emmanuel, G.: Ce:Nd:YAG side-pumped solar laser. J. Photon. Energy **11**(1), 1–9 (2021). https://doi.org/10.1117/1.JPE.11.018001
65. Mareš, J.A., Kubelka, J., Kvapil, J.: About the luminescence properties of YAG:Nd, Ce and YAG:Nd single crystals and their relation to laser properties. CzJPB **36**(9), 1079–1089 (1986). https://doi.org/10.1007/BF01597772
66. Weber, M.J.: Nonradiative decay from 5d states of rare earths in crystals. Solid State Commun. **12**(7), 741–744 (1973). https://doi.org/10.1016/0038-1098(73)90326-8
67. Jacobs, R.R., Krupke, W.F., Weber, M.J.: Measurement of excited-state-absorption loss for Ce^{3+} in $Y_3Al_5O_{12}$ and implications for tunable 5d→4f rare-earth lasers. Appl. Phys. Lett. **33**(5), 410–412 (1978). https://doi.org/10.1063/1.90395
68. Bachmann, V., Ronda, C., Meijerink, A.: Temperature quenching of yellow Ce3+ luminescence in YAG:Ce. Chem. Mater. **21**(10), 2077–2084 (2009). https://doi.org/10.1021/cm8030768
69. Chen, L., Chen, X., Liu, F., Chen, H., Wang, H., Zhao, E., Jiang, Y., Chan, T.-S., Wang, C.-H., Zhang, W., Wang, Y., Chen, S.: Charge deformation and orbital hybridization: intrinsic mechanisms on tunable chromaticity of $Y_3Al_5O_{12}$:Ce^{3+} luminescence by doping Gd^{3+} for warm white LEDs. Sci. Rep. **5**(1), 11514 (2015). https://doi.org/10.1038/srep11514
70. Tanner, P.A., Fu, L., Ning, L., Cheng, B.-M., Brik, M.G.: Soft synthesis and vacuum ultraviolet spectra of YAG:Ce^{3+} nanocrystals: reassignment of Ce^{3+} energy levels. J. Phys.: Condens. Matter **19**(21), 216213 (2007). https://doi.org/10.1088/0953-8984/19/21/216213
71. Dorenbos, P.: Electronic structure and optical properties of the lanthanide activated $RE_3(Al_{1-x}Ga_x)_5O_{12}$ (RE=Gd, Y, Lu) garnet compounds. J. Lumin. **134**, 310–318 (2013). https://doi.org/10.1016/j.jlumin.2012.08.028
72. Dorenbos, P.: Relating the energy of the $[Xe]5d^1$ configuration of Ce^{3+} in inorganic compounds with anion polarizability and cation electronegativity. PhRvB **65**(23), 235110 (2002). https://doi.org/10.1103/PhysRevB.65.235110
73. Lin, Y.-C., Karlsson, M., Bettinelli, M.: Inorganic phosphor materials for lighting. In: Armaroli, N., Bolink, H.J. (eds.) Photoluminescent Materials and Electroluminescent Devices, pp. 309–355. Springer International Publishing, Cham (2017)
74. Chen, D., Wang, Y., Yu, Y., Huang, P., Weng, F.: Quantum cutting downconversion by cooperative energy transfer from Ce^{3+} to Yb^{3+} in borate glasses. J. Appl. Phys. **104**(11), 116105 (2008). https://doi.org/10.1063/1.3040005
75. Wang, L., Xia, C., Xu, P., Di, J., Sai, Q., Mou, F.: Energy transfer in Ce, Nd, and Yb co-doped YAG phosphors. Chin. Opt. Lett. **11**(6), 061604 (2013)
76. Payziyev, S., Sherniyozov, A., Bakhramov, S., Zikrillayev, K., Khalikov, G., Makhmudov, K., Ismailov, M., Payziyeva, D.: Luminescence sensitization properties of Ce: Nd: YAG materials for solar pumped lasers. Opt. Commun. **499**, 127283 (2021). https://doi.org/10.1016/j.optcom.2021.127283
77. Zhao, G., Zhu, B., Peng, X., Xu, J., Xu, C., Yi, L., Yang, S., Chen, X.: Mechanism of compact solid state laser with increasing efficiency at higher surrounding temperature. In: Proc. SPIE, Photonics China '98 (1998)
78. Vistas, C.R., Liang, D., Garcia, D., Catela, M., Tibúrcio, B.D., Costa, H., Guillot, E., Almeida, J.: uniform and non-uniform pumping effect on Ce:Nd:YAG side-pumped solar laser output performance. Energies **15**(10), 3577 (2022)
79. Almeida, J., Liang, D., Garcia, D., Tibúrcio, B.D., Costa, H., Catela, M., Guillot, E., Vistas, C.R.: 40 W continuous wave Ce:Nd:YAG solar laser through a fused silica light guide. Energies **15**(11), 3998 (2022)
80. Liang, D., Vistas, C.R., Garcia, D., Tibúrcio, B.D., Catela, M., Costa, H., Guillot, E., Almeida, J.: Most efficient simultaneous solar laser emissions from three Ce:Nd:YAG rods within a single pump cavity. Sol. Energy Mater. Sol. Cells **246**, 111921 (2022). https://doi.org/10.1016/j.solmat.2022.111921
81. Almeida, J., Liang, D., Vistas, C.R., Guillot, E.: Highly efficient end-side-pumped Nd:YAG solar laser by a heliostat-parabolic mirror system. Appl. Opt. **54**(8), 1970–1977 (2015). https://doi.org/10.1364/ao.54.001970

82. Villars, B., Steven Hill, E., Durfee, C.G.: Design and development of a high-power LED-pumped Ce:Nd:YAG laser. Opt. Lett. **40**(13), 3049–3052 (2015). https://doi.org/10.1364/OL.40.003049
83. Garcia, D., Liang, D., Vistas, C.R., Costa, H., Catela, M., Tibúrcio, B.D., Almeida, J.: Ce:Nd:YAG Solar Laser with 4.5% Solar-to-Laser Conversion Efficiency. Energies **15**(14), 5292 (2022)
84. Pruss, D., Huber, G., Beimowski, A., Laptev, V.V., Shcherbakov, I.A., Zharikov, Y.V.: Efficient Cr^{3+} sensitized Nd^{3+}:GdScGa-garnet laser at 1.06 μm. Appl. Phys. B **28**(4), 355–358 (1982). https://doi.org/10.1007/BF00686366
85. Zharikov, E.V., Il'ichev, N.N., Laptev, V.V., Malyutin, A.A., Ostroumov, V.G., Pashinin, P.P., Pimenov, A.S., Smirnov, V.A., Shcherbakov, I.A.: Spectral, luminescence, and lasing properties of gadolinium scandium gallium garnet crystals activated with neodymium and chromium ions. SvJQE **13**(1), 82–85 (1983). https://doi.org/10.1070/qe1983v013n01abeh004020
86. Struve, B., Huber, G.: The effect of the crystal field strength on the optical spectra of Cr^{3+} in gallium garnet laser crystals. Appl. Phys. B **36**(4), 195–201 (1985). https://doi.org/10.1007/BF00704574
87. Krupke, W.F., Shinn, M.D., Marion, J.E., Caird, J.A., Stokowski, S.E.: Spectroscopic, optical, and thermomechanical properties of neodymium- and chromium-doped gadolinium scandium gallium garnet. J. Opt. Soc. Am. B **3**(1), 102–114 (1986). https://doi.org/10.1364/JOSAB.3.000102
88. Laporta, P., Magni, V., Svelto, O.: Comparative study of the optical pumping efficiency in solid-state lasers. IEEE J. Quantum Electron. **21**(8), 1211–1218 (1985). https://doi.org/10.1109/JQE.1985.1072800
89. Reed, E.: A flashlamp-pumped, Q-switched Cr:Nd:GSGG laser. IEEE J. Quantum Electron. **21**(10), 1625–1629 (1985). https://doi.org/10.1109/JQE.1985.1072565
90. Caird, J.A., Shinn, M.D., Kirchoff, T.A., Smith, L.K., Wilder, R.E.: Measurements of losses and lasing efficiency in GSGG:Cr, Nd and YAG: Nd laser rods. Appl. Opt. **25**(23), 4294–4305 (1986). https://doi.org/10.1364/AO.25.004294
91. Kim, K.H., Venable, D.D., Brown, L.A., Lee, J.H.: Thermal effects on cavity stability of chromium- and neodymium-doped gadolinium scandium gallium garnet laser under solar-simulator pumping. J. Appl. Phys. **69**(5), 2841–2848 (1991). https://doi.org/10.1063/1.348619
92. Cooke, D.: Sun-pumped lasers: revisiting an old problem with nonimaging optics. Appl. Opt. **31**(36), 7541–7546 (1992). https://doi.org/10.1364/AO.31.007541
93. Walling, J.C., Jenssen, H.P., Morris, R.C., O'Dell, E.W., Peterson, O.G.: Tunable-laser performance in $BeAl_2O_4$:Cr^{3+}. Opt. Lett. **4**(6), 182–183 (1979). https://doi.org/10.1364/OL.4.000182
94. Walling, J., Peterson, O., Jenssen, H., Morris, R., Dell, E.O.: Tunable alexandrite lasers. IEEE J. Quantum Electron. **16**(12), 1302–1315 (1980). https://doi.org/10.1109/JQE.1980.1070430
95. Hwang, I.H., Lee, J.H.: Efficiency and threshold pump intensity of CW solar-pumped solid-state lasers. IEEE J. Quantum Electron. **27**(9), 2129–2134 (1991). https://doi.org/10.1109/3.135171
96. Lando, M., Shimony, Y., Benmair, R.M.J., Abramovich, D., Krupkin, V., Yogev, A.: Visible solar-pumped lasers. Opt. Mater. **13**(1), 111–115 (1999). https://doi.org/10.1016/S0925-3467(99)00019-1
97. Payziyev, S., Makhmudov, K., Kasimov, A.: Performance analysis of solar pumped alexandrite laser: a new way for lowering the threshold power. Recent Adv. Photonics Opt. **2**(1), 26–30 (2019)

Chapter 5
Primary Solar Concentrators

Dário Garcia

Introduction

Optical apparatus such as concentrators can collect solar energy into a compact form, which is very desirable for some applications that operate at high temperatures. However, the amount of concentrated energy is dependent on various uncontrollable factors, such as the unpredicted atmospheric conditions on Earth or the degradation of the concentrating medium over time.

The speed of light is a constant of 3.00×10^8 m/s when traveling in a vacuum, with a refractive index of $n_\lambda = 1$. When the propagating ray enters a different refractive material ($n_\lambda > 1$), it reduces the phase velocity by $v = c/n_\lambda$. Typical values of n_λ for air at normal pressure are around 1.0003, 1.33 for water, and 1.45–1.8 for glass and plastics, respectively. Moreover, the n_λ is different for each wavelength.

Snell's law of refraction follows the principle of least time (from Fermat's principle). The refracted incident ray travels from the interface between the refractive index media of n_1 and n_2, as shown in Eq. (5.1).

$$n_i \sin(\theta_i) = n_t \sin(\theta_t) \tag{5.1}$$

where θ_i is the incidence angle (measured from the normal on medium i) and the refracted angle θ_t (measured from the normal on medium t). The incident beam splits into a reflected beam and a transmitted beam, both subject to Snell's Law, as shown in Fig. 5.1.

Refraction

A portion of incident radiation is transmitted through the next interface from the previous. If the second interface (medium) has the same refraction index (i.e., $n_i = n_t$), then the ray continues to travel without changing its course, i.e., $\theta_i = \theta_t$. If $n_i < n_t$, due to Snell's law, then the refractive radiation will have a slight bent or a deviation of the angle about the normal axis, as shown in Fig. 5.1. Refractive materials such as fused silica lenses with $n_\lambda \approx 1.47$ and poly methyl methacrylate (PMMA) at $n_\lambda \approx 1.49$ are commonly used in solar-pumped lasers.

© The Author(s), under exclusive license to Springer Nature Switzerland AG 2023

D. Liang et al., *Solar-Pumped Lasers*, Green Energy and Technology,
https://doi.org/10.1007/978-3-031-24785-9_5

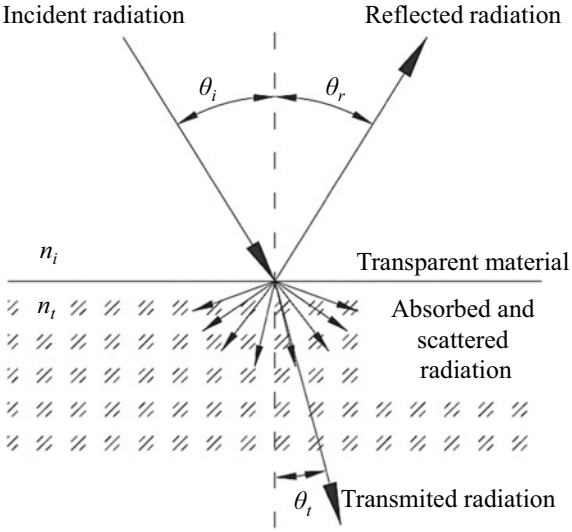

Fig. 5.1 Incident radiation is incoming from angle θ_i normal to the surface of the material. Reflected radiation bouncing with θ_r (same value as θ_i). The transmitted radiation shifts θ_t in its trajectory due to snell's law. The intensity of the transmitted radiation is reduced due to the absorption and scattering nature of the refractive medium

Absorption

Light with a certain energy, intensity, and wavelength passing through a medium (other than a vacuum) would have small or sizable portions of its energy absorbed by the material. The transmitted wavelength intensity ($I_{t(\lambda)}$) is proportional to the standard exponential decay of the incident intensity ($I_{i(\lambda)}$) by the coefficient of absorption of the material (α_λ) at a depth length (l):

$$I_{t(\lambda)} = I_{i(\lambda)} e^{-\alpha_\lambda l} \tag{5.2}$$

Reflection

The reflected radiation remains the same n_i section after interacting with the reflective medium. A small portion of the reflected energy is lost due to the absorption of the material. The reflected angle is mostly the same as the angle of incidence, $\theta_i = \theta_r$.

Mirror

The mirror is an optical device with the primary function of reflecting light. Most mirrors found in the market are flat and through special demand, curved-shaped mirrors can be obtained. The amount of energy reflected by the mirror measures the reflectivity, i.e., the amount of energy reflected compared to the initial energy. Front surface mirrors (or first surface mirrors) are metal-coated mirrors with a thin layer of metal coating, mostly produced by vacuum evaporation or by a sputtering technique. The metallic coating adheres to a substrate, mostly glass (fused silica), as shown in Fig. 5.2a. Mirror coating of aluminum, silver, or gold is commonly found in the market, and less common materials such as beryllium, copper, chrome, or nickel/chrome alloys are more difficult to acquire. Dielectric layers are often used to

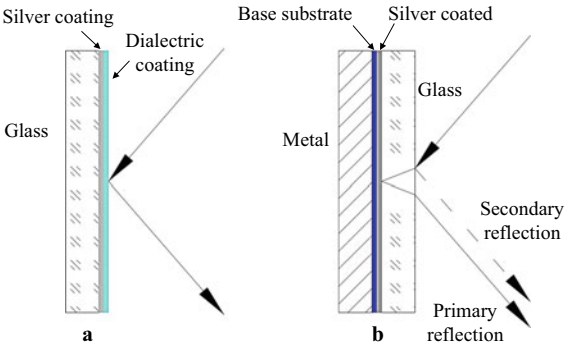

Fig. 5.2 **a** First surface and **b** back surface mirrors

protect or/and enhanced the metallic coating. Metallic mirror (first surface mirror) provides larger reflective broadband, negligible low achromatic dispersion, and weak angular dependency on reflectivity.

Another type of mirror is the back surface metallic mirror, which has an added protective glass layer on top of the metallic surface, as shown in Fig. 5.2b. Household mirrors are silver coated on the back.

Advantages of first surface mirrors compared to back surface mirrors:

- The substrate of the mirror does not contribute to the reduction of reflectivity by absorption in certain broadband regions. This type of mirror has a much lower loss of reflection band in the infrared region.
- Wavefront distortion from reflection caused by inhomogeneities of the substrate cannot occur.
- in non-normal incidence light. It does not generate ghost images due to the weaker front surface reflection from the mirror surface.
- Light in normal incidence. It does not cause strong chromatic dispersion based on the interference contribution from the front and back surface reflection of the glass substrate.

Disadvantages:

- The touched surface creates fingerprints that can easily cause oxidation. It may not be possible to clean such mirrors, losing the optical quality.
- Moisture and aggressive gases may cause oxidation in the mirror coating.
- The degradation of reflectivity in the function of time is faster than that of the back surface mirror.
- Harder to clean.

Sun Shaped By Angle

The Sun shape image should be taken into the utmost consideration for any solar-based research and technology. The acceptance half-angle subtended by the Sun dictates the absolute angle at which the solar rays arrive at the Earth's atmosphere.

The Sun–Earth subtended acceptance half-angle of 0.27° can be determined by the mathematical relationship between the radial size of the Sun and its distance to the Earth [1–3]. It stands valid from a theoretical and mathematical perspective; and considered by most researchers in the field of solar energy concentration [1–16]. However, this angle could only be true if the Earth had no atmosphere. The sudden change from vacuum to Earth's atmosphere significantly alters the trajectory of solar rays due to the law of refraction. Solar rays pass through various atmospheric layers, such as the thermosphere, mesosphere, stratosphere, and troposphere. The scattering dispersion randomness and the subsequent absorption lead to decreasing the original solar intensity from the Sun to the surface of the Earth, thus it is called diffuse sky radiation [2]. The radiation intensity decreases mostly by the absorption of the ozone (O_3) and by the atmosphere's water vapor, while the former absorbs at the ultraviolet band and the latter absorbs at the near-infrared band. Each layer's gaseous composition has its refractive index, influencing the refraction angle. Moreover, the acceptance of half-angle subtended by the Sun can be different depending on geographical location, time zone, and local atmospheric conditions, such as the presence of clouds, humidity, sand particles, and pollution in the troposphere. Therefore, at the Earth's surface, the acceptance half-angle should be larger than 0.27°. These complex systems influencing the refraction of sunlight on Earth were widely neglected by most researchers in this field, who had adopted the half-angle of 0.27° as the gold standard for their works [1–17].

Gaussian Distribution Sun Shape

The Sun shape image is inconsistent, and it is difficult to analyzed due to unpredictable and uncontrollable atmospheric factors. The systematic and averaging measurement of the image size approximates a near-exact representation of the image of the Sun. One of the alternative approximations was done by Vittitoe and Biggs [18], which treats the Sun as a superposition of six Gaussian terms.

The approximation of the Sun shape in Gaussian distribution form described in Eq. (5.3), this Gaussian form sets the behavior of the Sun distribution of the solar radiation emitting from a generic source:

$$I(l, m) \approx I_0 e^{-(G_x l^2 + G_y m^2)} \tag{5.3}$$

where l and m are the direction cosines of the rays in the X and Y axis direction with G_x and G_y as the Gaussian distribution in function of the root-mean-square width (δ_{RMS}), given by Eq. (5.4):

$$G_x = G_y = \frac{1}{2 \times \delta_{RMS}^2} \tag{5.4}$$

The larger the value of G_x and G_y, the narrower the distribution in that respective direction. The overall distribution collimated form when both G_x and G_y are infinite (values of zero in Zemax®).

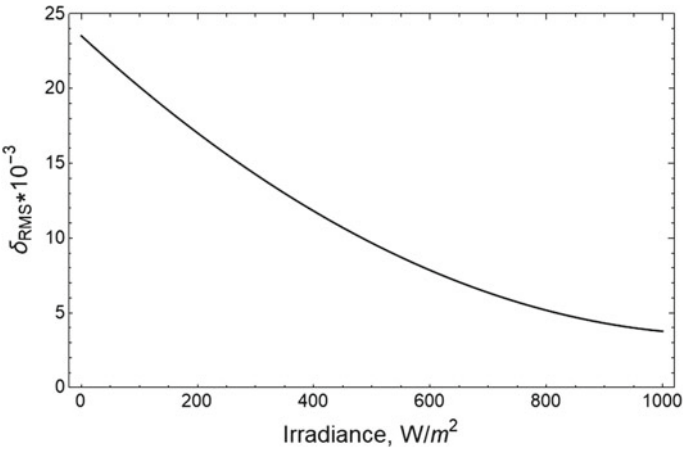

Fig. 5.3 Variation of δ_{RMS} at different solar irradiances (I)

The δ_{RMS} described and obtained by [18], where the correlation of δ_{RMS} with the solar irradiation (I) is shown in Fig. 5.3, where the curve is given by

$$\delta_{RMS} \times 10^3 \approx 3.7648 - 0.0038413(I - 1000) + 1.5923 \times 10^{-5}(I - 1000)^2 \tag{5.5}$$

with I is the current solar irradiance in W/m^2. This curve is a generalized reference to the Sun's shape at a given solar irradiance. The actual δ_{RMS} value may change dependently not only through the current measured irradiation (insolation), but also the time and location where the measurement was carried out, as referenced in [18].

Zemax® ray tracing software approximates the Sun shape in a mathematical and computational form. Considering a parabolic mirror of 2 m diameter, a focal length of 850 mm, and a reflectivity of 59% [19], the same as the medium-sized solar furnace (MSSF) parabolic mirror in PROMES, where a typical local irradiance of 1000 W/m^2 is normally attained on a normal clear day [20, 21]. The Sun shape image of this concentrator would have a δ_{RMS} of 0.0037648 according to Eq. (5.5) then the G_x and the G_y would be 35,276.6 through Eq. (5.4). The simulation and experimentally measured onsite results show similar outcomes for both cases (see 5.2.1 Solar concentration principles). Alternatively, the Gaussian distribution of G_x and G_y can be manually adjusted in Zemax® until the simulated result is the same as the experimental measurements [22].

The terrestrial solar half-angle (θ_E) found by using the effective size of the solar-terrestrial image (d_E) at a distance (L), as represented in Eq. (5.6).

$$\theta_E = \tan^{-1}\left(\frac{0.5d_E}{L}\right) \tag{5.6}$$

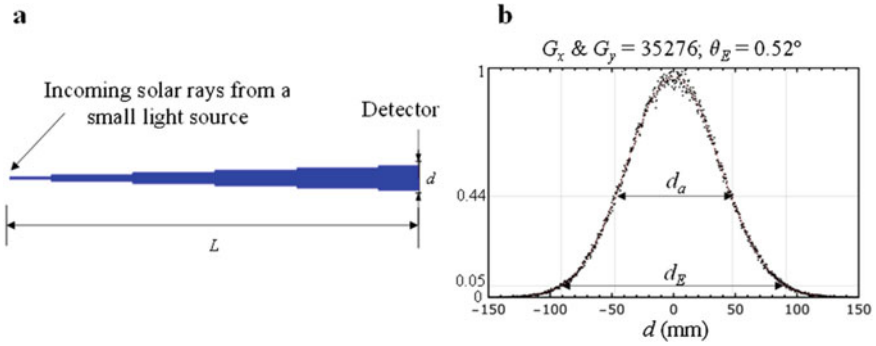

Fig. 5.4 **a** Light propagation from a small light source towards a detector of size d at a distance L. **b** Solar-terrestrial image with solar half-angle (θ_E) of 0.52°

θ_E calculated through a simple simulation in Zemax® by using a detector at a distance (L) away from a small solar light source, as shown in Fig. 5.4a. For example, consider a 0.002 mm diameter source (a small hole) at $L = 10$ m away from 150 × 150 mm^2 with a precision of 1001 × 1001 pixels. The calculation of θ_E is independent of the distance L since d_E is adjusted by the inverse-square law.

Figure 5.4b shows the solar distribution in Zemax® of a solar source by using the $G_x = G_y = 35{,}276$ as the Gaussian distribution calculated from Eq. (5.4) at a consideration of 1000 W/m^2 irradiance. For a correct calculation of the terrestrial solar angle, considering 95% of the total distribution then a width of $d_E = 91$ mm, which is equivalent to $\theta_E = 0.52°$. It is important to note that the acceptance half-angle (θ_a) of 0.27° can be found at the effective size (d_a) at 56% effective of focal Gaussian distribution [23].

5.1 Parabolic Concentrator

5.1.1 Solar Concentration Principles

The simplest and most efficient solar concentrator is a reflector shaped like a parabolic dish. This reflective concentrator enables all paraxial rays striking its surface then reflected toward the same common focal spot. The parabolic shape is straightforward to analyze, easy to build (depending on its size), conservative of material, and provides an adequate concentrations ratio for many high-power applications [24] (Fig. 5.5).

The sag Eq. (5.7) generalizes the parabolic shape in the x–z plane. Let z point toward the Sun.

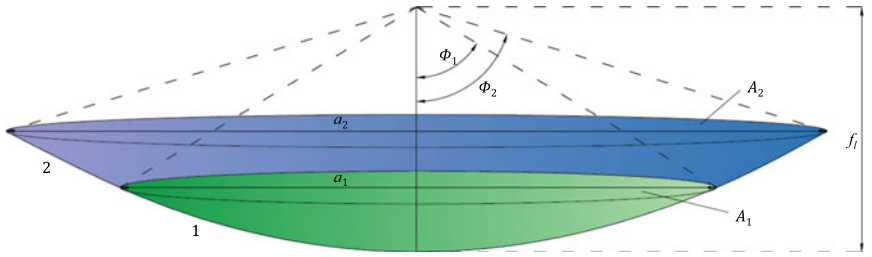

Fig. 5.5 Parabolic geometry. Each parabolic concentrator has the same focal length but with different aperture sizes

$$z = \frac{ca^2}{1 + \sqrt{1 - (1+k)c^2a^2}} + \sum_{i=1}^{M} \alpha_i a^i \tag{5.7}$$

where c is the curvature of the surface, k is the conic constant, a is the radial aperture coordinate, and the terms α are aspheric coefficients. A pure parabolic geometry attained by $k = -1$ and considered the coefficients α as zero, then the simplify equation shows as:

$$z = \frac{ca^2}{2} = \frac{a^2}{2RoC} = \frac{a^2}{4f_l} \tag{5.8}$$

Most concave geometry uses the radius of curvature (RoC) to design its surface line, which is the inverse of c. In this case, the RoC would be twice the value of the focal length (f_l) (Fig. 5.6).

5.1.2 Example of Numerical Analysis with Zemax®

In this section, a parabolic mirror with the same specification as the MSSF parabolic concentrator used in PROMES evaluated in Zemax® Non-Sequential ray tracing environment and compared to that of a measured counterpart.

Concentrating object

The *Aspheric surface* object in the NSC editor in Zemax® was used to simulate the MSSF parabolic concentrator with a 1000 mm radial aperture; a hole of 150 mm radius; a focal distance of 850 mm; and a measured reflectivity of 59% (I41 in Zemax® coating file, see Sect. 2.1.1.3) [19, 20]. The parameters used in Zemax® presented in Table 5.1.

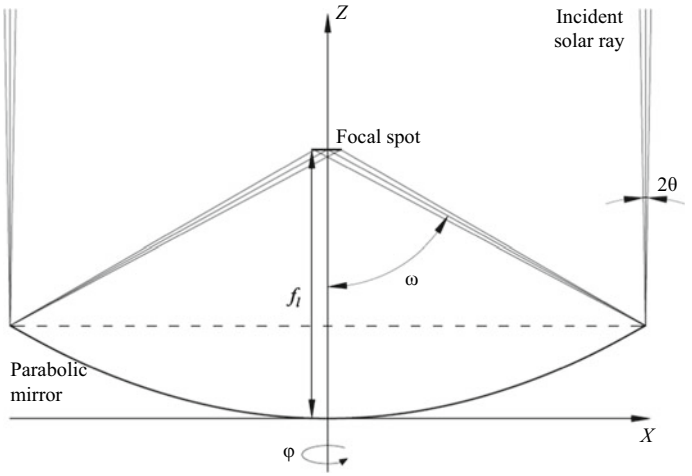

Fig. 5.6 Parabolic geometry. ω is the rim angle or aperture angle, f_l is the focal length, and the θ half solar angle

Table 5.1 Non-sequential parameter for MSSF parabolic concentrator

Parameters	Values
Object	Aspheric surface
X, Y, Z (mm)	0, 0, 0 [a]
T_x, T_y, T_z (°)	0, 0, 0
Material	Mirror [b]
The radius of curvature (mm)	1700
Conic	– 1
Maximum aperture (mm)	1000
Minimum aperture (mm)	150

[a]—The vertex of the parabolic mirror at its origin
[b]—The coating of *I41* was set as the 41% absorption for the reflective surface of the mirror

Source object

The *Source Ellipse* object used as the source for ray tracing. 1000 W/m^2 solar irradiance used to power the source. Over twenty-one key, solar spectrums ranging from 325 μm to 2.223 μm, with their respective weights consulted in the standard solar spectrum ASTMG173 at AM1.5 [25] were used to represent the solar spectrum. Over 40 million analysis rays were traced for simulation. Table 5.2 listed all the necessary parameters for modeling the source used.

Table 5.2 Solar source over the MSSF parabolic concentrator

Parameters	Values
Object	Source ellipse
X, Y, Z (mm)	0, 0, 294.2[a]
T_x, T_y, T_z (°)	0, 0, 0
Material	–
# Layout rays	20
# Analysis rays	40,000,000
Power (W)	3070.91[b]
X and Y half width (mm)	1000
Gaussian distribution G_x and G_y	35,276.6

[a]—The sag equation from Eq. (5.7) provides the precise position of the source
[b]—The total power of the source calculated by the reflective area with the irradiance, $P = I_0 \times \pi({a_{\max}}^2 - {a_{\min}}^2)$, with a_{max} and a_{min} as the maximum and minimum aperture of the parabolic mirror, respectively

Detector object

An absorbing 20 × 20 mm with a precision of 150 × 150 pixels *Rectangular detector* object positioned at the focal spot of the parabolic concentrator. Table 5.3 shows the parameters used for this detector.

Figure 5.7a shows the non-sequential 3D layout of the parabolic concentrator (same specs as the MSSF) with a source emitting twenty blue layout rays.

Figure 5.7b shows the focal distribution (Sun shape) in incoherent irradiance on the *Detector viewer*. The concentrated solar flux of 16.2 W/mm^2 and 15 mm diameter at 5 mm FWHM (full width at half maximum) in size, were in a very similar range claimed by [20, 21 and 26].

Table 5.3 Detector at the MSSF focal spot

Parameters	Values
Object	Rectangular detector
X, Y, Z (mm)	0, 0, 850
T_x, T_y, T_z (°)	0, 0, 0
Material	Absorb
X and Y half width (mm)	10
#X and #Y Pixels	150

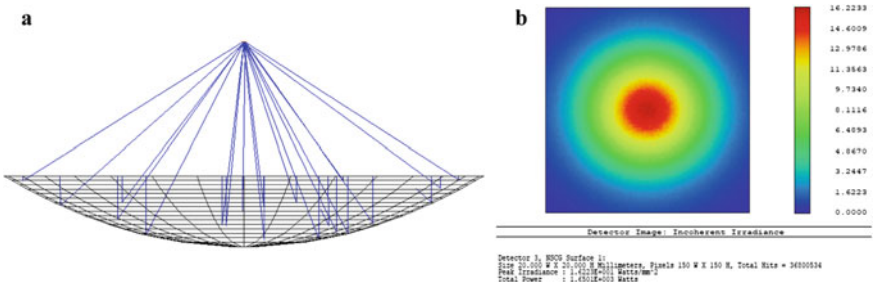

Fig. 5.7 **a** Zemax® NSC 3D layout representation of the parabolic concentrator of 1 m radius, a focal length of 0.85 m, and a radius of curvature of 1.7 m. **b** Focal spot of a rectangular detector of 20×20 mm^2 with 150×150 pixels at the focal spot of the MSSF parabolic concentrator with 40 million analysis rays, at typical solar irradiance of 1000 W/m^2

5.2 Fresnel Lenses

5.2.1 Solar Concentration Principles

The Fresnel lens is a refractive optical apparatus with few millimeters in thickness. This concentrator conceptually produced by removing the non-essential parts of dielectric material from a conventional lens, as shown in Fig. 5.8. The dielectric surface of the resulting thin facetted lens intercepts the rays of light with the same incidence angle as the original would have and performs identical refractive and focus functions.

Both the standard lens and the Fresnel lens share the same sag expression from Eq. (5.7). However, this type of lens uses refractive optics with Snell law as a means of focusing. The achromatic aberration is inevitable and amplified with the inclusion of a large bandwidth of wavelengths such as the Sun.

Glass/silica is the preferred material for Fresnel lenses before 1950. Those lenses had grooves grounded and polished. To cut production costs, a cheaper method was to cast and press the glass into molds. The casting process receives no further treatment,

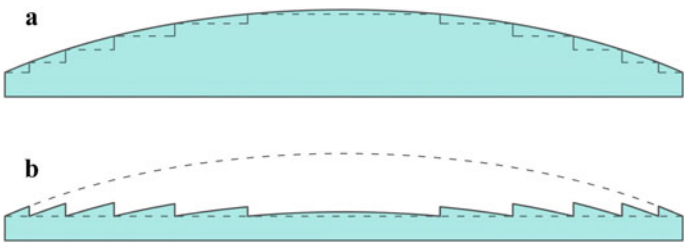

Fig. 5.8 **a** Standard focusing lens and dashed lines divide the steeped surface design by Buffon. **b** Fresnel lens uses the stepped surface onto a thin substrate

Fig. 5.9 Fresnel lens. **a** Grooves-in design. **b** Grooves-out design

which leads to a final product with a lower optical quality. Furthermore, due to the high surface tension of the glass, problems arise during solidification at the rounded grooves and tips.

Nowadays, plastics and new molding techniques, and computer-aid diamond-turning machines have vastly improved the quality of Fresnel lenses. The reduction of weight and cost enables new uses for Fresnel lenses. Various plastic Fresnel lenses can be pressure-molded, injection-molded, cut, or extruded. Fresnel lenses found and used at: overhead projectors; copy machines; camera-focused screens; magnifiers and reading lenses; holography; communications (data transfer); lighthouses; solar collectors for thermal and/or photovoltaic use; and solar-pumped lasers.

The flat Fresnel lens has two design orientations, the "grooves-in" (steeped facet facing towards the target) or "grooves-out" (steeped facet facing toward the Sun), as shown in Fig. 5.9. The grooved-out design offers advantages in terms of optical efficiency and tolerance. Grooves-in is more common in the market for being less prone to soiling problems, and easier to clean and maintain.

The efficiency of the Fresnel lens affected by the refractive change of the material due to the prolonged exposure at various temperatures; this may alter both the focal distance and the size of the focal spot; thermal expansion of the lens may cause further deformation of its image profile. It is preferable to design a lens while considering the operating temperature of the optical material. Moreover, the lifetime of the concentrator drops due to prolonged exposure at higher temperatures [27].

Most of the Fresnel lens modeling sequences and parameters found in the industry, including the Zemax® Fresnel lens are based on Claytor's patent [28, 29]. The variables used in Zemax® are (Fig. 5.10):

- r, the aperture defines the radial size of the Fresnel lens.
- RoC, the radius of curvature defines the focal length.
- k, the conic curvature constant defines the shape of the Fresnel lens facet.
- d_t, is the thickness of the substrate below the grooves.
- θ_p, pitch (degrees) defines the "inactive" faces (those faces nominal parallel to the local z-axis).
- d_m, the frequency of the grooves per lens diameter defines the total number of slope facets and their size.

The Fresnel lens's focal image is wavelength sensitive due to the chromatic Snell's deviation caused by the difference in refraction index. Figure 5.11 shows the achromatic aberration of wavelengths from 0.3 μm to 1.5 μm. The Y = 0 mm is the mathematical focus calculated for 0.5 μm (red line) and all other wavelengths scattered around on its focus. The position Y = 100 mm has the sharpest concentration size and the highest concentration intensity.

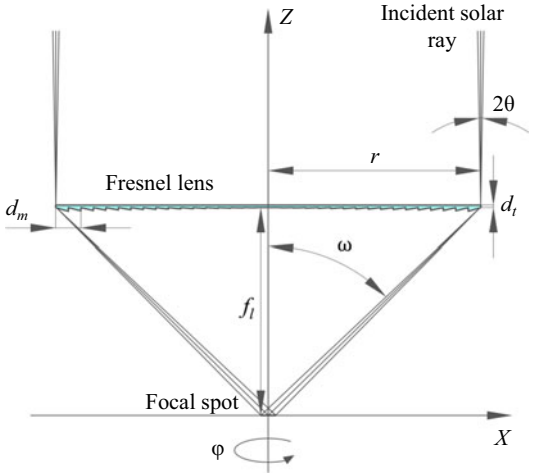

Fig. 5.10 Fresnel lens with radial aperture (r) with an incident solar ray at the edge with a solar half-angle of θ. The f_l is the focal length of the lens, ω is the rim angle, d_t is the thickness of the lens and d_m is the groove frequency

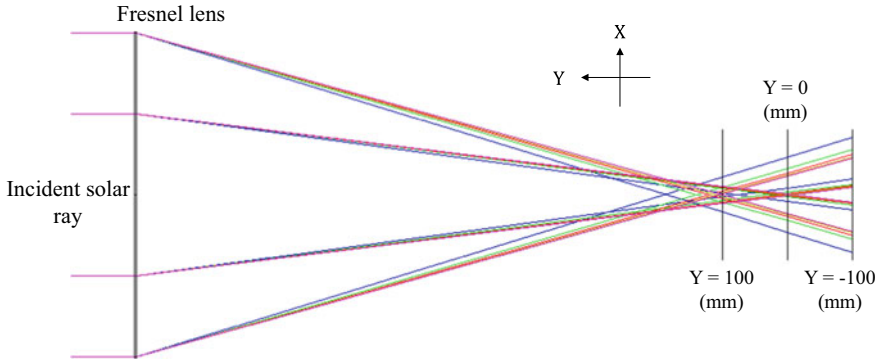

Fig. 5.11 Achromatic aberration is caused by various collimated wavelengths by a Fresnel lens

5.2.2 *Example Numerical Analysis with Zemax®*

In this section, the output data of concentrated solar flux and the focal spot size reproduced by a Fresnel lens is the same as an experimentally measured lens in Zemax® under the same environmental conditions.

Concentrating object

The *Fresnel lens* object used was identical to that of *Centro Nacional de Investigaciones Metalúrgicas* (CENIM) in the Complutense University of Madrid, which was a PMMA Fresnel lens of 889 mm diameter, a focal length of 757 mm, the thickness

Table 5.4 Non-sequential parameters of the Fresnel lens used in CENIM

Parameters	Values
Object	Fresnel 1
X, Y, Z (mm)	0, 757, 0
T_x, T_y, T_z (°)	−90, 0, 0
Material	PMMA
Radial height (mm)	444.5
+Depth/-Freq	−2[a]
Pitch (°)	7.1
Thickness (mm)	3.17
The radius of curvature (mm)	378.5
Conic constant	−2

[a] About 889 groves

of 3.17 mm and grooves numbers of 50 in 25 mm faced toward the focus [30–32]. This Fresnel lens generated over 2.60 W/mm^2 of concentrated solar flux with a focal size of 8 mm diameter, under a cloudless day with a solar irradiance of 1000 W/m^2. The Non-Sequential parameters of this lens are shown in Table 5.4.

Zemax® provides two types of Fresnel lens objects, *Fresnel 1*, and *Fresnel 2*, only the former was considered. The Fresnel lens object positioned at 757 mm above the origin point in the Y axis. The tilt axis (T_x) was set as "−90" so the grooves are facet toward the focus. PMMA material used. The radial height was set as 444.5 mm as the radius of the Fresnel lens. The "X half-width" was set as zero since the actual Fresnel lens was radially symmetrical instead of a line-focus Fresnel lens. The "+ Depth/-Freq" parameter serves to design each groove, if the value was positive, then each groove would have that value of depth (vertical facet), while in a negative value, the grooves were designed by the number of grooves per millimeter; in this case, the "+ Depth/-Freq" was –2, for 50 grooves in 25 mm which was about 2 grooves per 1 mm width. The radius of curvature had half of the focal length value. Both pitch and conic constant values were not given by the authors and were hidden by the manufacturer of the lens, however, both values could be tweaked to achieve the target output value. In this case, the pitch was set as 7.1° (normally it ranges from 2° to 20°), and the conic was set as –2.

Source object

Table 5.5 shows the parameters needed to model the source over the Fresnel lens. The source positioned 765 mm above the origin and eight millimeters above the groove tip of the Fresnel lens. Over 40 million rays were used in this ray tracing simulation. The total power of the source proportionally calculated with the area of the Fresnel lens and the solar irradiance of 1000 W/mm^2.

Table 5.5 Solar source over the CENIM Fresnel lens

Parameters	Values
Object	Source Ellipse
X, Y, Z (mm)	0, 765, 0
T_x, T_y, T_z (°)	90, 0, 0
Material	–
# Layout rays	1000
# Analysis rays	40,000,000
Power (W)	620.727
X and Y half width (mm)	444.50
Gaussian distribution G_x and G_y	35,276.6

Detector object

A *rectangular detector* of material set as ABSORB with a size of 20 × 20 mm and precision of 150 × 150 pixels, the same as Table 5.3, was positioned at the focal spot of the Fresnel lens (at the origin point).

Figure 5.12 shows the traced data. It attains a concentrating solar flux of over 2.65 W/mm^2, which has the same range as the measured concentrating solar flux of 2.60 W/mm^2 and the focal shape size has a comparable size of 8 mm diameter claimed by the CENIM Fresnel lens.

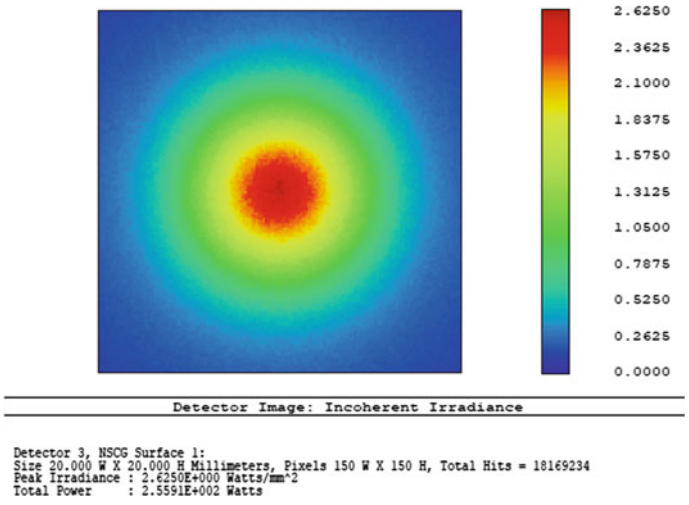

Fig. 5.12 Focal spots of a rectangular detector of 20 × 20 mm^2 with 150 × 150 pixels at the focal spot of the CENIM Fresnel lens with 40 million analysis rays, at typical irradiance of 1000 W/m^2

5.3 Elliptical-Shaped Fresnel Lens (ESFL)

See Fig. 5.13.

5.3.1 Solar Concentration Principles

The shaped Fresnel lens is as a chain of a well-defined prism (grooves) aligned along an outline, such as a semicircle or an ellipse. Each prim individual prism is designed and optimized so that most of the refracted light will focus on the same focal position.

The advantages of a shaped Fresnel lens with a flat Fresnel lens are:

- Reduction of the achromatic aberration effect.
- Have higher structural integrity and mechanical stability.
- Non-imaging lens.

The disadvantages of the shaped Fresnel lens include (Fig. 5.14):

- The complexity of manufacturing this type of lens, and the precision required would be quite expensive.
- Non-imaging lens.

The general parameters to model an ESFL are:

- *r*—Radial aperture (mm) defines the size of the concentrator.

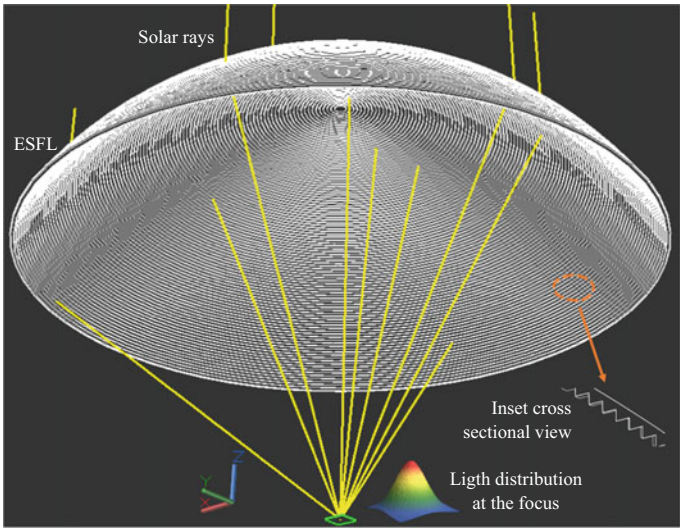

Fig. 5.13 Elliptical shaped fresnel lens

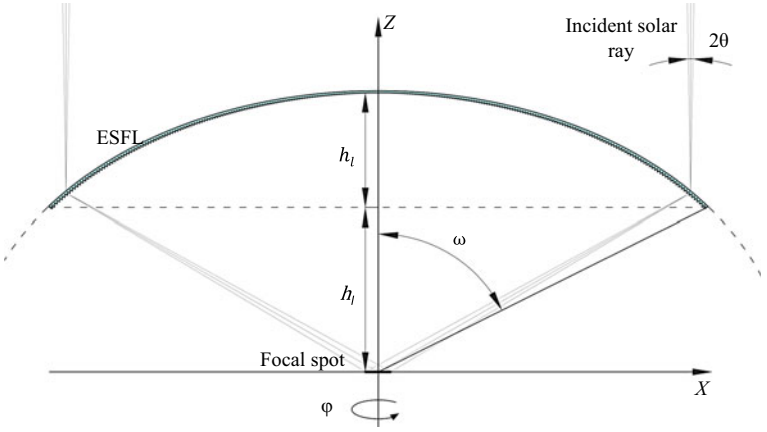

Fig. 5.14 Elliptical-shaped Fresnel lens. θ is the half angle from the Sun to Earth, ω is the aperture angle, f_l is the focal length, h_d is the height of the lens, and φ the angular rotation of the lens

- h_f—Focal length (mm), which defines the vertical distance between the focus and the outmost prism of the concentrator.
- h_l—Lens height (mm) defines the height of the "arch".
- d_t—Lens thickness (mm), is the thickness of the substrate below the grooves.
- n_λ—Refraction index of medium and wavelength dependents.
- $\delta\omega$—Division angle (°), defines the size of each groove.
- θ_P—Pitch angle (°), or "draft angle".

Number of prisms/grooves

The prims aligned or chained through the outline of the ellipse arch with the input facets facing toward the Sun. The number of prims or grooves (N) defined by the divisions of the aperture angle with the angular segments ($\delta\omega$), shown in Eq. (5.9).

$$N = \frac{\omega}{\delta\omega} \tag{5.9}$$

Each prism is parametrically calculated through Eqs. (5.10), (5.11), and (5.12) to obtain the coordinates of points A, B, and D, respectively, as shown in Fig. 5.15. The calculation of these equations are explained in [23].

$$\begin{cases} x_{n,A} = AO_n \sin(\omega - (n-1)\delta\omega) \\ y_{n,A} = AO_n \cos(\omega - (n-1)\delta\omega) \end{cases} \tag{5.10}$$

$$\begin{cases} x_{n,B} = BO_n \sin(\omega - (n)\delta\omega) \\ y_{n,B} = BO_n \cos(\omega - (n)\delta\omega) \end{cases} \tag{5.11}$$

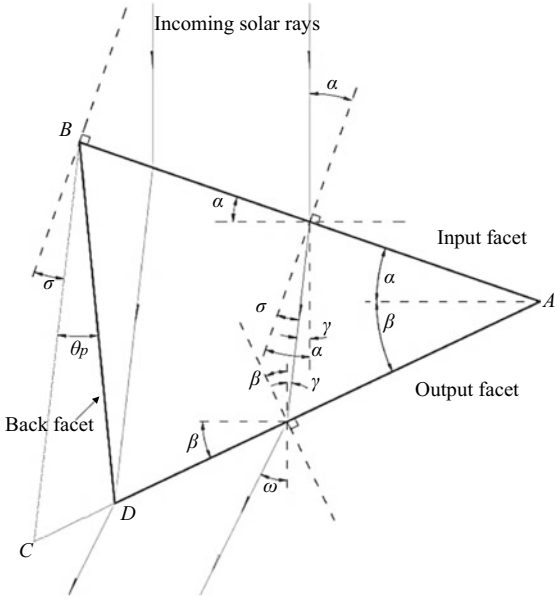

Fig. 5.15 The light path getting in and out through the ABD prism. The angles α, β, γ, σ, θ_p and ω are the characteristic angles for the Snell's law equations that the vertical incoming ray would exit at angle ω

$$\begin{cases} x_{n,D} = x_{n,A} - BD_n \cos(\beta_n) \\ y_{n,D} = y_{n,A} - BD_n \sin(\beta_n) \end{cases} \tag{5.12}$$

Thickness

The ideal prism shown in Fig. 5.15 is not physically capable of joining a neighboring prism. Expanding the output and the back facet at a thickness (d_t) with the input facet, changes the triangular prism shape into a new type of prism, as shown in Fig. 5.16. Vertex E and F is the direct increment of d_t of point B and A, respectively.

Prism chaining, coordinate extraction, and automation

The chaining process starts with joining the facet BE_n to the next prism facet AF_{n+1}, as shown in Fig. 5.16. It shows the first four segments of ESFL coordinates imported into AutoCAD®. The *Polyline* command outlines by following the 2D coordinates. A complete ESFL would follow the coordinates A_1, D_1, A_2, and D_2, until D_N, then it continues from F_N to F_1 and finally ends by closing the *Polyline*. If done correctly, all the coordinates of the ESLF should end in the positive quadrant of the cartesian space.

The conceptual model of the ESFL is no more than a list of coordinates of prisms chained together at one end to another end, forming a semi-arch. The coordinates of the ESFL build by a simple recursive code, where all the vertices of the prism

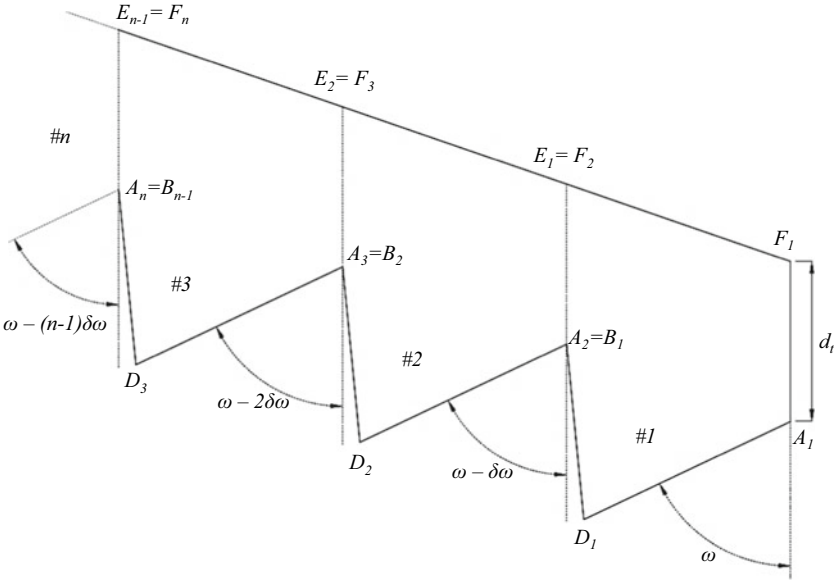

Fig. 5.16 The prism-chaining process of the first three polygons

calculated incrementally achieving the calculated number of prisms. Figure 5.17 shows the flowchart for ESFL modeling.

The newly drawn 2D wire-shaped ESFL converts into a 3D form of shape or slab shape in any CAD software, such as Autocad®

- Dome shape: Use the *Revolve* command on the 2D ESFL outline and revolve it for 360° along the Y axis to make a dome shape solid object, as shown in Fig. 5.18a.
- Slab shape: Use the *mirror* command on the 2D ESFL outline along the Y axis to make a duplicate, then use the *Extrude* command to make a 3D slab ESFL, as shown in Fig. 5.18b.

Note: Use the *Facetress* command then change the value to a maximum (10) to achieve the highest polygon count possible before exporting. Any optical design exported from a CAD should be as fine as possible.

Note: The exporting file should be in *.IGES format.

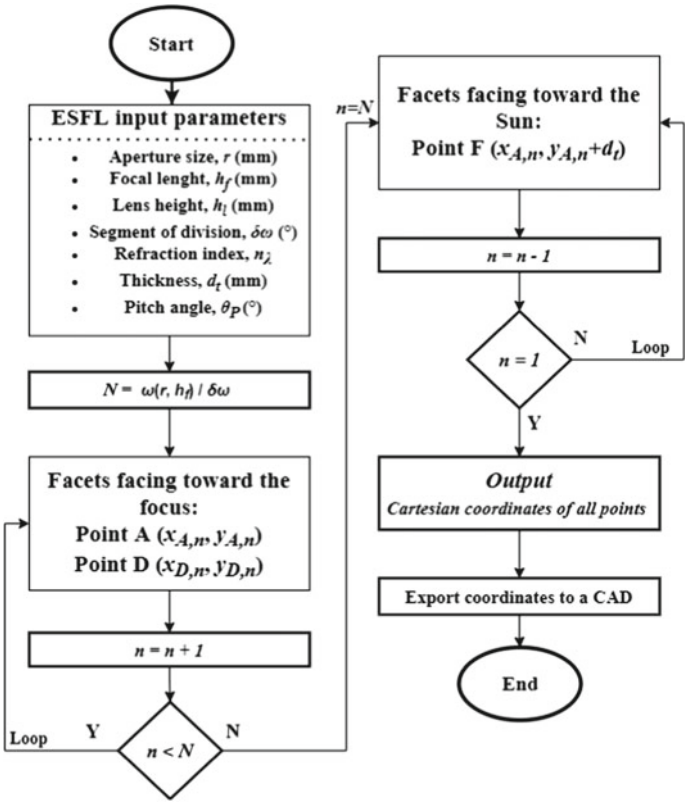

Fig. 5.17 A flow chart of the calculation of the ESFL coordinates

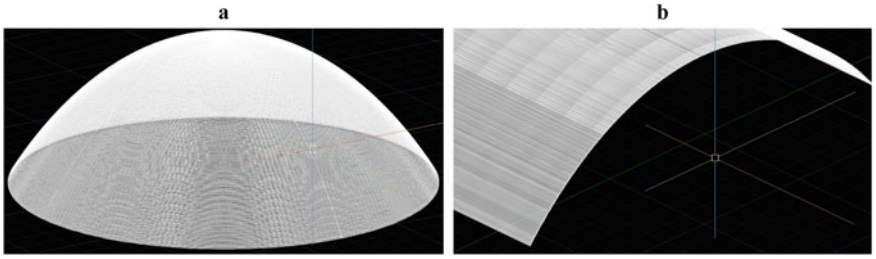

Fig. 5.18 3D views of the ESFL in AutoCAD®. **a** The ESFL is in dome shape. **b** ESFL in slab shape

Note: Importing an enormous number of grooves may slow down the Zemax® software.

5.3.2 *Example Numerical Analysis with Zemax®*

In this section, the output data of the concentrated solar flux and the focal spot size produced by the ESFL in Zemax® compared with the Fresnel lens of the same specification used in the previous section.

Concentrating object

The ESFL specifications are shown in Table 5.6, and the resulting CAD *IGES* object is used in Fig. 5.19.

Table 5.6 Specification of the Elliptical Shaped Fresnel lens

Parameters	Values
r (mm)	450
h_f (mm)	757
h_l (mm)	300
$\delta\omega$ (°)	0.034[a]
n_λ	1.491756[b]
d_t (mm)	3
θ_P (°)	7

[a] About 903 groves
[b] Refractive index of PMMA from Zemax®

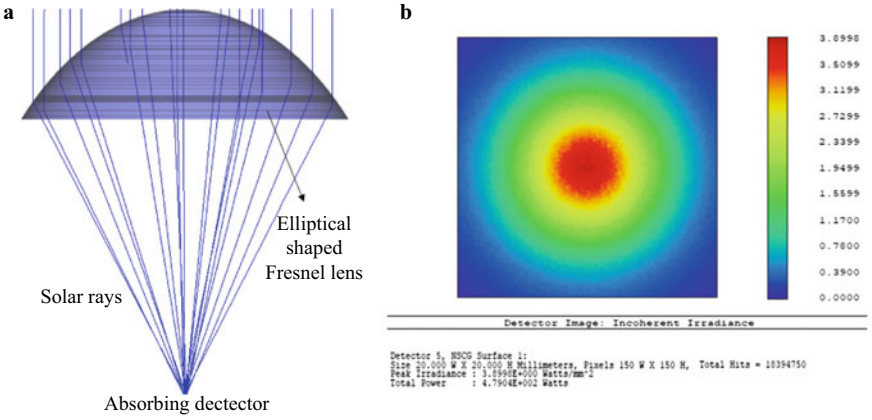

Fig. 5.19 **a** Light concentration of the imported ESFL in the NSC shaded model. **b** Concentration profile of the detector at focus

Source object

The parameters of the source are the same as in Table 5.5. This source positioned at 1020 mm above the origin, only 10 mm above the central highest point of the ESFL ($h_f + h_l + d_t + 10 = 1020$) in the Y axis.

Detector object

A *rectangular detector* of material set as ABSORB with a size of 20 × 20 mm and precision of 150 × 150 pixels, the same as Table 5.3, was positioned at the focal spot of the ESFL (at the origin point).

According to Fig. 5.19b, a 3.89 W/mm^2 peak concentrated in solar flux and total absorbed power of 479.04 W numerically calculated at the focus. Note: The concentrated solar flux of the ESFL was much higher than that of the Fresnel lens of the size and focal length from the previous section.

5.4 Single-Ring Array Concentrator

See Fig. 5.20.

5.4.1 Solar Concentration Principles

The reflective type of optics proves to be more efficient in concentrating light compared to refractive optics. A downside of the reflective type is the reduction of concentrating power due to shadowing effects caused by any receiver and the associated mechanical apparatus positioned in front of the concentrator.

The ring array concentrator (RAC) consists of a batch of concentric parabolic ring mirrors with an addition of a Fresnel lens at the center, which concentrates the lights onto a focal spot, shown in Fig. 5.21. The RAC mitigates the shadowing effect caused by the receiver apparatus [33].

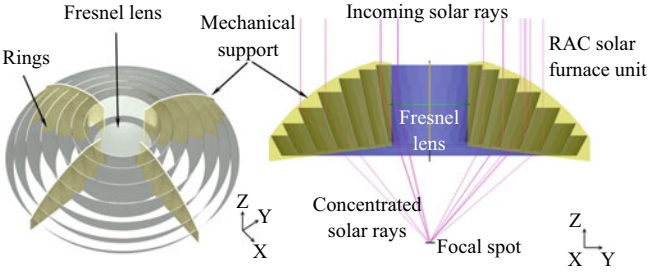

Fig. 5.20 Seven-ring RAC represented in NSC shaded model by Zemax®

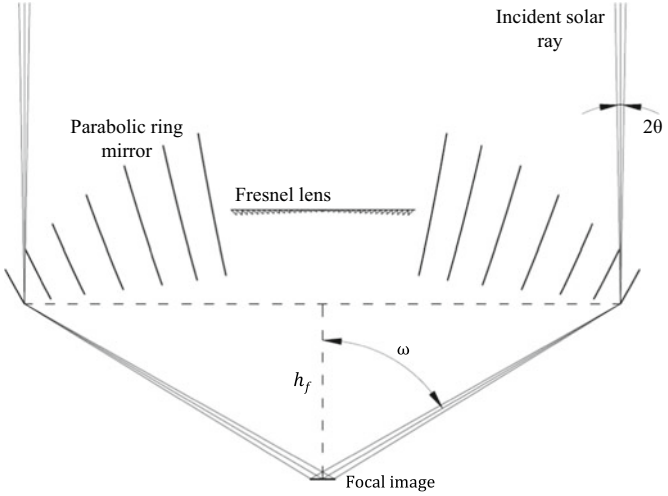

Fig. 5.21 RAC focusing methods with parabolic ring mirrors and Fresnel lenses. θ is the Sun-Earth half-angle, h_f is the focal distance of the concentrating media and ω is the aperture angle

Each ring is modeled in that all the concentrated light would focus onto a common focal spot, while none of that reflected solar radiation would be obstructed by the adjacent ring, as shown in Figs. 5.22 and 5.23. Depending on the number of rings given into the RAC configuration, a Fresnel lens could be added to further concentrate the remaining solar radiation at the center of the innermost ring [33].

The general parameters used in RAC are similar to that of a parabolic mirror:

- r—Radial aperture (mm) defines the size of the concentrator.
- R—Radial aperture reference (mm).
- h_f—Focal length (mm), defines the vertical distance between the focus and the outmost parabolic ring of the concentrator.
- d_w—Ring width modifier, defines the width of each ring of the RAC.
- h_d—Ring height modifier, defines the height of each inner ring beside the outermost ring.
- d_t—Lens thickness (mm) is the thickness of each ring.

Δa_1 is the ring width of the first ring, a_{out1} is the outer aperture of the first ring, a_{in1} is the inner aperture of the first ring, h_f is the focal length, h_{a1} is the first ring height deviation, H_1 is the height of the first ring, d_t is the thickness of the ring and $r_{fresnel}$ is the radius of the Fresnel lens.

The RAC design process is summarized by the following flowchart shown in Fig. 5.24 [33]. First defines the RAC parameters, such as the number of desired rings, concentrator radial size, focal length, the width of the ring, internal height of each ring, ring thickness, and the thickness of the Fresnel lens. Then, the first ring model gives the necessary information for the next ring. The neighboring ring model

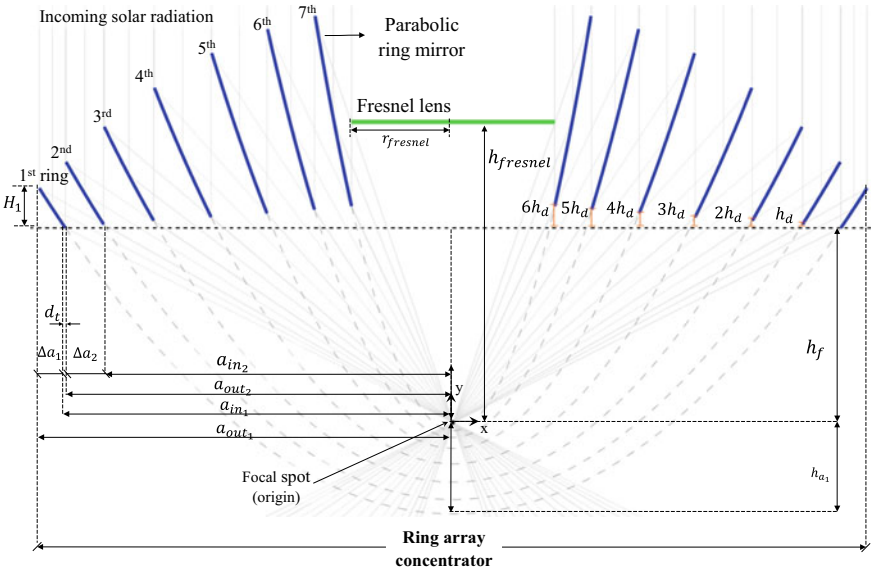

Fig. 5.22 Cross section of the RAC unit with seven rings. The blue lines represent the cross-section of the parabolic rings, and the green line represents the Fresnel lens

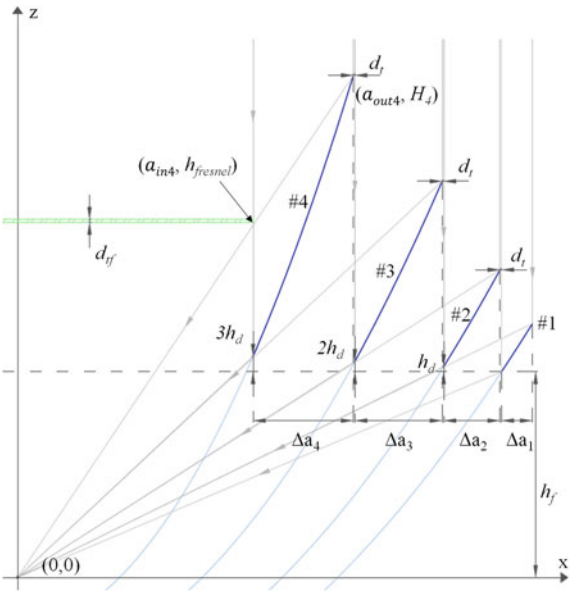

Fig. 5.23 Fresnel lens occupying the remaining space within the four-ring RAC. The radial size is the same as the inner aperture of the fourth ring (a_{in4}). Fresnel lens positioned at the $h_{fresnel}$ to the origin. d_{tf} is the thickness of the Fresnel lens

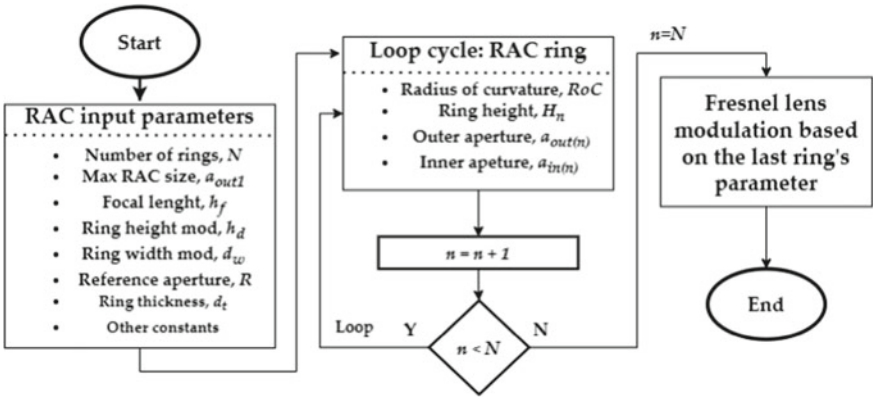

Fig. 5.24 Flowchart of RAC design modeling process

will give out all the information about each successive ring up until the last ring. The last ring will give the necessary information for the conception of the Fresnel lens.

5.4.2 *Example Numerical Analysis with Zemax®*

In this section, a numerical evaluation of the RAC under a virtual Sun calculated in Zemax® ray-tracing software.

Concentrating object

Consider a seven-ring RAC of 1.0 m radius (a_{out1}) with a h_f of 0.5 m and an h_d of 20 mm, shown in the following Table 5.7.

There were not any built-in objects that directly modeled the RAC in Zemax®. Then single a ring was adapted as a section of a parabolic mirror, hence the use of the *aspheric surface* object. Seven *aspheric surface* objects were listed within the *NSC editor* with a conic constant of –1 to attain a parabolic curvature; the object material was set to *MIRROR* with the reflectivity/coating of *I41* (59% reflectivity, the same

Table 5.7 RAC parameters

Parameter	Value
N	7
a_{out1} (mm)	1000
h_f (mm)	500
d_w (mm)	30
R (mm)	500
d_t (mm)	3
h_d (mm)	20

was used by the parabolic mirror in the Sect. of 5.1.2 Example of numerical analysis with Z) at a *tilt about X* angle at −90°. Table 5.8 shows the seven ring's relative Y position, RoC, maximum aperture $\left(a_{out_n}\right)$ and minimum aperture $\left(a_{in_n}\right)$.

The *Fresnel 1* object added after the last *Aspheric surface* object, with the following parameters shown in Table 5.9.

Source object

Table 5.10 shows the parameters used to configure the *Source Ellipse* object. The source positioned in Y-axis at 1110.75 mm above the origin point, only 10 mm above the highest point of the seventh ring ($H_7 = 1100.746$ mm).

Detector object

A *rectangular detector* of material set as ABSORB with a size of 20 × 20 mm and precision of 150 × 150 pixels, the same as Table 5.3, was positioned at the focal spot of the RAC (at the origin point).

Table 5.8 Non-sequential parameters of aspheric surface objects to model the seven-ring RAC in the NSC editor

Ring #n	Y Position (mm)	RoC (mm)	a_{out_n} (mm)	a_{in_n} (mm)
1	−282.353	564.707	1000	940
2	−239.839	479.677	937	850.975
3	−187.010	374.021	847.975	732.362
4	−130.532	261.064	729.362	593.897
5	−81.338	162.676	590.897	456.794
6	−46.389	92.778	453.794	339.563
7	−25.152	50.304	336.563	248.775

Table 5.9 Non-sequential parameters of the Fresnel lens used in RAC

Parameters	Values
Object	Fresnel 1
X, Y, Z (mm)	0, 816.634, 0
T_x, T_y, T_z (°)	− 90, 0, 0
Material	PMMA
Radial height (mm)	248.775 [a]
X half-width (mm)	0
+Depth/-Freq	0.3
Pitch (°)	12
Thickness (mm)	3
The radius of curvature (mm)	408.317
Conic	− 0.7

[a] The radial size is the same as the last ring's inner aperture

Table 5.10 Solar source over RAC

Parameters	Values
Object	Source Ellipse
X, Y, Z (mm)	0, 1110.746, 0
T_X, T_y, T_Z (°)	90, 0, 0
Material	–
# Layout rays	20
# Analysis rays	40,000,000
Power (W)	3063.507
X and Y half width (mm)	500
Gaussian distribution G_x and G_y	35,276.6

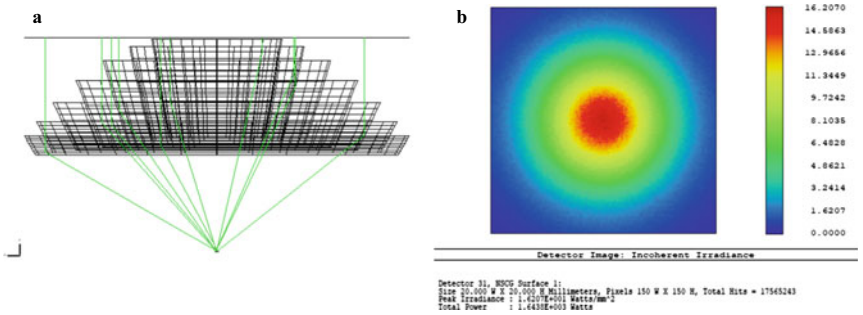

Fig. 5.25 **a** Zemax® NSC 3D layouts represent the seven-ring RAC with a 1000 mm radius and 500 mm focal length. **b** Focal spot of a rectangular detector of 20 × 20 mm^2 with 150 × 150 pixels at the focal spot of the RAC with 40 million analysis rays, at typical solar irradiance of 1000 W/m^2. The focal distribution has a peak concentrating solar flux of 16.2 W/mm^2

Results

Figure 5.25a shows the layout of the RAC by following the setup of the object. The green lines(rays) represent the reflected solar rays. Figure 5.25b shows the resulting data on the detector after ray tracing, obtaining over 16.20 W/mm^2 of solar concentrating flux.

5.5 3D Ring Array Concentrator

5.5.1 Solar Concentrator Principle

Figure 5.26 shows the 3D RAC solar furnace in a three-dimensional view, consisting of five RAC units. This configuration forms a compact box-shaped solar furnace with an opening at the rear side for easy access to a focal spot in the center. Figure 5.27

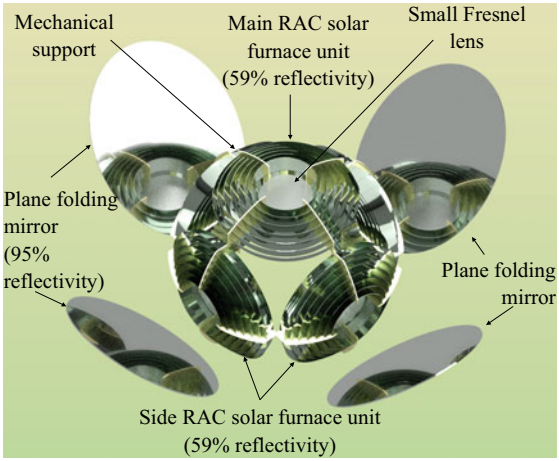
Mechanical support
Main RAC solar furnace unit (59% reflectivity)
Small Fresnel lens
Plane folding mirror (95% reflectivity)
Plane folding mirror
Side RAC solar furnace unit (59% reflectivity)

Fig. 5.26 3D RAC solar furnaces are composed of five identical seven-ring RAC and four folding mirrors

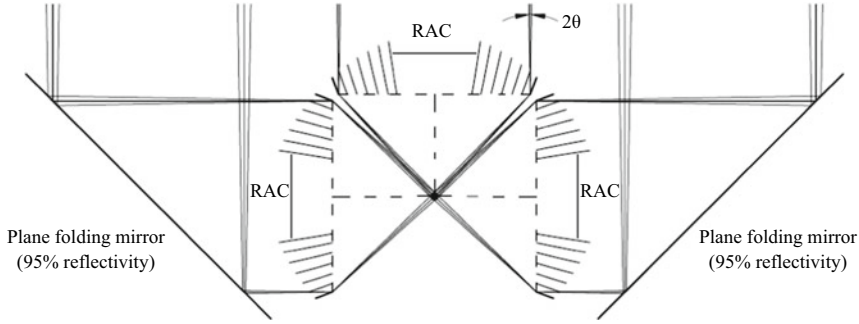

Fig. 5.27 3D RAC solar furnace combinations, with three RAC units and the associated folding mirror, θ is half acceptance angle from the Sun to Earth

shows the cross-section view of three RAC units focusing on a common focal spot. A single RAC unit receives solar rays directly from the Sun and the lateral RAC units receive reflected light from the plane's folding mirror.

5.5.2 Example Numerical Analysis with Zemax®

Consider five sets of seven-ring RAC of 0.447 m radius (0.628 m^2 collection area each, and a total collection area of 3.14 m^2) with a focal length of 0.447 m and all the ring positioned at the same focal height ($h_d = 0$ mm) in Zemax®, as shown in Fig. 5.28.

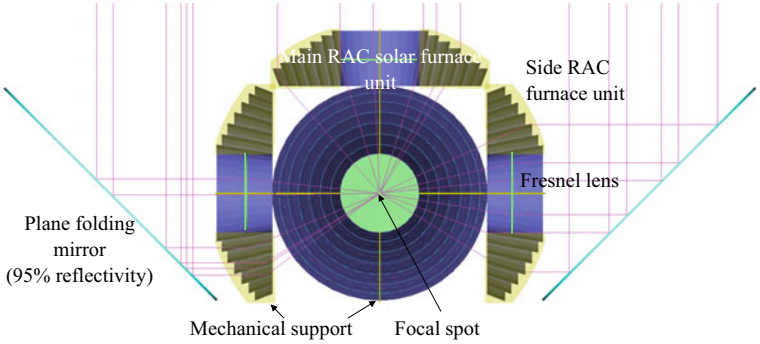

Fig. 5.28 Schematics of the cross-sectional view of the 3D RAC solar furnace with concentrating solar rays onto a common spot

Concentrating object—RAC unit

Table 5.11 shows the parameters of a single RAC and Table 5.12 shows its ring parameters.

Table 5.13 shows the parameters of the *Fresnel 1* object at the center of the RAC unit.

Table 5.11 Parameters of a single RAC

Parameter	Value
N	7
a_{out1} (mm)	447.21
h_f (mm)	447.21
d_w (mm)	31.5
R	500
d_t (mm)	1.32
h_d (mm)	0

Table 5.12 Non-sequential parameters of the seven aspheric surface objects for the RAC

Ring #n	Y position (mm)	RoC (mm)	a_{out_n} (mm)	a_{in_n} (mm)
1	−82.821	165.642	447.210	419.036
2	−70.671	141.342	417.694	382.618
3	−57.423	114.854	381.276	340.454
4	−44.254	88.507	339.113	294.951
5	−32.363	64.727	293.610	249.163
6	−22.563	45.125	247.822	205.906
7	−15.101	30.201	204.565	167.107

Table 5.13 Non-sequential parameters of the Fresnel lens used in the RAC

Parameters	Values
Object	Fresnel 1
X, Y, Z (mm)	0, 556.603, 0
T_x, T_y, T_z (°)	−90, 0, 0
Material	PMMA
Radial height (mm)	167.107 [a]
X half-width (mm)	0
+Depth/-Freq	0.3
Pitch (°)	12
Thickness (mm)	3
The radius of curvature (mm)	278.302
Conic	−0.7

[a] The radial size is the same as the last ring's inner aperture

Source object

Table 5.14 shows the source parameter for a single RAC. The source positioned at 687.685 mm above the origin, only 10 mm above the highest point of the seventh ring ($H_7 = 686.685$ mm).

Detector object

Due to the multiple-side pumping, a simple *rectangle volume* detector nor a *cylinder volume* detector could not be able to correctly measure the total concentration produced by the 3D RAC. The detector must be a three-dimensional sphere. Zemax® does not have a *sphere* object as the detector. However, an imported object with known localized pixels could serve as a detector (see Sect. 2.1.4.3). A "*Standard Tessellation Language*" (STL) sphere of 2.84 mm radius with a total of 5624 superficial pixels (or facets) designed in AutoCAD® and then imported and positioned at the

Table 5.14 Solar source over each RAC unit

Parameters	Values
Object	Source Ellipse
X, Y, Z (mm)	0, 687.685, 0
T_x, T_y, T_z (°)	90, 0, 0
Material	–
# Layout rays	1000
# Analysis rays	40,000,000
Power (W)	609.39
Maximum X and Y half-width (mm)	447.21
Minimum X and Y half-width (mm)	0
Gaussian distribution G_x and G_y	35,276.6

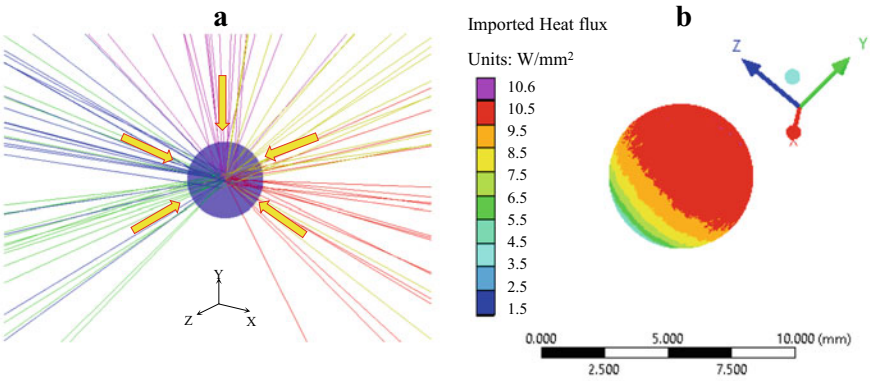

Fig. 5.29 **a** Spherical receiver at the focal spot in Zemax®. **b** The imported heat flux data of the spherical receiver retrieved from Zemax® shown in ANSYS™

center of the focus, as shown in Fig. 5.29a. The imported object in detector mode can only provide data in text form, showing only coordinates including the associated absorbing power data (Sect. 2.1.5.2). Figure 5.29b shows the map of the imported heat flux in ANSYS™ over the sphere. It was important to note that the data from Zemax® was not compatible with ANSYS™ and the data had to be transformed into an acceptable form for ANSYS™.

5.6 Focal Spot Analysis of Primary Solar Concentrators with ANSYS™ Software

This chapter will show the minimum operating procedure of Zemax® to ANSYS™ interaction. The 2D detector data collected from Zemax® at the focus of the MSSF parabolic mirror (see 5.1.2 Example of numerical analysis with Z) placed on top of a cylinder of the same size to calculate the temperature.

The ANSYS™ is an engineering simulation software that uses Finite Element Analysis (FEA) to simulate models of structures, electronics, or machine components for analyzing the strength, toughness, elasticity, temperature distribution, electromagnetism, fluid flow, and other innate or user-implemented attributes.

All the ANSYS™ simulations performed on the ANSYS™ workbench. Figure 5.30 shows the two sets of operations necessary for interacting with the Zemax® data. Figure 5.30a, shows two linked analysis systems for FEA calculation. The external data in group A serves the function of importing any External Data. The transient thermal group B is one of the methods of FEA calculation, which calculates the propagation and distribution of temperature as a function of time.

Unlike LASCAD©, the native Zemax® detector file is not compatible with ANSYS™ input. However, ANSYS™ accepts any universal text-based file such as

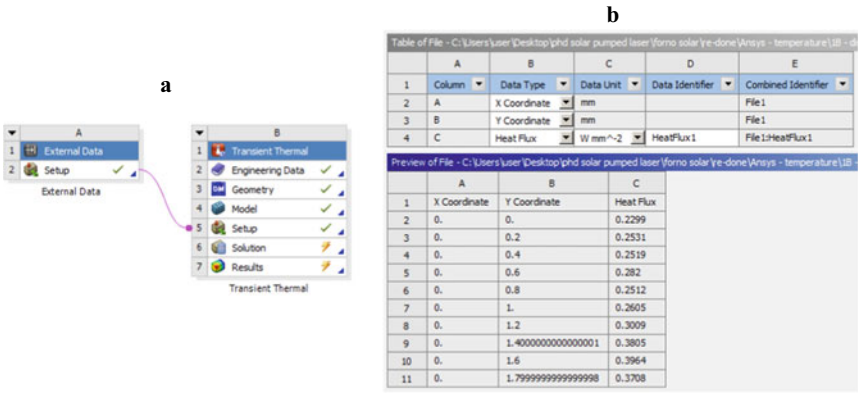

Fig. 5.30 **a** ANSYS™ workbench project schematic setup for temperature calculation in Transient Thermal analysis system influenced by the imported Zemax® file at External data analysis system. **b** ANSYS™ external data configuration by accepting three data columns extracted from the Zemax® detector data file

*.DAT file extension, by importing through the External Data function. Figure 5.30b shows the reading configuration of the External Data over the file, it reads the content from column to column. In this case, column A considered as the X axis in millimeter length, column B as the Y axis, and column C as the heat flux in W/mm^2. A single line corresponds to a single heat flux pixel at position X and Y coordinates on the detector.

The detector in Zemax® shows the data in matrix form and can easily converted into the required data form for ANSYS™, as shown in Fig. 5.31. The conversion process is automated by Microsoft Excel or any other programming process, such as Matlab®, Mathematica®, JavaScript, C++, etc.

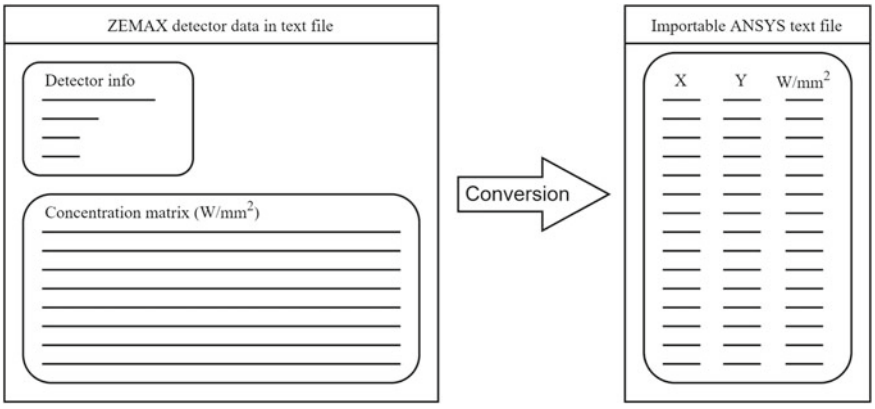

Fig. 5.31 Zemax® matrix data converted into importable/readable form for ANSYS™

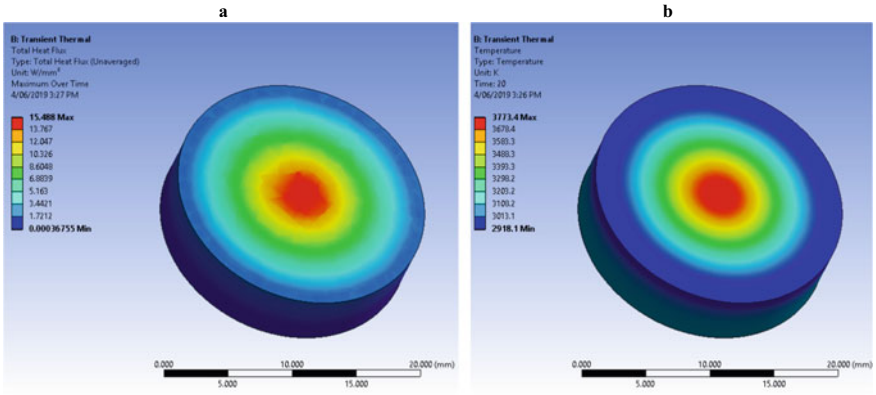

Fig. 5.32 **a** The imported heat flux data on top of the solid cylinder detector. **b** Temperature of the detector

Figure 5.32a shows the imported heat flux map data from Zemax® on top of the cylindrical temperature detector. The cylinder designed within the Geometry window in ANSYS™, and it was modeled with matching coordinates of that found in Zemax® data. The cylinder was about 4 cm in diameter, meshed in the Tetrahedrons method with 0.4 mm of the element size. The imported data introduced into the Transient Thermal analysis system as one of the setup conditions.

Other conditions assigned to the cylinder before executing the FEA simulation. The cylinder detector was considered a Graphite material with an emissivity of 0.85, which was the average emissivity of graphite at a working temperature above 3000 K [34]. Boundary conditions of convection used onto the disk surface of a constant heat transfer of 5×10^{-6} W/mm^2/K, which was equivalent to natural stagnant air convection. The radiation exchange between the surface in ANSYS™ restricted by a gray-diffuse surface. Figure 5.32b is the simulated temperature. A maximum temperature of 3773.4 K is attained at the center of the cylinder [22].

References

1. Kalogirou, S.: Solar energy engineering processes and systems (2014)
2. Rabl, A.: Active solar collectors and their applications (1985)
3. Winston, R.: Principles of solar concentrators of a novel design. Sol. Energy **16**(2), 89–95 (1974). https://doi.org/10.1016/0038-092X(74)90004-8
4. Viera-González, P.M., Sánchez-Guerrero, G.E., Martínez-Guerra, E., Ceballos-Herrera, D.E.: Mathematical analysis of nonimaging fresnel lenses using refractive and total internal reflection prisms for sunlight concentration. Math. Probl. Eng. **2018**, 4654795 (2018). https://doi.org/10.1155/2018/4654795
5. Kritchman, E.M., Friesem, A.A., Yekutieli, G.: Highly concentrating fresnel lenses. Appl. Opt. **18**(15), 2688–2695 (1979). https://doi.org/10.1364/AO.18.002688

6. Leutz, R., Suzuki, A., Akisawa, A., Kashiwagi, T.: Design of a nonimaging Fresnel lens for solar concentrators. Sol. Energy **65**(6), 379–387 (1999). https://doi.org/10.1016/S0038-092X(98)00143-1
7. Yeh, N.: Analysis of spectrum distribution and optical losses under Fresnel lenses. Renew. Sustain. Energy Rev. **14**(9), 2926–2935 (2010). https://doi.org/10.1016/j.rser.2010.07.016
8. Akisawa, A., Hiramatsu, M., Ozaki, K.: Design of dome-shaped non-imaging Fresnel lenses taking chromatic aberration into account. Sol. Energy **86**(3), 877–885 (2012). https://doi.org/10.1016/j.solener.2011.12.017
9. Romero, M., Steinfeld, A.: Concentrating solar thermal power and thermochemical fuels. Energy Environ. Sci. **5**(11), 9234–9245 (2012). https://doi.org/10.1039/c2ee21275g
10. Languy, F., Habraken, S.: Nonimaging achromatic shaped Fresnel lenses for ultrahigh solar concentration. Opt Lett **38**(10), 1730–1732 (2013). https://doi.org/10.1364/OL.38.001730
11. Leutz, R., Suzuki, A.: Nonimaging Fresnel Lenses: Design and Performance of Solar Concentrators (2001)
12. Cheng, Y., Zhang, X.D., Zhang, G.X.: Design and machining of Fresnel solar concentrator surfaces. Int. J. Precis. Technol. **3**(4), 354–369 (2013). https://doi.org/10.1504/IJPTECH.2013.058257
13. Zheng, H., Feng, C., Su, Y., Dai, J., Ma, X.: Design and experimental analysis of a cylindrical compound Fresnel solar concentrator. Sol. Energy **107**, 26–37 (2014). https://doi.org/10.1016/j.solener.2014.05.010
14. Yeh, N.: Illumination uniformity issue explored via two-stage solar concentrator system based on Fresnel lens and compound flat concentrator. Energy **95**, 542–549 (2016). https://doi.org/10.1016/j.energy.2015.12.035
15. Yeh, N., Yeh, P.: Analysis of point-focused, non-imaging Fresnel lenses' concentration profile and manufacture parameters. Renew. Energy **85**, 514–523 (2016). https://doi.org/10.1016/j.renene.2015.06.057
16. Ma, X., Jin, R., Liang, S., Zheng, H.: Ideal shape of Fresnel lens for visible solar light concentration. Opt. Express **28**(12), 18141–18149 (2020). https://doi.org/10.1364/OE.386599
17. Yeh, N.: Optical geometry approach for elliptical Fresnel lens design and chromatic aberration. Sol. Energy Mater. Sol. Cells **93**(8), 1309–1317 (2009). https://doi.org/10.1016/j.solmat.2009.02.012
18. Vittitoe, C.N., Biggs, F.: Six-gaussian representation of the angular-brightness distribution for solar radiation. Sol. Energy **27**(6), 469–490 (1981). https://doi.org/10.1016/0038-092X(81)90043-8
19. Almeida, J., Liang, D., Vistas, C.R., Guillot, E.: Highly efficient end-side-pumped Nd:YAG solar laser by a heliostat-parabolic mirror system. Appl. Opt. **54**(8), 1970–1977 (2015). https://doi.org/10.1364/AO.54.001970
20. Flamant, G., Ferriere, A., Laplaze, D., Monty, C.: Solar processing of materials: opportunities and new frontiers. Sol. Energy **66**(2), 117–132 (1999). https://doi.org/10.1016/S0038-092X(98)00112-1
21. Ferriere, A., Sanchez Bautista, C., Rodriguez, G.P., Vazquez, A.J.: Corrosion resistance of stainless steel coatings elaborated by solar cladding process. Sol. Energy **80**(10), 1338–1343 (2006). https://doi.org/10.1016/j.solener.2005.06.009
22. Garcia, D., Liang, D., Tibúrcio, B.D., Almeida, J., Vistas, C.R.: A three-dimensional ring-array concentrator solar furnace. Sol. Energy **193**, 915–928 (2019). https://doi.org/10.1016/j.solener.2019.10.016
23. Garcia, D., Liang, D., Almeida, J., Tibúrcio, B.D., Costa, H., Catela, M., Vistas, C.R.: Elliptical-shaped fresnel lens design through gaussian source distribution. **15**(2), 668 (2022)
24. Winter, C.J., Sizmann, R.L., Vant-Hull, L.L.: Solar Power Plants. Springer, Berlin Heidelberg (1991)
25. International, A.: Standard Tables for Reference Solar Spectral Irradiances: Direct Normal and Hemispherical on 37° Tilted Surface. In: ASTM G173–03(2012) (2012)
26. PROCÉDÉS, M.E.É.S.U.: MSSF horizontal—PROMES. https://www.promes.cnrs.fr/index.php?page=mssf-horizontal (2018). Accessed 7 Mar 2019

27. Hornung, T., Steiner, M., Nitz, P.: Estimation of the influence of Fresnel lens temperature on energy generation of a concentrator photovoltaic system. Sol. Energy Mater. Sol. Cells **99**, 333–338 (2012). https://doi.org/10.1016/j.solmat.2011.12.024
28. N. Claytor, R.: Fresnel lens with apseheric grooves. United State of America Patent
29. Zemax Manual, vol. 13. Zemax, Radiant Zemax (2014)
30. López-Delgado, A., López-Andrés, S., Padilla, I., Álvarez, M., Galindo Llorach, R., Vázquez, A.: Dehydration of gypsum rock by solar energy: preliminary study. Geomaterials **4**, 82 (2014)
31. Sierra, C., Vázquez, A.: NiAl coatings on carbon steel by self-propagating high-temperature synthesis assisted with concentrated solar energy: Mass influence on adherence and porosity. Solar Energy Mater. Solar Cells **86**, 33–42 (2005). https://doi.org/10.1016/j.solmat.2004.06.003
32. Sierra, C., Vázquez, A.: NiAl coating on carbon steel with an intermediate Ni gradient layer. Surf. Coat. Technol. **200**, 4383–4388 (2006). https://doi.org/10.1016/j.surfcoat.2005.02.176
33. Garcia, D., Liang, D., Almeida, J., Tibúrcio, B.D., Costa, H., Catela, M., Vistas, C.R.: Analytical and numerical analysis of a ring-array concentrator. Int. J. Energy Res. **45**(10), 15110–15123 (2021). https://doi.org/10.1002/er.6787
34. Kostanovskii, A.V., Zeodinov, M.G., Kostanovskaya, M.E.: The determination of thermal conductivity and emissivity of graphite at high temperatures. High Temp. **43**(5), 793–795 (2005). https://doi.org/10.1007/s10740-005.0125.1

Chapter 6
Multimode Solar-Pumped Lasers

Joana Almeida and Dawei Liang

Milestone multimode solar-pumped laser designs and their laser output performances are introduced in this chapter. Since the knowledge of imaging and nonimaging primary, secondary and tertiary concentrators are vital for successful solar laser designs, Zemax® and LASCAD™ numerical analysis examples are provided in order to ensure student's clear understandings of how concentrated solar radiation is optically coupled and absorbed by the laser medium by Zemax® software and, consequently, how solar laser output power is numerically calculated by LASCAD™ software.

6.1 Solar-Pumped Lasers with Imaging and Nonimaging Primary, Secondary and Tertiary Concentrators

The optical pumping of solar lasers relies on primary, secondary and tertiary concentrators to achieve enough pumping intensity for the lasing threshold [1–24]. These solar concentrators can be classified into two types: imaging and nonimaging, depending on whether the image of the sun is focused on the receiver or not [25]. The imaging and nonimaging concentrators responsible for the main advances in solar-pumped lasers will be addressed in the next sections.

6.1.1 Configurations for Solar Energy Collection and Concentration

The Sun appears to move across the sky during the day due to the rotational motion of the Earth. The Sun's path across the sky also varies seasonally and with geographical location. The Earth's axial tilt of approximately 23.5° and its elliptical orbit around the Sun ensure that observers at different locations will see the apparent Sun motion

© The Author(s), under exclusive license to Springer Nature Switzerland AG 2023

D. Liang et al., *Solar-Pumped Lasers*, Green Energy and Technology,
https://doi.org/10.1007/978-3-031-24785-9_6

differently throughout the year [26]. For these reasons, solar systems (including solar-pumped lasers) require sun-tracking systems for the efficient capture of the solar radiation during the day and along the year. The solar energy collection by these systems can be done in two different ways: through direct tracking or indirect solar tracking by heliostat.

6.1.1.1 Direct Solar Tracking Type

In direct solar tracking systems, the primary concentrator and the receiver (the solar laser head in solar-pumped lasers) are both assembled to the solar tracker with their optical axes aligned with the position of the Sun in the sky, as illustrated in Fig. 6.1. This implicates that all the components of the laser system are movable.

In the early stages of solid-state solar lasers, direct solar tracking systems were adopted [1, 2]. In 1966, Young used an equatorial mount mechanism to support the first Neodymium (Nd): Yttrium Aluminum Garnet (YAG) solar laser system with a 0.61 m diameter paraboloidal mirror as primary concentrator [2]. The equatorial tracking, also known as polar or spinning-elevation tracking, is commonly used in telescopes, where the principal axis—the polar axis—is always oriented towards the North Star, by which the Earth's axis of rotation is oriented. Therefore, this axis tracks the Sun in East–West direction. A secondary axis, named as declination axis and perpendicular to the polar axis, is also needed to correct the solar declination angle that changes along the year, tracking the Sun in North–South direction [27, 28].

Between the middle 1980s and early 2000s, solar laser systems with stationary focus have gained strength with the use of large size mirrors as primary concentrators, for which heliostats were required to redirect the solar radiation towards the static laser head [3–8]. Nevertheless, as of 2007, direct solar tracking systems were employed again in solar-pumped lasers with the adoption of the economically competitive Fresnel lenses as primary concentrators [9–14]. The low weight of the Fresnel lenses facilitated their assembly on solar trackers, allowing the development of much lighter and more compact solar laser systems and avoiding additional power

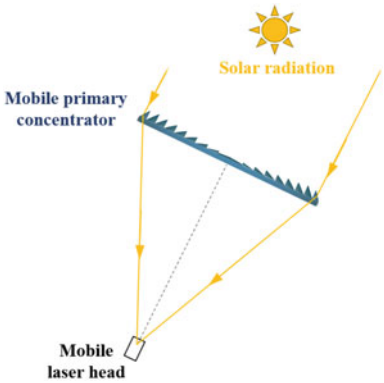

Fig. 6.1 Direct solar energy collection and concentration configuration

losses with the use of heliostats. Moreover, unlike the reflective concentrators, the focal spot of Fresnel lenses lies in their rear side. Consequently, the laser head along with the laser resonator and mechanical support are positioned behind the Fresnel lens, as shown in Fig. 6.1, enabling its easy access during the experiments.

6.1.1.2 Heliostat Type

A Heliostat, from *helios* (the Greek word for Sun) and *stat* (stationary), is a device composed of one or more mirrors that redirects the solar radiation towards a static receiver [29]. The mirrored surface of the heliostat is kept perpendicular to the bisector of the angle between the Sun's position in the sky and the stationary receiver, as illustrated in Fig. 6.2.

The conventional heliostat configuration is based on the variation of two axes simultaneously [30]: The azimuth axis and the elevation axis. The azimuth axis is vertical relative to the heliostat base, tracking the angle bisector between the Sun and the receiver in the East–West direction. The elevation (or altitude) axis is normal to the azimuth axis, tracking the Sun in North–South direction. The configuration azimuth-elevation is also used in direct solar tracking systems with Fresnel lenses, with the azimuth axis tracking the Sun position [13].

Heliostats begun to be implemented in solar laser systems in the mid-1980s [3, 4]. In order to reach higher solar laser output power levels, large size mirror concentrators were used to pump the laser medium, for which direct solar tracking became inappropriate. The attachment of heavy solar laser systems on a solar tracker structure would lead to higher energy requirements for tracking [27]. Besides, the focusing method of reflective concentrators requires the receiver to be placed in their front (Fig. 6.2), which would make the direct tracking even more troublesome, especially

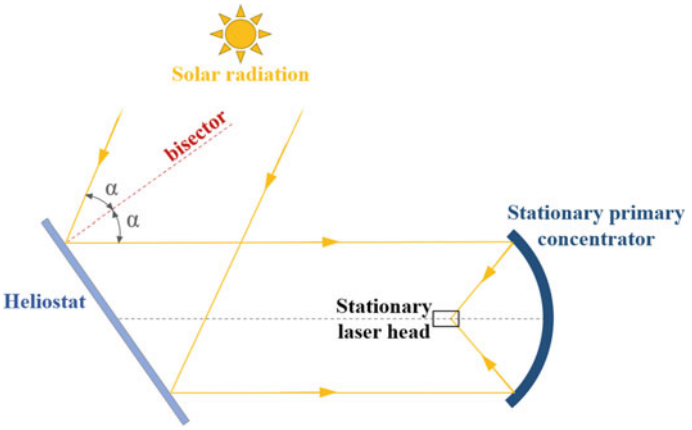

Fig. 6.2 Indirect solar energy collection and concentration configuration via heliostat

in the daily hours of greatest solar irradiance when the Sun reaches its highest position in the sky, obliging the receiver to be located above the primary concentrator. Therefore, heliostats were needful to redirect the solar radiation towards the laser head [3–8].

Despite the progress in solar laser collection efficiency that led to a reduction in primary mirror concentrator area, heliostats are still used in solar laser systems with reflective concentrators, guaranteeing steady solar laser head within the laboratory [15–22, 24].

6.1.2 Parabolic Mirrors and Fresnel Lens as Primary Imaging Concentrators

Solar pumping of lasers requires primary concentrators with high concentration ratios to obtain sufficient gain in the irradiated active medium.

Primary mirror concentrators of paraboloidal shape have long been exploited by solar laser researchers to stimulate the laser medium, as summarized in Table 6.1. In 1966, Young used a Ø 0.61 m aluminized parabolic mirror to pump the first Nd:YAG solar laser of 1 W in continuous wave (cw) mode [2]. Between the mid and late 1980s, large-size stationary mirror concentrators with apertures up to 10 m were adopted as primary concentrators [3, 4]. This permitted obtaining high solar powers at the focus and cw laser output power levels of more than 60 W [4]. The highest solar laser output power of 500 W cw was further achieved in 1993 by Krupkin et al. [6] using 64 paraboloidal mirrors in the heliostat field of Weizmann Institute (WIS) Solar Tower with total collection area of 660 m^2. Nevertheless, the solar laser collection efficiency (the laser output power per unit of primary concentrator area) was only 0.76 W/m^2 [7]. Besides, the solar tower configuration has the drawback of causing astigmatic aberration and focal spot increase [31]. To overcome this problem, Lando and his co-workers built an Astigmatic Corrected Target Aligned (ACTA) solar concentrator [31]. In this device, a segmented primary mirror with 3.4 m aperture was mounted on a two-axis positioner which tracked the solar orbit. The primary concentrator focused the incoming solar radiation towards a plane folding mirror, which in turn deflected the light towards the stationary solar laser head within an enclosure, as shown in Table 6.1. Through this collection and concentration system, with primary concentrator aperture much smaller than the previous ones [3, 4, 6], 6.7 W/m^2 collection efficiency was reached, constituting a substantial progress in solar laser efficiency at that decade [7]. Since the work of Lando et al. [7], solar laser researchers started to pay more attention to the solar laser efficiency rather than the laser output power for the assessment of the solar laser performance [9–23].

Significant progress in solar laser collection efficiency and reduction in the collection area have occurred with the adoption of Fresnel lenses as primary concentrators in direct solar tracking systems, as summarized in Table 6.2. Solar laser collection efficiency of 32.1 W/m^2 with Fresnel lens system was reached in 2018 by Guan

Table 6.1 Solar collection and concentration systems of milestone solar lasers with primary mirror concentrators

Year	Authors [Ref.]	Milestones
Primary concentrator (image) Place		Parameters
1966	Young [2]	First 1 W cw Nd:YAG solar laser
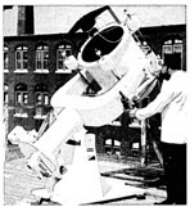 American Optical Company, USA		Solar tracking: Direct **Primary concentrator: Parabolic mirror** Diameter: 0.61 m Full collection area: ~0.293 m^2 Focal length: 0.915 m Focal spot diameter: ~9 mm Reflectivity: 85%
1984	Arashi et al. [3]	18 W cw solar laser power
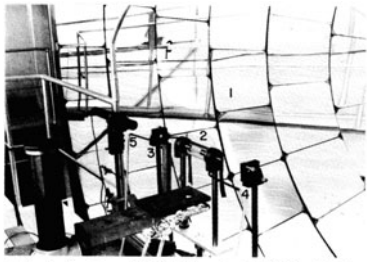 **1.** Parabolic mirror; **2.** Nd:YAG laser head; **3.** High reflection mirror; **4.** Output mirror; **5.** He-Ne laser for optical alignment Tohoku University (TU), Japan		Solar tracking: Heliostats (Segmented flat mirror) **Primary concentrator: Segmented paraboloidal mirror** [3] Diameter: 10 m Full collection area: ~78.5 m^2 Focal length: 3.2 m Rim-angle: 76° [33] FWHM[1] focal spot : ~40 mm Maximum power at the focus: 55 kW **Effective solar power for pumping:** 1.1 kW **Effective collection area**: ~13.1 m^2
1988	Weksler and Schwartz [4]	> 60 W cw solar laser power
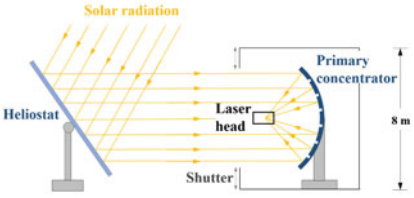 Weizmann Institute of Science (WIS), Israel		Solar tracking: Heliostats (10×10 m^2 segmented flat mirror) **Primary concentrator: Segmented mirror** made of 600 small spherical mirrors Diameter: 7.3 m [34] Full collection area: ~38.5 m^2 [7] Focal length: 3.5 m Rim-angle: 65° [34] FWHM focal spot: ~40 mm Maximum power: >15 kW **Effective solar power for pumping:** ~5 kW **Effective collection area**: ~12.8 m^2

[1] FWHM—Full Width at Half Maximum.

(continued)

Table 6.1 (continued)

1993	Krupkin et al. [6]	500 W cw solar laser power
 WIS, Israel		Solar tracking: Heliostats **Primary concentrator: Heliostat parabolic mirrors field** [6] Full collection area: 3500 m^2 [6] Maximum power: ~2.8 MW [35] **Effective collection area**: ~660 m^2 [7]
2003	Lando et al. [7]	6.7 W/m^2 solar laser collection efficiency
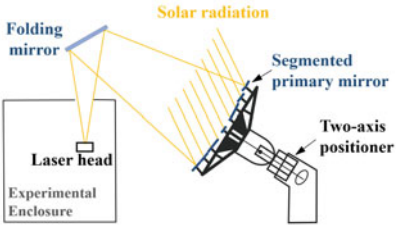 WIS, Israel		Solar tracking: ACTA solar concentrator **Primary concentrator: Segmented mirror** composed of 61 hexagonal mirrors spherically curved Diameter: 3.4 m Full collection area: 6.85 m^2 Focal length: 8.5 m **Effective collection area**: 6.75 m^2
2012	Almeida et al. [23]	0.29 W multimode laser beam brightness
2017	Liang et al. [17]	31.5 W/m^2 solar laser collection efficiency 5.25% slope efficiency
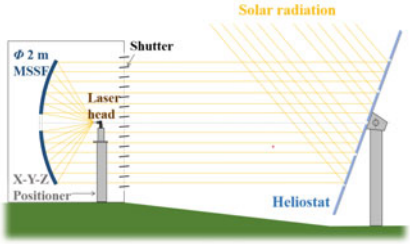 PROMES-CNRS, France		Solar tracking: Heliostat (Flat mirror with 36 segments of 0.5×0.5 m^2 each) **Primary concentrator: Parabolic mirror** Diameter: 2.0 m; Full collection area: ~3.07 m^2 Focal length: 0.85 m Rim-angle: 60° FWHM focal spot: ~10 mm [36] Maximum power: ~2 kW [36] Combined reflectivity (heliostat plus parabolic mirror): 59% **Effective collection areas**: 2.88 m^2 [23] 1.18;m^2 [17]
2018	Liang et al. [21]	32.5 W/m^2 Cr:Nd:YAG solar laser collection efficiency 6.7% slope efficiency
2019	Liang et al. [15]	Side-pumped solar laser with 5.4% slope efficiency

(continued)

Table 6.1 (continued)

2020	Liang et al. [18]	Simultaneous solar laser emissions from three Nd:YAG rods
2021	Vistas et al. [16]	Ce:Nd:YAG side-pumped solar laser with 23.6 W/m^2 collection efficiency
2022	Garcia et al. [19]	Single-rod Ce:Nd:YAG solar laser with 4.5% conversion efficiency Lowest threshold solar power
2022	Liang et al. [20]	Most efficient simultaneous emissions from three Ce:Nd:YAG laser rods 4.64% solar-to-laser conversion efficiency 41.3 W/m^2 solar laser collection efficiency 7.64% slope efficiency
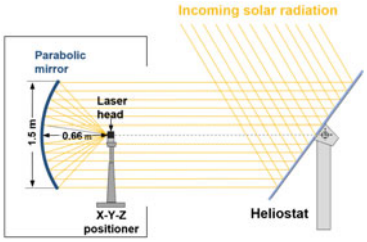 NOVA School of Science and Technology (FCT NOVA), Portugal		Solar tracking: Heliostat (Flat mirror with two segments) **Primary concentrator: Parabolic mirror** Diameter: 1.5 m Full collection area: 1.767 m^2 Focal length: 0.66 m Rim-angle: 60° Maximum power: ~1.2 kW Combined reflectivity (heliostat plus parabolic mirror): 75% **Effective collection areas:** 1.0 m^2 [21]; 0.9 m^2 [15]; 1.0 m^2 [18]; 0.7 m^2 [16]; 0.29 m^2 [19]; 0.4 m^2 [20]

Images adapted from [2–4, 7, 21, 24, 32]

et al. using an effective collection area of only 1.03 m^2 to end-side-pump a bonding Nd:YAG/YAG laser rod [14].

Compared with parabolic mirror systems, Fresnel lens systems reduce complexity, weight, and cost of solar lasers. However, they have chromatic aberration, i.e., spreading the solar radiation spectrum along its focal zone, which may impair the transfer efficiency of the pump radiation to the laser medium. Parabolic mirrors, instead, collect all pumping wavelengths to a small focal spot without dispersion. For these reasons, the solar laser researchers from FCT NOVA have insisted on enhancing the solar laser efficiency using parabolic mirror as primary concentrators. Since 2017, several important milestone solar lasers occurred at the solar facilities of FCT NOVA and PROMES-CNRS (Table 6.1), both composed of an heliostat and a stationary parabolic mirror with 1.5 and 2.0 m maximum diameter, respectively [15–21, 37]. Records in solar-to-laser conversion, collection, and slope efficiencies of 4.64%, 41.3 W/m^2, and 7.64% were, respectively, attained in 2022 by the simultaneous end-side-pumping of three Cerium (Ce):Nd:YAG laser rods through the NOVA solar facility [20].

Table 6.2 Solar collection and concentration systems of milestone solar lasers with primary Fresnel lens concentrators

Year	Authors [Ref.]	Milestones
Primary concentrator (image) Place		Parameters
2007	Yabe et al. [9]	18.7 W/m^2 solar laser collection efficiency with Cr:Nd:YAG active medium
 Tokyo Institute of Technology (TIT), Japan		Solar tracking: Direct **Primary concentrator: Fresnel lens** Aperture: 1.4×1.05 m^2 Focal length: 1.2 m FWHM focal spot: 11.2 mm Transmission: 66.4% **Effective solar power for pumping:** ~865 W **Effective solar collection area:** ~1.3 m^2
2011	Liang and Almeida [13]	19.3 W/m^2 solar laser collection efficiency with Nd:YAG active medium
 FCT NOVA, Portugal		Solar tracking: Direct **Primary concentrator: Fresnel lens** Diameter: 0.9 m Focal length: 1.2 m FWHM focal spot: ~12 mm Transmission: 78.6% **Effective solar power for pumping:** ~445 W **Effective solar collection area:** 0.636 m^2
2012	Dinh et al. [10]	30 W/m^2 solar laser collection efficiency
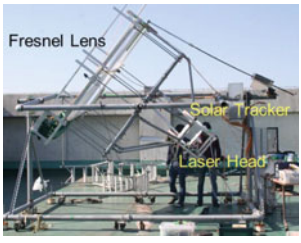 TIT, Japan		Solar tracking: Direct **Primary concentrator: Fresnel lens** Aperture: 2×2 m^2 Focal length: 2 m FWHM focal spot: ~20.4 mm [11] Transmission: 50% **Effective solar power for pumping:** 1840 W **Effective solar collection area:** 4 m^2

(continued)

Table 6.2 (continued)

2018	Guan et al. [14]	32.1 W/m^2 Nd:YAG solar laser collection efficiency
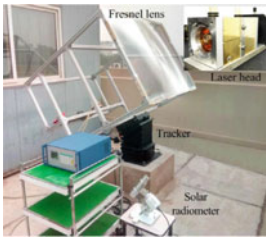 Beijing Institute of Technology (BIT), China		Solar tracking: Direct **Primary concentrator: Fresnel lens** Aperture: 1.4×1.05 m^2 Focal length: 1.2 m FWHM focal spot: 11.5 mm **Effective solar collection area:** 1.03 m^2

Images adapted from [9, 11, 13, 14]

6.1.3 Secondary Imaging Concentrators

The concentrated solar intensity of the primary concentrator is limited by the Sun image at the focus, which can lead to a significant mismatch between the sizes of the focal spot and the laser active medium. Thence, for efficient coupling of the solar rays into the laser medium, the focal image must be reduced, which requires secondary optics. In this section, the secondary imaging concentrators that contributed to the most significant advances in solar lasers are presented.

6.1.3.1 Hyperbolic-Cylindrical Reflector for Side-Pumping Scheme

The first 1 W cw Nd:YAG solar laser was pumped through a modified Cassegrain sun-tracking telescope consisting of a 0.61 m diameter paraboloidal primary mirror, a water-cooled hyperbolic-cylindric secondary mirror and a hemicircular cylindric tertiary mirror, as shown in Fig. 6.3 [2]. The aluminized secondary concentrator, as well as the primary concentrator, had an average reflection of 85% in the pump bands.

In this solar laser system, a side-pumping configuration was adopted, which means that the solar radiation was injected into the laser medium transversely to its optical axis. Thus, to refocus and redistribute the concentrated solar radiation along the 3 mm diameter, 30 mm length, 1.0 at.% Nd:YAG rod, both secondary and tertiary concentrators were two-dimensional. The resultant image at the focus of the hyperbolic-cylindric reflector was 3 mm by 24 mm, which was coincident with the exposed portion of the active medium [2]. The laser resonator was formed by the highly and partially reflective coatings in the laser emission wavelength (1064 nm) deposited on the convex end surfaces of laser rod with 5 cm radius of curvature [2].

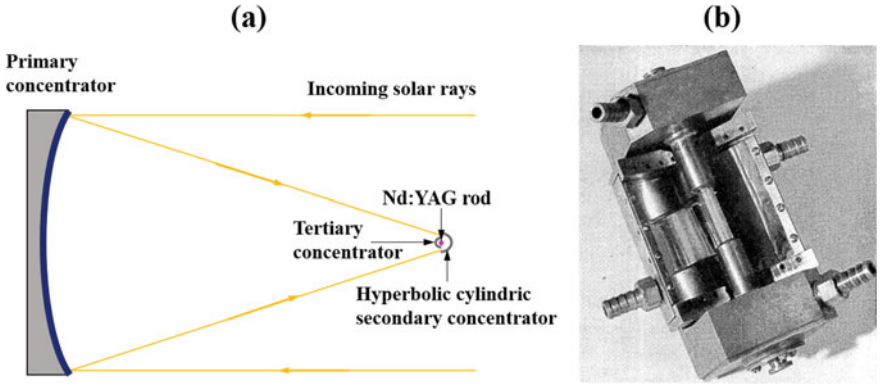

Fig. 6.3 **a** Schematic design of the 1 W cw Nd:YAG solar laser system (adapted from [2]) **b** Assembly of the hyperbolic-cylindric secondary concentrator [2]

6.1.3.2 Meniscus Plus Hyper Hemispherical Aplanatic Refractors for End-Side-Pumping Scheme

An aplanatic lens is free of both spherical and coma aberrations, being widely used in microscope objectives. They are usually made of at least two or three air-spaced lens elements [38].

In 1964 and 1966, Simpson [1] and Young [2] utilized this type of lenses as secondary concentrators in their solar laser experiments with Nd:glass medium, combining a meniscus converging lens with a hyper semispherical lens to pump the laser rod, as shown in Table 6.3. A meniscus converging lens is a convex-concave lens thicker at the center than at the edges, being free from both spherical and comma aberrations [39]. When combined with the hyper hemispherical lens, which has a very wide field of view angle [40], the focal length of the solar laser system is shortened and, consequently, the focal spot is reduced. With this configuration, the more external solar rays could ricochet along the rod, allowing multipass pumping to the thin laser rod.

Young succeeded in obtaining Nd:glass solar laser output power of 1.25 W [2]. However, no provisions were made to cool the laser rod in both experiments [1, 2]. Therefore, laser operation lasted less than 1.0 s before cessation owing to excessive temperature.

6.1.3.3 Fused Silica Aspheric Lens for Both End- and Side-Pumping Schemes

Aspherical lenses encompass any lens with rotational symmetry that has a non-spherical surface, in which the radius of curvature varies radially from the center to the edge. These lenses can focus all the incident light on the same focal region,

Table 6.3 Milestone solar lasers with meniscus plus hyper hemispherical aplanat refractors as secondary concentrators

Year	Authors [Ref.]	Milestones
Secondary concentrator (image)		Solar laser system parameters
1964	Simpson [1]	First Nd:glass solar laser
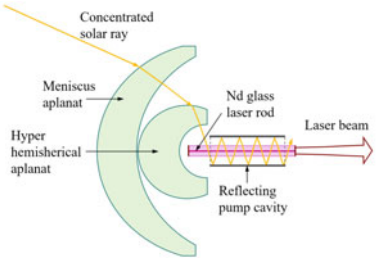		Primary concentrator: 0.61 m diameter Parabolic mirror **Secondary concentrator: Meniscus plus hyper hemispherical aplanats** SF-4 glass material Tertiary concentrator: Silvered reflector Active medium: Ø 0.1 mm × 30 mm Nd-doped barium crown glass core clad by Ø 1.0 mm soda-lime silicate glass
1966	Young [2]	1.25 W Nd:glass solar laser
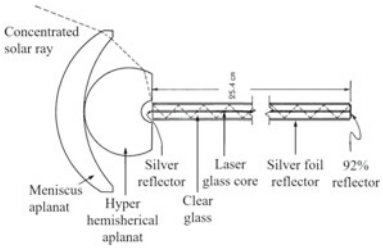		Primary concentrator: 0.61 m diameter Parabolic mirror **Secondary concentrator: Meniscus plus hyper hemispherical aplanats** SF-4 glass material Tertiary concentrator: Silver foil reflector Active medium: Ø 0.4 mm Nd:glass core clad by Ø 4.0 mm clear glass

Images adapted from [1] and [2], respectively

reducing spherical aberration and providing true diffraction-limited spot sizes. The concentrated solar radiation can hence be collected and compressed efficiently from the focal zone of the primary concentrator into the laser medium. For these reasons, fused silica aspherical lenses have been used as secondary concentrators in several solar-pumped laser systems with either side-pumping or end-side-pumping configurations [15–20], summarized in Table 6.4. Fused silica material is suitable for solar-powered lasers since it has a wide transparency range over the laser media absorption spectra. Furthermore, it is very resistant to high temperature and thermal shock [41].

The curvature surface of the aspheric lenses (z) utilized in these solar laser systems followed Eq. (6.1) [19]:

$$z = \frac{RoCr^2}{1 + \sqrt{1 - (1 + k)RoC^2r^2}} + \alpha_1 r^2 \tag{6.1}$$

Table 6.4 Milestone solar lasers with aspherical lenses as secondary concentrators

Year	Authors [Ref.]	Milestones
Secondary concentrator (image) **Laser head configuration**		Solar laser system parameters
2017	Liang et al. [17]	31.5 W/m^2 collection efficiency 5.25% slope efficiency
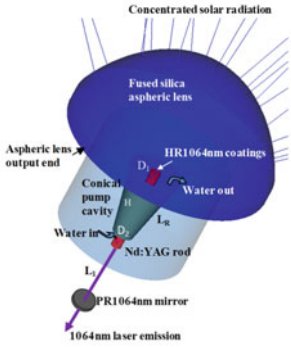 **End-side-pumping**		Primary Concentrator, effective collection area: PROMES-CNRS parabolic mirror, 1.18 m^2 **Secondary concentrator: Aspheric Lens** Radius of curvature *RoC*: 45 mm Flat output surface Radial aperture *r*: 42 mm Conic constant *k*: 0 Height: 38 mm Aspheric coefficient α_i: -0.005 Tertiary concentrator: Conical reflector Active medium: Ø 4 mm × 35 mm Nd:YAG
2019	Liang et al. [15]	Side-pumped Nd:YAG solar laser with 5.4% slope efficiency
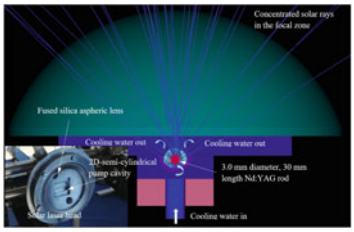 **Side-pumping**		Primary Concentrator, effective collection area: FCT NOVA parabolic mirror, 0.9 m^2 **Secondary concentrator: Aspheric Lens** Radius of curvature *RoC*: 44 mm Flat output surface Radial aperture *r*: 40 mm Conic constant *k*: 0 Height: 31 mm Aspheric coefficient α_i: -0.002 Tertiary concentrator: Semi-cylindrical reflector Active medium: Ø 3 mm × 30 mm Nd:YAG

(continued)

where *RoC* is the radius of curvature, *r* is the radial aperture, *k* the conic constant, and α_i the aspheric coefficient.

The most efficient Nd:YAG solar laser with parabolic mirror as primary concentrator was obtained with the use of a secondary aspherical lens in an end-side-pumping scheme [17]. In end-side-pumping configurations, most of the concentrated solar radiation is directly focused onto the end face of the laser rod, i.e., parallel to the laser beam. Therefore, the optical path of solar rays within the laser medium is much longer than that of side-pumping scheme, enabling higher pumping efficiency.

Table 6.4 (continued)

2020	Liang et al. [18]	First simultaneous solar laser emissions from three Nd:YAG rods
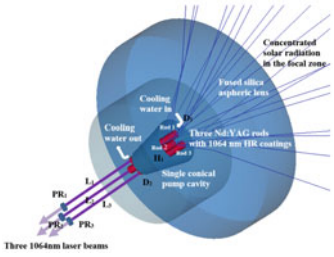 **End-side-pumping**		Primary Concentrator, effective collection area: FCT NOVA parabolic mirror, 1.0 m^2 **Secondary concentrator: Aspheric Lens** Radius of curvature *RoC*: 60 mm Flat output surface Radial aperture *r*: 42 mm Conic constant *k*: 0 Height: 34 mm Aspheric coefficient α_i: -0.003 Tertiary concentrator: Conical reflector Active medium: Three Ø 3.0 mm × 25 mm Nd:YAG
2022	Garcia et al. [19]	Single-rod Ce:Nd:YAG solar laser with 4.5% conversion efficiency Lowest threshold solar power
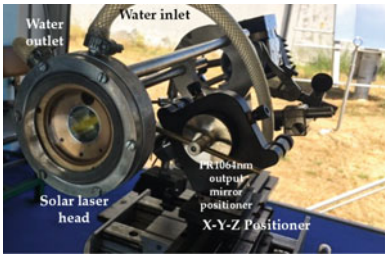 **End-side-pumping**		Primary Concentrator, effective collection area: FCT NOVA parabolic mirror, 0.293 m^2 **Secondary concentrator: Aspheric Lens** Radius of curvature *RoC*: 43 mm Flat output surface Radial aperture *r*: 41 mm Conic constant *k*: 0 Height: 37 mm Aspheric coefficient α_i: -0.004 Tertiary concentrator: Conical reflector Active medium: Ø 2.5 mm × 25 mm Ce:Nd:YAG
2022	Liang et al. [20]	Most efficient simultaneous emissions from three Ce:Nd:YAG laser rods 4.64% solar-to-laser conversion efficiency 41.3 W/m^2 solar laser collection efficiency 7.64% slope efficiency
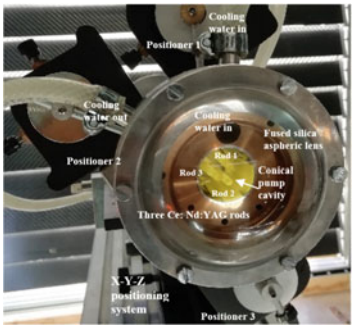 **End-side-pumping**		Primary Concentrator, effective collection area: FCT NOVA parabolic mirror, 0.4 m^2 **Secondary concentrator: Aspheric Lens** Radius of curvature *RoC*: 43 mm Flat output surface Radial aperture *r*: 42 mm Conic constant *k*: 0 Height: 37 mm Aspheric coefficient α_i: -0.005 Tertiary concentrator: Conical reflector Active medium: Three Ø 2.5 mm × 25 mm Ce:Nd:YAG

Images adapted from [15, 17–20]

Nevertheless, end-side-pumping can lead to severe thermal loading issues in single solid-state laser media of cylindrical geometry [42, 43], due to the non-homogenous pumping light distribution along the laser rod's length, precluding these laser systems to scale to high power. To attenuate this drawback, the potential of multirod solar laser systems based on the simultaneous pumping of several laser media has been recently investigated [18, 20]. In these systems, each rod absorbs only a portion of the concentrated solar radiation incident on the pumping cavity, reducing significantly the thermal induced effects. The records in solar-to-laser conversion, collection, and slope efficiencies of 4.64%, 41.3 W/m^2, and 7.64%, respectively, were attained through the simultaneous pumping of three Ce:Nd:YAG laser rods using an aspherical lens as secondary concentrator (Table 6.4) [20].

Side-pumping configuration is also suitable for laser power scaling once it spreads the solar radiation along the laser rod, hence improving the thermal performance. The most efficient side-pumped Nd:YAG solar laser with 2.43% solar-to-laser power conversion efficiency, 17.7 W/m^2 collection efficiency and 5.4% slope efficiency had also an aspheric lens as secondary concentrator (Table 6.4) [15].

6.1.3.4 Liquid Light Guide Lens for End-Side-Pumping Scheme

The liquid light guide lens can be considered as a laser flow tube. Nonetheless, it can also work as a lens due to the difference of refraction index n between the air ($n_{air} = 1$) and the coolant (usually water, $n_{water} = 1.33$), as shown in Fig. 6.4.

In 2012, Dinh and his co-workers utilized a liquid light guide lens to improve the performance of an end-side-pumping solar laser system, composed of a Fresnel lens primary concentrator and a secondary conical mirror (Fig. 6.4) [10, 11]. In this case, the liquid light guide lens worked essentially as a tertiary concentrator, helping to refocus the reflected solar rays by the conical cavity into the laser rod. With this configuration, 120 W cw laser power was produced from a 6 mm diameter, 100 mm length Nd:YAG rod, resulting in 30 W/m^2 collection efficiency. Such result was 2 times higher than that without the glass tube, i.e., with the conical cavity flooded with water [10, 11].

In 2018, Guan et al. [14] and Liang et al. [21] developed liquid light guide lenses with hemispherical front surfaces to end-side-pump a bonding Nd:YAG/YAG [14] and a Cr:Nd:YAG rod [21], respectively, within a conical cavity. The curved front

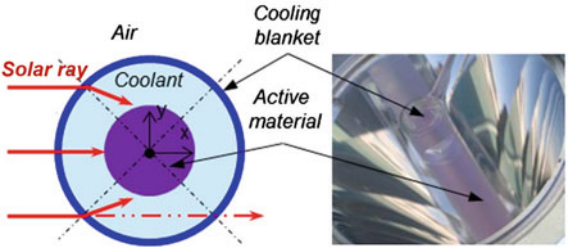

Fig. 6.4 Liquid light guide lens configuration. Adapted from [11]

Table 6.5 Milestone solar lasers with liquid light guide lens as secondary concentrators

Year	Authors [Ref.]	Milestones
Secondary concentrator (image)		Solar laser system parameters
2018	Guan et al. [14]	32.1 W/m^2 Nd:YAG/YAG solar laser collection efficiency
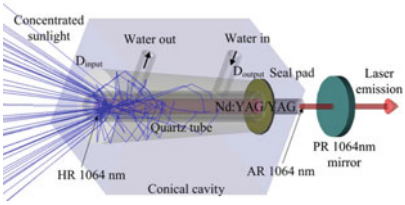		Primary Concentrator, effective collection area: BIT Fresnel lens, 1.03 m^2 **Secondary concentrator: Liquid light guide lens** Material: quartz Hemispherical input surface; *RoC*: 6 mm External/internal diameters: 12 mm / 10mm Length: 81 mm Tertiary concentrator: Conical reflector Active medium: Ø 6 mm × 95 mm bonding Nd:YAG/YAG
2018	Liang et al. [21]	32.5 W/m^2 Cr:Nd:YAG solar laser collection efficiency 6.7% slope efficiency
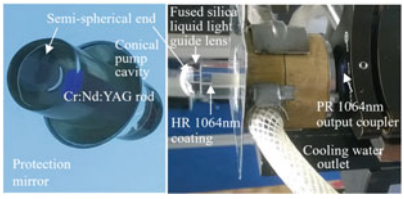		Primary Concentrator, effective collection area: FCT NOVA parabolic mirror, 1.0 m^2 **Secondary concentrator: Liquid light guide lens** Material: Fused silica Hemispherical front surface; *RoC*: 8.5 mm Flat output surface Tertiary concentrator: Conical reflector Active medium: Ø 4.5 mm × 35 mm Cr:Nd:YAG

Images adapted from [14] and [21], respectively

surface allowed the concentrated solar rays to be more efficiently focused on the top region of the laser rod, so the light guide lens acted as a secondary concentrator. These pumping configurations led to the records in solar laser collection efficiencies of 32.1 and 32.5 W/m^2 with Nd:YAG [14] and Cr:Nd:YAG laser materials [21], respectively, as summarized in Table 6.5. Similar configuration with liquid light guide lens as a secondary concentrator was also adopted for the first Ce:Nd:YAG solar laser [22].

6.1.4 Secondary Nonimaging Concentrators

Nonimaging concentrators can be considered as a funnel for light, sacrificing the image of the source in order to concentrate the light to intensities approaching the

theoretical limit [44]. They have played an important role in the advancement of solar-pumped lasers, acting as secondary and/or tertiary concentrators. In this section, the secondary nonimaging concentrators that contributed to the most significant advances in solar lasers are presented.

6.1.4.1 Three-Dimensional Compound Parabolic Concentrator (3D-CPC) for Side-Pumping Scheme

One of the most representative nonimaging type concentrators is the compound parabolic concentrator (CPC), also known as Winston-type collector [45]. The three-dimensional (3D) CPC shape is derived from the CPC design principle for a flat receiver, represented in Fig. 6.5. It is based on the intersection of two parabolas facing each other, the axes of which are inclined at angles $\pm\ \theta_a$ with respect to optical axis of the collector. The angle θ_a is the acceptance angle of the concentrator, i.e., the angle at which the incoming sunlight can be captured by a concentrator and reflected to the absorber. Because of the CPC shape, all the incident solar rays within the maximum concentration angle θ_a can be transmitted to a small output aperture emitting into a larger angle. This implies that irradiance is larger at the output aperture than at the entrance aperture, leading to a net concentration of the pump radiation [46].

The use of secondary 3D-CPCs concentrators has contributed to the advances of solar lasers in the 90's and early 2000s [6, 7], as summarized in Table 6.6.

In 2003, Lando et al. reached 6.7 W/m^2 by using a 3D-CPC combined with a 2D-CPC tertiary concentrator to side-pump a Nd:YAG laser rod [7]. Similar archetype has been previously utilized by Krupkin et al. in 1993 to side-pump an array of laser rods at the WIS solar tower, reaching 500 W cw solar laser power [6].

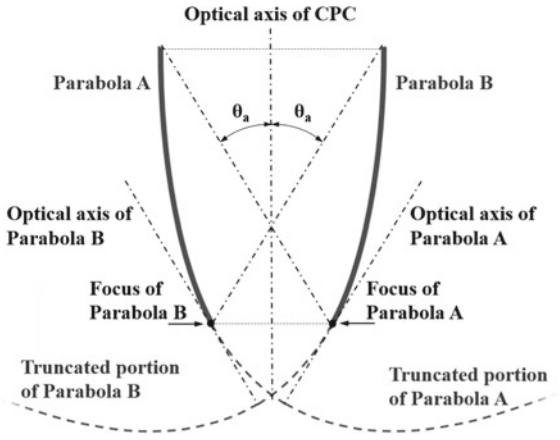

Fig. 6.5 Schematic design of a compound parabolic concentrator (CPC) for a flat receiver

Table 6.6 Milestone solar lasers with secondary three-dimensional compound parabolic concentrators (3D-CPCs)

Year	Authors [Ref.]	Milestones
Secondary concentrator (image)		Solar laser system parameters
1993	Krupkin *et al* [6]	500 W Nd:YAG solar laser power
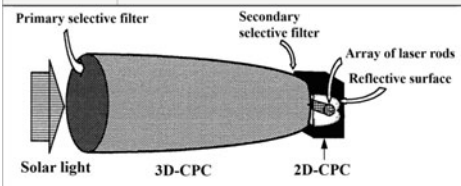		Primary concentrator, effective collection area: WIS heliostat parabolic mirrors, 660 m^2 **Secondary concentrator: 3D-CPC** Tertiary concentrator: 2D-CPC Active medium: Array of laser rods
2003	Lando *et al* [7]	6.7 W/m^2 Nd:YAG solar laser collection efficiency
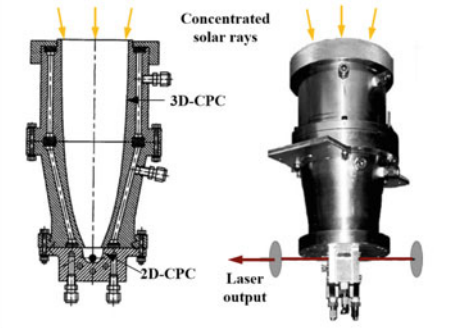		Primary concentrator, effective collection area: WIS ACTA solar concentrator, 6.75 m^2 **Secondary concentrator: 3D-CPC** Input aperture:100 mm Output aperture: 24 mm Maximum output half angle: 55° Tertiary concentrator: 2D-CPC Active medium: Ø 6.0 mm × 72 mm Nd:YAG

Images adapted from [6] and [7], respectively

6.1.4.2 Two-Dimensional Compound Parabolic Concentrator (2D-CPC) for Side-Pumping

The CPC can take a variety of shapes depending on the receiver geometry [47]. For solar-pumped lasers, the classical two-dimensional (2D) CPC profile is based on the design principle for tubular receivers, illustrated in Fig. 6.6. This CPC type has two different segments that smoothly join at point *B(B')* related to θ_a. The lower segment, from the bottom of the receiver, *A*, to point *B (B')* is an involute of the receiver's cylindrical cross-section. The upper segment, from point *B(B')* to *C(C')*, is of parabolic shape.

A light ray entering the 2D-CPC with an angle $\theta_i = \theta_a$ will strike the tubular receiver of radius r tangentially. The distance along the tangent from the receiver (*P'*) to the last intersection point of the ray with the concentrator (*P*) is represented by ρ, which is given by the following equation for the two CPC segments [48], where θ is the angle between the radius to the bottom of the receiver and the radius to the tangential point *P'*:

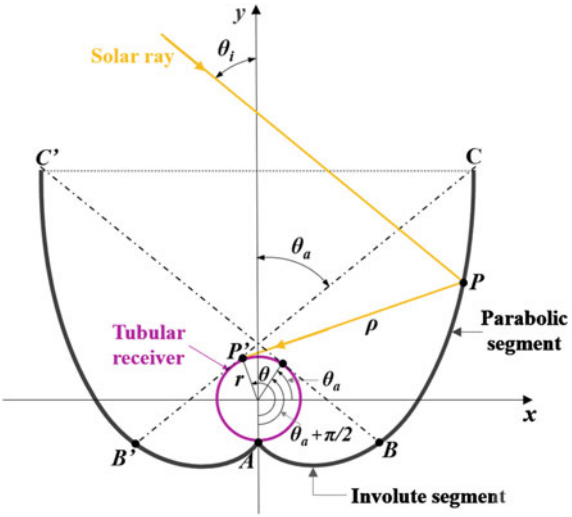

Fig. 6.6 Cross-section of a two-dimensional compound parabolic concentrator (2D-CPC) classical design for a tubular absorber. Adapted from [48]

$$\rho = \begin{cases} r\theta & \text{if } |\theta| \leq \theta_a + \pi/2 \\ r\left[\frac{\theta+\theta_a+\pi/2-\cos(\theta-\theta_a)}{1+\sin(\theta-\theta_a)}\right] & \text{if } \theta_a + \pi/2 \leq |\theta| \leq 3\pi/2 - \theta_a \end{cases} \tag{6.2}$$

As observed in Eq. (6.2), the classical 2D-CPC profile only depends on the acceptance angle θ_a and on the absorber radius r. With $\overline{CC'}$ being the 2D-CPC entrance width, the rod radius is given by Eq. (6.3),

$$2\pi r = \overline{CC'} \sin(\theta_a) \tag{6.3}$$

The 2D-CPC was first implemented in solar-pumped lasers as a secondary concentrator in 1988 by Weksler and Schwartz, to increase the coupling of solar rays from the WIS concentrator into the Nd:YAG rod in a side-pumping configuration [4], as shown in Table 6.7. This has contributed to more than 60 W of solar laser power, the highest to that date. Later, Lando et al. has also utilized this concentrator type at the focus of the ACTA solar concentrator for side-pump Nd:YAG solar laser experiments, achieving 6.7 W/m^2 collection efficiency, which constituted a record in 2003 [7].

6.1.4.3 Conical Pump Cavity for End-Side-Pumping Scheme

In the previous works, non-imaging secondary CPCs were used to further concentrate and redistribute the sunlight from primary mirror concentrators along the laser rods in side-pumping configurations [4, 6, 7]. However, the pump radiation passes through the active medium only once in a CPC chamber. Besides, the optical path in side-pumping configuration is less than that in end-pumping configuration, resulting in

Table 6.7 Milestone solar lasers with secondary two-dimensional compound parabolic concentrators (2D-CPCs)

Year	Authors [Ref.]	Milestones
Secondary concentrator (image)		Solar laser system parameters
1988	Weksler and Schwartz [4]	> 60 W Nd:YAG solar laser power
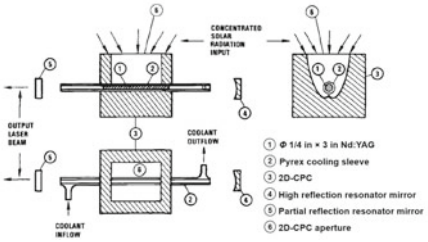		Primary concentrator, effective collection area: WIS mirror concentrator, ~12.8 m^2 **Secondary concentrator: Dry 2D-CPC** Active medium: Ø 6.35 mm × 76.2 mm Nd:YAG
2003	Lando et al. [7]	6.7 W/m^2 Nd:YAG solar laser collection efficiency
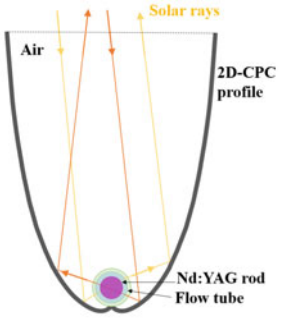		Primary concentrator, effective collection area: WIS ACTA solar concentrator, 6.75 m^2 **Secondary concentrator: Dry 2D-CPC** Aperture: 98 × 89 mm^2 Length: 131 mm Active medium: Ø 10 mm × 130 mm Nd:YAG

Images adapted from [4] and [7] respectively

lower pumping efficiency. These concerns became even more challenging with the introduction of Fresnel lens as primary concentrator [9], due to the dependence of the focal length on the solar spectrum wavelength. To overcome this issue, in 2007 Yabe et al. adopted a secondary conical mirror to end-side-pump a Cr:Nd:YAG rod at the focus of a 1.3 m^2 Fresnel lens [9], as illustrated in Fig. 6.7.

This type of concentrator provided the confinement of light by multiple reflections inside the pumping cavity, enhancing the absorption efficiency. The solar laser collection efficiency was boosted to 18.7 W/m^2, representing a 2.8 times enhancement over the previous record of 6.7 W/m^2 by Lando et al. [7]. Since then, the conical cavity has been widely used by solar laser researchers, either as a secondary [9–12] or tertiary concentrator [13, 14, 17–22].

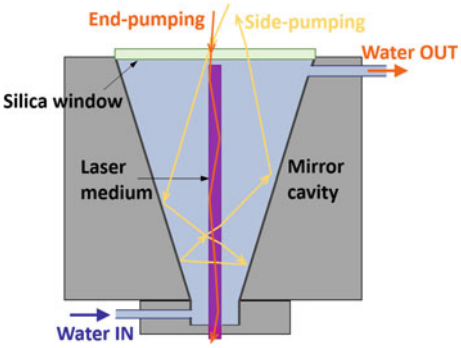

Fig. 6.7 Schematic design of a secondary conical pump cavity for end-side-pumping, with Fresnel lens primary concentrator (adapted from [10])

6.1.4.4 Dielectric Totally Internally Reflecting Secondary Concentrator (DTIRC) for End-Side-Pumping Scheme

Dielectric totally internally reflecting concentrator (DTIRC) was originally designed for photovoltaic applications with the goal of reducing the cost of electricity generated through photovoltaic conversion [49]. DTIRCs combine the front surface refraction with total internal reflection from the sidewall to achieve concentrations close to the theoretical limits [50]. Unlike dielectric CPCs, which has a flat front surface, the curved front surface of the DTRICs works like a lens, concentrating the solar rays before their reflection on the sidewalls. Therefore, the more curved the front surface, the shorter the DTRIC [50].

In 2011, Liang and Almeida employed a modified version of the DTIRC with an aspherical front surface and a conical section to efficiently concentrate the solar radiation from a 0.636 m^2 Fresnel lens primary concentrator to the upper end-region of the 25 mm length Nd:YAG laser rods with either 3 or 4 mm diameter [13], as illustrated in Fig. 6.8. The previous progress in solar-pumped laser with economical Fresnel lens has revitalized solar laser researches [9]. However, chromatic aberration of the Fresnel lens hinders the coupling of the different solar pump wavelengths into a small laser rod by a conventional lens. The modified DTIRC was therefore designed to overcome this difficulty [13]. For end-pumping, one part of the radiation was directly focused onto the upper end-face of the laser rod through the curved surface of the DTRIC, represented by ray A, while another part was focused indirectly through total internal reflection from the conical section of the DTIRC, represented by ray B. The solar radiation that does not hit the end face of the rod, represented by ray C, was guided into the small conical cavity, ensuring a multi-pass side-pumping to the rod.

As shown in Fig. 6.8, the end face of the DTRIC was in direct contact with cooling water, which ensured an efficient light coupling to the rod. The laser resonator was formed by the high reflection (HR) coating at 1064 nm on the upper end-face of the laser rod and the partial reflection (PR) coating on the concave output mirror. This solar laser system permitted to obtain 12.3 W cw laser power from a

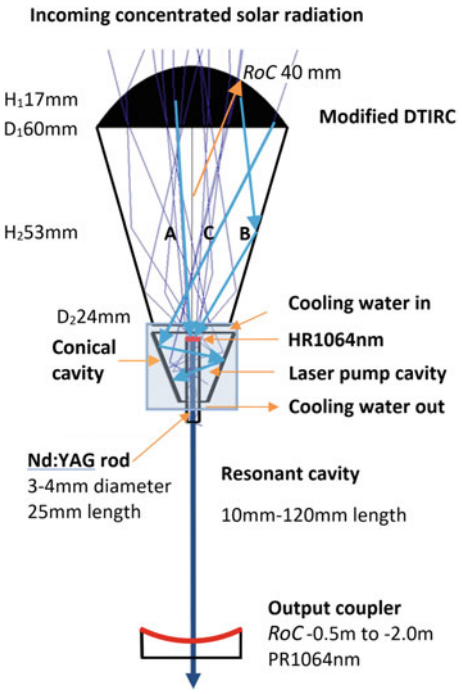

Fig. 6.8 The Nd:YAG laser head composed of the secondary DTIRC and the tertiary conical concentrator where a 3–4 mm diameter rod is efficiently pumped. RoC, radius of curvature; H_1, height of the aspherical section of the DTRIC; H_2, height of the conical section of the DTRIC; D_1, DTIRC input diameter; D_2, DTIRC output diameter. HR, high reflection; PR, partial reflection

Ø 4 mm × 25 mm laser rod, corresponding to a record solar laser collection efficiency of 19.3 W/m^2 at that time.

6.1.5 Tertiary Imaging and Nonimaging Concentrators

Tertiary concentrators are indispensable for increasing the solar laser pumping efficiency since they can either compress or wrap the solar radiation from the secondary concentrator to the laser medium. The imaging and nonimaging tertiary concentrators that played a key role in the solar laser advances are addressed in this section.

6.1.5.1 Semi-Cylindrical Mirror as an Imaging Tertiary Concentrator

Semi-cylindrical tertiary mirrors have been implemented in some solar laser systems with side-pumping configuration to both redirect and refocus the transmitted solar radiation from imaging secondary concentrators back to the laser rod [2, 3, 15], as summarized in Table 6.8.

This tertiary concentrator was first adopted by Young in 1966 for the first Nd:YAG solar laser emission [2]. To prove the advantage of using the semi-cylindrical mirror,

Table 6.8 Milestone solar lasers with semi-cylindrical mirror as tertiary concentrators

Year	Authors [Ref.]	Milestones
Secondary concentrator (image)		Solar laser system parameters
1966	Young [2]	First 1 W Nd:YAG solar laser
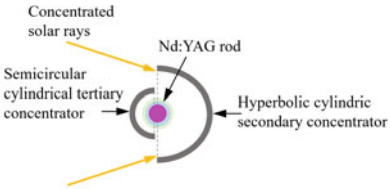		Primary concentrator: Ø 0.61 m Parabolic mirror Secondary concentrator: Hyperbolic cylindric mirror **Tertiary concentrator: Dry semi-cylindrical reflector** Active medium: Ø 3 mm × 30 mm Nd:YAG
1984	Arashi et al. [3]	18 W Nd:YAG solar laser power
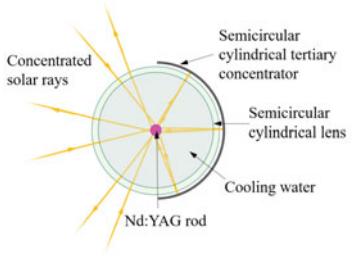		Primary Concentrator, effective collection area: TU segmented paraboloidal mirror, ~13.1 m^2 Secondary concentrator: Cylindrical lens **Tertiary concentrator: Semi-cylindrical reflector** Active medium: Ø 4 mm × 75 mm Nd:YAG
2019	Liang et al. [15]	Side-pumped Nd:YAG solar laser with 5.4% slope efficiency
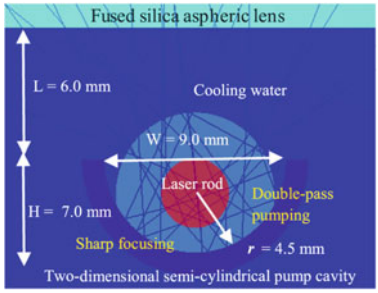		Primary Concentrator, effective collection area: FCT NOVA parabolic mirror, 0.9 m^2 Secondary concentrator: Aspherical lens **Tertiary concentrator: Water-cooled semi-cylindrical reflector** Material: silver-coated aluminum foil Reflectivity: 94% Width W: 9.0 mm Radius of curvature *r*: 4.5 mm Height H: 7.0 mm Length: 18 mm Active medium: Ø 3 mm × 30 mm Nd:YAG

Images adapted from [2, 3, 15], respectively

Young decided to compare the output performance of the Nd:YAG solar laser system with and without it. This experiment has revealed 1.5 times increase in the laser output power over that obtained with the hyperbolic cylindric secondary concentrator alone.

In 1984, Arashi et al. placed a semi-cylindrical concentrator just behind the secondary cylindrical lens to refocus the transmitted solar radiation to the side-pumped Nd:YAG laser rod [3]. With this combination, 18 W cw solar laser power was measured, the highest at that time.

In 2019, Liang et al. used a water-cooled semi-cylindrical tertiary concentrator for the most efficient side-pumped solar laser [15]. This pump cavity showed great usefulness in both refocusing and reflecting the pump rays from the secondary aspherical lens towards the Nd:YAG rod. One part of the concentrated solar radiation from the parabolic mirror was directly focused onto the laser rod by the secondary lens, but the pump rays were only partially absorbed. Double-pass pumping was possible by the semi-cylindrical mirror, once it could refocus the transmitted pump rays from the secondary lens back to the laser rod. Besides, a significant part of the pump rays exiting the aspherical lens did not pass directly through the laser rod. Therefore, the tertiary concentrator had also a fundamental role in redirecting those pump rays to the laser rod.

6.1.5.2 Two-Dimensional Compound Parabolic Nonimaging Concentrator (2D-CPC)

Tertiary concentrators with 2D-CPC shape were also used in conjunction with either secondary 3D-CPCs [6, 7] or rectangular fused silica light-guide homogenizers [23] to side-pump the laser rod, as summarized in Table 6.9.

In 1993 and 2003, Krupkin et al. [6] and Lando et al. [7] combined the 3D-CPC secondary concentrators with 2D-CPC tertiary concentrators for side-pumping of Nd:YAG laser rods. The experimental results from these solar laser systems constituted records in solar laser power [6], collection efficiency [7] and brightness figure of merit [7].

Later, in 2012, Almeida et al. resort a modified version of the classic 2D-CPC as a tertiary concentrator in combination with a secondary fused silica rectangular light guide to improve the absorbed pump distribution along a Nd:YAG laser rod [23].

The classic 2D-CPC design is based on the edge ray principle, which requires the extreme incident rays at the entrance aperture to be tangent to the tubular receiver [44], as demonstrated in Fig. 6.6 (Sect. 6.1.4.2). In a solar laser system, this prevents the most extreme solar rays from being absorbed by the laser medium, impairing the absorption efficiency. The modified 2D-CPC was designed to overcome this drawback, allowing the coupling of the pump rays with high incidence angles coming from the light guide into the laser rod [23]. This design configuration contributed to multimode solar laser beam brightness figure of merit of 0.29 W, which was three times higher than that of the previous solar-pumped Nd:YAG laser by a Fresnel lens [13] and nine times more than that from the previous side-pumped Nd:YAG solar laser with 2D-CPC as tertiary concentrator [7].

Table 6.9 Milestone solar lasers with two-dimensional compound parabolic concentrators (2D-CPCs) as tertiary concentrators

Year	Authors [Ref.]	Milestones
Secondary concentrator (image)		Solar laser system parameters
2003	Lando et al. [7]	6.7 W/m^2 solar laser collection efficiency 0.032 W multimode solar laser beam brightness
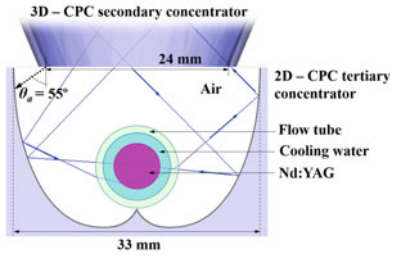		Primary concentrator, effective collection area: WIS ACTA solar concentrator, 6.75 m^2 Secondary concentrator: 3D-CPC **Tertiary concentrator: Dry 2D-CPC** Input aperture: 33×24 mm^2 Active medium: Ø 6.0 mm × 72 mm Nd:YAG
2012	Almeida et al. [23]	0.29 W multimode laser beam brightness
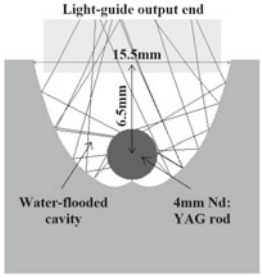		Primary concentrator, effective collection area: PROMES-CNRS parabolic mirror, 2.88 m^2 Secondary concentrator: Rectangular light-guide **Tertiary concentrator: Water-flooded 2D-CPC** Material: silver-coated aluminum foil Reflectivity: 94% Input aperture: 15.5 × 23 mm^2 Active medium: Ø 4.0 mm × 30 mm Nd:YAG

Images adapted from [7] and [23], respectively

6.1.5.3 Conical Nonimaging Concentrator for End-Side-Pumping Scheme

Tertiary concentrators with conical shape have been the most widely used in end-side-pumping solar laser systems since the utilization of this type of concentrators in 2007 by Yabe et al. [9]. Conical reflectors of different dimensions have been attached to different secondary concentrators, such as DTRIC [13], aspheric lenses [17–20] and liquid light guide lenses [14, 21, 22], with the common purpose of increasing the absorption efficiency by enabling multi-pass pumping to the laser medium, as shown in Fig. 6.9.

Most of these tertiary concentrators consisted of a silver-coated aluminum foil of 94% reflectivity [13, 17–22] that covered the inner walls of the conical pump cavity. Except the solar laser schemes with a liquid light guide lens as secondary

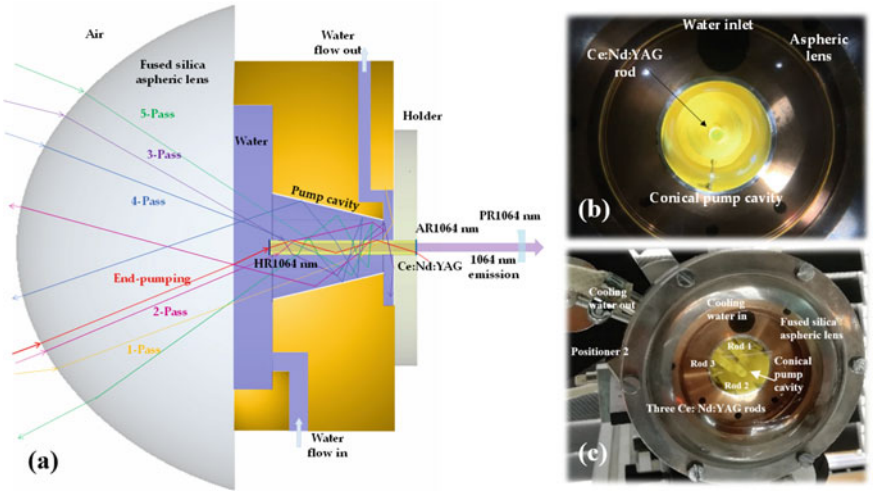

Fig. 6.9 **a** Schematic design and **b** front image of the laser head of the most efficient single-rod Ce:Nd:YAG solar laser with primary parabolic mirror concentrator (adapted from [19]). **c** Front image of the laser head of the most efficient solar laser with three Ce:Nd:YAG rods simultaneously pumped (adapted from [20]). Both solar laser prototypes had an aspheric lens and a conical cavity as secondary and tertiary concentrators, respectively

concentrator, which had a dry tertiary conical cavity [14, 21, 22], the remaining prototypes had a water-flooded conical cavity [18–20], as demonstrated in Fig. 6.9.

The use of the conical cavity as a tertiary concentrator contributed to the most important milestone solar lasers in multimode regime:

- The most efficient Nd:YAG solar lasers with parabolic mirror [17] and Fresnel lens [14] as primary concentrators;
- The most efficient Cr:Nd:YAG solar laser [21];
- The most efficient single-rod Ce:Nd:YAG solar laser with primary parabolic mirror concentrator [19], in Fig. 6.9a, b;
- The most efficient simultaneous solar laser emissions with Ce:Nd:YAG as laser media [20], in Fig. 6.9c.

6.2 Examples of Numerical Analysis of Milestone Solar-Pumped Lasers

In this section, examples of the modelling and numerical analysis of some milestone solar-pumped lasers are given. The design parameters of the solar laser prototypes here presented were first optimized in Zemax® ray-tracing software in non-sequential mode. LASCAD™ laser cavity analysis software was then used to find out the optimum laser resonator parameters.

6.2.1 Zemax® and LASCAD™ Numerical Analysis of 12.3 W Solar Laser with DTIRC Secondary and Conical Tertiary Concentrators

The layout from Zemax® of the 12.3 W solar laser [13] is represented in Fig. 6.10. It was composed of the 0.9 m diameter Fresnel lens primary concentrator, the DTIRC secondary concentrator and the conical tertiary mirror, within which the 4 mm diameter, 25 mm length, 1.0 at.% Nd:YAG laser rod was end-side-pumped. This design configuration contributed to the record in solar laser collection efficiency of 19.3 W/m^2 with Nd:YAG laser medium in 2011 [13].

For modeling the solar laser system, its components are defined by the non-sequential objects of Zemax® in the Non-Sequential Component Editor window, as

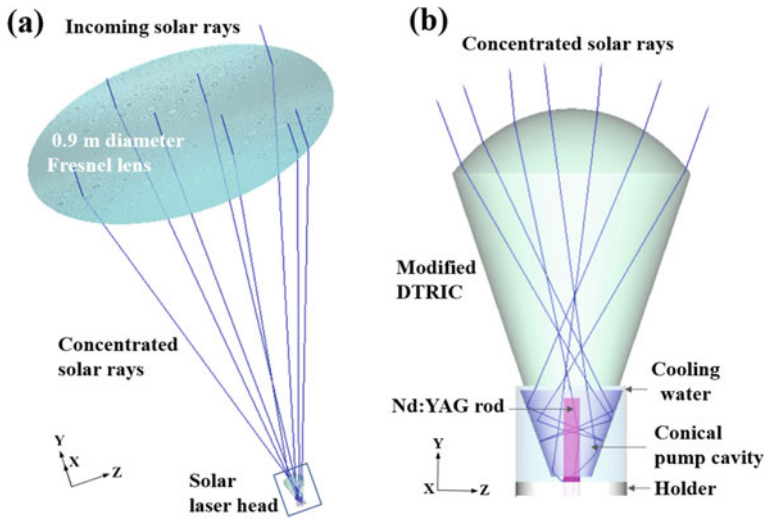

Fig. 6.10 Shaded model layout of the 12.3 W solar laser components [13]: **a** Solar laser system; **b** Laser head with the fused silica modified DTIRC and the conical tertiary mirror

Non-Sequential Component Editor

Edit Solves Tools View Help

	Object Type	Comment	Material
1	Source Ellipse	Solar source	-
2	Fresnel 1	Primary concentrator	PMMA
3	Annular Aspheric Lens	DTIRC (Aspheric lens)	SILICA
4	Cylinder Volume	DTIRC (Conical section)	SILICA
5	Cylinder Volume	Cooling water	WATER
6	Cylinder Pipe	Conical pump cavity	MIRROR
7	Cylinder Volume	Rod holder	MIRROR
8	Detector Volume	Transversal Nd:YAG detector	WATER
9	Detector Volume	Longitudinal Nd:YAG detector	WATER
10	Cylinder Volume	Nd:YAG rod	NDYAG_1.0AT%

Fig. 6.11 List of Zemax® objects in the non-sequential component editor to simulate the components of the 12.3 W solar laser [13]

explained in Sect. 2.1.1.1 of Chap. 2. The list of Zemax® non-sequential objects utilized to design the 12.3 W solar laser system, as well as the respective materials, are given in Fig. 6.11.

For the light source, 22 peak absorption wavelengths of the Nd:YAG material were added in the source wavelength data: 527, 531, 569, 579, 586, 592, 732, 736, 743, 746, 753, 758, 790, 793, 803, 805, 808, 811, 815, 820, 865, and 880 nm. The weight of each wavelength was defined based on its spectral irradiance value in the standard direct solar spectrum for one-and-a-half air mass (AM1.5 D) [51]. The absorption coefficients of each of those wavelengths [52] were defined in the glass catalog data for the 1.0 at.% Nd:YAG (see Sects. 2.1.1.2 and 2.1.1.4 of Chap. 2 for more details). The absorption spectra and wavelength-dependent refractive indices of PMMA, fused silica and water [19] were also included in the glass catalog data to account for absorption losses in those media. For the conical tertiary concentrator, 94% reflectivity was assumed [13], using the coating I.06 in the section Coat/Scatter of the object properties (see Sect. 2.1.1.3 of Chap. 2 for more details).

The X, Y, Z positions and directions (Tilt About X, Y and Z) of the 12.3 W solar laser components in Zemax® space are indicated in Fig. 6.12. The optimal parameters of the 12.3 W solar laser [13] components defined in Zemax® are indicated in Table 6.10.

For the ray-tracing analysis of the absorbed pump power and light distribution within the active medium, detector volumes divided into several voxels were used. The number of analysis rays in the source and the number of voxels in the detectors were adjusted in order to attain accurate results and good image resolution. To estimate the absorbed pump power by the laser rod, the radiation absorbed in each voxel was summed up.

Figure 6.13 shows the absorbed pump flux distributions along seven transversal cross sections and one longitudinal central cross section of the 4 mm diameter, 25 mm length, 1.0 at.% Nd:YAG laser rod. Red color means near maximum pump

Non-Sequential Component Editor

Edit Solves Tools View Help

	Object Type	X Position	Y Position	Z Position	Tilt About X	Tilt About Y	Tilt About Z
1	Source Ellipse	852.100	1988.000	7.000	90.000	0.000	0.000
2	Fresnel 1	852.100	1987.000	7.000	-90.000	180.000	-90.000
3	Annular Aspheric Lens	852.100	793.690	7.000	-90.000	0.000	0.000
4	Cylinder Volume	852.100	740.700	7.000	-90.000	0.000	0.000
5	Cylinder Volume	852.100	716.800	7.000	-90.000	0.000	0.000
6	Cylinder Pipe	852.100	718.100	7.000	-90.000	0.000	0.000
7	Cylinder Volume	852.100	713.050	7.000	-90.000	0.000	0.000
8	Detector Volume	852.100	725.500	7.000	90.000	0.000	0.000
9	Detector Volume	852.100	725.500	7.000	180.000	90.000	0.000
10	Cylinder Volume	852.100	713.000	7.000	-90.000	0.000	0.000

Fig. 6.12 Example of the position and rotation of the 12.3 W solar laser [13] components in Zemax® non-sequential component editor

absorption, whereas blue means little or no absorption. The 4 mm diameter, 25 mm length 1.0 at.% Nd:YAG rod absorbed a maximum power of 48.6 W. Due to the rotational symmetry of the end-side-pumping configuration, a symmetric absorbed pump profile was attained. In the central region of the laser rod, maximum absorbed pump intensity of 0.436 W/mm^3 was detected.

The absorbed pump flux data from the Zemax® analysis was then processed by LASCAD™ to quantify the thermal effects applied in the active medium, previously defined in LASCAD™ (see Sects. 2.2.3 and 2.2.4 of Chap. 2 for more details). A fluorescence lifetime of 230 μs [42] and the mean absorbed and intensity-weighted solar pump wavelength of 660 nm [4] were considered. These values were used for the LASCAD™ numerical analysis of all the solar laser schemes [13, 17, 20, 23]. The reported values of the Nd:YAG stimulated emission cross-section range from 2.7 to 8.8×10^{-19} cm^2 [53]. Therefore, the value of the stimulated emission cross-section used in LASCAD™ depended on the values given by the laser rod manufacturers. In the present case, a stimulated emission cross-section of 2.8×10^{-19} cm^2 was assumed [13].

Based on the information from the Finite Element Analysis (FEA) of LASCAD™, the optimal laser resonator beam parameters, represented in Fig. 6.14, were found.

The high reflection (HR 1064 nm) coating on the end face of the laser rod and the partial reflection (PR 1064 nm) coating on the output mirror, together with the Nd:YAG laser rod, formed the laser resonator. L_{ROD} represents the rod length and L represents the separation length between the antireflection (AR 1064 nm) coating on the end face of the rod and the PR 1064 nm output mirror. In the experiments, maximum laser power of 12.3 W was extracted from a PR mirror with 98% reflectivity (R) and −0.5 m radius of curvature (RoC).

For accurate calculation of the laser power in LASCAD™, a simulation of the laser beam profile, based on the beam propagation method (BPM), was performed to find the correct laser beam width at the output mirror. The following procedure (also explained in Sect. 2.3.2 of Chap. 2) was adopted:

1. Accounting for apertures in the laser resonator (Fig. 6.15).
2. Starting BPM analysis (see Sect. 2.2.5 of Chap. 2 for more details).

Table 6.10 12.3 W solar laser [13] components defined in Zemax® non-sequential component editor

Solar source				
Parameters / Object Type	Analysis Rays	Power (W)	X / Y Half Width (mm)	Gauss Gx / Gy
Source Ellipse	20000000	90.545[1]	450 /450	40000 / 40000[2]

Primary concentrator							
Parameters / Object Type	Radial Height (mm)	X Half-Width (mm)	+Depth/ -Freq	Pitch (deg)	Thickness (mm)	Radius (mm)	Conic
Fresnel 1[3]	450	0	0.3	12	3	640	-0.7

DTIRC (Aspherical lens section)							
Parameters / Object Type	Min / Max Front Aper (mm)	Min / Max Back Apert (mm)	Thick Aper (mm)	Rear Radius (mm)	Rear Conic	Thickness (mm)	Rear r^2
Annular Aspheric Surface	0 / 30	0 / 30	0	-40	0	17	-0.003

DTIRC (Conical section)			
Parameters / Object Type	Front R (mm)	Z Length (mm)	Back R (mm)
Cylinder Volume	12	53	30

Cooling water			
Parameters / Object Type	Front R (mm)	Z Length (mm)	Back R (mm)
Cylinder Volume	14	24	14

Conical pump cavity			
Parameters / Object Type	Front R (mm)	Z Length (mm)	Back R (mm)
Cylinder Pipe	5	22	12

Rod holder			
Parameters / Object Type	Front R (mm)	Z Length (mm)	Back R (mm)
Cylinder Volume	14	3.8	14

Transversal detector		
Parameters / Object Type	X / Y / Z Half Width (mm)	# X / # Y / # Z Pixels
Detector Volume	2 / 2 / 12.5	80 / 80 / 25

Longitudinal detector		
Parameters / Object Type	X / Y / Z Half Width (mm)	# X / # Y / # Z Pixels
Detector Volume	2 / 12.5 / 2	40 / 250 / 5

1.0 at.% Nd:YAG rod			
Parameters / Object Type	Front R (mm)	Z Length (mm)	Back R (mm)
Cylinder Volume	2	25	2

[1] The source power was calculated by using Eq. (2.4) from Chap. 2: $P_{source,\,Nd:YAG} = A_{ef} \times I_s \times \eta_{overlap,Nd3+}$.

$A_{ef} = 0.636\ m^2$ is the effective collection area of primary Fresnel lens concentrator with 0.9 m in diameter. I_s is the solar irradiance, whose reported value was 890 W/m^2 [13]. $\eta_{overlap,Nd3+}$ is the spectral overlap of the Nd^{3+} absorption spectrum with solar emission spectrum, which is 16% (See Sect. 4.3.2 of Chap. 4).

[2] G_x and G_y parameters define the Gaussian distribution of the solar rays in X and Y axes. $G_x = G_y = 40{,}000$ were defined to account for the apparent half angle of 0.27° subtended by the Sun on the Earth surface.

[3] The parameters of a Fresnel lens are described in Sect. 5.2 of Chap. 5.

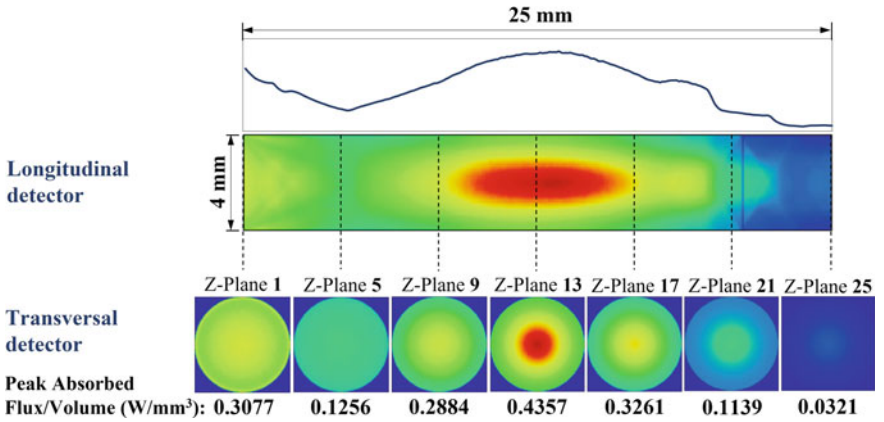

Fig. 6.13 Absorbed pump flux distributions along the longitudinal central cross-section and seven transversal cross sections of the 4.0 mm diameter, 25 mm length, 1.0 at.% Nd:YAG rod of the 12.3 W solar laser [13], obtained through Zemax® numerical analysis

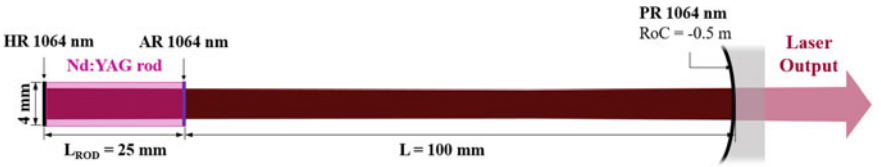

Fig. 6.14 Schematic design of the 12.3 W solar laser resonator [13]. The image is not at scale

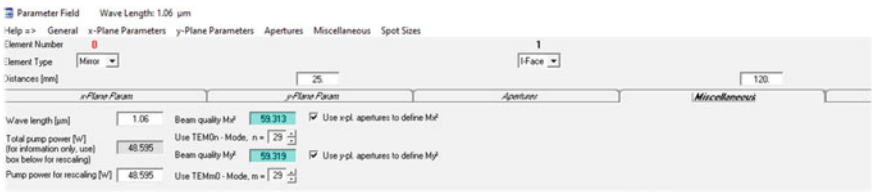

Fig. 6.15 Accounting for apertures in the 12.3 W solar laser resonator [13] in LASCAD™ *Parameter Field*

3. Finding the beam waist, W, of the laser beam profile. It is calculated by multiplying the half width of the BPM computational window (4080 µm) by the quotient between the number of squares of the grid representing the maximum oscillating laser modes in X, Y directions (~20 squares) and the total number of squares in the grid (42 squares), illustrated in Fig. 6.16.
4. Modifying the M_x^2, M_y^2 factors in the *Parameter Field* window until the spot sizes are coincident with the beam waist from BPM analysis, as illustrated in Fig. 6.17.

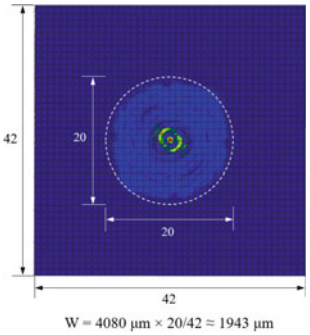

Fig. 6.16 Top-view of the 12.3 W solar laser beam profile from BPM analysis of LASCAD™

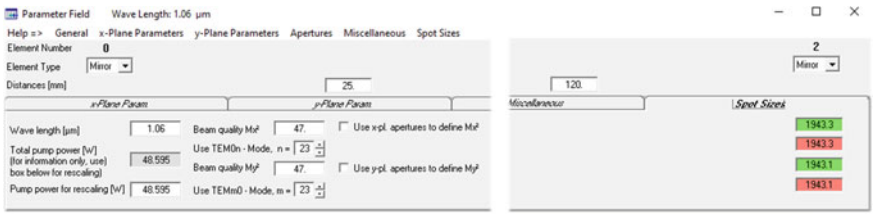

Fig. 6.17 Correction of the beam waist in LASCAD™ *Parameter Field* by changing the M_x^2, M_y^2 factors

5. Calculating multimode laser power in the *Laser Output Power* window, with account for apertures unchecked, as indicated in Fig. 6.18.

For accurate calculation of the laser power, the total roundtrip losses (given by Eq. (2.7) in Chap. 2) must be defined in this window. By considering a typical absorption and scattering loss α of 0.002 cm^{-1}, a two-way loss of 1% was found for the 4.0 mm diameter, 1.0 at.% Nd:YAG rod with 2.5 cm length. Assuming 0.4% of imperfect HR and AR coatings, the total round-trip loss increased to 1.4%. The diffraction losses depend on rod diameter, resonator length and radius of curvature (RoC) of the resonator mirrors. For the present solar laser resonator, 0.04% of diffraction losses was calculated by LASCAD™ BPM analysis. A total round-trip loss of 1.404% was hence defined in the *Laser Output Power* window (Fig. 6.18).

Based on this procedure, 12.26 W was numerically obtained from an output mirror with R = 98% and RoC = −0.5 m, matching well with the experimental solar laser power value with similar PR mirror characteristics [13].

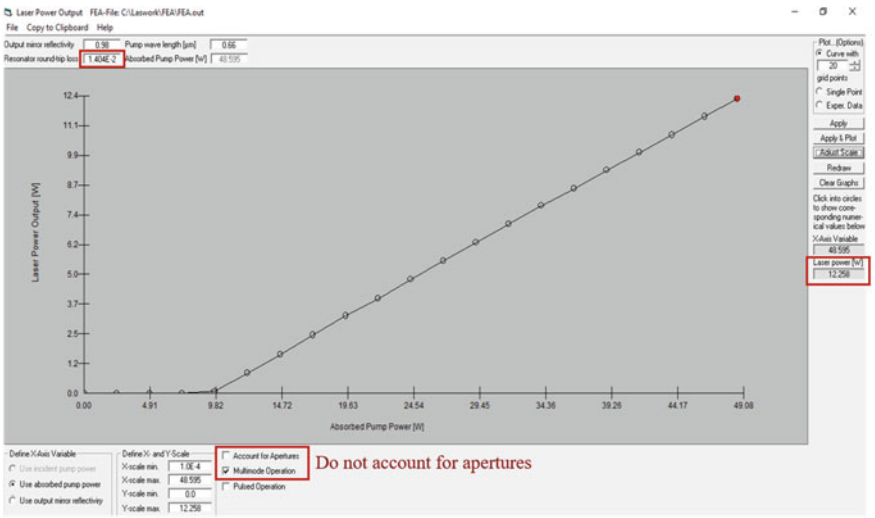

Fig. 6.18 Numerically calculated laser output power in LASCAD™ as a function of the absorbed solar power, for the output mirror reflectivity (R) of 98%

6.2.2 Zemax® and LASCAD™ Numerical Analysis of 28 W Solar Laser with a Fused Silica Light Guide Homogenizer and a 2D-CPC Pump Cavity

The layout from Zemax® of the 28 W solar laser [23] is represented in Fig. 6.19. The fused silica light guide of 14 mm × 22 mm rectangular cross-section was used to both transmit and homogenize, through total internal reflection, the concentrated solar radiation from the focal zone of the 2.0 m diameter parabolic mirror to the entrance aperture of a modified 2D-CPC water-flooded pump cavity, within which the 4 mm diameter, 30 mm length, 1.1 at.% Nd:YAG laser rod was side-pumped. This design configuration contributed to record solar laser brightness figure of merit of 0.29 W in 2012 [23].

The list of Zemax® non-sequential objects utilized to design the 28 W solar laser components, as well as the respective materials, are given in Fig. 6.20.

The X, Y, Z positions and directions (Tilt about X, Y and Z) of the 28 W solar laser components in Zemax® space are indicated in Fig. 6.21.

The optimal parameters of the 28 W solar laser [23] components defined in Zemax® are indicated in Table 6.11.

All the solar laser components were parameterized using objects existent in the Zemax® list, except for the 2D-CPC pump cavity, which was designed in AUTOCAD and imported to Zemax® (see Sect. 2.1.3.2 of Chap. 2 for more details). The solar wavelength data and the media materials were defined in the same way as in the previous example in Sect. 6.2.1. For the primary concentrator, 64% reflectivity was assumed, which accounted for the absorption losses in both the heliostat and parabolic

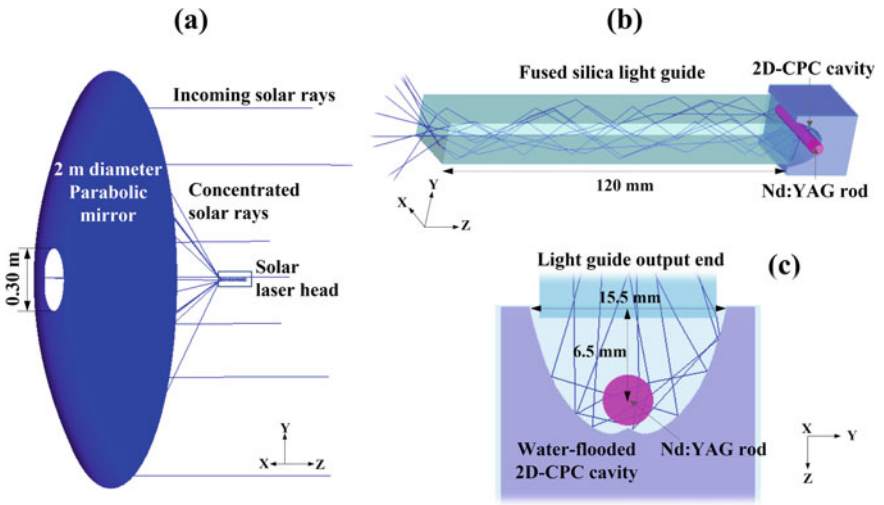

Fig. 6.19 Shaded model layout of the 28 W solar laser components [23]: **a** Solar laser system; **b** Laser head with the fused silica light guide homogenizer and the 2D-CPC pump cavity; **c** Detailed view of the modified 2D-CPC pump cavity

Non-Sequential Component Editor

Edit Solves Tools View Help

	Object Type	Comment	Material
1	Source Ellipse	Solar source	-
2	Aspheric Surface	Primary concentrator	MIRROR
3	Rectangular Volume	Cooling water	WATER
4	Rectangular Volume	Rectangular light guide	SILICA
5	Detector Volume	Transversal Nd:YAG detector	WATER
6	Detector Volume	Longitudinal Nd:YAG detector	WATER
7	Cylinder Volume	Nd:YAG rod	NDYAG_1.1AT%
8	CAD Part: STL	Modified 2D-CPC.STL	MIRROR

Fig. 6.20 List of Zemax® objects in the non-sequential component editor to simulate the components of the 28 W solar laser [23]

Non-Sequential Component Editor

Edit Solves Tools View Help

	Object Type	X Position	Y Position	Z Position	Tilt About X	Tilt About Y	Tilt About Z
1	Source Ellipse	0.000	0.000	1310.00	180.000	0.000	0.000
2	Aspheric Surface	0.000	0.000	0.000	0.000	0.000	0.000
3	Rectangular Volume	-11.500	0.000	979.000	90.000	90.000	0.000
4	Rectangular Volume	0.000	0.000	849.500	0.000	0.000	90.000
5	Detector Volume	0.000	0.000	976.000	-90.000	90.000	0.000
6	Detector Volume	0.000	0.000	976.000	0.000	0.000	90.000
7	Cylinder Volume	-15.000	0.000	976.000	0.000	90.000	0.000
8	CAD Part: STL	13.500	12.050	991.500	180.000	0.000	90.000

Fig. 6.21 Example of the position and rotation of the 28 W solar laser [23] components in Zemax® non-sequential component editor

Table 6.11 28 W solar laser [23] components defined in Zemax® non-sequential component editor

Solar source				
Parameters / Object Type	Power (W)	X / Y Half Width (mm)	Gauss Gx / Gy	Minimum X / Y Half Width (mm)
Source Ellipse	456.2[1]	1000 /1000	40000 / 40000	150 / 150[2]
Primary concentrator				
Parameters / Object Type	Radius (mm)	Conic	Max / Min Aper (mm)	
Aspheric Surface[3]	1700	-1	1000 / 150	
Cooling water				
Parameters / Object Type	X1 / Y1 Half Width (mm)	Z Length (mm)	X2 / Y2 Half Width (mm)	
Rectangular Volume	10.5 / 10.5	23	10.5 / 10.5	
Rectangular light guide				
Parameters / Object Type	X1 / Y1 Half Width (mm)	Z Length (mm)	X2 / Y2 Half Width (mm)	
Rectangular Volume	7 / 11	120	7 / 11	
Transversal detector				
Parameters / Object Type	X / Y / Z Half Width (mm)	# X / # Y / # Z Pixels		
Detector Volume	2 / 2 / 15	80 / 80 / 30		
Longitudinal detector				
Parameters / Object Type	X / Y / Z Half Width (mm)	# X / # Y / # Z Pixels		
Detector Volume	2 / 15 / 2	40 / 300 / 5		
1.1 at.% Nd:YAG rod				
Parameters / Object Type	Front R (mm)	Z Length (mm)	Back R (mm)	
Cylinder Volume	2	30	2	
Modified 2D-CPC				
Parameters / Object Type	Scale	Is Volume?		
CAD Part: STL	1	1		

[1] For the 28 W solar laser, an effective collection area of 2.88 m^2 and maximum direct solar irradiance of 990 W/m^2 were measured [23]. Therefore, $P_{source,\,Nd:YAG} = 2.88\ m^2 \times 990\ W.m^{-2} \times 0.16 = 456.2$ W was calculated.

[2] Minimum X/Y Half Width of 150 mm was defined in the source, since the solar rays from this region are not collected by the primary parabolic mirror, which has a central hole of 300 mm in diameter (Fig. 6.19).

[3] The parameters of a parabolic mirror are described in Sect. 5.1 of Chap. 5.

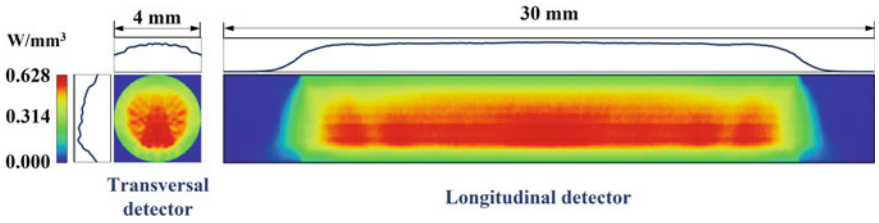

Fig. 6.22 Absorbed pump flux distributions along the central transversal and longitudinal cross-sections of the 4.0 mm diameter, 30 mm length, 1.1 at.% Nd:YAG rod of the 28 W solar laser [23], obtained through Zemax® numerical analysis

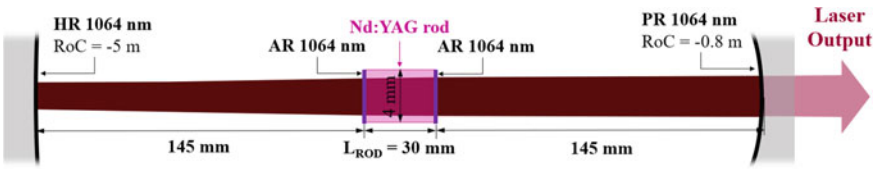

Fig. 6.23 Schematic design of the 28 W solar laser resonator [23]. The image is not at scale

mirrors [23]. Therefore, the coating I.36 was defined in the section Coat/Scatter of the object properties. For the 2D-CPC, 94% reflectivity (I.06) was considered [23].

The absorbed pump flux distributions along one central transversal cross section and one central longitudinal cross section of the 4 mm diameter, 30 mm length, 1.1 at.% Nd:YAG laser rod is shown in Fig. 6.22. The rectangular fused silica light guide behaved like a beam homogenizer by transforming the near-Gaussian profile of the concentrated light spot from the parabolic mirror, incident on its input face, into a uniform rectangular light distribution at its output end [23], enabling a homogeneous absorbed pump light distribution along the Nd:YAG laser rod, as demonstrated in Fig. 6.22. This helps to reduce the thermal induced effects in the laser rod and meliorate the laser beam quality. Therefore, the output laser beam brightness can be higher compared to solar lasers with no light homogenizer [7, 13].

The modified 2D-CPC also played a crucial role in improving the absorbed pump distribution by coupling efficiently the pump rays into the center of the laser rod, as shown by the transversal cross-section (Fig. 6.22).

A symmetric concave-concave laser resonator of 320 mm length was adopted in this case, as illustrated in Fig. 6.23. The HR coated mirror with RoC =–5 m, the Nd:YAG laser rod and the PR mirror formed the laser resonator. The PR mirror with R = 94% and RoC = –0.8 m led to the maximum measured laser output power of 27.7 W [23].

In the present case, a stimulated emission cross-section of 2.8×10^{-19} cm^2 was assumed for LASCAD™ analysis [23]. Based on the procedure described in 6.2.1, multimode laser output power of 29.48 W was numerically extracted from the PR mirror with R = 94% and RoC = –0.8 m at maximum absorbed pump power of 121.2 W, as shown in Fig. 6.24, which agrees reasonably well with the experimental value [23].

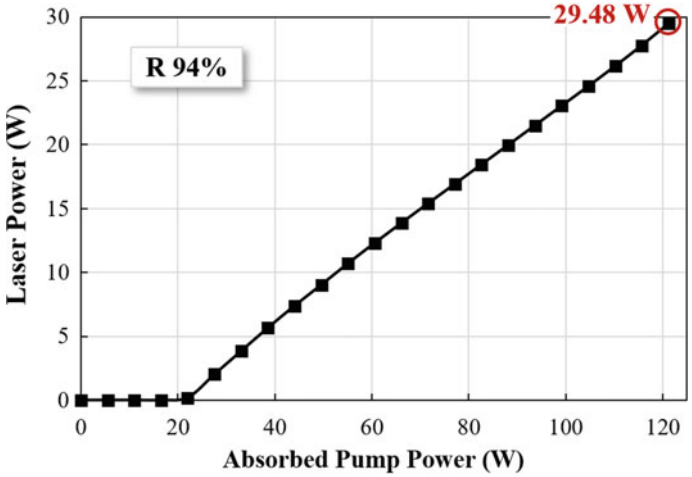

Fig. 6.24 Numerically calculated laser output power from the 4 mm diameter, 30 mm length, 1.1 at.% Nd:YAG rod in LASCAD™ as a function of the absorbed solar power, for the output mirror reflectivity (R) of 94%

6.2.3 Zemax® and LASCAD™ Numerical Analysis of Simultaneous Solar Laser Emissions from Three Ce:Nd:YAG Laser Rods Within a Single Pump Cavity

The design of the 16.5 W solar laser [20], composed of the 0.8 m diameter parabolic mirror as primary concentrator, the secondary aspheric lens and the conical tertiary mirror, within which the three 2.5 mm diameter, 25 mm length, 0.1 at.% Ce: 1.1 at.% Nd:YAG laser rods were end-side-pumped, is represented in Fig. 6.25. This design configuration contributed to the current records in solar-to-laser conversion, collection and slope efficiencies of 4.64%, 41.25 W/m^2 and 7.64%, respectively [20].

The list of Zemax® non-sequential objects utilized to design the 16.5 W three-rod Ce:Nd:YAG solar laser system, as well as the respective materials, are given in Fig. 6.26.

In this case, two sources were defined. Source 1 represents the relevant solar emission wavelengths that overlaps with the Nd^{3+} ion absorption spectrum, as well as those correspondent to the Ce^{3+} non-radiative transfer to Nd^{3+} by quantum cutting down conversion. Source 2 is related to the solar wavelengths corresponding to the radiative transfer from Ce^{3+} to Nd^{3+} (see Sect. 4.5 of Chap. 4 for more details). For such, the wavelength data was defined in two spectrum files, one for each source. The spectrum file for source 1 is similar to the wavelength data of the previous examples, i.e., with 22 peak absorption wavelengths of Nd^{3+}, whose weight is decided by the solar spectral irradiance value. For source 2, six wavelengths were defined in the spectrum file, corresponding to the most relevant Nd^{3+} peak absorption wavelengths that matches with the Ce^{3+} fluorescence spectrum: 527, 531, 569, 579, 586, and

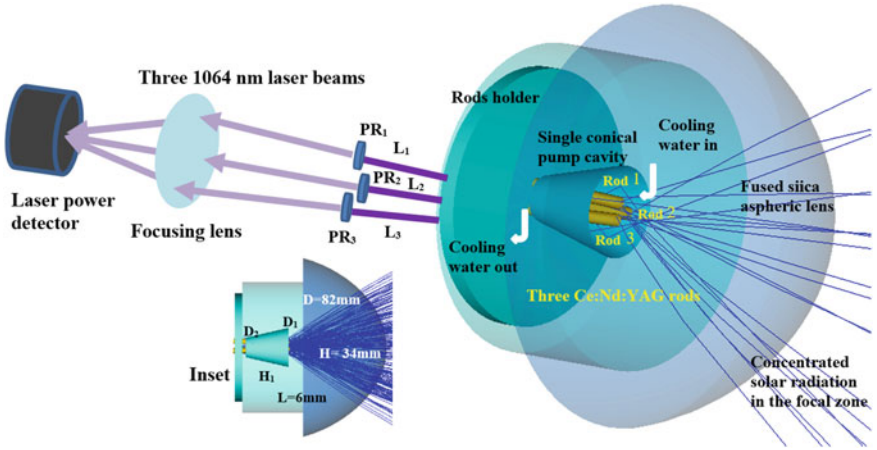

Fig. 6.25 Design of the three-rod Ce: Nd:YAG laser head, composed of the fused silica aspheric lens, the conical pump cavity and the Ce:Nd:YAG rods, actively cooled by water [20]

Non-Sequential Component Editor

Edit Solves Tools View Help

	Object Type	Comment	Material
1	Source Ellipse	Nd absorption spectrum	-
2	Source Ellipse	Ce fluorescence spectrum	-
3	Aspheric Surface	Primary concentrator	MIRROR
4	Annular Aspheric Lens	Aspheric lens	SILICA
5	Cylinder Volume	Cooling water	WATER
6	Cylinder Volume	3-Rod holder	MIRROR
7	Detector Volume	Transversal rod 1 detector	WATER
8	Cylinder Volume	Rod 1	NDYAG_1.1AT%
9	Detector Volume	Transversal rod 2 detector	WATER
10	Cylinder Volume	Rod 2	NDYAG_1.1AT%
11	Detector Volume	Transversal rod 3 detector	WATER
12	Cylinder Volume	Rod 3	NDYAG_1.1AT%
13	Cylinder Pipe	Conical pump cavity	MIRROR

Fig. 6.26 List of Zemax® objects in the Non-Sequential Component Editor to simulate the components of the most efficient solar laser from three Ce:Nd:YAG rods [20]

592 nm [19, 20]. In this case, the weight of each wavelength was defined based on its spectral irradiance in the Ce^{3+} fluorescence spectrum [54]. It is worth noting that the Nd^{3+} material programmed in the glass catalog data in Zemax® software can also be used to represent the Ce:Nd:YAG material. This is possible thanks to the energy transfer mechanism from Ce^{3+} to Nd^{3+} ions in Ce:Nd:YAG medium.

For the primary concentrator, 75% reflectivity was assumed, which accounted for the absorption losses in both the heliostat and parabolic mirrors [20]. Therefore, the

Non-Sequential Component Editor

Edit Solves Tools View Help

	Object Type	X Position	Y Position	Z Position	Tilt About X	Tilt About Y	Tilt About Z
1	Source Ellipse	852.100	855.900	1000.000	180.000	0.000	90.000
2	Source Ellipse	852.100	855.900	1000.000	180.000	0.000	90.000
3	Aspheric Surface	852.100	855.900	-648.000	0.000	0.000	0.000
4	Annular Aspheric Lens	852.100	855.900	0.000	180.000	0.000	0.000
5	Cylinder Volume	852.100	855.900	0.000	0.000	0.000	0.000
6	Cylinder Volume	852.100	855.900	27.000	0.000	0.000	0.000
7	Detector Volume	852.100	853.481	18.488	2.400	0.000	45.000
8	Cylinder Volume	852.100	854.005	6.000	2.400	0.000	0.000
9	Detector Volume	854.207	857.087	18.488	-1.200	2.078	75.000
10	Cylinder Volume	853.754	856.825	6.000	-1.200	2.078	0.000
11	Detector Volume	849.994	857.087	18.488	-1.200	-2.078	15.000
12	Cylinder Volume	850.446	856.825	6.000	-1.200	-2.078	0.000
13	Cylinder Pipe	852.100	855.900	6.500	0.000	0.000	0.000

Fig. 6.27 Example of the position and rotation of the most efficient solar laser emissions from three Ce:Nd:YAG rods [20] in Zemax® Non-Sequential Component Editor

coating I.25 was defined in the section Coat/Scatter of the object properties. For the conical pump cavity, 94% reflectivity (I.06) was considered [20].

The X, Y, Z positions and directions (Tilt about X, Y and Z) of the simultaneous 16.5 W solar laser system in Zemax® space are indicated in Fig. 6.27. The optimal parameters of the simultaneous 16.5 W solar laser [20] components defined in Zemax® are indicated in Table 6.12.

The absorbed pump flux distributions along five transversal cross-sections of the three Ce:Nd:YAG rods are given in Fig. 6.28. Non-uniform distributions along the end-side-pumped laser rods were numerically calculated with a peak absorbed pump flux of 0.68 W/mm^3. Nevertheless, these were the distributions that ensured the maximum absorbed solar power by the three rods.

In the present case, a stimulated emission cross-section of 2.8×10^{-19} cm^2 was assumed for LASCAD™ analysis [20]. The laser resonator configuration for maximum multimode solar laser extraction from one of the three Ce:Nd:YAG laser rods is illustrated in Fig. 6.29, which is similar for all the three laser rods. PR mirrors with 97.5% reflectivity and RoC = –0.5 m were adopted. Each one was optically aligned with its respective laser rod 15 mm away from the AR1064 nm output face.

With this laser resonator configuration, maximum multimode laser power of 5.64 W was numerically calculated for each one of the Ce:Nd:YAG rods, as shown in Fig. 6.30, corresponding to 16.92 W (3×5.64 W) total multimode solar power, which is close to the experimental value of 16.5 W.

Table 6.12 Components of the most efficient solar laser emissions from three Ce:Nd:YAG rods [20] defined in non-sequential component editor

Solar source (Nd^{3+} absorption spectrum)			
Parameters / Object Type	Power (W)	X / Y Half Width (mm)	Gauss Gx / Gy
Source Ellipse	95.15[1]	400 / 400	40000 / 40000
Solar source (Ce^{3+} fluorescence spectrum)			
Parameters / Object Type	Power (W)	X / Y Half Width (mm)	Gauss Gx / Gy
Source Ellipse	16.35[2]	400 / 400	40000 / 40000

Primary concentrator			
Parameters / Object Type	Radius (mm)	Conic	Max / Min Aper (mm)
Aspheric Surface	1320	-1	410 / 0

Aspherical lens							
Parameters / Object Type	Min / Max Front Aper (mm)	Min / Max Back Apert (mm)	Thick Aper (mm)	Rear Radius (mm)	Rear Conic	Thickness (mm)	Rear r^2
Annular Aspheric Surface	0 / 41	0 / 41	0	-43	0	37	-0.004

Cooling water			
Parameters / Object Type	Front R (mm)	Z Length (mm)	Back R (mm)
Cylinder Volume	35	27	35

3-Rod holder			
Parameters / Object Type	Front R (mm)	Z Length (mm)	Back R (mm)
Cylinder Volume	20	3.5	20

Transversal detectors of Rods 1, 2 and 3		
Parameters / Object Type	X / Y / Z Half Width (mm)	# X / # Y / # Z Pixels
Detector Volume	1.25 / 1.25 / 12.5	50 / 50 / 25

Ce:Nd:YAG laser rods			
Parameters / Object Type	Front R (mm)	Z Length (mm)	Back R (mm)
Cylinder Volume	1.25	25	1.25

Conical pump cavity			
Parameters / Object Type	Front R (mm)	Z Length (mm)	Back R (mm)
Cylinder Pipe	9	19	4.5

[1] The source1 power was calculated by using Eq. (2.5) from Chap. 2: $P_{source1,\,Ce:Nd:YAG} = A_{ef} \times I_s \times (\eta_{overlap,Nd3+} + \eta_{overlap,Ce3+} \times \eta_{NR:Ce3+\rightarrow Nd3+})$, where $\eta_{overlap,Ce3+} = 15.3\%$ is the spectral overlap of the Ce^{3+} absorption spectrum with the solar emission spectrum and $\eta_{NR:Ce3+\rightarrow Nd3+} = 70\%$ is the percentage of absorbed energy by Ce^{3+} ions that could be transferred to Nd^{3+} non-radiatively [19, 20]. Since $A_{ef} = 0.4$ m^2 and $I_s = 890$ W/m^2 were accounted [20], then $P_{source1,\,Ce:Nd:YAG} = 95.15$ W was calculated.

[2] The source2 power was calculated by using Eq. (2.6) from Chap. 2: $P_{source2,\,Ce:Nd:YAG} = A_{ef} \times I_s \times \eta_{overlap,Ce3+} \times \eta_{R:Ce3+\rightarrow Nd3+}$, where $\eta_{R:Ce3+\rightarrow Nd3+} = 30\%$ is the percentage of absorbed energy by Ce^{3+} ions that could be transferred to Nd^{3+} radiatively [19, 20]. $P_{source1,\,Ce:Nd:YAG} = 16.35$ W was hence calculated.

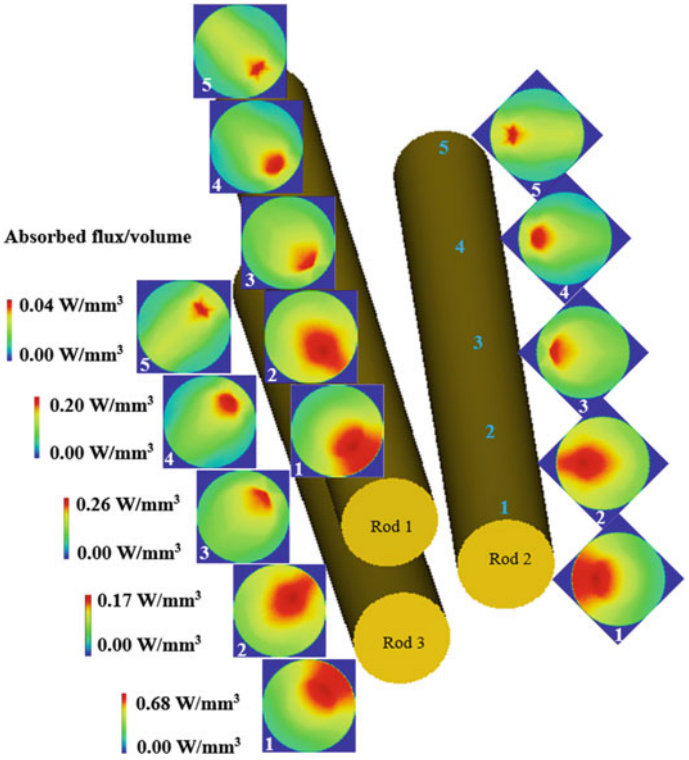

Fig. 6.28 Absorbed pump-flux distributions along five transversal cross-sections (1, 2, 3, 4 and 5) of the three 2.5 mm diameter, 25 mm length Ce:Nd:YAG rods, obtained through Zemax® numerical analysis [20]

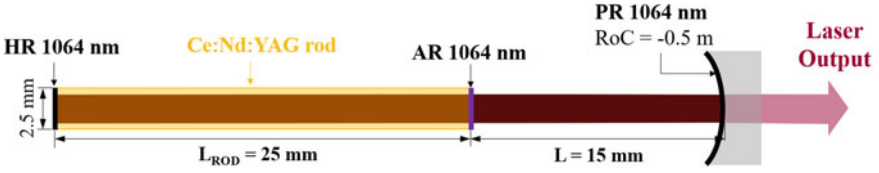

Fig. 6.29 Schematic design of the laser resonator for multimode solar laser extraction from one of the three Ce:Nd:YAG rods [20]

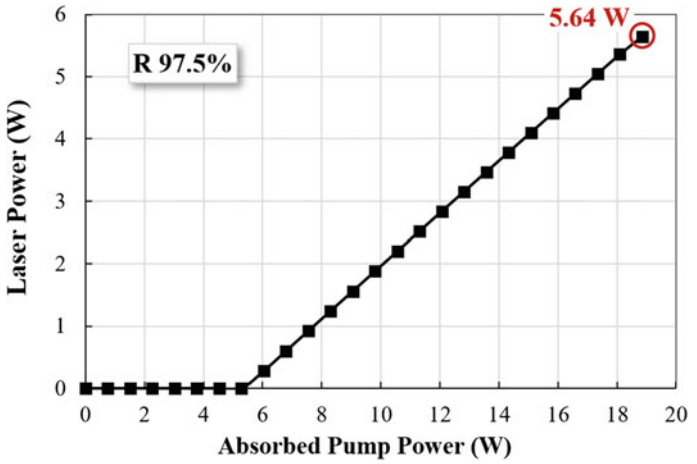

Fig. 6.30 Numerically calculated laser output power from one of the three Ce:Nd:YAG rods in LASCAD™ as a function of the absorbed solar power, for the output mirror reflectivity (R) of 97.5%

References

1. Simpson, G.R.: Continuous sun-pumped room temperature glass laser operation. Appl. Opt. **3**(6), 783–784 (1964). https://doi.org/10.1364/AO.3.000783
2. Young, C.G.: A sun-pumped cw one-watt laser. Appl. Opt. **5**(6), 993–997 (1966). https://doi.org/10.1364/AO.5.000993
3. Arashi, H., Oka, Y., Sasahara, N., Kaimai, A., Ishigame, M.: A solar-pumped cw 18 W Nd:YAG laser. Jpn. J. Appl. Phys. **23**(Part 1, No. 8), 1051–1053 (1984). https://doi.org/10.1143/jjap.23.1051
4. Weksler, M., Shwartz, J.: Solar-pumped solid-state lasers. IEEE J. Quantum Electron. **24**(6), 1222–1228 (1988). https://doi.org/10.1109/3.247
5. Benmair, R.M.J., Kagan, J., Kalisky, Y., Noter, Y., Oron, M., Shimony, Y., Yogev, A.: Solar-pumped Er, Tm, Ho:YAG laser. Opt. Lett. **15**(1), 36–38 (1990). https://doi.org/10.1364/OL.15.000036
6. Krupkin, V., Kagan, J., Yogev, A.: Nonimaging optics and solar laser pumping at the Weizmann Institute, vol. 2016. SPIE's 1993 International Symposium on Optics, Imaging, and Instrumentation. SPIE, (1993). https://doi.org/10.1117/12.161945
7. Lando, M., Kagan, J., Linyekin, B., Dobrusin, V.: A solar-pumped Nd:YAG laser in the high collection efficiency regime. Optics Communications **222**(1), 371–381 (2003). https://doi.org/10.1016/S0030-4018(03)01601-8
8. Lando, M., Shimony, Y., Benmair, R.M.J., Abramovich, D., Krupkin, V., Yogev, A.: Visible solar-pumped lasers. Opt. Mater. **13**(1), 111–115 (1999). https://doi.org/10.1016/S0925-3467(99)00019-1
9. Yabe, T., Ohkubo, T., Uchida, S., Yoshida, K., Nakatsuka, M., Funatsu, T., Mabuti, A., Oyama, A., Nakagawa, K., Oishi, T., Daito, K., Behgol, B., Nakayama, Y., Yoshida, M., Motokoshi, S., Sato, Y., Baasandash, C.: High-efficiency and economical solar-energy-pumped laser with Fresnel lens and chromium codoped laser medium. Appl. Phys. Lett. **90**(26), 261120 (2007). https://doi.org/10.1063/1.2753119
10. Dinh, T.H., Ohkubo, T., Yabe, T., Kuboyama, H.: 120 watt continuous wave solar-pumped laser with a liquid light-guide lens and an Nd:YAG rod. Opt. Lett. **37**(13), 2670–2672 (2012). https://doi.org/10.1364/OL.37.002670

11. Dinh, T.H., Ohkubo, T., Yabe, T.: Development of solar concentrators for high-power solar-pumped lasers. **53**, 2711 (2014). https://doi.org/10.1364/ao.53.002711
12. Xu, P., Yang, S., Zhao, C., Guan, Z., Wang, H., Zhang, Y., Zhang, H., He, T.: High-efficiency solar-pumped laser with a grooved Nd:YAG rod. Appl. Opt. **53**(18), 3941–3944 (2014). https://doi.org/10.1364/AO.53.003941
13. Liang, D., Almeida, J.: Highly efficient solar-pumped Nd:YAG laser. Opt. Express **19**(27), 26399–26405 (2011). https://doi.org/10.1364/OE.19.026399
14. Guan, Z., Zhao, C., Li, J., He, D., Zhang, H.: 32.1 W/m^2 continuous wave solar-pumped laser with a bonding Nd:YAG/YAG rod and a Fresnel lens. Opt. Laser Technol. **107**, 158–161 (2018). https://doi.org/10.1016/j.optlastec.2018.05.039
15. Liang, D., Vistas, C.R., Almeida, J., Tiburcio, B.D., Garcia, D.: Side-pumped continuous-wave Nd:YAG solar laser with 5.4% slope efficiency. Solar Energy Mater. Solar Cells **192**, 147–153 (2019). https://doi.org/10.1016/j.solmat.2018.12.029
16. Vistas, C., Liang, D., Almeida, J., Tibúrcio, B., Garcia, D., Catela, M., Costa, H., Guillot, E.: Ce:Nd:YAG side-pumped solar laser. J. Photonics Energy **11**(1), 018001 (2021). https://doi.org/10.1117/1.JPE.11.018001
17. Liang, D., Almeida, J., Vistas, C.R., Guillot, E.: Solar-pumped Nd:YAG laser with 31.5W/m^2 multimode and 7.9W/m^2 TEM$_{00}$-mode collection efficiencies. Solar Energy Mater. Solar Cells **159**, 435–439 (2017). https://doi.org/10.1016/j.solmat.2016.09.048
18. Liang, D., Almeida, J., Garcia, D., Tibúrcio, B.D., Guillot, E., Vistas, C.R.: Simultaneous solar laser emissions from three Nd:YAG rods within a single pump cavity. Sol. Energy **199**, 192–197 (2020). https://doi.org/10.1016/j.solener.2020.02.027
19. Garcia, D., Liang, D., Vistas, C.R., Costa, H., Catela, M., Tibúrcio, B.D., Almeida, J.: Ce:Nd:YAG Solar Laser with 4.5% solar-to-laser conversion efficiency. **15**(14), 5292 (2022). https://doi.org/10.3390/en15145292
20. Liang, D., Vistas, C.R., Garcia, D., Tibúrcio, B.D., Catela, M., Costa, H., Guillot, E., Almeida, J.: Most efficient simultaneous solar laser emissions from three Ce:Nd:YAG rods within a single pump cavity. Sol. Energy Mater. Sol. Cells **246**, 111921 (2022). https://doi.org/10.1016/j.solmat.2022.111921
21. Liang, D., Vistas, C.R., Tibúrcio, B.D., Almeida, J.: Solar-pumped Cr:Nd:YAG ceramic laser with 6.7% slope efficiency. Solar Energy Mater. Solar Cells **185**, 75–79 (2018). https://doi.org/10.1016/j.solmat.2018.05.020
22. Vistas, C.R., Liang, D., Garcia, D., Almeida, J., Tibúrcio, B.D., Guillot, E.: Ce:Nd:YAG continuous-wave solar-pumped laser. Optik **207**, 163795 (2020). https://doi.org/10.1016/j.ijleo.2019.163795
23. Almeida, J., Liang, D., Guillot, E.: Improvement in solar-pumped Nd:YAG laser beam brightness. Opt. Laser Technol. **44**(7), 2115–2119 (2012). https://doi.org/10.1016/j.optlastec.2012.03.017
24. Almeida, J., Liang, D., Garcia, D., Tibúrcio, B.D., Costa, H., Catela, M., Guillot, E., Vistas, C.R.: 40 W Continuous wave Ce:Nd:YAG solar laser through a fused silica light guide. **15**(11), 3998 (2022). https://doi.org/10.3390/en15113998
25. Kalogirou, S.A.: Solar thermal collectors and applications. Prog. Energy Combust. Sci. **30**(3), 231–295 (2004). https://doi.org/10.1016/j.pecs.2004.02.001
26. Mousazadeh, H., Keyhani, A., Javadi, A., Mobli, H., Abrinia, K., Sharifi, A.: A review of principle and sun-tracking methods for maximizing solar systems output. Renew. Sustain. Energy Rev. **13**(8), 1800–1818 (2009). https://doi.org/10.1016/j.rser.2009.01.022
27. Reddy, D.S., Khan, M.K.: Stationary point focus solar concentrators—a review. **46**(5), 5678–5702 (2022). https://doi.org/10.1002/er.7612
28. Bouzakri, H., Abbou, A., Tijani, K., Abousserhane, Z.: Biaxial equatorial solar tracker with high precision and low consumption: modelling and realization. Int. J. Photoenergy **2021**, 6679576 (2021). https://doi.org/10.1155/2021/6679576
29. Chang, C.: 5—Tracking solar collection technologies for solar heating and cooling systems. In: Wang, R.Z., Ge, T.S. (eds.) Advances in Solar Heating and Cooling. pp. 81–93. Woodhead Publishing, (2016). https://doi.org/10.1016/B978-0-08-100301-5.00005-9

30. Grigoriev, V., Milidonis, K., Blanco, M.: Sun tracking by heliostats with arbitrary orientation of primary and secondary axes. Sol. Energy **207**, 1384–1389 (2020). https://doi.org/10.1016/j.solener.2020.07.086
31. Lando, M., Kagan, J., Linyekin, B., Sverdalov, L., Pecheny, G., Achiam, Y.: An astigmatic corrected target-aligned solar concentrator. Opt. Commun. **180**(1), 127–132 (2000). https://doi.org/10.1016/S0030-4018(00)00686-6
32. The Canadian Institute for the Energies and Applied Research. https://wis-wander.weizmann.ac.il/content/harnessing-sun (1997)
33. Arashi, H., Cooke, D., Naito, H.: Fivefold increase in solar laser output with a nonimaging concentrator. Jpn. J. Appl. Phys., **34**(Part 1, No. 9A), 4795–4798 (1995). https://doi.org/10.1143/jjap.34.4795
34. Levitan, R., Rosin, H., Levy, M.: Chemical reactions in a solar furnace—direct heating of the reactor in a tubular receiver. Sol. Energy **42**(3), 267–272 (1989). https://doi.org/10.1016/0038-092X(89)90017-0
35. Epstein, M., Vishnevetsky, I., Segal, A., Rubin, R., Lieberman, D.: Research and development in the solar research facilities unit of the weizmann institute of science: past, present, and future. The Int. J. Environ. Sustain. **9**, 97–116 (2014). https://doi.org/10.18848/2325-1077/CGP/v09i04/55113
36. Solar furnaces and concentrating solar systems. https://www.promes.cnrs.fr/en/infrastructure-solaire/moyens-solaires/solar-furnaces-and-concentrating-solar-systems/ (2022)
37. Johnson, S.C.: Solar pumping converts broadband sunlight into efficient laser light. In: Laser Focus World: Lasers and Sources. (2022). https://www.laserfocusworld.com/lasers-sources/article/14283698/solar-pumping-converts-broadband-sunlight-into-efficient-laser-light
38. Aieta, F., Genevet, P., Kats, M., Capasso, F.: Aberrations of flat lenses and aplanatic metasurfaces. Opt. Express **21**(25), 31530–31539 (2013). https://doi.org/10.1364/OE.21.031530
39. Rocha, M.C., Goncharov, A.V.: Aplanatic meniscus lens corrector for Ritchey-Chrétien telescopes. Opt. Express **30**(4), 6076–6089 (2022). https://doi.org/10.1364/OE.450473
40. Pernechele, C.: Hyper hemispheric lens. Opt. Express **24**(5), 5014–5019 (2016). https://doi.org/10.1364/OE.24.005014
41. Heraeus: Properties of fused silica. https://www.heraeus.com/en/hca/fused_silica_quartz_knowledge_base_1/properties_1/properties_hca.html (2022)
42. Koechner, W.: Solid-State Laser Engineering. Springer (2006). https://doi.org/10.1007/0-387-29338-8
43. Clarkson, W.A.: Thermal effects and their mitigation in end-pumped solid-state lasers. J. Phys. D Appl. Phys. **34**(16), 2381–2395 (2001). https://doi.org/10.1088/0022-3727/34/16/302
44. Winston, R., Minano, J.C., Benitez, P.G.: Nonimaging Optics. Elsevier (2005). https://doi.org/10.1016/B978-0-12-759751-5.X5000-3
45. Winston, R.: Principles of solar concentrators of a novel design. Sol. Energy **16**(2), 89–95 (1974). https://doi.org/10.1016/0038-092X(74)90004-8
46. Welford, W.T.: High Collection Nonimaging Optics. Elsevier, (1989). https://doi.org/10.1016/B978-0-12-742885-7.X5001-3
47. Rabl, A., Goodman, N.B., Winston, R.: Practical design considerations for CPC solar collectors. Sol. Energy **22**(4), 373–381 (1979). https://doi.org/10.1016/0038-092X(79)90192-0
48. McIntire, W.R.: Truncation of nonimaging cusp concentrators. Sol. Energy **23**(4), 351–355 (1979). https://doi.org/10.1016/0038-092X(79)90130-0
49. Ning, X., O'Gallagher, J., Winston, R.: Optics of two-stage photovoltaic concentrators with dielectric second stages. Appl. Opt. **26**(7), 1207–1212 (1987). https://doi.org/10.1364/AO.26.001207
50. Ning, X., Winston, R., O'Gallagher, J.: Dielectric totally internally reflecting concentrators. Appl. Opt. **26**(2), 300–305 (1987). https://doi.org/10.1364/AO.26.000300
51. ASTM Standard G173–03 (2020), Standard Tables for Reference Solar Spectral Irradiances: Direct Normal, and Hemispherical on 37º Tilted Surface (2020). https://doi.org/10.1520/G0173-03R20

52. Prahl, S.: Nd:YAG—Nd:$Y_3Al_5O_{12}$. https://omlc.org/spectra/lasermedia/html/052.html (2017)
53. Rapaport, A., Zhao, S., Xiao, G., Howard, A., Bass, M.: Temperature dependence of the 1.06-μm stimulated emission cross section of neodymium in YAG and in GSGG. Appl. Opt. **41**(33), 7052–7057 (2002). https://doi.org/10.1364/AO.41.007052
54. Tai, Y., Zheng, G., Wang, H., Bai, J.: Near-infrared quantum cutting of Ce3+–Nd3+ co-doped Y3Al5O12 crystal for crystalline silicon solar cells. J. Photochem. Photobiol., A **303–304**, 80–85 (2015). https://doi.org/10.1016/j.jphotochem.2015.02.009

Chapter 7
High Brightness Solar-Pumped Lasers

Cláudia R. Vistas

High brightness solar-pumped lasers are introduced in this chapter. The pumping configurations and the output performances of TEM_{00}-mode and low-order modes solar lasers are described. Techniques for the efficient extraction of TEM_{00}-mode solar laser power are discussed in this chapter. Readers will understand how thermal lensing, resonant cavity parameters, solar pumping conditions and laser rod dimensions affect the TEM_{00}-mode laser output performance.

7.1 Solar Laser Pumping Configurations for TEM_{00}-mode

Solar lasers have been designed with different pumping configurations, based on whether the active medium is end-, side- or end-side-pumped. In an end-pumped laser, the pump light is introduced through one end-face of the active medium [1, 2]; however, it leads to strong thermal lensing effects, contributing to poor solar laser brightness. In a side-pumping configuration, the pump light enters through the side walls of the active material. The uniform absorption along the longitudinal rod axis improves the thermal performance of solar lasers, leading to advances in solar laser beam brightness [3–8] and output power stability [9, 10]. In an end-side-pumped laser, the pump light is injected through one end-face and the side walls of the active medium. This configuration has allowed major breakthroughs in solar laser efficiency [11–18].

The TEM_{00}-mode is one of the most preferred beam modes for laser applications because of its low divergence, smooth intensity profile, high power density and hence high brightness. The first TEM_{00}-mode solar laser operation was attained in 2013 by side pumping a Nd:YAG rod through a fused silica aspherical lens secondary concentrator [4]. Since then, the side-pumping configuration has been used to produce the TEM_{00}-mode solar laser emission, using as secondary concentrators the fused silica light guides [5, 6, 9, 10], fused silica cylindrical or ellipsoidal lenses [7, 8]. The

© The Author(s), under exclusive license to Springer Nature Switzerland AG 2023

D. Liang et al., *Solar-Pumped Lasers*, Green Energy and Technology,
https://doi.org/10.1007/978-3-031-24785-9_7

end-side-pumping configuration was able to produce a record in solar laser collection efficiency (7.9 W/m^2), using a fused silica aspherical lens [16].

In Table 7.1 is summarized the performance of the TEM_{00}-mode solar laser systems.

7.1.1 Side-Pumping Configuration

In a side-pumping configuration, the pump radiation enters through the side walls of the active medium, being perpendicular to the laser beam direction. The main advantage of this design is that the absorbed pump radiation is well spread along the laser rod axis, leading to a homogenous pump absorption profile. Therefore, the heat deposition along the rod is uniform, which results in a reduction of the thermal load issues. This allows the scalability of laser power. In addition, the free access to both ends of the active medium allows an efficient optimization of the laser resonator parameters. Thus, the extraction of low laser modes is facilitated, and the laser beam quality is easily improved. Another advantage of side-pumped solar laser is the good solar tracking error compensation capacity. The absorbed pump radiation is not significantly affected by the tracking errors in azimuth axis if the focal spot remains within the pump cavity.

The side-pumping configuration allows a high uniform light distribution along the rod, but it is the secondary concentrator that plays a key role in the distribution and uniformization of the solar light rays from the focal zone of the primary concentrator to the active medium, as explained in previous chapters. The TEM_{00}-mode solar laser has been achieved by using the two most used secondary concentrators in side-pumped solar lasers, the fused silica aspherical lens and light guide, as well as cylindrical and ellipsoidal lenses. This section is divided by the secondary concentrators used in TEM_{00}-mode side-pumped solar laser heads.

7.1.1.1 Aspherical Lens Secondary Concentrator

Most lenses have at least one spherical surface. However, some lenses have non-spherical surfaces and are so called aspherical lenses. Their radius of curvature gradually changes from the center of the lens to the edge, having a shape slightly divergent from spherical. The role of the asphere surface profile is to reduce or eliminate spherical aberration, an optical effect that causes incident light rays to focus on different points (Fig. 7.1). Therefore, aspherical lenses have an improved spot size, smaller than that of spherical lenses.

Aspherical lenses are one of the main secondary concentrators in solar-pumped lasers since they collect and compress the concentrated solar radiation from the focal zone of the primary concentrator into a small spot with true diffraction-limited size and the lowest wavefront error. Therefore, the absorbed pump light profile within

Table 7.1 Summary of TEM_{00}-mode solar laser pumping schemes

Year/Source	Laser head configuration	Primary concentrator–effective collection area	Secondary concentrator	Tertiary concentrator	Pump cavity	Active medium	TEM_{00}-mode laser power	TEM_{00}-mode collection efficiency	Slope efficiency	Brightness figure of merit	Beam quality factor M^2
2013 Liang and Almeida [4]	Side-pumping	Fresnel lens–0.78 m^2	Fused silica aspherical lens	2D-CPC	V-shaped pump cavity	Nd:YAG rod 3 mm diameter, 30 mm length	2.3 W	2.9 W/m^2	NA	1.9 W	≤1.10
2015 Liang et al. [5]	Side-pumping	Parabolic mirror–2.30 m^2	Fused silica light guide	2D-CPC	V-shaped pump cavity	Nd:YAG rod 3 mm diameter, 30 mm length	4.4 W	1.9 W/m^2	0.81%	4.0 W	≤1.05
2015 Almeida et al. [6]	Side-pumping 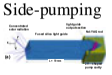	Parabolic mirror–1.92 m^2	Fused silica light guide	2D-trapezoidal output section of light guide	2V-shaped pump cavity	Nd:YAG rod 4 mm diameter, 30 mm length	5.5 W	2.8 W/m^2	1.27%	3.5 W	≤1.25
2016 Vistas et al. [7]	Side-pumping 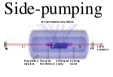	Parabolic mirror–1.00 m^2	Fused silica cylindrical lens	NA	2V-shaped pump cavity	Nd:YAG grooved rod 4 mm diameter, 34 mm length	3.4 W	3.4 W/m^2	1.90%	2.8 W	≤1.10
2016 Liang et al. [8]	Side-pumping	Parabolic mirror–1.13 m^2	Fused silica ellipsoid-shaped lens	NA	2V-shaped pump cavity	Nd:YAG grooved rod 4 mm diameter, 34 mm length	4.5 W	4.0 W/m^2	2.36%	3.7 W	≤1.10
2017 Bouadjemine et al. [9]	Side-pumping 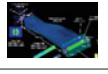	Parabolic mirror–1.18 m^2	Fused silica twisted light guide	2D-CPC	2V-shaped pump cavity	Nd:YAG rod 3 mm diameter, 50 mm length	2.3 W	1.9 W/m^2	NA	2.2 W	≤1.05

(continued)

Table 7.1 (continued)

Year/Source	Laser head configuration	Primary concentrator–effective collection area	Secondary concentrator	Tertiary concentrator	Pump cavity	Active medium	TEM_{00}-mode laser power	TEM_{00}-mode collection efficiency	Slope efficiency	Brightness figure of merit	Beam quality factor M^2
2017 Mehellou et al. [10]	Side-pumping 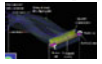	Parabolic mirror–1.18 m^2	Fused silica twisted light guide	2D-CPC	2V-shaped pump cavity	Nd:YAG rod 3 mm diameter, 50 mm length	2.7 W	2.3 W/m^2	NA	2.5 W	≤1.05
2017 Liang et al. [16]	End-side-pumping	Parabolic mirror–1.18 m^2	Fused silica aspherical lens	NA	Conical pump cavity	Nd:YAG rod 4 mm diameter, 35 mm length	9.3 W	7.9 W/m^2	NA	6.45 W	≤1.20
2018 Almeida et al. [19]	Side-pumping	Parabolic mirror–1.10 m^2	Fused silica semispherical lens	NA	Trapezoidal-shaped pump cavity	Nd:YAG grooved rod 4 mm diameter, 34 mm length	2.0 W	1.8 W/m^2	NA	NA	NA
2019 Liang et al. [20]	Side-pumping 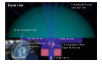	Parabolic mirror–0.90 m^2	Fused silica aspherical lens	NA	Semi-cylindrical pump cavity	Nd:YAG rod 3 mm diameter, 30 mm length	2.8 W	3.1 W/m^2	NA	NA	NA
2019 Vistas et al. [21]	End-side-pumping	Parabolic mirror–1.00 m^2	Fused silica liquid light guide lens	NA	Conical pump cavity	Nd:YAG rod 4 mm diameter, 35 mm length	3.0 W	3.0 W/m^2	NA	NA	NA

NA - not available

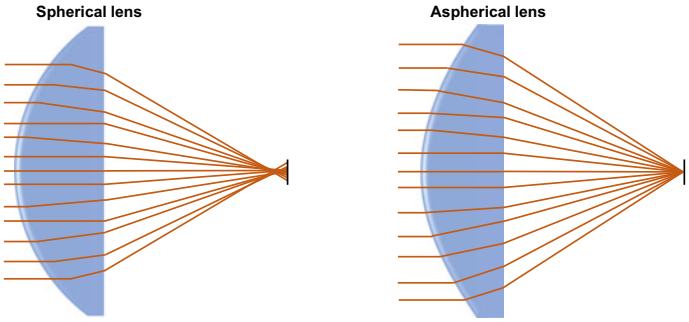

Fig. 7.1 Spherical aberration in a spherical lens (left) versus an aspherical lens (right)

the laser rod is more concentrated on its central region because this concentrator preserves the near-Gaussian profile of the pump source.

The first solar laser in fundamental mode, reported by Liang and Almeida in 2013, used an aspherical lens to side pump a 3 mm diameter, 30 mm length Nd:YAG rod [4]. The TEM_{00}-mode Nd:YAG solar laser system was composed of a first-stage Fresnel lens with 0.78 m^2 area, a second-stage fused silica aspherical lens with an input face of 43 mm radius and r^2 rear parameter of −0.0005, and a third-stage 2D-compound parabolic concentrator (2D-CPC), as shown in Fig. 7.2. The 2D-CPC was used to convert the rays from 18 × 23 mm^2 large aperture emitting into a small angle, 25°, to 8 × 23 mm^2 small aperture emitting into a large angle, 70°, preserving thus the source etendue. This preservation implies that irradiance is larger at the output aperture than the one at the input aperture, leading to a net concentration of the pump radiation [22]. Moreover, a V-shaped pump cavity was used to achieve an efficient multi-pass absorption of the highly concentrated pump radiation from the 2D-CPC output aperture [4].

This laser system produced 2.3 W TEM_{00}-mode laser power. The near-field laser beam output profile is shown in Fig. 7.3. The laser beam quality factor $M^2 \leq 1.1$ was attained, corresponding to a brightness figure of merit of 1.9 W [4].

7.1.1.2 Light Guide Secondary Concentrator

Light guides transmit the incident light from a light source to a particular area, through internal refractive and total internal reflection principles. In solar-pumped lasers, they convert the near-Gaussian profile of the concentrated solar radiation from the focal zone into a uniform light distribution at its output end, as demonstrated in Fig. 7.4. This facilitates the efficient light coupling into a long and thin laser rod, producing a uniform absorbed pump light profile within the active medium. This uniformity helps to minimize the thermal load issues.

The light guide serves as a beam homogenizer, minimizing also the problems associated with solar tracking error. This is a critical factor that influences the resonator stability of a solar laser, moving the center of the absorption distribution inside the

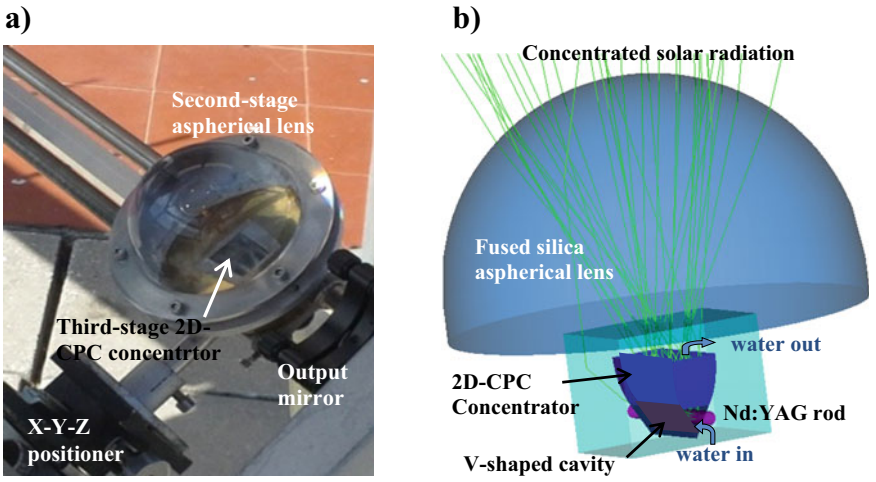

Fig. 7.2 **a** Photograph and **b** scheme of the TEM_{00}-mode Nd:YAG solar laser head [4]

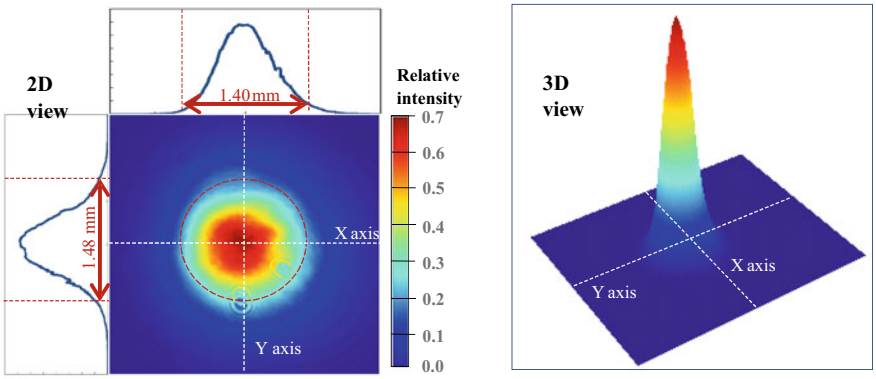

Fig. 7.3 Measured output laser beam 2D and 3D profiles 40 mm away from the output coupler [4]

crystal, which results in low output power and non-uniform beam profile. Light guides have been used not only to overcome the issues associated with tracking error and thermal load, but also to attain TEM_{00}-mode solar laser emission [5, 6, 9, 10].

Using a rectangular light guide as secondary concentrator to side pump a 3 mm diameter, 30 mm length Nd:YAG rod, significant advances in solar pumped laser beam brightness and beam quality factors were achieved by Liang et al. in 2015 [5]. The solar laser head was composed of a fused silica rectangular light guide with 10×15 mm^2 input end, 12×18 mm^2 output end and 100 mm length, a 2D-CPC tertiary concentrator with 14×20 mm^2 input aperture, 8×20 mm^2 output aperture and 10 mm height, and a V-shaped pump cavity (Fig. 7.5). A parabolic mirror with 2.3 m^2 effective collection area was used as primary concentrator.

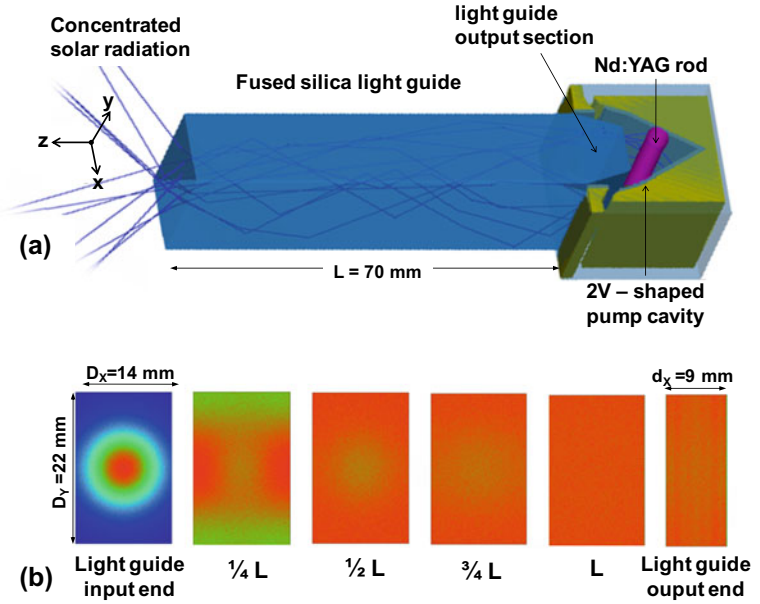

Fig. 7.4 **a** Scheme of a TEM_{00}-solar laser head with a rectangular light guide of length L as secondary concentrator. **b** Pump light distribution at different sections along the rectangular light guide [6]

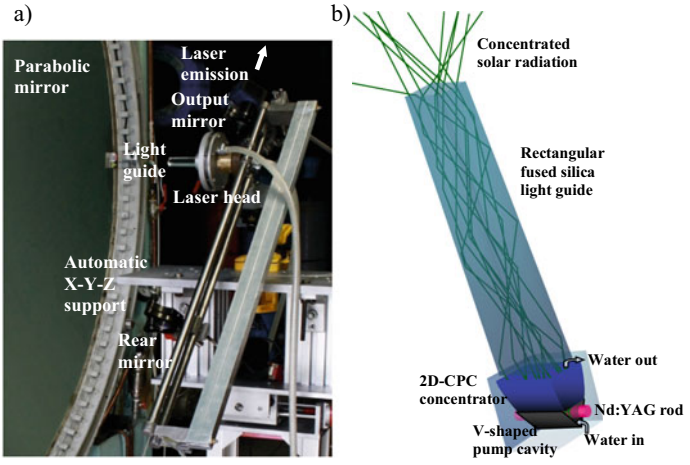

Fig. 7.5 **a** Photograph and **b** scheme of the of the TEM_{00}-mode Nd:YAG solar laser head [5]

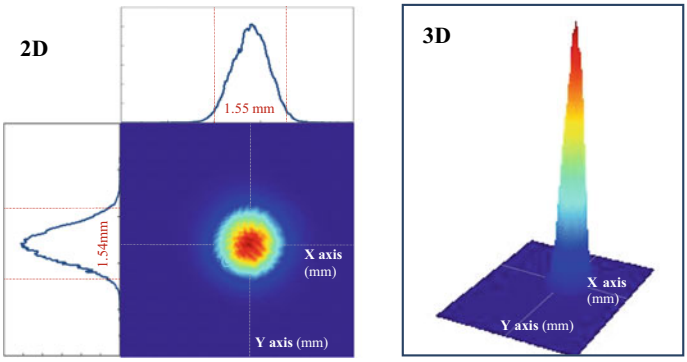

Fig. 7.6 Measured output laser beam 2D and 3D profiles 40 mm away from the output coupler [5]

With this solar laser system, a TEM_{00}-mode laser power of 4.4 W was obtained. The near-field laser beam output profile is shown in Fig. 7.6. Excellent laser beam quality factor $M^2 \leq 1.05$ was attained, resulting in a beam brightness figure of merit of 4.0 W, which is the record to date for a side-pumped solar laser [5].

Twisted light guides have been developed to improve the laser beam stability of solar-pumped lasers. Two side-pumping schemes composed of a monolithic fused silica twisted light guide, a tertiary 2D-CPC concentrator, a 2V-shaped pump cavity, and a thin and long Nd:YAG rod, with 3 mm diameter, 50 mm length, were investigated (Fig. 7.7). Both used a parabolic mirror with 1.18 m^2 effective collection area as primary concentrator [9, 10].

One twisted light guide was symmetrical, having one straight light guide and two twisted light guides, with 16 × 16 mm^2 input face, 8 × 32 mm^2 output end and 110 mm length (Fig. 7.7a, b) [10]. The other was non-symmetrical, having one straight light guide and one twisted light guide, with 19.4 × 16.6 mm^2 input face, 8.3 × 38.6 mm^2 output end and 119.3 mm length (Fig. 7.7c) [9]. Both had square inlet face and rectangular outlet end that distribute and uniformize the concentrated solar light at the focus into a homogenized light distribution at its output end (Fig. 7.7).

The laser system with symmetric twisted light guide produced 2.7 W TEM_{00}-mode laser power with beam quality factor $M^2 \leq 1.05$, corresponding to a beam brightness figure of merit of 2.4 W [10]. While the laser system with non-symmetric twisted light guide produced 2.3 W TEM_{00}-mode laser power with beam quality factor $M^2 \leq 1.05$, corresponding to a beam brightness figure of merit of 2.1 W [9].

The combination of both twisted light guide and small diameter rod helped to overcome the thermal lensing problems by providing a uniform pumping distribution along the thin laser rod, which allowed the production of a stable continuous-wave TEM_{00}-mode solar laser. This in turn led to significantly low solar pumping intensity, and consequently low heat load, low thermal stress and working temperature [9, 10].

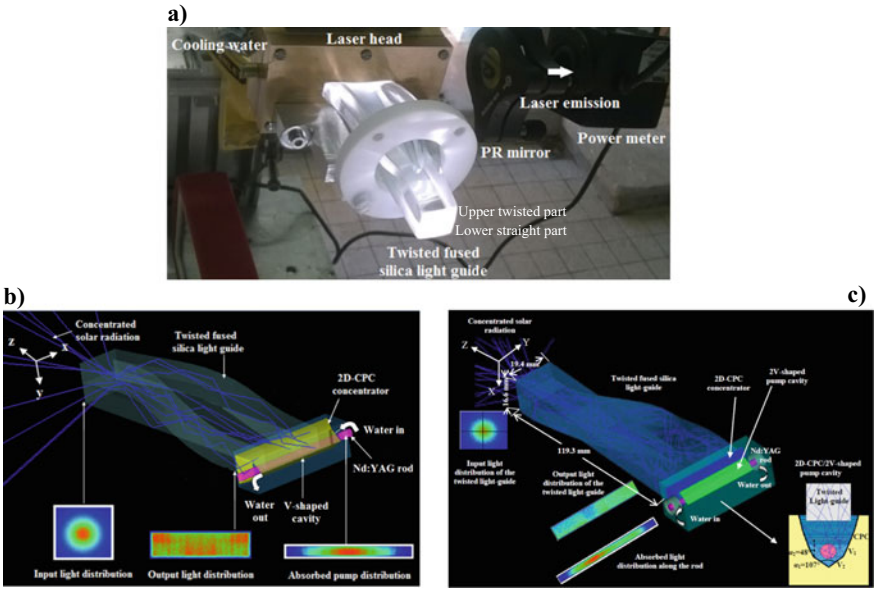

Fig. 7.7 **a** Photograph of the solar laser head with symmetric twisted light guide [10], and design of solar laser heads with **b** symmetric [10] and **c** non-symmetric [9] twisted light guides

7.1.1.3 Cylindrical/Ellipsoidal Lenses Secondary Concentrators

A cylindrical lens has at least one curved surface in one direction. Therefore, the light is focused on a single dimension or axis. Ellipsoidal or elliptic cylindrical lenses are cylinder lenses with an ellipse as its cross-section.

Vistas et al. combined a cylindrical lens with the multi-pass pumping ability of a 2V-shaped cavity to provide efficient side pumping along a 4.0 mm diameter, 34 mm length grooved Nd:YAG crystal rod (Fig. 7.8), using the heliostat-parabolic mirror system as the primary concentrator [7].

The fused silica cylindrical lens, with 37 mm outer diameter, 19 mm inner diameter and 68.5 mm length, collected and compressed the concentrated solar radiation along the laser rod. The two-dimensional 2V-shaped cavity had an entrance aperture of 10×22 mm^2 and 6 mm depth, being much more effective in coupling highly concentrated solar rays with different incidence angles into the laser rod than a single V-shaped reflector. The grooved surface of the laser rod offers a large interface with cooling liquid, compared to common rods, and hence improved heat dissipation and reduced thermal lensing effect, which in turn can enhance the laser beam quality of solar laser [23]. Using a parabolic mirror with 1.0 m^2 effective collection area, 3.4 W TEM_{00}-mode laser power was attained with beam quality factor $M^2 \leq 1.1$, corresponding to a beam brightness figure of merit of 2.8 W.

To improve the TEM_{00}-mode solar laser efficiency, Liang et al. used an ellipsoid-shaped lens [8]. The solar laser head was composed of a fused silica truncated

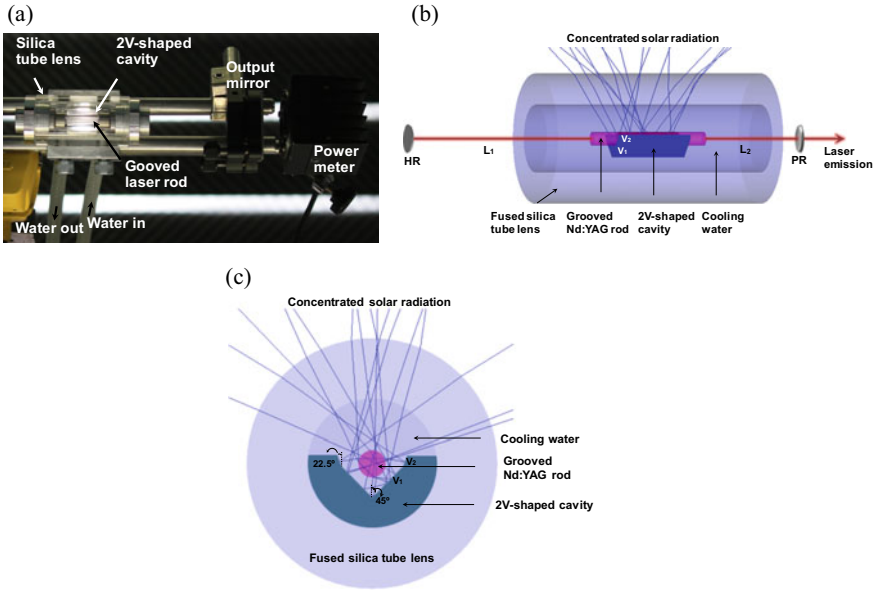

Fig. 7.8 **a** Photograph of the Nd:YAG laser head composed of the fused silica cylindrical lens, the 2V-shaped pumping cavity and the grooved Nd:YAG rod, and **b** side-view and **c** front-view of the solar laser head design. The 2V-shaped cavity is composed of a V-shaped reflector V_1 and two upper planar reflectors V_2. L_1 and L_2 represent the separation length of the high reflection (HR) mirror and partial reflection (PR) mirror, respectively, to their nearest end face of the laser rod [7]

ellipsoid-shaped concentrator, a 2V-shaped pump cavity, and a 4.0 mm diameter, 34 mm length grooved Nd:YAG rod (Fig. 7.9), using the heliostat-parabolic mirror system as the primary concentrator.

The ellipsoid-shaped lens was mathematically defined by $a = b = 17.5$ mm semi-minor axes and $c = 50$ mm semi-major axis, and was truncated from two sides to 60 mm length. The central water-cooling channel had 16 mm diameter. The two-dimensional 2V-shaped cavity had an entrance aperture of 10×22 mm^2 and 8 mm depth. Using a parabolic mirror with 1.13 m^2 effective collection area, 4.5 W TEM_{00}-mode laser power was obtained, corresponding to 4.0 W/m^2 collection efficiency, which is the record to date for side-pumping solar laser. A beam quality factor $M^2 \leq 1.1$ was achieved, resulting in a 3.7 W beam brightness figure of merit [8]. The far-field laser beam profile is shown in Fig. 7.10.

7.1.2 End-Side-Pumping Configuration

In an end-side-pumping configuration, the central part of the pump radiation is directly injected into the end-face of the laser rod, in the same direction as the

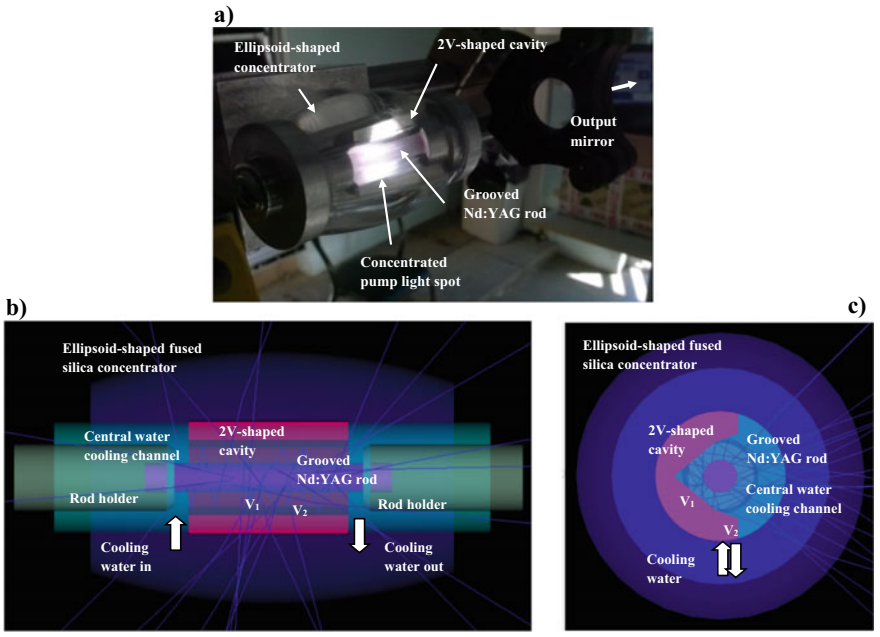

Fig. 7.9 **a** Photograph of the Nd:YAG laser head composed of the ellipsoid-shaped fused silica concentrator, the 2V-shaped pumping cavity and the grooved Nd:YAG rod, **b** front-view and **c** side-view of the solar laser pumping approach illustrated by Zemax® shaded models [8]

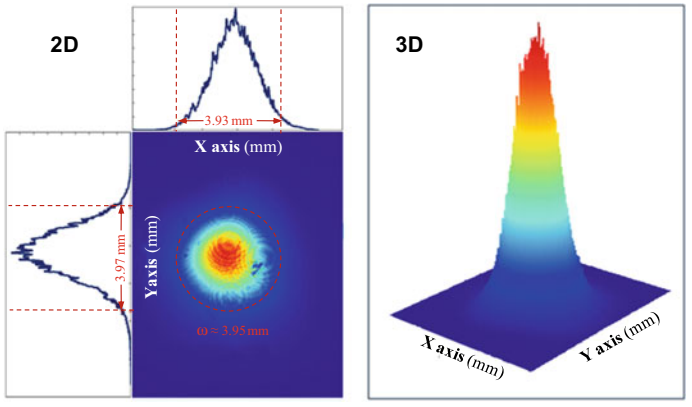

Fig. 7.10 Measured TEM_{00}-mode output laser beam 2D and 3D profiles 2.5 m away from the output coupler [8]

emerging laser beam, while another part of the radiation is injected into the side walls of the rod, in directions approximately perpendicular to the laser beam.

End-side-pumping configuration offers highly efficient continuous-wave laser operation because the pump power can be effectively concentrated in the laser mode volume. Efficient TEM_{00}-mode operation can thus be greatly benefited using this configuration, since the good spatial match between the pump region and the resonator TEM_{00}-mode allows the maximum utilization of the concentrated solar energy. However, this has a downside, the high pump power irradiance incident on the laser rod end results in high thermal load on its input face. This non-uniform heat deposition leads to strong thermal lensing and thermally induced birefringence, which drive to the degradation of the beam quality. The high thermal stress can cause the ultimate fracture of the laser rod end.

Another drawback of this configuration is the low solar tracking error compensation capacity compared to that of the side-pumping. For end-side-pumping, a small solar tracking error in either azimuth or altitude axis can cause a substantial reduction in the laser output power and thus in its stability. This occurs because the main part of the concentrated solar radiation is directly focused onto the end face of the laser rod.

7.1.2.1 Aspherical Lens Secondary Concentrator

Aspherical lens has a non-spherical surface, as explained in Sect. 7.1.1.1.

With the goal to boost the solar laser efficiency, Liang et al. used an aspherical lens to end-side pump a Nd:YAG laser rod [16]. As shown in Fig. 7.11, the laser head was composed of the fused silica aspherical lens and a conical-shaped pump cavity, inside which was a 4 mm diameter, 35 mm length Nd:YAG rod. The fused silica aspherical lens was 84 mm in diameter, 38 mm in height, 45 mm in front surface radius of curvature and -0.005 in rear r^2 parameter. The conical cavity had 22 mm input diameter, 9 mm output diameter and 29 mm height.

Using a parabolic mirror with 1.18 m^2 effective collection area, TEM_{00}-mode laser output power of 9.3 W was achieved, corresponding to 7.9 W/m^2 collection efficiency, which is the record to date for an end-side-pumped solar laser. A beam quality factor $M^2 \leq 1.2$ was achieved, resulting in a 6.46 W beam brightness figure of merit [16]. The respective laser beam profile is shown in Fig. 7.12.

7.2 Solar Laser Pumping Configurations for Doughnut-Shaped and Low-Order Modes Emissions

Other low beam modes have been obtained by solar-pumped lasers, such as doughnut-shaped and petal-like beams [19–21]. Doughnut-shaped beam (TEM_{01*}-mode) has

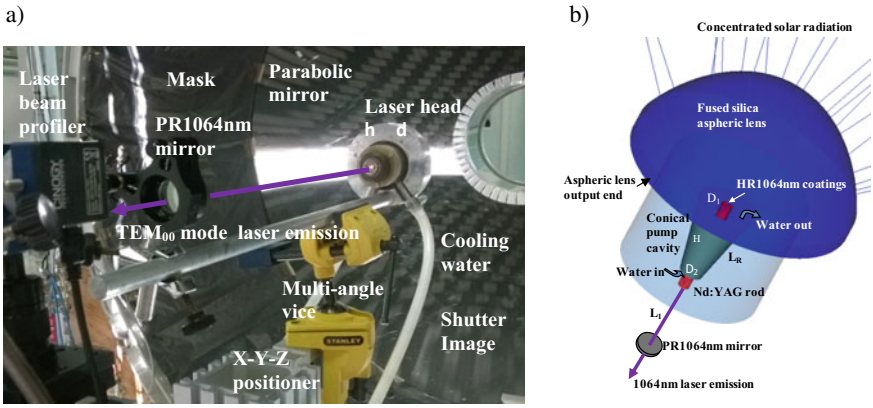

Fig. 7.11 **a** Photograph and **b** design of the Nd:YAG laser head [16]

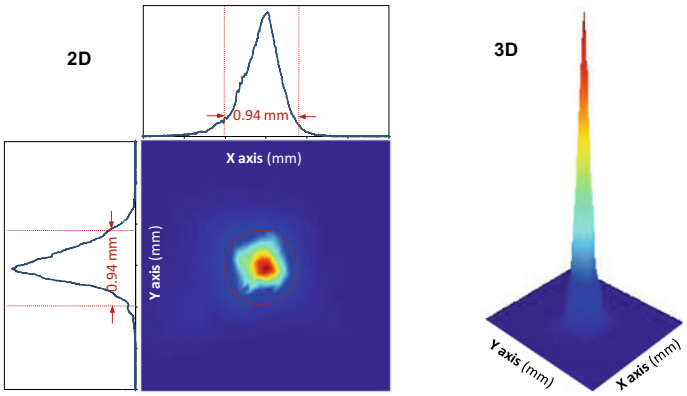

Fig. 7.12 Measured TEM_{00}-mode output laser beam 2D and 3D profiles 284 mm away from the output mirror [16]

an intensity distribution concentrated in a ring with no on-axis intensity. This beam offers new perspectives on fundamental laser-matter interactions, being useful for applications in advanced trapping techniques, deep-hole drilling, photopolymerization and nanopatterning [24]. Doughnut-shaped beams can be generated using apertures, spatial light modulators or by inserting additional phase elements into a laser cavity [24–28]. However, these methods have the disadvantages of involving accurate laser cavity alignment and wasting significant output power due to insertion losses. The first production of a doughnut-shaped beam by a solar laser was reported in 2018, by side pumping a grooved Nd:YAG rod with a semispherical lens [19]. In the following year, the same group improved the efficiency of the doughnut-shaped solar laser beam, using an end-side-pumping configuration with a fused silica liquid light guide lens [21]. The technique used in both works required no

additional optical elements, reducing thus laser power losses and system complexity. Moreover, the doughnut-shaped beam was produced with less diffraction losses than that of a Gaussian beam. The selective oscillation of laser modes can be explained in terms of mode-dependent thermal lens effects of the active material and spatial mode-matching efficiency [19, 21].

Other interesting laser light patterns have been studied, which are described as petal-like beams [29–31], optical ring lattice structures [32], necklace beams [33], etc. This kind of patterns has been used in optical tweezing experiments [30] and atom optics applications [32], and they can be generated using spatial light modulators. Vistas et al. reported the formation of a four-petal Gaussian solar laser beam using the same technique to produce the doughnut-shaped solar laser beam [21].

7.2.1 Side-Pumping Configuration

7.2.1.1 Semispherical Lens Secondary Concentrator

A semispherical lens is spherical on one surface and flat on the other.

Almeida et al. used a double-stage semispherical lens/2D-trapezoidal-shaped pumping cavity to produce, for the first time, a doughnut-shaped solar laser beam [19]. The heliostat-parabolic mirror system was used as the primary concentrator with an effective solar radiation reception area of 1.1 m^2. The solar laser head consisted of a fused silica semispherical lens with 40 mm radius of curvature, 80 mm output face diameter and 35 mm length, a 2D-trapezoidal-shaped pumping cavity with 12.2 × 22.0 mm^2 entrance aperture and 13.3 mm depth, inside which was a 4.0 mm diameter, 34 mm length grooved Nd:YAG rod, as shown in Fig. 7.13.

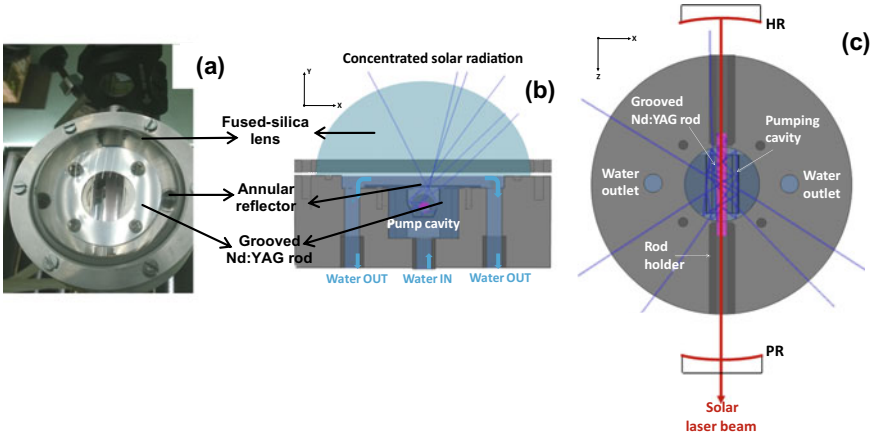

Fig. 7.13 **a** Photograph of the Nd:YAG solar laser head. **b** Front-view and **c** top-view design of the solar laser head [19]

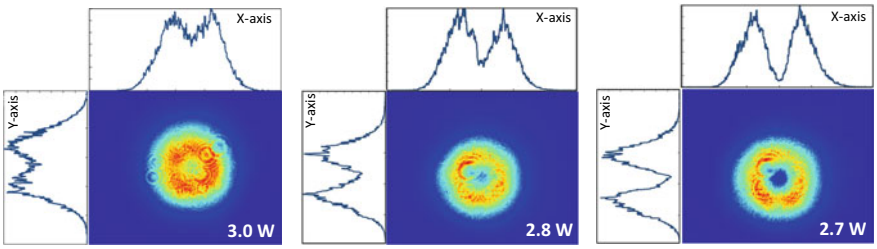

Fig. 7.14 Different doughnut-shaped output laser beam profiles. Influenced by the slight angular adjustment of the end mirror [19]

Solar laser beams at low-order mode are produced by operating the laser near to the edge of the optically stable region. The resonant cavity length needs to be long to provide a large spatial overlap between the pump mode and low-order mode volumes. Doughnut-shaped solar laser beam with 3.0 W solar laser power was produced using an asymmetric and long resonant cavity length. The intensity distribution of the doughnut-shaped beam can be changed with slight adjustments in the optical resonator alignment, as shown in Fig. 7.14. A slight angular adjustment of the output mirror led to a doughnut-shaped with an almost null intensity at the center; however, at the cost of slightly low laser output power (Fig. 7.14) [19].

This solar laser head was also able to produce TEM_{00}-mode using a longer resonant cavity length than that of the doughnut-shaped beam, at the limit of thermally stable zone, producing 2.0 W TEM_{00}-mode laser power [19].

7.2.2 End-Side-Pumping Configuration

7.2.2.1 Liquid Light Guide Lens Secondary Concentrator

The liquid light guide lens has the structure of a cylinder, surrounding a laser rod with coolant. One of the extremities could have a semispherical face.

Vistas et al. used a liquid light guide lens assembled in a conical pump cavity to end-side pump a 4 mm diameter, 35 mm length Nd:YAG rod [21]. The heliostat-parabolic mirror system was used as the primary concentrator, with an effective solar radiation reception area of 1.0 m^2. As shown in Fig. 7.15, the solar laser head was composed of a fused silica liquid light guide lens that had a semispherical input face of 11 mm radius of curvature, a plane output face and a height of 37 mm, and a conical pump cavity with 34 mm input diameter, 23 mm output diameter and 13 mm height.

A long resonant cavity length was used to produce a doughnut-shaped solar laser beam with 4.5 W laser power, corresponding to 4.5 W/m^2 collection efficiency [21].

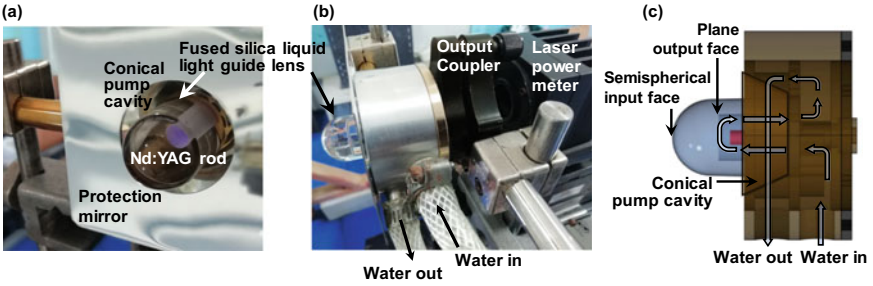

Fig. 7.15 **a**, **b** Photographs and **c** mechanical design of the Nd:YAG solar laser head [21]

This efficiency was higher than the previous one obtained by a side-pumping configuration [19]. Slight angular adjustments in the output mirror influenced the intensity distribution of the doughnut-shaped beam and consequently the laser power (Fig. 7.16). A doughnut-shaped with 18% of the maximum intensity at the center was produced at the expense of slightly low laser power of 4.2 W (Fig. 7.16) [21].

Using a longer resonant cavity length, closer to the border of the resonator stable zone, than that of the doughnut-shaped beam, TEM_{00}-mode solar laser power of 3.0 W was produced, as shown in Fig. 7.17 [21]. It is also important to note that the resonant cavity was 1.6 times longer than that of the previous TEM_{00}-mode end-side-pumping scheme [16]. Therefore, the mode-matching efficiency was less sensitive to small changes in thermal lensing near the asymptote, and thus stable solar laser emission at low-order modes were more often observed.

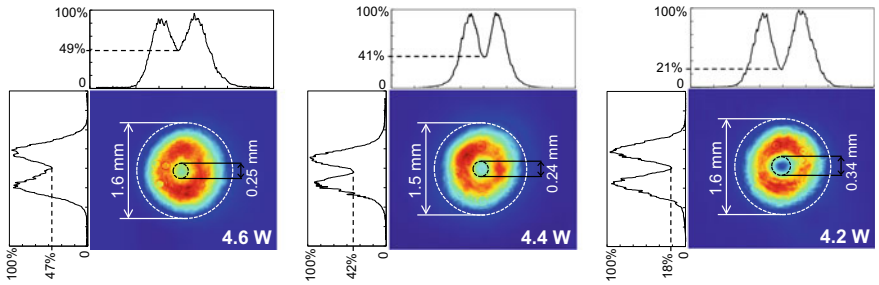

Fig. 7.16 Doughnut-shape solar laser beam profiles at a resonant cavity length of 600 mm. Influenced by the slight angular adjustment of the output mirror [21]

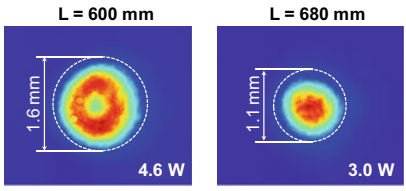

Fig. 7.17 Solar laser beam profile at two different resonant cavity length (L) 600 mm and 680 mm [21]

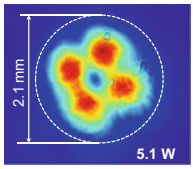

Fig. 7.18 Four-petal solar laser beam profile at a resonant cavity length of 545 mm [21]

A kind of four-petal Gaussian solar laser beam with 5.1 W laser power was also produced, using a shorter resonant cavity length than that of the doughnut-shaped beam, as shown in Fig. 7.18 [21].

The selective oscillation of laser modes was produced without the need of inserting additional optical phase elements to the laser cavity. The adoption of a long resonant cavity length allows the optimization of the overlap between the desired resonator mode and the pump mode volumes, enabling thus the formation of the selected low-order mode beams.

7.3 Techniques of TEM_{00}-Mode Solar Laser Power Extraction

7.3.1 Thermal Lensing Effect and Thermal Focal Length

In solid-state lasers, heat is generated in the active medium as a consequence of optical pumping. The underlying reasons for this event are [34, 35]:

(1) difference between pump and lasing photons energies—quantum defect. This is converted into heat by interactions with phonons in the upper (the difference between the pump and the upper metastable state level) or in the lower levels (the difference between the lower laser level and the ground state);
(2) non-radiative relaxation from the upper level to the ground state—owing to concentration quenching—and from the pump bands to the ground state;
(3) non-radiative relaxation from non-radiative sites (also called "dead sites"). These are ions that absorb pump photons but do not contribute to inversion;
(4) background absorption by the host material in unusable spectrum of pumping system. This is particularly valid for lamp- and solar-pumped systems because of their broadband pump radiation, which can also be absorbed by impurity atoms and color centers, increasing thus the heating.

The heat generated must be dissipated by a coolant flowing along the active medium. Therefore, depending on the configuration of the laser material and the cooling system, the heat is extracted through a specific direction within the active medium. This leads to a temperature gradient that produces different effects: (1) thermo-optic effect—temperature-induced change in refractive index; (2) stress- or strain-optic effect—temperature-induced stress/strain that leads to a variation in

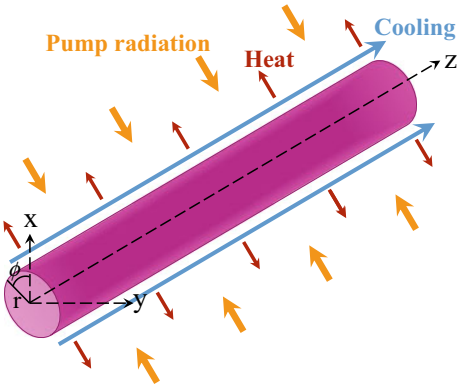

Fig. 7.19 Scheme of the heating and cooling of a side-pumped cylindrical laser rod

refractive index; (3) end bulging—physical deformation of the rod ends flatness. These effects contribute to the thermal lensing of the rod, and the net result is the distortion of the laser beam. Moreover, the generated stresses induce birefringence, and the final sequel is the rod fracture at the maximum stress point.

Koechner [34] and Foster and Osterink [36] were the pioneers in developing a theoretical model for the thermal lensing in the isotropic Nd:YAG crystal, deriving expressions that quantify the three effects noted above. They restrained the attention to the classic case of a long cylindrical laser rod with uniform internal heat generation and cooling along the rod surface, corresponding to the case of the side-pumped, edge-cooled rod under steady-state conditions (Fig. 7.19). The long cylindrical rod with uniform heat deposition and constant surface temperature develops a quadratic radial temperature profile, which leads also to a quadratic variation in the refractive index with the radial coordinate. This causes the laser rod to act as a lens with variable focal length. The optical power of the thermal lens is proportional to pump power [34].

The combination of the three effects—temperature- and stress-dependent variation in the refractive index and end bulging of the rod—leads to the following expression for the focal length (f) of the thermal lens formed in the laser rod [34]:

$$f = \frac{KA}{P_h}\left[\frac{1}{2}\frac{dn}{dT} + \alpha C_{r,\phi} n_0^3 + \frac{\alpha r_0 (n_0 - 1)}{l}\right]^{-1}, \tag{7.1}$$

where K is the thermal conductivity, A is the rod cross-sectional area and P_h is the power dissipated as heat in the rod ($P_h = \eta P_{in}$, where η is the fraction of the electrical input power P_{in} that is dissipated as heat in the rod). α is the thermal coefficient of expansion, $C_{r,\phi}$ is the photoelastic coefficient in the radial and tangential directions, n_0 is the refractive index at the center of the rod, r_0 and l are the radius and length of the rod, respectively. The first term d_n/d_T in the bracket of Eq. (7.1) represents the contribution of the temperature (T)-dependent change in refractive index (n). The second term represents the stress-dependent change in refractive index, and the third term refers to the effects in the laser rod caused by distortion of the rod ends flatness.

The major contribution to thermal lensing arises from the temperature-dependent variation in refractive index, whereas the stress-dependent term contributes only to the extent of about 20% [37]. The contribution due to the end bulging term remains less than about 10% for the typical dimensions of laser rods [37, 38].

7.3.2 *Influence of Laser Resonant Cavity Parameters*

Thermal lensing is an important parameter that must be considered in the design of the laser resonator. The thermal lensing effect distorts the mode structure in the resonator, affecting the laser stability, oscillation mode size, output beam quality, and the maximum achievable average power [37, 39–41].

The TEM_{00}-mode Gaussian beam has the smallest beam radius and divergence in a resonant cavity. The resonator design for an efficient TEM_{00}-mode laser system implies an optimal overlap of the fundamental mode of the cavity with the pump profile while the rod is used to apodize higher-order spatial modes. This increases the volume of the active medium involved in lasing.

Classically, the laser operation in fundamental mode is achieved by the insertion of an aperture in the resonant cavity to prevent high-order modes from oscillating. In this case, the laser extraction efficiency is reduced because of poor utilization of the stored energy in the active medium. Nonetheless, for efficient TEM_{00}-mode emission, several resonator configurations have been investigated in an attempt to maximize the energy extraction from solid-state lasers at the TEM_{00}-mode as well as maintain the resonator insensitive as possible to focal length and alignment perturbations. In solid-state lasers, the thermal lens effect has been compensated by using concave-convex resonators [41, 42], negative lenses ground at the rod ends [43], specific mirror curvatures [42, 44], or by insertion of a telescope in the resonator [45].

In side-pumped solar lasers, the asymmetric resonator with concave end mirrors of large radius of curvature (Fig. 7.20) has found to be an excellent configuration for achieving fundamental mode laser operation, because it provides a large spatial overlap between the fundamental mode and pump mode volumes [4–10].

L_1 and L_2 represent the separation length of the high reflection (HR) or partial reflection (PR) mirrors to their nearest end face of the laser rod, respectively. L_2 is

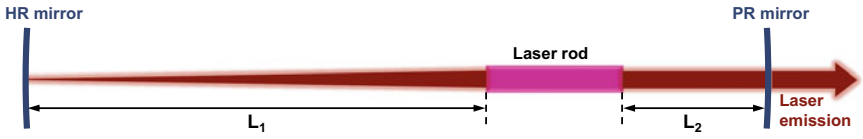

Fig. 7.20 Schematic diagram of the TEM_{00}-mode beam propagation along the asymmetric laser resonator with large radius of curvature end mirrors. L_1 and L_2 represent the separation length of the high reflection (HR) mirror and partial reflection (PR) mirror, respectively, to the end face of the laser rod

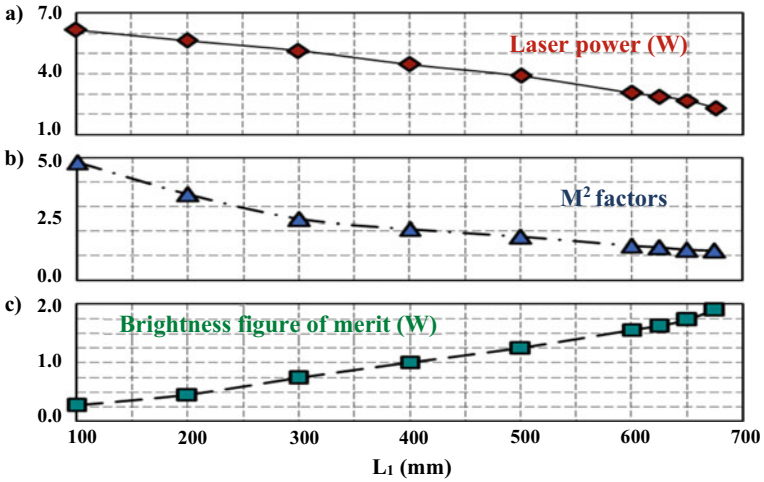

Fig. 7.21 Dependence of **a** laser power, **b** M^2 factors and **c** brightness figure of merit on the separation length of the high reflection mirror to its nearest end face of the laser rod (L_1) [4]

maintained short, usually no longer than 100 mm. L_1 is the key parameter to attain the optimum mode overlap. As shown in Fig. 7.21, the increase in L_1 leads to a decrease in both output laser power and M_2 factors, leading to an increase in brightness figure of merit—the overall result is the improvement of the laser beam quality and thus the generation of the TEM_{00}-mode [4].

High multimode and low TEM_{00}-mode laser output power levels are achieved with short L_1, consequently small L_1/L_2 (≈ 1) ratio (Fig. 7.22), where the Gaussian beam waist radius poorly matches the laser rod radius. This comes at the expense of high beam quality M^2 factor values and thus poor laser beam quality [4, 6, 7]. Nonetheless, as shown in Fig. 7.22, enhancing L_1, and consequently enhancing L_1/L_2 ratio, leads to an increase in the fundamental mode beam waist radius within the rod because high-order modes are suppressed by large diffraction losses at the rod edges, particularly for high input powers. Therefore, the fundamental mode size increases to a value suitable for TEM_{00}-mode operation, enhancing the TEM_{00}-mode laser output power (Fig. 7.22d) [6, 7].

In Table 7.2 is also shown the influence of L_1 on the output laser power and the respective beam profile, confirming that L_1 plays a fundamental role in controlling the number of lasing modes and laser power [20]. Using a side-pumped solar laser head, Liang et al. demonstrated that varying L_1, the laser beam pattern can change from a doughnut-shaped profile to a TEM_{00}-mode [20].

Therefore, to obtain efficient extraction of TEM_{00}-mode laser, the laser should operate with large L_1 (Table 7.2, Figs. 7.21 and 7.22), close to the edge of the resonator stable zone, where the fundamental mode size is more sensitive to thermal focus fluctuations, increasing towards an asymptote (Fig. 7.22) [46]. Consequently, the

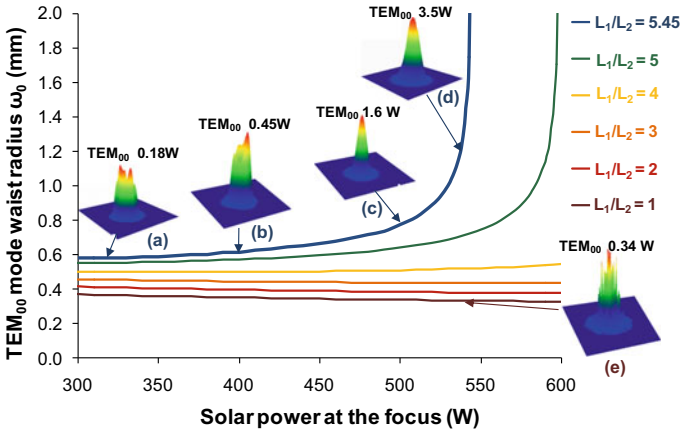

Fig. 7.22 TEM_{00}-mode beam waist radius ω_0 in the rod as a function of solar power at the focus, for different L_1/L_2 resonators, numerically obtained by LASCAD™ analysis. **a–d** Output laser beam profiles at different pump powers for $L_1/L_2 = 5.45$ resonator. **e** Output laser beam profile for $L_1/L_2 = 1$ resonator. Numerically calculated TEM_{00}-mode laser power values are given for **a–e** [7]

spatial overlap between the pump and the resonator TEM_{00}-mode volumes becomes larger and the few-order modes are also suppressed, generating a single mode.

The beam overlap efficiency has also a strong dependence on the radius of curvature (RoC) of both HR and PR mirrors [47, 48]. It is noteworthy that different RoCs are associated with different diffraction losses, although absorption, scattering and imperfect coating losses remain equal for the asymmetric resonator. End mirrors with small RoC lead to low TEM_{00}-mode laser power despite the low diffraction losses associated [47, 48]. This is explained by the large mismatch between the pump beam and the small TEM_{00}-mode volumes along the central region of the laser rod. Large RoC mirrors allow the maximum extraction of TEM_{00}-mode solar laser power from all the available absorbed solar pump power within the rod, because of the large oscillation mode volume [47, 48]. This is in line with the use of flat–flat (infinite RoC) cavity mirrors for TEM_{00}-mode operation [49].

7.3.3 Influence of Solar Pumping Conditions

As explained above, optical pumping leads to a radial temperature gradient in the active medium. In consequence, the rod behaves as a positive lens with an effective focal length that is inversely proportional to pump power [34, 46].

Almeida et al. used the LASCAD™ software to assess the focal length, temperature and heat load in the laser rod as a function of pump power, as shown in Fig. 7.23 [6]. In LASCAD™, the focal length of the rod lens can be determined through the stability limits of the resonator. As illustrated in Fig. 7.20, PR mirror was fixed at a

Table 7.2 Influence of the separation length of the high reflection mirror to the end face of the laser rod (L_1) and the solar irradiance (I) on the output laser power (P), and the respective beam profile (adapted from [20])

Increase in solar irradiance

TEM_{01}^*-mode	P = 2.9 W L_1 = 380 mm I = 700 W/m^2	P = 2.7 W L_1 = 380 mm I = 720 W/m^2	P = 2.6 W L_1 = 380 mm I = 760 W/m^2	P = 2.7 W L_1 = 380 mm I = 810 W/m^2
TEM_{01}-mode	P = 3.2 W L_1 = 390 mm I = 700 W/m^2	P = 2.8 W L_1 = 390 mm I = 760 W/m^2	P = 2.6 W L_1 = 390 mm I = 800 W/m^2	P = 2.5 W L_1 = 390 mm I = 840 W/m^2
TEM_{00}-mode	P = 2.8 W L_1 = 400 mm I = 770 W/m^2	P = 2.5 W L_1 = 400 mm I = 790 W/m^2	P = 2.4 W L_1 = 400 mm I = 820 W/m^2	P = 2.3 W L_1 = 400 mm I = 830 W/m^2

Increase in L_1

close distance to the rod lens, L_2. The focal length of the rod lens was assumed by L_1 at the point where the resonator becomes unstable [6]. The increase in pump power generates an enhance in both temperature and heat load in the laser rod, which in turn causes a decrease in focal length (Fig. 7.23).

Changes in the pump power in a solid-state laser lead to fluctuations in the rod focal length, exerting substantial variations in the spot size and hence in the mode volume and output power [46]. Almeida et al. [6] and Vistas et al. [7] numerically evaluated the TEM_{00}-mode solar laser beam waist radius as a function of the input solar power at the focus. The increase in pump power generates an enhance in the fundamental mode size to a value suitable for TEM_{00}-mode operation, obtaining very good beam quality (Fig. 7.22). When pump power levels are near laser emission threshold, the fundamental mode radius is small, leading to a low TEM_{00}-mode laser power (Fig. 7.22a). As pump power increases towards the resonator stability limit, the fundamental mode size at the center of the rod becomes larger, so the pump power extracted by the low-order mode laser is higher than that from the high-order mode laser, allowing the oscillation of the only possible lowest-order mode at higher output power: TEM_{00}-mode (Fig. 7.22d).

Several works have investigated the evolution of the laser beam profile with solar pump power [6, 7, 20], as shown in Table 7.2 and Fig. 7.24. No aperture is used

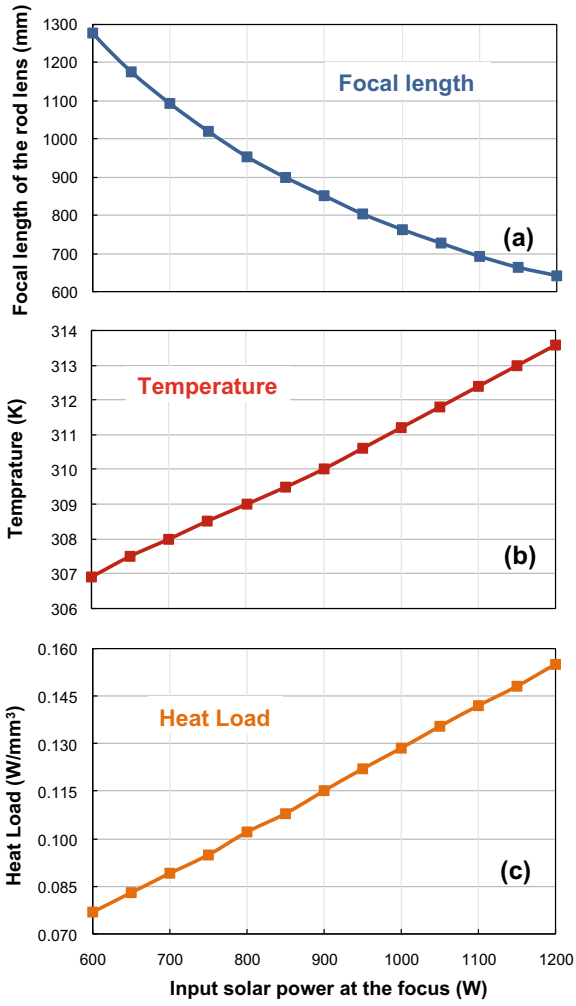

Fig. 7.23 Numerically calculated **a** focal length, **b** temperature and **c** heat load in the laser rod as a function of input solar power, assuming T = 300 K water cooling [6]

in the laser resonator besides the rod itself, and thus high-order modes oscillate at low output powers because of the small overlap between the fundamental mode and pump mode volumes (Fig. 7.24a). The pump power increase causes the oscillation of only few modes (Fig. 7.24b, c and Table 7.2) because of the increase in diffraction losses. As pump power approaches the thermal stability limit, the resonator modes originate only one mode of higher intensity (Fig. 7.24d and Table 7.2).

As illustrated in Fig. 7.25, the TEM_{00}-mode laser output power increases nonlinearly with the pump power, mainly because of the change in the radius of the transverse cavity mode at the HR rear mirror and at the laser rod, which is caused by the thermal lensing effect. Just as the pump mode-laser mode overlap and the diffraction losses depend on the thermal lensing effect, they also depend on the pump

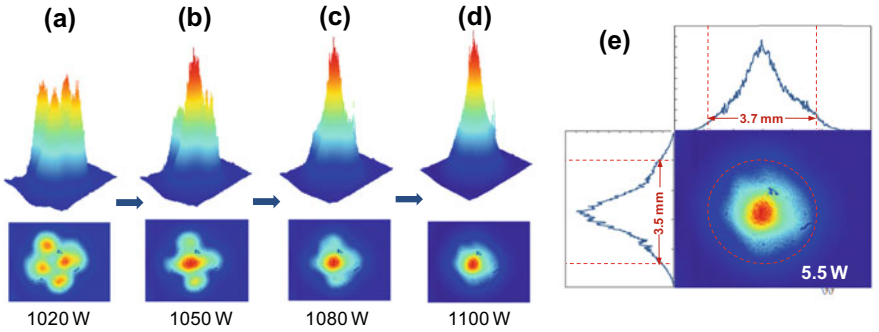

Fig. 7.24 **a–d** Evolution of output laser beam profile (taken 1.7 m away from the output coupler) with solar pump power as it approaches the resonator stability limit. **e** 2D analysis of the measured TEM_{00}-mode profile with indication of the output power [6]

intensity [50]. Once the output laser power reaches a peak value, further increase in pump power leads to an abrupt drop in output power (Fig. 7.25). The decrease in the extracted power from the laser rod is a result of excessive diffraction losses, caused by strong thermally induced aberrations, which makes the laser resonator unstable and stops the laser oscillation.

The dependency of the TEM_{00}-mode laser power on the input solar power from a side-pumped solar laser scheme was compared with that from an end-side-pumped scheme, as shown in Fig. 7.26 [10]. In a conical-shaped end-side-pumped laser [16], the TEM_{00}-mode solar power was very sensitive to the variation in input solar power at the focus (Fig. 7.26a). Low input power alleviates considerably the thermal lensing effect, permitting either two-mode or other low-order mode laser operation within the laser cavity (Fig. 7.26a). A slight increase in input solar power above a certain

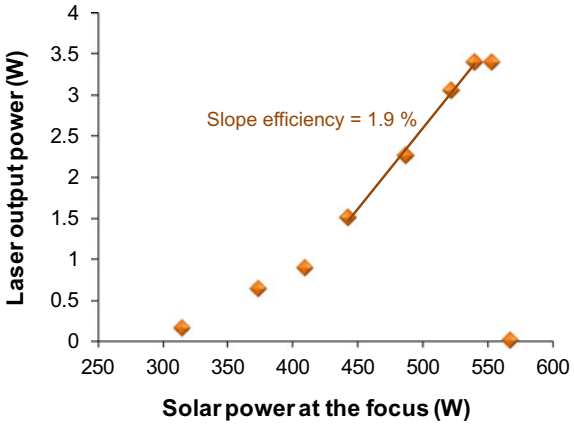

Fig. 7.25 TEM_{00}-mode laser output power as a function of the solar input power at the focus [7]

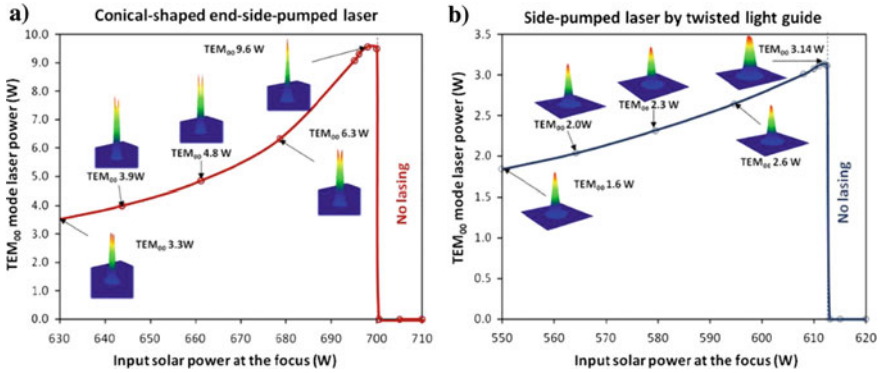

Fig. 7.26 TEM_{00}-mode solar laser power as a function of input solar power and beam profiles from both the **a** conical-shaped end-side-pumped laser [10, 16] and **b** side-pumped laser by the twisted light guide [10]

threshold leads to a shorter thermal length, causing the extinction of solar laser output power. For the side-pumped solar laser by a twisted light guide [10], the TEM_{00}-mode Gaussian profile remained nearly stable with the increase in input solar power up to a certain threshold, from which solar laser stopped lasing because of the thermal lensing effect (Fig. 7.26b). The TEM_{00}-mode laser power and beam profile from the side-pumping configuration are more tolerant to pump input variations than those from the end-side-pumping configuration.

7.3.4 Influence of Laser Rod Dimensions

The use of the laser rod as the limiting aperture in the resonator is essential to obtain the maximum efficiency in a TEM_{00}-mode system. Acting as an aperture, small diameter laser rods can easily suppress high-order resonator modes due to the large diffraction losses, improving the beam quality and enabling the efficient extraction of TEM_{00}-mode laser power [4–10, 47, 48].

Small diameter rods tend to allow a more uniform absorption profile that is not centrally peaked, which reduces the temperature on the axis, resulting thus in low thermal lensing at the center, few high-order aberrations at the periphery, and low stress in the laser rod [48, 51].

The laser beam quality M_x^2, M_y^2 factors are influenced by the rod diameter, as proved by several numerical analyses [47, 48, 52]. Asymmetries in the X-axis and Y-axis spot sizes increase with the diameter rod, resulting in discrepancies in the M_x^2, M_y^2 factors and thus in the laser beam divergence. Overall, small diameter rods tend to enable the emission of TEM_{00}-mode laser with high power and high brightness figure of merit [47, 48, 52].

References

1. Gleckman, P.: Achievement of ultrahigh solar concentration with potential for efficient laser pumping. Appl. Opt. **27**(21), 4385–4391 (1988). https://doi.org/10.1364/AO.27.004385
2. Smyth, C.J.C., Mirkhanov, S., Quarterman, A.H., Wilcox, K.G.: 27.5 W/m^2 collection efficiency solar laser using a diffuse scattering cooling liquid. Appl. Opt. **57**(15), 4008–4012 (2018). https://doi.org/10.1364/AO.57.004008
3. Lando, M., Kagan, J., Linyekin, B., Dobrusin, V.: A solar-pumped Nd:YAG laser in the high collection efficiency regime. Opt. Commun. **222**(1), 371–381 (2003). https://doi.org/10.1016/S0030-4018(03)01601-8
4. Liang, D., Almeida, J.: Solar-pumped TEM$_{00}$ mode Nd:YAG laser. Opt. Express **21**(21), 25107–25112 (2013). https://doi.org/10.1364/oe.21.025107
5. Liang, D., Almeida, J., Vistas, C.R., Guillot, E.: Solar-pumped TEM$_{00}$ mode Nd:YAG laser by a heliostat-parabolic mirror system. Sol. Energy Mater. Sol. Cells **134**, 305–308 (2015). https://doi.org/10.1016/j.solmat.2014.12.015
6. Almeida, J., Liang, D., Vistas, C.R., Bouadjemine, R., Guillot, E.: 5.5 W continuous-wave TEM$_{00}$-mode Nd:YAG solar laser by a light-guide/2V-shaped pump cavity. Appl. Phys. B-Lasers O. **121**(4), 473–482 (2015). https://doi.org/10.1007/s00340-015-6257-z
7. Vistas, C.R., Liang, D., Almeida, J., Guillot, E.: TEM$_{00}$ mode Nd:YAG solar laser by side-pumping a grooved rod. Opt. Commun. **366**, 50–56 (2016). https://doi.org/10.1016/j.optcom.2015.12.038
8. Liang, D., Almeida, J., Vistas, C.R., Oliveira, M., Goncalves, F., Guillot, E.: High-efficiency solar-pumped TEM$_{00}$-mode Nd:YAG laser. Sol. Energy Mater. Sol. Cells **145**, 397–402 (2016). https://doi.org/10.1016/j.solmat.2015.11.001
9. Bouadjemine, R., Liang, D., Almeida, J., Mehellou, S., Vistas, C.R., Kellou, A., Guillot, E.: Stable TEM$_{00}$-mode Nd:YAG solar laser operation by a twisted fused silica light-guide. Opt. Laser Technol. **97**, 1–11 (2017). https://doi.org/10.1016/j.optlastec.2017.06.003
10. Mehellou, S., Liang, D., Almeida, J., Bouadjemine, R., Vistas, C.R., Guillot, E., Rehouma, F.: Stable solar-pumped TEM$_{00}$-mode 1064 nm laser emission by a monolithic fused silica twisted light guide. Sol. Energ. **155**, 1059–1071 (2017). https://doi.org/10.1016/j.solener.2017.07.048
11. Ohkubo, T., Yabe, T., Yoshida, K., Uchida, S., Funatsu, T., Bagheri, B., Oishi, T., Daito, K., Ishioka, M., Nakayama, Y., Yasunaga, N., Kido, K., Sato, Y., Baasandash, C., Kato, K., Yanagitani, T., Okamoto, Y.: Solar-pumped 80 W laser irradiated by a Fresnel lens. Opt. Lett. **34**(2), 175–177 (2009). https://doi.org/10.1364/ol.34.000175
12. Dinh, T.H., Ohkubo, T., Yabe, T., Kuboyama, H.: 120 watt continuous wave solar-pumped laser with a liquid light-guide lens and an Nd:YAG rod. Opt. Lett. **37**(13), 2670–2672 (2012). https://doi.org/10.1364/ol.37.002670
13. Almeida, J., Liang, D., Guillot, E., Abdel-Hadi, Y.: A 40 W cw Nd:YAG solar laser pumped through a heliostat: a parabolic mirror system. Laser Phys. **23**(6), 065801 (2013). https://doi.org/10.1088/1054-660x/23/6/065801
14. Almeida, J., Liang, D., Vistas, C.R., Guillot, E.: Highly efficient end-side-pumped Nd:YAG solar laser by a heliostat-parabolic mirror system. Appl. Opt. **54**(8), 1970–1977 (2015). https://doi.org/10.1364/ao.54.001970
15. Liang, D., Almeida, J., Vistas, C.R.: 25 W/m^2 collection efficiency solar-pumped Nd:YAG laser by a heliostat-parabolic mirror system. Appl. Opt. **55**(27), 7712–7717 (2016). https://doi.org/10.1364/ao.55.007712
16. Liang, D., Almeida, J., Vistas, C.R., Guillot, E.: Solar-pumped Nd:YAG laser with 31.5 W/m^2 multimode and 7.9 W/m^2 TEM00-mode collection efficiencies. Sol. Energy Mater. Sol. Cells **159**, 435–439 (2017). https://doi.org/10.1016/j.solmat.2016.09.048
17. Liang, D., Vistas, C.R., Tiburcio, B.D., Almeida, J.: Solar-pumped Cr:Nd:YAG ceramic laser with 6.7% slope efficiency. Sol. Energy Mater. Sol. Cells **185**, 75–79 (2018). https://doi.org/10.1016/j.solmat.2018.05.020

18. Liang, D., Vistas, C.R., Garcia, D., Tibúrcio, B.D., Catela, M., Costa, H., Guillot, E., Almeida, J.: Most efficient simultaneous solar laser emissions from three Ce:Nd:YAG rods within a single pump cavity. Sol. Energy Mater. Sol. Cells **246**, 111921 (2022). https://doi.org/10.1016/j.solmat.2022.111921
19. Almeida, J., Liang, D., Vistas, C.R.: A doughnut-shaped Nd:YAG solar laser beam. Opt. Laser Technol. **106**, 1–6 (2018). https://doi.org/10.1016/j.optlastec.2018.03.029
20. Liang, D., Vistas, C.R., Almeida, J., Tiburcio, B.D., Garcia, D.: Side-pumped continuous-wave Nd:YAG solar laser with 5.4% slope efficiency. Sol. Energy Mater. Sol. Cells **192**, 147–153 (2019). https://doi.org/10.1016/j.solmat.2018.12.029
21. Vistas, C.R., Liang, D., Almeida, J., Tibúrcio, B.D., Garcia, D.: A doughnut-shaped Nd:YAG solar laser beam with 4.5 W/m^2 collection efficiency. Sol. Energ. **182**, 42–47 (2019). https://doi.org/10.1016/j.solener.2019.02.030
22. Welford, W.T., Winston, R.: High Collection Nonimaging Optics. Academic Press, London (1989)
23. Xu, P., Yang, S., Zhao, C., Guan, Z., Wang, H., Zhang, Y., Zhang, H., He, T.: High-efficiency solar-pumped laser with a grooved Nd:YAG rod. Appl. Opt. **53**(18), 3941–3944 (2014). https://doi.org/10.1364/ao.53.003941
24. Duocastella, M., Arnold, C.B.: Bessel and annular beams for materials processing. Laser Photonics Rev. **6**(5), 607–621 (2012). https://doi.org/10.1002/lpor.201100031
25. Rioux, M., Tremblay, R., Bélanger, P.A.: Linear, annular, and radial focusing with axicons and applications to laser machining. Appl. Opt. **17**(10), 1532–1536 (1978). https://doi.org/10.1364/AO.17.001532
26. Okida, M., Hayashi, Y., Omatsu, T., Hamazaki, J., Morita, R.: Characterization of 1.06 μm optical vortex laser based on a side-pumped Nd:$GdVO_4$ bounce oscillator. Appl. Phys. B **95**(1), 69–73 (2009). https://doi.org/10.1007/s00340-009-3438-7
27. Litvin, I.A., Ngcobo, S., Naidoo, D., Ait-Ameur, K., Forbes, A.: Doughnut laser beam as an incoherent superposition of two petal beams. Opt. Lett. **39**(3), 704–707 (2014). https://doi.org/10.1364/OL.39.000704
28. Cherezova, T.Y., Chesnokov, S.S., Kaptsov, L.N., Kudryashov, A.V.: Doughnut-like laser beam output formation by intracavity flexible controlled mirror. Opt. Express **3**(5), 180–189 (1998). https://doi.org/10.1364/OE.3.000180
29. Duan, K., Lü, B.: Four-petal Gaussian beams and their propagation. Opt. Commun. **261**(2), 327–331 (2006). https://doi.org/10.1016/j.optcom.2005.12.037
30. Yu, J., Zhou, C., Jia, W., Wu, J., Zhu, L., Lu, Y., Xiang, C., Li, S.: Generation of controllable rotating petal-like modes using composited Dammann vortex gratings. Appl. Opt. **54**(7), 1667–1672 (2015). https://doi.org/10.1364/AO.54.001667
31. Sabatyan, A., Rafighdoost, J.: Azimuthal phase-shifted zone plates to produce petal-like beams and ring lattice structures. J. Opt. Soc. Am. B **34**(5), 919–923 (2017). https://doi.org/10.1364/JOSAB.34.000919
32. Franke-Arnold, S., Leach, J., Padgett, M.J., Lembessis, V.E., Ellinas, D., Wright, A.J., Girkin, J.M., Öhberg, P., Arnold, A.S.: Optical ferris wheel for ultracold atoms. Opt. Express **15**(14), 8619–8625 (2007). https://doi.org/10.1364/OE.15.008619
33. Wang, H., Bai, Y., Wu, E., Wang, Z., Liu, P., Liu, C.: Terahertz necklace beams generated from two-color vortex-laser-induced air plasma. Phys. Rev. A **98**(1), 013857 (2018). https://doi.org/10.1103/PhysRevA.98.013857
34. Koechner, W.: Solid-State Laser Engineering, 6th edn. Springer, New York (2006)
35. Fan, T.Y.: Heat generation in Nd:YAG and Yb:YAG. IEEE J. Quantum Electron. **29**(6), 1457–1459 (1993). https://doi.org/10.1109/3.234394
36. Foster, J.D., Osterink, L.M.: Thermal effects in a Nd:YAG laser. J. Appl. Phys. **41**(9), 3656–3663 (1970). https://doi.org/10.1063/1.1659488
37. Koechner, W.: Thermal lensing in a Nd:YAG laser rod. Appl. Opt. **9**(11), 2548–2553 (1970). https://doi.org/10.1364/AO.9.002548
38. Uppal, J.S., Monga, J.C.: Contribution of stress-dependent variation of refractive index to thermal lensing in Nd:glass laser rods. Appl. Opt. **24**(22), 3690–3692 (1985). https://doi.org/10.1364/AO.24.003690

39. Innocenzi, M.E., Yura, H.T., Fincher, C.L., Fields, R.A.: Thermal modeling of continuous-wave end-pumped solid-state lasers. Appl. Phys. Lett. **56**(19), 1831–1833 (1990). https://doi.org/10.1063/1.103083
40. Tidwell, S.C., Seamans, J.F., Bowers, M.S., Cousins, A.K.: Scaling CW diode-end-pumped Nd:YAG lasers to high average powers. IEEE J. Quant. Electron. **28**(4), 997–1009 (1992). https://doi.org/10.1109/3.135219
41. Tuan, P.H., Chang, C.C., Lee, C.Y., Cho, C.Y., Liang, H.C., Chen, Y.F.: Exploiting concave-convex linear resonators to design end-pumped solid-state lasers with flexible cavity lengths: application for exploring the self-mode-locked operation. Opt. Express **24**(23), 26024–26034 (2016). https://doi.org/10.1364/OE.24.026024
42. Chesler, R.B., Maydan, D.: Convex-concave resonators for TEM_{00} operation of solid-state ion lasers. J. Appl. Phys. **43**(5), 2254–2257 (1972). https://doi.org/10.1063/1.1661486
43. Osterink, L.M., Foster, J.D.: Thermal effects and transverse mode control in a Nd:YAG laser. Appl. Phys. Lett. **12**(4), 128–131 (1968). https://doi.org/10.1063/1.1651922
44. Lörtscher, J.P., Steffen, J., Herziger, G.: Dynamic stable resonators: a design procedure. OQE **7**(6), 505–514 (1975). https://doi.org/10.1007/BF00619328
45. Hanna, D.C., Sawyers, C.G., Yuratich, M.A.: Telescopic resonators for large-volume TEM_{00}-mode operation. OQE **13**(6), 493–507 (1981). https://doi.org/10.1007/BF00668347
46. Magni, V.: Resonators for solid-state lasers with large-volume fundamental mode and high alignment stability. Appl. Opt. **25**(1), 107–117 (1986). https://doi.org/10.1364/AO.25.000107
47. Liang, D., Almeida, J., Vistas, C.R.: Scalable pumping approach for extracting the maximum TEM_{00} solar laser power. Appl. Opt. **53**(30), 7129–7137 (2014). https://doi.org/10.1364/ao.53.007129
48. Almeida, J., Liang, D.: Design of TEM_{00} mode side-pumped Nd:YAG solar laser. Opt. Commun. **333**, 219–225 (2014). https://doi.org/10.1016/j.optcom.2014.07.091
49. Golla, D., Bode, M., Knoke, S., Schöne, W., Tünnermann, A.: 62-W cw TEM_{00} Nd:YAG laser side-pumped by fiber-coupled diode lasers. Opt. Lett. **21**(3), 210–212 (1996). https://doi.org/10.1364/OL.21.000210
50. Kaneda, Y., Oka, M., Masuda, H., Kubota, S.: 7.6 W of continuous-wave radiation in a TEM_{00} mode from a laser-diode end-pumped Nd:YAG laser. Opt. Lett. **17**(14), 1003–1005 (1992). https://doi.org/10.1364/OL.17.001003
51. Liang, D., Almeida, J., Garcia, D.: Design of a high-power, high-brightness Nd:YAG solar laser. Appl. Opt. **53**(9), 1856–1861 (2014). https://doi.org/10.1364/AO.53.001856
52. Vistas, C.R., Liang, D., Almeida, J.: Solar-pumped TEM_{00} mode laser simple design with a grooved Nd:YAG rod. Sol. Energ. **122**, 1325–1333 (2015). https://doi.org/10.1016/j.solener.2015.10.049

Chapter 8
Solar Tracking Error in Solar-Pumped Lasers

Bruno D. Tibúrcio

8.1 Brief Introduction

In this chapter are discussed the solar tracking errors and the compensation techniques in solar-pumped lasers. Solar tracking error displaces the focal spot away from its optimal position, shifting the center of the absorption distribution within the laser rod, resulting in less laser output power and poor laser beam quality. The multi-rod approach is here discussed numerically and experimentally, in order to compensate the solar tracking error and enhance stable solar laser emission. A numerical modeling example of solar-pumped laser with tracking error compensation capacity is finally given in this chapter.

8.2 Sun Trajectory and Error Formation in Solar Energy Collection and Concentration Systems

8.2.1 Sun Trajectory in the Sky During the Day

The conceptualization of the apparent movement of the Sun is of paramount importance in the development of solar energy systems and solar tracking error systems. The discussion that follows is made within the context of orientating a solar tracker with respect to the Sun at any location on the earth and on any given time of the day. In the Fig. 8.1 below is shown the schematics of the Sun-Earth relationship. As seen from the Earth, the Sun disk forms an angle of 32 min of a degree. The Sun cannot be considered as a point source, due to even this small angle is significant in the analysis of the optical efficiency of a solar concentration system.

Knowledge of the variation in the Sun's position along the time and through the sky is necessary to calculate the solar radiation falling on a surface. The relative motions of the sun and earth are not simple, but they are systematic and thus predictable [1].

© The Author(s), under exclusive license to Springer Nature Switzerland AG 2023

D. Liang et al., *Solar-Pumped Lasers*, Green Energy and Technology,
https://doi.org/10.1007/978-3-031-24785-9_8

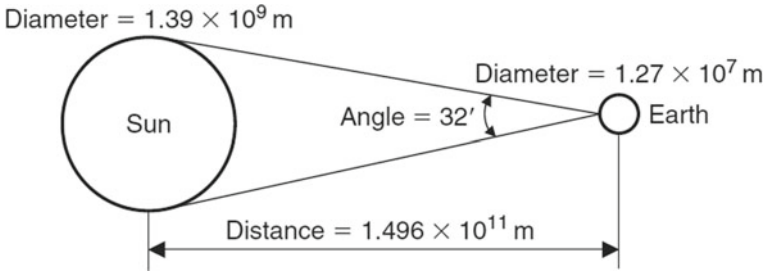

Fig. 8.1 Sun-earth relationship, adapted from [1]

The Ptolemaic view of the Sun's motion is used in the analysis for simplicity; since all motion is relative, it is convenient to consider the Earth fixed and to describe the Sun's apparent motion in a coordinate system fixed to the earth with its origin at the site of interest. Solar tracking systems (STS), such as the altitude-azimuth dual axis, use solar tracking algorithms to ensure that the Sun's passage through the sky is calculated and followed with high precision in automated solar tracker applications. A high precision solar position calculator or algorithm uses a software program routine to align the solar tracker to the sun and is an important component in the design and construction of an automatic solar tracking system. Solar position computer software for tracing the sun is available as open source codes.

The Earth makes one rotation about its axis every 24 h and completes a revolution about the sun in a period of approximately 365.25 days. The eccentricity, e, of the earth's orbit is very small, equal to 0.01673. Therefore, the orbit of the earth around the sun can be approximated as circular. Any location on the surface of the earth then can be defined by the intersection of a longitude angle and a latitude angle [2].

The Sun is constrained to move with 2 degrees of freedom on the celestial sphere; therefore, its position with respect to an observer on earth can be fully described by means of two astronomical angles, the solar altitude (h) and the solar azimuth (α) angles. Before giving the equations of solar altitude and azimuth angles, the solar declination and hour angle need to be defined.

8.2.2 Error Formation in Solar Energy Collection and Concentration Systems

The movement of the earth affects the collected solar radiation on solar systems, and consequently on the efficient solar concentration. The variation of the Sun's position in the sky during the day, or its apparent movement, generates errors in the alignment of the solar energy concentration system and the Sun, which any STS is designed to attenuate with a certain degree of accuracy with its automatic movement. The necessity of a high precision STS become a critical key for the developing and

deploying of solar concentration systems with the smallest integrated error in the STS.

Declination, δ

The earth axis of rotation (the polar axis) is always inclined at an angle of 23.45° from the ecliptic axis, which is normal to the ecliptic plane [1]. The ecliptic plane is the plane of orbit of the earth around the sun. The solar declination (δ) is the angle between the line joining the centers of the Sun and the Earth and its projection on the equatorial plane, as shown in Fig. 8.2. Declinations north of the equator (summer in the Northern Hemisphere) are positive, and those south are negative, and is given by:

$$\delta = 23.45 \sin\left[\frac{360}{365}(284 + N)\right] \tag{8.1}$$

The declination, δ, in degrees for any day of the year (N) can be calculated approximately by the equation [1]:

The solar declination during any given day can be considered constant in engineering calculations [4, 5]. The variation of the solar declination throughout the year is shown in Fig. 8.3.

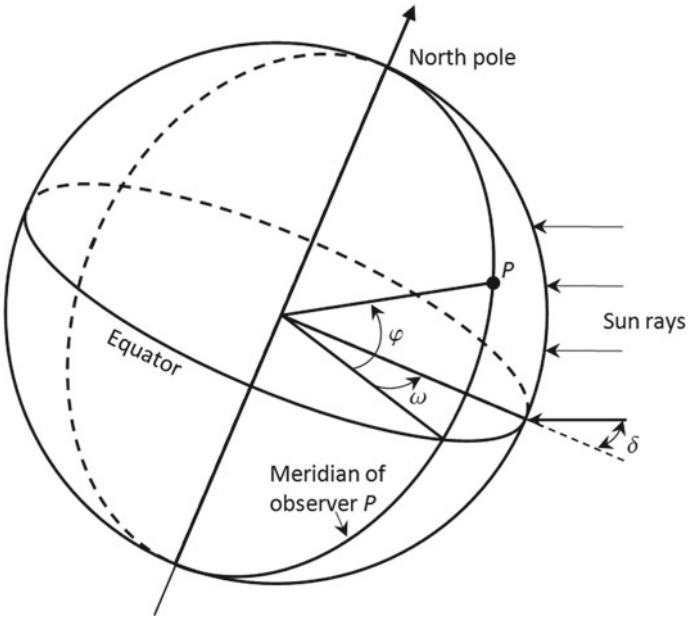

Fig. 8.2 Representative drawing of latitude, solar declination and hour angle, adapted from [3]

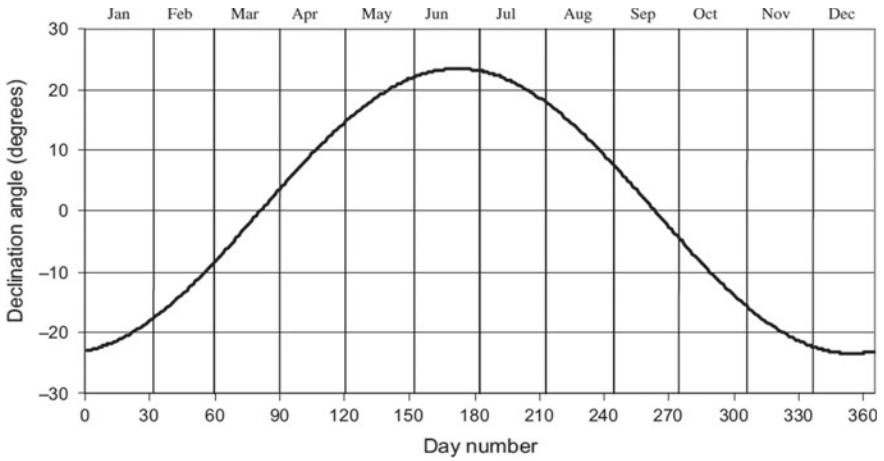

Fig. 8.3 Solar declination angle of the Sun [1]

Hour angle, ω

The hour angle, ω, of a point on the earth's surface is defined as the angle through which the earth would turn to bring the meridian of the point directly under the sun. To describe the Earth's rotation about its polar axis the concept of hour angle (ω) is used, which is the angle between the meridian passing through the Sun and the meridian of the observer P, as shown in Fig. 8.2, and is given by [1]:

$$\omega = \pm 0.25^{\circ} \times number\ of\ minutes\ from\ local\ solar\ noon \tag{8.2}$$

where the plus sign applies to afternoon hours and the minus sign to morning hours. The hour angle at local solar noon is zero, with each 360/24 or 15° of longitude equivalent to 1 h, afternoon hours being designated as positive.

Solar altitude angle, h

The solar rays are characterized by two astronomical angles: solar azimuth angle and the solar altitude angle [1, 6]. The solar altitude angle (h) is defined as the vertical angle between the projection of the Sun's rays on the horizontal plane, as shown in the Fig. 8.4. It is related to the solar zenith angle (θ_Z) which is the angle between the Sun's rays and the vertical [1]:

$$\theta_Z = 90^{\circ} - h \tag{8.3}$$

The solar altitude angle at the time of Sunrise and Sunset is 0°. The solar altitude angle has its maximum value at noon time in all seasons. The elevation angle is related to both the declination angle and the hour angle by the following expression [1].

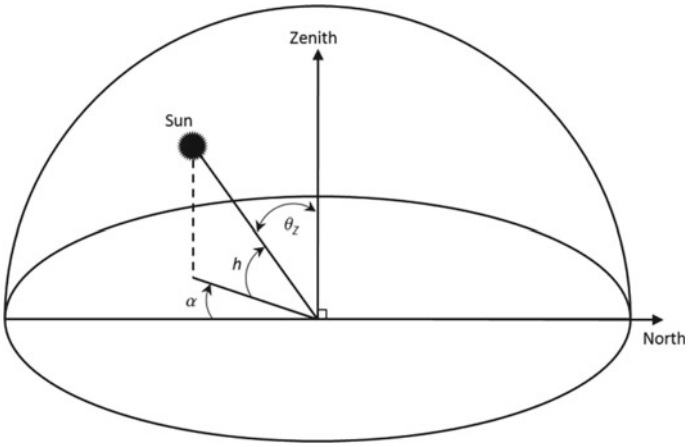

Fig. 8.4 Solar altitude h, azimuth α and zenith angles θ_Z

$$\sin(h) = \cos(\varphi)\cos(\delta)\cos(\omega) + \sin(\varphi)\sin(\delta) \tag{8.4}$$

where φ is the local latitude in degrees. The solar altitude angle at the time of sunrise and sunset is 0°, and has its maximum value at noon time in all seasons.

Solar azimuth angle, α

The solar azimuth angle, α, is the angle of the sun's rays measured in the horizontal plane from due south (true south) for the Northern Hemisphere or due north for the Southern Hemisphere; westward is designated as positive. For a geographical location, the azimuth angle α is the horizontal angle of the Sun's rays, and is given by the following equation [1]:

$$\sin(\alpha) = \frac{\cos(\delta)\sin(\omega)}{\cos(h)} \tag{8.5}$$

The output power produced by high-concentration solar systems is directly related to the amount of solar energy collected by the system, and it is necessary to track the sun's position with a high degree of accuracy, thus decreasing the errors in the alignment of the Sun and the solar concentration system.

8.3 Solar Tracking Systems

8.3.1 Direct Solar Tracking Mode

Solar-pumped lasers have additional problems not seen in commercial lasers in achieving the maximum solar energy transfer and absorption efficiencies from the pump source to the laser medium. The resonator stability of solar lasers depends on how well the Sun is tracked to continuously pump the laser crystal. The output power produced by high-concentration solar thermal and solar laser and photovoltaic systems is directly related to the amount of solar energy collected by the system. Many solar tracking systems (STS) have been proposed to implement this task over the past 60 years. STS thus have an important role in the development and efficiency of solar concentration applications [6]. STS enable solar collectors to accurately point towards the Sun and compensate for time (day and season) changes observed in altitude and azimuth angles of the Sun, thus decreasing the errors formed by the apparent movement of the Sun.

In this chapter, the STS will be presented regarding the fact if the primary collectors continuously follow the Sun directly pointed to it (or are tilted in a determined angle in order to increase its efficiency), or if the collectors are fixed, but irradiated by heliostats continuously moving to track the Sun's apparent movement in the sky.

There are different classifications of tracking systems regarding the strategies implemented to increase the energy collected by solar systems. Passive STS have simple operation principles, without mechanical parts or sensing units to help it to orient towards the Sun [7, 8], however, they have lower accuracy and energy gain compared to their more complex counterparts [9]. Active STS usually have optical sensors that help them to continuously determine the position of the Sun and use the motors to adjust the axes orientation [2]. In relation to the control strategies used to implement STS, there are the closed loop systems and the open-loop systems, the former based on feedback control principles, receiving input signals from the sensors which determine the position of the Sun [10–12]. The latter are algorithm-based systems, without feedback control to correct errors or disturbances in the operation [13–15].

STS can also be classified regarding to the number of movable axis following the Sun. They are generally classified in those implemented by using single-axis STS, and for higher accuracy, double-axis STS. There are several configurations of motion of single-axis trackers: horizontal, tilted-horizontal, vertical, tilted and polar aligned, parallel to earth's axis, with east–west tracking [1, 9]. Studies have demonstrated that single-axis STS [16–20] can increase their energy produced of between 12 and 20% [21] compared with fixed/optimally inclined installations.

Although single-axis trackers are cheaper and easier to build and implement, the increase in efficiency provided is lower than that of the double-axis STS [9]. These systems have been studied using Fresnel lenses [22] or concentrator photovoltaic (CPV) system [23], solar panels [24] or solar-pumped lasers [25–27], (Fig. 8.5). In 2012, a high accuracy solar tracking system was developed which achieved 0.01%

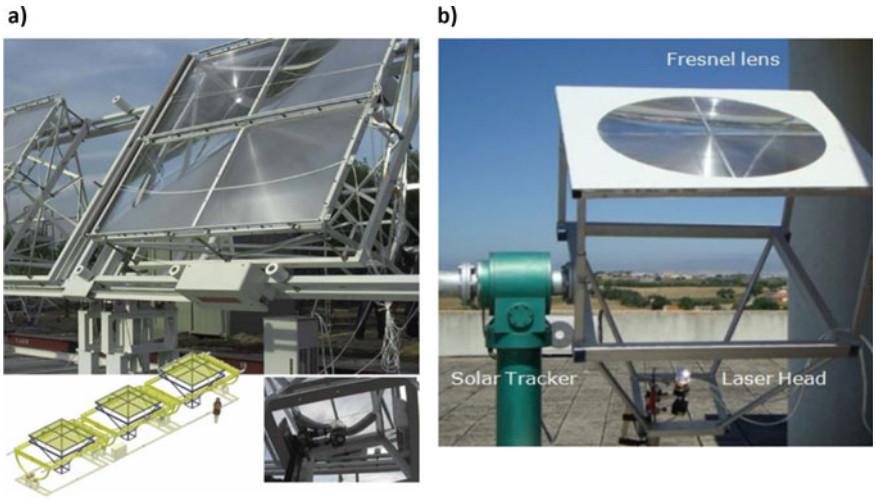

Fig. 8.5 Solar-pumped laser setups using Fresnel lenses and direct solar tracking systems from [25, 27]

standard deviation between the simulated and measured values of the available solar radiation [28].

The conclusion is that double-axis STS always achieved good performances with greater efficiencies between 20 and 50% energy gains when compared to fixed flat panels and/or CSP systems [9]. In 2014, Yao proposed a multipurpose double-axis STS that can be applied to solar power systems. Results of the accuracy test indicate that the tracking error of the normal tracking strategy is within 0.15°. Furthermore, in the test on the output of the PV modules, it is found that the average energy efficiency of the normal tracking PV, compared with the fixed PV, is more than 23.6%, as shown in Fig. 8.6. The average energy efficiency of the daily adjusted PV is more than 31.8% [29].

The direct tracking mode has the advantage of higher solar irradiation upon the receiver, due to the primary collector being continuously pointed directly to the Sun, discarding another mirror while is in use. However, indirect tracking mode has the advantage of protecting the most expensive and sensible primary solar concentrator, altogether with the receiver and all components of the solar application inside an infrastructure, and a more stable solar energy delivery in any application.

8.3.2 Indirect Solar Tracking Mode by Heliostats

The contents in this section are classified in solar tracking systems which use heliostats whose track the Sun, reflecting the solar radiation toward the collector, as shown in Fig. 8.7.

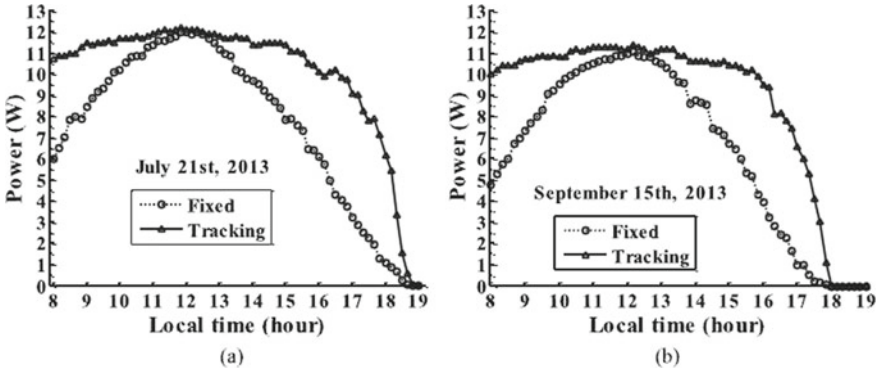

Fig. 8.6 Output of the normal tracking and fixed PV module on the days of **a** July 21st; **b** September 15th [29]

Fig. 8.7 Photograph of a heliostat tracking the Sun and reflecting the solar radiation to a medium size parabolic mirror in Almeria solar plant, Spain

Since the first STS, introduced in 1962 [30] using single heliostats, showing very little increased performance over fixed systems, many other researchers have investigated solar trackers in order to improve their solar collection efficiency [31, 32], with the tracking error tolerances varying between 0.5° and 1°. Significant improvement on the accuracy of STS was noticed since 1985, after Badescu et al. demonstrated the influence of the astronomical and constructive parameters on the concentration of solar radiation with plane heliostats on the tracking surfaces of PV systems [33]. Solutions were investigated to correct the heliostat offset errors and the reflected solar radiation images to the receiver using cameras. The system had a digital camera capturing the real time Sun images projected by the heliostats and supplied it to the computer. These images were then compared to the inbuilt reference images where

the solar radiations were perpendicular to the heliostat. The difference between these two images generated a control signal which was used by the control system to activate the servo-motors and reorient the collector back to 90° with respect to the solar radiation beam [34]. Chen in 2005 derived general Sun tracking formula for heliostats with arbitrarily oriented axes [35].

A solar double axis tracker was developed in 2007, with a higher concentration of solar energy using a tracking master mirror surrounded by several other slave mirrors, which reflected collected solar radiation onto a stationary target. The solar image reflected by the master mirror was used as a reference for all slave mirrors. The rotational axis was configured pointing to the target and the other one was the elevation axis parallel to the reflector [36]. Using two photo-sensors and a heliostat, reflecting the solar radiation to a 70 m away target screen, system's tracking error was evaluated at 0.11° in a clear weather [37]. In 2014, a beam characterization system was used to evaluate the tracking error of two heliostats from a central tower solar plant with an estimated accuracy of about 2% for the positioning angle measurement [38].

For extremely high inputs of radiant energy, a multiplicity of flat mirrors, or heliostats, using altitude-azimuth mounts can be used to reflect their incident direct solar radiation onto a common target, as shown in Fig. 8.8. This is called the heliostat field or central receiver collector. The heliostat field typically represents 30–50% of the capital cost of the system and the required size of the heliostat field for a given nominal power of a solar plant is reduced with an increased optical efficiency. Similarly, increasing thermal performance of the receiver decreases the required size of the heliostat field and the associated capital cost [39].

Central receivers have several advantages [40]:

Fig. 8.8 Photograph of a large parabolic mirror in PROMES CNRS, France: the heliostat field reflects their incident direct solar radiation onto a parabolic mirror, which concentrates the solar radiation onto a target at its focal zone

1. They collect solar energy and transfer it to a single receiver, thus minimizing thermal energy transport requirements.
2. They typically achieve concentration ratios of 300–1500 and so are highly efficient.
3. They can conveniently store thermal energy.
4. They are quite large (generally more than 10 MW) and thus benefit from economies of scale.

The heliostats collect and concentrate Sunlight onto the receiver, which absorbs the concentrated solar energy, transferring its energy to a heat transfer fluid. A thermal storage system typically stores the collected energy as sensible heat for later delivery to the power conversion system.

8.4 Tracking Error in Different Primary Solar Concentrators

8.4.1 Solar Tracking Error in Parabolic Mirrors

Solar concentration systems as point-focusing concentrators need to employ some form of solar tracking mechanism with sufficient accuracy [41], usually with less than 0.05° [15, 42], for enabling the achievement of higher concentration ratios, radiation flux and thus conversion efficiency [1]. Consequently, it becomes necessary to follow the daily apparent motion of the sun in both altitude and azimuth directions, requiring a solar tracking system [1, 43]. Parabolic collectors generally use a method in which the sun tracker moves in both altitude and azimuth direction.

Parabolic trough collectors (PTCs) generally use a one-axis tracking system, which follows the sun in only one direction. PTCs are a well established solar energy technology, implemented in many places to produce electricity via solar cells or thermal processes. Significant advancements have been demonstrated in the last decades with several approaches and strategies to increase the output power harvested from these collectors [44–46]. 68.8% higher in heat gain achieving 15–17% more in collector efficiency or an enhanced optical efficiency of 0.81% were obtained using double-axis STS [47, 48]. Solar tracking systems have been also developed in order to improve the solar collection and concentration efficiency of parabolic dish solar concentrators, which have attracted much interest for many researchers, as a mean to reach high concentration ratios [10, 49–51]. In 2019, Natarajan et al. obtained 86% of short circuit current value of the concentrated panel compared with conventional PV panel [52].

In Fig. 8.8a is shown a two-axis heliostat and a stationary parabolic mirror with 1.5 m diameter, 60° rim angle and 660 mm focal length and its two axis of rotation. It also shown in Fig. 8.9b the position of the focal spot at its optimal alignment, in the absence of solar tracking error, and in two extreme cases for the maximum solar tracking errors of $\Delta Y = 0.3^{\circ}$ and $\Delta X = 0.3^{\circ}$.

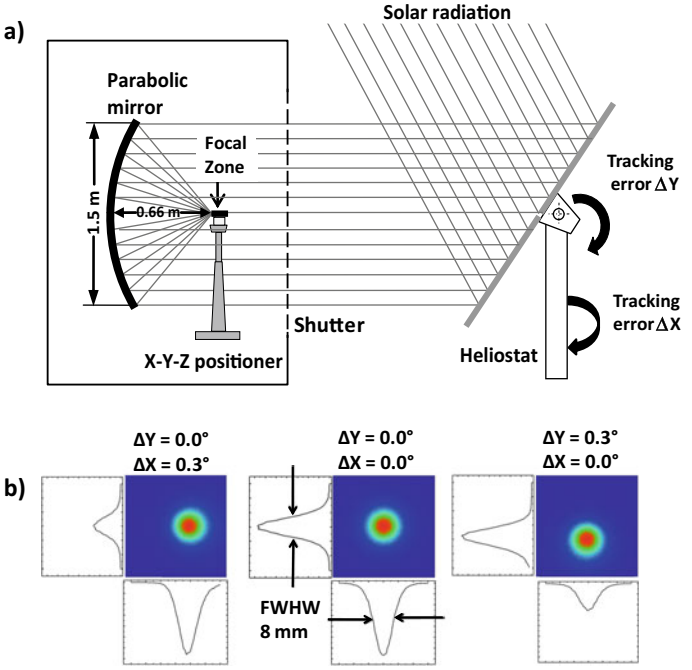

Fig. 8.9 **a** Schematics of a heliostat-parabolic solar energy collection and concentration system and the heliostat orientation error direction at ΔY and ΔX. **b** The focal spot of the parabolic mirror at its optimal alignment, in the absence of solar tracking error and at two extreme cases for solar tracking errors of $\Delta X = 0.3^{\circ}$ and $\Delta Y = 0.3^{\circ}$

Motohiro, aiming to attain efficient solar energy conversion to laser light and utilizing originally designed μSPLs, developed a precise direct solar tracking system with an error smaller than 0.06°, required because of the high concentration ratio: 1 = 10626 of the μSPL collector mirror. Thus, a prototype system with precision < 0.06° for 25 μSPLs in an array was successfully fabricated in that study.

Studying the tracking error influence in solar lasers with two types of secondary concentrators, cylindrical and aspherical at the focus of a parabolic dish, Tiburcio et al. [53, 54], have numerically investigated the solar laser output power using a dual-rod scheme as a function of the tracking errors, in order to develop a tracking error compensation capacity solar laser scheme. The tracking error width at 10% laser power loss ($TEW_{10\%}$) was chosen to analyze the tracking error compensation capacity of the schemes. For a fused silica cylindrical lens as a secondary concentrator, a large improvement in tracking error compensation capacity was numerically attained with that approach, leading to 2.57 and 3.00 times enhancement in tracking error width at 10% laser power loss in ΔY (altitude) and ΔX (azimuth) errors, respectively, as compared to the most efficient end-side-pumped scheme by the same collection area. Using aspherical fused silica lens as a secondary concentrator, this results were improved with, where the $TEW_{10\%}$ was improved 1.66 and 1.21 times at altitude

(ΔY) and azimuth (ΔX) tracking errors, respectively, as compared to the numerically simulated side-pumped single-rod scheme. In 2022, the first experimental results of tracking error compensation capacity of a solar-pumped laser pump by a heliostat-parabolic mirror were demonstrated, which it will be given in Sect. 8.5.2.1 [55].

8.4.2 Solar Tracking Error in Fresnel Lenses

In the field of concentrated solar energy applications, Fresnel lenses have been one of the best choices because of the advantages such as small volume, light-weight, mass production with low cost, despite the chromatic aberration that is produced at the focus [56]. Point-focus concentrating systems with azimuth-elevation tracking can obtain a high energy density and overall efficiency, but, in return, this results in an increase in the initial and operational costs. Compared with the azimuth-elevation tracking, the advantage of polar-axis tracking is the best one-axis tracker, delivering around 97% of the yearly energy of azimuth-elevation trackers, and its cost is approximately half that of the azimuth-elevation one [2].

Several researchers have studied and developed STS for Fresnel lens concentrators over the years [57–62]. Yabe et al. proposed a solar laser system that uses the Fresnel lens with a double-axis direct tracking system to demonstrate a fossil-fuel-free energy cycle with magnesium and laser [63, 64]. Perini presented a model for a novel linear Fresnel lens collector with dual-axis tracking capability, where the optical and thermal models of the Fresnel lens collector with 2D tracking are presented and validated using experimental data. The conclusion was that both single and dual axis tracking remain an option [65].

Liang et al. improved several times the solar-pumped laser efficiency using a Fresnel lenses with a double-axis direct tracking system, presented in Fig. 8.10 [25, 26].

8.4.3 Solar Tracking Error in Ring-Array Concentrators

A ring-array solar concentrator, introduced and developed by Vasylyev et al. [66] consists of a set of concentric rings disposed in such way that the inner reflective surfaces do not mutually shade, shaping its focal spot through superposition of rays to a common point in the rear side of the collector, as shown in Fig. 8.11. This configuration allows efficient integration of components, decreasing the shadow areas between incoming solar rays and the laser head, as compared with heliostat-parabolic mirror.

In 2018, it was studied a typical tracking error from 0.05° to 0.2° in either azimuthal and altitude axes through the laser output power variation. Figure 8.11 represents the RAC designed in [67], which is composed of 13 rings, each with off-axis parabolic profile, 0.6 mm thickness and protective-silver coated with 95% reflectivity. In the

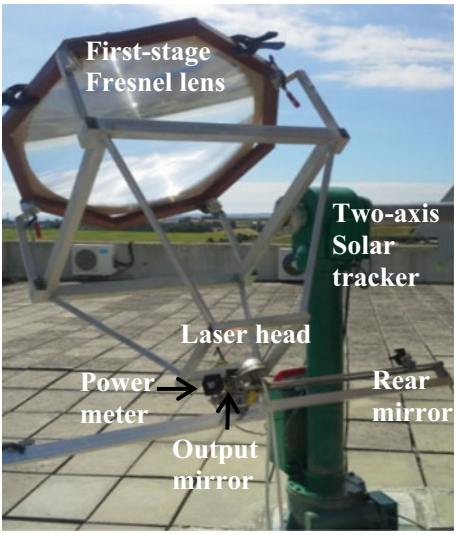

Fig. 8.10 The solar-pumped Nd:YAG solar laser system from [26]

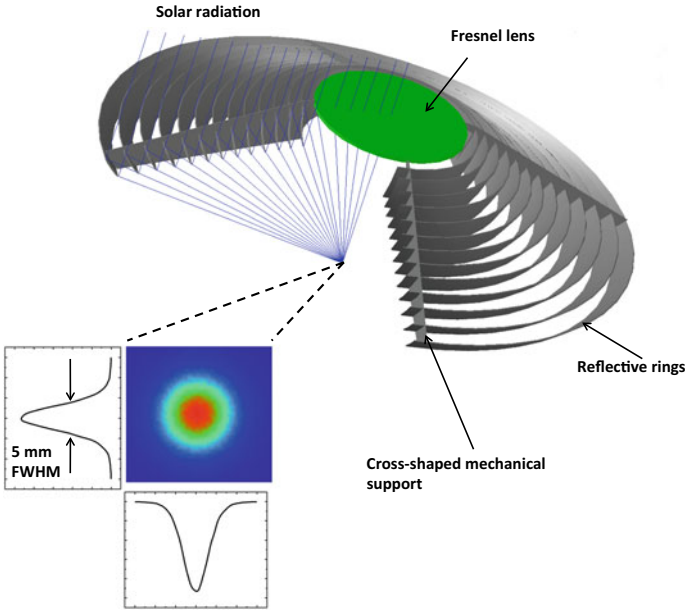

Fig. 8.11 The ring-array concentrator is composed of 13 rings and a small Fresnel lens. Inset picture with the pump light distribution at its focal point

central region of the RAC a small Fresnel lens is also mounted. A mechanical structure connecting all these rings and the Fresnel lens is also given in Fig. 8.11. The influence of tracking error on the output laser power for the 5.0 mm diameter, 20 mm length Nd:YAG rod was studied. At the maximum tracking error of 0.2° in both azimuth and altitude axes, 48.5 W was attained, corresponding to 28% laser power loss, using an end-side-pumping scheme. De Matos et al. proposed in 2018 a modified RAC [68]. It was studied a typical tracking error from 0.05° to 0.20° in either azimuthal and altitude axes. At the maximum tracking error of 0.2° in both azimuth and altitude axes, 50.4 W was attained, corresponding to 25.7% laser power loss. To correctly evaluate the tracking error associated laser output power, a 1.5 m diameter Fresnel lens was also designed to pump the same 5.0 mm diameter 20 mm length Nd:YAG rod. Therefore, a very clear advantage of the modified ring-array system in both solar laser output power enhancement and tracking error associated laser power reduction was demonstrated in comparison to Fresnel lenses.

Garcia et al. analyzed is the efficiency loss of the spherical receiver of 15 mm diameter as function of tracking error in altitude and azimuth directions for MSSF parabolic mirror and 3D RAC solar furnace [69]. At the extreme case of tracking error by 0.5° on both axes, the efficiency was nearly extinguished for the MSSF parabolic mirror and a 60% loss was obtained for 3D RAC. Tiburcio et al. studied the same RAC designed before to investigate the dual-rod side-pumping concept as an interesting alternative to attain an improved solar laser output power, with better beam quality and tracking error compensation capacity [70]. In Fig. 8.12 is shown the 3D normalized solar laser power for both the single and the dual-rod side-pumping schemes from this work and the end-side-pumping scheme from reference [71], as a function of the simultaneous altitude and azimuth solar tracking errors ranging from 0.0° to 0.3°.

The influence of tracking error on RAC side-pumping solar laser performance was also investigated, showing only 2% power loss for a tracking error of 0.1° at altitude and azimuth directions simultaneously. The dual-rod side-pumping concept is an interesting alternative to attain an improved solar laser output power with better beam quality and tracking error compensation capacity, comparatively not only with the single-rod side-pumping scheme but also with the end-side-pumping scheme from [71]. The significant improvement in the thermal performance of the laser media helps to increase the laser performance and stability.

8.5 Tracking Error Compensation Techniques

8.5.1 Monolithic Fused Silica Twisted Light Guide

In order to improve the overall stability and tracking error tolerance on solar lasers, in 2008 Geraldes et al. designed and simulated nine fused silica light guides of square cross-section are used to form the light guide assembly, as shown in Fig. 8.13 [72].

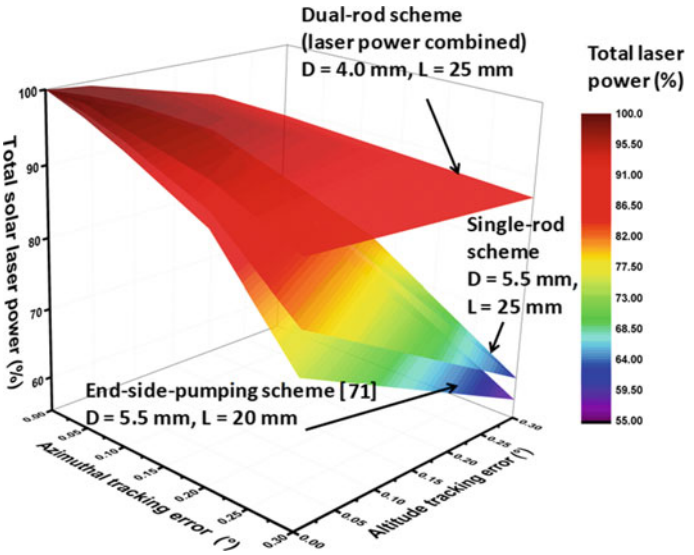

Fig. 8.12 The normalized total solar laser output power in percentage, for both the single and the dual-rod side-pumping schemes, and the end-side pumping scheme [71], as a function of the simultaneous variation in altitude and azimuth solar tracking errors, ranging from the optimal alignment (0.0°) to 0.3°, using the same RAC solar energy collection and concentration system

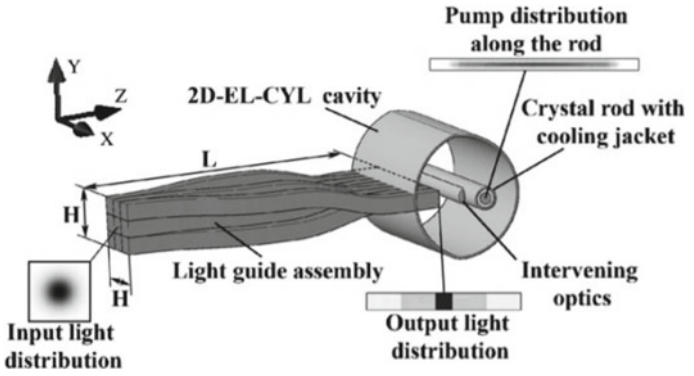

Fig. 8.13 Light guide assembly 2D-CYL-EL cavity with intervening optics. End plates have been removed for better illustration

The input ends of the light guides were packed together to form a 20 × 20 mm^2 square input face. The input face of the assembly is placed at the focal spot of the primary mirror and the output end coupled to the first focal line of the 2D-ELCYL cavity. Figure 8.14a shows both the input and output pump light distributions of the light guide assembly, corresponding to the optimum alignment between the heliostat and the primary parabolic concentrator. For the combined tracking errors in XY-axes,

the focal spot is located near the center of the four upper left light guides, resulting in the strongly shifted output distribution as given in Fig. 8.14d.

In 2017, a fused silica twisted light guide was experimentally simulated and tested with tracking error compensation capacity [73, 74]. The concentrated solar radiation was firstly collected by the twisted fused silica light guide with 16 mm 16 mm input face. It was then transmitted along 110 mm length, observing both refraction and total internal reflection principles, to its rectangular output end with 8.0 mm, 32 mm, as illustrated in Fig. 8.15. The near-Gaussian profile of the concentrated light spot incident on the input face of the light guide assembly was therefore transformed into a rectangular pump light column at the assembly output end.

For the combined tracking errors of 0.2° in both X and Y axes, the focal spot was shifted obliquely from the center of the input face of the lower straight part of the light guide, causing a reduction in laser output power and a modification of the fundamental mode beam profile.

8.5.2 Multi-Rod Pumping Approach

8.5.2.1 Multi-Rod Pumped Through a Fused Silica Cylindrical Secondary Concentrator

Multi-rod concepts have been numerically investigated using different secondary concentrators in order to improve the solar laser emission stability and tracking error compensation capacity. Tiburcio et al. in 2019 had numerically investigated a cylindrical concentrator in a dual-rod side-pumping configuration [53]. The tracking error of the optimized dual and single-rod schemes was firstly studied and then was compared to that of the most efficient end-side-pumped laser [71]. All these schemes were pumped by NOVA heliostat-parabolic solar collection and concentration system with the same collection area of 1.56 m^2. The tracking error width at 10% laser power loss ($TEW_{10\%}$) was chosen to evaluate the tracking error compensation capacity of the schemes.

In Fig. 8.16 is shown the influence of the solar tracking error on the dual-rod scheme in altitude (ΔY) and azimuth (ΔX) directions. With the tracking error at ΔY, the focal spot moved upwards (Fig. 8.16a), from the lower rod to the upper rod in the dual-rod scheme. With the tracking error at ΔX, the focal spot moved in the azimuthal direction of the dual-rod scheme (Fig. 8.16b). With the simultaneous tracking error in ΔY and ΔX, the focal spot moved upwards to the upper rod and also to the right in azimuthal directions (Fig. 8.16c).

In Fig. 8.17 is shown the absorbed pump flux distribution along the longitudinal cross-section of the dual-rod and the single-rod pumped with solar tracking error at ΔY, ΔX and ΔY and ΔX, simultaneously. The laser output powers are also indicated.

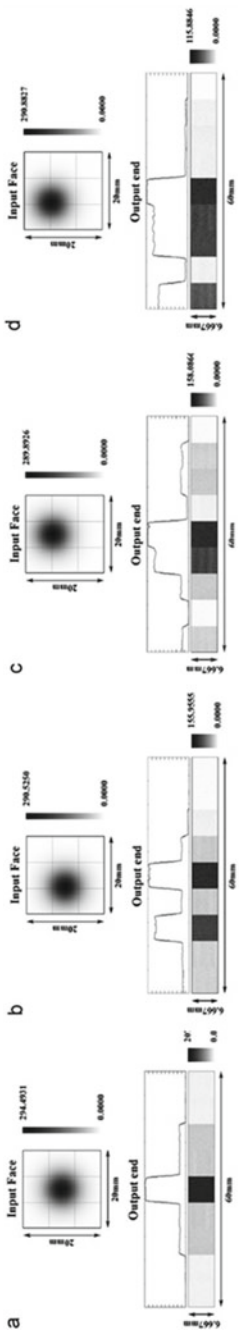

Fig. 8.14 Input and output light distributions for the cases of **a** zero tracking error, **b** *X*-axis 3 mm displacement, **c** *Y*-axis 3 mm displacement and **d** combined *X*–*Y* axes 3 mm displacement

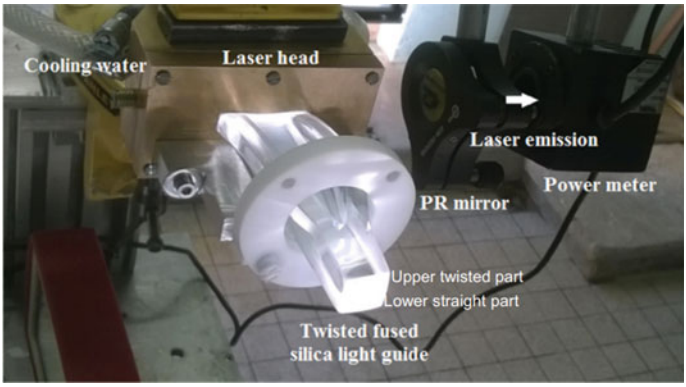

Fig. 8.15 Solar-pumped Nd:YAG laser head composed of the monolithic light guide, the solar laser head and the laser resonant cavity [73]

8.5.2.2 Multi-Rod Pumped Through a Fused Silica Aspherical Secondary Concentrator

The single and the dual-rod schemes were studied regarding to the tracking error capacity using an aspherical lens as a secondary concentrator [54]. In Fig. 8.18 is shown an example of the influence of the solar tracking error on the dual-rod scheme in altitude (ΔY) and azimuth (ΔX) directions individually, and at ΔY and ΔX directions simultaneously. With the tracking error at only ΔY, the focal spot moved upwards, from the lower rod to the upper rod (Fig. 8.18a). With the tracking error at ΔX, the focal spot moved along the laser rods (Fig. 8.18b). With the simultaneous tracking error in ΔY and ΔX, the focal spot moved upwards to the upper rod and also to the right (Fig. 8.18c).

The normalized total multimode laser output power as a function of the ΔY and ΔX solar tracking errors (from the optimal alignment to 0.35° tracking error) for both the single and the dual-rod schemes and also for the 3.5 mm diameter, 25 mm length Nd:YAG from the previous dual-rod scheme are shown in Fig. 8.19 [53].

In 2022, the first experimental results of tracking error compensation capacity of a solar-pumped laser were demonstrated, with a largely enhanced tracking error tolerance achieved by pumping two laser rods simultaneously [55]. A large aspherical fused silica lens, with an input face of 46 mm radius of curvature and 84 mm diameter, provided an efficient focusing of the concentrated solar radiation from the focal spot of the parabolic mirror onto the two laser rods, mounted within two semicylindrical pump cavities.

In Fig. 8.20 is presented a photograph of the dual-rod solar laser head and the two laser power meters used to measure the solar laser output powers from each one of the rods.

The altitude h and the azimuthal α position of the Sun were calculated in two moments during the experiment: when the system was optimally aligned (t_0), and

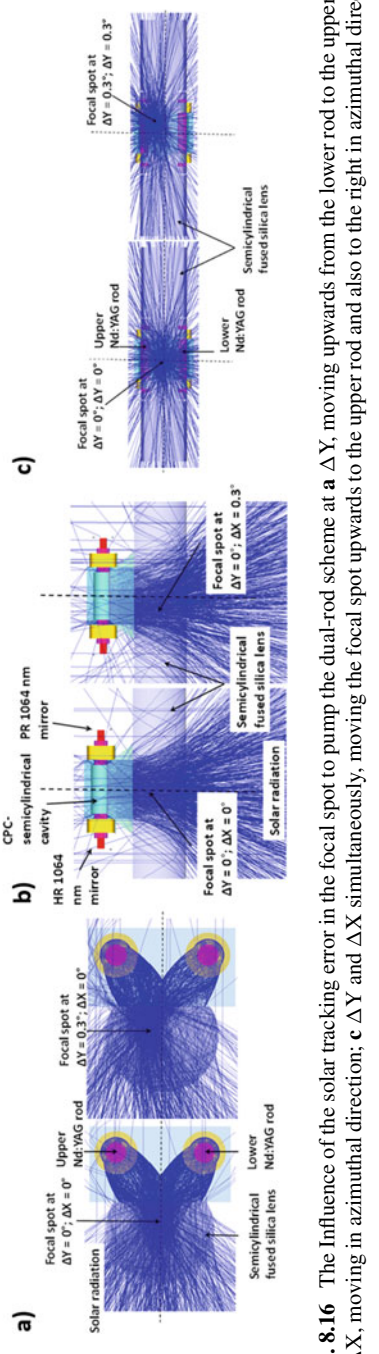
a)
Solar radiation
Focal spot at ΔY = 0°; ΔX = 0°
Upper Nd:YAG rod
Focal spot at ΔY = 0.3°; ΔX = 0°
Semicylindrical fused silica lens
Lower Nd:YAG rod
b)
HR 1064 nm mirror
CPC-semicylindrical cavity
PR 1064 nm mirror
Focal spot at ΔY = 0°; ΔX = 0°
Solar radiation
Semicylindrical fused silica lens
Focal spot at ΔY = 0°; ΔX = 0.3°
c)
Focal spot at ΔY = 0°; ΔY = 0°
Upper Nd:YAG rod
Lower Nd:YAG rod
Semicylindrical fused silica lens
Focal spot at ΔY = 0.3°; ΔY = 0.3°

Fig. 8.16 The Influence of the solar tracking error in the focal spot to pump the dual-rod scheme at **a** ΔY, moving upwards from the lower rod to the upper rod; **b** ΔX, moving in azimuthal direction; **c** ΔY and ΔX simultaneously, moving the focal spot upwards to the upper rod and also to the right in azimuthal direction

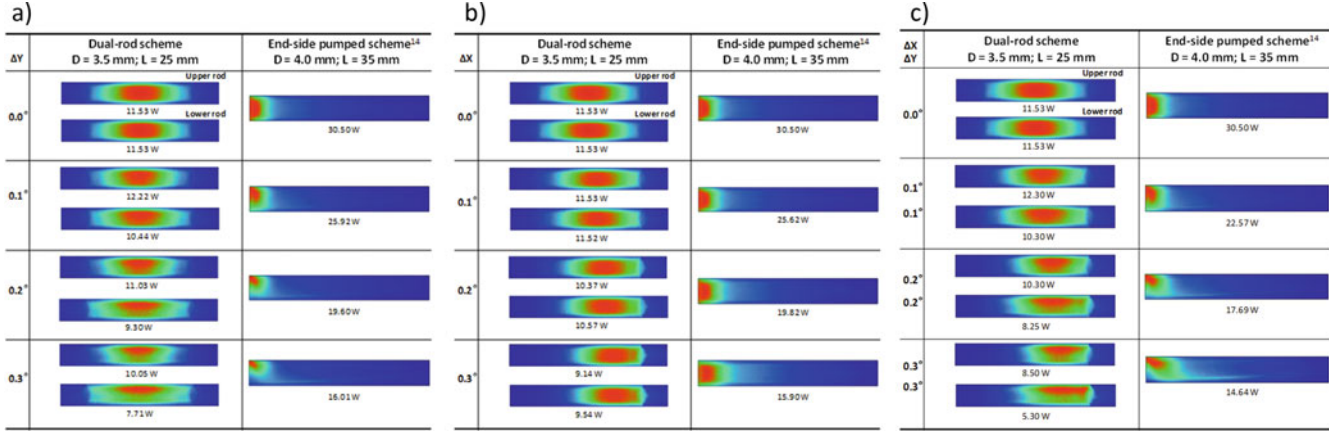

Fig. 8.17 The absorbed pump flux distribution along the longitudinal cross-section of the Nd:YAG crystal rods, pumped with solar tracking error at **a** ΔY, **b** ΔX and **c** ΔY and ΔX simultaneously, for the dual-rod and the end-pumped scheme [71], with the same collection area of NOVA solar system. The numerically obtained laser output powers are also indicated

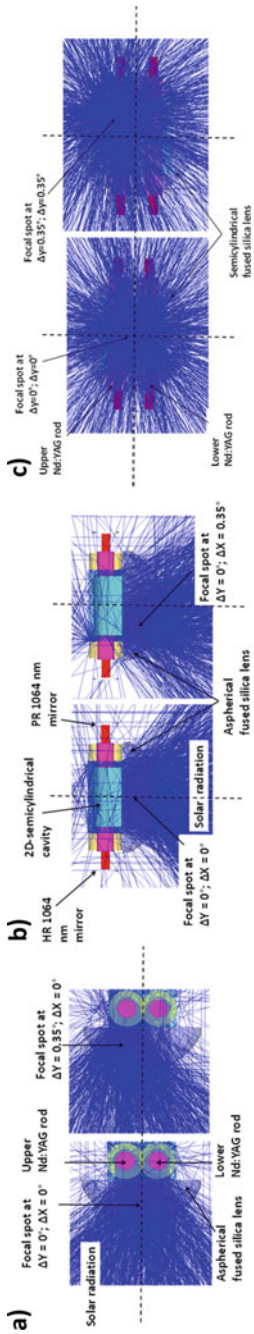
a)
Solar radiation
Focal spot at ΔY = 0°; ΔX = 0°
Upper Nd:YAG rod
Focal spot at ΔY = 0,35°; ΔX = 0°
Aspherical fused silica lens
Lower Nd:YAG rod
b)
HR 1064 nm mirror
2D-semicylindrical cavity
PR 1064 nm mirror
Focal spot at ΔY = 0°; ΔX = 0°
Solar radiation
Aspherical fused silica lens
Focal spot at ΔY = 0°; ΔX = 0,35°
c)
Upper Nd:YAG rod
Focal spot at Δy=0°; Δy=0°
Focal spot at Δy=0,35°; Δy=0,35°
Lower Nd:YAG rod
Semicylindrical fused silica lens

Fig. 8.18 Solar tracking error and its influence in the focal spot to pump the dual-rod scheme at **a** altitude direction (ΔY), **b** azimuth direction (ΔX) and **c** ΔY and ΔX simultaneously

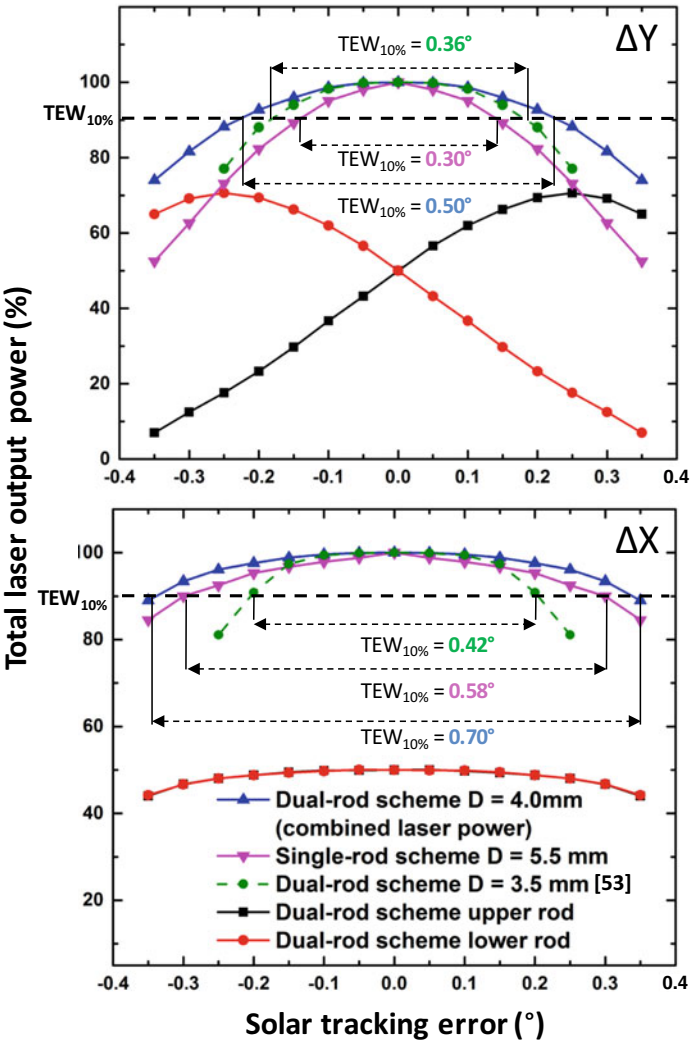

Fig. 8.19 Normalized total multimode laser output power, from the optimal alignment (0.0°) of the solar laser head, as a function of the ΔY and ΔX solar tracking errors, for the single and the dual-rod schemes and also for the previous dual-rod scheme [53]. It is also shown the normalized power for each laser rod from the dual-rod scheme (both upper and lower rod), as well the tracking error width at 10% laser power loss ($TEW_{10\%}$)

after one minute (t_1), with the heliostat stopped [1]. The dual-rod side-pumping tracking error compensation capacity was tested using two setups: one vertical (i.e. the solar laser beams emitted vertically), and one horizontal (the laser beams emitted horizontally). In Fig. 8.21 is shown the solar laser head and the schematics for two maximum displacements of the focal spot, due to the solar tracking error in both

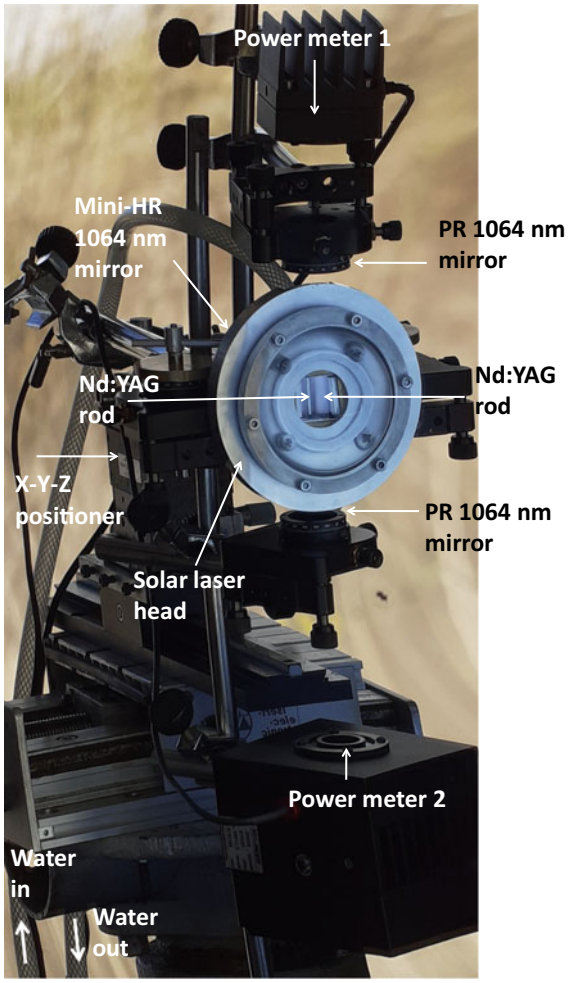

Fig. 8.20 Photograph of the solar laser head showing the two Nd:YAG rods, the water cooling scheme, the laser resonator mirrors and the laser power meters 1 and 2

altitude and azimuth directions are presented, corresponding to the positions 1 and 3 in Fig. 8.21a–c, respectively. The optimal alignment is represented by the position 2 in Fig. 8.21b. In Fig. 8.21d is shown the normalized total solar laser power from the left and the right laser rods, as well as the normalized solar laser power from each rod.

With the tracking error in altitude, the pump flux distribution moved only slightly along the laser rods of the dual-rod scheme. The largest tracking error occurred in the azimuth direction, which displaced the pump flux distribution from the left rod to the right rod. In Fig. 8.22 is presented the solar laser head and the schematics for two maximum displacements of the focal spot due to the solar tracking error in both altitude and azimuth directions in the horizontal setup, corresponding to the positions 1 and 3 in the Fig. 8.22a–c, respectively. The optimal alignment corresponds to the

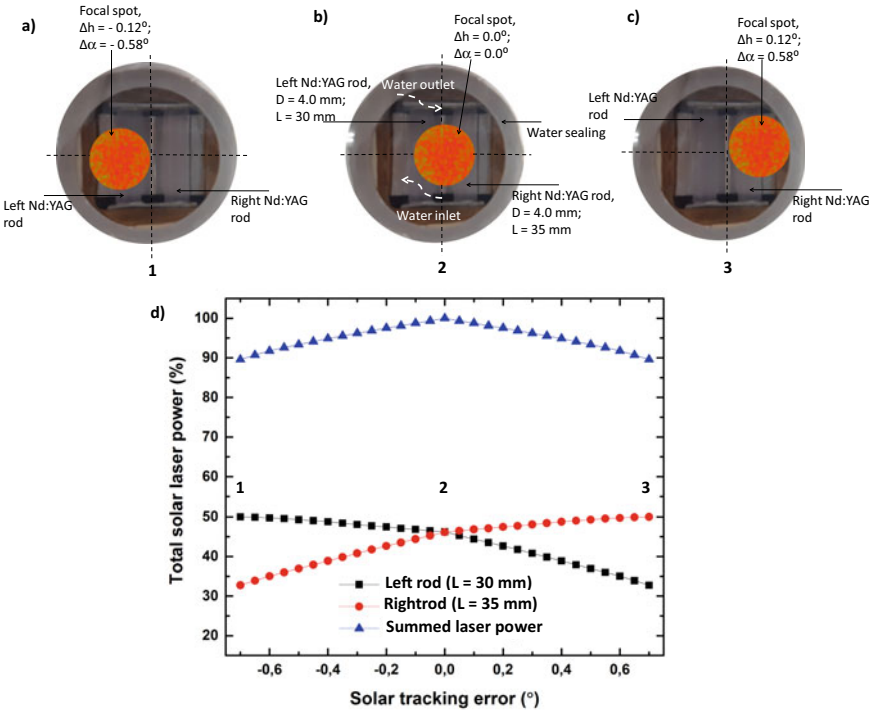

Fig. 8.21 The solar laser head and the schematics for **a**, **c** two maximum displacements of the focal spot due to the solar tracking error in both altitude and azimuth directions in the vertical setup, corresponding to the positions 1 and 3; **b** optimal alignment of the focal spot, corresponding to the position 2; **d** normalized total solar laser power for the left and the right laser rods

position 2 in Fig. 8.22b. In Fig. 8.22d is shown the normalized total solar laser power from the upper and the lower laser rods, as well as the normalized laser power from each laser rod. With the tracking error in altitude, the pump flux distribution moved from the lower rod to the upper rod of the dual-rod scheme. The tracking error in azimuth displaced the pump flux distribution along the rods.

The dual-rod side-pumping experiments resulted in a largely enhanced tracking error tolerance, as shown in Fig. 8.23, where the vertical and the horizontal setups presented a $TEW_{10\%}$ of 1.4˚ and 0.6˚, respectively, and a more stable solar laser emission as compared to the numerical models from a previous dual-rod scheme [54].

In comparison with the other numerical dual-rod side-pumping solar laser, with cylindrical lens and one pump cavity to each one of the laser rods in a horizontal setup [53], the experimental dual-rod side-pumping had also shown a significantly improved tracking error stability, as given in Fig. 8.24. The comparison with

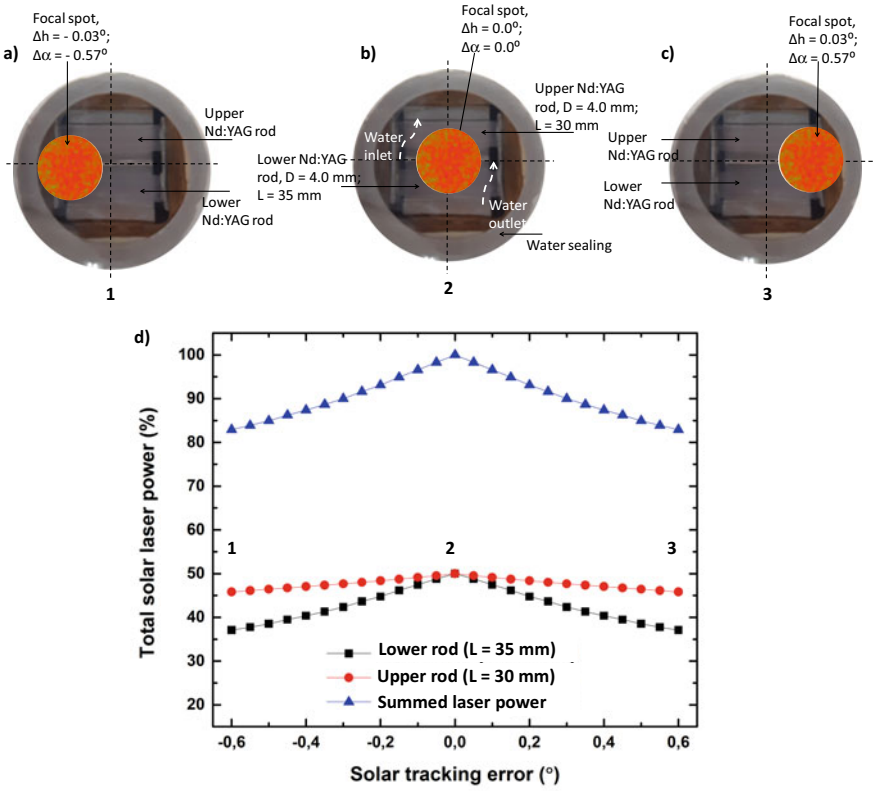

Fig. 8.22 The solar laser head and the schematics for **a**, **c** two maximum displacements of the focal spot due to the solar tracking error in both altitude and azimuth directions in the horizontal setup, corresponding to the positions 1 and 3; **b** optimal alignment, corresponding to the position 2; **d** normalized total solar laser power for the upper and the lower laser rods, as well as the normalized laser power from each laser rod

the numerically calculated tracking error compensation capacity of the most efficient experimental solar-pumped laser in an end-side-pumping configuration is also represented [53, 71].

Both the vertical and the horizontal setups had shown a substantially improved tracking error tolerance, providing a stable solar laser emission, even with large tracking error displacements of the focal spot.

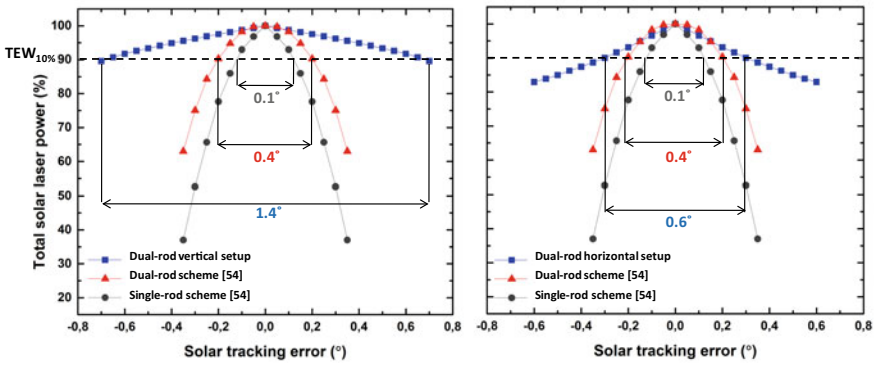

Fig. 8.23 Normalized solar laser output power from the vertical and horizontal setups with no Sun tracking, compared to the previous numerical results of the single-rod and the dual-rod side-pumping using a small aspherical lens as secondary concentrator [54]

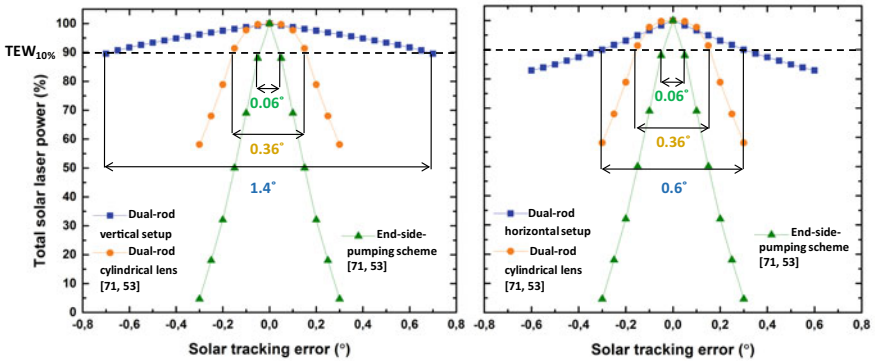

Fig. 8.24 Normalized solar laser output power with vertical and horizontal setups with no Sun tracking, compared to the previous numerical results of the solar laser approach using cylindrical lens as secondary concentrator [53], and that of the most efficient end-side-pumping solar laser [53, 71]

8.6 Example of Numerical Modeling of Solar-Pumped Lasers with Tracking Error Compensation Capacity

8.6.1 Zemax® and LASCAD™ Analysis of the Tracking Error Compensation Capacity Using Multi-Rod Configurations

In this section, it will be given an example, based on modeling in Zemax® and LASCAD™ software, of numerical tracking error compensation capacity using a multi-rod configuration with fused silica aspherical lens. Non-sequential ray-tracing

is performed in Zemax® to analyze both the absorption efficiencies and the absorbed pump distributions within the Nd:YAG laser rod, then this information is exported to LASCAD™ in order to analyze the solar laser output and its dependency on the solar tracking error generated.

First, the primary solar concentrator composed of heliostat-parabolic mirror combined need to be programmed. The heliostat tracks the Sun continuously and reflects the solar radiation to the primary parabolic mirror. The combined reflectivity of the two reflective mirrors can be assumed as 80%, and this combined heliostat-parabolic system will be modeled to investigate a variation on the solar pumping based on the variation of the Sun's position. The primary mirror has 1.3 m diameter, 60° rim angle, 655 mm focal distance and 1.33 m^2 collection area. The divergence of the solar rays between [30000, 40000] can be assumed for the circular source to simulate the incoming solar radiation in Zemax® ray-tracing software, depending of the diffusivity. Considering 950 W/m^2 terrestrial solar irradiation, the concentrated light spot at the focus of the primary mirror can reach 1264 W.

In order to carry out the solar tracking error study of this solar laser system, the altitude and azimuth variations from the optimally aligned solar laser system to a certain amount of time need to be defined. For this case, the equations given in the Sect. 8.1.1 can be used, choosing a specific day and time of measurement, so that the other variables can also be determined to have a real coordinate variation for the tracking error study of the solar laser system. Alternatively, a solar position computer software, or algorithm, for tracing the sun is available as open source codes on internet. As an example, it is presented a table with calculated values for a given day and time of measurement, from [55]. In this way determining the values to be introduced in the X and Y tilt variations of the light source on Zemax® software for the simulations. In Table 8.1 is given time of measurement, latitude, declination, hour angle, azimuth and altitude variations in the Sun's position along one minute for August 18.

The dual-rod solar-pumped laser can be studied as an example of multi-rod configuration, assembled with a large fused silica aspherical lens as a secondary concentrator. Figure 8.25 gives the key dimensions of the Zemax® simulation model to be numerically tested.

Using the Table 8.1 and the values for the tracking error and solar irradiation conditions, the dual-rod horizontal scheme can be tested for tracking error compensation

Table 8.1 Values used for the calculation of the variation in the Sun's position along one minute for August 18, for the two dual-rod configurations used in the experimental measurements in [55]

Variables	Values (°)	
	t_0	t_1
$\varphi(°)$	38	38
$\delta(°)$	12.83	12.83
$\omega(°)$	12.25	12.50
$\Delta h(°)$	0.03	
$\Delta\alpha(°)$	0.57	

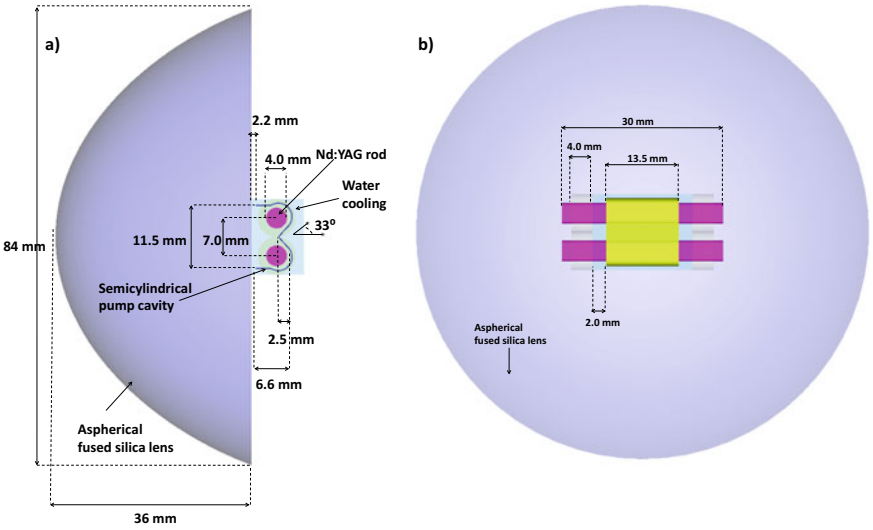

Fig. 8.25 **a** Front view of the solar laser head model of the Nd:YAG dual-rod side-pumping scheme and its key dimensions; **b** top view of the solar laser head

capacity, by inserting the calculated solar tracking errors at azimuth and altitude axis in the tilt about X and Y in the solar source of the Zemax® non-sequential component editor, respectively, simulating in this way a displacement on the solar pumping of the laser rods due to the displacement of the solar source in both axis. In the Fig. 8.26 is given the pump flux absorption distribution of the solar laser head model of the Nd:YAG dual-rod side-pumping scheme for the calculated solar tracking errors for August 18, around midday.

Alternatively, the vertical configuration can be also tested, by inserting the calculated solar tracking errors at azimuth and altitude axis in the tilt about Y and X in the solar source, respectively. In Fig. 8.26 is given the absorbed pump flux distribution along the longitudinal cross-sections of both the laser rods in Zemax® software, for the optimal alignment and two maximum displacements of the focal spot due to the solar tracking error in both altitude and azimuth directions, for the horizontal and vertical schemes. The larger tracking error in azimuth direction displaced the pump flux distribution along the rods for the horizontal scheme. In the case of the vertical scheme, the tracking error in azimuth direction displaced the pump flux distribution from the left/right rod to the right/left rod.

The laser resonant cavity analysis and optimization of the laser output power can be carried out using LASCAD™ software. Through the adoption of a symmetrical laser resonant cavity, the multimode solar laser output power can be efficiently extracted and analyzed. Different radius of curvature (RoC) and resonant cavity lengths can be studied for several rod diameters and lengths. The maximized numerical multimode solar laser output power for the dual-rod scheme was achieved with a 50 mm total length resonant cavity, being 10 mm as the separation lengths amongst

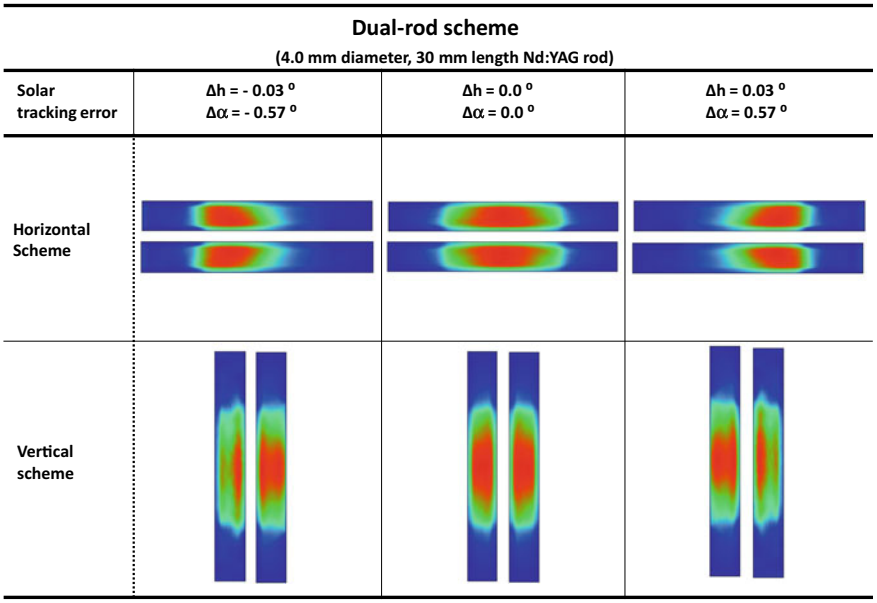

Fig. 8.26 Absorbed pump flux distribution along the longitudinal cross-sections of both the laser rods, for the optimal alignment ($\Delta h = 0.0^{\circ}$; $\Delta\alpha = 0.0^{\circ}$) and two maximum displacements ($\Delta h = 0.03^{\circ}$; $\Delta\alpha = 0.57^{\circ}$ and $\Delta h = -0.03^{\circ}$; $\Delta\alpha = -0.57^{\circ}$) of the focal spot due to the solar tracking error in both altitude and azimuth directions, for the horizontal and vertical schemes

the end-mirror and the output mirror to the end-faces of the laser rod, and RoC $= -$ 10 m for both mirrors, as shown in Fig. 8.27.

The solar laser output powers obtained for the tracking error study are presented in Table 8.2.

The Zemax® and LASCAD™ models presented in this section give numerical results which corresponds to the obtained experimental data from [55]. Other intermediate values of solar tracking error for that day can also be simulated, in this way

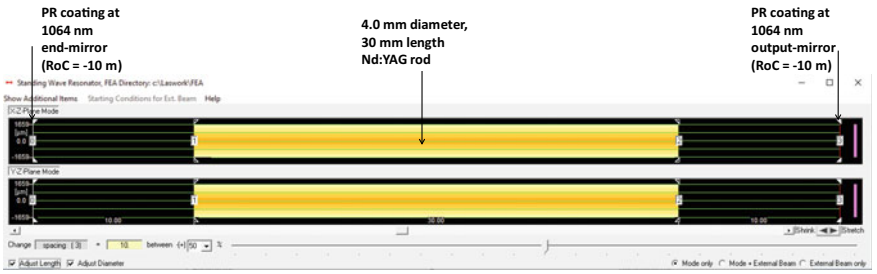

Fig. 8.27 Symmetric laser resonant cavity for the solar laser output power in LASCAD™ software: 10 mm was the separation lengths among the end-mirror and the output mirror to the end-faces of the laser rod. It is also indicated the RoC's used for the extraction of the solar laser

Table 8.2 Numerically calculated laser output power influenced by the calculated solar tracking errors for the dual-rod scheme in horizontal and vertical configurations

Solar tracking error (°)	Configurations					
	Dual-rod horizontal scheme			Dual-rod vertical scheme		
	Laser power (W)		Total power (W)	Laser power (W)		Total power (W)
	Nd:YAG Left rod	Nd:YAG Right rod		Nd:YAG Left rod	Nd:YAG Right rod	
$\Delta h = -0.03°$ $\Delta\alpha = -0.57°$	4.36	4.89	9.26	0.18	6.49	6.66
$\Delta h = 0.0°$ $\Delta\alpha = 0.0°$	6.91	6.92	13.83	6.91	6.92	13.83
$\Delta h = 0.03°$ $\Delta\alpha = 0.57°$	4.89	4.36	9.26	6.49	0.18	6.66

plotting a graph to determine the tracking error width at 10% for a given solar laser system for a specific day and time. Other experimental conditions for other days can also be simulated.

References

1. Kalogirou, S.: Solar Energy Engineering, vol. 1, 2nd edn. Academic Press, Massachusetts (2013)
2. Mousazadeh, H., Keyhani, A., Javadi, A., Mobli, H., Abrinia, K., Sharifi, A.: A review of principle and sun-tracking methods for maximizing solar systems output. Renew. Sustain. Energy Rev. **13**(8), 1800–1818 (2009). https://doi.org/10.1016/j.rser.2009.01.022
3. Hussein, M.T., Albarqouni, S.N.: Enhanced model of one axis-two positions manual tracking photovoltaic panels for lighting projects in Palestine. In: IASTED International Conference on Solar Energy 2010, pp. 15–17
4. Kreith, F., Kreider, J.F.: Principles of Solar Engineering (1978)
5. Duffie, J.A., Beckman, W.A.: Solar Engineering of Thermal Processes. Wiley, New York (1980)
6. Skouri, S., Ben Haj Ali, A., Bouadila, S., Ben Salah, M., Ben Nasrallah, S.: Design and construction of sun tracking systems for solar parabolic concentrator displacement. Renew Sustain Energy Rev **60**, 1419–1429 (2016). https://doi.org/10.1016/j.rser.2016.03.006
7. Poulek, V.: Testing the new solar tracker with shape memory alloy actors. In: Proceedings of 1994 IEEE 1st World Conference on Photovoltaic Energy Conversion-WCPEC (A Joint Conference of PVSC, PVSEC and PSEC), pp. 1131–1133. IEEE (1994)
8. Mwithiga, G., Kigo, S.N.: Performance of a solar dryer with limited sun tracking capability. J. Food Eng. **74**(2), 247–252 (2006). https://doi.org/10.1016/j.jfoodeng.2005.03.018
9. Nsengiyumva, W., Chen, S.G., Hu, L., Chen, X.: Recent advancements and challenges in solar tracking systems (STS): a review. Renew. Sustain. Energy Rev. **81**, 250–279 (2018). https://doi.org/10.1016/j.rser.2017.06.085
10. Agarwal, A.K.: Two axis tracking system for solar concentrators. (1992). https://doi.org/10.1016/0960-1481(92)90104-B
11. Abdallah, S., Nijmeh, S.: Two axes sun tracking system with PLC control. Energy Convers. Manage. **45**(11), 1931–1939 (2004). https://doi.org/10.1016/j.enconman.2003.10.007

12. Roth, P., Georgiev, A., Boudinov, H.: Design and construction of a system for sun-tracking. Renew. Energy **29**(3), 393–402 (2004). https://doi.org/10.1016/S0960-1481(03)00196-4
13. McCluney, R.: Passive optical solar tracking system. Appl. Opt. **22**(21), 3433–3439 (1983). https://doi.org/10.1364/AO.22.003433
14. Beshears, D.L., Capps, G.J., Earl, D.D., Jordan, J.K., Maxey, L.C., Muhs, J.D., Leonard, T.M.: Tracking Systems Evaluation for the Hybrid Lighting System. Paper presented at the ASME 2003 International Solar Energy Conference
15. Reda, I., Andreas, A.: Solar position algorithm for solar radiation applications. Sol. Energy **76**(5), 577–589 (2004). https://doi.org/10.1016/j.solener.2003.12.003
16. Baltas, P., Tortoreli, M., Russell, P.E.: Evaluation of power output for fixed and step tracking photovoltaic arrays. Sol. Energy **37**(2), 147–163 (1986). https://doi.org/10.1016/0038-092X(86)90072-1
17. Michaelides, I.M., Kalogirou, S.A., Chrysis, I., Roditis, G., Hadjiyianni, A., Kambezidis, H.D., Petrakis, M., Lykoudis, S., Adamopoulos, A.D.: Comparison of performance and cost effectiveness of solar water heaters at different collector tracking modes in Cyprus and Greece. Energy Convers. Manage. **40**(12), 1287–1303 (1999). https://doi.org/10.1016/S0196-8904(99)00020-5
18. Huang, B.J., Ding, W.L., Huang, Y.C.: Long-term field test of solar PV power generation using one-axis 3-position sun tracker. Sol. Energy **85**(9), 1935–1944 (2011). https://doi.org/10.1016/j.solener.2011.05.001
19. Chin, C.S., Babu, A., McBride, W.: Design, modeling and testing of a standalone single axis active solar tracker using MATLAB/Simulink. Renew. Energy **36**(11), 3075–3090 (2011). https://doi.org/10.1016/j.renene.2011.03.026
20. Kalogirou, S.A.: Design and construction of a one-axis sun-tracking system. Sol. Energy **57**(6), 465–469 (1996). https://doi.org/10.1016/S0038-092X(96)00135-1
21. Lazaroiu, G.C., Longo, M., Roscia, M., Pagano, M.: Comparative analysis of fixed and sun tracking low power PV systems considering energy consumption. Energy Convers. Manage. **92**, 143–148 (2015). https://doi.org/10.1016/j.enconman.2014.12.046
22. Yeh, P., Yeh, N.J.R.E.: Design and analysis of solar-tracking 2D Fresnel lens-based two staged, spectrum-splitting solar concentrators. **120**, 1–13 (2018).
23. Lv, H., Zheng, Y., Wang, J., Chen, B., Sheng, F., Cheng, C., Lv, Q.: Tracking control and output power optimization of a concentrator photovoltaic system with polar axis. Optik **127**(8), 3840–3843 (2016). https://doi.org/10.1016/j.ijleo.2016.01.092
24. Alexandru, C., Pozna, C.: Simulation of a dual-axis solar tracker for improving the performance of a photovoltaic panel. Proc. Inst. Mech. Eng., Part A: J. Power Energy **224**(6), 797–811 (2010). https://doi.org/10.1243/09576509JPE871
25. Liang, D., Almeida, J.: Highly efficient solar-pumped Nd:YAG laser. Opt. Express **19**(27), 26399–26405 (2011). https://doi.org/10.1364/oe.19.026399
26. Liang, D., Almeida, J.: Solar-pumped TEM_{00}-mode Nd:YAG laser. Opt. Express **21**(21), 25107–25112 (2013). https://doi.org/10.1364/oe.21.025107
27. Yabe, T., Bagheri, B., Ohkubo, T., Uchida, S., Yoshida, K., Funatsu, T., Oishi, T., Daito, K., Ishioka, M., Yasunaga, N., Sato, Y., Baasandash, C., Okamoto, Y., Yanagitani, K.: 100 W-class solar pumped laser for sustainable magnesium-hydrogen energy cycle. J. Appl. Phys. **104**(8), 083104 (2008). https://doi.org/10.1063/1.2998981
28. Missbach, T., Jaus, J.: New sensor for measuring tracking accuracy, tracker vibration, and structural deflection. AIP Conf. Proc. **1477**(1), 262–266 (2012). https://doi.org/10.1063/1.4753882
29. Yao, Y., Hu, Y., Gao, S., Yang, G., Du, J.: A multipurpose dual-axis solar tracker with two tracking strategies. Renew. Energy **72**, 88–98 (2014). https://doi.org/10.1016/j.renene.2014.07.002
30. Finster, C.J.S.: El heliostato de la Universidad santa maria. **119**, 5–20 (1962)
31. McFee, R.H.: Power collection reduction by mirror surface nonflatness and tracking error for a central receiver solar power system. Appl. Opt. **14**(7), 1493–1502 (1975). https://doi.org/10.1364/AO.14.001493

32. Semma, R.P., Imamura, M.S.: Sun tracking controller for multi-kW photovoltaic concentrator system. In, January 01, 1981 1981, p. 375
33. Badescu, V.: Influence of certain astronomical and constructive parameters on the concentration of solar radiation with plane heliostats fields. (1985)
34. Berenguel, M., Rubio, F.R., Valverde, A., Lara, P.J., Arahal, M.R., Camacho, E.F., López, M.: An artificial vision-based control system for automatic heliostat positioning offset correction in a central receiver solar power plant. Sol. Energy **76**(5), 563–575 (2004). https://doi.org/10.1016/j.solener.2003.12.006
35. Chen, Y.T., Lim, B.H., Lim, C.S.: General sun tracking formula for heliostats with arbitrarily oriented axes. J. Sol. Energy Eng. **128**(2), 245–250 (2005). https://doi.org/10.1115/1.2189868
36. Omar, A., Ismail, D., Muzamir, I., Mohd Rafi, A.: Simplification of sun tracking mode to gain high concentration solar energy. Am. J. Appl. Sci. **4**(3) (2007). https://doi.org/10.3844/ajassp.2007.171.175
37. Aiuchi, K., Yoshida, K., Onozaki, M., Katayama, Y., Nakamura, M., Nakamura, K.: Sensor-controlled heliostat with an equatorial mount. Sol. Energy **80**(9), 1089–1097 (2006). https://doi.org/10.1016/j.solener.2005.10.007
38. Sun, F., Wang, Z., Guo, M., Bai, F., Xu, Z.J.E.P.: Determination of tracking errors with respect to the geometrical errors based on optimization algorithm. Energy Procedia **49**, 2211–2220 (2014)
39. Pavlović, T.M., Radonjić, I.S., Milosavljević, D.D., Pantić, L.S.: A review of concentrating solar power plants in the world and their potential use in Serbia. Renew. Sustain. Energy Rev. **16**(6), 3891–3902 (2012). https://doi.org/10.1016/j.rser.2012.03.042
40. De Laquil, P., III, Kearney, D., Geyer, M., Diver, R.: Solar-thermal electric technology. Island Press, Washington, DC (United States), United States (1993)
41. Chemisana, D.: Building integrated concentrating photovoltaics: a review. Renew. Sustain. Energy Rev. **15**(1), 603–611 (2011). https://doi.org/10.1016/j.rser.2010.07.017
42. Aiuchi, K., Yoshida, K., Katayama, Y., Nakamura, M., Nakamura, K.: Sun tracking photo-sensor for solar thermal concentrating system
43. Rabl, A.: Active Solar Collectors and Their Applications, vol. 1. Oxford University Press, New York (1985)
44. Ibrahim, S.M.J.R.E.: The forced circulation performance of a sun tracking parabolic concentrator collector. **9**(1–4), 568–571 (1996)
45. Brunotte, M., Goetzberger, A., Blieske, U.: Two-stage concentrator permitting concentration factors up to 300x with one-axis tracking. Sol. Energy **56**(3), 285–300 (1996). https://doi.org/10.1016/0038-092X(95)00107-3
46. Grass, C., Schoelkopf, W., Staudacher, L., Hacker, Z.: Comparison of the optics of non-tracking and novel types of tracking solar thermal collectors for process heat applications up to 300 °C. Sol. Energy **76**(1), 207–215 (2004). https://doi.org/10.1016/j.solener.2003.07.031
47. Sun, J., Wang, R., Hong, H., Liu, Q.: An optimized tracking strategy for small-scale double-axis parabolic trough collector. Appl. Therm. Eng. 1408–1420 (2017). https://doi.org/10.1016/j.applthermaleng.2016.10.187
48. Ullah, F., Min, K.: Performance evaluation of dual-axis tracking system of parabolic trough solar collector. In: IOP Conference Series: Materials Science and Engineering 2018, vol. 1, p. 012166. IOP Publishing
49. Badescu, V.: Different tracking error distributions and their effects on the long-term performances of parabolic dish solar power systems. Int. J. Solar Energy **14**(4), 203–216 (1994). https://doi.org/10.1080/01425919408909811
50. Jamil, U., Ali, W.: Performance tests and efficiency analysis of solar invictus 53S—a parabolic dish solar collector for direct steam generation. In: AIP Conference Proceedings 2016, vol. 1, p. 070018. AIP Publishing LLC
51. Yan, J., Cheng, Z.-R., Peng, Y.-D.: Effect of tracking error of double-axis tracking device on the optical performance of solar dish concentrator. Int. J. Photoenergy **2018**, 9046127 (2018). https://doi.org/10.1155/2018/9046127

52. Natarajan, S.K., Thampi, V., Shaw, R., Kumar, V.S., Nandu, R., Jayan, V., Rajagopalan, N., Kandasamy, R.K.J.I.J.O.E.R.: Experimental analysis of a two-axis tracking system for solar parabolic dish collector. **43**(2), 1012–1018 (2019)
53. Tibúrcio, B.D., Liang, D., Almeida, J., Garcia, D., Vistas, C.R.: Dual-rod pumping approach for tracking error compensation in solar-pumped lasers. J. Photonics Energy **9**(02) (2019). https://doi.org/10.1117/1.Jpe.9.028001
54. Tibúrcio, B.D., Liang, D., Almeida, J., Garcia, D., Vistas, C.R., Morais, P.J.: Highly efficient side-pumped solar laser with enhanced tracking-error compensation capacity. Opt. Commun. **460**, 125156 (2020). https://doi.org/10.1016/j.optcom.2019.125156
55. Tibúrcio, B.D., Liang, D., Almeida, J., Garcia, D., Catela, M., Costa, H., Vistas, C.R.: Tracking error compensation capacity measurement of a dual-rod side-pumping solar laser. Renew. Energy **195**, 1253–1261 (2022). https://doi.org/10.1016/j.renene.2022.06.114
56. Xie, W.T., Dai, Y.J., Wang, R.Z., Sumathy, K.: Concentrated solar energy applications using Fresnel lenses: a review. Renew. Sustain. Energy Rev. **15**(6), 2588–2606 (2011). https://doi.org/10.1016/j.rser.2011.03.031
57. Al-Jumaily, K.E.J., Al-Kaysi, M.K.A.: The study of the performance and efficiency of flat linear Fresnel lens collector with sun tracking system in Iraq. Renew. Energy **14**(1), 41–48 (1998). https://doi.org/10.1016/S0960-1481(98)00045-7
58. James, L.W., Williams, J.K.: Fresnel optics for solar concentration on photovoltaic cells. In, 1978/01/1, pp. 673–679. (1978)
59. Hiramatsu, M., Miyazaki, Y., Egami, T., Akisawa, A., Mizuta, Y.: Development of non-imaging Fresnel lens and sun-tracking device. In: 3rd World Conference on Photovoltaic Energy Conversion, 2003. Proceedings of, 11–18 May 2003, vol. 2383, pp. 2383–2385 (2003)
60. Whitfield, G.R., Bentley, R.W., Weatherby, C.K., Hunt, A.C., Mohring, H.D., Klotz, F.H., Keuber, P., Miñano, J.C., Alarte-Garvi, E.: The development and testing of small concentrating PV systems. Sol. Energy **67**(1), 23–34 (1999). https://doi.org/10.1016/S0038-092X(00)00045-1
61. Huang, F., Li, L., Huang, W.: Optical performance of an azimuth tracking linear Fresnel solar concentrator. Sol. Energy **108**, 1–12 (2014). https://doi.org/10.1016/j.solener.2014.06.028
62. Wang, H., Huang, J., Song, M., Hu, Y., Wang, Y., Lu, Z.: Simulation and Experimental study on the optical performance of a fixed-focus fresnel lens solar concentrator using polar-axis tracking. Energies **11**(4) (2018). https://doi.org/10.3390/en11040887
63. Yabe, T., Ohkubo, T., Uchida, S., Yoshida, K., Nakatsuka, M., Funatsu, T., Mabuti, A., Oyama, A., Nakagawa, K., Oishi, T., Daito, K., Behgol, B., Nakayama, Y., Yoshida, M., Motokoshi, S., Sato, Y., Baasandash, C.: High-efficiency and economical solar-energy-pumped laser with Fresnel lens and chromium codoped laser medium.**90**(26), 261120 (2007). https://doi.org/10.1063/1.2753119
64. Yabe, T., Uchida, S., Ikuta, K., Yoshida, K., Baasandash, C., Mohamed, M.S., Sakurai, Y., Ogata, Y., Tuji, M., Mori, Y., Satoh, Y., Ohkubo, T., Murahara, M., Ikesue, A., Nakatsuka, M., Saiki, T., Motokoshi, S., Yamanaka, C.: Demonstrated fossil-fuel-free energy cycle using magnesium and laser. Appl. Phys. Lett. **89**(26), 261107 (2006). https://doi.org/10.1063/1.2423320
65. Perini, S., Tonnellier, X., King, P., Sansom, C.J.S.E.: Theoretical and experimental analysis of an innovative dual-axis tracking linear Fresnel lenses concentrated solar thermal collector **153**, 679–690 (2017)
66. Vasylyev, V.P., Tovmachenko, O.G., Vasylyev, S.V.: Expected optical performances of novel type multi-element high-heat solar concentrators. In: Proceedings ASES Conference (2002)
67. Tiburcio, B.D., Liang, D., Almeida, J., Matos, R., Vistas, C.R.: Improving solar-pumped laser efficiency by a ring-array concentrator. J. Photonics For. Energy **8**(1) (2018). https://doi.org/10.1117/1.Jpe.8.018002
68. Matos, R., Liang, D., Almeida, J., Tibúrcio, B.D., Vistas, C.R.: High-efficiency solar laser pumping by a modified ring-array concentrator. Opt. Commun. **420**, 6–13 (2018). https://doi.org/10.1016/j.optcom.2018.03.027

69. Garcia, D., Liang, D., Tibúrcio, B.D., Almeida, J., Vistas, C.R.: A three-dimensional ring-array concentrator solar furnace. Sol. Energy **193**, 915–928 (2019). https://doi.org/10.1016/j.solener.2019.10.016
70. Tibúrcio, B.D., Liang, D., Almeida, J., Garcia, D., Catela, M., Costa, H., Vistas, C.R.: Improving side-pumped solar lasers using ring-array concentrators. Int. J. Sustain. Energy 1–21 (2021). https://doi.org/10.1080/14786451.2021.1987435
71. Liang, D., Almeida, J., Vistas, C.R., Guillot, E.: Solar-pumped Nd:YAG laser with 31.5 W/m^2 multimode and 7.9 W/m^2 TEM$_{00}$-mode collection efficiencies. Solar Energy Mater. Solar Cells **159**, 435–439 (2017). https://doi.org/10.1016/j.solmat.2016.09.048
72. Geraldes, J.P., Liang, D.: An alternative solar pumping approach by a light guide assembly elliptical-cylindrical cavity. Sol. Energy Mater. Sol. Cells **92**(8), 836–843 (2008). https://doi.org/10.1016/j.solmat.2008.01.019
73. Mehellou, S., Liang, D., Almeida, J., Bouadjemine, R., Vistas, C.R., Guillot, E., Rehouma, F.: Stable solar-pumped TEM$_{00}$-mode 1064 nm laser emission by a monolithic fused silica twisted light guide. Sol. Energy **155**, 1059–1071 (2017). https://doi.org/10.1016/j.solener.2017.07.048
74. Bouadjemine, R., Liang, D., Almeida, J., Mehellou, S., Vistas, C.R., Kellou, A., Guillot, E.: Stable TEM00-mode Nd:YAG solar laser operation by a twisted fused silica light-guide. Opt. Laser Technol. **97**, 1–11 (2017). https://doi.org/10.1016/j.optlastec.2017.06.003